THÈSE

Pour l'obtention du grade de
DOCTEUR DE L'UNIVERSITÉ DE POITIERS
École nationale supérieure d'ingénieurs (Poitiers)
Pôle poitevin de recherche pour l'ingénieur en mécanique, matériaux et énergétique - PPRIMME (Poitiers)
(Diplôme National - Arrêté du 25 mai 2016)

École doctorale : Sciences et ingénierie en matériaux, mécanique, énergétique et aéronautique - SIMMEA (Poitiers)
Secteur de recherche : Sciences de l?ingénieur

Cotutelle : Université technique nationale de recherche du nom de A. N. Tupolev

Présentée par :
Nikolai Adiutantov

Développement d'une instrumentation et méthodologie par l'étude des bruits électrochimiques pour le diagnostic des stacks de pile à combustible de type PEMFC

Directeur(s) de Thèse :
Sergueï Martemianov, Yury Evdokimov

Soutenue le 19 décembre 2017 devant le jury

Jury :

Président	**Mikhail A. Vorotynsev**	Professor, Mendeleev Chemical Technology University, Moscow
Rapporteur	**Sergey A. Grigoriev**	Professeur, MPEI, Moscou
Rapporteur	**Gael Maranzana**	Professeur, LEMTA, Université de Lorraine
Membre	**Sergueï Martemianov**	Professeur, IC2MP, ENSIP, Université de Poitiers
Membre	**Yury Evdokimov**	Professor, KNRTU-KAI, Kazan, Russia
Membre	**Anthony Thomas**	Maître de conférences, PPRIME, ENSIP, Université de Poitiers
Membre	**Lingai Luo**	Directeur de recherche CNRS, Université de Nantes
Membre	**Evgenii Denisov**	Associate professor, KNRTU-KAI, Kazan, Russia

Pour citer cette thèse :

Nikolai Adiutantov. *Développement d'une instrumentation et méthodologie par l'étude des bruits électrochimiques pour le diagnostic des stacks de pile à combustible de type PEMFC* [En ligne]. Thèse Sciences de l?ingénieur. Poitiers : Université de Poitiers, 2017. Disponible sur Internet <http://theses.univ-poitiers.fr>

Université de Poitiers
Kazan National Research Technical University named after A. N. Tupolev-KAI

Doctoral School **SIMMEA**

University Department **Institut Pprime**

Thesis defended by **Nikolai Adiutantov**

Defended on **19th December, 2017**

In order to become Doctor from Université de Poitiers and from Kazan National Research Technical University named after A. N. Tupolev-KAI

Academic Field **Engineering**

Speciality **Energetic**

Thesis Title

Development of instrumentation and methodology for noise diagnostic of PEMFC stacks

Thesis supervised by	Serguei Martemianov	Supervisor
	Yury Evdokimov	Co-Supervisor

Committee members

Referees	Sergey Grigoriev	Professor at MPEI (Moscow)
	Gaël Maranzana	Professor at University of Lorraine
Examiners	Lingai Luo	Professor at University of Nantes
	Anthony Thomas	Assistant Professor at University of Poitiers
	Evgenii Denisov	Associate Professor at KNRTU-KAI
	Mikhail Vorotyntsev	Professor at Mendeleev University of Chemical Technology (Moscow)
Supervisors	Serguei Martemianov	Professor at University of Poitiers
	Yury Evdokimov	Professor at KNRTU-KAI

Université de Poitiers
Kazan National Research Technical University named after A. N. Tupolev-KAI

Doctoral School **SIMMEA**

University Department **Institut Pprime**

Thesis defended by **Nikolai Adiutantov**

Defended on **19th December, 2017**

In order to become Doctor from Université de Poitiers and from Kazan National Research Technical University named after A. N. Tupolev-KAI

Academic Field **Engineering**

Speciality **Energetic**

Thesis Title

Development of instrumentation and methodology for noise diagnostic of PEMFC stacks

Thesis supervised by	Serguei Martemianov	Supervisor
	Yury Evdokimov	Co-Supervisor

Committee members

Referees	Sergey Grigoriev	Professor at MPEI (Moscow)
	Gaël Maranzana	Professor at University of Lorraine
Examiners	Lingai Luo	Professor at University of Nantes
	Anthony Thomas	Assistant Professor at University of Poitiers
	Evgenii Denisov	Associate Professor at KNRTU-KAI
	Mikhail Vorotyntsev	Professor at Mendeleev University of Chemical Technology (Moscow)
Supervisors	Serguei Martemianov	Professor at University of Poitiers
	Yury Evdokimov	Professor at KNRTU-KAI

Université de Poitiers
Kazan National Research Technical University named after A. N. Tupolev-KAI

École doctorale **SIMMEA**
Unité de recherche **Institut Pprime**

Thèse présentée par **Nikolai Adiutantov**
Soutenue le **19 décembre 2017**

En vue de l'obtention du grade de docteur de l'Université de Poitiers et de l'Kazan National Research Technical University named after A. N. Tupolev-KAI

Discipline **Sciences de l'ingénieur**
Spécialité **Énergétique**

Titre de la thèse

Développement d'une instrumentation et méthodologie par l'étude des bruits électrochimiques pour le diagnostic des stacks de pile à combustible de type PEMFC

Thèse dirigée par	Serguei Martemianov	directeur
	Yury Evdokimov	co-directeur

Composition du jury

Rapporteurs	Sergey Grigoriev	professeur au MPEI (Moscow)
	Gaël Maranzana	professeur à l'University of Lorraine
Examinateurs	Lingai Luo	professeure à l'University of Nantes
	Anthony Thomas	Assistant Professor à l'University of Poitiers
	Evgenii Denisov	Associate Professor au KNRTU-KAI
	Mikhail Vorotyntsev	professeur au Mendeleev University of Chemical Technology (Moscow)
Directeurs de thèse	Serguei Martemianov	professeur à l'University of Poitiers
	Yury Evdokimov	professeur au KNRTU-KAI

The Université de Poitiers and the Kazan National Research Technical University named after A. N. Tupolev-KAI neither endorse nor censure authors' opinions expressed in the theses: these opinions must be considered to be those of their authors.

Keywords: electrochemical noise, instrumentation, methodology, statistical descriptors, diagnostic, prognostic, fuel cell, pemfc stack

Mots clés : bruit électrochimique, instrumentation, méthodologie, descripteurs statistiques, diagnostic, pronostic, pile à combustible, stack pemfc

This thesis has been prepared at

Institut Pprime
SP2MI - Téléport 2
11 boulevard Marie et Pierre Curie
BP 30179 F86962 Futuroscope Chasseneuil Cedex
France

☎ (33)(0)5 49 49 74 16
(33)(0)5 49 49 74 18
secretariat.direction@cnrs.pprime.fr
Web Site http://www.pprime.fr/

To my family and beloved Christina without whom it would not be possible to complete this work

Remerciements

This book is the result of a doctoral thesis performed in the frame of cooperation agreement between University of Poitiers(France) and Kazan National Research Technical University named after A.N. Tupolev-KAI (KNRTU-KAI, Russia). This work has been supported by the ANR project PROPICE (ANR-12-PRGE-0001) funded by the French National Research Agency.

I would, first of all, like to thank my two thesis supervisors Serguei MARTEMIANOV and Yury EVDOKIMOV for helping me, directed, and enriched throughout the thesis work. Serguei for his good humor, support and for assistance at all stages of the thesis. Yury for his scientific ideas and his talents as an experimentalist. A big thanks to all the team from FCLAB Laboratory and especially to Elodie PAHON for her help in Belfort. As well as a huge thanks to Anthony THOMAS for his active participation in the discussion of the experimental results and help in writing the thesis. The author also thanks his parents for their help and support. And special thanks to my beloved Christina for her support and love.

Development of instrumentation and methodology for noise diagnostic of PEMFC stacks

Abstract

Fuel cell technology development requires adequate diagnostic tools, in particular for monitoring the state of health of industrial systems (stacks) under operating conditions. Traditional diagnostic tools require to stop or disrupt the system operating. This thesis aims at the development of an innovative and non-intrusive approach for the diagnostic of PEM (Proton Exchange Membrane) fuel cell stacks. The methodology is based on the measurement of small electrical fluctuations (electrochemical noise). To measure this noise, a high frequency signal acquisition system was used without prior analog filter. These measurements were obtained within the ANR project « Propice » using four measurement campaigns with the collaboration of FCLAB and CEA LITEN. Electrochemical noise Measurements, over several weeks, made it possible to build a rich database. To process these data, different statistical approaches in time, frequency and tempo-frequency domains have been used for the generation of reliable and robust descriptors. It has been shown that the measurement of noise makes it possible to obtain a rich signature of the PEM stacks in a wide frequency range. This signature reflects the various physico-chemical phenomena and it is very sensitive to the operating parameters of the system. The evolution of this signature in short time analysis can be used for an in-situ diagnostic of the state of health of commercial stacks under real operating conditions and for the development of prognostic strategies.

Keywords: electrochemical noise, instrumentation, methodology, statistical descriptors, diagnostic, prognostic, fuel cell, pemfc stack

Développement d'une instrumentation et méthodologie par l'étude des bruits électrochimiques pour le diagnostic des stacks de pile à combustible de type PEMFC

Résumé

Le développement de la technologie « piles à combustible » nécessite l'utilisation d'outils de diagnostic adéquats notamment pour le monitoring de l'état de santé des systèmes industriels (stacks) dans les conditions réelles de fonctionnement. L'utilisation des moyens traditionnels de diagnostic nécessite l'arrêt ou la perturbation du fonctionnement du système. Le travail de cette thèse vise le développement d'une approche innovante non intrusive pour le diagnostic des stacks PEM (Proton Exchange Membrane), basée sur la mesure des petites fluctuations électriques (bruits électrochimiques). Pour mesurer les bruits, un système d'acquisition des faibles signaux à haute fréquence a été utilisé sans filtrage analogique préalable. Ces mesures ont été dans le cadre du projet ANR « Propice » pour quatre campagnes de mesures avec la collaboration du FCLAB et du CEA LITEN. Les mesures des bruits électrochimiques, sur plusieurs semaines, ont permis de construire une base de données extrêmement riche. Pour traiter ces données, différents approches statistiques dans le domaine temporel, fréquentiel et tempo-fréquentiel ont été utilisés pour la génération de descripteurs fiables et robustes. Il a été démontré que la mesure des bruits permet d'obtenir une riche signature des stacks PEM dans un vaste domaine fréquentiel. Cette signature reflète les différents phénomènes physico-chimiques et est très sensible aux paramètres de fonctionnement du système. L'évolution de cette signature au court de temps peut être utilisée pour le diagnostic in-situ de d'état de santé des stacks commerciaux dans les conditions réelles de fonctionnement et pour le développement des moyens de pronostic.

Mots clés : bruit électrochimique, instrumentation, méthodologie, descripteurs statistiques, diagnostic, pronostic, pile à combustible, stack pemfc

Institut Pprime
SP2MI - Téléport 2 – 11 boulevard Marie et Pierre Curie – BP 30179 F86962 Futuroscope Chasseneuil Cedex – France

Contents

List of Tables

List of Figures

Introduction

In a background where the energy demand, based essentially on fossil energy, is irreparably increasing and that an environmental crisis is likely to upset our habits, a new energy mix must be imagined. Indeed, today global energy management is embedded in a sustainable development strategy that includes, beyond the ecological aspect, social and economic aspects. This is why over the past ten years, many alternatives have been developed to overcome this possible energy shortage, particularly through the use of renewable energies such as wind, hydro, or solar. However, the unique use of renewable energies does not make it possible today to meet global energy demand due to their low efficiency and variabilities. So, new forms of energy production are developed, in particular fuel cells associated with the hydrogen vector.

Indeed, Fuel Cell (FC) technology obtains high potential to become one of main bases for power sources because of many reasons such as environmentally friendly behavior, high efficiency, and silent operation due to absence of moving parts. One of the most perspective systems in this area is the Proton Exchange Membrane Fuel Cells (PEMFC). Proton Exchange Membrane Fuel Cells (PEMFC) are a promising technology for converting chemical energy into electrical energy and heat for movable applications (transportation, portable electronics) and stationary applications (auxiliary generator, conversion / storage energy). Despite the undeniable progress made in recent decades, some technological impediments need to be overcome to enable an economical feasible development. Among the various aspects currently studied, we can mention needs to provide manufacturing reduction costs, to increase the reliability and the lifetime of the fuel cell systems as well as to develop the implementation of diagnostic and prognostic reliable tools.

This thesis work is therefore part of this issue and concerns more particularly the development of instrumentation and methodology for noise diagnostic of PEMFC stacks. Fuel cell technology development requires adequate diagnostic tools, in particular for monitoring the state of health of industrial systems (stacks) under operating conditions. This thesis aims at the development of an innovative and non-intrusive approach for the diagnostic of PEM (Proton Exchange Membrane) fuel cell stacks. The methodology is based on the measurement of small electrical fluctuations (electrochemical noise). To measure this noise, a high frequency signal acquisition system was used without prior analog filter. Fundamental aspect is to understand through the use of noise analysis the internal physical phenomena taking place within the stack, as similar to the electrochemical impedance but with the advantage of electrochemical noise to be non-intrusive (no disturbance of the system with an exciter signal).

These measurements were obtained within the ANR project «PROPICE» using four measurement campaigns with the collaboration of FCLAB, EIFER and CEA LITEN. Three of these campaigns are based on microcogeneration profile and the fourth is based on automobile profile. Electrochemical noise measurements, over several weeks (1000h) for each campaign, made it possible to build a rich database. Surely, difficulties of storage (big data) and long-time analysis is met and overcome in this work.

To process these data, different statistical approaches in time, frequency and tempo-frequency domains have been used for the generation of reliable and robust descriptors. It has been shown that the measurement of noise makes it possible to obtain a rich signature of the PEM stacks in a wide frequency range. This signature reflects the various physico-chemical phenomena and it is very sensitive to the operating parameters of the system. The evolution of this signature in short time analysis can be used for an in-situ diagnostic of the state of health of commercial stacks under real operating conditions and for the development of prognostic strategies.

This manuscript is divided into six chapters. Chapter 1 introduces the state of art of fuel cell technologies. Chapter 2 highlights principle, limitations and diagnostic of the PEMFC. This chapter focus on the methods that allow the diagnostic of PEMFC technology. Chapter 3 is dedicated to the electrochemical noise analysis and its application on the diagnostic of fuel cells. This chapter is based on the presentation of different signals methodology and particularly about the detrending and the mathematical methods for the statistical descriptors generation is explained. In the chapter 4 the statistical descriptors generated during experiments provided under the ANR project "PROPICE" are presented in time and frequency domains. These descriptors and their evolutions are shown for the four campaign and provided different signatures for each analysis, in time domain and frequency domain and for each campaign. Chapter 5 is focus on the utilization of time-frequency methods to generate statistical descriptors in both domains at the same time. This application of time-frequency analysis gives some signature as painting of the fuel cell stacks for the four campaign of the project. In chapter 6, the crossing of all methods and all results is done. This aim of this chapter is give some conclusions about the statistical descriptors and signatures in time, frequency and time-frequency domain. The comparison of signatures generated by statistical descriptors between operating points of the four campaign highlights the power of electrochemical noise analysis to provide very interesting and remarkable signs of the physics phenomena within a PEMFC stack, essential elements for its proper diagnostic and its future prognostic. Finally, a general conclusion summarizes the work carried out during this thesis and suggests perspectives for future works.

Chapter 1

Fuel Cell Technologies: state of art

Contents

Figures

1.1 State of art of energy in the world

Coal was the first of fossil fuels used by humans. As long as coal was a low-cost primary energy source in the beginning of the 18th century, there was a heavy growth of using this type of fossil fuel that led to the industrial revolution, which, in turn, contributed to the development and modernization of the coal industry. This transitional revolution from manual labour to production by machine got its completion after the creation and democratization of engines. Integrated to steam engines, coal provided energy in mines, industries, and allowed the development of new transportation. The development of new machines involve scientists to face the issues and created a ne science - the technical thermodynamics, that in the sequel led to the creation of piston engine involving internal-combustion engines developments. In the early 20th century, the internal combustion engine replaced the steam engines, that remains the only engine used during the 19th century. Thereby, car coal was replaced by oil, with many advantages such as lightness, simplicity of storage and transportation. Thanks to these characteristics, oil was the main energy source in the last decades of the 20th century, that was used in all scope of activity. However, today energy consumption is increased due to rapid growth of population and the scale of socio-economic progress. Thereby, due to limited quantities of non-renewable resources, there is a new issue to resolve: research of new energy resources that would satisfy all energy requirements. In the past years, there were a lot of researches in the field of developing and implementing new energy sources such as power of sun, wind, water, etc. However, these solutions need to be implement at a large scale to resolve problem of consumption. Nowadays, industries are not ready to replace oil by renewable energy resources due to the high cost of new developed systems and insufficient operational characteristics. Nevertheless, the problem of replacement of traditional fossil fuels and development of clean energy consumption becomes very important for the society.

1.1.1 Power energy sources and energy consumed

The influence of energy sources is important in all areas of our activity that scarcity of fossil fuels affect our daily lives. There are several types of energy sources that can be separated in three subdivisions that are presented in the Fig. 1.1. One of these important subdivisions is the energy from fossil fuels which was stocked and formed during millions years by nature and cannot be restored during the human's time scales. Among these are oil, natural gas and coal. Energy was principally produced by these fossil resources that are depleted. These circumstances pushed the world community to develop new systems using renewable resources or secondary power sources. Renewable resources and energy vectors can become promising in near future to replace current energy carriers (coal, oil and gas). Solar, wind, biomass and hydraulic energies are renewable resources that are inexhaustible by definition. Energy vectors are power sources which do not exist in natural state. They occur from transformation of available primary energy to form energy suitable for storage, transportation and final consumption. Examples of sustainable vectors are hydrogen, ethanol, formic acid, ammonia. Hydrogen is a leader among advanced energy vectors.

The general consumption of energy in the world has increased to 97.5 quadrillion Btu and will continue to increase to the 105 quadrillion Btu[1] in accordance with preliminary data (Fig. 1.2) from Annual Energy Outlook 2015[1]. This increase is a little bit lower than 10 percent and the main part is an higher consumption of natural gas and renewable energy. All these data depend on rate of economic growth, which leads to variations in estimation of energy consumption in the area of all fuels. Today, China and India are the main engine of economic growth in the world. Indeed, the main factors of increasing energy consumption are the growth of the world

[1] A BTU is the energy amount that is needed to heat one pound of water on one degree Fahrenheit.

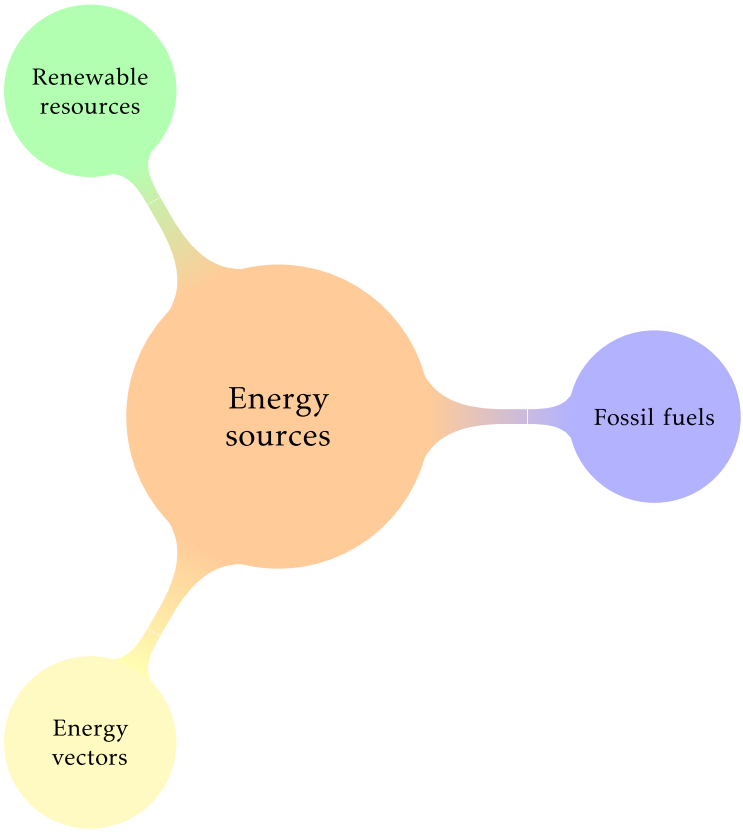

Figure 1.1 – Types of energy sources

population and the strong development of new economics, that's why China and India account for the majority of the energy consumption.

Quantity of global reserves, consumption and production of primary sources are presented in Table 1.1 that are reported by World Energy Council[2].It is estimated that global explored reserves of oil are enough for mankind for the next 56 years, gas for the next 55 years, coal for next 100 years, preliminarily. This information accentuates the importance of requirements aimed at energy saving and efficiency. In addition, we need to remember that growth of consumption involves numerous environmental and climatic problems.

1.1.2 Problems related with energy consumption and CO_2 emissions

World energy demanding for fossil fuels is a key factor in the upward trend of global CO_2 emissions affecting the environment. According to information from Intergovernmental Panel on Climate Change, one of the scenarios implies increasing environment temperature on 2 degrees in 2100 relative to pre-industrial levels, which is a critical threshold in climate change[3].

The emissions of carbon dioxide depend not only of the intensities of energy consumption, but also from the energy intensity of economic output and the level of economic output. Actual economic system is based on intense competition motivating to expand production and to accumulate capital by larger scales increasing. In this system, any decline of energy intensity tends to make energy products cheaper, thereby to encourage people to consume more energy

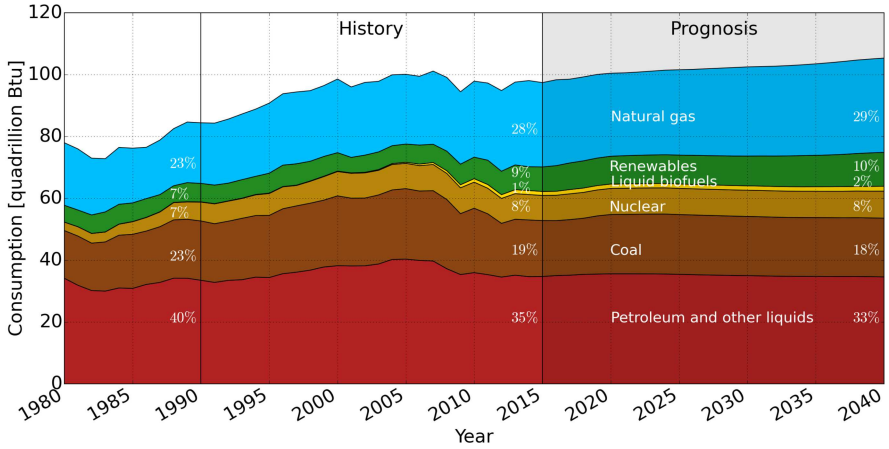

Figure 1.2 – Consumption evolution until 2040[1]

Primary source	Annual Production	Annual Consumption	Global reserves
Coal	7520 [Mt]	7513.8 [Mt]	891530 [Mt]
Oil	3973 [Mt]	4153.5 [Mt]	223454 [Mt]
Gas	3518 [bcm]	3375 [bcm]	209741 [bcm]

Table 1.1 – Global reserves, consumption and production of the main primary source (bcm -billion cubic metres, Mt - million tonnes)[1]

at long term. Thus, falling energy intensity (or rising energy efficiency) is simply translated into a higher capital accumulation (economic growth) and rarely leads to absolute declines in energy consumption. International Energy Agency registered zero growth in global carbon emissions in 2014. It had been invariable for the first time in 40 years, even though economic growth was at 3 percent[4], that behavior was achieved by using clean energy. In 2005, many industrialized countries had ratified the Kyoto protocol, requiring the reducing or limiting greenhouse emissions gases by 5 percent from 1990 to 2012. Among all countries, who ratified the Kyoto protocol, only Russia substantially reduced emissions since 1990 due to collapse of the Soviet Union in 1992. Russia's emissions fell by one-third from 1990 to 2005, with an annual rate of reduction of 2.7 percent[5]. The European Union is currently committed to a reduction of emissions by 20 percent (from the 1990 levels) by 2020. Therefore, there is an important issue which main goal is to develop new eco-friendly energy resources that could replace fossil energies and could be generated from sources that cannot be depleted as renewable energy sources.

1.1.3 Alternative energy with Energy Returned On Invested(EROI)

Nowadays, different power systems are used, but nuclear, hydro, coal, and natural gas power systems are on one order of magnitude more effective than photovoltaic (solar energy) and wind power. This is due to the energy efficiency of solar cells that is not sufficiently and wind energy

remains limited to the regions where winds are strong and constant.

The "Energy returned on invested" (EROI) is the most important parameter that describes the overall life-cycle efficiency of a power supply technique, independent from temporary economical fluctuations or politically motivated influence(Fig.1.3). Meaning of EROI is quantity of obtained useful energy for a certain effort to make this energy available[6].

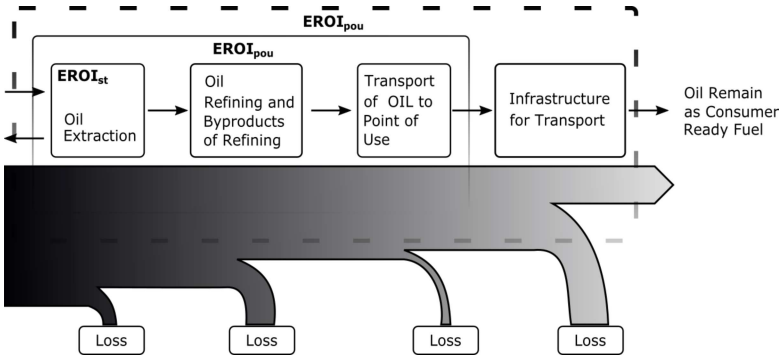

Figure 1.3 – Boundaries of various types of EROI analyses (standard EROI ($EROI_{st}$), EROI at the point of use ($EROI_{pou}$) and extended EROI ($EROI_{ext}$)) and energy loss associated with the processing of oil as it is transformed from "oil at the well-head" to consumer ready fuels

1.2 Hydrogen vector

Hydrogen is a clean and promising energy vector that respect (if it is produced by renewable energy) the environment expressed by low environmental impact, and by effective means of storing energy thanks to high specific heat of combustion that is near 120 MJ/kg. Therefore, level of attention in the world of science applying hydrogen vector during the last twenty years has increased due to the way of the most effective application of available power sources. In spite of these advantages, there are disadvantages. Hydrogen does not exist above on the Earth. This always combine to other molecules (CH_4, H_2O), CnH_2n,...) that leads to loss a part of energy to produce it. In addition, some problems remains with its delivery and storage that are very considerable coercing to build appropriate infrastructure. Therefore, hydrogen like some other commercial product goes through several levels between production and consumption. In the beginning, it must be packaged by compression and/or liquefaction, after transported by different ways and stored in a tank waiting to be transferred to the consumer for its using.

1.2.1 Production of Hydrogen

Global warming forces us to switch to alternative energy sources. Thereby, transition to the using of hydrogen allows to reduce the use of fossil fuel and the concentration of carbon dioxide. Hydrogen can be obtained from many sources as water and electricity, biomass, natural gas, etc. However, its production requires difficult ways. Nowadays, there are four main ways to produce hydrogen, reliant on cost and inquiry requirements. The main methods of hydrogen production are reminded in Fig.1.4.

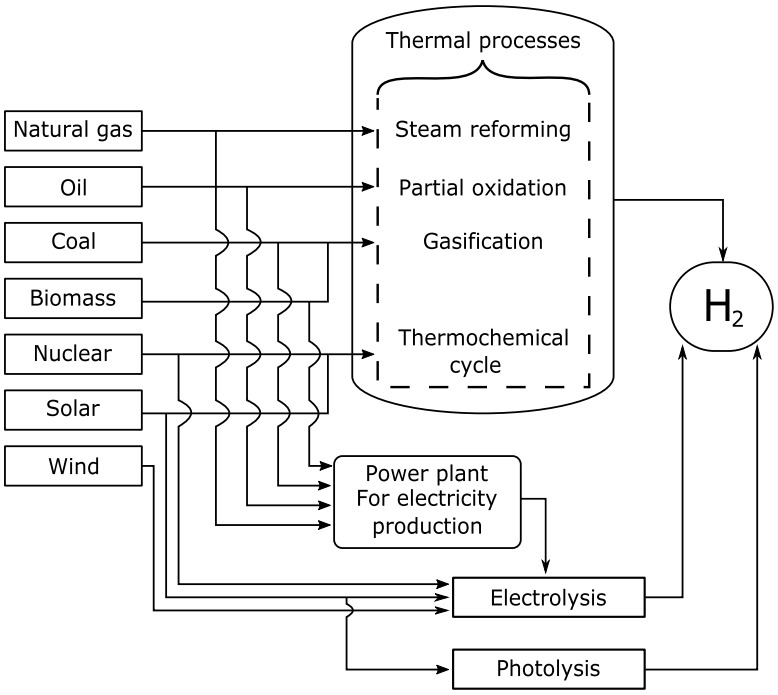

Figure 1.4 – Flowsheet of the main hydrogen production technologies [7]

They can be classified as: (i) thermal, (ii) electrolytic or (iii) photolytic processes.
At the moment, the most popular way for hydrogen production is method based on the use of depleted fossil fuels (conversion natural gas, methanol, diesel fuel, gasoline, etc.), that is not efficient in a long term point of view. Another way to obtain H_2 consists to produce hydrogen by water electrolysis or water decomposition, using water-reacting metals. Nowadays, this method remains marginal due to the cost of electrolysis compared to hydrogen production by reforming natural gas. In addition, hydrogen can be obtained from another promising source - biomass, but to replace of traditional methods some barriers have to be resolved, such as: seasonality, energy losses for drainage water, large-scale production, costs for fertilizers, harvest, transportation and storage.

These advantages and disadvantages, highlights the difficulties to find the replacement of fossil fuels. Everything depends on the cost and efficiency. It is possible that such marginal method as, for example, water electrolysis combined with renewable energy resources may replace the traditional method of hydrogen production.

1.2.2 Storage, delivery, distribution and use of hydrogen

Hydrogen can be stored in various forms as a gas under high-pressure, liquid, fixation of hydrogen molecules hydride metals for example. Hydrogen is the lightest of all gases and if hydrogen is loaded in a tank, he tries to leave it and passes through the metals, rubber, plastic and even glass. Thereby it is required complex additional efforts to prevent leaks. The fill of hydrogen tanks is quick and easy process depending on the required pressure. Fuel cell using hydrogen provides autonomy, and a vehicle equipped with them can be recharged in a short

time period. This makes hydrogen as an effective solution for energy storage. However, there is a barrier to use hydrogen in social life. Hydrogen has the lowest ignition point, which is 20 times lower than gasoline that can provoke explosion, which is unsafe. To a compact point of view, eight liters of hydrogen with pressure of 400 atmospheres are equivalent to one liter petrol[8]. To reduce the volume, it is necessary to use high pressure.

Compression of hydrogen is a multistage complex process, on which spending 15 % of the energy containing in hydrogen. Thereby, use of trucks for transportation of gaseous hydrogen near atmospheric pressure is inefficient, because it suffices only for several dozen cars. Moreover, usage of trucks with gas form are not efficient, because to deliver fuel with distance in 250 km requires at least 20 % of its energy. In comparison truck with gasoline, it sufficient to fill 800 cars[8]. Other alternative - pipelines. However, it is necessary to have huge funds to construct infrastructure . Earlier built pipelines cannot be used for pumping hydrogen because they are made of metal which are too fragile for hydrogen, and because of its fragility they can provoke leakage. The most important parameter of the accumulator or fuel tank is the power content, i.e. how much energy contains in 1 kg of weight or 1 l of volume. Liquid hydrogen has less energy density by volume than hydrocarbon fuels, such as gasoline by approximately a factor of four. Thereby, nowadays internal combustion engines are still most popular.

In addition, it is known that reduction of the vehicle weight increases the economy of fuel consumption. Thereby, it is necessary to take into account the tank. When you compress more hydrogen to reach high pressure, you need to use tanks with sufficient thickness to eliminate problem of security and leakage. This impact the weight and cost. For example, modern hydrogen car can pass preliminary 100 km with 1 kg of hydrogen. Volume of tank allows to contain 3 kg of compressed gas, which is enough for 300 km of trip with 400kg of tank weight. In comparison with standard 50 liters of fuel tank in car that is sufficient at least 600 km of a way with full tank, which weight without fuel is near 10 kg. The main way to transport the hydrogen from production places to places of usage consists to use liquid hydrogen circulating through the pipelines. There are about 1500 km of built pipelines in Europe and about 900 km in North America. Usage of liquid hydrogen increases the amount of energy of hydrogen in a smaller volume, but creation of this state includes inevitable losses, which are about 30-40 %. The liquefaction process also requires advanced security and a very low temperature - 20K. For applying liquid hydrogen in vehicles it's necessary to have complex heavy cryogenic system that also adds significant weight of insulation for already heavy tank.

The third method of hydrogen storage is the fixation of hydrogen molecules in hydride metals. Under the influence of pressure and/or temperature hydrogen molecules can be adsorbed in the hydride, thereby eliminating the problem in security.

Difficulties of gas storage and its transportation do not allow to use hydrogen widely, however, nowadays, hydrogen is exclusively being used as industrial gas for production of ammonia, purification of oil products and production of methanol.

1.3 Fuel cell technology

1.3.1 Brief history

As mentioned above, hydrogen is an energy rich molecule, and despite of the fact that there are still problems of production, storage and distribution, hydrogen vector remains a promising alternative energy source. From a technologic point of view, a fuel cell converts energy of hydrogen directly into electricity by means of electrochemical reaction producing chemical

water and heat (reverse electrolysis process). Electrochemical reaction is presented by Eq.1.1:

$$2H_2(\text{gas}) + O_2(\text{gas}) \longrightarrow 2H_2O + \text{electricity} + \text{heat} \tag{1.1}$$

Schönbein and Grove, who became friends through their exchange of experiences, systematically researched what we nowadays refer to as fuel cells. At that time, they were still called gas batteries. In 1838 Christian Friedrich Schönbein observed the fuel cell principle inverse electrolysis process shortly before William Grove constructed his gaseous voltaic battery in 1839 based on Schönbein's ideas [9]. Thus, Christian Friedrich Schoenbein is link to the discoverer of the fuel cell principle and William Robert Grove as the fuel cell inventor. Francis T. Bacon started working on practical fuel cells in 1930s and he successfully developed a 5 kW stationary fuel cell by the end of the 1950s. However, the first big step in fuel cell technology happened in the end of 1950s and the beginning of 1960s. The first practical applications of fuel cell has in the field of astronautics. Fuel cells with various designs were used on the American spacecraft Gemini, Apollo and Shuttle, and created in Soviet reusable space Shuttle "Buran". The depletion of fossil fuels caused interest in fuel cells for commercial purposes, and that's why several companies and institutions started to intensify their effort into further researches. The result of this effort is the creation of new membranes from Nafion®for polymer electrolyte membrane (PEM) fuel cell that allow using fuel cell technology not only for space program, but also for terrestrial applications. First - fuel cell-powered buses was build by Ballard Power Systems and first passenger car running on PEM fuel cells is due to Energy Partners development in 1993. In spite of the low prices for oil, this tendency will not be continued for a long time (due to limited fossil fuels) and in the future this situation will provoke a sharp rise in energy prices. Thereby, this marginal method of using hydrogen energy could become one of the remaining reliable method to replace traditional energy resources.

The development of fuel cells is being carried out in all countries, in particular in Russia and in France. Nowadays, Russia is the most promising and profitable market for the introduction of fuel cell technologies because Russia has an unrivaled base of energy and natural resources, a professional scientific and research experience gained over several decades. At present time activity in PEM development in France is significantly increased that is conformed by introducing by developing experimental train of Coradia iLint based on fuel cells in 2016.

1.3.2 Types of fuel cells

There are several types of fuel cell, which can be distinguished to six main fuel cell types that are classified by the nature of the electrolyte:

1. Alkaline Fuel Cells (AFC);
2. Phosphoric Acid Fuel Cells (PAFC);
3. Molten Carbonate Fuel Cells (MCFC);
4. Solid Oxide Fuel Cells (SOFC);
5. Direct Methanol Fuel Cells (DMFC);
6. Polymer Electrolyte Membrane Fuel Cells (PEMFC);

Brief comparative information is presented in the Table 1.2. These fuel cells differ in their electrolyte and the nature of the exchanged ions, as well as in their architecture, operating conditions and fields of applications[9]. More detailed information about each of them briefly indicated in the next section.

Table 1.2 – Main characteristics of the six fuel cell types[9]

Type of FC	AFC	PEMFC	DMFC	PAFC	MCFC	SOFC
Name	Alkaline Fuel Cell	Polymer Exchange Membrane Fuel Cell	Direct Methanol Fuel Cell	Phosphoric Acid Fuel Cell	Molten Carbonate Fuel Cell	Solid Oxide Fuel Cell
Electrolyte	KOH Solution (Aqueous solution of potassium hydroxide in a matrix)	Polymer Membrane proton conductive (Perfluorosulfonic acid)	Polymer Membrane proton conductive	Phosphoric acid (Phosphoric acid soaked in a matrix)	Li_2CO_3 and K_2CO_3 melted in a matrix of $LiAlO_2$ (solution of litium, and/or potassium carbonates, soaked in a matrix)	ZrO_2 and Y_2O_3 (Yttria stabilized zirconia)
Catalyst	Nikel, Platine-palladium	platine	platine, platine/Ruthénium	platine	Nikel-Chrome	Lanthanum strontium manganite
Ions in the electrolyte	OH^-	H^+	H^+	H^+	CO_3^{2-}	O^{2-}
Operating temperature	80 °C-90 °C	50 °C-90 °C, typically 80 °C	60 °C-130 °C	150 °C-210 °C	600 °C-700 °C	700 °C-1000 °C
Fuel	H_2	H_2 (pure or reformed)	Methanol	H_2 (pure or reformed)	H_2 (pure or reformed)	H_2 (pure or reformed)
Oxidants	O2 (pure)	Air	Air	Air	Air	Air
Applications	space, transport, military	portable, transport, stationary	portable	transport, stationary (distributed generation)	stationary (distributed generation)	transport (APU), stationary (auxillary power, distributed generation)
Power range	10 W-100 kW	1 W-300 kW	1 W-300 kW	1 kW-300 kW, 100 kW module	300 kW-3 MW, 300 kW module	1 kW-2 MW
Electrical efficiency	60-70 %	50-65 %	FC: 20-30%	40-50 %	55-65 %	55-65 %
Advantages	very high performance at the cathode low cost components	high energy density, quick start/stop, low temp	low operating range, easy storage and transportation,	Mature technology, good reliability, low cost electrolyte	high efficiency, large choice of catalyst, fuel flexibility, suitable for CHP	high efficiency, large choice of catalyst, fuel flexibility, suitable for CHP
Disadvantages	usage pure gas, sensitivity to impurities, electrolyte management	expensive components, water management	expensive catalyst, methanol crossover	expensive catalyst, evaporation of the acid, long start-up time, low power density	long start-up time, corrosion, low power density	long start-up time, high temperature, components relatively expensive

Alkaline Fuel Cell (AFC)

Alkaline Fuel Cell (AFC) uses an electrolyte of alkaline type, such as potassium hydroxide solution (KOH) or odium hydroxide (NaOH), in which hydroxide ions (OH^-) are the mobile charge carriers [10]. However, usage sodium hydroxide has not obtained wide application due to low solubility of sodium carbonate compared to potassium carbonate. Hydrogen is supplied into the anode side, while oxygen or purified air is provided to the cathode side that led the generation of water, electrical energy, and heat. Chemical reactions occurring in the alkaline fuel cell (Fig. 1.5):

Anodic reaction: $H_{2(g)} + 2\,(OH)^-_{(aq)} \longrightarrow 2H_2O_{(liq)} + 2\,e^-$

Cathodic reaction: $\frac{1}{2}\,O_{2(g)} + H_2O_{(liq)} + 2\,e^- \longrightarrow 2\,(OH)^-_{(aq)}$

Overall reaction: $H_{2(g)} + \frac{1}{2}\,O_{2(g)} \longrightarrow H_2O_{(liq)}$

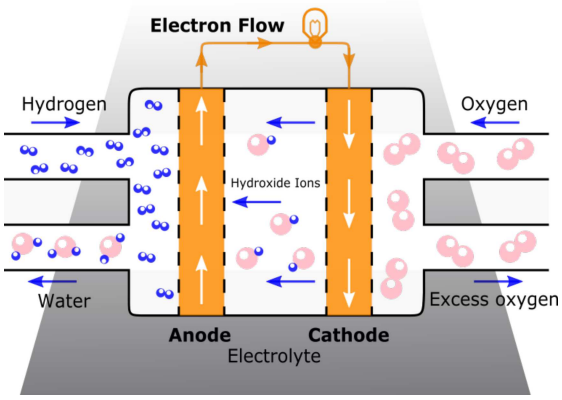

Figure 1.5 – Principe of AFC operation

Nowadays, alkaline solution is widely used in various applications due to its accessibility and price, but on the other hand, precious metals, such as platinum, are used for catalyst. Therefore, AFCs are relatively inexpensive. This barrier can be eliminated by using nickel that is cheaper than expensive platinum catalyst[11, 12]. This type of fuel cell can operate between 60 °C and 250 °C, but mostly it seldom excess 100 °C. Its operating temperature ranges around 80-90 °C [13]. Working under low operational temperature, systems based on AFC can easily be launched and stopped. However, it is necessary to provide pure reactants without any contaminants, such as carbon oxides, that aggravate operation working coupling by dissolving in the electrolyte and decreasing OH^- concentration. Thereby, these fuel cells can be fed only with pure H_2 and O_2 as well as they must regularly replenished electrolyte to have sufficient ionic conductivity[14]. Moreover, another disadvantage is that when nickel is exposed to air. This situation leads to the increase of the electrode resistance. This problem can be eliminated by covering it with a protective layer of chromium oxide[11]. In spite of these mentioned limitations, the alkaline fuel cell was the first fuel cell used in space operations in the US Apollo Space Program utilized pure reactants and diluted electrolyte (85% KOH) allowing operation at a lower pressure without electrolyte boiling [14]. Similar developments were also make in Russia. Russian fuel cell system, namely as "Photon", was built for its national space plane "Buran", but this project has already been stopped[10]. Nowadays, lifetime of AFC systems surpass several thousand operating hours, but for large-scale utility applications it is necessary to achieve at least 40 000 hours.

Proton Exchange Membrane Fuel Cell (PEMFC)

One of the most perspective systems among others is the Proton Exchange Membrane Fuel Cell (PEMFC), since they operate at a relatively low temperature range 50-90 °C, have a high power density and fast output power response on changing energy needs. PEMFC consists of a polymer membrane, ionic acid, electrodes, gas diffusion layers, bipolar plates and sealing gaskets. A more detailed study of fuel cell type PEM is carried out in Chapter 2. The proton exchange membrane fuel cell (PEMFC) uses membranes as its electrolyte that are ionomers and the most used is based on perfluorosulfonic acid (PFSA) such as the Nafion. Popular catalyst used in electrode is platinum for electrodes and PEMFC are usually fed with (pure) hydrogen (H_2) and O_2/air. Supplied hydrogen to anode side where are oxidated into protons and electrons, then the protons travel through the membrane to the cathode side where meet electrons traveled in an external circuit and make reduction reaction with oxygen produce water and heat. Chemical reactions occurring in the Proton Exchange Membrane Fuel Cell (Fig. 1.6):

Anodic reaction: $\mathrm{H_{2(g)}} \longrightarrow 2\,\mathrm{H^{+}_{(aq)}} + 2\,\mathrm{e^{-}}$

Cathodic reaction: $\frac{1}{2}\,\mathrm{O_{2(g)}} + 2\,\mathrm{H^{+}_{(aq)}} + 2\,\mathrm{e^{-}} \longrightarrow \mathrm{H_2O_{(liq)}}$

Overall reaction: $\mathrm{H_{2(g)}} + \frac{1}{2}\,\mathrm{O_{2(g)}} \longrightarrow \mathrm{H_2O_{(liq)}}$

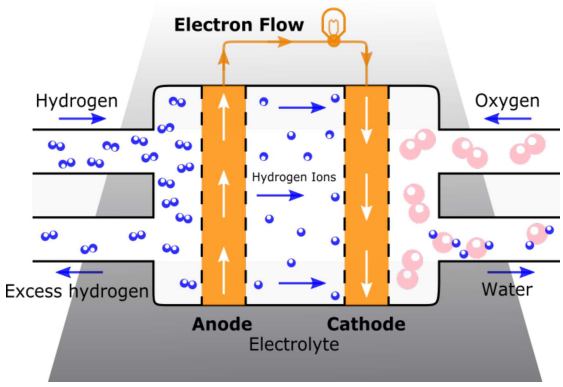

Figure 1.6 – Principe of PEMFC operation

In spite of the fact that PEMFCs have high performance, small level of environment pollution, very high efficiency up to 83 % [15], they have insufficient operational characteristics namely reliability and durability, that impede their wide utilization. Another disadvantages are the usage of precious metal-based electrodes and water and thermal management issues. Nowadays, lifetime of PEMFCs has not yet achieved with appropriate parameters for a wide utilization on light duty and materials handling vehicles and for stationary applications. However, research in this technology developments is carried out.

Direct Methanol Fuel Cell (DMFC)

Direct Methanol Fuel Cell is a relatively recent development in field of fuel cell technologies. The design and structure of DMFC is like the PEMFC that includes a proton-conducting solid polymer electrolyte membrane with two catalyst-coated electrodes. Methanol is used as the main fuel for DMFC, thereby it gives several advantages such as cheapness of usage, simpleness of transporting and storing (absence of additional using of safety). Operating temperature of

DMFC ranges around 60-130 °C. Main chemical reactions occurring within DMFC contain the following steps. Liquid solution of methanol and water are supplied at the anode side where methanol is oxidized by 1 mol of water and presence of a catalyst, producing 1 mol of carbon dioxide (CO_2), six protons of hydrogen (H^+) ans six electrons (e^-). After that electrons go through external power circuit toward the cathode where meet the ions of protons traveled through electrolyte membrane and made reduction reaction with oxygen to form 3 mol of water with the presence of a catalyst at the cathode side. Chemical reactions occurring in the direct methanol fuel cell (Fig. 1.7):

Anodic reaction: $CH_3OH + H_2O \longrightarrow CO_2 + 6\,H^+ + 6\,e^-$

Cathodic reaction: $O_2 + 6\,H^+ + 6\,e^- \longrightarrow 3\,H_2O$

Overall reaction: $CH_3OH + O_2 \longrightarrow 2\,H_2O + CO_2$

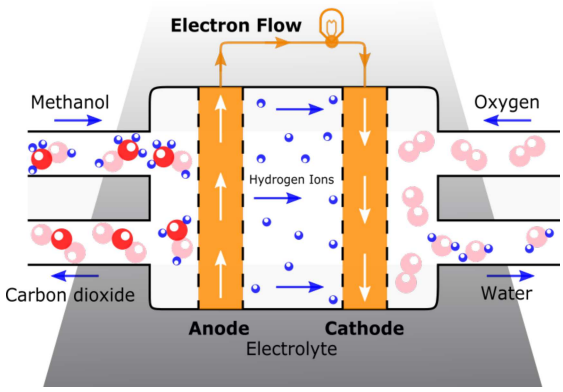

Figure 1.7 – Principe of DMFC operation

Thanks to supplying water with methanol to anode side, there is no need in maintaining water balance in membrane, which can have dry issues due to the migration of water from the anode to the cathode. Thanks to the low operating temperature, this type of fuel cell can be used in applications with frugal power requirements, such as mobile devices, portable power banks. Since methanol is in liquid state with temperature range between −97 °C and 64 °C, it will simplify process of storage and transportation without additional costs on security. However, one of the significant challenges of using DMFC systems is the absence of robust and low-cost catalyst. Nowadays, the most common catalyst in DMFC is platinum-ruthenium (PtRu) catalyst with ratio one by one. However, even with these catalysts, efficiency of DMFC systems is lower than PEMFCs due to low electrochemical activity for fully methanol oxidation to form six electrons and due to high water electro-osmosis (up to 19 water molecules per proton) which causes significant flooding at cathode side. Regarding this last comment, use of water balance systems can be raised. Another disadvantage is the presence of methanol crossover that leads to a heat of generation due to methanol combustion reaction and causes damages on the membrane. Also, methanol crossover and combustion reaction at the cathode side lead to a reducing of oxygen concentration and reduce the electrochemical activity that affects its effectiveness. Produced water formed at cathode side can be used for supplying water at anode side and for impact water management systems. Nowadays, DMFC systems are being applied widely in warehouse as lifting-and-shifting machines. Compared with batteries, DMFC systems can be refueled in a couple of minutes what is important for commercial goals. Recently, Lohoff et al.[16] developed a 1.3 kW direct methanol fuel cell (DMFC) system with a proven lifetime of 20,000 h.

Molten-Carbonate Fuel Cell (MCFC)

Molten-carbonate fuel cells (MCFCs) are one of the high-temperature fuel cells which operate at temperature range of 600-700 °C with high efficiency of 65%. MCFCs include two porous electrodes (nichrome NiCr for anode, nickel oxide NiCr for cathode) separated by liquid electrolyte consisting of carbonate salt, e.g. Na_2CO_3, Li_2CO_3, K_2CO_3, CO_3^{2-},suspended in a porous ceramic matrix. High operating temperature improves kinetics reaction and allows to use less active and low cost catalysts based on nickel. MCFC can work with different fuels such as oil, natural gas, methanol, coal gas after a rough reforming stage to obtain hydrogen. The principle is based on oxidation of hydrogen at anode side by combining with incoming carbonate ions CO_3^{2-},which have been transmitted in electrolyte, producing water and carbon dioxide with two electrons that travel through external circuit. After that at the cathode side, supplying oxygen undergoes reduction reaction by combining with carbon dioxide and incoming electrons and releasing carbonate ions[17]. Chemical reactions occurring in the alkaline fuel cell (Fig. 1.8):

Anodic reaction: $H_{2(g)} + CO_3^{2-} \longrightarrow H_2O_{(g)} + CO_{2(g)} + 2\,e^-$

Cathodic reaction: $\frac{1}{2}\,O_{2(g)} + CO_{2(g)} + 2\,e^- \longrightarrow CO_3^{2-}$

Overall reaction: $H_{2(g)} + \frac{1}{2}\,O_{2(g)} + CO_{2(g)} \longrightarrow H_2O_{(g)} + CO_{2(g)}$

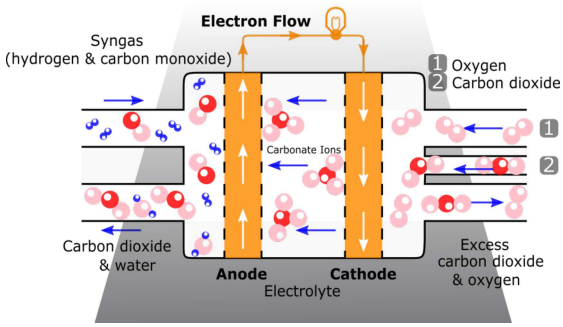

Figure 1.8 – Principe of MCFC operation

As we can see, CO_2 production and consumption at the anode and cathode sides (respectively) require the applying of a recycling loop, which increases the cost of MCFC installations. Problems of corrosion of the electrodes remain at high-enough temperature during operation. Thanks to high operating temperature MCFCs suits for co-generation of applications, heat and electrical power where overall efficiencies can be over 80 %. However, thermo-mechanical stress, that appears inside the electrolyte during the start-up and shutdown, narrows its wide utilization. Thereby, these fuel cells are more appropriate for stationary and continuous power applications. Wide utilization of these types of fuel cell have been proven by stability and durability, lifetime these technology is at least 40 000 hours.

Phosphoric Acid Fuel Cell (PAFC)

Phosphoric Acid Fuel Cell (PAFC) is the most experienced fuel cell technology in commercial area compared to others since the early 90's. PAFC includes two Pt porous electrodes separated by phosphoric acid (H_3PO_4) solution embedded in a porous SiC matrix, providing the ionic conductivity, to minimize crossover of the reactant gases, and to eliminate short circuit of the electrodes. The operation temperature is controlled by air or an other fluid between 150 °C and

250 °C to have a good electric efficiency near 40 °C and overall efficiencies near 80 °C if the heat of this process is harnessed for co-generation. The supplied hydrogen is oxidize at the anode side, starts to release electrons (e^-) and protons (H^+). The phosphoric acid conducts protons to the stage where it reacts with oxygen and electrons at the cathode side to form water. The chemical reactions occurring in the Phosphoric Acid Fuel Cell (Fig. 1.9):

Anodic reaction: $2\,H_{2(g)} \longrightarrow 4\,H^+_{(aq)} + 4\,e^-$

Cathodic reaction: $O_{2(g)} + 4\,H^+_{(aq)} + 4\,e^- \longrightarrow 2H_2O_{(liq)}$

Overall reaction: $H_{2(g)} + O_{2(g)} + CO_2 \longrightarrow 2\,H_2O_{(liq)} + CO_2$

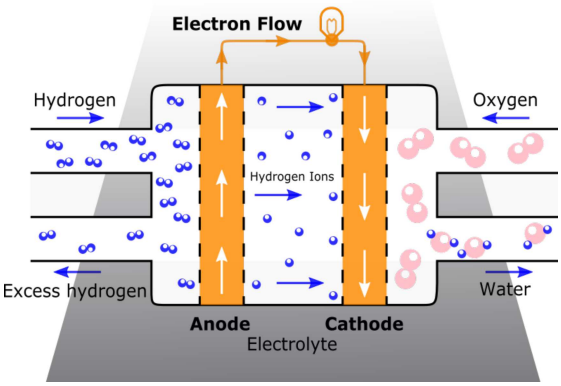

Figure 1.9 – Principe of PAFC operation

However, over a long period of operation, there are losses of acid. The temperature is controlled through a fluid (air, water or oil circulating in the cooling plates interspersed between the cells) to avoid the evaporation of the electrolyte. Among the various noble metal catalysts that are stable under acidic conditions, Pt is still the most active electro-catalyst for the hydrogen oxidation reaction

Operating of PAFC systems must be maintained at sufficiently high temperatures to avoid the solidification of the electrolyte (pure H_3PO_4 solidifies at 42 °C) and to prevent damage to the electrodes. However, these barriers can be eliminated by a dilution of the electrolyte to lower the concentration and to reduce its freezing point of acid. On the other hand, working at high temperatures entails processes of evaporation and that's why it is needed to replenish it regularly. Due to this constraint, PAFC systems are appropriate only for those stationary power plants, where these systems can work for a long time without interruptions. Problem of water management in the PAFC is not a major concern as PEMFCs. The main problem of such systems, like PEMFCs, which impedes their wide utilization is the price of materials, including the separator, bipolar plate, and Pt-based electrode-catalyst. As was mentioned above, these systems commonly used for stationary power generation as well as for combined heat and power (CHP). In spite of all problems with price, these systems closest to the wide-ranging use have a high reliability and achieved 40 000 hours of operation. Thereby they reach their application in banks, hospitals, and computing facilities.

Solid Oxide Fuel Cell (SOFC)

Solid Oxide Fuel Cell (SOFC) is a high-temperature fuel cell that operates at a temperature range of 700-1000°Cwith high efficiency over 60 °C when converting fuel to electricity, and overall efficiencies near 80 °C for co-generation profile. SOFCs use a solid ceramic electrolyte, such as zirconium oxide stabilized with yttrium oxide $Y_{0.1}Zr_{0.9}O_2$, capable to conduct oxygen ions. High operating temperature allows using various form of fuels which can be reformed within the fuel cell itself that eliminates the usage of external reforming and thereby reduces cost of SOFC systems. Main chemical reactions following steps. At the beginning, supplied oxygen picks up electrons and forms a negatively charged oxygen ion O^{2-} which travels through solid oxide ion-conducting membrane electrolyte toward the anode where it reacts with hydrogen gas, producing water and electrons that transports to the cathode through the external electrical circuit. Chemical reactions occurring in the Solid Oxide Fuel Cell (Fig. 1.10):

Anodic reaction: $H_{2(g)} + O^{2-} \longrightarrow H_2O_{(g)} + 2\,e^-$

Cathodic reaction: $\frac{1}{2}\,O_{2(g)} + 2\,e^- \longrightarrow O^{2-}$

Total: $H_{2(g)} + \frac{1}{2}\,O_{2(g)} \longrightarrow H_2O_{(g)}$

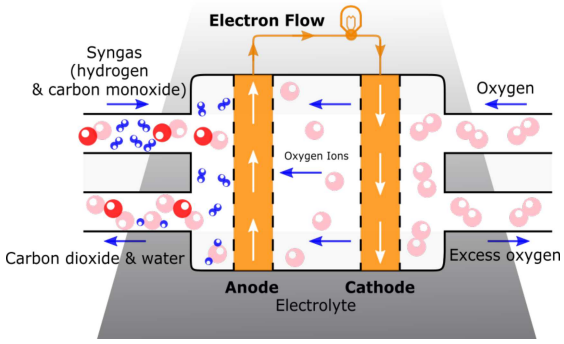

Figure 1.10 – Principe of SOFC operation

One of the main challenges of using SOFC systems is choice of materials for electrolyte, electrode, gasket seals for enhanced performance and operating characteristics, namely reliability and durability, and reducing of price. Mostly SOFCs are used for stationary application due to the waiting for the start-up and reaching the operating temperature. Reducing operating temperature to 800°C, allows us to make wide selection of materials that are robust and heat-resistant. Thereby, it allows using materials which are less expensive but have the same operating characteristics. Consequently, this increases the possibility of using SOFCs for a wide variety of applications, including stationary and automotive applications. Power generation of these systems can achieve from several kilowatt to hundred megawatt what is enough for small co-generation applications.

1.4 Conclusion

To resolve problem with depleted fossil fuels it has required the research of higher power effective power plants, engines that allow to build new necessary infrastructure from the power source to end-consumer. For example, for hydrogen vector it is required construction of infrastructure for storage, pipeline or cargo transportation for delivery, plants for hydrogen production.

Nowadays, researchers tries to implement fuel cells as PEMFC systems in the area of transport thanks to its very low influence on ecology. Table 1.3 shows obviously that FC emissions are very low. However, it should be noted that FCs can be combined another fuel, for example, methanol. Lack of hydrogen infrastructure is one of the main obstacles of development of hydrogen transport.

Table 1.3 – Prospective emissions for the car on FC and standards of emissions (g/mile)

Type of setup	Type of emission		
	organic components	CO_2	NO_x
Petrol internal combustion engine	0.755	7.553	0.704
Hydrogen power installation	0.004	0.003	0.001
Methanol power installation	0.023	0.004	0.001
Petrol power installation	0.371	0.005	0.001

Creation of a wide hydrogen infrastructure of filling stations at modern level of technologies is extremely expensive and there are a lot of unresolved tasks in technical, economic and safety providing areas. Really, hazard of explosions of «a rattling mix» in case of leakage of hydrogen with air/oxygen at mass use of the compressed hydrogen is very high. Safety methods of storage of hydrogen either are too expensive, or are non-technologically robust. Nevertheless, there is intensive development in this direction, and it is theoretically possible to expect emergence of safer storage of hydrogen on board of the car. Recent emergency of fast-charged lithium, ion accumulators, made possible the serial release of city electrical cars, which can be charged practically in living conditions. Low costs of a transport network of electrical cars and low (in comparison with petrol) cost of kilometer allows to approve creation that this future of this transport niche.

SOFCs offer the best prospects for further improvement and for a future large-scale deployment. MCFCs and SOFCs offer the best performance for stationary high power applications. Due to their high power density and their compact design (MEA thickness less than 1 mm), PEMFCs seem to be the most promising creation for small-scale stationary, residential and portable power applications and, of course, for transportation. They are currently also the most studied fuel cells.

A further disadvantage of all kinds of these fuel cells is their expected lifetime. To compete with conventional technologies on the UPS market, it will be necessary to reach a lifetime of ten years (discontinuous operation).

In spite of the fact that PEMFCs have high performances and small level of environment pollution, they have insufficient operational characteristics namely reliability and durability, that impedes their wide utilization for automotive and for stationary applications.

Therefore, any device meet problems, and FC is not an exception. Typical FC problems can be divided into two groups: damaging of construct elements and disoperation mode. Failures of the first group arise due to three main reasons: first, incorrect assembly of FC, which can give rise to increasing mechanical stress of FC components; second, defects of FC components (for example,

unequal distribution of the catalyst and mechanical defects), and third - corrosion of materials of the fuel cell. For eliminating these failures, FC running has to stop for repair or replace its components. Failures of the second group oftenly arise due to wrong water balance (for example, drying and flooding of Membrane-Electrodes Assembly and gas transport channels) and can be eliminated by FC's operating mode correction.

Based on review results we can conclude that we can observe different degradation mechanisms depending on the operating conditions (OCV, fuel starvation, potential hold). Moreover, the membrane electrode assembly is the most critical component within PEMFC system, that can lead to the death of stack due to a lot of factors which is difficult of distinguish. The most detailed review of all these components allows to distinguish which components are necessary to control and to manage for PEMFC lifetime(Fig. 1.11).

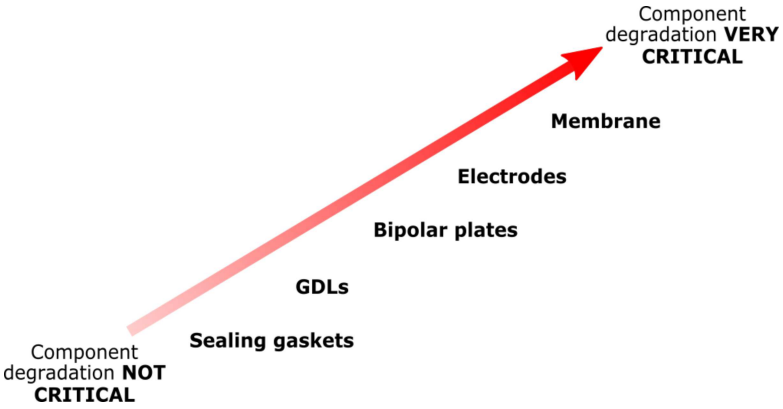

Figure 1.11 – Hierarchy of critically components

There are a lot of processes occurred during fuel cell operation, however it is emphasize one is the water management which is still not completely understood and remains hardly assessed. A good knowledge of PEMFC water management allows to improve its reliability and performance. This is why there are a lot of continuous and significant researches in this field in which different techniques are devoted to the evaluation of cell state-of health or water management[18].

This problem can be solved by means of the PEMFC technical state diagnostics adapted to detect and possibly to predict failures at the initial stages and to try to neutralize effects of failures to keep high operational characteristics.

Chapter 2

Proton Exchange Membrane (PEM) Fuel Cells: Principle, limitations and diagnostic

Contents

Figures

2.1 Proton Exchange Membrane Fuel Cell Assembly

As was mentioned above, fuel cell converts directly the chemical energy of hydrogen into electrical energy with an efficiency near 50 percent for electricity and 98 percent in co-generation applications (heat and electricity). Fuel cells can currently replace or come in addition of batteries to power electrical systems . PEMFC technology allows to produce electricity with low emission but each parts of the systems and functioning remains complex. Indeed, all components, which compose the fuel cell assembly (Fig.2.1), have often antagonist functions and different phenomena within them. Moreover, auxiliaries (air pumps and fans, mass flow controllers, reactant storages, gas humidifiers and purifiers, a temperature controlling system etc.) need to be implemented for accurate working of the system. All these auxiliaries are responsible to maintain the stack at its nominal operating conditions and thereby optimize of the system performance and life-time. Stability of all components is necessary for large and extreme functioning regimes and for long-term operation of the fuel cells. For a technological point of view, one of the main important factor for a system is its simplicity and its efficiency and auxiliary components can increase its complexity and power consumption. This is why, especially in small-scale applications, it is used passive controlling and operating methods. Due to its passive operation, free-breathing PEMFC is a potential power source for small-scale applications[19]

An elementary assembly of single cell of PEMFC produces a power-limited, usually less than one volt. To obtain required output voltage it is necessary to multiply unit cells and connected often in series and constitute a stack. Quantity of these cells may varied from a single one to several hundred depending of the output power require.

2.1.1 Sealing gaskets

Structure and role

One of the parts which is commonly neglected during long-term utilization of PEMFC system, is the sealing gasket. This component is responsible for gas tightness and mechanical rigidity that influence not only the electricity output performance and security of the fuel cell, but also affects the durability and reliability of the system. Bolts and nuts are used for compress components to obtain a mechanical support of all components, minimize their bending and maintain an appropriate clamping of the cell. Moreover, sealing gaskets are necessary to avoid gas mixing, leakage and crossover[20]. Typical sealing materials are some rubbers, Ethylene Propylene Diene Monomer (EPDM) and silicone[21]. Nonuniform contact pressure can lead to increase

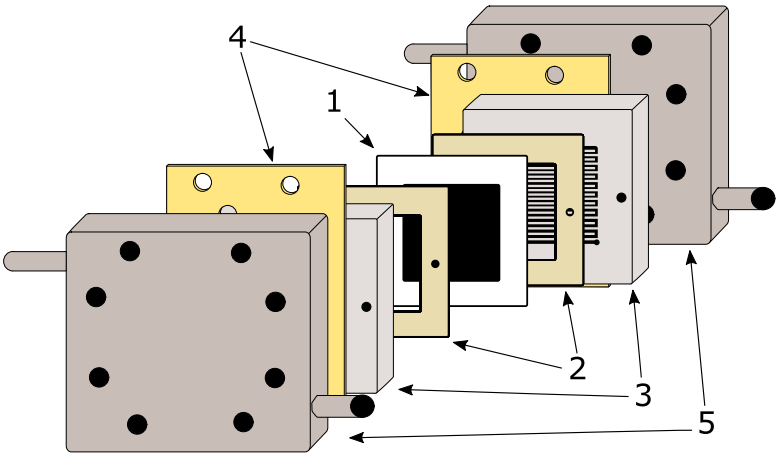

Figure 2.1 – PEM fuel cell assembly: 1. - membrane electrodes assembly; 2. - gaskets; 3. - bipolar plates with gas transport channels; 4. - current collector plates; 5 - anode and cathode end plates.

the contact resistance and also an over-compression of the gas diffusion layers (GDLs) increase the diffusion resistance of gases, that are influence at large current density[22]. Appropriate reasonable design of the sealing gaskets should be suitable for mass production, convenient for fuel cell stack assembly and should have a low cost. This is why material characteristics, structures and sizes of all components should be chosen and designed with precaution.

Degradation phenomena, failures, and their diagnosis

Poor, faulty or inappropriate sealing gaskets cause the loss of their own force retention and can lead to compression loss, external leaks of coolant, gas crossover. Thereby sealing defaults can lead to obtain detonating mixture and also reduced voltage due to the formation of a mixed potential at the electrodes[22] and eventually accelerating the degradation of the fuel cell. There are only few articles focusing on the structures of gasket sealing available in the literature, but some of them are distinguish[21].

Schulze et al. [20] investigated in details the degradation of silicon-based seals during long-term fuel cell operation using X-ray photoelectron spectroscopy (XPS). Its usage clearly showed that residues of the silicone were detected in the anode catalyst layer and cathode GDL that lead to the poisoning of the catalysts and changing the hydrophilic/hydrophobic characteristic of the electrodes.

Bograchev et al. [23] studied the influence of seal joints stiffness in the Nafion membrane during the start-up phase. He noted, that in the transient regime the influence of the joint stiffness was more pronounced than during the pre-heating stage, which may reach its maximal level.

The compression of the seal in a PEMFC was investigated experimentally by Chien et al. [24]. The results showed that impact of sealing force was not significantly affected during the period between assembly and normal operation of the PEMFC, excluding a stress relaxation effect. In addition, it was shown that changes in all dimensions caused by thermal expansion was negligible.

Investigation of several commercially available gasket materials was performed by Tan et al. [25]. They investigated the chemical degradation and its mechanisms of the materials in a

simulated FC environment. Characteristics of some sealing gaskets are strongly dependent on temperature and it was shown that stress in the sample could accelerate the degradation of the materials, which can degrade faster under high-applied stress. Optical microscopy reveals that the degradation starts with surface roughness from the beginning of the exposure and finally results in cracks on the surface over time.

Cleghorn et al. [26] observed the degradation silicone/glass re-enforced gasket during 26 300 hours single cell lifetime experiments. As a results they were detected silicone particles on the surface of the gas diffusion layers (GDL). They reported, after disassembly of the cell, that the gasket thickness was typically reduced by approximately 25 µm.

2.1.2 Gas Diffusion Layers (GDLs)

Structure and role

Gas Diffusion Layers (GDLs), inserted between the catalyst layers (CLs) and the flow fields plates, allow to insure electrical contact and reactants gases distribution to the catalyst layers (CLs) through its porous nature. GDL is a porous carbon fibber/cloth which is typically treated with polytetrafluoroethylene (PTFE, Teflon)[27] to enhance its hydrophobicity for better water management properties, and then coated with a micro-porous layer (MPL)[28]. The GDL has the following key features, such as reactant/product permeability, electrical/thermal conductivity and mechanical support[29]. On the one hand, the porous structure must allow the transport of the reactants and water to ensure an adequate supply of reactants and hydration of polymer electrolyte membrane to obtain a good ionic conductivity. On the other hand, a certain hydrophobicity is required for removing water of saturated pores to the flow field. Water transport behavior affects the gas transport and the electrochemical activity of the electrodes. So liquid water is transported through hydrophilic pores, whereas in gas-phase reactants are distributed homogeneously through hydrophobic pores of GDL[30]. In addition, GDL conducts electrons and heat between the catalyst layer and the current collectors via the bipolar plate and gives mechanical support to the membrane electrode assemble (MEA) and protect the membrane from damage during assembly and avoid its deflection into the flow field channels during cell compression [29]. Thereby, GDL under strong pressure constraint to ensure the sealing, may undergo a decrease of 10 to 40 % of their thickness. Thereby, it constraints impose a selection of required materials that have good electrical and heat conductivities and also allows plastic deformations and gas permeability. Adding a micro porous layer (MPL) made of carbon carrier modified with hydrophobic material between the GDL and catalyst layer significantly improves water removal from the catalyst layer and reduces site flooding and thereby improves cell performance[31]. Thus, MPL enhances the water management (better humidification of the anode and enhanced water removal from the cathode) and improves the electronic contact between the GDL and the catalyst layer[32]. However, there is no clear explanation in the literature about the optimal GDL thickness and pore sizes of the MPL for enhancing the water management and thereby the cell performance. It depends on operating conditions, for high current density (wet condition) is better to use thin GDLs, and thick GDLs preferred on low current density (dry condition).

Degradation phenomena, failures, and their diagnosis

Identification and understanding of degradation phenomena in PEMFC require more efforts, but also it is necessary to understand that there is absence of understanding concerning the cause of degradation of each PEMFC component impacting on performance loss[21]. Thereby, there are not a lot of works related to degradation of the GDL, among the public literature,

because the major difficulty is separating GDL degradations from membrane-electrode assembly degradations that is why most of research works on GDL are ex-situ measurements.

Several mechanisms of GDL degradation have been observed during aging test, including: mechanical degradation [33], carbon corrosion [27], and hydrophobic agent decomposition [34]. Pauchet et al. [34] showed that the loss of hydrophobicity in a GDL, influencing on water behavior modifications, is a very suitable factor to explain performance loss rates observed during long-term tests. Schulze et al. [35] concluded that loss of hydrophobicity can induce a performance loss two times higher than catalyst dissolution and agglomeration in the active layer. Due to carbon oxidation and PTFE decomposition, there is modification of liquid water transport properties with time, so the electrodes become more prone to flooding since evacuation of water becomes difficult[34, 36]. Lee et al.[33] investigated effects of changing the GDL on the PEMFC performance under different bolt torques. Results showed that the main impact factor is the difference in thickness between the gasket and the diffusion layer effects on the contact pressure within PEMFC to insure impermeability. Consequently, GDLs compressed unevenly, cause a change the gas permeability and porosity due to the channel-rib structure of the flow field plate and is responsible for its impermeability. Thus, compression increases the electrical and thermal conductivity of the GDL, and decreases electrical and thermal contact resistances between components. Yan et al. [28] studied the impact of the presence of a significant quantity of PTFE on appearance of cracks in the MPLs. Thus, the degradation of GDL must be taken into account to evaluate global performance loss.

2.1.3 Bipolar plates

Structure and role

External element of PEMFC stack is the bipolar plate. In single cell configuration, two plates are placed on each side of the membrane electrode assembly and can be considered as two halves of a bipolar plate. Bipolar plates or flow field plates have generally, on their surfaces, channels of flow field of reactant gas. Because of the harsh working environment of the PEMFC, materials for bipolar plates must meet the following requirements[21]:

1. Good electrical and thermal conductivity;
2. A low permeability to reactant gases and no brittleness;
3. Good mechanical and chemical stability to products oxidant reducers.

Flow field plate are usually made from metals, carbon, carbon/graphite-based composites, and organic polymer based materials. These materials allow electrical and heat conduction and are chemically stable. The choice of material determines the compromise between performance, efficiency, size, lifetime, cost and operational range flexibility. Metallic bipolar plates are cheaper than graphite and graphite composites, typically made of stainless steel. They have a good thermal conductivity, can be mass-produced and can allow to create a compact stack design. However, they have an high electrical contact resistance and a lower resistance to oxidation than graphite. Graphite satisfies the requirements, but due to its brittleness, graphite is difficult and expensive to produce massively, due to process of molding , and also a sufficient thickness for mechanical resistance is required. Bipolar plates are key components used for distribute of supplied reactants, for collect excess water and reagents of the cel.l they assure the thermal regulation of the cell, provide the mechanical stability and conduct the electrical current within the stack. Its geometry and their flow direction may strongly influence the performance of the PEMFC, particularly thanks to management of water and gas distribution on the electrodes[21]. Lasbet et al. [37] analyzed the hydrodynamic characteristics of commercial bipolar plates and showed that the flow regime is laminar (Reynolds number near 200). There are only few research

papers concerning the optimization of flow channels. Kumar et al. [38], for example, investigated the impact of channel dimensions and concluded that the optimum channel width, land width and channel depth were close to values of 1.5, 0.5 and 1.5 mm, respectively.

Degradation phenomena, failures, and their diagnosis

Degradation of bipolar plates can be occurred by mechanical and chemical stresses caused by contact pressure, excessive temperature and extreme operating conditions. There are few degradation phenomena that can be distinguished: corrosion[39], appearance of the resistive surface layer[21] and fracture/deformation of the bipolar plates[40]. Corrosion of bipolar plates with further appearance of contaminants causes membrane pollution by water transport. The formation of a resistive surface layer leading the increase of the ohmic resistance and becomes an important factor in performance losses. Other common challenges related to bipolar plates is the deformation or cracks of the plates caused by compressive forces that are used to ensure a good clamping and low electric contact during its operation[41]. Mostly, these mechanical degradation phenomena can appeared from such factors as thermal cycles, bad temperature distributions or nonuniform currents[42]. Thermal cycle's regime also can effect the coating material that is used on bipolar plate to allow a good electric contact. We can observe expansion or shrinkage of this coating material with different rates due to the difference in their thermal expansion coefficients [21] that leading to form micro-pores and cracks.

2.1.4 Electrodes

Structure and role

The electrodes (active layers or catalyst layers) are considered as one of the main PEMFC components where electrochemical reactions such as reactions of oxidation of hydrogen at the anode and oxygen reduction at the cathode take place. Electrodes are deposit on the membrane (CCM) or on the GLD (GDE) and use platinum as a catalyst. Platinum (Pt) is an expensive noble metal that is usually used at both electrode, the anode and the cathode. Also for reducing the catalyst cost, platinum alloy with particles of nanometer size is used to improve efficiency of platinum utilization, for a similar cost, by increasing the electrochemical active surface area (EASA)[43]. Thereby, it can allow to establish the commercialization of PEMFCs. Electrodes are physically constituted by a triple phase boundary with particles of carbon, for the electrical conductor with very small Pt particles on it to form the catalyst, ionomer suspension for the proton conductivity. This triple phase is usually made thanks to an ink and support by carbon to form a porous structure to facilitate the diffusion of the reactants onto the catalyst it is known as the GDL[40]. This structure plays a major role in transportation of reactants (hydrogen, oxygen) and products (vapor and liquid water) between the catalyst sites and the GDL, as well as for transportation of protons and electrons between the active sites and the membrane, and respectively between the reaction sites and the GDL. Antolini et al. [44] investigated the effect of Nafion content in the catalyst layer and suggested an empirical equation (Eq.2.1) to calculate optimum loading, expressed as follows:

$$\text{optimum Nafion loading (mg cm}^{-2}) = 56 \cdot \frac{L_{Pt}}{P_{Pt}} \tag{2.1}$$

where L_{Pt} is the platinum loading (mg cm^{-2}) and P_{Pt} the wt.% of Pt supported on carbon. The optimum Nafion loading calculated using this equation, expressed in wt.%, is 36 wt.% for all platinum loadings.

Degradation phenomena, failures, and their diagnosis

Catalyst layers durability is still not satisfactory for tight operating conditions, such as, high humidity, low pH values, elevated temperature, and dynamic loads[21]. Its durability influences the performance in a long term point of view and it is a major barrier for worldwide commercialization of PEM fuel cells. Kocha et al. [45] have distinguished two main group of phenomena that are responsible for the lost of performance due to electrodes : the catalyst layer's degradation and the carbon support's degradation. Corrosion of the Pt catalyst is one of the fundamental mechanisms that contributes to degradation due to the loss and modification in its structure and the agglomeration of Pt distribution on the carbon support leading to decrease the electrochemical active surface area (ECSA) of the electrode[40].

After research works of Wu et al. [21] and Jouin et al. [42], we can distinguish four operating modes that impact the catalyst degradation: idling, transition between startup and shutdown cycles, a continual load of cycling mode at high frequency in rapid changes of potentials , starvation of fuel due to blockage at anode side due to continuous operation. Last regime can occur uneven flow sharing between cells during high overall stack utilization [21]. Load cycling mode is one of the most important factors contributing to platinum agglomeration and/or oxidation and in the sequel to a decrease in ECSA [40, 46, 47] that can be achieved of around 40% of losses after 1500 potential cycles from 0.1 to 1.0 V. Kocha et al. [45] investigated the contribution for catalyst degradation for load cycling mode and for continuous operation. They concluded, for observed cycled profile, that the degradation is higher (by time unit) than for a constant current at the same range and duration. Consequently, it shows a significant contribution to the degradation by the increasing and decreasing ramps of current transitions. Degradation provoked by starting/stopping cycles can be observed due to nonuniform distribution of fuel on the anode and due to oxygen crossover occurring generally during startup and shutdown of the PEM fuel cell. Idling mode that represent system functioning near circuit voltage (OCV) conditions, provides a minimal power (current). Thereby, this condition creates a favorable environment for the reactions of Pt degradation[42]. In addition, different cell temperatures and humidification level of the incoming reactants during operation also have an impact on the ECSA. Increasing of temperature helps to kinetics in leading to fast growth of Pt-particles, but the reducing of relative humidity (RH) of the gases leads to reducing these particles, thereby low RH helps to increase the lifetime of the catalyst layer[40].

There are a lot of works concerning degradation modeling of electrodes. One of them is the work of Dhanushkodi et al. [46] where they investigated the degradation phenomena. They proposed a model, which they call the fingerprint of the carbon degradation, that were obtained by related the amount of voltage loss to the amount of CO_2 that is generated during an accelerated stress test. Their results show that the loss of PEMFC performance can be linked to the losing of carbon at the catalyst layer by an exponential law. Another interesting result was presented by Bi et al. [48] that suggested degradation model including following processes: (1) electrochemical dissolution and re-deposition in the cathode; (2) Pt ion transport by diffusion in MEA; and (3) Pt ion chemical reduction in membrane by hydrogen that permeates from the anode.

2.1.5 Membrane

Structure and role

The proton exchange membrane plays a very important role in a fuel cell which is a thin layer of solid electrolyte that is sandwiched between two electrodes transporting ions from one side to the other thanks to its hydrophilic and hydrophobic domains, but preventing electron

transport and crossover of the reactant gases, H_2 and O_2[49]. For reliability's sake, membrane must be able to withstand harsh conditions and thereby has to be stable against chemical and mechanical degradations over the range of operating conditions, and has to have high proton conductivity when membrane are well-hydrated , a good mechanical resistance, flexibility, a low permeability to gases and a low water drag[21]. Nowadays, the most commonly used membranes for PEMFCs is Nafion ®so-called the perfluorosulfonic acid (PFSA) membrane developed by DuPont Company (USA) that has an aliphatic perfluorinated backbone with ether-linked side chains ending in sulfonate cation exchange sites [50]. Nafion membranes are classified according to their equivalent weight EW (in terms of molecular mass) per sulfonic acid group and thickness: Nafion XYZ where first two digits XY represent the EW and the last digit Z is its thickness. For example, Nafion 117 means a material with 1100 g EW with thickness of 0.007 inches[51]. Another promising membranes satisfying all requirements [21] are Gore-Select®(USA), Aciplex®(Japan), Flemion®(Japan) for example.

The ionic conductivity of such membranes is strongly dependant on the temperature, the concentration of the acid group and the water content. When the membrane absorbs water, the ionic domains swells and forms proton-conducting channels. This conductivity increases until its limit value. Moreover, with further increasing water content can be caused its own swelling that can lead to mechanical stress and thereby the concentration of protons will be diminished and the conductivity will be lowered[50]. Thereby, water management of membrane is an important factor of its lifetime, in particular is noted significantly at high current densities.

The structure of Nafion is represented by the following general formula Fig. 2.2:

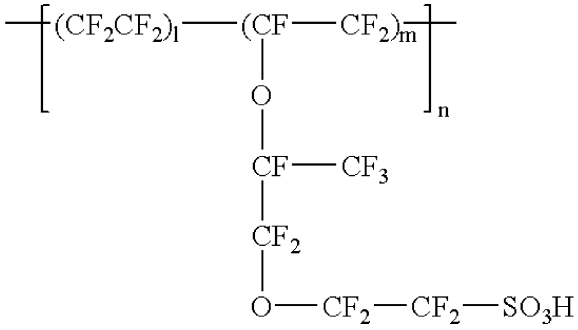

Figure 2.2 – Nafion structure

The water adsorption is characterized by the (dimensionless) concentration λ representing the number of adsorbed water molecules per sulfonate head group SO_3^-:

$$\lambda = \frac{n_{H_{20}}}{n_{SO_3^-}} \tag{2.2}$$

where $n_{H_{20}}$ and $n_{SO_3^-}$ designate the number of adsorbed water molecules and the number of sulfonate groups, respectively[51]. Mostly, proton conduction is usually observed when excess protons can move on the counter- ion clusters, i.e. for $\lambda \geq 2$.

As was mentioned above, lifetime of the membrane determines the life of PEMFC, so that is why it is so important to understand the mechanism of its degradation.

Degradation phenomena, failures, and their diagnosis

On this day, insufficient operational characteristics, namely durability and reliability of the membrane, are still one of the critical issues impeding the commercialization of PEM fuel cells. To eliminate this barrier it is necessary to have a lifetime durability more than 40 000 and 8000 hours of uninterrupted operation at power more than 80 % for stationary applications. Reasons of the leading degradation processes has not been fully understood so far and it is the subject of much discussion of many researchers. Membranes are more vulnerable and degradations are more rapid in automotive applications during a load cycling and starting/stopping phases[40]. Collier et al. [50] investigated membrane operating under nominal conditions and supposed the new classification of critical degradation mechanisms: chemical degradation, mechanical degradation, and thermal degradation. Early failures is often caused by mechanical degradation that can happen due to substandard membrane fabrication, non-accurate stack assembly, varying of operation conditions especially in terms of temperature and humidity variations. As a consequence, it can lead to swelling/shrinkage of the membrane causing mechanical constrains and hydrothermal fatigue. Mechanical failures appear under different forms such as cracks, tears, punctures or blisters[47]. All of them can cause propagating microscopic cracks responsible of gas crossovers and unequal water balance that, under lack of water, can be fragile and brittle the membrane. Maximum temperature of Nafion membrane under which structure preserves its characteristics makes up 120 °C that's why it is not a big problem for PEM fuel cells working on favorable temperature zone is usually from 60 °C to 80 °C
. Thereby, this range is most suitable for maintaining well-hydrated PFSA membranes. Thus, thermal degradation does not impact strongly on appearing of membrane failures, but its transient operation can lead to local heat build-up that with the subsequent on a presence of local dehydrated spot within the membrane, causing structural changes in it and thereby a loss of proton conductivity that may affect the stability, performance, and lifetime[52].

Chemical degradation may be occurred under normal functioning causing serious originates from chemical attack initiated by active oxygen species (oxygen radicals, hydrogen peroxide)[21]. This chemical degradation leads to catastrophic problems[49] such as the decomposition of the membrane, the reduction of the thickness and the formation of impurities and contamination, can resulted as a reduction of proton conductivity[50], an increase of gas crossovers and a mechanical weakness favorable for failures (short-circuit).

Regarding appearance of shorting, indicator of passage of electronic current goes directly from the anode to the cathode through the membrane due to over-compression of cell or topographical irregularities of the neighboring PEMFC components causing over-compression and creep during assembly or thermal variations. Gittleman et al. [[49]] distinguished two families of shorting: soft that is not critical and does not lead to the failure immediately; and hard appearing which can affect increasing gas crossover with subsequent to its failure.

Concerning crossover, hydrogen and oxygen crossover are present, however hydrogen crossover is the most primary cause leading to the stack death. Due to local pinholes and perforations on the membrane, hydrogen can easily travel to the cathode side where it meets with oxygen occurring combustion reaction and cause the generation of local hot-points leading rapidly to the death of the stack. The most severe degradation mechanisms have been considered and based on this review. We can conclude that membrane degradation mostly can appear when our system stays on transient operation than steady state operation. Thereby, further research works are necessary for understanding the impact of membrane degradation with different operating conditions.

2.2 Objectives and problems related with fuel cell diagnostic

Nowadays, the fuel cell is considered as an alternative technology, that allows to solve environmental problems, but the application of these technologies in industry is complicated and needs to be optimized, in particular by the increase of remaining useful file (RUL). As the result, new era of science and technology is appeared: Prognostics and Health Management (PHM), which aims to make estimation of system operation and prognostics of fuel cell lifetime. Despite of the rapid development of PHM, implementation of this technology on Fuel cell at the international level is not carried out. This fact can be explained by the absence of knowledge of behavior of these systems. This is why the development of the predictive tool with consideration of the many uncertainties is complicated due to the ability to estimate the functioning of the system without an irreversible depreciation of equipment. Therefore, at this moment, international efforts are put in advance on the following tasks:

- development of reliable predictive approaches to PEMFC
- easiness of implementation,
- allowing of this approach for industrial deployment

The first direction aims not only to realize estimation of RULs, but also to expand the capabilities of the developed predictive tools. To estimate a priori quantitatively an error or to control the distribution of this error. Several approaches are considered: a model-oriented predictive, data-oriented approach of prediction.

The second direction is aimed to increase the applicability of these prognostic systems, thereby to develop the usage of approaches which can be possible use as a tool in the design of these systems at high characteristics of prognostics.

The third direction is aimed to a distribution and a transfer of predictive tool results to industry. This direction cannot be develop without a clear understanding of their expectations.

Implementation of the prediction is based on the assessment of the current state of the fuel cell, which is quantitatively determined by various parameters (descriptors). Therefore, obtaining these descriptors thanks to methods that are not disturbing operation of the fuel cell, is critical. Generation of descriptors refers to the tasks of diagnosis, there are various approaches, which are discussed below. Thereby, the main objective of the thesis is to obtain statistical descriptors using electrochemical noise diagnostic.

This part presents traditional methods using for diagnosis and prediction of the PEMFC technical state. Methods are presented in the followed list: structural techniques and chemical analysis, direct recording of physical parameters, current-voltage and impedance measurements, current interruption method and water balance.

2.3 Structural techniques and chemical analysis

Imaging and spectroscopic techniques are widely used to characterize the composition and chemical state of fuel cell components. In this section, we mention some of them[41, 53]:

- Scanning electron microscopy (SEM) and transmission electron microscopy (TEM), which are used to characterize materials on a micron and nanoscale, respectively. SEM is commonly used to analyze the pore structure in the GDL as well as membrane and electrode structure in cross-section [54]. TEM is also used for research of the particle size and distribution of the electrocatalyst on the carbon support;
- X-ray diffraction (XRD) is used to examine the crystalline materials, such as the electrocatalyst and the membrane structure in PEM fuel cells. This method is based on the diffraction of electromagnetic X-rays radiation, which are comparable to the interatomic spacing.

- X-ray photoelectron spectroscopy (XPS) and energy dispersive X-ray spectroscopy (EDX), generate energy signature obtained from the energy of photoelectrons ejected from the sample for XPS whereas for EDX, operating in the opposite to XPS mode, being used the energy of X-rays, emitted when an electron beam impinges on the surface sample;
- X-ray absorption spectroscopy (XAS) is based on measuring of energy of transmitted beam received from incident of X-ray beam on the sample and forming function of transmitted energy from incident beam;
- Secondary ion mass spectrometry (SIMS) which detects secondary ions emitted from the surface by mass spectrometry whereas a primary ion beam bombard sample surface. If the mass spectrometer is configured for detection of a certain element, a depth profile may be obtained as the sputtering time is increasing, what allows us to investigate chemical state of fuel cell materials for further detection of chemical degradation in fuel cell components in long term tests.

Implementation of these techniques requires strict monitoring or adaptation of the operation state and components of PEMFC and using complex measurement equipment. Some techniques require full destruction of the fuel cell assembly.

2.4 In-situ measuring of physical parameters (direct descriptors)

Different types of sensors are usually integrated in a PEMFC stack for the full control of it. These sensors provide information to diagnose the fuel cell state and for further prognostic of the remaining useful life (RUL). Commonly, the typical test benches are equipped with sensors for temperature, pressure, humidity, flow rate measurements. Nowadays, the main information is generated with the help of the voltage measurements of the whole stack and/or certain cell of the stack (in galvanostatic mode of operation). We want to note that the typical data acquisition frequency is 1 Hz. The diagram of a PEMFC stack equipped by different sensors is presented in Fig. 4.1.

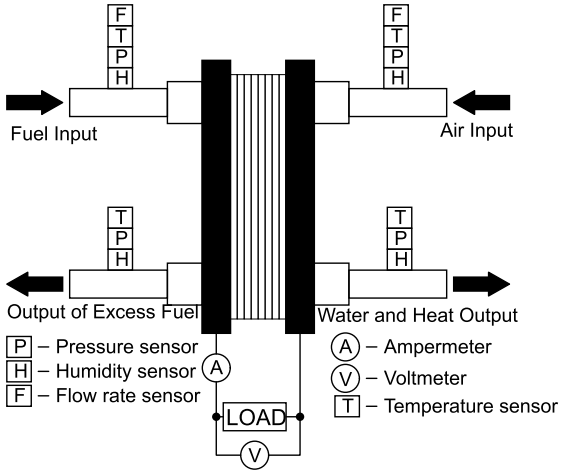

Figure 2.3 – Acquisition of thermo-physical parameters for generating direct descriptors

In Fig. 2.4a some measured physical parameters are presented and obtained thanks to sensors

integrated in a CEA stack in the framework of ANR PROPICE project in Belfort. In this case the test is performed when current I is equal to 170A in the normal operating conditions. In the sequel on the basis of these obtained data, it is possible to generate a descriptor database. Mean value of physical parameter measured by each sensor may be considered as a "direct" descriptor. The temporal evolution of these descriptors gives the possibility of a RUL prognostic. However, calculation of mean value of parameter, which is changed over time, is an nontrivial problem. Indeed, the existence of random fluctuations, drift and/or low-frequency of quasi-periodic components highlights a problem of the correct choice of time windows for the calculation of the mean value. It is clearly demonstrated on Fig. 2.4b, where the number of point (m = 5, 10, 20 and 40) corresponding to the number of intervals on which mean value is calculated, that the size of time windows impact the results. Some methods for calculation of mean value will be described further.

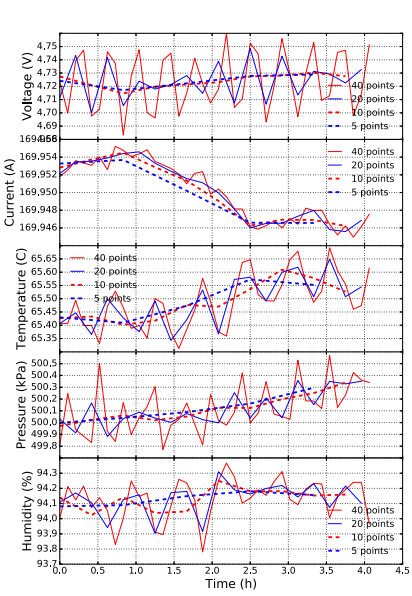

(a) raw recordings

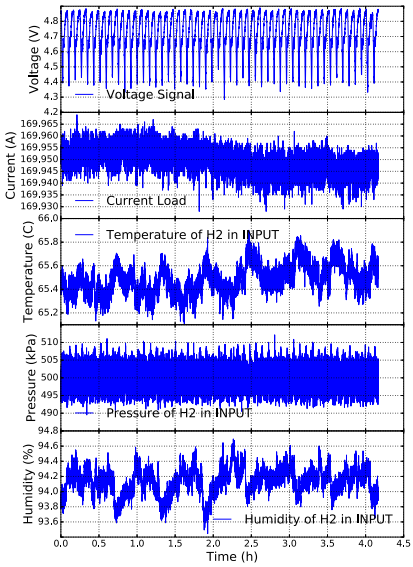

(b) Calculation of average values with different temporal windows

Figure 2.4 – Acquisition of thermo-physical parameters for generation of direct descriptors.

Most of the research works use the mean value of the stack voltage and/or monocellules voltage to calculate the stack power and obtain a base of values for RUL prognosis[55–58]. However, there are some approaches in which the recording of other physical parameters is being used, such as, for example, the pressure [59]. Obviously, an increasing of the number of sensors and, due to that, a direct availability of descriptors, improves the robustness of the prognosis methods. However, in this case the problem of system cost arises. A compromise between the efficiency of the prognosis and the price of the system remains important.

2.5 Electrochemical methods

The generation of descriptors by direct measurements of physical parameters is the most effective method for industrial applications. However, these descriptors are non relevant to give information about the physical phenomena that govern the state of health of the system and determine its remaining useful life. In this section, we present methods allowing generation of descriptors for this purpose. However, these methods require the stop or perturbation of system operation as well as a sophisticated instrumentation.

2.5.1 Current – voltage curve (polarization curve)

The current-voltage curve also known as a polarization curve, is the main characteristic of the performance of electrochemical systems. Fig. 2.5 presenta an example of current-voltage curve which has been measured in the framework of the ANR PROPICE project in Belfort. Polarization curve allows to characterize the influence of operating condition such as flow rate, temperature, and relative humidity of the reactants on the losses of system performance and to interpret these losses in terms of governing electrochemical parameters[60]. It can be noticed from Fig. 2.5 that polarization curve can be divided into three specific sections responsible for different effects[9]:

- kinetic zone ("activation polarization");
- ohmic zone ("ohmic polarization");
- effects related to mass transport limitations ("concentration polarization").

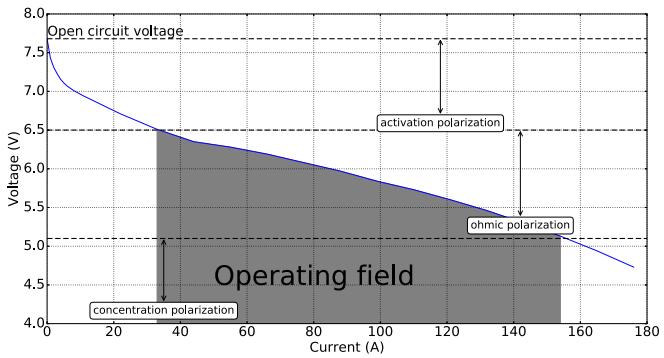

Figure 2.5 – current-voltage curve of the stack. The measurements are performed after stopping of the stack.

There are several methods for interpretation of the current-voltage curves [9], all of them need the usage of some semi-empirical equations describing the governing electrochemical phenomena, as for example Eq. 2.3:

$$V_{FC} = E_0 - A(ln(I_{FC}) - ln(i_0)) - I_{FC} \cdot R_M - \frac{R \cdot T}{2 \cdot F} ln(1 - \frac{I_{FC}}{i_{lim}}) \tag{2.3}$$

where: V_{FC} - FC operating potential (V); I_{FC} - FC electrical current (A);
E_0 - open circuit voltage (V);
R_M - ohmic resistance of fuel cell (Ohm);
T - fuel cell temperature (K); R - universal gas constant (8.314 $J \cdot mol^{-1} K^{-1}$);
F - Faraday constant (96485 $C \cdot mol^{-1}$);

i_0 - exchange current (A);
A - kinetic parameter of electrochemical reaction;
i_{lim} - limiting current (A).

Using the fitting of Eq. 2.3 with experimental polarization curve (Fig. 2.5) it is possible to determine different electrochemical parameters of the system (R_M ,i_0,A,i_{lim}, etc.). Each parameter can be considered as a descriptor for the prediction of the PEMFC technical state.

Also, it has been shown [9] that effect of hysteresis takes place in polarization curve measurements. It can be clearly observed in Fig. 2.6. It is supposed that this effect is caused by excess or insufficient humidification of MEA.

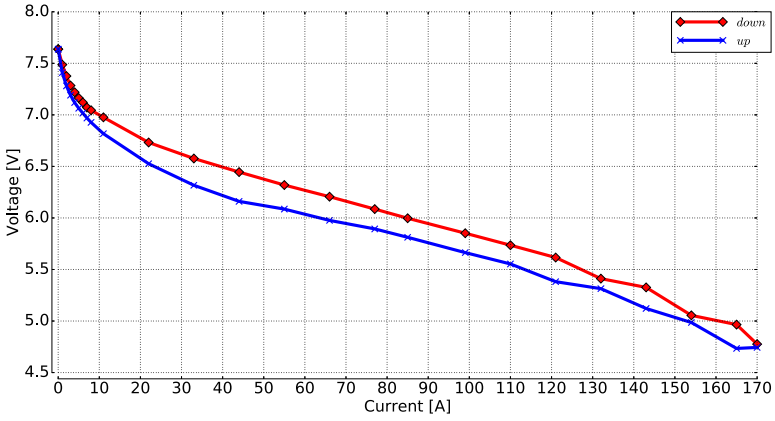

Figure 2.6 – Hysteresis of polarization curves measurement

In spite of advantages, that were mentioned above, the polarization curve has a number of disadvantages that limits their wide utilization in practical applications. Firstly, perturbation of FC normal operation is required. Secondly, there are some difficulties related with interpretation of results. For example, flooding and drying inside a fuel cell cannot be distinguished by a single polarization curve[60]. Finally, difficulties with using rather sophisticated instrumentation.

2.5.2 Impedance spectroscopy

Electrochemical impedance spectroscopy (EIS) is another method which is widely used for characterization of electrochemical systems. EIS is based on applying small AC voltage or current signal to the cell for further measuring the amplitude and phase of the resulting signal as a function of frequencies.

$$Z(jw) = \frac{V_{\mathrm{FC}} jw}{I_{\mathrm{FC}} jw}, \tag{2.4}$$

where w is the excitation frequency (Hz). EIS of fuel cells has been used [60, 61] for:

1. studying oxygen reduction reaction (ORR) mechanism;
2. characterization of transport (diffusion) losses;
3. evaluation of FC ohmic losses, charge transfer resistance and double-layer capacitance.

Example of measurements of electrochemical impedance, which was carried out in the framework of the ANR PROPICE project is presented in Fig. 2.7. Interpretation of impedance measurements is based usually in using of appropriate equivalent circuit (EC), one example

is given on Fig. 2.8. Fitting experimental EIS curves by the numerical simulations based on equivalent circuits allows determining different elements of these circuits (charge transfer resistance R_{CT}), the electric double layer capacity (C_{DL}), the ohmic resistance of the cell (R_M), the impedance of Warburg (W), etc). Each of these parameters can be considered as a descriptor for prognosis.

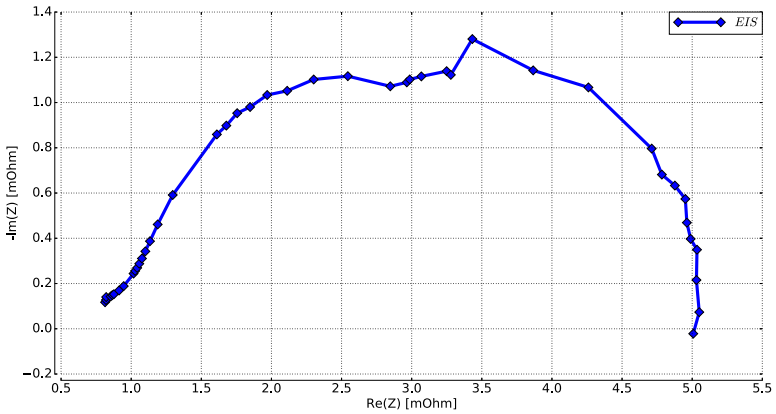

Figure 2.7 – Example of impedance measurements (Nyquist diagram). The tests are performed after stopping of the stack running.

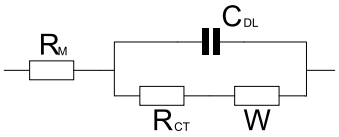

Figure 2.8 – Example of electrical diagram equivalent

However, interpretation of impedance spectra is still difficult, for example, it is complicated to separate contributions related with anode and cathode electrodes[60].

EIS measurements meet the same principal difficulty as the recording of polarization curves: the method needs the stop or perturbation of system running. In addition, EIS requires usage of sophisticated measuring devices, as well as correct recording of impedance spectra is low frequency range that can takes some hours.

2.5.3 Current interruption method

Another method using for characterization of the state of FC is current interruption method. The method of the current interruption (CI) is based on the measurements of the voltage drop due to a step change of the current[60] for a short period (about several milliseconds). Ratio of occurred voltage drop ΔV to the current value I_0 before interruption is associated with MEA electrical resistance R_M.

$$R_M = \frac{\Delta V}{I_0} \tag{2.5}$$

The example of CI measurements performed in the framework of the ANR PROPICE project is presented in Fig. 2.9. This curve allows to determine an effective resistance of the electrochemical source which can be used further as a descriptor.

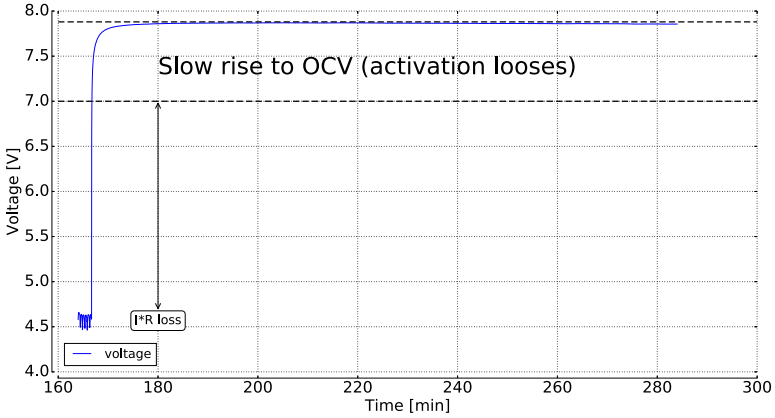

Figure 2.9 – Example of use of the method of interruption of the current. The test under the conditions of a change of the operating regime of the stack

An advantage of the CI technique is related with the usage of an inexpensive equipment.

Implementation of CI measurements requires accurate measurement of time moment of voltage drop ΔV, after which a slow increase of voltage caused by activation losses is observed[60]. Wu et al.[60] have described in details this phenomenon by an equivalent circuit consisting of two resistors and a capacitor, where one of these resistors is responsible for the effective resistance, connected in serial to another one, responsible for the activation losses, that is connected in parallel to a capacity. Rubio et al.[62] successfully applied CI measurement for fuel cell, where in subsequent, have been proposed an equivalent circuit with a procedure for the estimation of all parameters of their model. They applied this methodology for the diagnosis of the cathode flooding phenomenon.

CI method meets the same difficulty as current-voltage and impedance measurements, namely perturbation of operating system.

2.6 Water balance

The principle of the water balance measurement is presented in Fig. 2.10a [63–65]. A mass balance between the input and output channels for the supplied gas allows determines the water fluxes, N_a and N_c, passed through the GDLs at the anode and the cathode side, respectively(Fig. 2.10b).

The water flux density through the anode and cathode GDLs, respectively N^a and N^c, were calculated by knowledge of two water balances between the inlet and the outlet of the anode (n^a_{in} and n^a_{out}) and cathode (n^c_{in} and n^C_{out}) channels, respectively (Eq. 2.6 and Eq. 2.7):

$$N^a = (n^a_{out} - n^a_{in})/S \tag{2.6}$$

$$N^c = (n^c_{out} - n^c_{in})/S \tag{2.7}$$

Here S is the active area of the MEA. N^a, and N^c are linked between each other through the water flux flowing through the membrane (M) denoted as N^m that is equal to N^a, (see Eq. 2.8)

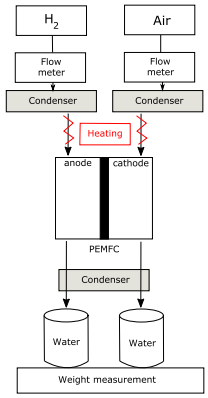

(a) Principle schema of water balance method

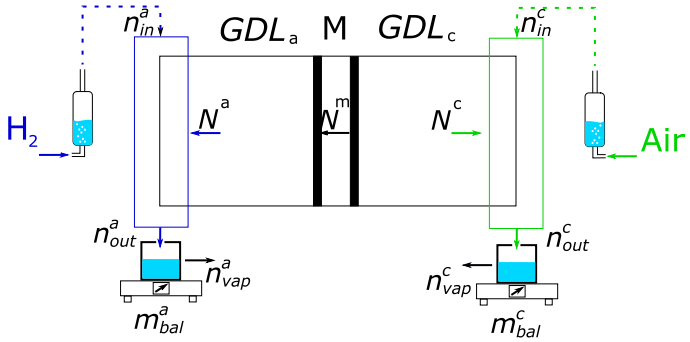

(b)

Figure 2.10 – Water balance: a - schema of experimental setup, b - Directions of water flux

and the water production at the cathode denoted as N^{prod} (see Eq. 2.9)

$$N^a = N^m \tag{2.8}$$

$$N^{prod} = N^m + N^c \tag{2.9}$$

where N^{prod} is the amount of water produced by the oxygen reduction reaction which is a function of the current density.

Figure 2.11 shows the variation of N^a and N^c as a function from the current density j.

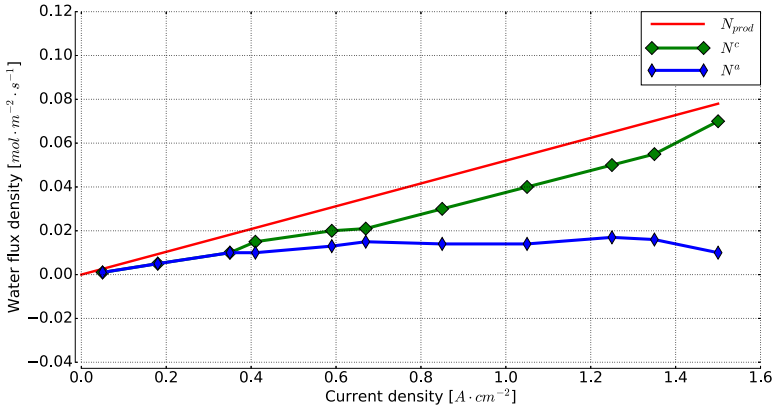

Figure 2.11 – Example of measurement of the water balance:water fluxes measured at the anode and at the cathode

Applying the water balance allows to determine the water flux, N^a, and N^c, to determine what coefficient dominate in this time, and thereby to make diagnosis technical state of MEA (flooding or drying state). Further, each of these parameters can be considered as a descriptor for diagnosis and prognosis.

The water balance method needs complicated instrumentation and is not well adapted for transient regimes and industrial applications.

2.7 Conclusion

In the context of implementation of prognostics, the available diagnostic methods can be divided into three classes:

- destructive
- non-destructive, but invasive to a normal operation of the fuel cell
- passive (non-destructive and noninvasive methods)

It is clear that from the point of view to build up a prognostics system, only passive methods are relevant to monitor industrial objects. At the same time, tool management of relevant prognostic systems should not be expensive and bulky (e.g. water balance). The value of destructive and invasive methods consists in accumulation of information, allowing to make interpretation of the results obtained with the sue of passive methods.

The main goal of this thesis is the development of a passive method for fuel cell diagnostics. The instrumentation base which is developed in this work is not much more complicated in comparison with traditional techniques of direct recording of physical parameters (direct descriptors). However, in spite of registration of the average values and their slowly changing trend, we offer to register high frequency fluctuations of the physical parameters, namely, noise.

Complication of the hardware is mainly connected with an "in-situ storage" of big data and their statistical treatment. This task can be successfully solved by using a PC and appropriate software without significant increase of cost of the system. On the other hand, on this basis, it is possible to generate a very large quantity of statistical descriptors, thereby extending the prognostic and ability of fuel cells.

More information will be given in next chapter.

Chapter 3

Electrochemical noise analysis apply to fuel cells diagnostic

Contents

Figures

3.1 Noise of physical systems

Random behaviors of signals, also known as noise, reflects character of physical systems. Measurements of noise characteristics can be used to understand the physical processes, diagnostic system's structure and prediction of its evolution. Nowadays we can distinguish several types of noise sources[66–68]:

- thermal noise;
- shot noise;
- generation-recombination noise;
- flicker noise;
- popcorn noise;

Some of them will be briefly considered below using power spectral density (PSD) for identification of the noise type. Concerning the shape of PSD, noise can be divided into two classes: white and pink noises. White noise, that includes thermal and shot noise, is characterized by a uniform spectral density with the same energy of the noise signal at any given frequency band. Whereas pink noise is characterized by spectral density that increases with decreasing of frequency. Flicker noise and noise caused by random jumps of current (popcorn noise) are examples of pink noise.

3.1.1 Thermal noise

John Bertrand Johnson has discovered this type of noise in 1928[69]. During experiments, he observed spontaneous motion of the electricity in a conducting material at thermodynamic equilibrium. Heat motion of the atoms induces fluctuations of electric potential. The same year, Harry Nyquist explains the results of the Johnson who worked at the same laboratory, Bell Labs[70]. He found out that the mean-square potential fluctuations over the conductor are proportional to the electrical resistance and to the absolute temperature of the conductor. This

type of noise does not depend on the size, shape and conductor nature. In honor of these two scientists, this thermal noise is named Johnson-Nyquist noise.

The noise power spectral density $S_V(f)$ ($A^2\,Hz^{-1}$) of the thermal noise is given by Eq. 3.1. Thermal noise is a white noise, PSD is uniform with frequency (Fig. 3.1).

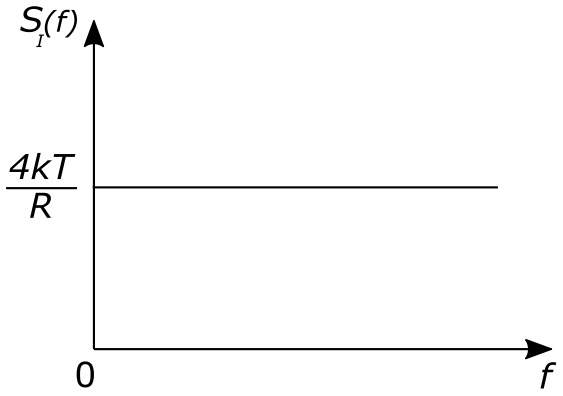

Figure 3.1 – Power spectral density of thermal noise

$$S_V(f) = 4\mathrm{KTR} \tag{3.1}$$

where R is an electrical resistance of observed object(Ω), k is Boltzmann constant that equal to $1.38 \times 10^{-23}\,J\,K^{-1}$, T is absolute temperature (K). As can be seen from this equation, for minimization of the influence of thermal noise it is necessary to decrease the temperature of the object. In the case of a well-known resistance value, it is possible to determine local temperature of the observed object using noise measurements[71].

3.1.2 Shot noise

Shot noise, also known as Schottky noise ,is related to the corpuscular nature of the electrical charge carriers and can be observed when electrical current causes collective movement of the electrical charge carriers to overcome some potential barrier. Mostly, it can be encountered in semiconductor devices. Shot noise is generated due to the fact that the flow of electrical charge carriers passing through the transition is not continuous. It is formed by electrons, the arrival time of which is a random variable, what leads to appearance of the shot noise. In fact, constant current I_0 flowing through p-n junction that we see on a macroscopic level, represents the sum of many microscopic random impulses of current[71]. Thereby, shot noise has Gaussian uniform spectral density (white noise) caused by variations of current, level of which increases with current. PSD of shot noise does not depend on a frequency. Example of this PSD is presented on Fig. 3.2, that is expressed by Eq. 3.2.

$$S_I(f) = 2\mathrm{q}I_0 \tag{3.2}$$

where I_0 is a constant current flowing through the barrier (A), q = 1.6×10^{-19} C is an electron charge.

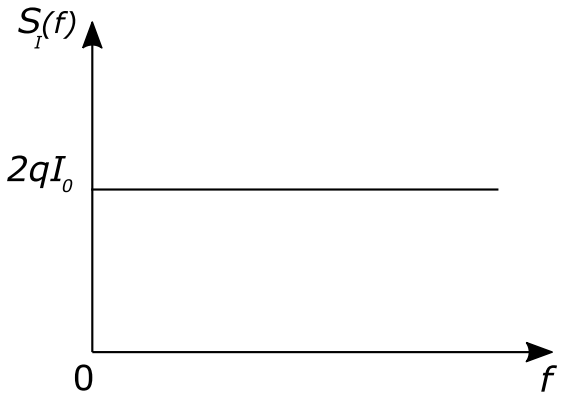

Figure 3.2 – Power spectral density of shot noise

3.1.3 Flicker noise

In this well-understood field of noise research, with agreement between experiment and theory almost everywhere, there is one notorious exception: $1/f$ noise. Flicker noise a spontaneous fluctuation in electrical conductance which dominates other types of noises at low frequencies , let us say below 1 kHz, in many electronic devices. For higher frequencies flicker noise at the background of white noise, since its spectral density is inversely proportional to the frequency. Mostly, $1/f$ noise is generated by semiconductors devices. Till now there is no accepted theory explaining the appearance of this phenomena. However, Hooge et al. partially explained this phenomena [66]. Power Spectrum Density of flicker noise is expressed by the empirical Hooge formula(Eq. 3.3):

$$S_I(f) = \frac{\alpha_H I_0^2}{Nf} \tag{3.3}$$

where I_0 is a current flowing through the investigated object (A), N is a number of independent charge carriers and α_H is Hooge parameter. Hooge found that this ratio is quasi-constant $\alpha_H = 5 \times 10^{-3}$, which suggests that the flicker noise caused by a fundamental mechanism of unknown origin[66]. Example of PSD is presented in Fig. 3.3.

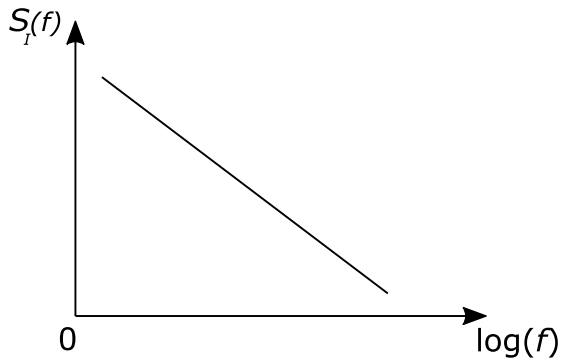

Figure 3.3 – Power spectral density of the flicker noise

The frequency in which the intensity of the flicker noise begins to exceed the intensity of white noise is named the corner frequency, that generally is in the range 0.1 Hz … 1 kHz and varies depending on the sources of noise. There are two type of flicker noise that spectra are described by the $1/f^{\gamma}$:

- the equilibrium flicker noise (EFN);
- non-equilibrium flicker noise (NEFN).

EFN is characterized by equilibrium processes in the object and does not depend on the current flowing through the object, its γ parameter in this case is the near one. Quite the contrary happens with the non-equilibrium flicker noise, where the mechanism of occurrence is directly linked to the current flowing through the object or other external influence, for this case its parameter γ can has values more than $\gamma \geq 2$. Du et al.[72] suggested a new technique of separation $1/f$ noise from the thermal noise. In comparison with the white noise, current value of which is independent on previous values, the flicker noise has its own memory.

3.1.4 Popcorn noise

This type of noise is caused by random jumps of the current, also known as burst noise, with constant amplitude. Most often this type of noise occurs in bipolar transistors caused by the contamination of semiconductor materials by ions of heavy metals. That is why this noise has been named like popcorn noise due to "clicks" produced in the dynamics. These clicks are random with a frequency below 100 Hz and are characterized by discrete amplitude and duration of 1 ms to 1 s. Power spectral density of popcorn noise increases with decreasing frequency and is expressed by Eq. 3.4

$$S_I(f) = \frac{2\Delta I^2/\nu}{1 + (\pi f/\nu)^2} \tag{3.4}$$

where ΔI is the fluctuations amplitude (A), ν is the average quantity of junctions from one level to another one during 1 s. Example of popcorn noise is given in Fig. 3.4, that looks like as large, low frequency, long duration of current jumps.

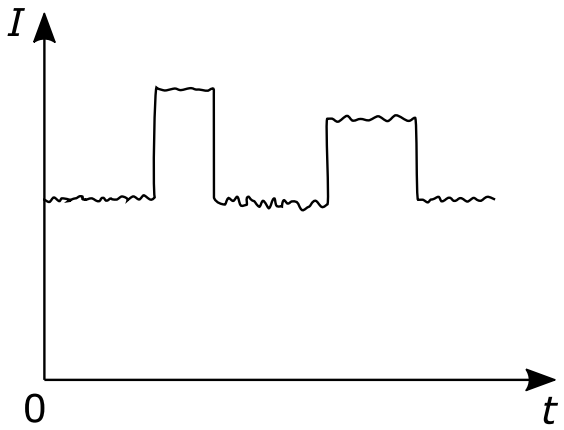

Figure 3.4 – Example of the popcorn noise

3.1.5 Electrochemical noise

As was mentioned above, all of energy sources produce electric noise, and electrochemical energy sources, such as the PEMFCs, are not an exception. Noise that is produced by these systems is named electrochemical noise (EN) and is defined as the spontaneous fluctuations of potential and/or current caused by electrochemical processes within PEMFCs[73].

In recent times, methods of diagnosis based on EN measurements have been used widely for studying of various phenomena such as turbulent mass transport[74–78], particle impact[79], investigation of metal films and electrode corrosion[80, 81], estimation of charge level and detection of overcharging of electrochemical batteries [82, 83]. These works showed that electric noise reflect physical processes occurring in the object and can be used for studying these processes and diagnostics of the system state.

EN was employed to investigate PEM single cell under various operating conditions at different humidification levels with respect to study flooding or drying tendencies[68, 84]. EN is sensitive to changes in the PEMFC operating conditions, the electrochemical noise increases during the drying of the fuel cell and increases with the current level. Moreover, its PSDs seem to be sensitive to changes in the water production inside the cell[18, 68, 84, 85]. Tan et al. [86] used the EN to investigate real-time performances of a glucose biofuel cells. Implementation of EN does not obtain wide utilization for diagnostic of batteries, although EN have been adapted for investigation of fuel cells. One of the reason is the decrease of EN amplitude with the increase of active surface area[74]. Usually EN measurements concern low frequency range. For example, Cottis[79] noticed that a lot of experiment with noise measurement was implemented typically in the range of 10^{-3} Hz to 1 Hz. There is an important limitation of EN diagnostic because the information about high frequency processes will be lost. In present work we shall extend noise measurements to high frequency domain also.

3.2 Data acquisition of electrochemical noise

As was described above, noise measurement contains a lot of information about investigated object allowing to make a diagnosis more precisely. Concerning PEMFC, this technique of diagnosis is not fully developed. Usually, test benches for PEMFC experiments have a sensors that measure signals with sampling frequency in the range of 1 Hz. In this way only low internal noise can be measured.

For these reasons in this chapter, a focus will be done on electrochemical noise including high frequency range and generation of descriptors obtained by statistic methods. The main advantages of the noise measurements are its non-intrusiveness, rapidity and its high informatively. Of course there are several barriers limiting today this method for a wide usage . Firstly, it is the difficulties of measurement of very low-level noise signals (for example, noise from Li-ion battery with a range of nanovolt). Secondly, it is the non-stationary of signals that requires a complex technique of measurements (for example, usage of analog filtration without impact on the filtered signal). Thirdly, noise measurements require a large set of data to have a good statistics for low-frequency analysis. Fourthly, it is a limited theoretical background. Therefore, new development of instrumentation and methodology for EN diagnostic is needed. The utilization of traditional methods of PEMFC diagnostic usually perturbate the system and requires complex equipment.

3.2.1 Instrumentation for noise measurement

The goal of the present work is the usage of statistical descriptors obtained thanks to EN measurements. Development of instrumentation for noise measurements meets some problems, namely:

- the weakness of the signal level
- a collection of large statistics at high sampling frequency (Big Data)
- Nonstationary of signals

The distinct benefit of statistical descriptors lies in the possibility of using simple equipment without perturbation of the system running. Sensors configuration previously used for the generation of the direct descriptors is sufficient. Initial information is obtained by simple sensor, for example by measurement of the voltage of the stack and/or single cells. However, this initial raw data are used not only for detection of the mean value, but also for extraction the fluctuations of the recorded signal. Fluctuated component of signal can be performed by another method (for example, analog filtration). Usually signal processing filtration is used to obtain the high frequency part of the signal with subsequent processing. However, usage analog filters influence the signal, and reduce useful information (high pass filter role). Moreover, due to the complexity of the signal (drift, non stationary), there are limitations on the use of filters. This is why, in the present work, we use an equipment to measure directly the raw signal. Sure, this way meets some barrier. One of them is accuracy, because it is complicated to build the system that can measure signal with very high resolution (high digits and bits, low noise of equipment, high sampling, anti-aliasing filter). Everything depends on applications. In our case, the required resolution can be achieved using DAQ 9239 developed by National Instruments (NI) with characteristic of 4 channels +-10 V, 24 bits, sample rate of 50 kHz, anti-aliasing filter.

As was said before, most of fuel cell systems use a sampling frequency about 1 Hz for data measurements. It can be explained by difficulties related with data transportation and storage if measurements are on a lot of parameters during long time period. Voltage was chosen as a raw signal of PEMFC because it is easy to measure this parameter without any perturbations of the system. Sample frequency of measurements has been selected on 50 kHz. Huge problem for using this high sample frequency is data storage (billions of points - Tera octets data). Measurement system was implemented on LabView software from NI. All 3 minutes, measured data are recorded and directly saved in hard drive using for every file special HDF format that is used for storage of huge information. In parallel, each hour another program analyzed folder for presenting old files older than 3 hours. If this folder is presented it means last file was older than 3 hours, all files were transformed and transferred to an external hard drive, thereby we restore new place for saving in computer hard drive. During first experiments and analysis on obtained data, we conclude that the use of this high sample frequency is not necessary, and in subsequent we decrease the sample frequency at 2 kHz. The use of 2 kHz allows us to record data of 4 channels each 15 minutes, that also allow us to use this long signal to implement other diagnostic methods (frequency or tempo-frequency domains). Then, statistics descriptors will be generated by analysis of the signal (voltage) fluctuations ("noise analysis"). Experimental setup is presented in Fig. 3.5 wherein DAQ acquisition, laptop and fuel cell bench from FCLab are presented.

3.3 Methodology of signal processing for detrending

Noise measurement allows to create a good basis for further researches in non-invasive on-line diagnosis and prognosis field. However, as was mentioned above, there is difficulty with shape of signal that requires complex techniques to prepare it for further signal processing. In this

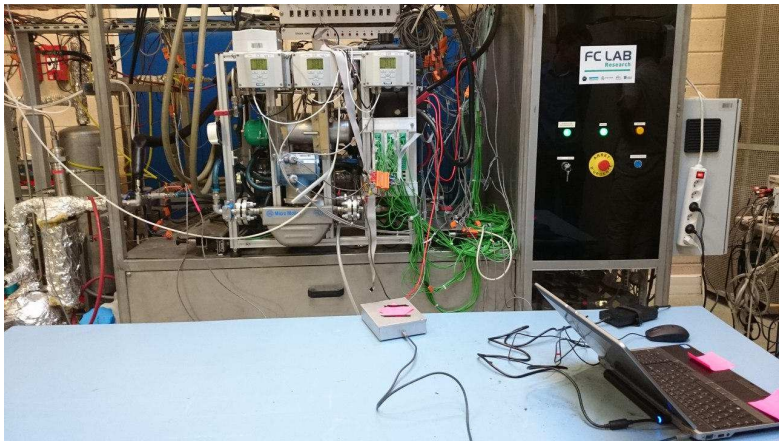

Figure 3.5 – Experimental setup

work, fluctuations of current and voltage (electrical fluctuations) have been observed. Typical signals from PEMFC are presented on Fig. 3.6. Signals can have different structures. Some of them have low amplitude Fig. 3.6 a, others have significantly low-frequent quasi-periodic component Fig. 3.6 b. Moreover, signals could have slow alteration of the system under study during experiment. Indeed, working with DC signal also can create some difficulties with EN analyzing.

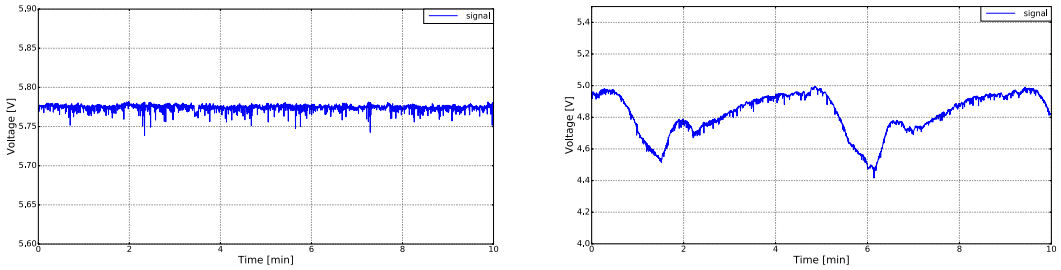

(a) Voltage measuremnts without low-frequency component

(b) Voltage measurements with quasi-periodic structure

Figure 3.6 – Evolution of voltage signal for 10 min

The diagnosis and prognosis of a PEMFC is commonly based on the temporal evolution of a descriptor. This implies a main problem when we want to use descriptors from temporal fluctuations ("noise"). Indeed, it is no longer possible to assume that the signal is stationary. Therefore, it is necessary to perform the extraction of the fluctuations taking into account the evolution with time of the average value. For this reason, the DC drift in measured signal should be removed before the analysis of EN data. Therefore, it is required special techniques to emphasize fluctuation component. Fluctuation signal in potential-time record can be deduced as following Eq. 3.5

$$U_{\text{noise}} = U - \overline{U} \tag{3.5}$$

However, we must take into account complexity of the signal and its non-stationarity for

selecting techniques for detrending the mean component. Accordingly, how to effectively extract $\overline{U}$ and deduct from raw data to obtain necessary signal U_{noise} is still a challenging task and is not a trivial issue. If its average value on specific time windows is not removed perfectly, error in EN analysis may be appeared and can be expressed by an increase of the low frequency value in the power spectral density (PSD). AC signal can be obtained by hardware filtration or by mathematical techniques (see Fig. 3.7). Electrical circuit of high pass filter can be selected for hardware filtration but impact of this analogical filter need to be take in account. However, in this case, the choice was made to work with the DC signal, because implementation of hardware filtration can modify original nature our signal. Concerning digital filter, it is also influence on signal nature.

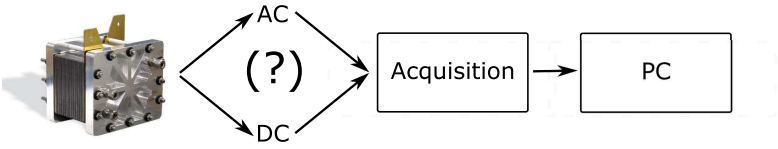

Figure 3.7 – Diagram of acquisition of raw data

Therefore, set of techniques for detrending signal will be considered with their advantages and disadvantages.

3.3.1 Detrending procedures

There are a lot of methods to remove trend in complex signal, but Xia et al.[73] distinguished some of them for an optimal trend removing technique:

1. Average Trend Removal (ATR);
2. Liner Trend Removal;
3. Polynominal Trend Removal;
4. Wavelet Analysis;
5. Empirical Mode Decomposition.

Moreover, it can be add another good method named structure function, that is suggested by Kolmogorov[87, 88]. Further we will briefly investigate average trend removal thanks to moving average procedure, polynomial trend removal, use of structure function as well as emphasize theirs advantages and disadvantages.

One method is the Average Trend Removal, which is based on the usage of a sliding window ("moving average"). The average value ATR(t) of the signal fluctuating $x(t)$ is calculated by the Eq. 3.6:

$$ATR(t' = t + \frac{N}{2}) = \frac{2}{N} X \sum_{i=0}^{\frac{N}{2}-1} x_{t'-i} + \frac{2}{N} X \sum_{i=\frac{N}{2}}^{N-1} x_{t'+i} \tag{3.6}$$

After that, it is possible to extract the fluctuations of the signal from raw data by Eq. 3.7:

$$x'(t) = x(t) - ATR(t) \tag{3.7}$$

In general, ATR refers to a low-pass filtering method. The time length of many electrochemical processes is longer than 4 s, e.g. metastable pitting is about 5–7 s, diffusion process is about 32–64 s[89], that is require minimum quantity of points (p) that is determine as Eq. 3.8:

$$p = 32/dt \tag{3.8}$$

where dt is the time interval during sampling. Xia and Bertocci in their works [73, 89] concluded that ATR is not suitable for DC removal cause estimating non-uniform drift on longer times is impossible and has an affect on PSD.

Another method is based on Polynomial fitting procedure using the following model expressed by Eq. 3.9:

$$x(t) = a_0 + a_1 t + a_2 t^2 + \ldots + + a_n t^n \tag{3.9}$$

where a_n are the coefficients and n defines the polynomial order.

Bertocci [89] applied a lot of procedures for drift removal procedure and analyzed their effect on electronic and electrochemical signals. The results showed that the best technique appears to be is the polynomial detrending. Simplicity of application gives big advantage for wide range of application. When the drift is flat, linear detrending can also give satisfactory results, wherein order of polynomial is 1. However, if the polynomial is of order 5 or higher, the method can successfully suppress any low frequency component, whether the drift is linear or not. It is necessary to understand a physical meaning of each polynomial order, because using highest order can give the risk eliminating useful information.

Then, use of structure function can be considered. Structure function can be applied both for raw and filtered data. Structure function is a mathematical tool allowing to identify structure called coherent in turbulence chaos[87, 88]. In general case, structure function described by following expression:

$$S(\tau) = x(t+\tau) - x(t), \tag{3.10}$$

where x is observed signal, tau is the time shift. Thus, structure function acts as a filter role. With this technique, it is possible to use filtered data for further signal processing.

Thereby, it is required to make a new methodology of detrending signal that is allow to work with non-stationary complex signal and with no affect on PSD.

3.3.2 Detrending procedure by short-term analysis

Detrending procedures by short-term analysis had been suggested by Martemianov et al.[83], but modified for our needs. For signal processing, the total time domain have been divided into pieces with specific chosen duration and a special procedure for the extraction of the noise fluctuations have been performed. Figure 3.8 shows investigated signal (a) with its splitting (b) and the extracted voltage fluctuations for one piece (c). The procedure for the extraction of the noise fluctuations is the following: each of the splitted pieces being approximated by a n-order polynomial, and the signal fluctuations are being calculated with respect to the mean value determined by this polynomial. Total determined signal is obtained by concatenating of all fluctuated components from splitted pieces.

Influence time window and order of polynom on detrended signal Figure 3.9 illustrates the results of the signal processing when the different order (n) and time window (timeWin) are used as parameters for detrended procedures. It is clear that the polynomial procedure using an order higher than 3 is more efficient than mean (order is 0) and linear (order is 1) polynomial for fitting. For this reason, the high-order polynomials have been used for the fitting of the mean signal value. Moreover, it can be seen from Figure 3.9 a that for high-order polynomials (n=3, 5, 7), the results are not sensitive to the mathematical statistical parameters. For the following, the data processing has been performed using n=5 and timeWin=8s to extract the voltage fluctuations.

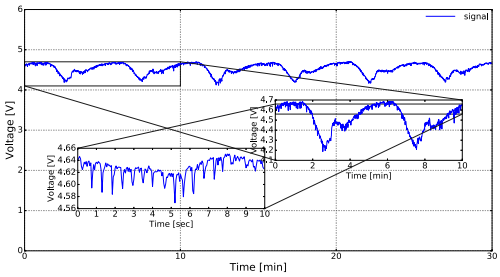

(a) Example of analyzed signal

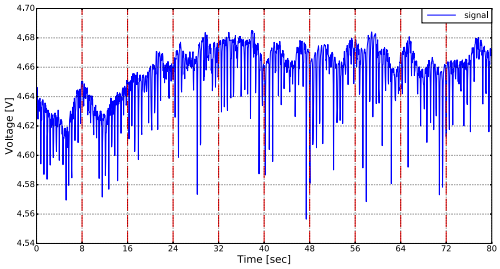

(b) Splitting the signal into 8 seconds

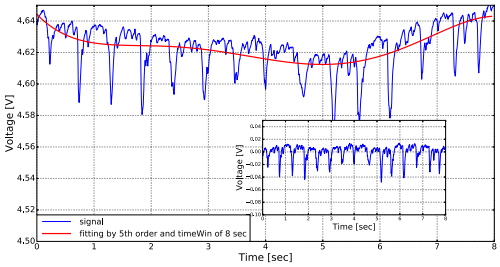

(c) Original and detrended signal during 8 seconds

Figure 3.8 – Detrending procedure (short-term analyzing)

3.3.3 Comparison of detrending procedures

Generally, DC drift in raw data is always nonlinear, so it is impossible to effectively remove the drift using linear detrended procedure because it cause some error in results, so it is not suitable for DC removal. Concerning polynomial, ATR, and digital filter signal after DC removal: they are similar. However, if the polynomial is of order 5 or higher, it can easily suppress any low frequency component, whether the drift is linear or not. Thereby it can cause a problem of to understand the physical meaning for each polynomial power, results become unclear, and sometimes it will result a risk of eliminating useful information[73]. Moreover, there are two other possible methods for achieving good DC removing: first is the digital filtering after acquiring the time series, and second is to use an analog filter in real time. Nowadays, it is possible to apply HP filtering in real time, but it's better to apply when you have a whole time record. There are a lot of papers concerning digital filtering, and no attempt will be made to summarize them. In our case, Butterworth filter with 5th order can be selected for DC removing. Depending on time window in which mean value is calculated, different noise signal can be obtained. Results comparison of different methods implementation of DC removing is presented in Fig.3.10.

Statistical parameters of detrended signal(see Table. 3.1) chosen as parameters for comparison. However, these descriptor are not well suited for the prognosis as it is difficult to follow the temporal evolution of a histogram. Inside each histogram, the red curve corresponds to histogram of a Gaussian signal with the same value of σ as for signal experimental (green). Detrending procedures by using digital filtration, Moving Average and short-term analyzing procedures showed preliminary the same results with a little bit difference. However, as was explained before with mean and linear detrending we have a opposite results due to complex of signal shape. Signal with polynomial detrended procedure has more left skewed distribution (skewness - -2.4) (Fig. 3.10e) comparatively to a Gaussian distribution where Skewness = 0, see section 3.4.1.

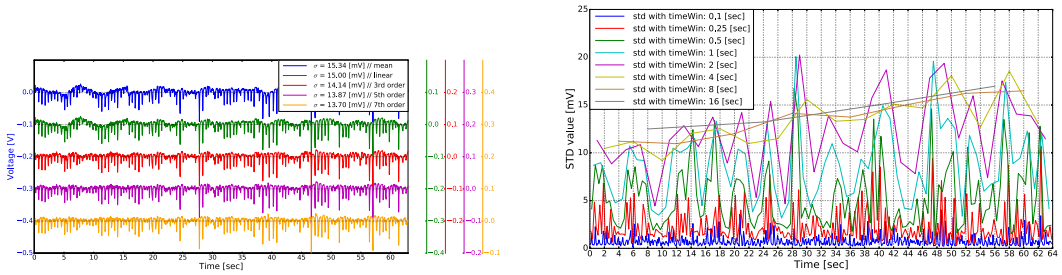

(a) Order of polynom fitting

(b) Time window

Figure 3.9 – Influence time window and order of polynom on detrended signal

It's mean that most values are concentrated on the right of the mean, with extreme values to the left. Also range of kurtosis is near to 10. It's leptokurtic distribution, that's sharper than a normal distribution, with values concentrated around the mean and thicker tails. This means high probability for extreme values. This explains why the shape of the histogram is very different from that of a signal Gaussian with the same value of σ as the signal experimental. In fact, it is possible to easily calculate these descriptors and to follow their temporal evolution.

In our case for detrending procedure, short-term analyzing technique had been chosen because it not depend on stationarity of signal (depends on time window), and also different between orders of 3,5 or higher is not significant, but for good detrending we have chosen a compromise, where power of polynom is 5. Results of preparing signal for their further signal processing can be used for the diagnosis of equipment over time, thereby it is possible to estimate the degree of degradation of the equipment that would allow control of life, changing the device settings.

3.3.4 Conclusion of detrending methodology

This work suggest a methodology of detrending by short-term analyzing with using polynomial fitting that is applied to raw signal, which subsequently can be used on all mathematical base for obtaining descriptors.

The developed data acquisition systems allows performing direct recording and storage of large volume of information provided by primary sensors without any filtering. It makes possible to collect information concerning electrochemical noise of fuel cells with frequency resolution up to 10 kHz. Sure, the data acquisition systems can be coupled with some filters. Nevertheless we prefer to avoid this way because the goal of the study is generation of statistical descriptors for the diagnostic of fuel cells and possibly for prognostic. It means that from the beginnings we should take into account that the signal is not stationary in statistical sense. Using any filter introduce some perturbations which are difficult to take into account when the signal is not stationary and its characteristics slowly vary in time. We prefer to work with non perturbed initial signals and put spec attention on the problem of characterization of non-stationary stochastic signal using differ mathematical methods of data treatment. So in this chapter we defined a mean of the noise, investigated their type of sources and moreover requirements for implementation of noise measurement have been observed. Several techniques for data pre-processing of measuring signal have been observed, and given the first results.

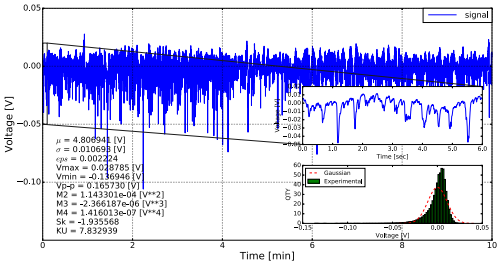

(a) Moving Average (ATR) with time window of 8 sec (linear)

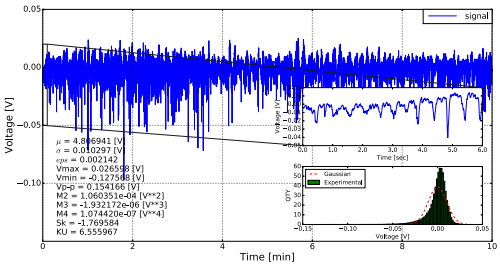

(b) digital filter (5th order, Butterworth)

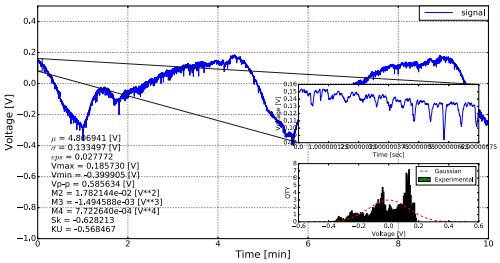

(c) Detrending by mean (polynomial order 0) with time window of 8 sec

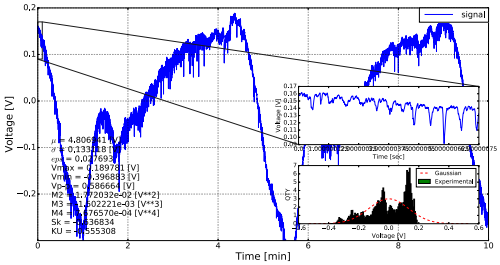

(d) Detrending by linear(polynomial order 1) with time window of 8 sec

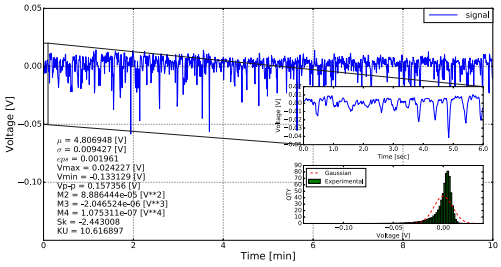

(e) Polynom of 5th order with time window of 8 sec

Figure 3.10 – Noise after implementation of trend removing techniques with histogram

3.4 Mathematical methods for generation of descriptors

After the pretreatment of data for further signal processing, methods of the descriptors generation need to be consider. There are a lot of different methods allowing statistical treatment of stochastic processes, but we consider only some of them. Special attention will be put on the problems related with non-stationary character of the signal. For illustration in this chapter we will use some examples of data recording obtained in our experiments which will be detailed in the next chapters. Methods of descriptor generations can be classified in several groups:

- descriptors in time domain range;
- descriptors in frequency domain range;
- descriptors in time-frequency domain range;
- descriptors obtained by using advanced methods.

More detailed information about these group will be given in the next chapter.

3.4.1 Descriptors in time domain range

This group can include a lot of parameters that can be calculated for observed signal and can be followed after that for its evolution by time. Commonly, standard statistical parameter such as standard deviation, mean is included, as well as higher order moments as skewness and kurtosis, which are characterized the shape of signal. For easiest understanding, it is smarter to use histogram. Descriptors in the time domain depend on the window wherein this parameter had been calculated.

Standard statistic parameters

One of the widespread technique that good for describing observed signal is moments that include a set of generalized statistical parameters derived from signal[79]. Generally, k^{th} moment can be expressed by following equation:

$$\mathrm{k}^{\mathrm{th}} = \frac{\sum_{n=1}^{\mathrm{N}} x(n)^{\mathrm{k}}}{\mathrm{N}} \tag{3.11}$$

where $x(n)^{\mathrm{k}}$ is the n^{th} measured point in set of measurement, and N is the number of experimental measured points in the measurement.

The moment of first order is mean, moment of highest order are related to other statistical parameters such as the variance (for the second moment - σ^2) from which can obtain standard deviation (σ) that is just the square root of variance[79]. However, the higher moments are strong depend on DC component, thereby to eliminate this problem commonly the central moment is used expressing by subtracting the mean from the raw data before calculating in according following Eq. 3.12

$$\mathrm{k}^{\mathrm{th}} = \frac{\sum_{n=1}^{\mathrm{N}} x(n)^{\mathrm{k}}}{\mathrm{N}} \tag{3.12}$$

Thus, mean value is expressed by Eq. 3.13 that can interpreted as direct descriptor.

$$\mu = \mathbb{E}[X] = \frac{1}{N}\sum_{i=1}^{N} x_i \tag{3.13}$$

To evaluate stationarity of signal is difficult task, because from that depending on extraction procedure of fluctuation, i.e. its mean value. To eliminate this difficulties it is required to select

part of signal and consider that in this part signal is stationary but for this we need to take into account quantity of measured data for calculation, thereby to find a compromise. After that calculation of statistic parameters may be performed. The standard deviation σ and the intensity ϵ of fluctuations are expressed by following equations:

$$\sigma = \mathbb{E}\left[(X-\mu)^2\right] = \frac{1}{N}\sum_{i=1}^{N}(x_i-\mu)^2 \tag{3.14}$$

$$\epsilon = \frac{\sigma}{\mu} = \frac{\mathbb{E}\left[(X-\mu)^2\right]}{\mathbb{E}[X]} = \frac{\frac{1}{N}\sum_{i=1}^{N}(x_i-\mu)^2}{\frac{1}{N}\sum_{i=1}^{N}x_i} \tag{3.15}$$

They can be interpreted as descriptors of basic statistics. Generally, for simplification of signal processing, these standard statistical parameters are widely used for analysis signal. In particular, the standard deviation characterizes the energy of the fluctuating signal which of value describes the “amplitude” of a noise signal. This parameter depends on the sampling frequency that is used for measurement. A higher range of frequencies in the measurement cause an increase the standard deviation value. It can be clear observed in power spectrum density which has a direct link with variance[79].

Moments of higher order

In additional to mean value, variance (standard deviation) and epsilon value, the moments of higher order can be used, in particular, the coefficients of asymmetry ("skewness", SK(X)) and coefficients of pointedness ("kurtosis", KU(X))[90].

Skewness Skew (or skewness) also known as coefficients of asymmetry that is derived as the third central moment divided by the cube of the standard deviation (Eq. 3.16). If define that X is a random sequence, then the skewness is derived by following Eq. 3.16:

$$\mathrm{SK(X)} = \mathbb{E}\left[\left(\frac{X-\mu}{\sigma}\right)^3\right] = \frac{E[(X-\mu)^3]}{E[(X-\mu)^2]^{3/2}} = \frac{\mu_3}{\sigma^3} = \frac{\mu_3}{\mu_2^{3/2}} \tag{3.16}$$

On histogram it can be clear to understand degree of coefficient of asymmetry of a random variable statistic. That is to say that if the skewness is positive, the distribution is leaning to the

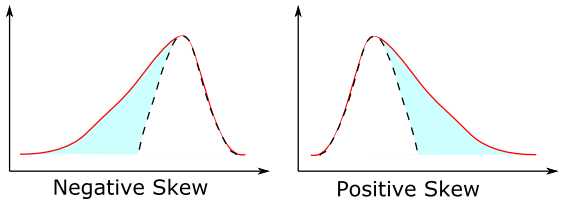

Figure 3.11 – Negative and Positive Skewness Distribution

left and spreading to the right; otherwise, it is leaning to the right and spreading to the left (see Fig. 3.11). Pearson had set an estimate of the skewness non-parametric as $\mathrm{SK(X)} = 3\frac{\mu-\nu}{\sigma}$, with μ the average, σ the standard deviation and ν the median. The median value is the probability value for which the density is divided into two equal areas. For distribution-focused, the median

μ	mean	V
σ	standart deviation	V
eps	epsilon	
V_{max}	Voltage maximum	V
V_{min}	Voltage minimum	V
V_{p-p}	Voltage peal-to-peak	V
M2	Signal Moment of 2nd order	V^2
M3	Signal Moment of 3rdd order	V^3
M4	Signal Moment of 4th order	V^4
Sk	Skewness	
KU	Kurtosis	

Table 3.1 – Description of statistical signs

is the average. This implies that a centered distribution has a skewness of zero. For the normal law, or any other symmetrical distribution, skewness is equal to zero.

Kurtosis KU (or kurtosis) also known as coefficients of pointedness that is derived as the ratio between the centered moment of order 4 and the square of the time centered of order 2. If define that X is a random sequence, then the kurtosis is derived by following Eq. 3.17:

$$\mathrm{KU(X)} = \mathbb{E}\left[\left(\frac{X-\mu}{\sigma}\right)^4\right] = \frac{E[(X-\mu)^4]}{E[(X-\mu)^2]^2} = \frac{\mu_4}{\sigma^2} = \frac{\mu_4}{\mu_2^2} \tag{3.17}$$

Similarly to skewness, coefficient of kurtosis easy to observe on the histogram.

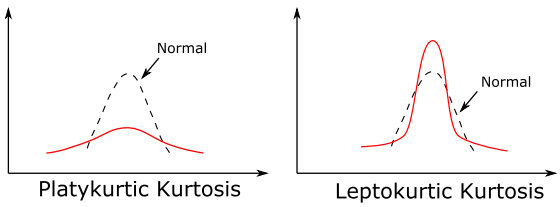

Figure 3.12 – Leptokurtic and Platykurtic Kurtosis Distribution

In case of normal law coefficient of kurtosis equal to 3 that is correspond kurtosis value of Gauss signal. Examples of distribution with high(leptokurtic) and less(platykurtic) kurtosis are presented in Fig. 3.12. The laws of distribution with a sharper peak than the normal have a coefficient of kurtosis is more than 3 and with less sharp peaks is less than 3.

Using structure function

Thanks to the utilization of structure function, it is possible extract information, for example, such as statistical descriptors like the moments of high order(skewness and kurtosis). The Fig. 3.13a and 3.13b illustrate the results of calculation of the coefficients of asymmetry and kurtosis of structure functions.

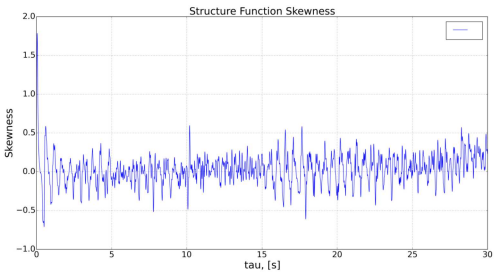

(a) Example of statistical treatment of the noise : skewness of the structure function

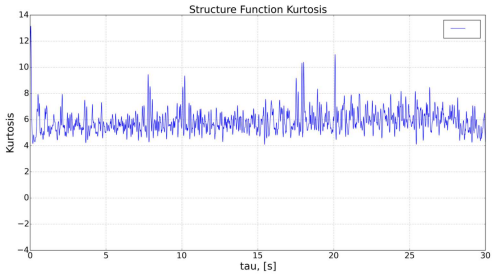

(b) Example of statistical treatment of the noise : the kurtosis of the structure function

Figure 3.13 – Implementation structure function for calculation skewness and kurtosis

As we can see from this results that kurtosis and skewness value do not change significantly depending on the signal shift

Results of implementation

In this section we can observe figures of implementation all methods in Fig.3.14.

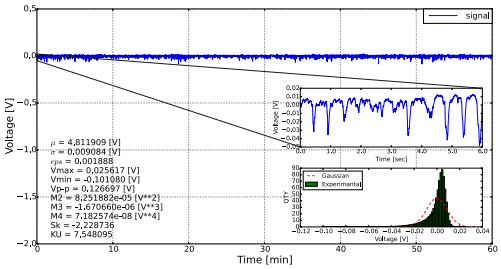

(a) Original signal

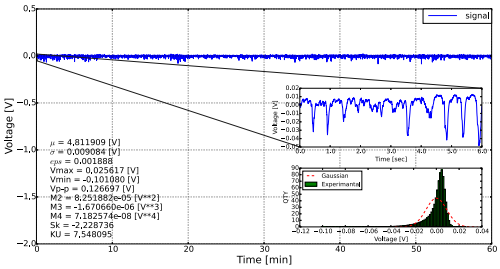

(b) Signal after detrendeding

Figure 3.14 – Signals

3.4.2 Descriptors in frequency domain range

Spectrum is mostly commonly used as descriptors in frequency domain range. Challenges concerning power spectrum estimation are still being discussed in literature. There is interest to search alternative methods of spectral analysis allowing to improve characteristics, in particular increase resolution, thereby enhance ability to detect weak signals with limited data. Spectral resolution is still major problem of power spectrum estimation, especially as applied to the analysis of short sequences of data. Generally, comparison of difference spectrum estimation is performed on the basis visual impressions. There are a lot of techniques of estimation, therefore it is necessary to make compromise between selection of window function, methods and parameters of averaging in time/frequency domains allowing to have acceptable spectral resolution.

Methods of spectrum estimation can be divided into two families: non-parametric and parametric methods of spectrum estimation. Each of these families has its advantages, disadvantages and application. We can note that, parametric methods based on priori model of observed system, allowing to improve the accuracy and resolution. Thus, the quality of the spectral analysis depends on the quality of matching between the selected model and the observed process.

Calculation of amount of power contained in the different frequency components of observed signal by spectral methods is named frequency analysis. Thus, PSD is a measure of the power($PSD(f)df$) contained in the frequencies($[f, f+df]$) of the signal $x(t)$. Power spectral density $S(\omega)$ can be defined as the average square of the spectral density of a random sequence that has theoretically infinite length ($N \to \infty$):

$$S(w) = \lim_{N\to\infty} \frac{1}{2N+1} \frac{\left|X(e^{j\omega T})\right|^2}{f_{\text{rate}}} \tag{3.18}$$

where $X(e^{j\omega T})$ is power spectrum density of sequence $x(n)$ and f_{rate} is rate:

$$X(e^{j\omega T}) = \sum_{n=-N}^{N} x(n)e^{-j\omega Tn} \tag{3.19}$$

In case of finite length of sequence, N, power spectrum density $\hat{S}(\omega)$ is performed. Like evaluation of PSD of random analog signal, estimation of PSD of random sequence gives a picture of distribution of average power by frequency, measured in watts per Hertz (W/Hz) or decibels per Hertz (dB/Hz)

Non-Parametric method of spectrum estimation

Nonparametric methods are based on calculating power spectrum directly to the samples of raw sequence, allowing usage to a wide class of stationary signals and noise, as well as to have high computational efficiency by using Fast Fourier Transform (FFT) algorithms.

Depending on methods of treatment of raw sequence, it can be distinguish following nonparametric methods of PSD estimation:

- periodogram method;
- modified periogogram methods, including:
  - Daniell periodogram method;
  - Bartlett periodogram method;
  - Welch periodogram method;
- Blackman-Tukey method, as known as correlogram method.

It is noted[91] that these methods give the most precise estimation of the spectrum when stochastic observed process is strictly stationary process.

Periodogram method Periodogram method consist in the calculation of PSD estimation $\hat{S}(\omega)$ of a finite random sequence of length N, which is called periodogram:

$$\hat{S}(\omega) = \frac{\left|X(e^{j\omega T})\right|^2}{N f_{\text{rate}}} \tag{3.20}$$

where $X(e^{j\omega T})$ is power spectrum density of sequence $x(n)$ and f_{rate} is rate:

$$X(e^{j\omega T}) = \sum_{n=0}^{N-1} x(n) e^{-j\omega T n} \tag{3.21}$$

Weight (window) function is applied to reduce the spreading effect of spectrum to have smoothing periodogram. These estimations are called modified periodogram $\hat{S}(\omega)$ that is expressed as:

$$\hat{S}(\omega) = \frac{\frac{1}{f_{\text{rate}}}\left|X_w(e^{jwT})\right|^2}{\sum_{n=0}^{N-1} |\omega(n)|^2} \tag{3.22}$$

where $w(n)$ is weight (window) function with length of N; $X_w(e^{j\omega T})$ is spectrum density of product $x(n)w(n)$

$$X_w(e^{j\omega T}) = \sum_{n=0}^{N-1} x(n) w(n) e^{-j\omega T n} \tag{3.23}$$

Daniell periodogram In the method of Daniell periodogram smoothing periodogram is consisted in averaging of neighboring $(2K+1)$ spectral frequencies, that are located symmetrically relative to the current frequency ω_k: $[\omega_{k-K} \cdots \omega_{k-1} \omega_k \omega_{k+1} \cdots \omega_{k+K}]$. Daniell periodogram is calculated based on the initial periodogram $\hat{S}(w)$ of Eq. 3.20 and expressed as:

$$\hat{S}_{DANIELL}(\omega_i) = \frac{1}{2K+1} \sum_{k=i-K}^{i+K} \hat{S}(\omega_k), \quad i = K, K+1, \cdots, N-1-K, \tag{3.24}$$

where N is length (samples number) of raw periodogram $\hat{S}(\omega)$, matching with length of raw sequence; ω_k is values of frequencies for averaging periodogram; its quntities for each value i equal to $(2K+1)$.

Bartlett periodogram Smoothing of periodogram $\hat{S}(\omega)$ by using Barlett periodogram is archieved by dividing the sequence of N samples into P non-overlapping segments with length of L.

$$x^{(p)}(n) = x(n + pL), \quad n = 0, \cdots, L-1; \quad p = 0, \cdots, P-1, \tag{3.25}$$

where p is number of segment, $P = N/L$ is their quantity and for each segment selective spectrum is calculated independently of in the frequency range:

$$\hat{S}^{(p)}_{BARTLETT}(\omega) = \hat{S}^{(p)}(\omega), \quad p = 0, \cdots, P-1. \tag{3.26}$$

Then at each frequency, P separated non-modified periodogram is averaged to archive final Bartlett periodogram:

$$\hat{S}_{BARTLETT}(\omega) = \frac{1}{P}\sum_{p=0}^{P-1}\hat{S}^{(p)}_{BARTLETT}(\omega). \tag{3.27}$$

Marple[91] argued that dispersion of Bartlett periodogram is inversely proportional to the number of segments of P, thereby Bartlett periodogram is more smoother Daniella periodogram. However, increasing of number of segments of P cause decrease of number of samples inside each segment, consequently it can lead diminish resolution frequency - increase $\Delta f = f_{rate}/L$. Thus, it is required to make compromise between resolution and decrease dispersion of PSD estimation.

Welch periodogram The third and is most effective method is Welch periodogram, which is different from Bartlett periodogram and consist of raw sequence with length of N divided by segments $x^p(n)w(n)$ with length l shifted on Q samples ($Q < L$) between neighboring segments with using smooth window $w(n)$.

$$x^{(p)}(n)w(n) = x(n+pQ)w(n), \quad n = 0,\cdots,L-1; \quad p = 0,\cdots,P-1, \tag{3.28}$$

where p is number of segment, P is their quantity with length L of raw signal that is equal to:

$$P = \frac{N-L}{Q} + 1, \tag{3.29}$$

. Thus, sample spectrum $\hat{S}^p_w(\omega)$of the weighted p_{th} segment in the frequency range is expressed:

$$\hat{S}^{(p)}_{Welch}(\omega) = \hat{S}^{(p)}_w(\omega), \quad p = 0,\cdots,P-1. \tag{3.30}$$

And then final view of Welch periodogram is defined as the average amount of segments periodogram:

$$\hat{S}_{Welch}(\omega) = \frac{1}{P}\sum_{p=0}^{P-1}\hat{S}^{(p)}_{Welch}(\omega). \tag{3.31}$$

Usage of weight function gives insufficient loss of resolution in frequency, however it leads to reduce the influence of the side-lobe spectrum of a rectangular window, which is indirectly being used when segmenting is performed. The aim of overlapping segments is to increase the number of averaged segments and thereby reducing the variance of the PSD estimation. Thus, the quality of the evaluation, compared to Bartlett periodogram (Eq. 3.27) that make Welch periodogram less oscillating than Bartlett periodogram. As we can understand from principe of calculation Welch periodogram, Bartlett periodogram can be seen as a special case of periodogram Welch which can obtained by calculation of periodogram of length N non-overlapping segments with length L and averaging periodogram segments.

Blackman-Tukey Method Blackman—Tukey based on the usage of the Wiener—Khinchine theorem, according to PSD of stationary signal $S(\omega)$ is Fourier transom of autocorrelation function (ACF) $R_x(m)$ of sequence $x(m)$ having infinite length:

$$S(\omega) = \frac{1}{f_{rate}}\sum_{m=-\infty}^{\infty}R_x(m)e^{-j\omega mT}. \tag{3.32}$$

In case of finite sequence length N, Eq. 3.32 have a expression as:

$$\hat{S}(\omega) = \frac{1}{f_{rate}} \sum_{m=-(N-1)}^{N-1} \hat{R}_x(m) e^{-j\omega mT}, \tag{3.33}$$

where $\hat{R}_x(m)$ is estimation of ACF, which is even function with length $L = 2N - 1$, and centered relative to $m = 0$. PSD of Blackman-Tukey method $\hat{S}_{BT}(\omega)$ involves using of weight function cal causing smoothing of PSD and expressed as::

$$\hat{S}_{BT}(\omega) = \frac{1}{f_{rate}} \sum_{m=-(N-1)}^{N-1} \hat{R}_x(m) w(m) e^{-j\omega mT}, \tag{3.34}$$

where $\hat{R}_x(m)$ is estimation of ACF, which is even function with length $L = 2N_1 - 1$, and centered relative to $m = 0$, and $w(m)$ is weight (window) function with length $L = 2N_1 - 1$, and centered relative to $m = 0$.

Biased estimator of ACF function is calculated by formula:

$$\hat{R}_x(m) = \frac{1}{N} \sum_{n=0}^{N-|m|-1} x(n)x(n+m), \quad -(N_1 - 1) \leq m \leq (N_1 - 1), \tag{3.35}$$

and unbias by another formula:

$$\hat{R}_x(m) = \frac{1}{N - |m|} \sum_{n=0}^{N-|m|-1} x(n)x(n+m), \quad -(N_1 - 1) \leq m \leq (N_1 - 1), \tag{3.36}$$

It is proved[91] that Biased estimator of ACF (Eq. 3.35) guarantees the non-negativity of the estimates of PSD (Eq. 3.34),but by using an unbiased estimator of the ACF (16.22) can lead to a negative evaluation of the PSD, which is at variance with the physical meaning of the PSD, which is non-negative.

Parametric method of spectrum estimation

As was mentioned above, parametric method of PSD estimation is based on the building math model of observed system and determination of their model parameters, which allow to approximate theoretic signal to analyzed according predefined criteria. Thus, parametric method allow to obtain more accurate PSD estimates with absence oscillations and distortion associated with applying weight function, as well as applying this method on short random sequence with good accuracy. However, as you can understand, the main difficulty is the right selection of mathematical model and criteria of their parameter estimation to obtain reliable estimates of PSD.

Depending on the type of mathematical model it can be distinguished different groups of parametric method of spectrum estimation, as following :

- Autoregressive (AR);
- Moving Average (MA);
- Autoregressive Moving Average (ARMA).

ARMA model is described by math model infinite impulse response (IIR) filter expressed as:

$$y(n) = -\sum_{k=1}^{M-1} a_k y(n-k) + \sum_{i=0}^{N-1} b_i e(n-i), \tag{3.37}$$

where $e(n)$ is input signal (influence), which is typically white noise with dispersion of σ^2; $y(n)$ is output signal (response, modeled sequence), a_k and b_i are parameters of ARMA model, $(M-1)$ is order of ARMA model when $(N-1) \leq (M-1)$ (by default).

ARMA model (Eq. 3.37) corresponds to IIR filter with rational transfer function, which block schematic diagram is presented in Fig. 3.15a:

$$H(z) = \frac{1 + \sum_{i=1}^{N-1} b_i z^{-i}}{1 + \sum_{k=1}^{M-1} a_k z^{-k}} = \frac{B(z)}{A(z)} \tag{3.38}$$

AR-model is described by Eq. 3.37 when $b_i = 0$, $i = 1, 2, \cdots, (N-1)$:

$$y(n) = -\sum_{k=1}^{M-1} a_k y(n-k) + e(n), \tag{3.39}$$

where a_k is parameters of AR-model, $(M-1)$ is its order. AR-model (Eq. 3.39) corresponds to IIR filter (recursive) with transfer function, which block schematic diagram is presented in Fig. 3.15b:

$$H(z) = \frac{1}{1 + \sum_{k=1}^{M-1} a_k z^{-k}} = \frac{1}{A(z)} \tag{3.40}$$

MA-model is described by Eq. 3.37 when $a_k = 0$, $k = 1, 2, \cdots, (M-1)$:

$$y(n) = e(n) + \sum_{i=0}^{N-1} b_i e(n-i), \tag{3.41}$$

where b_i is parameters of MA-model, $(N-1)$ is its order. MA-model (Eq. 3.39) corresponds to finite impulse response(FIR) filter with transfer function, which block schematic diagram is presented in Fig. 3.15c:

$$H(z) = 1 + \sum_{i=1}^{N-1} b_i z^{-i} = B(z) \tag{3.42}$$

At known parameters of the model[92] can determine frequency response of filter $H(e^{j\omega T})$ by substitutionally parameter $z = e^{j\omega T}$ to the transfer function $H(z)$ and then to calculate its PSD $S_y(\omega)$ of modeled sequence $y(n)$ by Eq. 3.43

$$S_y(\omega) = \frac{\sigma^2}{f_{rate}} \left| H(e^{j\omega T}) \right|^2, \tag{3.43}$$

There are various methods of estimating the parameters of AR model, however, we will focus on the more effective method as Berg method. This method is based on the calculation of the parameter estimates of AR-model directly on the samples of the sequence (without calculating ACF estimates); This can be done with linear prediction so as for forward and for backward, with minimizing the average summary of mean square error of linear prediction[91].

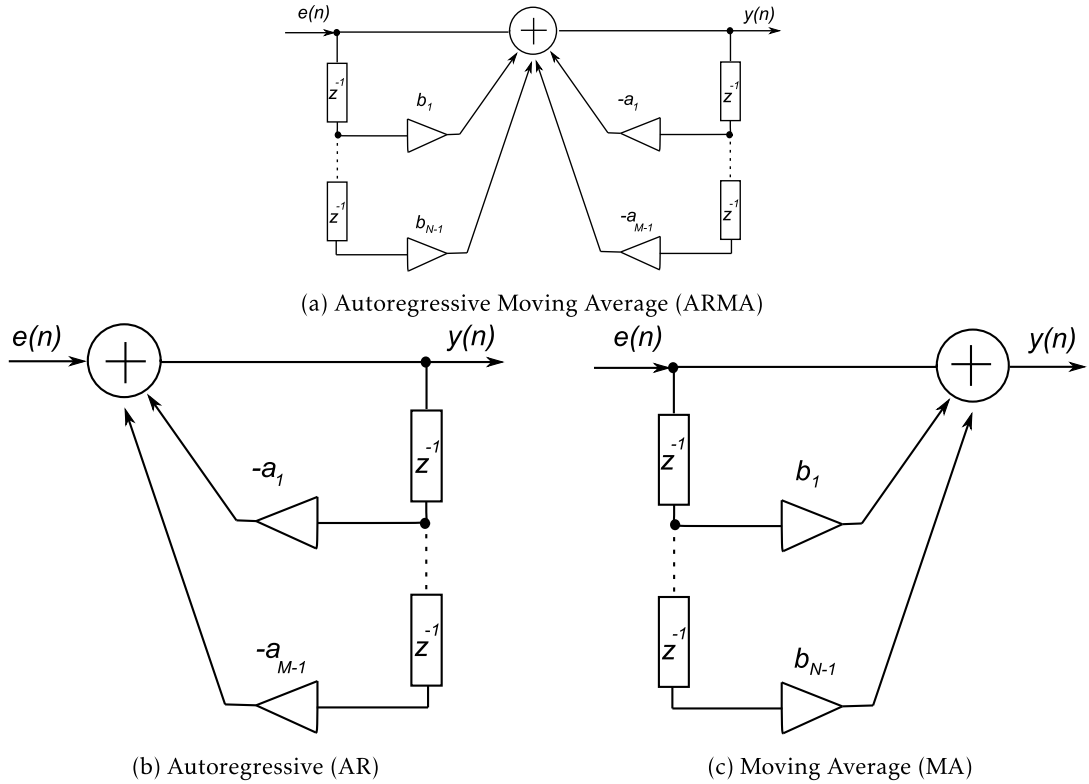

(a) Autoregressive Moving Average (ARMA)

(b) Autoregressive (AR)

(c) Moving Average (MA)

Figure 3.15 – Block schematic diagram of models:a - ARMA,b - AR and c - MA

Results of implementation

Here we can see results of implementation of calculation PSD by Welch and Burg methods(Fig.3.16) y to the voltage measurements of one stack of fuel cell.

Comparison of Burg and Welch In Fig.3.17 we can see difference results of calculation PSD by Burg and Welch methods. For calculation Burg PSD it is requires to have detrended signal. Detrending was obtained by suggested method by polynom. So this is why we see big difference between curves in low frequency range. But for range between 0.1 until 10 Hz, curves have the same shape, however Burg reveals some picks. Calculation PSD Burg requires high computational cost that is sufficient for analyzing in real time. Welch is faster that Burg by several orders.

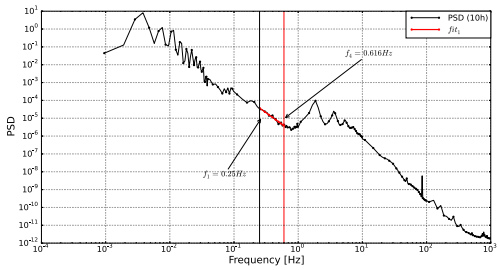

(a) PSD calculation of voltage signal with Welch method

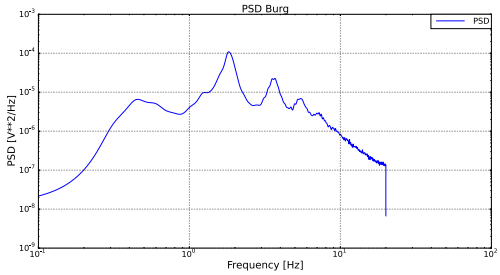

(b) PSD calculation of voltage signal after detrending with Burg method

Figure 3.16 – test

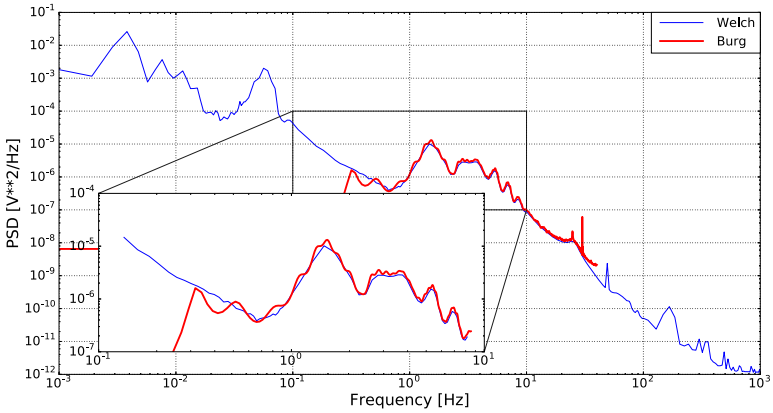

Figure 3.17 – Comparison PSD for Burg and Welch methods

3.4.3 Descriptors in time-frequency domain range

This group contain time-frequency representations (TFRs) with an underlying parametric model that has a some interest in recent years, Short-time Fourier Transform (STFT) and Time-Frequency Autoregressive (TFAR) and the analysis based on wavelets.

Short-time Fourier Transform (STFT) and Time-Frequency Autoregressive (TFAR)

There are a lot of techniques but we can distinguish some of them: Short-time Fourier Transform (STFT) and Time-Frequency Autoregressive (TFAR).

Short-time Fourier Transform (STFT) is a time-frequency analysis based on applying Fourier Transform to the short-term[93]. As a result, a spectrogram (like power spectral density in frequency domain) is obtained[94]. In practice, the procedure for computing STFTs is the implementation of Fourier analysis not on the whole signal, but only on a portion of shorter segments that the length is equal and divide the whole signal. So then weight function is applied on signal and slides to give the temporal parameter. As the results in graph we can observe changing spectra as a function of time

Time-Frequency Autoregressive (TFAR) is based on applying AR-model, for stationary signals, shows high resolution power spectral density (PSD) estimates even for short data records. Furthermore, researchers have developed efficient algorithms to compute the AR coefficients of nonstationary signals[95]. It is particularly the same idea like STFT, whole signal is divided on N pieces of signal. For each of them parametric method is applied. In our case Burg methods of estimation is selected. Result of implementation these techniques will be presented below.

Wavelets

Applying Wavelet allow us to evaluate in what time we have a transformation of signal in real time. This is one of the important advantages in wavelet. A wavelet ψ is defined as a function over energy with zero mean. There are a lot of types of wavelets which have different advantages and applications, but we can distinguish some of them: wavelet of Morley (Fig. 3.18a) and Mexican Hat (Fig. 3.18b). We note that these functions are oscillating on a support of a quasi-compact, that is to say, they tend very quickly to zero.

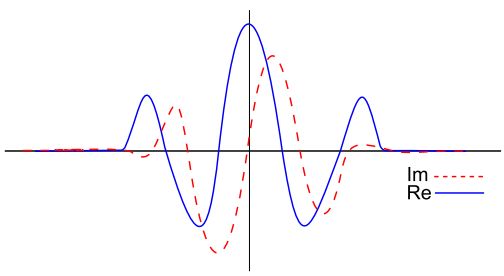

(a) Morlet wavelet, $\psi(t) = \frac{1}{\sqrt{2\pi}} e^{2i\pi\nu t - \frac{1}{2}\left(\frac{t}{\sigma}\right)^2}$ with $\nu = 1.5$ and $\sigma = 2$

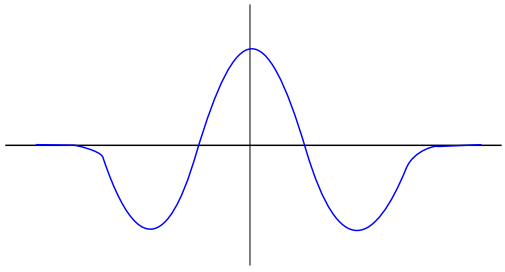

(b) Mexican cap wavelet, $\psi(t) = \sqrt{\frac{1}{3\sigma}} \cdot \left(1 - \frac{t^2}{\sigma^2}\right) \cdot e^{-\frac{t^2}{2\sigma^2}}$ with $\sigma = 2$

Figure 3.18 – Types of wavelets

Results of implementation

Here we can see results of implementation of calculation STFT and TFAR and Wavelet in Fig.3.19. Results of implementation of Morley wavelet on voltage fluctuation is shown in Fig. 3.19c, forming a scalogramme. As we can see on the results, there are moments that show us that there is an apparition of big spikes that can be consider as occurrences. With the analyze of these emissions, we can get a spectrum and also calculate statistical parameters. The difficulty of usage wavelets as descriptors statistics it can be lie in the interpretation of the scalogrammes.

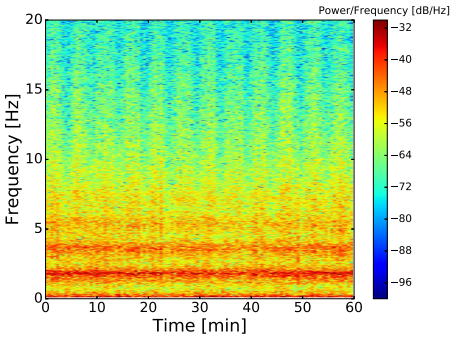

(a) STFT

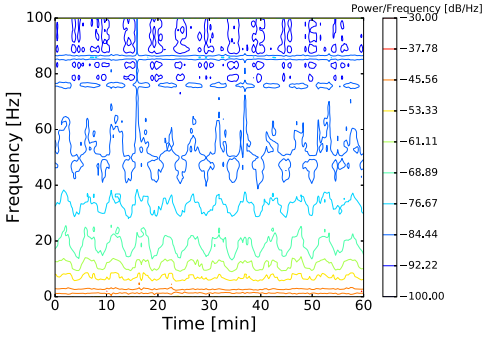

(b) TFAR

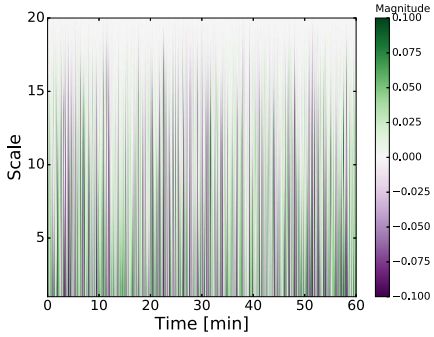

(c) Wavelet of Morley

Figure 3.19 – Implementation of STFT and TFAR and wavelet

3.4.4 Descriptors obtained by using advanced methods

In this section, we selected and present one of most promising technique that can be implement named Prony analysis. As was mentioned before, signals can have a different structure. Some of them have a significant low-frequency quasi-periodic component with high amplitude, others can have low amplitude. If our observed signal has a quasi-periodic (QP) component, it will be better to implement Prony method of signal characterization that suggested by Nigmatullin et al.[96, 97].

Prony analysis

Analysis of the available information sources shows that in the majority of cases PEMFC life tests are carried out in galvanostatic mode. Degradation processes in this case leads to a decrease of the cell voltage. These processes are usually observed with presence of voltage oscillations [98–100] especially when PEMFC is run with high current. This voltage oscillations are well known in many works [98–100] and results show a relationship between parameters of the oscillations and physical and chemical processes within FC. It is obvious that analysis of these phenomena can give a basis for developing an effective diagnostics tools for PEMFC allowing to monitor its technical state. Elaboration of this approach is limited by insufficient experimental database and difficulties of a proper model description for the oscillations which have usually a quasi-periodic nature. To overcome these barriers in frame of this work experimental investigation of PEMFC life tests has been carried out and a new approach for oscillation description on the basis QP processes analysis by the Prony's spectrum is proposed. The basic principle of the method is based on the properties of the functional equation [96, 97] describing results of real measurements:

$$F(t \pm LT) = aF(t) + b \tag{3.44}$$

Here T is a period of the process (its true value is calculated by the fitting procedure), a and b are some constants. In the result of this analysis we can describe the spectra (amplitude-frequency responses) of the voltage $U(t)$ or current $I(t)$ fluctuations for long term random sequences. The proposed method allows to increase accuracy of fluctuation processes description and can be considered as reliable and general diagnostic tool for PEMFC.

Analysis of typical PEMFC voltage signal (Fig. 3.20) shows that voltage reveals strong quasi-periodic components. Fourier's analysis for such signals is not applicable since they cannot be expanded into the desired Fourier's series having usually many additional frequencies not belonging to the phenomenon analyzed.

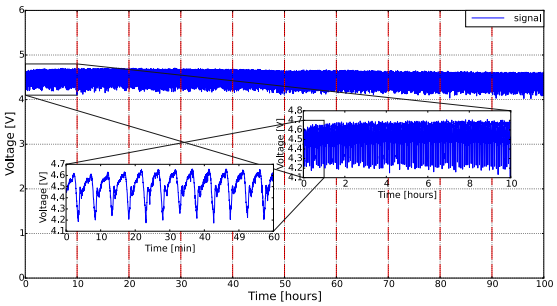

Figure 3.20 – Typical voltage signal measured for 8-cell PEMFC stack operated in galvanostatic mode (170A). Signal comprises clear strong quasi-periodic components.

It is known that pure-periodic process with period T satisfies the following functional equation:

$$Pr(t \pm LT) = Pr(t) \tag{3.45}$$

Generalized solution of this functional equation can be expressed in the form of the Fourier's series [97]. However, real measurements are described more accurately by more generalized functional Eq. 3.44, wherein a and b are real constants. It means that the temporal evolution of some process taking place on the interval $t > T$ is based on events that took place in the nearest past ($t < T$). The solution of functional Eq. 3.44 can be found as follows [97]:

$$\begin{aligned} &a \neq 1 : F(t) = exp(\lambda t)Pr(t) + c_0, \lambda = ln(a)/T, c_0 = b/(1-a); \\ &a = 1 : F(t) = Pr(t) + bt/T. \end{aligned} \tag{3.46}$$

It can be shown that solution Eq. 3.46 corresponds to Prony's series that includes exponential factors making the total process not pure periodical. One can derived from expression Eq. 3.46 that real measurements could be fitted by the following function

$$\begin{aligned} &y(x) \cong F(t) = B + A_0 exp(\lambda x/T_x) + \\ &+ \sum_{k=1}^{K} [Ac_k exp(\lambda x/T_x) cos(2\pi kx/T_x) + As_k exp(\lambda x/T_x) sin(2\pi kx/T_x)] \end{aligned} \tag{3.47}$$

here B, A_0, Ac_k, As_k are decomposition coefficients, T_x is a period of the process, λ is an exponential factor. Thus, real measurements can be described by a set of 2K+4 parameters, and we can have more or less parameters than the number of measurements. Therefore, the truncated Prony's series can be used as a fitting function for quantitative description of the measured signal. Traditionally, the main problem of expansion in Prony's series is extremely high computational cost especially for determination factor λ. This problem has been solved by co-author of this paper (R.R.N) who proposes an effective algorithm for accurate evaluation of the factor λ directly from raw experimental data. This approach significantly reduces calculation costs and increases accuracy of real signal description. Due to limitation in the size of the present publication we do not provide here complete proof of expression Eq. 3.45. The detailed explanation can be found in [96, 97].

Further details concerning the using Prony analysis can be found in our paper[101] which is presented in Annexe.

Results of implemenation

Results of implementation of Prony is shown Fig.3.21. As we can see this methodology allow to describe the quasi-periodic processes with a high accuracy using minimal number of modes and with reduced computational costs. Moreover, results of quasi-periodic processes fitting is presented and highlight a good accuracy on the fitting. By comparing these results to the values of Modulus decomposition coefficient that allow us to make an interpretation of operation state of the fuel cell and a possible prediction of the PEMFC failures.

3.4.5 Conclusion

In this chapter we considered several methods of descriptor generations and we decided to choose some of them. For example, statistical methods (STD, Sk, Ku,...), Burg and Welch

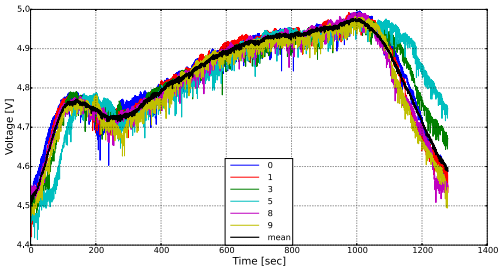

(a) Exemplary iterations of quasi-periodic process and corresponding mean curve

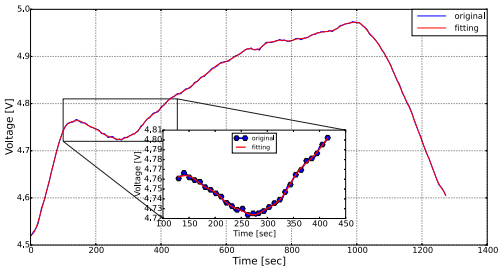

(b) Results of fitting

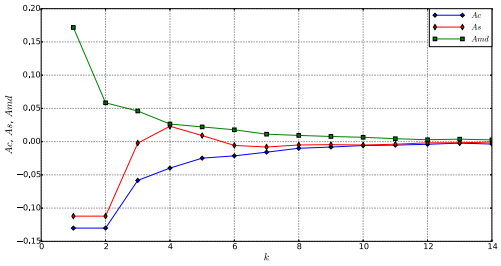

(c) Modulus decomposition coefficient for all modes

Figure 3.21 – Implementation of Prony method

spectrum, wime-frenquency analysis and Prony analysis. Each method of the statistical analysis generates statistical descriptors for the characterization of the studied phenomenon. These statistics descriptors can be used for the characterization of the state of health of the stack, for the characterization of the phenomenon of aging and for the prognosis of Remaining-useful-life (RUL). Certainly, a larger database needs to be obtained to achieve these goals. The following chapter will present implementation these methods of descriptor generation on several stacks and campaigns measurements done during ANR Propice.

Chapter 4

Statistical descriptors for noise diagnostic of PEM stacks in time and frequency domains

Contents

Figures

4.1 Experiments provided under ANR project "PROPICE"

4.1.1 ANR project "PROPICE": description and goals

PEMFC is a complex system that is difficult to describe fully, therefore experimental tests are very important. A lot of works are devoted to the tests with one cell[85, 98, 99, 102]. This is due to experiment simplification. Indeed, experiments with a single cell provide more understandable output behavior (for example, voltage) by changing input parameters (pressure, humidity, etc.). Sometimes special cell constructions (separated cells[63, 65, 103]) are used to understand evolution of the water formation inside bipolar plates. Therefore, work with a simple cell is the first step to understand PEMFC operation. Sure, it limits experiments to low power and makes difficult extrapolation of obtained results to real commercial applications related with highest power stacks.

Another important point deals with duration of fuel cell tests. Usually these tests are limited to few hours. These experiments allow to estimate the fuel cell performance and its components but leave an open question due to the system lifetime. Estimation of lifetime and its prognostic require experiments with long duration time (several months).

The present study is oriented on the development of advanced instrumentation to understand the behavior of FC stack with nominal power of 600 Watts containing 8 cells during its long operation. Experiments have been performed several times up to 1000 hours, to obtain characteristics describing stack durability and reliability. These type of experiments are very difficult and rarely reported in literature because a the lot of resources needed and special laboratory conditions for long running of stacks are necessary.

Another problem is related with the absence of suitable instrumentation for the estimation of system health state without perturbation of the running system. This problem has been discussed in previous chapters and the goal of this dissertation is the instrumentation developments for a permanent monitoring of PEM stacks based on noise diagnostic.

At last, we meet the problem of data storage because a huge quantity of raw data (several teraoctets) generated by means of noise diagnostics.

The present work has been realized in the frame of the scientific consortium during the French ANR project "PROPICE" with association of Russian partner.

ANR project "PROPICE" partners. This work has been supported by the ANR project PROPICE (ANR-12-PRGE-0001) funded by the French National Research Agency. The partners of this project are:

- The Alternative Energies and Atomic Energy Commission (CEA/LITEN), Grenoble
- EIFER European Institute for Energy Research, Karlsruhe
- Fuel Cell Laboratory (FCLAB), Belfort
- Institut Pprime, Poitiers
- Kazan National Research Technical University (KNRTU-KAI)
- The Laboratory of Automatic, Computer Engineering and Signal (LAGIS), Lille

Goals of "PROPICE" project The scientific objectives of the project are defined as follows:

- develop approaches for reliable prognostics of PEMFC stacks;
- facilitate their implementation;

Thereby, it will allow to move towards to develop a generic approach compatible with industrial constraints. Several ways will be considered to achieve these goals:

- processing for prognostic processes to develop new prognostics tools by quantifying and controlling their inherent error of estimation to obtain its remaining useful life;
- enhancing the applicability of prognostics tools enabling systematizing the building of a prognostics system while reducing the influence of arbitrary human choices, as well as reducing its learning and/or parametrization times;
- processing for industrial adaptation of fuel cells applicability.

The present dissertation is oriented on resolution of one of the mentioned above goals, namely on the development of noise diagnostic of PEM stack which can be suitable for in-situ monitoring and useful for prognostic purposes.

4.1.2 Description of PEMFC stack and experimental procedure

In framework of the project, observation of degradation process is performed using 8 cells hydrogen PEMFC stack (EPICEA v2) with cell surface of 220 cm^2 fabricated in CEA, Grenoble and run in FC laboratory (Belfort). The electrical parameters such as stack voltage and single cell voltage, electrical current, impedance, and etc. are measured in galvanostatic (0-170A) or potentiostatic (0-9V) modes. For development of prognosis methods information on the current technical state of PEM stack is required. Characterization of the stack is performed by data that are provided by the set of sensors. Test bench are equipped with sensors for

Characteristic	Value
Nominal Power	600 Watts
Current	0-170A
Relative humidity	50% or between 60%-70%)
Temperature of FC	75-80 °C
Absolute pressure	1,5 bar
Reagents stoichiometry of Anode/Cathode	1,5/2

Table 4.1 – Technical characteristics

measurements of temperature, pressure, humidity and flow rate of reactants. All sensors provide direct descriptors, i.e. record different physical parameters. Simplified diagram of sensors is shown in Fig.4.1. Main set-up parameters are presented in Table 4.1.

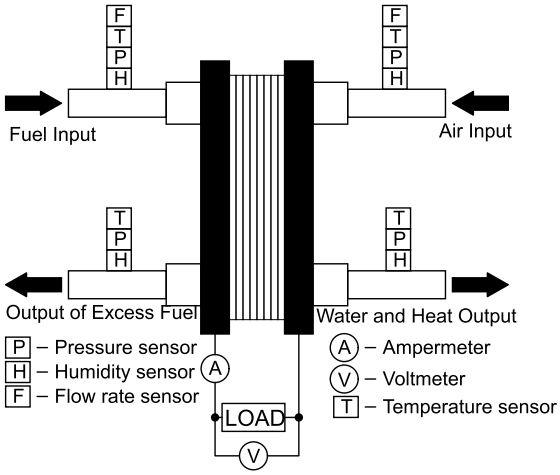

Figure 4.1 – Acquisition of thermo-physical parameters for generating direct descriptors

Two types of measurements have been provided in the frame of the project, namely micro-cogeneration profile and automotive profile. Campaign of measurements on the basis of the micro-cogeneration profile includes 4 consecutive stages corresponding to the micro-cogeneration system functioning during all year. This profile implies the experiments during 1000 hours and involve following stages:

- *Winter profile*, that implies the continuous operation of system during 250 hours;
- *Spring profile* consisting of 2 phases:
  - five-day cycles with 24 hours time period under maximum and middle power;
  - continuous operation during 120 hours;

- *Summer profile*, that involves 11-day cycles with 24 hours time period with start/stop profile:
  - 12 hours of functioning with middle power;
  - 12 hours of functioning without current load (open-circuit voltage);
- *Autumn profile*, that is the similar to spring profile with reversing phases (in the beginning continuous operation mode is performed and after periodic changing power between middle and maximum values).

The micro-cogeneration profile is presented in Fig.4.2.

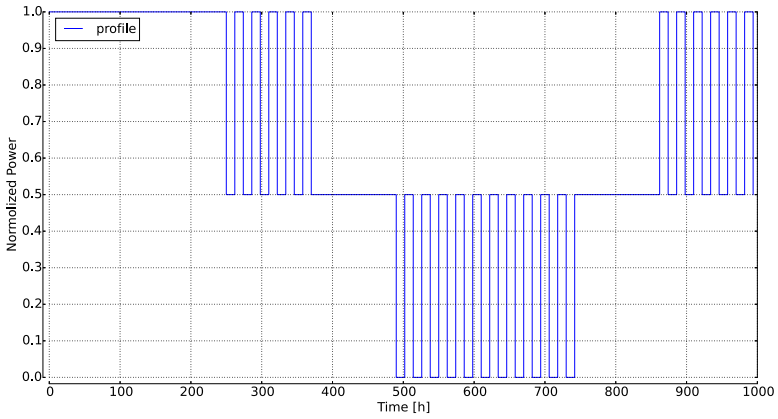

Figure 4.2 – Micro-cogeneration profile for 1000 hours

Automotive operation mode involves repetition of switching mode between two voltage values - 0.9 [V/cell] and 0.7 [V/cell]. The minimum cell voltage is defined at the value 0.3V/cell. In initial time it had been determined that these voltage values correspond to the voltages with currents j1=5A and j2=100A correspondingly. Repetition of switching mode during one minute is presented in Fig.4.3. It includes two stages: first stage is 10 seconds of operation under current load of j1 and second stage is 50 seconds of operation under current load of j2.

It is clear that studied profiles provide complex signal input and output. This is an obvious difficulty for system monitoring and traditional methods of diagnostic is not easy adapted for these types of measurements.

4.1.3 High-frequency measurements system and data storage

The goal of my personal work in the frame of the project is development of instrumentation and methodology for monitoring PEMFC stacks without perturbation of its running using noise measurements. A special system of data acquisition and storage has been developed. Voltage of PEMFC stack had been chosen as a criteria for diagnostic. The measurement system is based on data acquisition card (DAQ) from National Instruments (NI-9239) with acquisition frequency of 50kHz that is placed inside metal box for decreasing environmental influence. Root mean square value of intrinsic noise of the equipment is about 70 µV that is sufficient to measure FC voltage fluctuations (mV). Wires were connected to the output terminals of FC stack.

LabVIEW software from National Instruments was used for DAQ configuring as well as for data pre-storage. It is also possible to perform it by developed software on Python. All

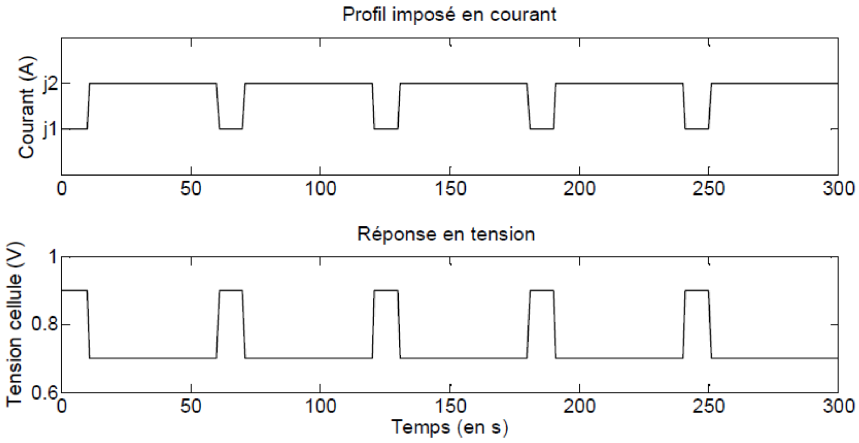

Figure 4.3 – Automotive profile for 5 minutes

data from DAQ automatically compressed and saved on corresponding folder for the following transfer to external hard drive. Storage and data management have been performed thanks to a laptop. Developed system allows to measure signals from 4 channels at the same time with high frequency of 50kHz. However, frequency rate of 2 kHz is sufficient for the provided experiments. Using several channels allows to measure not only total voltage from FC stack, but also voltages from specific cells, for example first, middle and last cell that mainly describe behavior of FC stack. Also it is possible to connect DAQ to other sensors that control and manage operation of FC stack (pressure, humidity and etc.). Obtained by this way additional information is important for understanding FC behavior with respect to the change of operational parameters.

4.1.4 Presentation of the experimental campaigns with associated noise measurements

ANR project "PROPICE" includes 4 campaigns of experiment in Belfort, 3 of them are co-generation profile, and a last one is an automotive profile. Some of profiles have been corrected during experiments in order to reach project goals or due to experimental difficulties.

For each experimental campaign a new stack has been fabricated. High speed noise measurements were performed continuously 24/7 and presented by red color in Fig. 4.4 4.5 4.6 4.7.

First campaign (Fig. 4.4) is co-generation profile, which includes continues operation with maximum current load of 170A (from 0 to 260 hours) and perform polarization procedure on the 170 hour that perturb operation during several hours. Cycles of operation between 85A and 170A take place after the 260 hour. Each cycle continues during 24 hours, 12 hours with 85A and 12 hours with 170A load. Polarization curve has been measured on the 335 hour. Continual operation with current load of 85A is performed during the 360 hour of total FC operation. High-speed measurements (noise measurements) had been started on the 380 hour and continued until the end of this experiment. There were two problems caused by absence of supplied reactants(hydrogen) on 391 hour and with low cell voltages on 480 hour due to cell drying.

Second campaign (Fig. 4.5) is also co-generation profile which consists from continual operation with maximum current load from the 55 to 300 hours. Polarization curve had been measured on 38, 183, 424, 431, 592, 736, 904, 911, 1072 and 1263 hour that perturb operation for

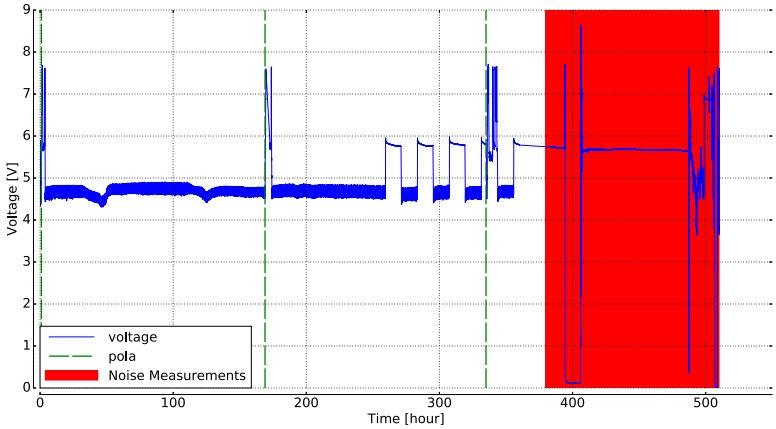

Figure 4.4 – 1st campaign

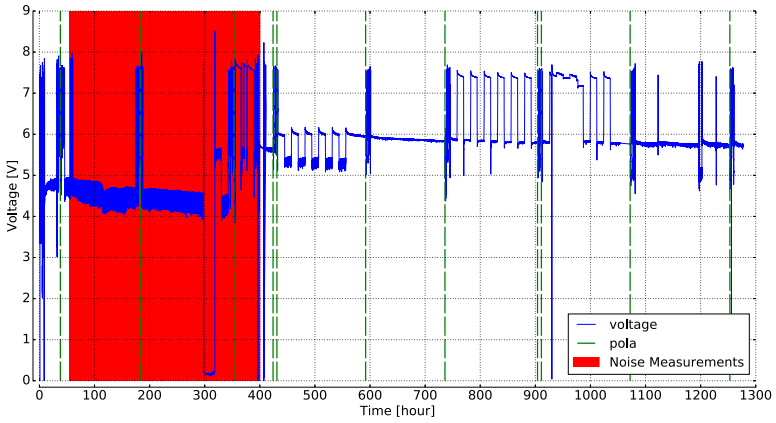

Figure 4.5 – 2nd campaign

several hours. This campaign also had some problems between the 300 and 350 hours occurred due to absence of supplied hydrogen and due to fast degradation of the stack. Experimental campaign had been performed after the 400 hour and includes cycles of changing current load during 24 hours, 12 hours with 85A and 12 hours with 110A until the 560 hour. After that, continues operation with 85A had been performed until the 736 hour. After cycle operation between 85A and 20A had been performed. Continual operation with current load of 85A is performed from the 1072 hour until the end of experiment.

Third campaign (Fig. 4.6) is also co-generation profile including in the beginning continual operation with maximum current load of 100A during 118 hours and after cycling operation between 50A and 100A of current load. This cycling is carried on until the 180 hour, wherein continual operation with current load of 50A is performed until the 230 hour. After that cycling between OCV and 50A is performed until the 355 hour. Each cycle takes 5 hours. After that continual operation with current load of 50A during 20 hours is performed until occurred problem at the 370 hour. After resolving this problem at the 405 hour, experiment had been continued during 20 hours with current load of 50A, after that operation cycle between 50A and 100A had been performed up to the end of experiment. Some problems take place at the 158

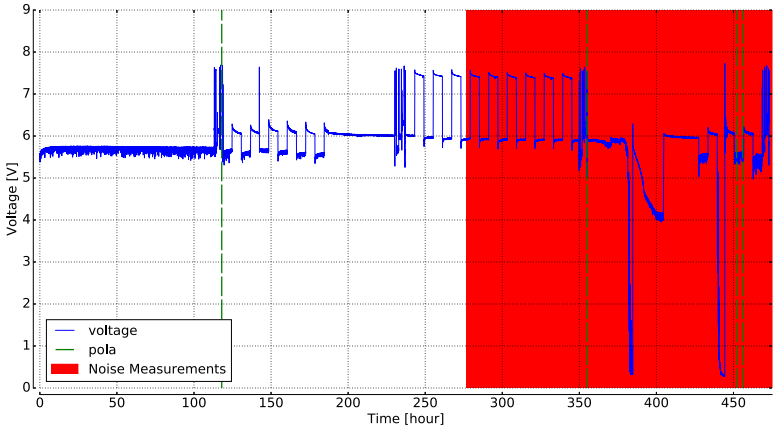

Figure 4.6 – 3rd campaign

hour that cut operation for 6 hour. High-speed measurements had been started on the 277 hour and continued until to the end of this experiment.

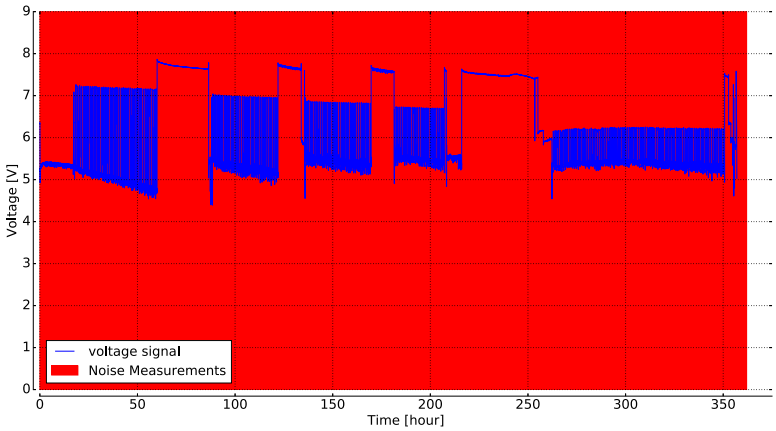

Figure 4.7 – 4th campaign

Fourth campaign (Fig. 4.7) is automotive profile that involves repetition of switching mode between two voltage values - 0.9 [V/cell] and 0.7 [V/cell]. In the beginning FC stack run during 20 hours with current load of 110A. After that subsequent of cycles between 5 and 100A is performed until 60 hour wherein operation with current load of OCV is performed during 26 hours. After that cycles between 5 and 50A is performed until the 123 hour wherein operation with current load of OCV is performed during 23 hours. After that cycles between 5 and 25A is performed until the 170 hour wherein operation with current load of OCV is performed during 25 hour. After cycles continual operation with current load of 20A is performed during 6 hours. After that OCV mode is performed until the 265 hour where operation with 5A is performed during 6 hours and after that cycles between 5 and 10A is performed until the 350 hour.

More detailed information about each campaigns will be considered in further sections.

4.2 Presentation of statistical descriptors recorded during different experimental campaigns

4.2.1 First campaign of measurements

Detailed description

This campaign had been performed for investigation of degradation processes of fuel cell stack under cogeneration profile. More clearly this campaign is explained in Fig.4.8. The goal of 1000 hours of continues operation was not reached due to fast degradation of the stack and problems occurred during experiment. Noise measurements were performed at the end of this campaign, total duration of these measurements is more than 100 hours.

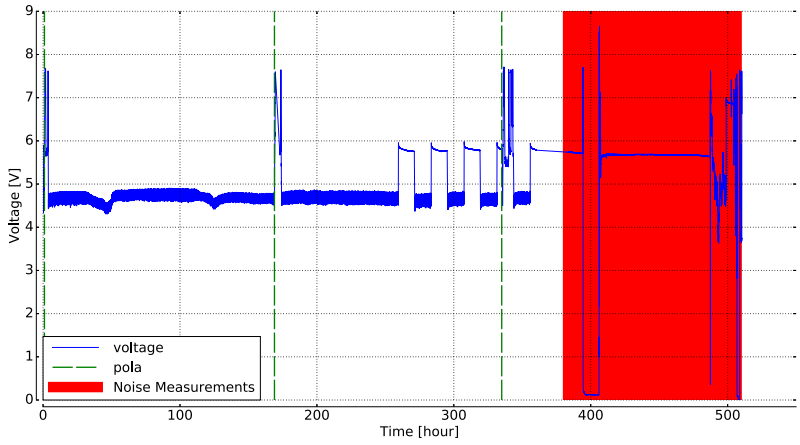

(a) voltage signal

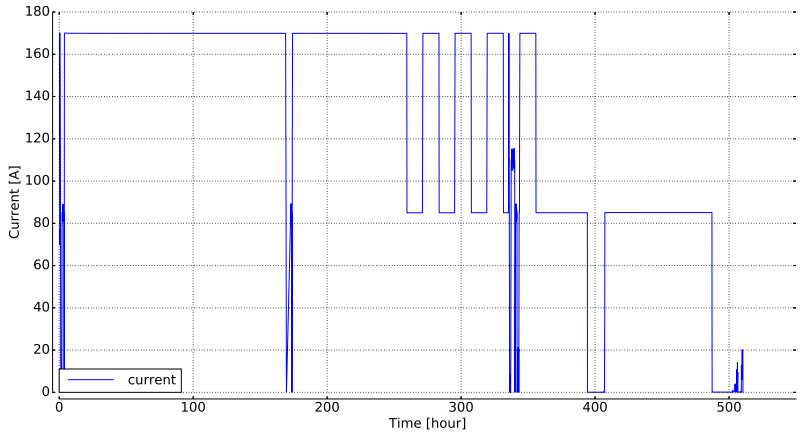

(b) current load

Figure 4.8 – Voltage signal and current load of FC stack during first campaign of measurements

This campaign includes continuous and cycles operations. Continual operation had been performed under maximum current load of 170A (from 0 to 260 hours) with measurement of polarization curve on the 170 hour that perturbs operation during several hours. Cycle operation

between 85A and 170A is performed after the 260 hour. Each cycle continues during 24 hours, 12 hours at 85A and 12 hours at 170A load. Polarization curve had been measured on the 335 hour. After that continual operation with current load of 85A is performed starting from the 360 hour. High-speed measurements have been started on the 380 hour and continued until the end of campaign. There were two problems caused by the absence of supplied reactants(hydrogen) on the 391 hour and due to low cell voltage on the 480 hour caused by cell drying. Last 20 hours is continue working during several hours until complete stop.

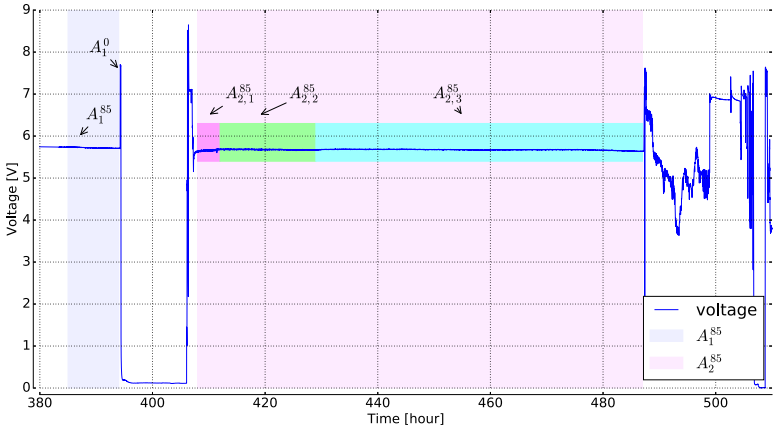

Figure 4.9 – Voltage signal for selected zones

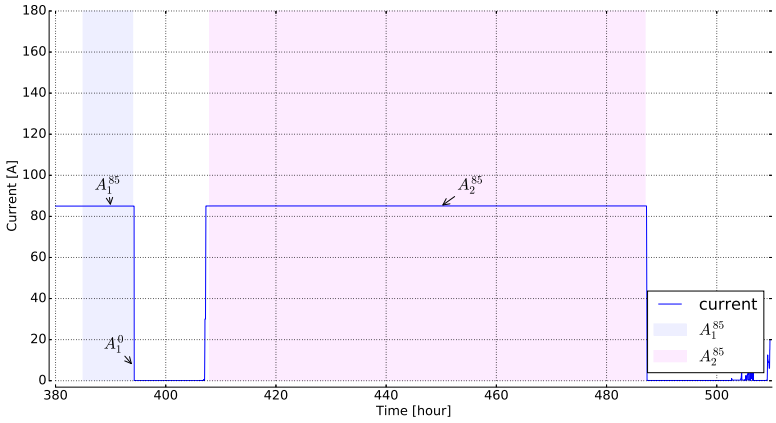

Figure 4.10 – Current load for selected zones

For further statistical treatment of recorded high-frequency noise measurements some zones had been selected, see Fig.4.9 and Fig.4.10. Zone A_1^{85} corresponds to the normal 85A operation mode before the problem with lack of hydrogen. Zone A_2^{85} is also 85A operation mode after resolution the problem with lack of hydrogen. Zone A_2^{85} is subdivided on 3 subzones ($A_{2,1}^{85}$, $A_{2,2}^{85}$, $A_{2,3}^{85}$). These subzones have been selected visually based on the shape of the signal, They reflect different stages of the recovering to the normal mode of operation after stack stopping. At last, zone A_1^0 corresponds to the OCV mode. The duration of this zone is rather short (1 min.)

compared to others. Nevertheless this zone is important for noise description of stack behavior. Visualizations of typical signals for selected zones are presented on Fig. 4.11

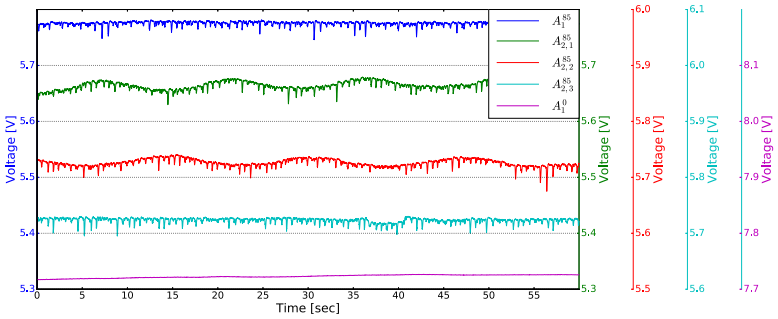

Figure 4.11 – Signal visualization for duration of 1 minute (A_1^{85},A_2^{85} and A_1^0 zones)

Typical signals with duration of 1 minute for selected zones are presented in Fig. 4.11. As we can see from this figure, the signals have a different shape and amplitude with some voltage drops. Signals corresponding OCV mode doesn't have a strong voltage drops and a huge fluctuations. Signals in A_1^{85} and $A_{2,3}^{85}$ have the same structure which is different from the one recorded for zones $A_{2,1}^{85}$ and $A_{2,2}^{85}$. It can be explained by stabilization of stack operation after stopping.

Fig. 4.12 presents visualization of typical signals for selected zones for duration of 1 hour. Unfortunately, for OCV mode we have no signals of this duration. The difference between different zones becomes more clear when using this time window. First zone corresponds to the normal mode, the $A_{2,1}^{85}$ has a pronounced low frequency component, the zone $A_{2,2}^{85}$ has a high frequency component with low amplitude and zone $A_{2,3}^{85}$ has a very low frequency component with low amplitude. Fluctuations in OCV mode have a very low amplitude in comparison to fluctuations recorded at 85A load mode. Another point concerns the voltage drops. These drops are clearly observed in 85A mode operation in comparison to OCV mode. We analyze in the present manuscript the signals for some selected zone. But raw data exist for other zones as well and can be used in the future.

Below we start to present and to discuss statistical descriptors which can be obtained using different statistical methods. A number of these methods is important, so a lot of descriptors can be generated for the signal. Sure, we should limited this manuscript for some of them and this choice is not easy. Finally, we have decided to present in this chapter the descriptors in time and in frequency domains. This is traditional approach. More advanced approaches based on descriptors in time-frequency domain will be presented in next Chapter 5.

Generation descriptors in time or in frequency domains meets the problem with signal detrending. Here we also have a lot of possibilities (see Chapter 3 and our papers in Annexes). At the first, we present the results obtained using detrending procedure with polynomial fitting of 5th order and different time windows (32, 8 , 2 and 0.3 s). Detrended signals for selected zones are presented in Fig. 4.13. As we can see all detrended signals have the same structure and it is difficult to compare these signals visually. Thus, statistical treatment is necessary. More detailed discussion on detrending procedure will be presented further.

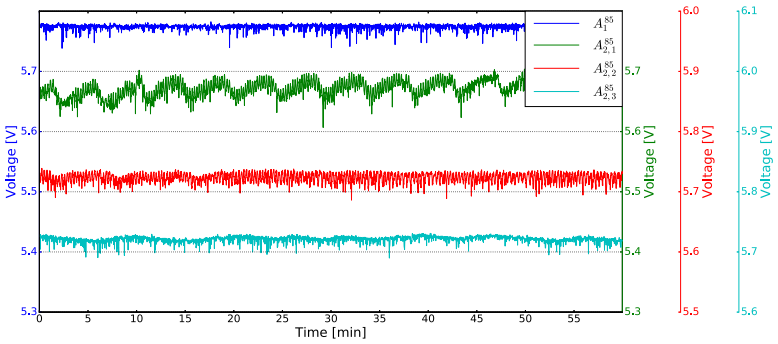

Figure 4.12 – Signal visualization for duration of 1 hour for current load of 85A (A_1^{85} and A_2^{85} zones)

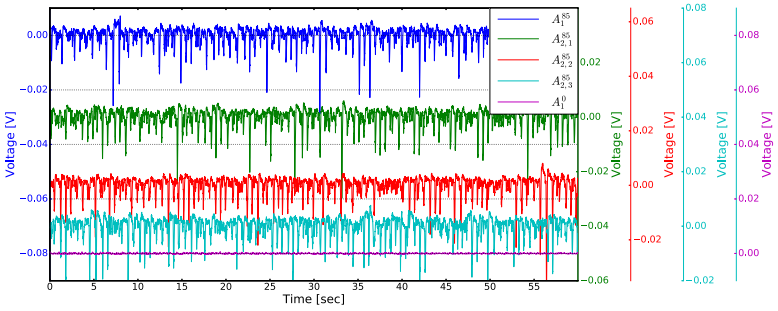

Figure 4.13 – Detrended signal for selected zones. Time window for detrending is 8 seconds.

Statistical descriptors in time domain

In these section generation of statistical descriptors in time domain will be presented for selected zones. As was mention, statistical descriptors depend on time window in which detrended procedure is provided. The results for time window of 8 seconds are presented below. Detrended signal with its histogram for current load of 85A is presented in Fig. 4.14. The signal has a negative skewness that is explained by set of voltage drops with different amplitudes and frequency. Signal distribution is not Gaussian, the last one is presented by dotted line on Fig. 4.14.

Another behavior has a signal for OCV mode that is presented in Fig. 4.15. There is no pronounced voltage drops that is confirmed with positive skewness value.

The presented above results for window of 8 seconds can be obtained for other time windows as well. It is interesting to see the dependence of statistical descriptors on time window. These results for selected above zones are presented below in the form of tables.

Zone A_1^{85} Tab. 4.2 presents calculation of statistical descriptors for A_1^{85}.

The "original" corresponds to signal without detrending, V_{max} and V_{min} are maximal and minimal voltage values of signal, V_{p-p} is the difference between the maximal and the minimal voltage, μ - mean value, σ - standard deviation fo signal, *eps* is the ratio of the mean value of signal to its standard deviation, M2, M3 and M4 are moments of seconds, third and forth order,

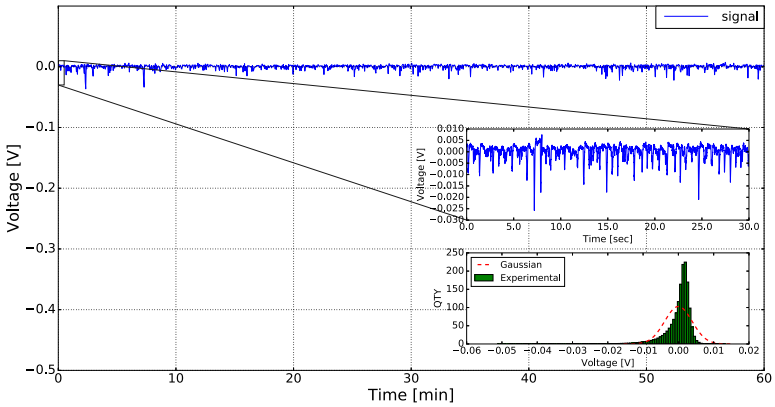

Figure 4.14 – Detrended signal with its histogram (5 order polynomial detrending with time window of 8 sec) for 85A load.

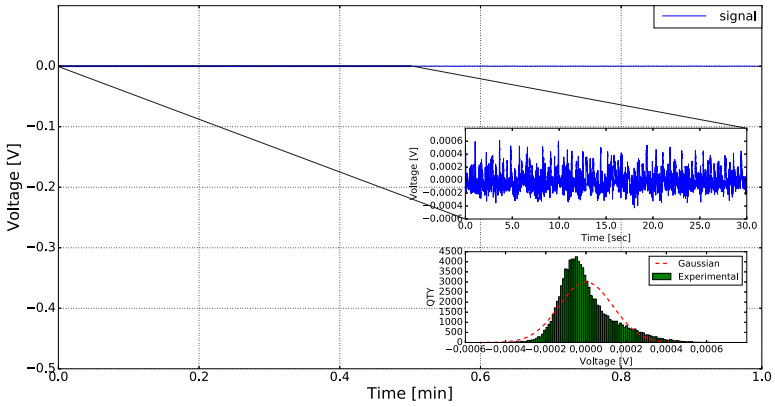

Figure 4.15 – Detrended signal with its histogram (5 order polynomial detrending with time window of 8 sec) for OCV mode.

Sk is Skewness, KU is kurtosis of signal.

We can see that standard deviation decreases with reducing of time window. It is related with the cut of low frequency fluctuations by short time windows. We can see drastic changes in signal character when detrending by window is applied. We can noted 3 zones : 1- Original 2-windows time of 32, 8 and 2 seconds and 3- time windows of 0.3 seconds. This behavior is illustrated by variation of *eps* and σ. For all time windows the signal is non-Gaussian.

Tables 4.3, 4.4 and 4.5 present statistical descriptors for zone A_2^{85}. We note an important change in signal character again in 3 zones and specially when 0.3s window is used. The decreasing of standard deviation with the reduction of the time window and non-Gaussian character of recorded signals are catch again. Some differences between different subzones can be noted as well. At last, Table 4.6 illustrates the results of calculations for OCV mode. An important difference for OCV mode and 85A mode can be noted.

	original	32 seconds	8 seconds	2 seconds	0.3 seconds
μ, V	5.774	5.774	5.774	5.774	5.774
σ, mV	4.2	3.99	3.88	3.59	0.93
eps, 10^{-6}	729	691	672	623	161
V_{max}, mV	5.784×10^3	10.3	13.3	27.6	15.1
V_{min}, mV	5.722×10^3	-52.4	-51.4	-45.1	-16.5
V_{p-p}, mV	61.742	62.7	64.7	72.8	31.7
M2, 10^{-6}	17.7	15.9	15.0	12.9	0.8
M3, 10^{-9}	-191	-183	-169	-116	-0.09
M4, 10^{-9}	4.6	4.4	3.9	2.5	0.01
Sk	-2.5	-2.9	-2.9	-2.5	-0.1
KU	11.7	14.3	14.3	12.3	11.8

Table 4.2 – Statistical descriptors for 85A load with normal operating conditions (A_1^{85}) after detrending procedure with different time windows

	original	32 seconds	8 seconds	2 seconds	0.3 seconds
μ, V	5.674	5.674	5.674	5.674	5.674
σ, mV	14.9	5.4	3.77	3.49	0.91
eps, 10^{-6}	2637	966	664	615	160
V_{max}, mV	5.721×10^3	19.6	10.3	28.6	13.8
V_{min}, mV	5.603×10^3	-51	-46.5	-42.0	-16.1
V_{p-p}, mV	117.6	70.7	56.8	70.6	30.0
M2, 10^{-6}	223	30.0	14.2	12.1	828
M3, 10^{-9}	-14.4	-148	-148	-104	-0.09
M4, 10^{-9}	138	5.57	3.15	2.13	0.01
Sk	0.004	-0.9	-2.76	-2.46	-0.12
KU	-0.24	3.18	12.5	11.42	11.95

Table 4.3 – Statistical descriptors for 85A load ($A_{2,1}^{85}$) after detrending procedure with different time windows

	original	32 seconds	8 seconds	2 seconds	0.3 seconds
μ, V	5.723	5.723	5.723	5.723	5.723
σ, mV	7.7	4.4	3.72	3.44	0.87
eps, 10^{-6}	1349	782	650	602	153
V_{max}, mV	5.740×10^3	15.1	9.5	33.6	14.1
V_{min}, mV	5.667×10^3	-52	-49.9	-41.6	-13.6
V_{p-p}, mV	73.3	67.8	59.5	75.2	27
M2, 10^{-6}	60	20.0	13.8	11.8	769
M3, 10^{-9}	-284	-155	-142	-98	-0.06
M4, 10^{-9}	12.4	4.0	3.0	1.99	0.008
Sk	-0.61	-1.7	-2.75	-2.41	-0.09
KU	0.49	7.14	12.76	11.13	11.71

Table 4.4 – Statistical descriptors for 85A load ($A_{2,2}^{85}$) after detrending procedure with different time windows

	original	32 seconds	8 seconds	2 seconds	0.3 seconds
μ, V	5.721	5.721	5.721	5.721	5.721
σ, mV	4.7	3.8	3.64	3.4	0.87
eps, 10^{-6}	823	667	637	593	152
V_{max}, mV	5.733×10^3	12.6	11.7	22.0	15.5
V_{min}, mV	5.668×10^3	-51.8	-49.3	-46.0	-13.4
V_{p-p}, mV	64.4	64.4	61.0	68.0	28
M2, 10^{-6}	22.1	14.5	13.2	11.5	759
M3, 10^{-9}	-181	-153	-140	-100	-0.06
M4, 10^{-9}	4.6	3.5	3.0	2.0	0.009
Sk	-1.74	-2.7	-2.9	-2.57	-0.09
KU	6.52	13.51	14.3	12.77	13.29

Table 4.5 – Statistical descriptors for 85A load ($A^{85}_{2,3}$) after detrending procedure with different time windows

	original	32 seconds	8 seconds	2 seconds	0.3 seconds
μ, V	7.723	7.723	7.723	7.723	7.723
σ, mV	2.6	0.25	0.13	0.12	0.075
eps, 10^{-6}	348	33	17	16	10
V_{max}, mV	7.726×10^3	0.9	0.6	0.6	0.36
V_{min}, mV	7.717×10^3	-0.8	-0.4	-0.5	-0.4
V_{p-p}, mV	9.7	1.8	1.0	1.1	0.8
M2, 10^{-6}	7.2	0	0	0	0
M3, 10^{-9}	-9.1	0	0	0	0
M4, 10^{-9}	0.1	0	0	0	0
Sk	-0.47	0.22	0.97	0.85	-0.01
KU	-0.99	0.19	1.01	1.00	1.46

Table 4.6 – Statistical results for OCV (A^0_1) after detrending procedure with different time window

Fig. 4.16 illustrates the obtained results in term of dependence of statistical descriptors on time window.

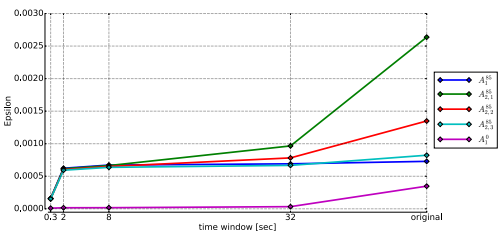

(a) Intensity of fluctuation, ϵ

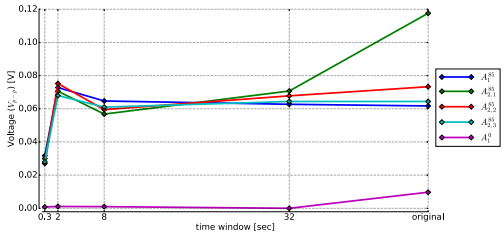

(b) Voltage peak-to-peak

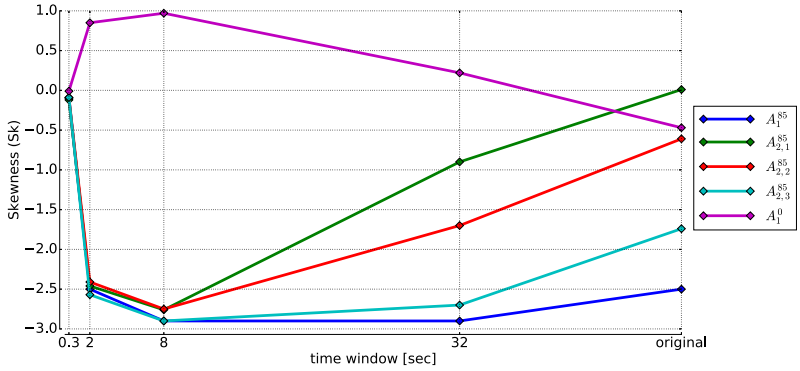

(c) Skewness

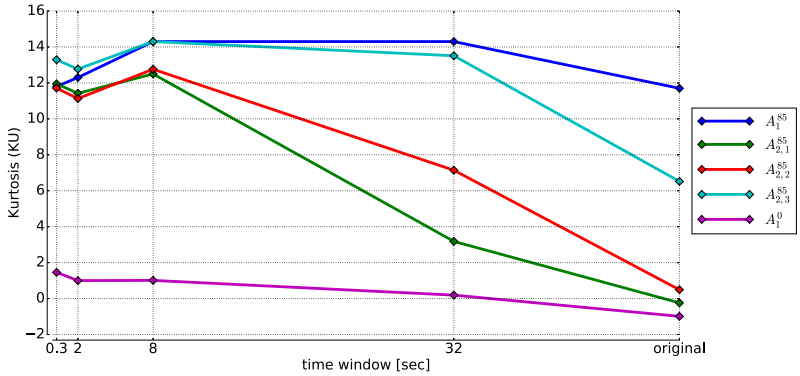

(d) Kurtosis

Figure 4.16 – Dependence of statistical descriptors on time window

This representation can provided more visualize information than Tables. We can see, and it will be the same in general for the others campaign, that changes for *eps* and σ due to time windows reduction highlights 3 different zones. High values for "original" signal, medium values for 32, 8 and 2s time windows and lower values for 0.3s time window. This behavior is due to the cut of the low-frequency of the signal due to the time windows detrending. Of course, apply a numerical filter (time windows) "clean" and decrease the variability of the statistical descriptors. Thanks to that we can better noted the difference between operating point like OCV and 85A in the present result. Skewness and Kurtosis variations with time windows duration

add another highlight. For the time windows in middle range (32, 8 and 2s) we can distinguish at the same operating point (here 85A), the different behavior between zones : A_1^{85}, A_2^{85} and A_3^{85}. To resume, changing the size of the time windows can highlighted different information on statistical descriptor. This play a role as a magnifying glass. Using a middle time windows (32, 8 and 2s) can clean the dispersion that can be observed in the original signal on *eps* and σ to distinguish easier differences between operating points. When these middle time windows are applied on Skewness and Kurtosis that allow to distinguish the differences between zones at the same operating point. This can provided the effect of ageing by given the evolution of the statistical descriptor (Sk and Ku) with time. This can be really useful for prognostic calculation.

For other campaigns, same table and figures will be done for the statistical descriptors evolution with time windows reduction. Globally, same behavior will be highlighted and comparison between campaigns will be done in the chapter 6. This chapter here is more focused to give a panel/list of all numerous results for all campaign to prepare the results crossing in chapter 6.

Statistical descriptors in frequency domain

This section presents the results of calculation descriptors in frequency domain, namely power spectral density (PSD). PSD can be obtained by different methods, such as Burg and Welch. The comparison between these methods will be done. Moreover, the dependence of PSD on time window will be studied for Welch method.

Zone A_1^{85} In Chapter 3 we have considered different methods of PSD calculations such as Burg and Welch methods. The results of implementation Burg and Welch methods are presented in Fig.4.17 for signal recorded during 3 hours on zone A_1^{85}. At first, we have provided calculations of PSD for 1 hour. Using 3 obtained PSD we have calculated the mean value and incertitude of estimation of PSD. After, PSD has been calculated for 3 hours time interval. The results of calculation are presented in Fig.4.17.

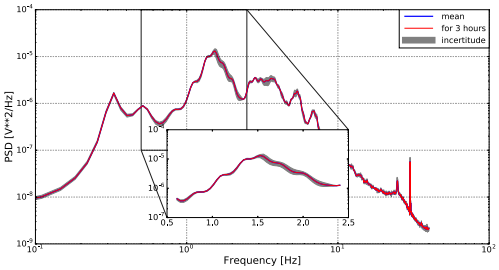

(a) Burg method

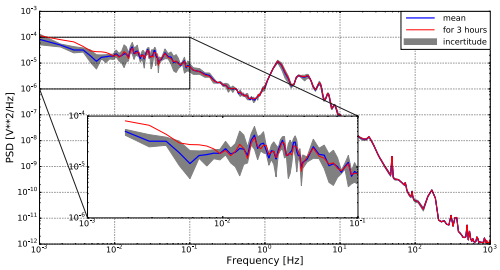

(b) Welch method

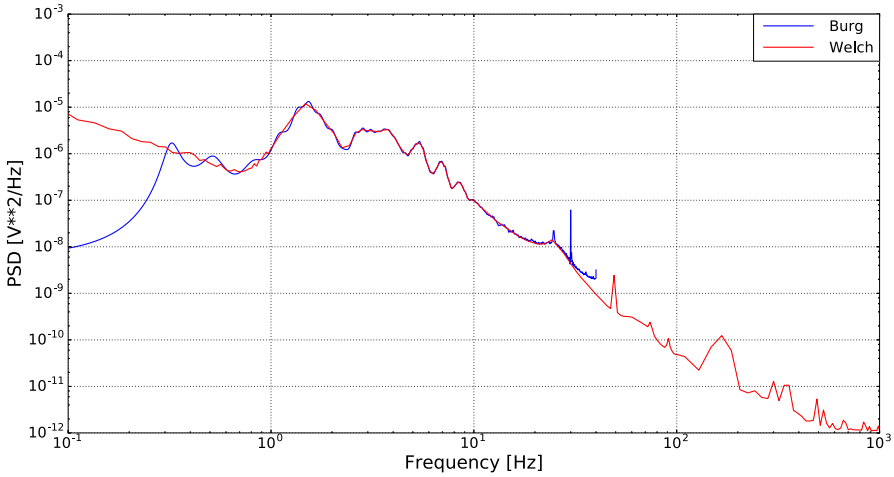

(c) comparison between Welch and Burg 3 hours

Figure 4.17 – PSDs for 3 hours; mean value and incertitude; comparison Welch and Burg.

The following conclusions can be done. PSD calculated for 3 hours is suited mainly within the interval of incertitude. Thus, 1h recording seems to be sufficient for correct estimation of PSD. This conclusion is supported by Fig. 4.18 which presents calculations of PSD for 1h, 3h and 9h signals (Welch method). Only in very low frequency range (less than 0.1 Hz) PSD for 3h and 9h differs from the one obtained for 1h. PSD obtained by Burg and Welch methods are the same in the main part of frequency region. Further we will use Welch method due to low calculation

costs. The results presented on Fig.4.17 and Fig. 4.18 deal with original (non-detrending) signal.

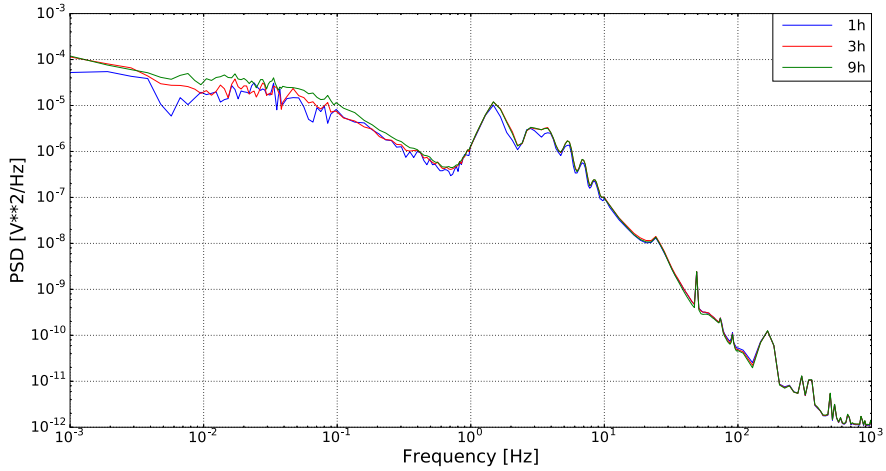

Figure 4.18 – PSD for signals with different time windows(1h, 3h, 9h)

Qualitative analyze of Fig. 4.18 allows to separate several zones, namely:
- flicker-noise component in low frequency range ($7 \cdot 10^{-2} - 7 \cdot 10^{-1}$ Hz) with slope $\alpha = 1.49$;
- a pick on $f \approx 1.8$ Hz with its subharmonics;
- flicker-noise component ($10 < f < 50$ Hz) with slope $\alpha = 3.23$;

For further analyzing it will be better to separate different phenomena. It can be done by signal detrending using different time windows. The results are presented on Fig. 4.19.

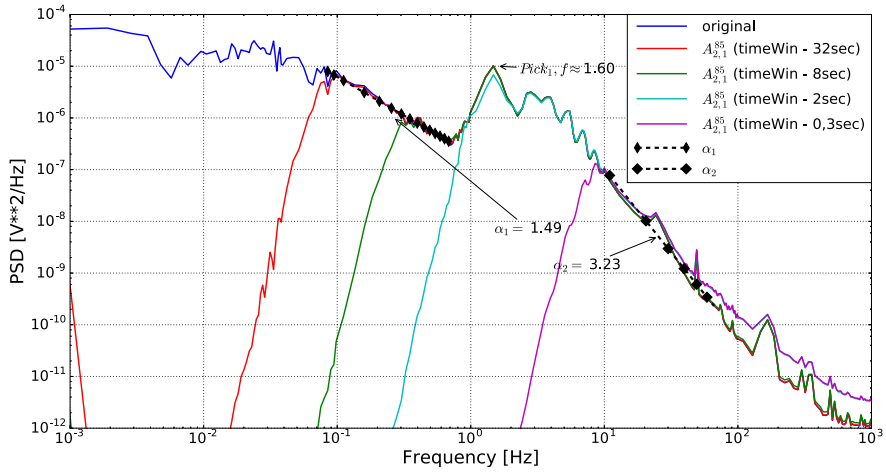

Figure 4.19 – PSD Welch with different time windows for 85A load (A_1^{85})

As we can see, detrending procedure cut low frequency signal but not influence on PSD with exception on high frequency range (f>50Hz). Detrending signals after implementing detrended procedure with different time windows are presented in Fig. 4.20.

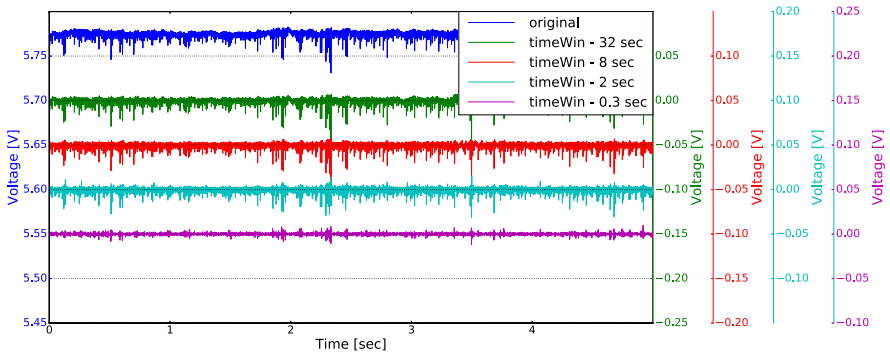

Figure 4.20 – Original signal and detrended signals with different time windows

Fig.4.21, Fig.4.22 and Fig.4.23 present the result of calculations of PSD for zone A_2^{85}. Below we discuss qualitatively the obtained results.

Zone $A_{2,1}^{85}$ The following phenomena can be noted:

- a pick on f=0.004Hz with its subharmonics that is explained by low serrated component in signal
- a pick on f=0.05Hz that is explained by quasi-periodic signal component
- in the frequency range f> 0.1Hz PSD is similar to the one obtained for zone I.

Zone $A_{2,2}^{85}$ The following phenomena can be noted:

- a pick on f=0.004Hz is not visible
- a pick on f=0.05Hz
- in the frequency range f> 0.1Hz PSD is similar to the one obtained for A_1^{85}.

Zone $A_{2,3}^{85}$ The following phenomena can be noted:

- a pick on f=0.05Hz is not visible
- PSD is similar to one obtained for A_1^{85}.

Thus, calculated PSD confirm existence of some relaxation process after stack stopping. This process manifests itself by low frequency signal components which disappear with time. In zone $A_{2,3}^{85}$ stack presents the same frequency signature as in zone A_1^{85}.

Zone A_1^0 Fig.4.24 presents PSD calculated for OCV mode with available duration of signal recording (T = 30 seconds). We can see, that calculated PSD differs significantly from the one obtained for the 85A load mode. Namely we note 3 flicker-noise components:

- in the range $0.03<f<0.7$ Hz with slope $\alpha = 3.27$;
- in the range $1<f<30$ Hz with slope $\alpha = 1.31$;
- in the range $30<f<60$ Hz with slope $\alpha = 4.39$;

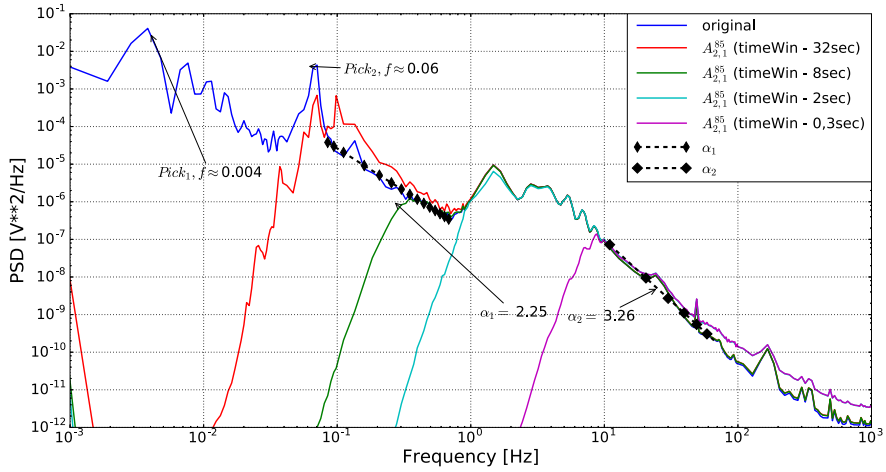

Figure 4.21 – PSD Welch with different time windows for 85A load ($A_{2,1}^{85}$)

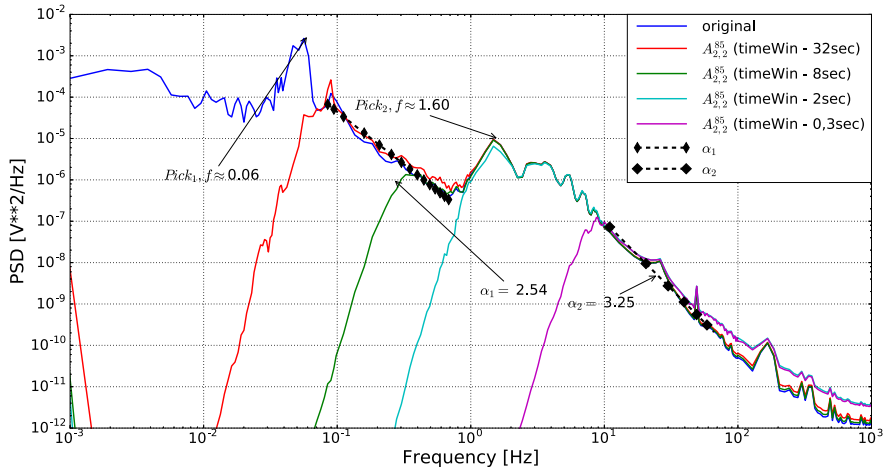

Figure 4.22 – PSD Welch with different time windows for 85A load ($A_{2,2}^{85}$)

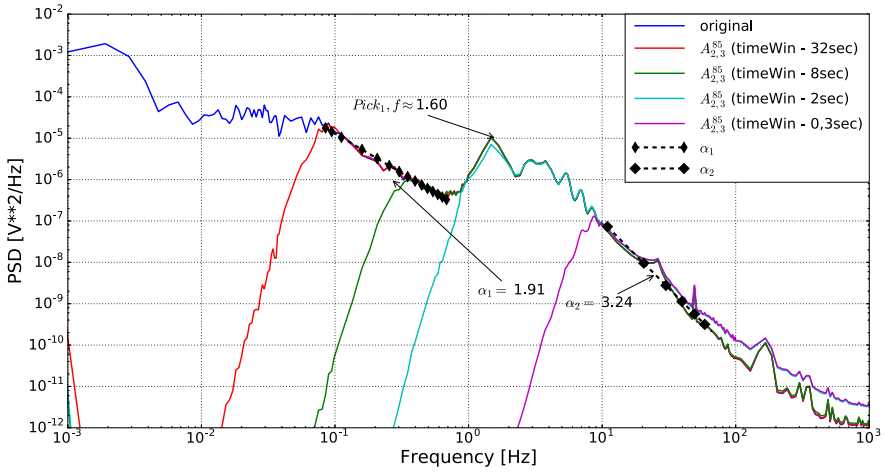

Figure 4.23 – PSD Welch with different time windows for 85A load ($A^{85}_{2,3}$)

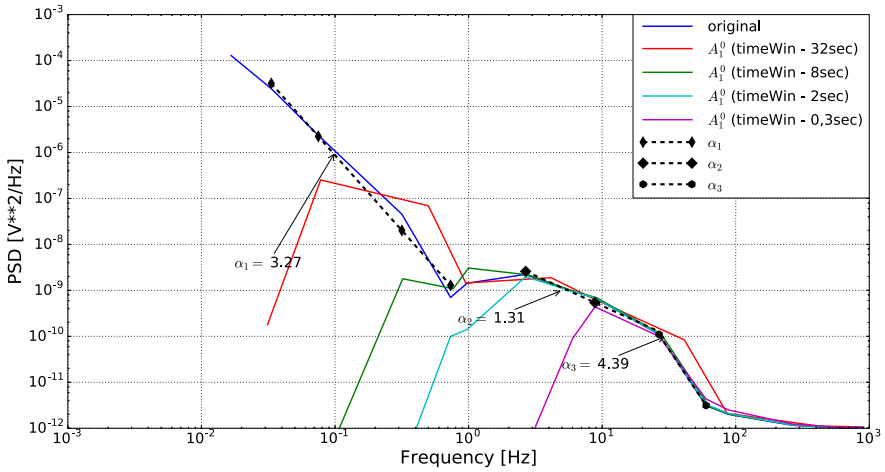

Figure 4.24 – PSD Welch with different time window for OCV mode (A^{0}_{1})

4.2.2 Second campaign of measurements

Detailed description

The goal of 1000 hours of continues operation had been reached in this campaign, however there were some interruptions during experiment. Profile of second campaign is presented in Fig.4.25. In accordance with the obtained data from first campaign, relative humidity was changed from 60-70% to 50%. Other parameters were remained invariable. Total duration of this measurement is 350 hours. The goal of archiving 1000 hours of continues operation has be done.

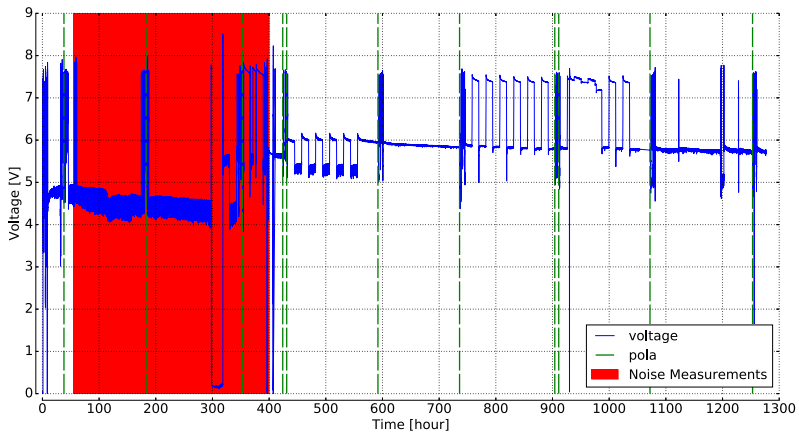

(a) voltage signal

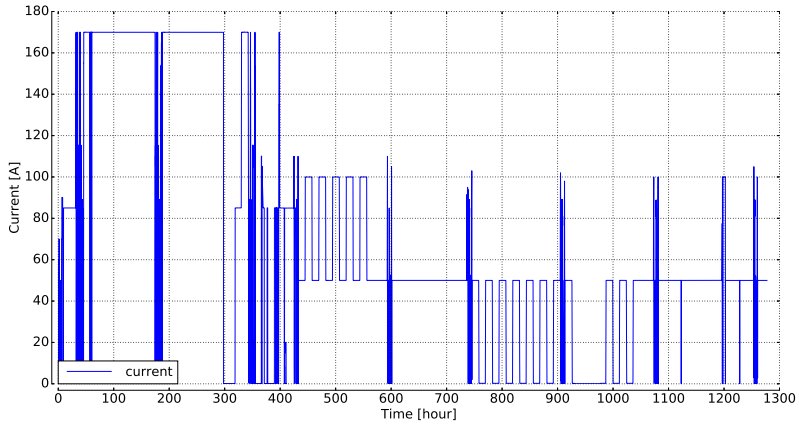

(b) current load

Figure 4.25 – Voltage signal and current load of FC stack during second campaign of measurements.

This campaign, like the previous one, includes continuous and cycles operations. Continual operation had been performed under maximum current load of 170A (from 60 to 300 hours) with performing polarization procedure on 180 hour that perturb operation during several hours. At the end of first 300 hours of operation, experiments had been interrupted due to the absence of hydrogen. After that, previously defined operational conditions had been redefined. The maximum current was changed from 170A to 100A and in order to reduce degradation processes

to achieve 1000 hours. Cycles operation between 50A and 100A was performed after the 410 hour. As like for the first campaign, each cycle continues 24 hours: 12 hours with 50A and 12 hours with 100A. After that, continues operation had been performed under 50A load (from 560 to 730 hours). After that, continual cycle operation between OCV and 50A was performed until the 1080 hour where continues operation under 50A was started until the end of campaign. Some measurements of polarization curve have been performed on 38, 183,353, 424, 592, 736, 904, 911, 1072 and 1253 hour that disturb operation during several hours. As we can see in Fig.4.25, high-speed noise measurements have been done during winter profile that corresponds to 170A load, during 200 hours that is split by polarization procedure in the middle of this period.

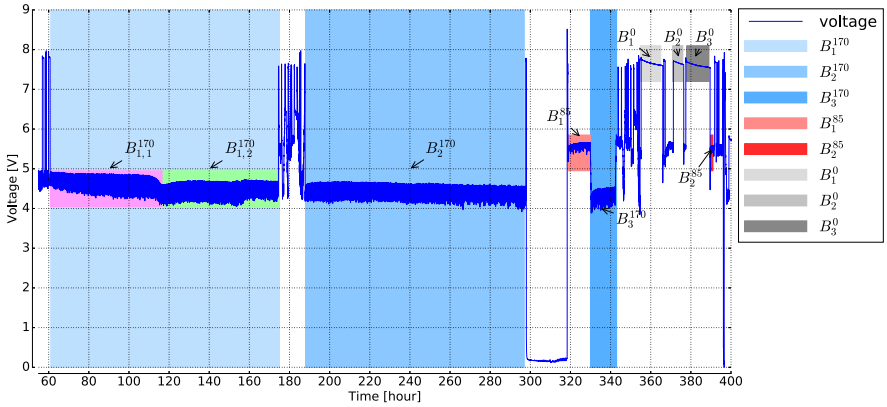

Figure 4.26 – Voltage signal for selected zones

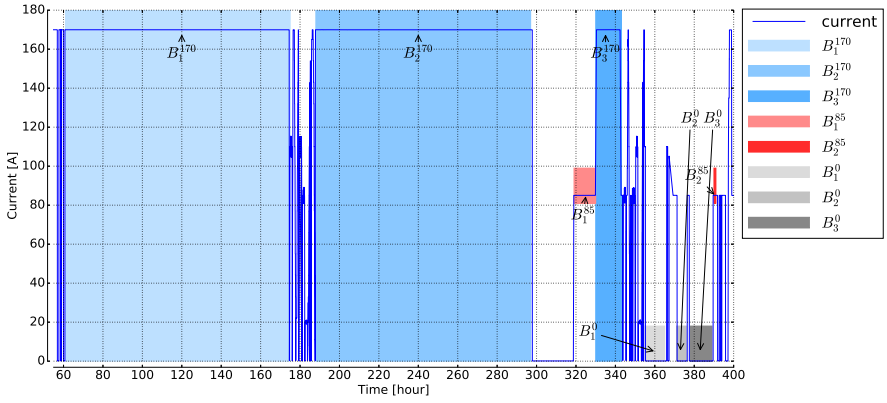

Figure 4.27 – Current load for selected zones

For further statistical treatment of recorded high-frequency noise measurements some zones had been selected, see Fig. 4.26 and Fig. 4.27 wherein current and voltage profiles are presented. Zones B_1^{170} and B_2^{170} correspond to the normal 170A operation mode before the problem with gas supply. Zone B_1^{170} is subdivided on 2 subzones ($B_{1,2}^{170}$ and $B_{1,2}^{170}$). These subzones have been selected visually based on a shift of voltage that is occurred. After stack repairing, operation under 85A and 170A loads have been performed that correspond to B_1^{85} and B_3^{170}. After the

problem related with absence of hydrogen has been solved, some non stable operation takes place done. For analyzing zones B_1^0, B_2^0 and B_3^0 have been chosen that correspond to operation under OCV mode. At last, zone B_2^{85} corresponds to operation with 85A. Visualizations of typical signals for selected zones are presented on Fig. 4.28, Fig. 4.29a and Fig. 4.29b.

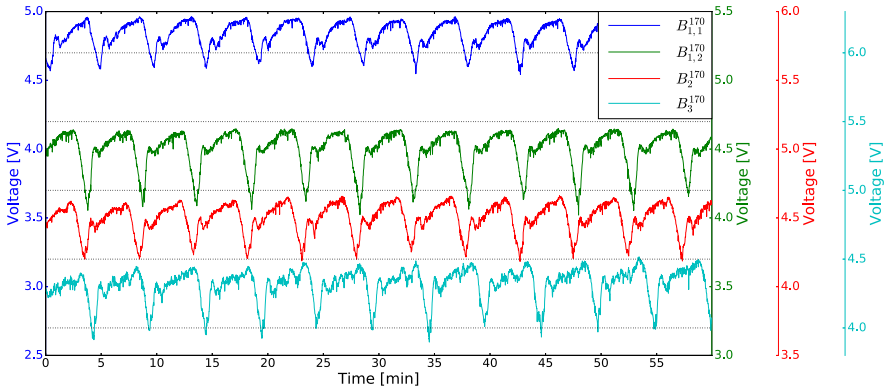

Figure 4.28 – Signal visualization for duration of 1 hour with current load of 170A (B_1^{170}, B_2^{170} and B_3^{170} zones)

As we can see from Fig. 4.28, signals for 170A load have a quasi-periodic component with different amplitude and shape due to limitation of pressure regulation. Signals for 85A load have some voltage drops but there is no clearly observed quasi-periodic component. Signals for OCV mode are presented in Fig. 4.29b wherein no problems with voltage drops, however there is a decreasing voltage trend. Fluctuations for OCV mode are lower than for 85A and 170A loads

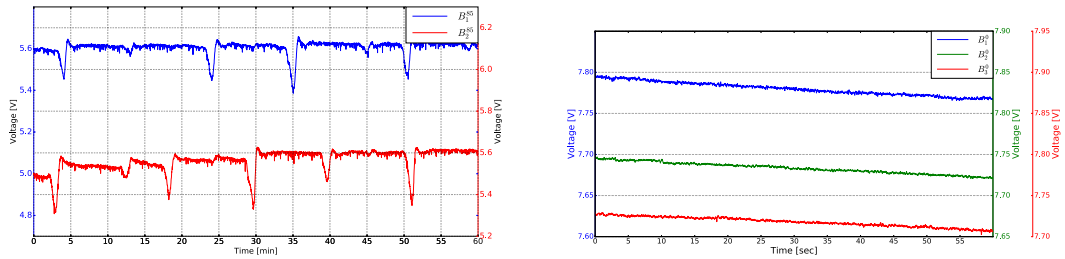

(a) B_1^{85} and B_2^{85} zones

(b) B_1^0, B_2^0 and B_3^0 zones

Figure 4.29 – Signal visualization for duration of 1 hour with current load of 85A (B_1^{85} and B_2^{85} zones) and with OCV mode (B_1^0, B_2^0 and B_3^0 zones)

In Fig. 4.30 and Fig. 4.31 are presented detrended signals for different loads and OCV mode. Detrending procedure is performed with 5th order polynomial fitting and time window of 8 seconds. As we can see all detrended signals have the same structure and it is difficult to compare them visually.

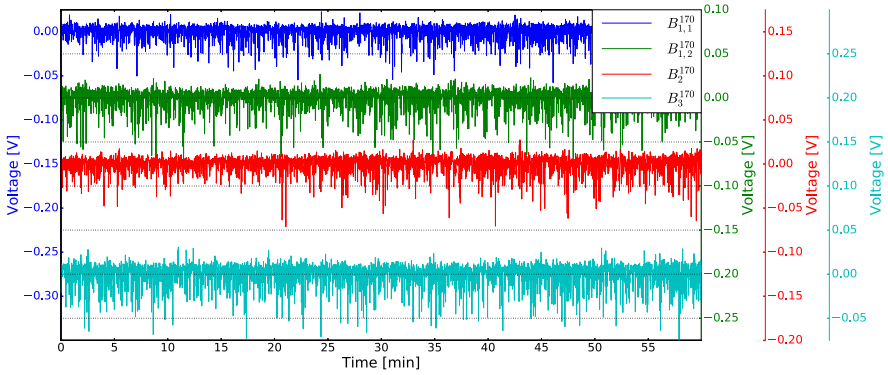

Figure 4.30 – Signal visualization for duration of 1 hour with current load of 170A after detrending (B_1^{170}, B_2^{170} and B_3^{170} zones)

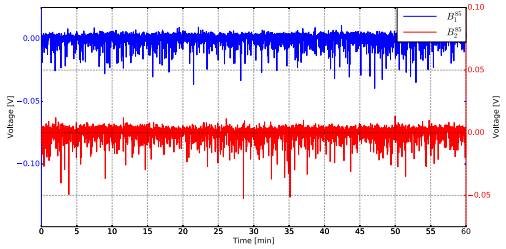

(a) B_1^{85} and B_2^{85} zones

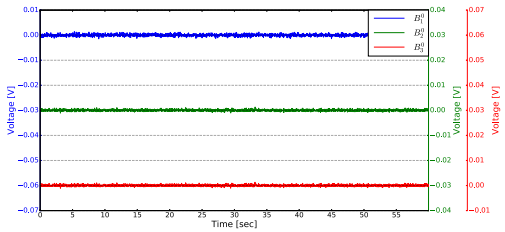

(b) B_1^0, B_2^0 and B_3^0 zones

Figure 4.31 – Signal visualization for duration of 1 hour with current load of 85A after detrending (B_1^{85} and B_2^{85} zones) and with OCV mode (B_1^0, B_2^0 and B_3^0 zones)

Statistical descriptors in time domain

Generation of statistical descriptors in time domain will be presented in this sections for selected zones. Typical detrended signals with their histogram are presented in Fig. 4.32 for 170A load and in Fig. 4.33 for 85A load. Negative distribution of skewness explained by set of voltage drops with different amplitudes and frequency. Distribution of signals is not Gaussian.

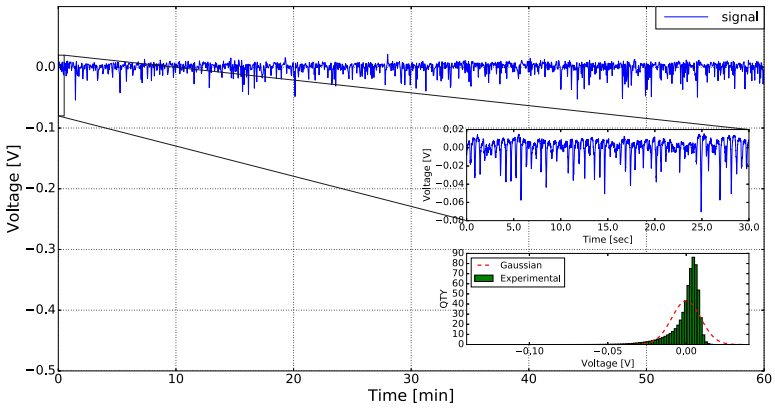

Figure 4.32 – Detrended signal with its histogram (5 order polynomial detrending with time window of 8 sec) for 170A.

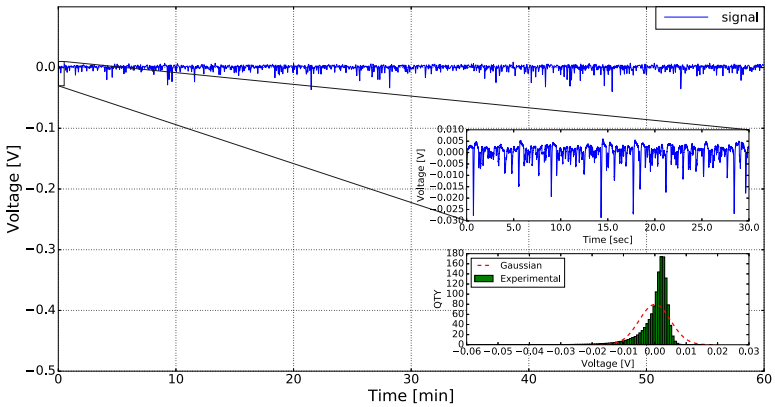

Figure 4.33 – Detrended signal with its histogram (5 order polynomial detrending with time window of 8 sec) for 85A.

Another behavior show signals for B_1^0, B_2^0 and B_3^0 zones that is presented in Fig. 4.34. There is no pronounced voltage drops that is confirmed by positive skewness.

The presented above results for window of 8 seconds can be obtained for other time windows. Results for different time windows for selected zones are presented further in the form of tables like for first campaign.

Tab. 4.7, Tab. 4.8, Tab. 4.9 and Tab. 4.10 correspond to $B_{1,1}^{170}$, $B_{1,2}^{170}$, B_2^{170} and B_3^{170} zones. They have at the same tendency. Values of skewness and kurtosis vary slightly in windows of 32s, 8s and 2s with a sharp jump for 0.3s window. Original signal is sensitive to selected zone and is

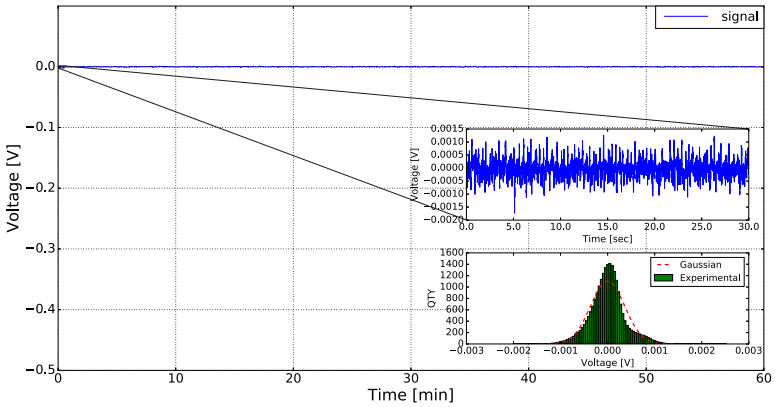

Figure 4.34 – Detrended signal with its histogram (5 order polynomial detrending with time window of 8 sec) for OCV.

different with comparison to detrending signals.

	original	32 seconds	8 seconds	2 seconds	0.3 seconds
μ, V	4.827	4.827	4.827	4.827	4.827
σ, mV	98	10.0	9.2	8.6	2.59
eps, 10^{-6}	20303	2086	1920	1789	538
V_{max}, mV	4.969×10^3	34.4	24.8	56.6	38.7
V_{min}, mV	4.498×10^3	-141.1	-137.5	-113.8	-34.2
V_{p-p}, mV	470.0	175.6	162.4	170.5	72.9
M2, 10^{-6}	9604	101.4	85.8	74.5	6.7
M3, 10^{-9}	-657613	-1997	-1825	-1367	-7
M4, 10^{-9}	235	100.2	82.9	59	0.5
Sk	-0.69	-1.95	-2.29	-2.12	-0.4
KU	-0.44	6.74	8.24	7.62	9.7

Table 4.7 – Statistical descriptors for 170A load ($B_{1,1}^{170}$) after detrending procedure with different time windows

Tab. 4.11 and Tab. 4.12 illustrate statistical descriptors for B_1^{85} and B_2^{85} zones. In general, statistical descriptors have the same tendency that for 170A, but all parameters are changed significantly. We note important decreasing of noise intensity in comparison with 170A load.

Tab. 4.13, Tab. 4.14 and Tab. 4.15 present statistical descriptors for B_1^0, B_2^0 and B_3^0 zones accordingly. Here we can see important difference with respect to results obtained for 85A and 170A that is expressed in standard deviation, skewness and kurtosis. Moreover, standard deviation decreased with time that it can be clearly observed by comparison of zones.

	original	32 seconds	8 seconds	2 seconds	0.3 seconds
μ, V	4.496	4.496	4.496	4.496	4.496
σ, mV	138	12.9	11.6	10.8	3.0
eps, 10^{-6}	30901	2885	2601	2420	685
V_{max}, mV	4.654×10^3	53.5	28.0	66.2	42.8
V_{min}, mV	3.963×10^3	-152.9	-146.4	-126.2	-55.7
V_{p-p}, mV	690.0	206.5	174.5	192.5	98.5
M2, 10^{-6}	19309	168.2	136.8	118.4	9.5
M3, 10^{-9}	-3598294	-3793	-3534	-2697	-11
M4, 10^{-9}	1454	243	193	142	1
Sk	-1.34	-1.73	-2.20	-2.09	-0.39
KU	-0.90	5.58	7.32	7.14	9.9

Table 4.8 – Statistical descriptors for 170A load ($B_{1,2}^{170}$) after detrending procedure with different time windows

	original	32 seconds	8 seconds	2 seconds	0.3 seconds
μ, V	4.500	4.500	4.500	4.500	4.500
σ, mV	107	11.4	9.7	8.9	2.7
eps, 10^{-6}	23956	2554	2172	1998	606
V_{max}, mV	4.664×10^3	48.7	35.3	76.7	39.0
V_{min}, mV	4.141×10^3	-142.5	-138.9	-129.8	-62.3
V_{p-p}, mV	522.8	191.3	174.2	206.5	101.3
M2, 10^{-6}	11625	132.1	95.5	80.9	7.4
M3, 10^{-9}	-1102121	-2403	-2140	-1602	-8
M4, 10^{-9}	409	152	109	78	0.7
Sk	-0.87	-1.58	-2.29	-2.2	-0.43
KU	0.03	5.75	9.01	8.96	11.0

Table 4.9 – Statistical descriptors for 170A load (B_2^{170}) after detrending procedure with different time windows

	original	32 seconds	8 seconds	2 seconds	0.3 seconds
μ, V	4.318	4.318	4.318	4.318	4.318
σ, mV	115	15.4	13.1	12.1	3.3
eps, 10^{-6}	26806	3577	3042	2813	768
V_{max}, mV	4.518×10^3	75.3	33.0	69.4	46.3
V_{min}, mV	3.835×10^3	-18.0	-177.2	-163.7	-74.6
V_{p-p}, mV	682.7	256.0	210.3	233.2	121.0
M2, 10^{-6}	13398	238.5	172.5	147.5	10.9
M3, 10^{-9}	-1933834	-5416	-4840	-3617	-16
M4, 10^{-9}	742644	445	297	213	1.8
Sk	-1.24	-1.47	-2.13	-2.0	-0.43
KU	1.13	4.82	6.99	6.79	12.0

Table 4.10 – Statistical descriptors for 170A load (B_3^{170}) after detrending procedure with different time windows

	original	32 seconds	8 seconds	2 seconds	0.3 seconds
μ, V	5.606	5.606	5.606	5.606	5.606
σ, mV	33.5	5.2	5.0	4.6	1.0
eps, 10^{-6}	5993	932	893	821	194
V_{max}, mV	5.661×10^3	12.6	15.1	36.2	19.2
V_{min}, mV	5.376×10^3	-61.1	-59.9	-54.6	-17.8
V_{p-p}, mV	284.4	73.8	75.0	90.9	37.1
M2, 10^{-6}	1128	27.3	25.0	21.1	1.1
M3, 10^{-9}	-127818	-380	-353	-245	-0.3
M4, 10^{-9}	20179	11	9.9	6.5	0
Sk	-3.37	-2.66	-2.81	-2.51	-0.25
KU	12.8	11.92	12.77	11.55	15.0

Table 4.11 – Statistical descriptors for 85A load (B_1^{85}) after detrending procedure with different time windows

	original	32 seconds	8 seconds	2 seconds	0.3 seconds
μ, V	5.563	5.563	5.563	5.563	5.563
σ, mV	53.2	5.8	5.6	5.1	1.2
eps, 10^{-6}	9568	1046	1010	929	230
V_{max}, mV	5.630×10^3	17.5	13.4	50.0	21.4
V_{min}, mV	5.274×10^3	-75.9	-74.0	-62.3	-21.4
V_{p-p}, mV	355.2	93.5	87.5	112.4	42.9
M2, 10^{-6}	2833	33.8	31.5	26.7	1.6
M3, 10^{-9}	-275393	-519	-484	-337	-0.5
M4, 10^{-9}	56439	17	15.3	10	0
Sk	-1.82	-2.63	-2.72	-2.44	-0.25
KU	4.0	11.91	12.35	11.0	15.4

Table 4.12 – Statistical descriptors for 85A load (B_2^{85}) after detrending procedure with different time windows

	original	32 seconds	8 seconds	2 seconds	0.3 seconds
μ, V	7.780	7.780	7.780	7.780	7.780
σ, mV	8.0	0.6	0.3	0.33	0.21
eps, 10^{-6}	1031	78	46	43	27
V_{max}, mV	7.797×10^3	3.0	2.5	1.6	1.3
V_{min}, mV	7.764×10^3	-3.6	-2.0	-1.8	-1.2
V_{p-p}, mV	32.4	6.7	4.5	3.4	2.6
M2, 10^{-6}	64.3	0.3	0.1	0	0
M3, 10^{-9}	79.8	0	0	0	0
M4, 10^{-9}	7.8	0	0	0	0
Sk	0.15	-0.19	0.11	0.10	-0.13
KU	-1.10	0.86	1.02	1.06	0.55

Table 4.13 – Statistical descriptors for OCV (B_1^0) after detrending procedure with different time windows

	original	32 seconds	8 seconds	2 seconds	0.3 seconds
μ, V	7.733	7.733	7.733	7.733	7.733
σ, mV	6.7	0.3	0.2	0.2	0.1
eps, 10^{-6}	874	48	37	33	11
V_{max}, mV	7.747×10^3	2.1	1.3	1.3	0.5
V_{min}, mV	7.719×10^3	-1.5	-1.3	-1.2	-0.5
V_{p-p}, mV	27.7	3.7	2.7	2.6	1.0
M2, 10^{-6}	45.6	136	0	0	0
M3, 10^{-9}	5.7	0	0	0	0
M4, 10^{-9}	4.0	0	0	0	0
Sk	0.01	0.25	0.59	0.61	0.19
KU	-1.08	0.39	0.74	0.76	1.50

Table 4.14 – Statistical descriptors for OCV (B_2^0) after detrending procedure with different time windows

	original	32 seconds	8 seconds	2 seconds	0.3 seconds
μ, V	7.733	7.733	7.733	7.733	7.733
σ, mV	5.8	0.4	0.3	0.3	0.1
eps, 10^{-6}	761	60	48	42	10
V_{max}, mV	7.729×10^3	3.4	1.8	1.6	0.5
V_{min}, mV	7.702×10^3	-3.3	-1.4	-1.5	-0.5
V_{p-p}, mV	27.5	6.7	3.2	3.1	1.0
M2, 10^{-6}	34.5	214	0.1	0.1	0
M3, 10^{-9}	-37.9	0	0	0	0
M4, 10^{-9}	2.2	0	0	0	0
Sk	-0.18	0.35	0.85	0.69	0.13
KU	-1.08	1.27	0.72	0.60	1.43

Table 4.15 – Statistical descriptors for OCV (B_3^0) after detrending procedure with different time windows

Fig. 4.35 illustrates the obtained results in term of dependence of statistical descriptors on time window.

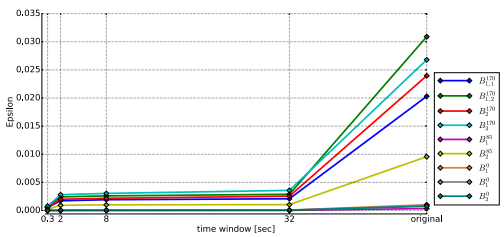

(a) Intensity of fluctuation, ϵ

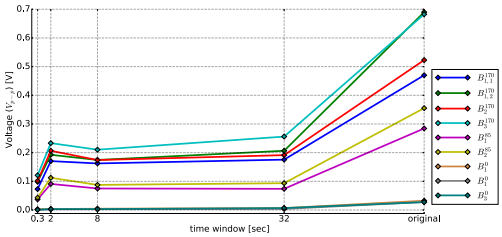

(b) Voltage peak-to-peak

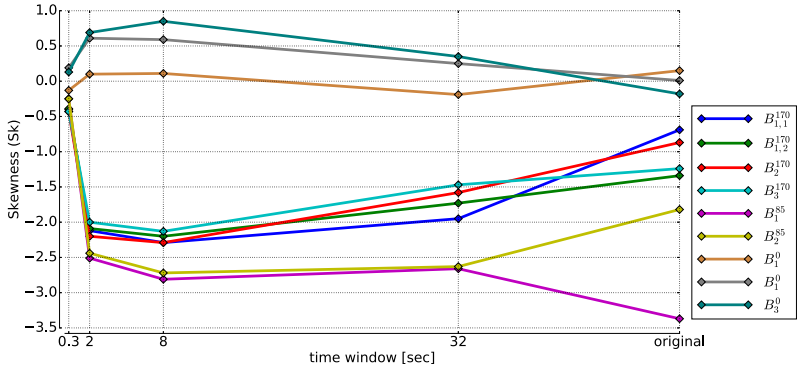

(c) Skewness

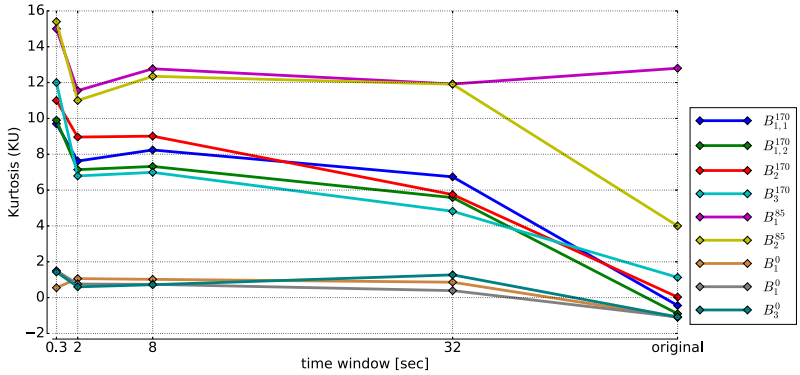

(d) Kurtosis

Figure 4.35 – Dependence of statistical descriptors on time window

Statistical descriptors in frequency domain

Fig. 4.36 and Fig. 4.37 present the result of calculation of PSD for $B^{170}_{1,1}$, $B^{170}_{1,2}$, B^{170}_{2} and B^{170}_{3} zones. All of them reflect the same phenomena, namely:

- a pick on f=0.004Hz with its subharmonics that is explained by low quasi-periodic component;
- flicker-noise component in low frequency range ($(7 \cdot 10^{-2} - 7 \cdot 10^{-1}$ Hz);
- a pick on f=1.7Hz or 1.8Hz that is explained by quasi-periodic signal component with high frequency;
- flicker-noise component ($10 < f < 50$ Hz).

For the first flicker-noise component the slope varies between 2.14 and 2.43. The slope for the second flicker-noise component is situated in the range between 3.58 and 3.66.

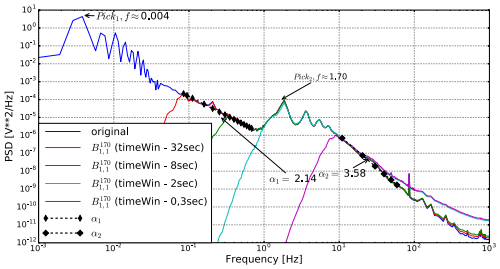

(a) $B^{170}_{1,1}$

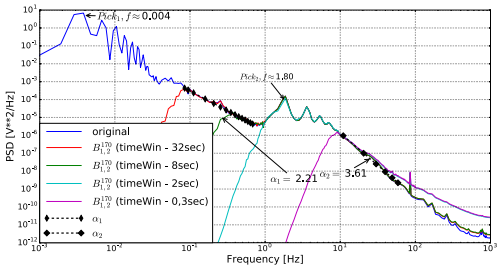

(b) $B^{170}_{1,2}$

Figure 4.36 – PSD Welch with different time windows for 170A load (B^{170}_{1})

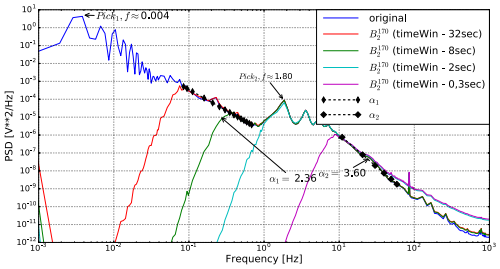

(a) B^{170}_{2}

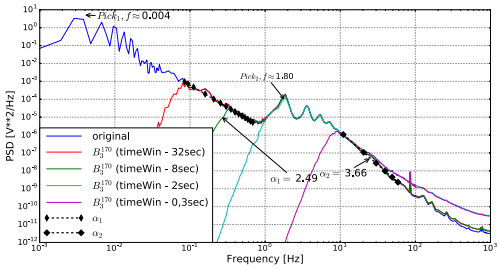

(b) B^{170}_{3}

Figure 4.37 – PSD Welch with different time windows for 170A load (B^{170}_{2} and B^{170}_{3})

Situation for 85A load (B_1^{85} and B_2^{85} zones) are presented in Fig. 4.38 and Fig. 4.39.We can note:

- a pick on f=0.004Hz is not visible;
- flicker-noise component in low frequency range (($7 \cdot 10^{-2} - 7 \cdot 10^{-1}$ Hz);
- a pick on f=1.7Hz that is explained by quasi-periodic signal component with high frequency;
- flicker-noise component ($10 < f < 50$ Hz).

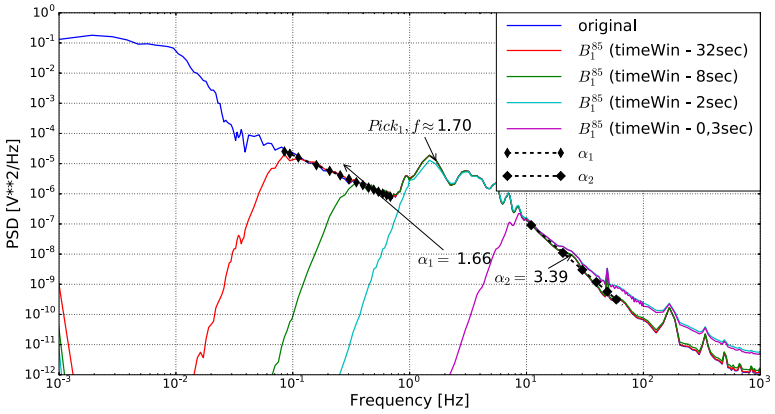

Figure 4.38 – PSD Welch with different time windows for 85 load (B_1^{85})

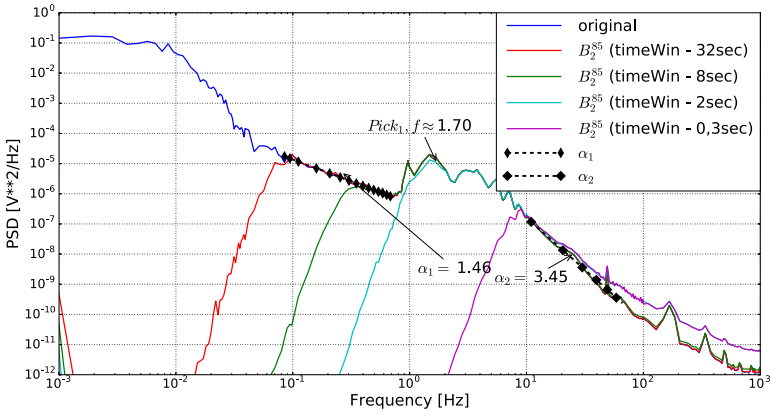

Figure 4.39 – PSD Welch with different time windows for 85 load (B_2^{85})

Slope for the first flicker-noise component is in the range between 1.66 and 1.46 and for the second flicker-noise component between 3.39 and 3.45.

And at last, the results for OCV mode are presented in Fig. 4.40 and Fig. 4.41 that correspond to B_1^0, B_2^0 and B_3^0. We note:

- a pick on f=0.004Hz is not visible;
- flicker-noise component in low frequency range (($7 \cdot 10^{-2} - 7 \cdot 10^{-1}$ Hz);
- a pick on f=2.5Hz that is explained by quasi-periodic signal component with high frequency;
- flicker-noise component ($10 < f < 50$ Hz).

Slope of first flicker-noise component varies from 3.36 to 2.41 and for the second flicker-noise component from 2.31 to 1.9.

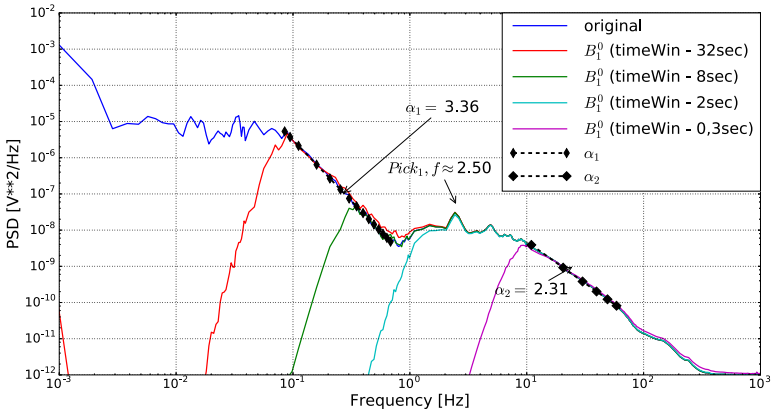

Figure 4.40 – PSD Welch with different time windows for OCV mode (B_1^0)

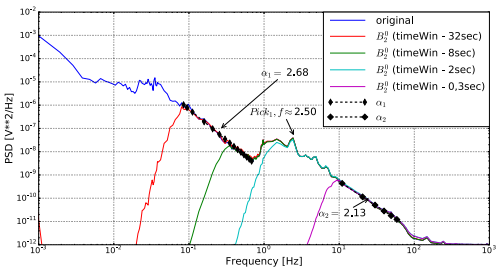

(a) B_2^0

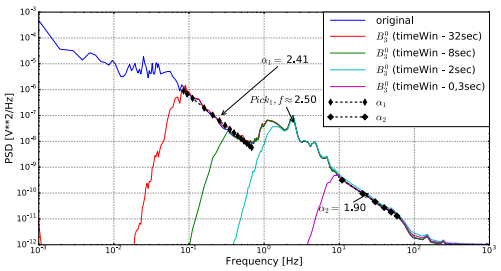

(b) B_3^0

Figure 4.41 – PSD Welch with different time windows for OCV mode (B_2^0 and B_3^0)

4.2.3 Third campaign of measurements

Detailed description

The goal of this campaign are achieved fully with exception of autumn profile at the end. High-speed noise measurement was made not at all time, and total duration of measurements is 200 hours. The profile of third campaign is presented in Fig.4.42.

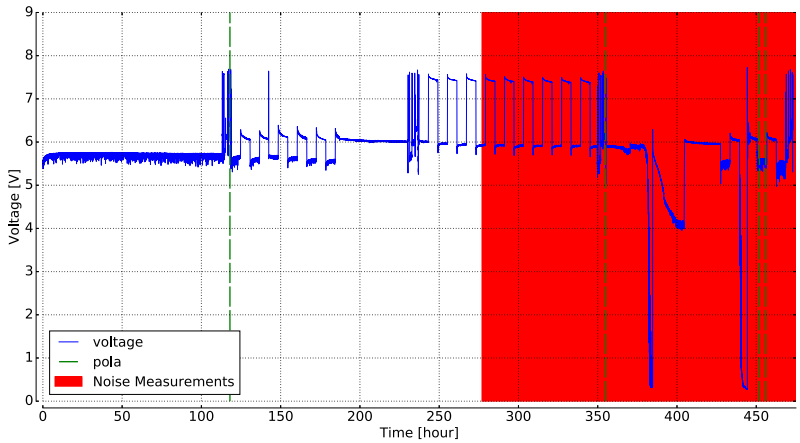

(a) voltage signal

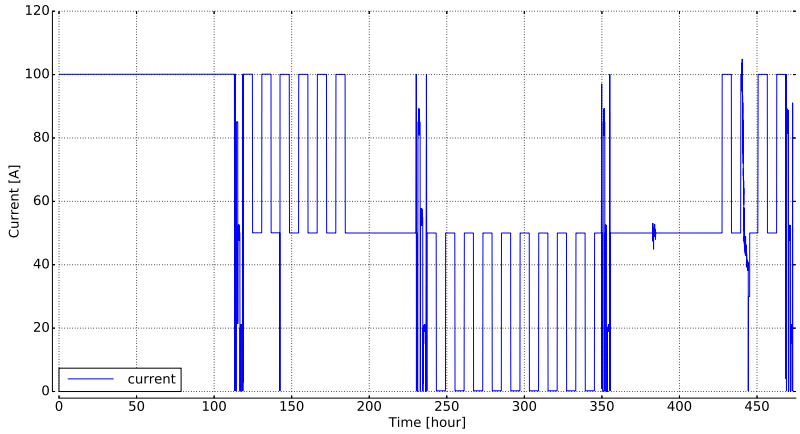

(b) current load

Figure 4.42 – Voltage signal and current load of FC stack during third campaign of measurements.

At the beginning continual operation had been performed under maximum current load of 100A (until 120 hours) with performing polarization procedure on the 118 hour that disturb operation during several hours. After that, cycles operation between 50A and 100A is performed until the 185 hour wherein again continual operation is performed under 50A. After the 230 hour, cycles operation between OCV and 50A is performed again until the 350 hour. After that, tests are performed during 20 hours when a problem of FC stack occurs. After correction, some cycles procedure between 100A and 50A are performed until full stack stop. Measurements of polarization curve have been performed on 118, 355, 452 and 456 hour that perturbate operation during several hours. As we can see in Fig.4.42, high-speed measurements have been

done during summer and autumn profiles that corresponds to cycle operation during 70 hour, continual operation under 50A and cycles operation between 50A and 100A.

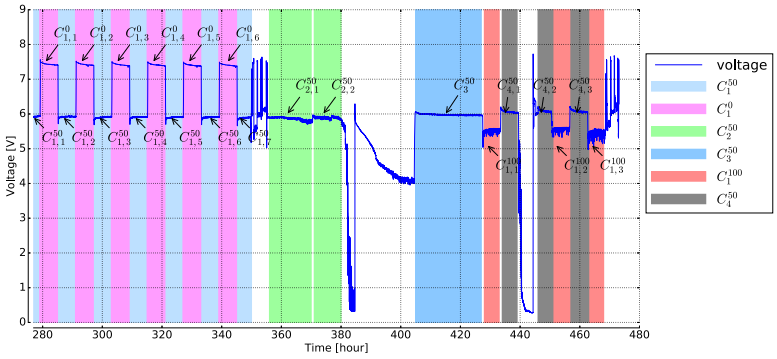

Figure 4.43 – Voltage signal for selected zones.

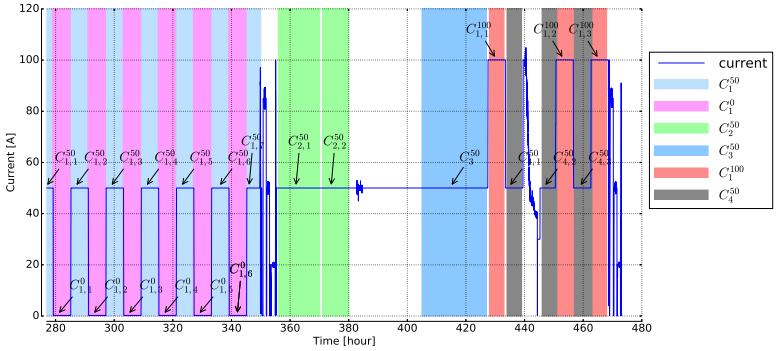

Figure 4.44 – Current load for selected zones.

Selected zones for statistical treatment of recorded high-frequency noise measurements are presented in Fig. 4.43 and Fig. 4.44. Zone C_1^{50} and C_1^0 correspond to operation under 50A load and OCV mode. These zones are divided on subzones which are followed each other. Zone C_2^{50} corresponds to continual operation under 50A load and is subdivided on 2 subzones ($C_{2,1}^{50}$ and $C_{2,2}^{50}$). These subzones have been selected visually based on shift of voltage that is occurred. Zone C_3^{50} is selected and corresponds to operation under 50A load after the interruption of FC stack operation and continues during 20 hours. And at last, Zone C_1^{100} and C_3^{50} correspond to cycle operation under 100A and 50A load, before the FC operation stop. Visualizations of typical signals for selected zones are presented on Fig. 4.45, Fig. 4.46, Fig. 4.47, Fig. 4.48 and Fig. 4.49.

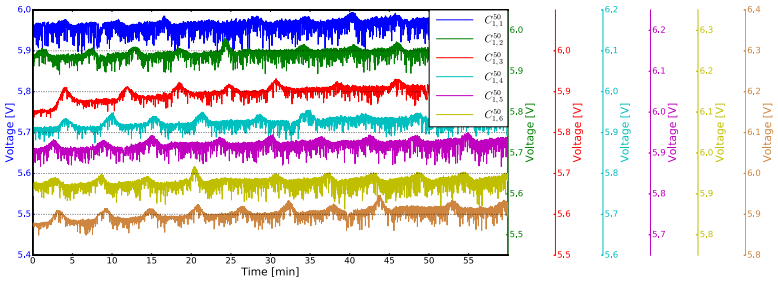

Figure 4.45 – Signal visualization for duration of 1 hour with current load of 50A (C_1^{50})

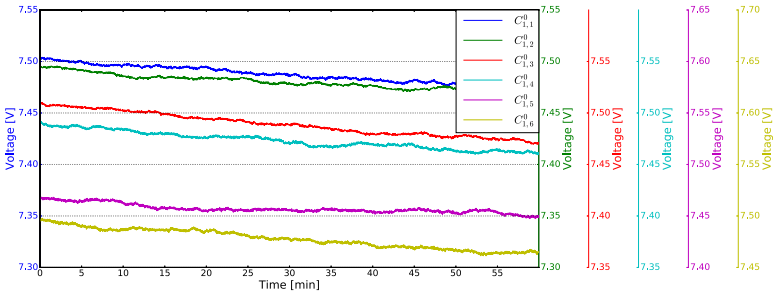

Figure 4.46 – Signal visualization for duration of 1 hour with OCV mode (C_1^0)

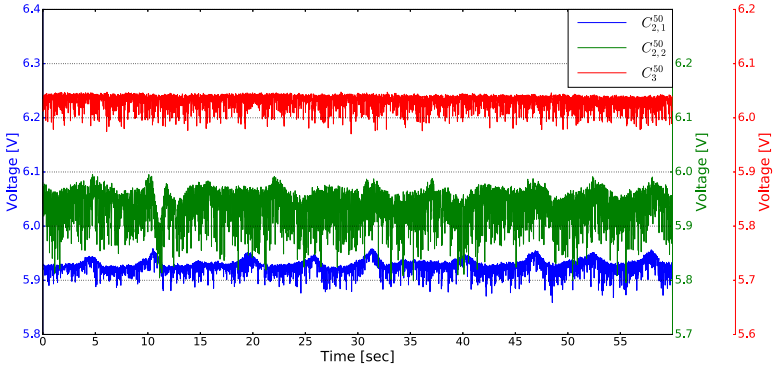

Figure 4.47 – Signal visualization for duration of 1 hour with current load of 50A (C_2^{50} and C_3^{50})

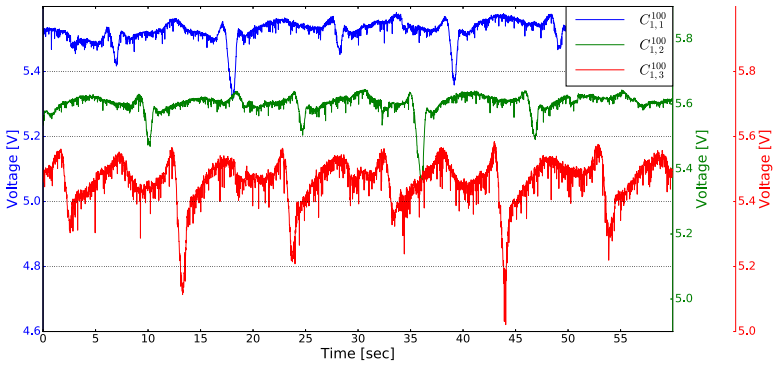

Figure 4.48 – Signal visualization for duration of 1 hour with current load of 100A (C_1^{100})

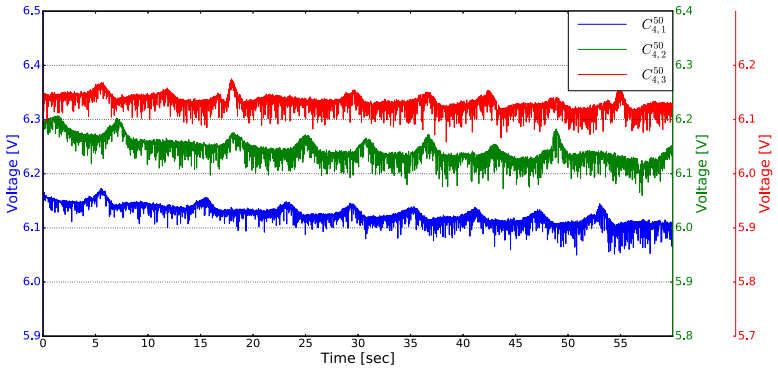

Figure 4.49 – Signal visualization for duration of 1 hour with current load of 50A (C_4^{50})

In Fig. 4.45, Fig. 4.46, Fig. 4.47, Fig. 4.48 and Fig. 4.49 are presented detrended signals. Detrending procedure is performed with polynomial fitting with 5th order and time window of 8 seconds. As we can see all detrended signals have the same structure and it is difficult to compare them visually.

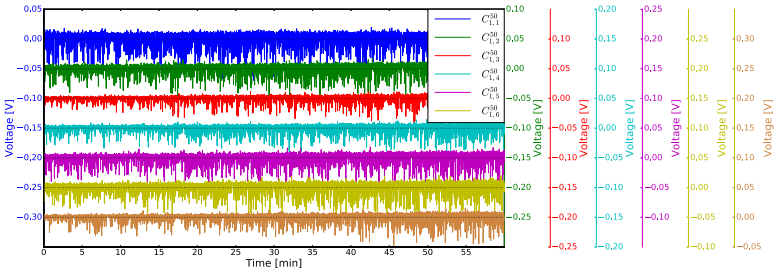

Figure 4.50 – Signal visualization for duration of 1 hour with current load of 50A after detrending (C_1^{50})

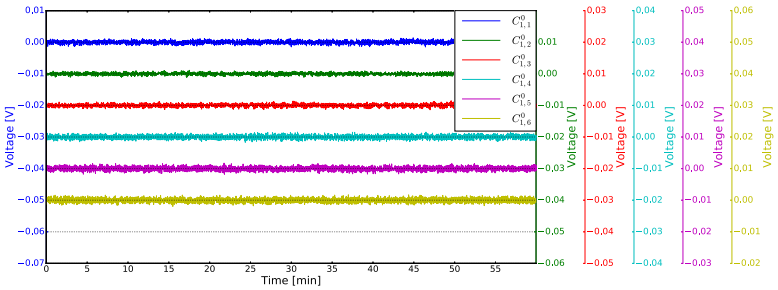

Figure 4.51 – Signal visualization for duration of 1 hour with OCV mode after detrending (C_1^0)

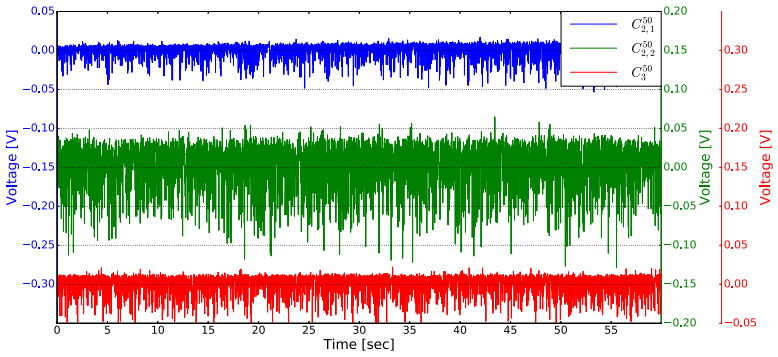

Figure 4.52 – Signal visualization for duration of 1 hour with current load of 50A after detrending (C_2^{50} and C_3^{50})

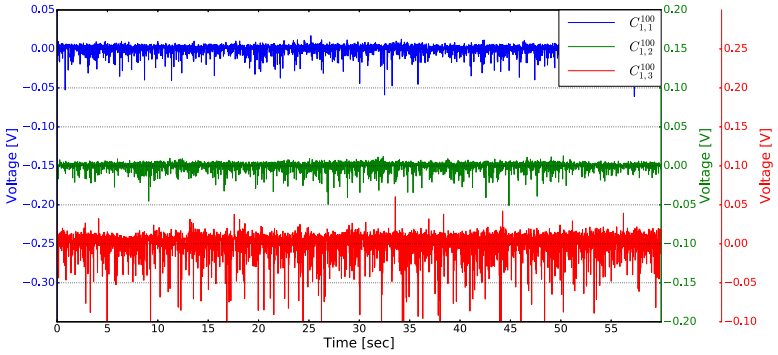

Figure 4.53 – Signal visualization for duration of 1 hour with current load of 100A after detrending (C_1^{100})

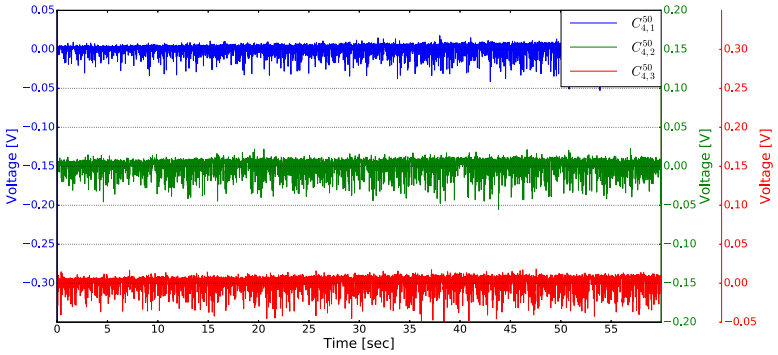

Figure 4.54 – Signal visualization for duration of 1 hour with current load of 50A after detrending (C_4^{50})

Statistical descriptors in time domain

Detrended signal with their histogram are presented further in Fig. 4.55 and Fig. 4.56 for C_1^{100} and C_1^{50} zones wherein negative skewness values can be noted. We can see a big difference in amplitude and frequency between 50A and 100A load. Another situation we can see in Fig. 4.57. Distribution of signals is non Gaussian. The signal for OCV zone has another character, see Fig. 4.57. This distribution is also non-Gaussian but near zero.

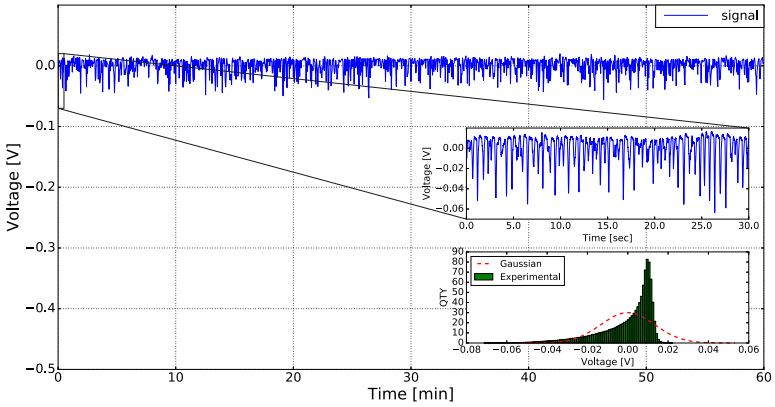

Figure 4.55 – Detrended signal with its histogram (5 order polynomial detrending with time window of 8 sec) for 100A.

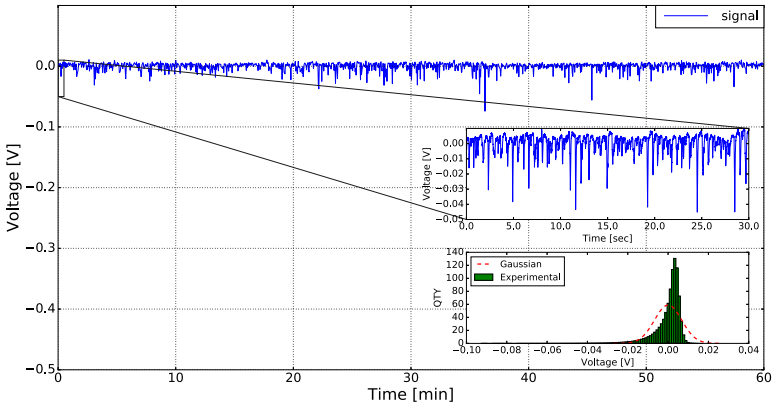

Figure 4.56 – Detrended signal with its histogram (5 order polynomial detrending with time window of 8 sec) for 50A.

Statistical descriptors obtained with different time windows are presented in tables below for selected zones.

Zone C_1^{50} shows a decreasing time tendency for standard deviation and increasing for skewness and kurtosis, see Tab. 4.16, Tab. 4.17 and Tab. 4.18. Another behaviour we can observe for C_4^{50} zone in Tab. 4.22, Tab. 4.23 and Tab. 4.24 wherein standard deviation is increased. Different tendencies we can see in C_2^{50} and C_3^{50} zones that are presented in Tab. 4.19, Tab. 4.20 and Tab. 4.21

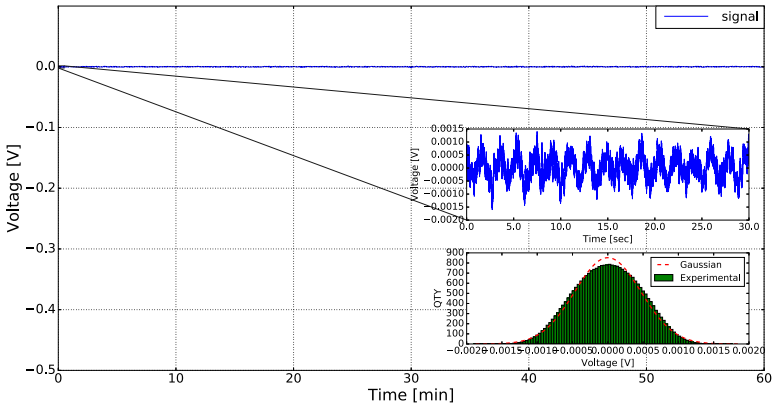

Figure 4.57 – Detrended signal with its histogram (5 order polynomial detrending with time window of 8 sec) for OCV.

	original	32 seconds	8 seconds	2 seconds	0.3 seconds
μ, V	5.963	5.963	5.963	5.963	5.963
σ, mV	15.2	13.4	13.3	12.4	1.7
eps, 10^{-6}	2562	2247	2231	2083	287
V_{max}, mV	5.996×10^3	22.0	22.6	58.0	20.8
V_{min}, mV	5.880×10^3	-72.8	-71.3	-74.3	-19.7
V_{p-p}, mV	116.1	94.8	93.9	132.3	40.5
M2, 10^{-6}	233	179	177	154	2.9
M3, 10^{-9}	-3988	-3760	-3585	-2646	-0.2
M4, 10^{-9}	245	167	159	120	0
Sk	-1.11	-1.56	-1.52	-1.38	0
KU	1.49	2.19	2.08	2.04	5.24

Table 4.16 – Statistical descriptors for 50A load ($C_{1,1}^{50}$) after detrending procedure with different time windows

In Tab. 4.25, Tab. 4.26 and Tab. 4.27 are presented statistical results for running under 100A load, namely zones $C_{1,1}^{100}$, $C_{1,2}^{100}$ and $C_{1,3}^{100}$ correspondingly. At the beginning, intensity of fluctuations (eps) decreases (for $C_{1,1}^{100}$ and $C_{1,2}^{100}$) and after increases ($C_{1,3}^{100}$) that is confirmed also visually. Moreover, kurtosis value increases.

In Tab. 4.28, Tab. 4.29 and Tab. 4.30 are presented statistical results for OCV mode $C_{1,1}^{0}$, $C_{1,4}^{0}$ and $C_{1,6}^{0}$ correspondingly. As we can see that all of parameters are very different from the ones recorded for running under the load.

	original	32 seconds	8 seconds	2 seconds	0.3 seconds
μ, V	5.925	5.925	5.925	5.925	5.925
σ, mV	12.1	8.1	8.1	7.5	1.3
eps, 10^{-6}	2054	1382	1372	1273	221
V_{max}, mV	5.960×10^3	16.7	16.6	41.9	15.1
V_{min}, mV	5.861×10^3	-60.5	-60.4	-55.6	-16.1
V_{p-p}, mV	98.9	77.2	77.0	97.5	31.2
M2, 10^{-6}	148	67	66	56	1.7
M3, 10^{-9}	-887	-1112	-1071	-761	-0.1
M4, 10^{-9}	72	34	33	23	0
Sk	-0.49	-2.0	-1.99	-1.77	0.08
KU	0.28	4.74	4.62	4.32	6.98

Table 4.17 – Statistical descriptors for 50A load $C_{1,4}^{50}$) after detrending procedure with different time windows

	original	32 seconds	8 seconds	2 seconds	0.3 seconds
μ, V	5.901	5.901	5.901	5.901	5.901
σ, mV	14.6	7.9	7.9	7.3	1.2
eps, 10^{-6}	2486	1351	1340	1239	216
V_{max}, mV	5.948×10^3	14.1	15.4	40.1	14.9
V_{min}, mV	5.838×10^3	-53.9	-52.6	-52.8	-15.7
V_{p-p}, mV	109.2	68.0	68.0	93.0	30.6
M2, 10^{-6}	215	63	62	53	1.6
M3, 10^{-9}	-574	-1038	-995	-705	-0.1
M4, 10^{-9}	134	31	30	21.5	0
Sk	-0.18	-2.05	-2.01	-1.8	-0.08
KU	0.10	4.91	4.79	4.54	7.0

Table 4.18 – Statistical descriptors for 50A load ($C_{1,7}^{50}$) after detrending procedure with different time windows

	original	32 seconds	8 seconds	2 seconds	0.3 seconds
μ, V	5.926	5.926	5.926	5.926	5.926
σ, mV	13.1	10.9	10.8	10.0	1.6
eps, 10^{-6}	2215	1840	1828	1698	284
V_{max}, mV	5.960×10^3	16.0	22.2	51.6	22.1
V_{min}, mV	5.847×10^3	-74.2	-71.8	-67.2	-18.1
V_{p-p}, mV	112.8	90.2	94.0	118.9	40.3
M2, 10^{-6}	172	118	117	101	2.8
M3, 10^{-9}	-2127	-2419	-2310	-1665	-0.5
M4, 10^{-9}	147	95	90	65	0
Sk	-0.94	-1.8	-1.81	-1.63	-0.11
KU	1.97	3.74	3.58	3.42	6.14

Table 4.19 – Statistical descriptors for 50A load ($C_{2,1}^{50}$) after detrending procedure with different time windows

	original	32 seconds	8 seconds	2 seconds	0.3 seconds
μ, V	5.933	5.933	5.933	5.933	5.933
σ, mV	33.1	31.1	30.8	28.3	2.8
eps, 10^{-6}	5583	5252	5206	4777	477
V_{max}, mV	6.001×10^3	48.9	64.8	128.5	41.9
V_{min}, mV	5.759×10^3	-165.0	-152.6	-143.6	-37.3
V_{p-p}, mV	242.1	213.9	217.5	272.1	79.3
M2, 10^{-6}	1097	971	954	803	8.0
M3, 10^{-9}	-34341	-31392	-29333	-19853	0.2
M4, 10^{-9}	4374	3448	3262	2360	0.4
Sk	-0.94	-1.0	-1.0	-0.87	0
KU	0.63	0.65	0.58	0.65	3.51

Table 4.20 – Statistical descriptors for 50A load ($C_{2,2}^{50}$) after detrending procedure with different time windows

	original	32 seconds	8 seconds	2 seconds	0.3 seconds
μ, V	6.030	6.030	6.030	6.030	6.030
σ, mV	13.3	13.2	13.1	12.2	1.6
eps, 10^{-6}	2218	2194	2178	2024	273
V_{max}, mV	6.050×10^3	17.0	23.8	53.5	19.5
V_{min}, mV	5.947×10^3	-78.0	-75.5	-71.4	-18.3
V_{p-p}, mV	242.1	95.0	99.4	125.0	37.9
M2, 10^{-6}	178	175	172	149	2.7
M3, 10^{-9}	-3526	-3484	-3317	-2397	-0.2
M4, 10^{-9}	156	151	143	106	0
Sk	-1.47	-1.5	-1.46	-1.31	0
KU	1.9	1.93	1.83	1.77	4.7

Table 4.21 – Statistical descriptors for 50A load (C_{3}^{50}) after detrending procedure with different time windows

	original	32 seconds	8 seconds	2 seconds	0.3 seconds
μ, V	6.123	6.123	6.123	6.123	6.123
σ, mV	18.0	8.6	8.5	7.9	1.2
eps, 10^{-6}	2950	1414	1403	1299	210
V_{max}, mV	6.174×10^3	13.6	21.2	45.9	17.8
V_{min}, mV	6.041×10^3	-63.9	-63.5	-59.0	-15.1
V_{p-p}, mV	132.8	77.6	84.7	105.0	33.0
M2, 10^{-6}	326	75	73	63	1.6
M3, 10^{-9}	-1325	-1189	-1132	-794	-0.1
M4, 10^{-9}	324	37	35	25	0
Sk	-0.2	-1.8	-1.8	-1.57	0
KU	0.04	3.7	3.5	3.3	6.3

Table 4.22 – Statistical descriptors for 50A load ($C_{4,1}^{50}$) after detrending procedure with different time windows

	original	32 seconds	8 seconds	2 seconds	0.3 seconds
μ, V	6.142	6.142	6.142	6.142	6.142
σ, mV	22.3	11.1	11.0	10.1	1.4
eps, 10^{-6}	3637	1812	1791	1658	231
V_{max}, mV	6.208×10^3	19.9	22.6	58.2	21.2
V_{min}, mV	6.043×10^3	-75.1	-72.7	-59.8	-14.7
V_{p-p}, mV	165.3	95.0	95.4	118.1	36.0
M2, 10^{-6}	498	123	121	103	2.0
M3, 10^{-9}	3211	-2084	-1967	-1407	-136
M4, 10^{-9}	83	78	72	52	0
Sk	-0.3	-1.5	-1.47	-1.3	0
KU	0.37	2.1	1.97	1.9	5.1

Table 4.23 – Statistical descriptors for 50A load ($C_{4,2}^{50}$) after detrending procedure with different time windows

	original	32 seconds	8 seconds	2 seconds	0.3 seconds
μ, V	6.129	6.129	6.129	6.129	6.129
σ, mV	15.3	10.8	10.71751	9.9	1.4
eps, 10^{-6}	2503	1764	1791	1625	240
V_{max}, mV	6.178×10^3	15.1	20.9	50.1	16.8
V_{min}, mV	6.047×10^3	-74.3	-72.7	-72.2	-15.4
V_{p-p}, mV	130.6	89.5	93.6	122.3	32.2
M2, 10^{-6}	235	116	115	99	2.1
M3, 10^{-9}	-2219	-2072	-1976	-1413	0
M4, 10^{-9}	22	76	72	53	0
Sk	-0.6	-1.6	-1.59	-1.43	0
KU	1.0	2.6	2.49	2.39	5.4

Table 4.24 – Statistical descriptors for 50A load ($C_{4,3}^{50}$) after detrending procedure with different time windows

	original	32 seconds	8 seconds	2 seconds	0.3 seconds
μ, V	5.529	5.529	5.529	5.529	5.529
σ, mV	35.1	7.0	6.7	6.3	1.8
eps, 10^{-6}	6356	1269	1226	1142	328
V_{max}, mV	5.592×10^3	16.7	17.0	45.1	29.2
V_{min}, mV	5.308×10^3	-93.8	-92.7	-87.4	-29.0
V_{p-p}, mV	283.6	110.5	109.8	132.5	58.3
M2, 10^{-6}	1235	49	45.9	39.8	3.2
M3, 10^{-9}	-92869	-908	-841	-622	-2
M4, 10^{-9}	16467	34	31	22	0.1
Sk	-2.13	-2.63	-2.7	-2.47	-0.33
KU	7.8	11.45	11.8	11.0	13.0

Table 4.25 – Statistical descriptors for 100A load ($C_{1,1}^{100}$) after detrending procedure with different time windows

	original	32 seconds	8 seconds	2 seconds	0.3 seconds
μ, V	5.601	5.601	5.601	5.601	5.601
σ, mV	31.5	6.1	5.8	5.4	1.6
eps, 10^{-6}	5630	1102	1052	977	291
V_{max}, mV	5.645×10^3	34.6	26.5	33.6	26.9
V_{min}, mV	5.329×10^3	-87.1	-86.5	-71.34	-26.7
V_{p-p}, mV	315.7	121.8	113.0	105.0	53.6
M2, 10^{-6}	994	38	34	29.9	2.6
M3, 10^{-9}	-110052	-618	-578	-417	-1.6
M4, 10^{-9}	21039	22	19	13	0.1
Sk	-3.5	-2.63	-2.2	-2.54	-0.37
KU	18.2	12.2	13.1	11.6	14.4

Table 4.26 – Statistical descriptors for 100A load ($C_{1,2}^{100}$) after detrending procedure with different time windows

	original	32 seconds	8 seconds	2 seconds	0.3 seconds
μ, V	5.462	5.462	5.462	5.462	5.462
σ, mV	69.6	17.7	16.9	15.3	3.3
eps, 10^{-6}	12756	3243	3096	2803	614
V_{max}, mV	5.588×10^3	45.6	60.4	101.7	51.3
V_{min}, mV	5.010×10^3	-194.3	-186.2	-155.3	-50.4
V_{p-p}, mV	578.7	240.0	246.6	257.0	101.7
M2, 10^{-6}	4855	313	286	234	11.2
M3, 10^{-9}	-57313	-14566	-13358	-8411	-9
M4, 10^{-9}	173988	1366	1195	698	2.3
Sk	-1.7	-2.62	-2.76	-2.34	-0.25
KU	4.37	10.8	11.6	9.7	15.46

Table 4.27 – Statistical descriptors for 100A load ($C_{1,3}^{100}$) after detrending procedure with different time windows

	original	32 seconds	8 seconds	2 seconds	0.3 seconds
μ, V	7.487	7.487	7.487	7.487	7.487
σ, mV	7.8	0.5	0.4	0.2	0.1
eps, 10^{-6}	1043	67	63	38	22
V_{max}, mV	7.504×10^3	1.8	1.8	1.2	0.7
V_{min}, mV	7.474×10^3	-2.4	-1.9	-1.1	-0.7
V_{p-p}, mV	109.2	4.3	3.8	2.4	1.4
M2, 10^{-6}	61	0	0	0	0
M3, 10^{-9}	121	0	0	0	0
M4, 10^{-9}	6.5	0	0	0	0
Sk	0.25	-0.07	-0.02	0.01	0
KU	-1.25	-0.39	-0.43	-0.33	-0.6

Table 4.28 – Statistical descriptors for OCV ($C_{1,1}^{0}$) after detrending procedure with different time windows

	original	32 seconds	8 seconds	2 seconds	0.3 seconds
μ, V	7.473	7.473	7.473	7.473	7.473
σ, mV	8.3	0.5	0.5	0.3	0.1
eps, 10^{-6}	1112	80	76	43	24
V_{max}, mV	7.492×10^3	2.1	1.9	1.2	0.8
V_{min}, mV	7.458×10^3	-2.2	-2.0	-1.3	-0.7
V_{p-p}, mV	33.8	4.4	3.9	2.6	1.6
M2, 10^{-6}	61	0	0	0	0
M3, 10^{-9}	121	0	0	0	0
M4, 10^{-9}	6.5	0	0	0	0
Sk	0.26	0	0	0.07	0.02
KU	-1.07	-0.62	-0.55	-0.35	-0.42

Table 4.29 – Statistical descriptors for OCV ($C^0_{1,4}$) after detrending procedure with different time windows

	original	32 seconds	8 seconds	2 seconds	0.3 seconds
μ, V	7.477	7.477	7.477	7.477	7.477
σ, mV	9.4	0.6	0.6	0.3	0.1
eps, 10^{-6}	1265	88	84	43	23
V_{max}, mV	7.498×10^3	2.2	2.1	1.3	0.8
V_{min}, mV	7.460×10^3	-2.5	-2.1	-1.3	-0.7
V_{p-p}, mV	37.0	4.8	4.3	2.6	1.5
M2, 10^{-6}	89	0	0	0	0
M3, 10^{-9}	42	0	0	0	0
M4, 10^{-9}	14	0	0	0	0
Sk	0.05	-0.02	-0.01	0.07	0.02
KU	-1.24	-0.71	-0.67	-0.35	-0.38

Table 4.30 – Statistical descriptors for OCV ($C^0_{1,6}$) after detrending procedure with different time windows

Fig. 4.58, Fig. 4.59, Fig. 4.60 and Fig. 4.61 illustrate the obtained results in term of dependence of statistical descriptors on time window.

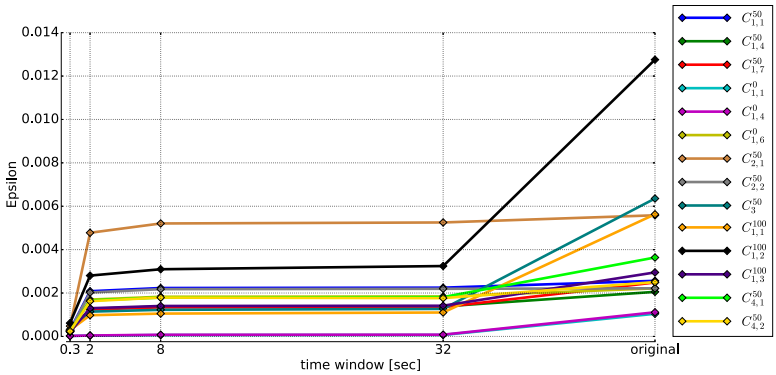

Figure 4.58 – Epsilon

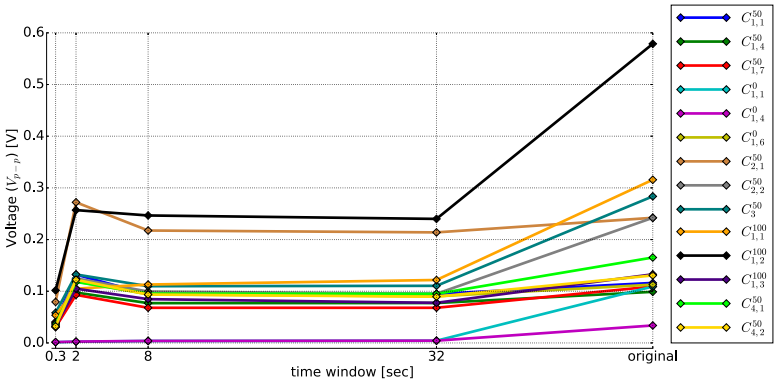

Figure 4.59 – Voltage peak-to-peak

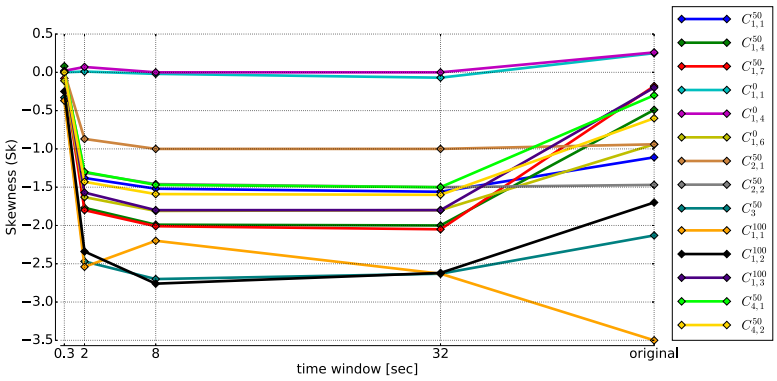

Figure 4.60 – Skewness

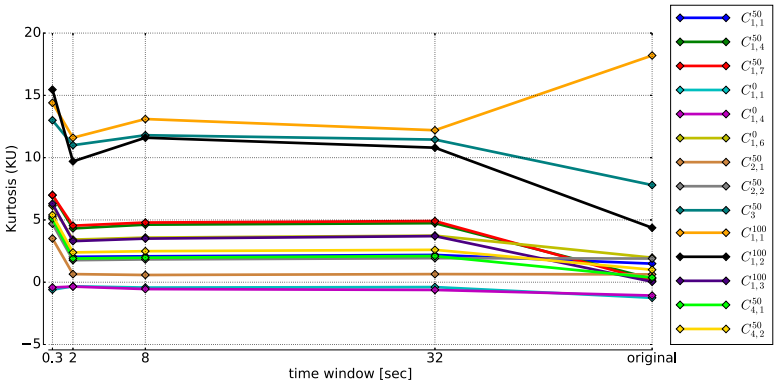

Figure 4.61 – Kurtosis

Statistical descriptors in frequency domain

In this section results of calculation descriptors in frequency domain are presented for selected zones.

Zones C_1^{50}, C_2^{50}, C_2^{50}, C_3^{50} and C_1^{100} have same shape of PSD curve but with some difference. All of them reflect at the same phenomena, namely:

- a pick on f=1.8Hz with its subharmonics;
- flicker-noise component in low frequency range ($(7 \cdot 10^{-2} - 7 \cdot 10^{-1}$ Hz);
- flicker-noise component ($10 < f < 50$ Hz).

Values of slope for flicker-noise components and pick frequency are presented in Fig. 4.62, Fig. 4.63, Fig. 4.64, Fig. 4.65, Fig. 4.66, Fig. 4.67, Fig. 4.68, Fig. 4.69, Fig. 4.70, Fig. 4.71

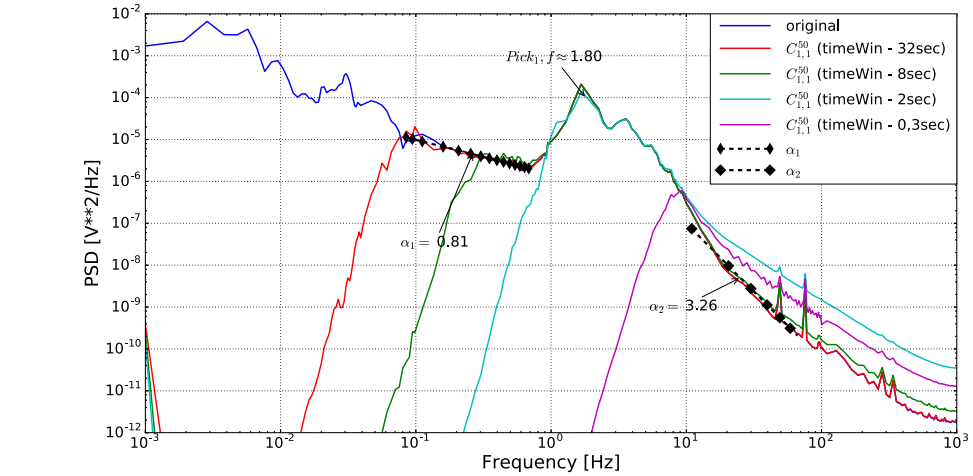

(a) $C_{1,1}^{50}$

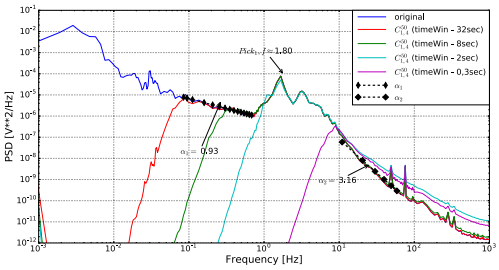

(b) $C_{1,4}^{50}$

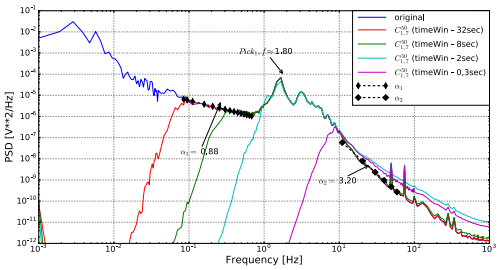

(c) $C_{1,7}^{50}$

Figure 4.62 – PSD Welch with different time windows for 50A load (C_1^{50})

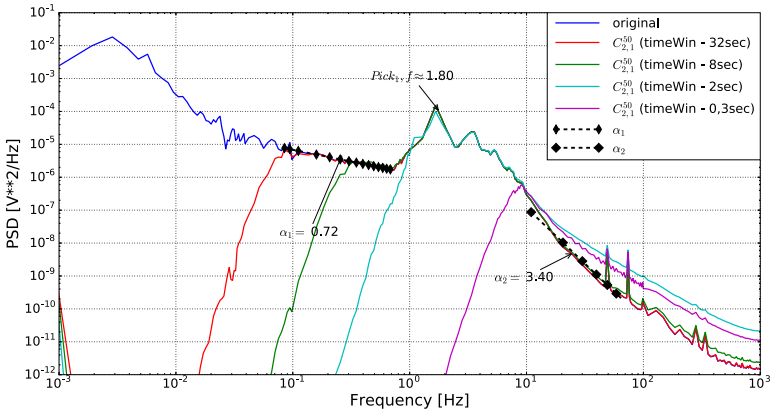

Figure 4.63 – PSD Welch with different time windows for 50A load ($C_{2,1}^{50}$)

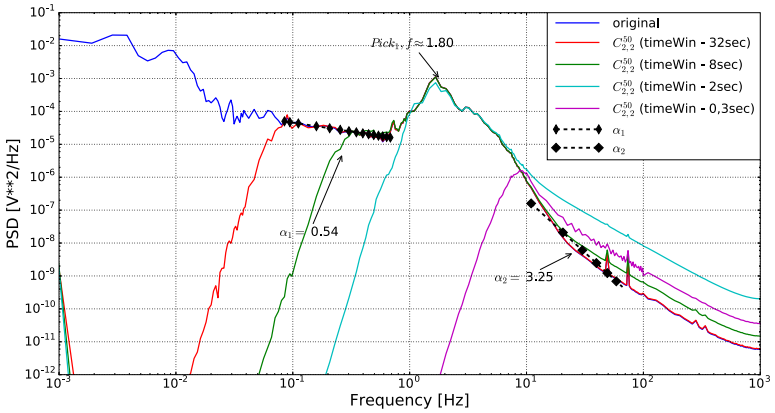

Figure 4.64 – PSD Welch with different time windows for 50A load ($C_{2,2}^{50}$)

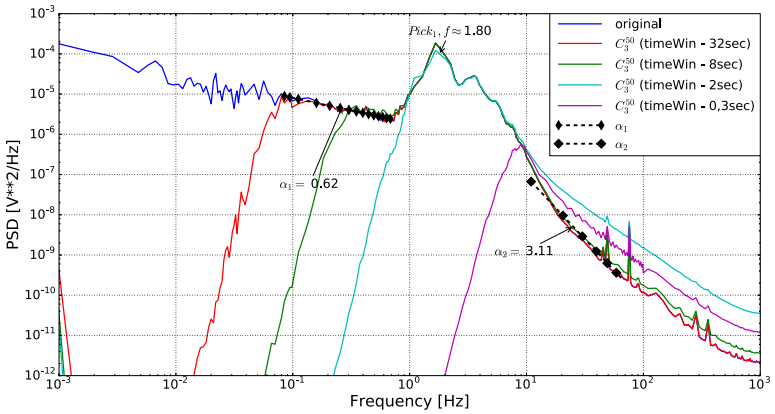

Figure 4.65 – PSD Welch with different time windows for 50A load (C_3^{50})

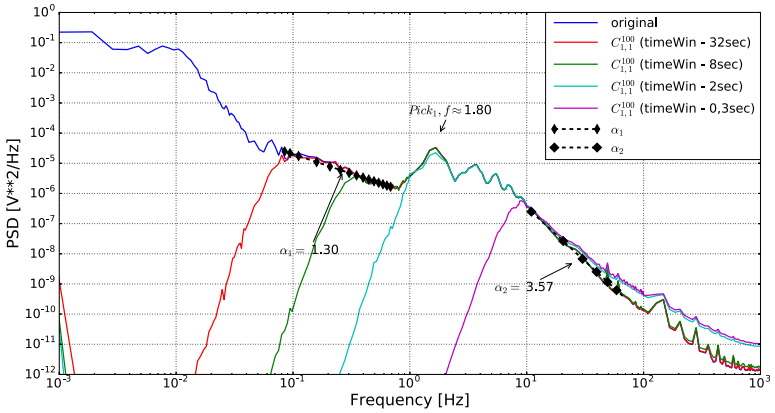

Figure 4.66 – PSD Welch with different time windows for 100A load ($C^{100}_{1,1}$)

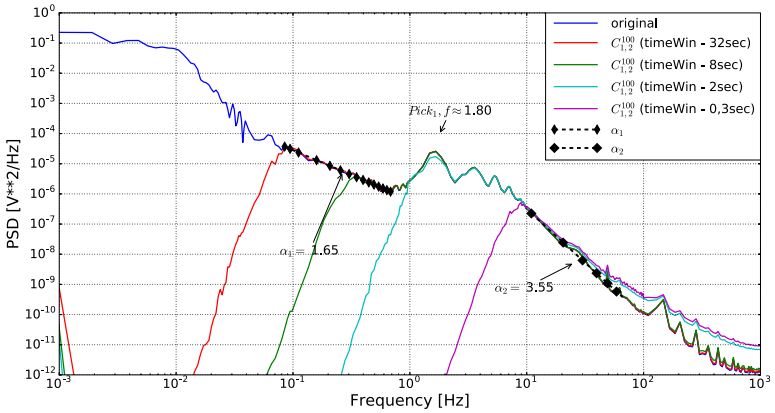

Figure 4.67 – PSD Welch with different time windows for 100A load ($C^{100}_{1,2}$)

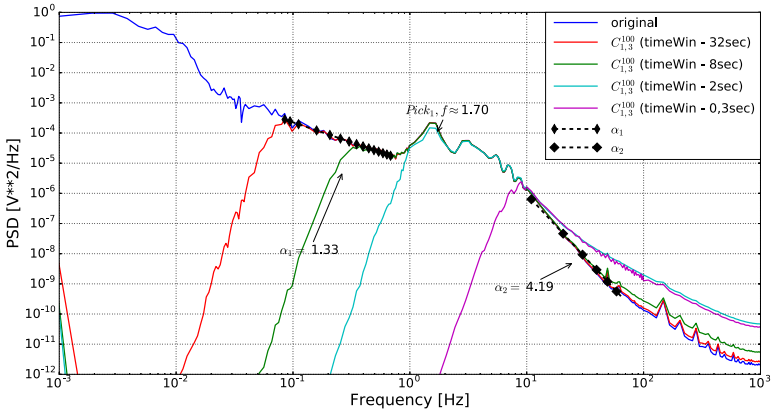

Figure 4.68 – PSD Welch with different time windows for 100A load ($C^{100}_{1,3}$)

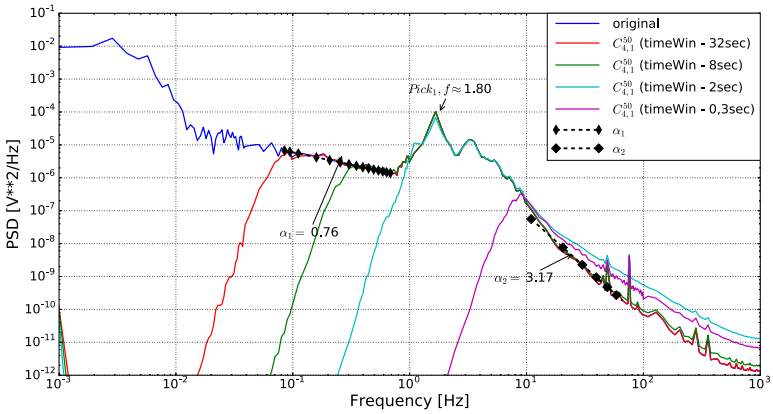

Figure 4.69 – PSD Welch with different time windows for 50A load ($C^{50}_{4,1}$)

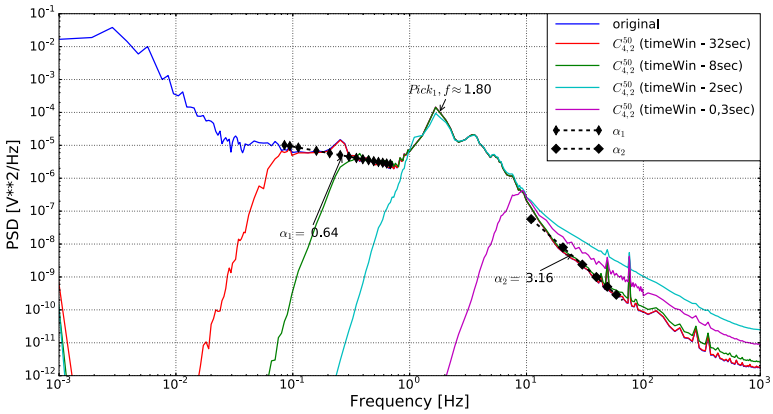

Figure 4.70 – PSD Welch with different time windows for 50A load ($C^{50}_{4,2}$)

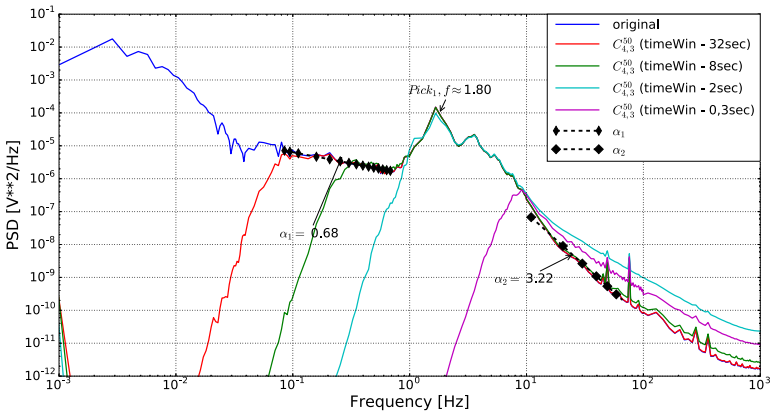

Figure 4.71 – PSD Welch with different time windows for 50A load ($C^{50}_{4,3}$)

And at last, we present PSD for OCV mode in Fig. 4.72. All of them have the same character, namely:

- a pick on f=0.5-0.6)Hz;
- a pick on f=1.8Hz is not visible;
- flicker-noise component in low frequency range ($(7 \cdot 10^{-2} - 7 \cdot 10^{-1}$ Hz);
- flicker-noise component ($10 < f < 50$ Hz).

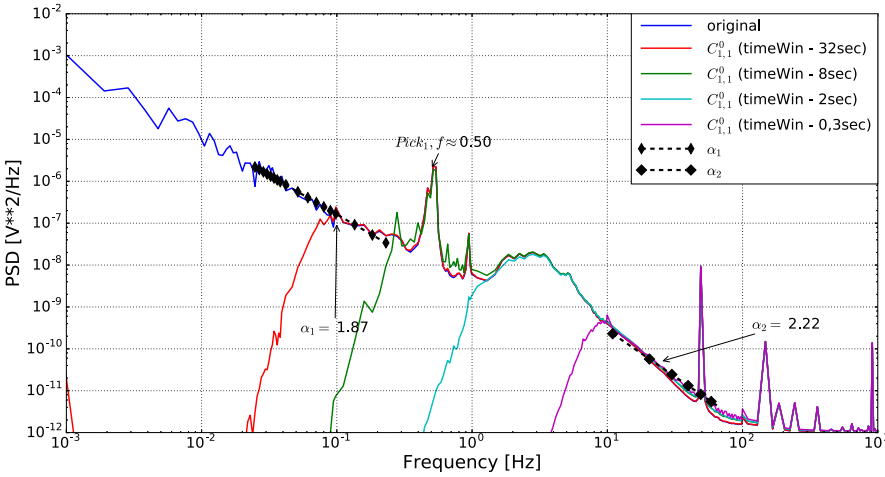

(a) $C^0_{1,1}$

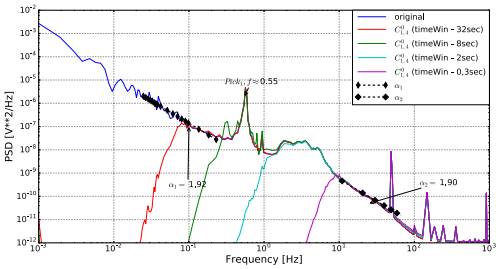

(b) $C^0_{1,4}$

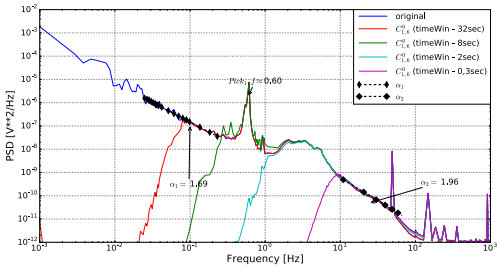

(c) $C^0_{1,6}$

Figure 4.72 – PSD Welch with different time windows for OCV mode (C^0_1)

4.2.4 Fourth campaign of measurements

Detailed description

In comparison with the previous campaigns, this campaign has been performed for automotive operation mode. The profile of fourth campaign is presented in Fig.4.73.

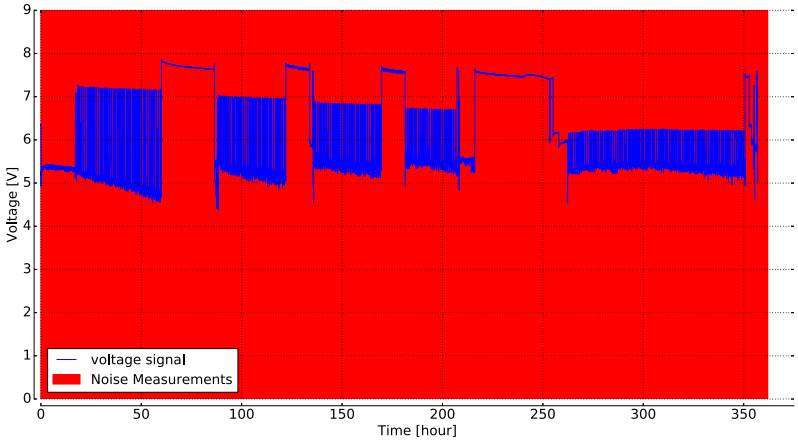

(a) voltage signal

Figure 4.73 – Voltage signal and current load of FC stack during seconds measurements campaign

This campaign includes continuous and auto mode operations. Continues operation had been performed under current load of 110A during 18 hours. Also continues operation under 85A load has been performed (zone D_1^{85}) during 10 hours just before the last OCV mode operation (zone D_4^0). After that, auto operation mode with some phases of operation with OCV mode take place. High-speed noise measurements were performed during all time. In framework of this campaign the applied load has been progressively diminished in order to reach project goals, that is why there are five different changing, see Fig.4.74.

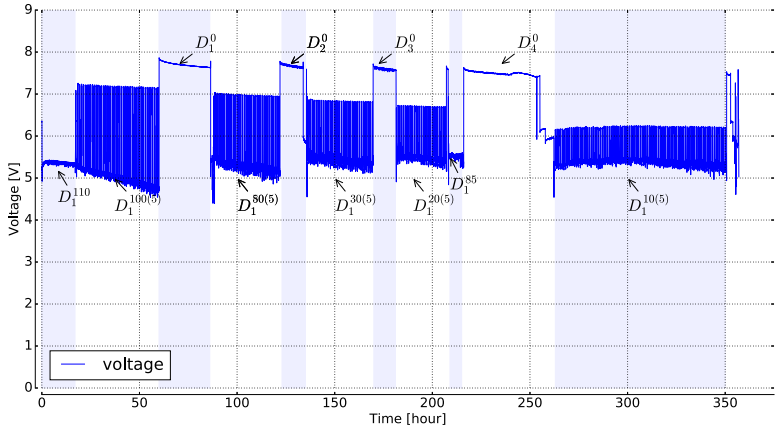

Figure 4.74 – Voltage signal for selected zones

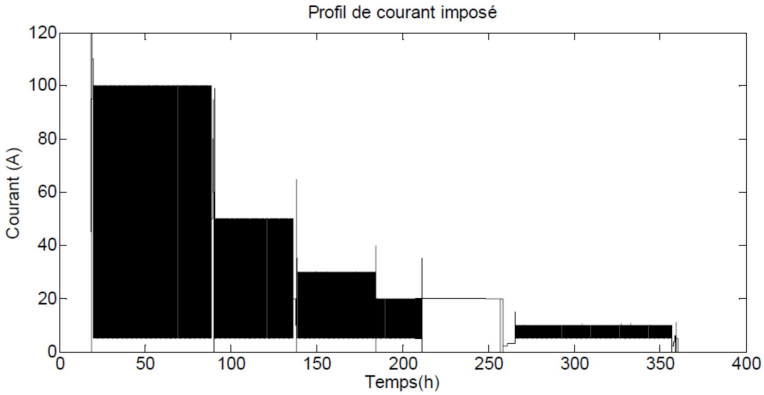

Figure 4.75 – Current load for selected zones

Fig. 4.74 presents the selected for analyzed zones. Zone D_1^{110} corresponds to the normal operation mode with current load of 170A after launching FC stack. During this period we can observe stabilization processes within FC stack. Zones $D_1^{100(5)}$, $D_1^{50(5)}$, $D_1^{30(5)}$, $D_1^{20(5)}$ and $D_1^{10(5)}$ zones corresponds to automotive mode operation with changing current load between 5A and applied maximal load, namely 100A, 50A, 30, 20 and 10A. In addition, OCV mode had been recorded in D_1^0, D_2^0, D_3^0 and D_4^0 zones.

Statistical descriptors for continuous operation and OCV mode.

Corresponding current profile for this selected zones is presented in Fig.4.75. For further statistical treatment following zones have been selected: D_1^{110}, D_1^{85}, D_1^0, D_2^0, D_3^0 and D_4^0. Visualizations of typical signals for selected zones are presented on Fig. 4.76, Fig. 4.77.

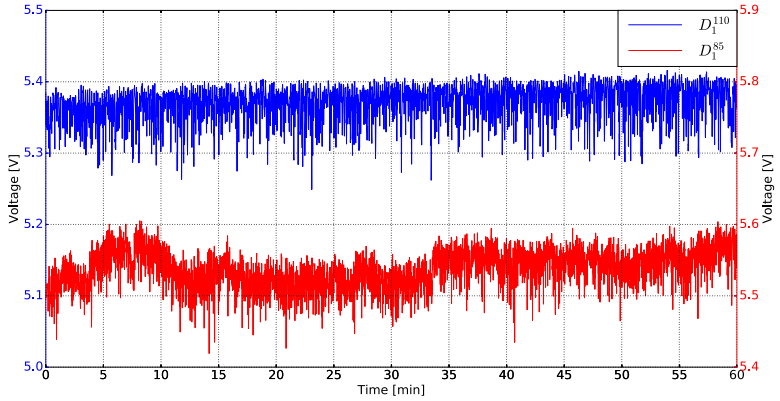

Figure 4.76 – Signal visualization for duration of 1 hour with current load of 110A (D_1^{110}) and 85A(D_1^{85}

As we can see different zones have a different structure of signals. First one (Fig. 4.76) is signals with 110A and 85A, there are different.

As we can see all of them have a different structure of signals. Zone D_1^{110} has a complex

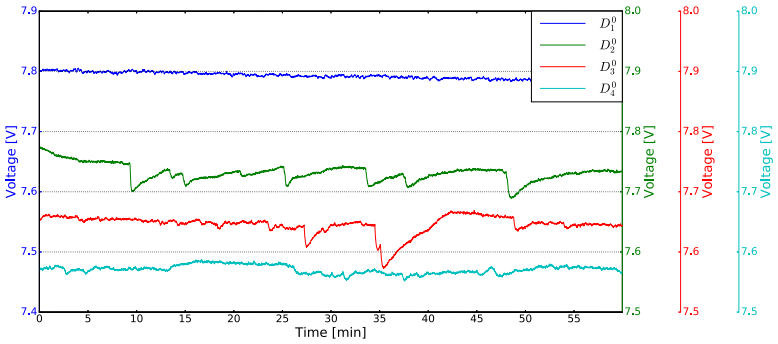

Figure 4.77 – Signal visualization for duration of 1 hour with OCV mode (D_1^0, D_2^0, D_3^0, D_4^0)

structure with low frequency component. Even signal under OCV mode has a different shape, some of them have a voltage drops that is increased by time, and at the end shape of signal is not smooth.

Detrended signals are presented in relation to mean value for selected zones in Fig. 4.78. Detrending procedure is performed with polynomial fitting with 5th order and time window of 8 seconds. As we can see all detrended signals has preliminary at the same structure and it is difficult to compare them visually.

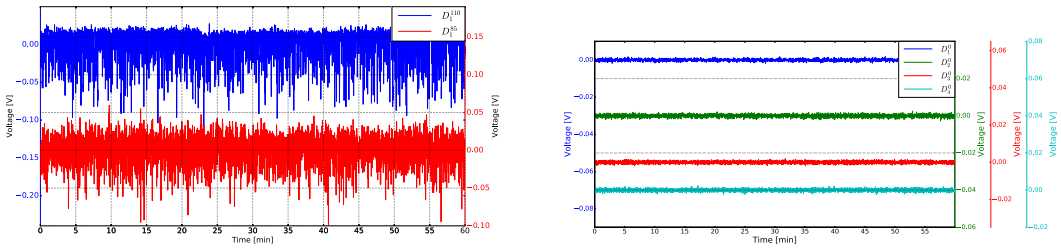

(a) D_1^{110} and D_1^{85} (b) D_1^0

Figure 4.78 – Duration of 1 hour with current load of 110A, 85A and with OCV mode after detrending (D_1^{110}, D_1^{85} and D_1^0)

Statistical descriptors in time domain Detrended signal with their histogram are presented further in Fig. 4.79 and Fig. 4.80 for D_1^{110} and D_1^{85} zones wherein negative skewness values can be noted. We can see a big difference in amplitude and frequency between 50A and 100A load. Another situation we can see in Fig. 4.81. Distribution of signals is non Gaussian. The signal for OCV zone has another character, see Fig. 4.81. This distribution is also non-Gaussian but centred near zero.

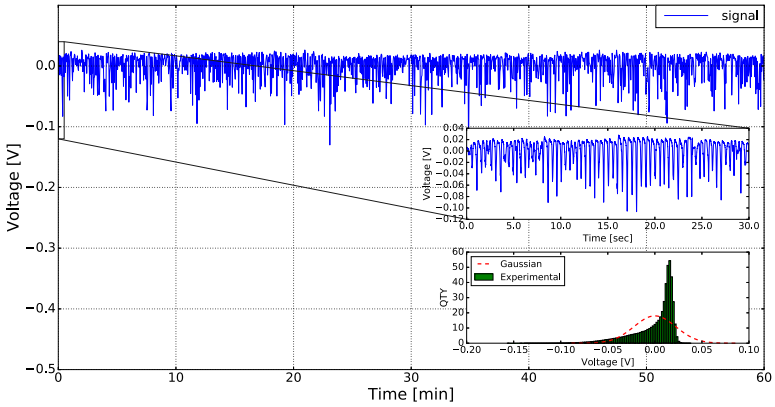

Figure 4.79 – Detrended signal with its histogram (5 order polynomial detrending with time window of 8 sec) for 110A.

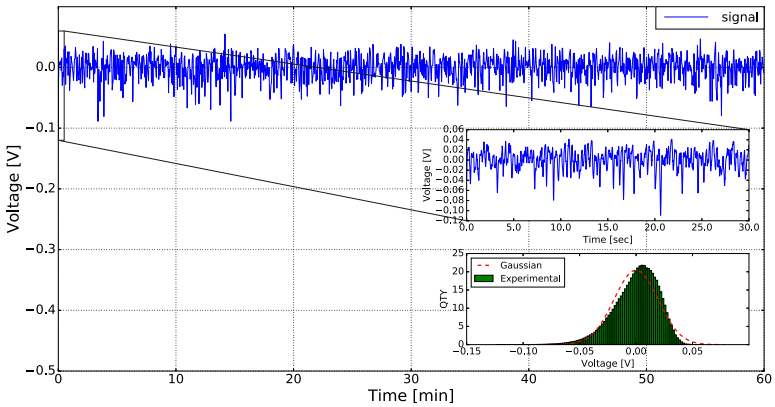

Figure 4.80 – Detrended signal with its histogram (5 order polynomial detrending with time window of 8 sec) for 85A.

Statistical descriptors obtained with different time windows are presented in tables below for selected zones.

Results for different time windows for selected zones are presented in the form of tables. Tab. 4.31 and Tab. 4.32 correspond to D_1^{110}, and D_1^{85} zones correspondingly. There is a big difference in all parameters.

Tab. 4.33, Tab. 4.34, Tab. 4.35 and Tab. 4.36 present statistical descriptors for D_1^0, D_2^0 and D_3^0 zones accordingly. Standard deviation value is decreased by time. Moreover, kurtosis value is decreased

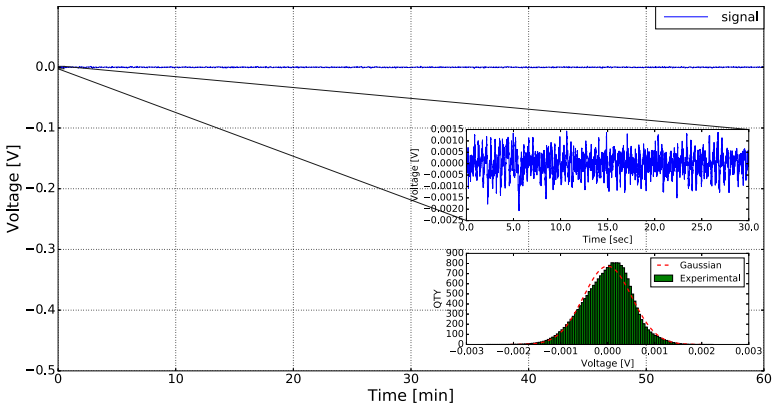

Figure 4.81 – Detrended signal with its histogram (5 order polynomial detrending with time window of 8 sec) for OCV.

	original	32 seconds	8 seconds	2 seconds	0.3 seconds
μ, V	5.372	5.372	5.372	5.372	5.372
σ, mV	24.4	23.2	22.1	21.2	4.0
eps, 10^{-6}	4548	4330	4127	3956	753
V_{max}, mV	5.417×10^3	40.7	38.4	83.4	50.1
V_{min}, mV	5.202×10^3	-161.1	-156	-146	-48.5
V_{p-p}, mV	215.0	201.8	195.1	230.0	98.6
M2, 10^{-6}	597	541	491	451	16
M3, 10^{-9}	-18740	-18147	-17223	-14245	0
M4, 10^{-9}	1702	1480	1270	1052	2
Sk	-1.28	-1.4	-1.58	-1.48	-0.2
KU	1.7	2.0	2.25	2.16	5.8

Table 4.31 – Statistical descriptors for 110A load(D_1^{110}) after detrending procedure with different time windows

	original	32 seconds	8 seconds	2 seconds	0.3 seconds
μ, V	5.537	5.537	5.537	5.537	5.537
σ, mV	26.7	20.2	19.5	16.8	2.5
eps, 10^{-6}	4836	3647	3529	3044	463
V_{max}, mV	5.615×10^3	50.5	59.4	76.5	24.2
V_{min}, mV	5.388×10^3	-133.0	-123.8	-110.4	-24.2
V_{p-p}, mV	227.4	183.6	183.2	186.9	48.4
M2, 10^{-6}	717	407	381	284	6.57
M3, 10^{-9}	-6635	-5958	-5404	-3824	0.4
M4, 10^{-9}	1609	642	557	332	0.2
Sk	-0.34	-0.72	-0.72	-0.8	0.02
KU	0.12	0.86	-0.82	1.12	1.51

Table 4.32 – Statistical descriptors for 85A load (D_1^{85}) after detrending procedure with different time windows

	original	32 seconds	8 seconds	2 seconds	0.3 seconds
μ, V	7.792	7.792	7.792	7.792	7.792
σ, mV	6.0	0.6	0.5	0.4	0.2
eps, 10^{-6}	770	80	66	62	25
V_{max}, mV	7.806×10^3	3.1	2.2	2.0	1.2
V_{min}, mV	7.776×10^3	-3.3	-2.6	-2.3	-1.3
V_{p-p}, mV	30.1	6.4	4.9	4.3	2.5
M2, 10^{-6}	36	0.4	0.3	0.2	0
M3, 10^{-9}	-6	0	0	0	0
M4, 10^{-9}	2	0	0	0	0
Sk	0	-1.4	-0.2	-0.15	-0.08
KU	-1.0	2.0	0.15	0.18	0.71

Table 4.33 – Statistical descriptors for OCV (D_1^0) after detrending procedure with different time windows

	original	32 seconds	8 seconds	2 seconds	0.3 seconds
μ, V	7.731	7.731	7.731	7.731	7.731
σ, mV	13.9	0.87	0.75	0.68	0.1
eps, 10^{-6}	1800	113	97	88	19
V_{max}, mV	7.776×10^3	7.4	2.9	2.8	0.9
V_{min}, mV	7.687×10^3	-6.0	-3.1	-2.7	-0.8
V_{p-p}, mV	88.7	13.3	6.0	5.6	1.7
M2, 10^{-6}	193	0.7	0.5	0.4	0
M3, 10^{-9}	461	0	0	0	0
M4, 10^{-9}	144	0	0	0	0
Sk	0.17	-0.1	-0.27	-0.17	-0.1
KU	0.83	1.4	-0.38	-0.33	0.44

Table 4.34 – Statistical descriptors for OCV (D_2^0) after detrending procedure with different time windows

	original	32 seconds	8 seconds	2 seconds	0.3 seconds
μ, V	7.645	7.645	7.645	7.645	7.645
σ, mV	15.3	0.8	0.61	0.52	0.07
eps, 10^{-6}	2002	104	80	68	9
V_{max}, mV	7.669×10^3	7.0	3.4	2.6	0.4
V_{min}, mV	7.571×10^3	-3.8	-2.4	-2.1	-0.4
V_{p-p}, mV	97.9	10.9	5.9	4.8	0.8
M2, 10^{-6}	234	0.6	0.3	0.2	0
M3, 10^{-9}	-7753	0	0	0	0
M4, 10^{-9}	490	0	0	0	0
Sk	-2.16	0	-0.15	0	0
KU	5.94	1.1	-0.41	-0.25	-0.1

Table 4.35 – Statistical descriptors for OCV (D_3^0) after detrending procedure with different time windows

	original	32 seconds	8 seconds	2 seconds	0.3 seconds
μ, V	7.570	7.570	7.570	7.570	7.570
σ, mV	6.9	0.8	0.6	0.2	0.06
eps, 10^{-6}	915	109	83	39	9
V_{max}, mV	7.587×10^3	3.3	2.4	1.5	0.3
V_{min}, mV	7.550×10^3	-3.4	-2.4	-1.5	-0.3
V_{p-p}, mV	37.2	6.8	4.8	3.0	0.7
M2, 10^{-6}	48	0.6	0.3	0	0
M3, 10^{-9}	18	0	0	0	0
M4, 10^{-9}	5.3	0	0	0	0
Sk	0.05	0	0	0.08	0
KU	-0.68	-0.16	-0.43	-0.06	-0.28

Table 4.36 – Statistical descriptors for OCV (D_4^0) after detrending procedure with different time windows

Fig. 4.82 illustrates the obtained results in term of dependence of statistical descriptors on time window.

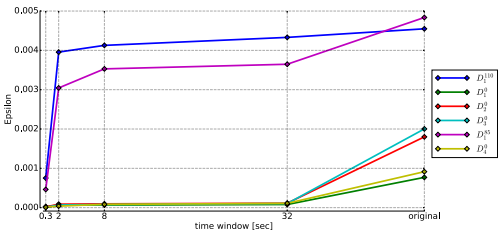

(a) Intensity of fluctuation, ϵ

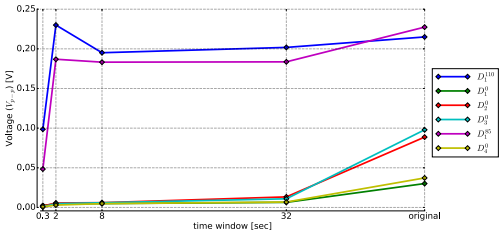

(b) Voltage peak-to-peak

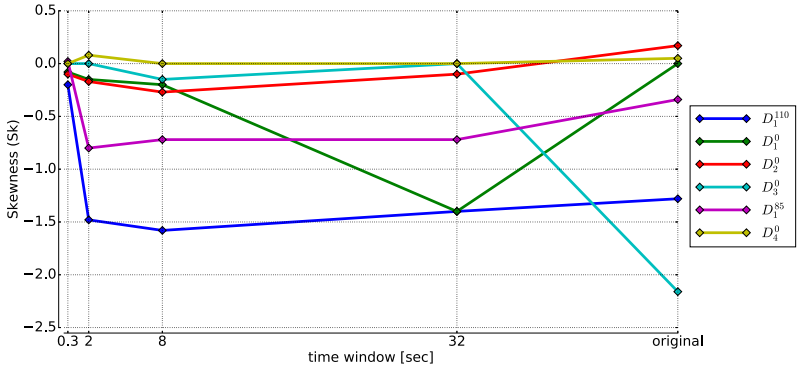

(c) Skewness

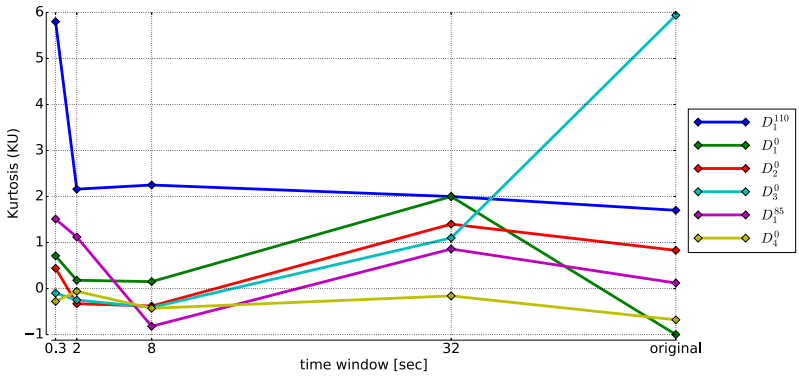

(d) Kurtosis

Figure 4.82 – Dependence of statistical descriptors on time window

Statistical descriptors in frequency domain In this section results of calculation descriptors in frequency domain has been presented for selected zones

PSD for D_1^{110} is presented in Fig. 4.83. Our curve has a lot zones that we can emphasize:

- a pick on f=0.09Hz;
- flicker-noise component in low frequency range from 0.15 until 0.4 Hz with slope of 2.83;
- a pick on f=1.9Hz;
- flicker-noise component in low frequency range ($8 < f < 50$ Hz) with slope of 4.28;

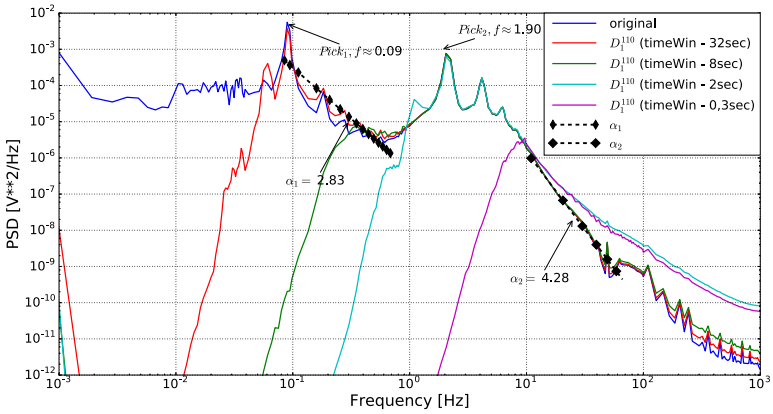

Figure 4.83 – PSD Welch with different time windows for 110A load (D_1^{110})

Another situation we can observe for D_1^{85} zone that is presented in Fig. 4.84. There are some phenomena that can emphasize:

- flicker-noise component in low frequency range until 0.4 Hz with slope of 0.99;
- a pick on f=0.5Hz;
- flicker-noise component in low frequency range ($8 < f < 15$ Hz) with slope of 4.98;
- flicker-noise component ($40 < f < 100$ Hz) with slope of 1.67.

Slopes of flicker-noise component are decreased from 1.66 to 1.46 and from 3.39 to 3.45 for first and seconds correspondingly.

Strange behaviors we can observe for D_1^0, D_2^0, D_3^0 and D_4^0 that are presented in Fig. 4.85, Fig. 4.85, Fig. 4.85 an. Below we discuss qualitatively the obtained results.

Zone D_1^0 The following phenomena can be noted:

- flicker-noise component in low frequency range until 0.4 Hz with slope of 2.31;
- a pick on f=2.3Hz with its subharmonics that is explained by low serrated component in signal
- flicker-noise component in low frequency range ($8 < f < 15$ Hz) with slope of 1.67;
- flicker-noise component ($40 < f < 100$ Hz) with slope of 2.74.

Zone D_2^0 The following phenomena can be noted:

- flicker-noise component in low frequency range until 0.4 Hz with slope of 2.88;
- a pick on f=2.3Hz with its subharmonics that is explained by low serrated component in signal
- flicker-noise component in low frequency range ($8 < f < 15$ Hz) with slope of 2.2;
- flicker-noise component ($40 < f < 100$ Hz) with slope of 3.74.

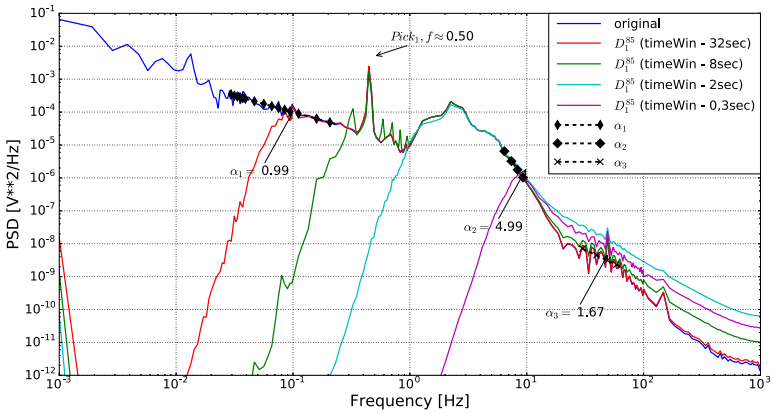

Figure 4.84 – PSD Welch with different time windows for 85A load (D_1^{85})

Zone D_3^0 The following phenomena can be noted:
- flicker-noise component in low frequency range until 0.4 Hz with slope of 2.69;
- a pick on f=2.3Hz is not visible
- flicker-noise component in low frequency range ($8 < f < 15$ Hz) with slope of 3.96;

Zone D_4^0 The following phenomena can be noted:
- flicker-noise component in low frequency range until 0.4 Hz with slope of 1.63;
- a pick on f=0.45Hz;
- a pick on f=2.3Hz is not visible
- flicker-noise component in low frequency range ($8 < f < 15$ Hz) with slope of 3.89;

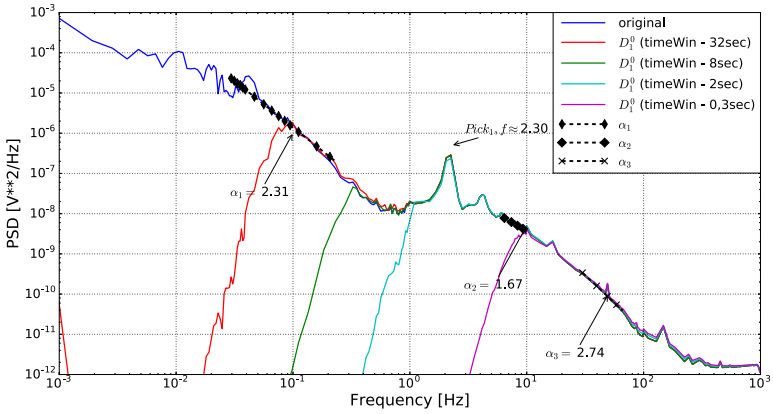

Figure 4.85 – PSD Welch with different time windows for OCV mode (D_1^0)

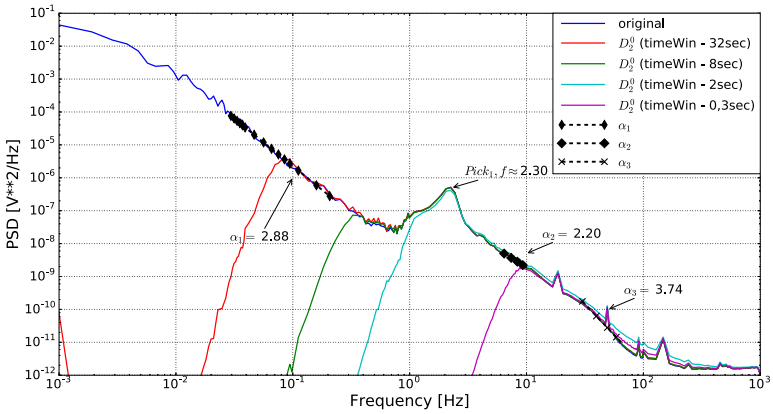

Figure 4.86 – PSD Welch with different time windows for OCV mode (D_2^0)

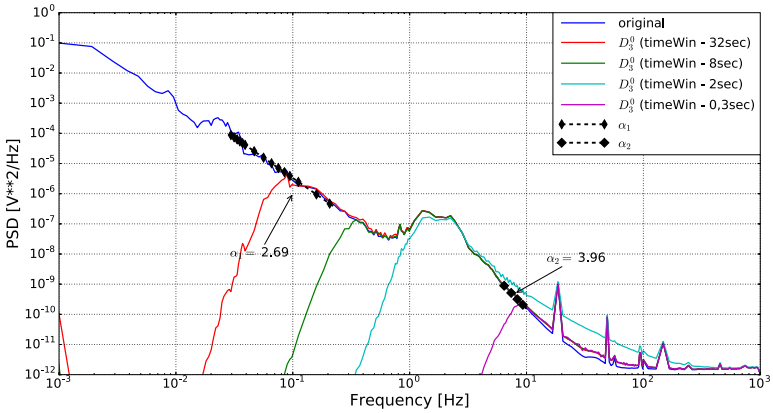

Figure 4.87 – PSD Welch with different time windows for OCV mode (D_3^0)

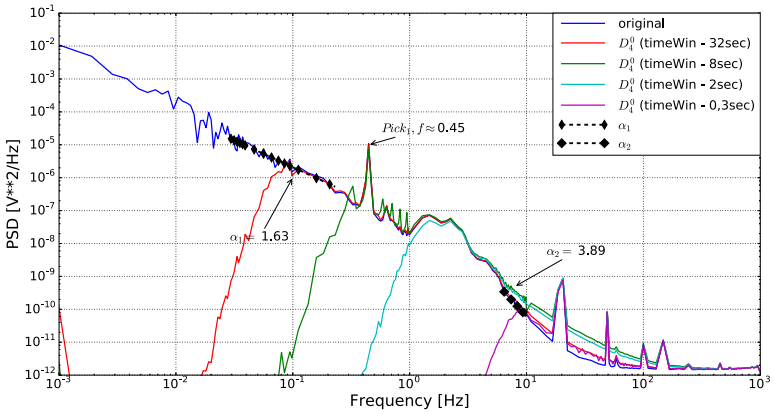

Figure 4.88 – PSD Welch with different time windows for OCV mode (D_4^0)

Statistical descriptors for automotive operation mode

This operation mode concerns zones $D_1^{100(5)}$, $D_1^{50(5)}$, $D^{30(5)_1}$, $D_1^{20(5)}$ and $D_1^{10(5)}$. During this operation mode the load of stack has been changed repetitively between maximum I_{max} (I_{max} = 100A, 50A, 30A, 20A and 10A) and I_{min}=5A values, the duration of each cycle is equal to 60s and total time duration of each zone is equal to 1 hour. All parts of cycling had been merged (we cut the parts of the signal which correspond to 1 minute). Results of merging are presented in Fig. 4.89, Fig. 4.90 and Fig. 4.91.

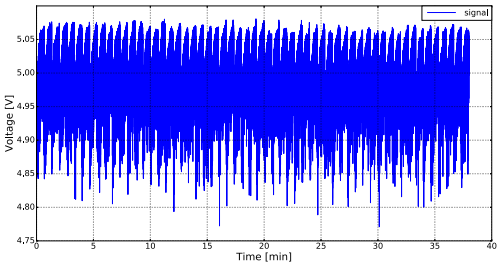

(a) 100A ($D^{100(5)_1}$)

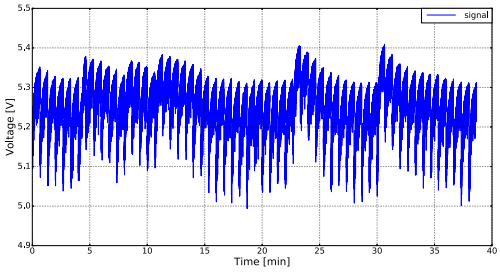

(b) 50A ($D^{50(5)_1}$)

Figure 4.89 – Signal visualization for automotive mode under 100A/5A ($D_1^{100(5)}$) and under 50A/5A($D_1^{50(5)}$)

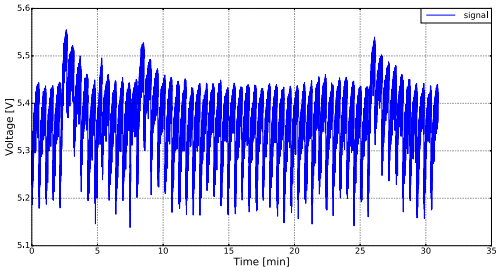

(a) 30A ($D^{30(5)_1}$)

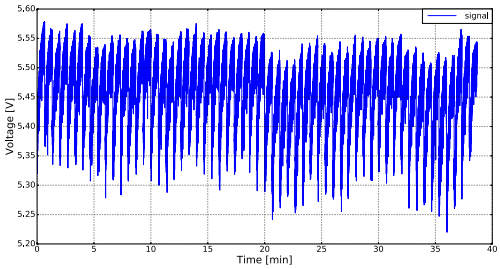

(b) 20A ($D^{20(5)_1}$)

Figure 4.90 – Signal visualization for automotive mode under 30A/5A ($D_1^{30(5)}$) and under 20A/5A($D_1^{20(5)}$)

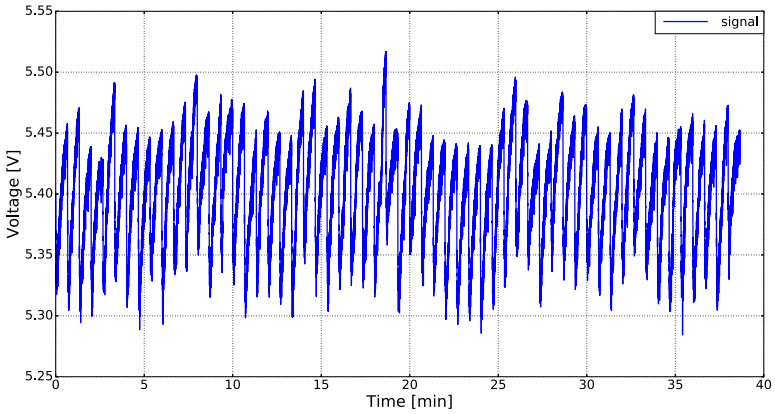

Figure 4.91 – Signal visualization for automotive mode under 10A/5A ($D_1^{10(5)}$)

Statistical descriptors in time domain Statistical descriptors in time domain are presented in Tab. 4.37,Tab. 4.38, Tab. 4.39, Tab. 4.40 and Tab. 4.41 As we can see that all of parameters are very different. There is tendency of decreasing intensity of energy (*eps*) with decreasing load in intermediate and high frequency range. Moreover, huge value of kurtosis is presented in high frequency range.

	original	32 seconds	8 seconds	2 seconds	0.3 seconds
μ, V	5.006	5.006	5.006	5.006	5.006
σ, mV	45.3	36.2	34.1	32.6	5.3
eps, 10^{-6}	9060	7232	6822	6525	5372
V_{max}, mV	5.081×10^3	87.1	54.3	126.4	117.6
V_{min}, mV	4.770×10^3	-205.0	-194.0	-182.1	-108.7
V_{p-p}, mV	310.5	292.1	248.3	308.5	226.3
M2, 10^{-6}	2057	1310	1166	1066	28.8
M3, 10^{-9}	-77811	-54935	-53389	-43495	-25
M4, 10^{-9}	14081	7184	5987	4946	11.5
Sk	-0.83	-1.15	-1.34	-1.24	-0.16
KU	0.32	1.18	1.4	1.34	10.9

Table 4.37 – Statistical descriptors for automotive mode under 100A/5A ($D_1^{100(5)}$) after detrending procedure with different time windows

	original	32 seconds	8 seconds	2 seconds	0.3 seconds
μ, V	5.258	5.258	5.258	5.258	5.258
σ, mV	64.0	32.7	25.2	23.8	4.0
eps, 10^{-6}	12186	6230	4798	4540	765
V_{max}, mV	5.409×10^3	124.6	47.3	96.1	127.1
V_{min}, mV	4.988×10^3	-170.2	-141.1	-129.7	-132.2
V_{p-p}, mV	421.4	294.8	188.5	225.9	259.3
M2, 10^{-6}	4106	1073	636	569	16.1
M3, 10^{-9}	-174412	-16087	-14128	-10713	5.9
M4, 10^{-9}	54302	4578	1390	1119	14.2
Sk	-0.66	-0.45	-0.87	-0.78	0.1
KU	0.22	0.97	0.43	0.44	51.3

Table 4.38 – Statistical descriptors for automotive mode under 50A/5A ($D_1^{50(5)}$) after detrending procedure with different time windows

	original	32 seconds	8 seconds	2 seconds	0.3 seconds
μ, V	5.368	5.368	5.368	5.368	5.368
σ, mV	65.5	20.0	19.2	17.6	3.2
eps, 10^{-6}	12218	3742	3592	3285	597
V_{max}, mV	5.555×10^3	86.0	56.7	83.0	95.3
V_{min}, mV	5.137×10^3	-133.2	-127.6	-110.8	-98.7
V_{p-p}, mV	418.0	219.2	184.3	193.9	194.1
M2, 10^{-6}	4301	403	371	311	10.2
M3, 10^{-9}	-121540	-9053	-8509	-5231	2.3
M4, 10^{-9}	52641	780	672	448	9.4
Sk	-0.43	-1.11	-1.18	-0.95	0
KU	-0.15	1.78	1.86	1.63	86.3

Table 4.39 – Statistical descriptors for automotive mode under 30A/5A ($D_1^{30(5)}$) after detrending procedure with different time windows

	original	32 seconds	8 seconds	2 seconds	0.3 seconds
μ, V	5.461	5.461	5.461	5.461	5.461
σ, mV	59.0	26.2	17.2	15.0	2.7
eps, 10^{-6}	10811	4800	3164	2759	508
V_{max}, mV	5.579×10^3	116.6	67.6	74.8	103.9
V_{min}, mV	5.219×10^3	-144.7	-110.5	-97.2	-86.3
V_{p-p}, mV	360.0	261.3	178.1	172.0	190.3
M2, 10^{-6}	3487	687	298	227	7.7
M3, 10^{-9}	-144864	-3437	-4397	-3077	7.2
M4, 10^{-9}	33898	2187	377	234	5.1
Sk	-0.7	-0.19	-0.85	-0.89	0.33
KU	-0.21	1.62	1.22	1.54	83.4

Table 4.40 – Statistical descriptors for automotive mode under 20A/5A ($D_1^{20(5)}$) after detrending procedure with different time windows

	original	32 seconds	8 seconds	2 seconds	0.3 seconds
μ, V	5.403	5.403	5.403	5.403	5.403
σ, mV	41.7	13.1	5.9	5.2	1.3
eps, 10^{-6}	7721	2426	1096	966	243
V_{max}, mV	5.517×10^3	75.7	22.4	22.9	44.5
V_{min}, mV	5.280×10^3	-55.3	-51.1	-41.0	-49.8
V_{p-p}, mV	236.5	131.0	73.6	63.9	94.4
M2, 10^{-6}	1740	171	35	27	1.7
M3, 10^{-9}	-17706	1572	-185	-123	0.4
M4, 10^{-9}	6609	193	5	3	0.2
Sk	-0.24	0.69	-0.89	-0.86	0.19
KU	-0.81	3.53	1.37	1.35	73.2

Table 4.41 – Statistical descriptors for automotive mode under 10A/5A ($D_1^{10(5)}$) after detrending procedure with different time windows

Statistical descriptors in frequency domain

Zone $D_1^{100(5)}$ The following phenomena can be noted:
- flicker-noise component in low frequency range until 0.4 Hz with slope of 2.31;
- a pick on f=1.9Hz with its subharmonics that is explained by low serrated component in signal;
- flicker-noise component in low frequency range ($8 < f < 15$ Hz) with slope of 3.82;
- third flicker-noise component in high frequency range with slope of 2.16.

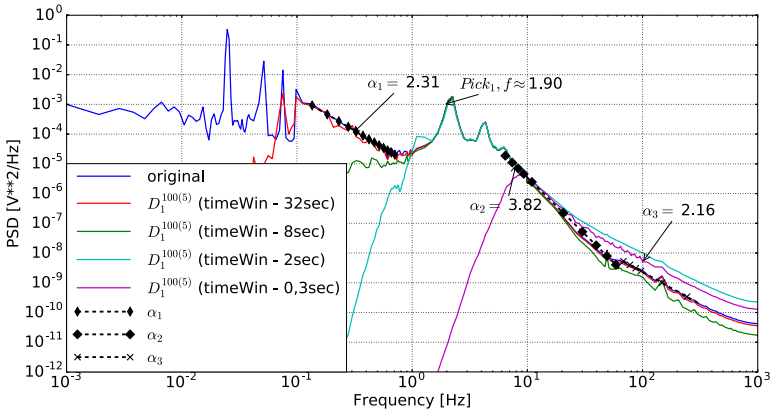

Figure 4.92 – PSD Welch with different time windows for 100A/5A automotive mode ($D_1^{100(5)}$)

Zone $D_1^{50(5)}$ The following phenomena can be noted:
- flicker-noise component in low frequency range until 0.4 Hz with slope of 2.39;
- a pick on f=1.9Hz with its subharmonics that is explained by low serrated component in signal
- flicker-noise component in low frequency range ($8 < f < 15$ Hz) with slope of 3.22;
- third flicker-noise component in high frequency range with slope of 2.05.

Zone $D_1^{30(5)}$ The following phenomena can be noted:
- flicker-noise component in low frequency range until 0.4 Hz with slope of 2.49;
- a pick on f=1.9Hz is not visible
- flicker-noise component in low frequency range ($8 < f < 15$ Hz) with slope of 3.67;
- third flicker-noise component in high frequency range with slope of 2.06.

Zone $D_1^{20(5)}$ The following phenomena can be noted:
- flicker-noise component in low frequency range until 0.4 Hz with slope of 2.17;
- a pick on f=1.9Hz is not visible
- flicker-noise component in low frequency range ($8 < f < 15$ Hz) with slope of 3.69;
- third flicker-noise component in high frequency range with slope of 2.09.

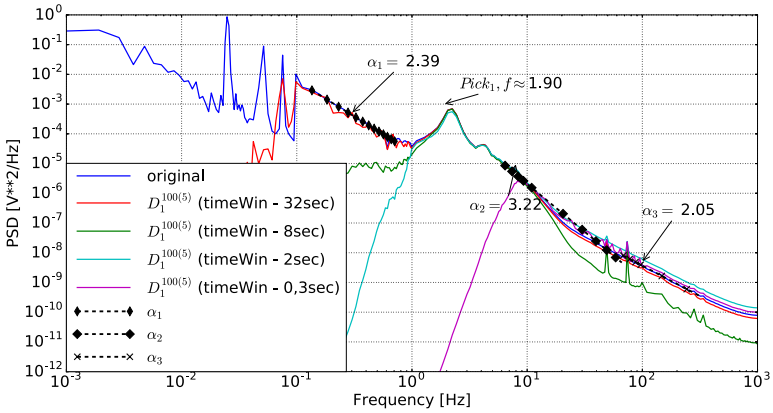

Figure 4.93 – PSD Welch with different time windows for 50A/5A automotive mode ($D_1^{50(5)}$)

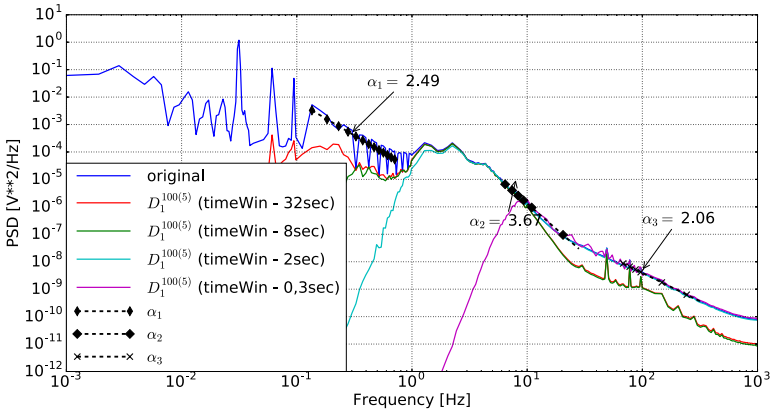

Figure 4.94 – PSD Welch with different time windows for 30A/5A automotive mode ($D_1^{30(5)}$)

Zone $D_1^{10(5)}$ The following phenomena can be noted:

- flicker-noise component in low frequency range until 0.4 Hz with slope of 2.65;
- a pick on f=1.9Hz is not visible
- flicker-noise component in low frequency range ($8 < f < 15$ Hz) with slope of 3.40;
- third flicker-noise component in high frequency range with slope of 3.58.

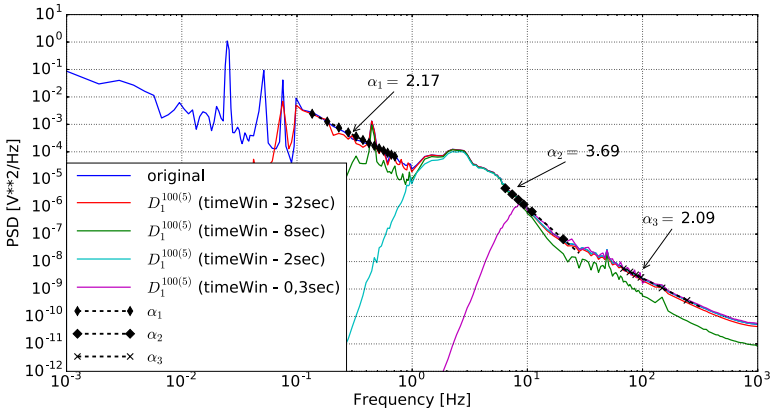

Figure 4.95 – PSD Welch with different time windows for 20A/5A automotive mode ($D_1^{20(5)}$)

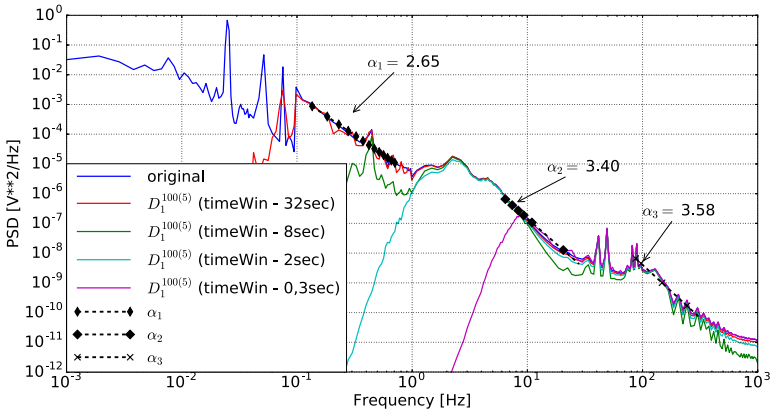

Figure 4.96 – PSD Welch with different time windows for 10/5A automotive mode ($D_1^{10(5)}$)

Chapter 5

Statistical descriptors for noise diagnostic of PEM stacks in time-frequency domains

Contents

Figures

5.1 General presentation of statistical descriptors recorded during different experimental campaigns

In the previous Chapter 4 statistical descriptors have been generated for time (moments) or for frequency (PSD) domains. It is interesting to use also generation statistical descriptors in time-frequency domain. The advantage is related with a possibility of simultaneous observation of frequency behavior of studied system in time domain. The disadvantage deals with significant increasing of time of calculations because more important volume of data should be treated. Sometimes it is necessary to look for a compromise between calculation costs and time-frequency resolution. For the same volume of data statistical descriptors in time and frequency domains provide better resolution and descriptors in time-frequency domain scarify partly this resolution in order to give a global overview. Thus, descriptors in time-frequency domain are complementary to ones generated in time or in frequency domains. In this chapter we present statistical descriptors obtained by STFT (time extension of Welch spectra), by TFAR (time extension of Burg spectra) and Wavelet analyze. Mathematical details concerning these methods are given in Chapter 3.

5.1.1 First campaign of measurements

Short-time Fourier Transform (STFT)

Short-time Fourier Transform (STFT) results are presented in Fig. 5.1. We can see (Fig. 5.1) that noise signature for FC under 85A load is very different in comparison to the one obtained for OCV mode. Also, it very clearly that noise intensity under load is much more important. We contrast existence of dominate frequencies and its subharmonics which are stable in time, All the zones under load demonstrate the same noise behavior (Fig. 5.1a and Fig. 5.1c).

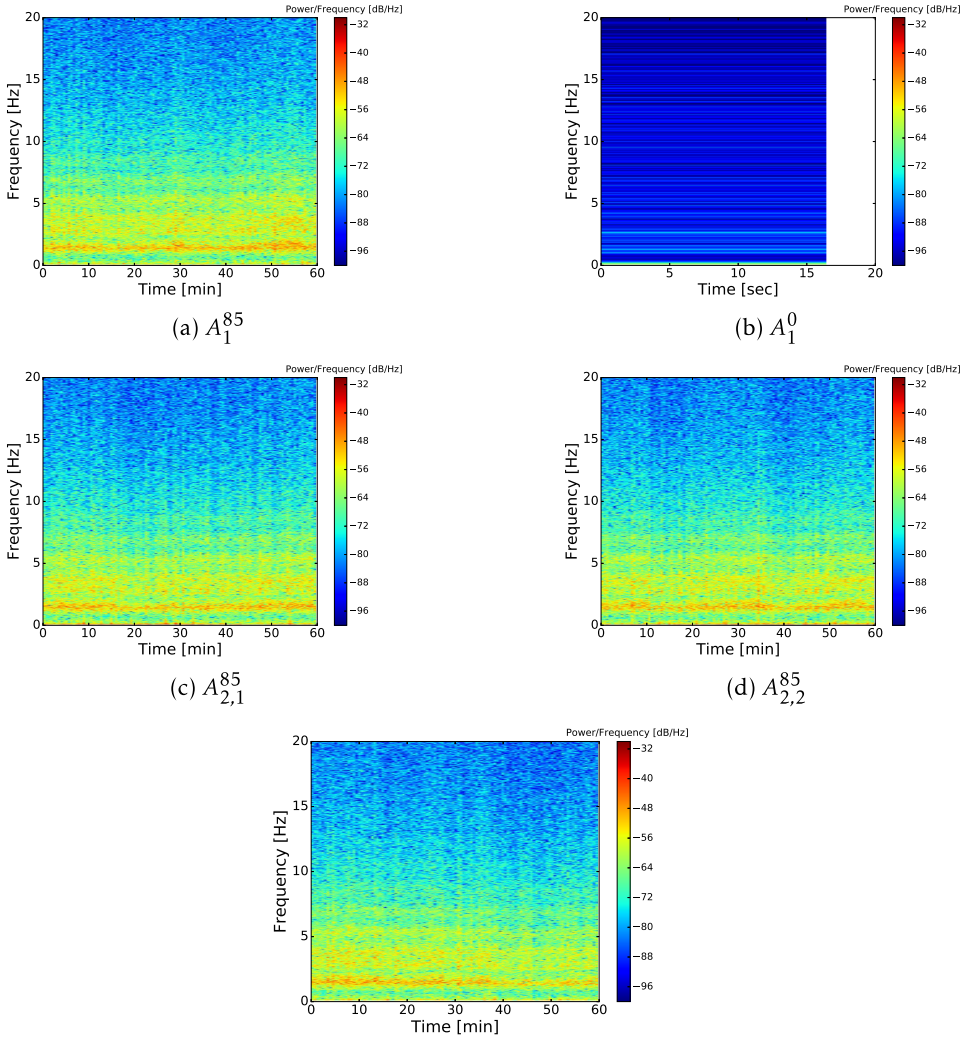

(a) A_1^{85}

(b) A_1^0

(c) $A_{2,1}^{85}$

(d) $A_{2,2}^{85}$

(e) $A_{2,3}^{85}$

Figure 5.1 – STFT for 85A load (A_1^{85}, A_2^{85}) and for OCV mode (A_1^0)

Time-Frequency Autoregressive (TFAR)

Time-Frequency Autoregressive (TFAR) results are presented in Fig. 5.2. These results are similar to the ones obtained by STFT. It is clear that dominant frequencies are more pronounces in comparison to STFT, especially for OCV mode.

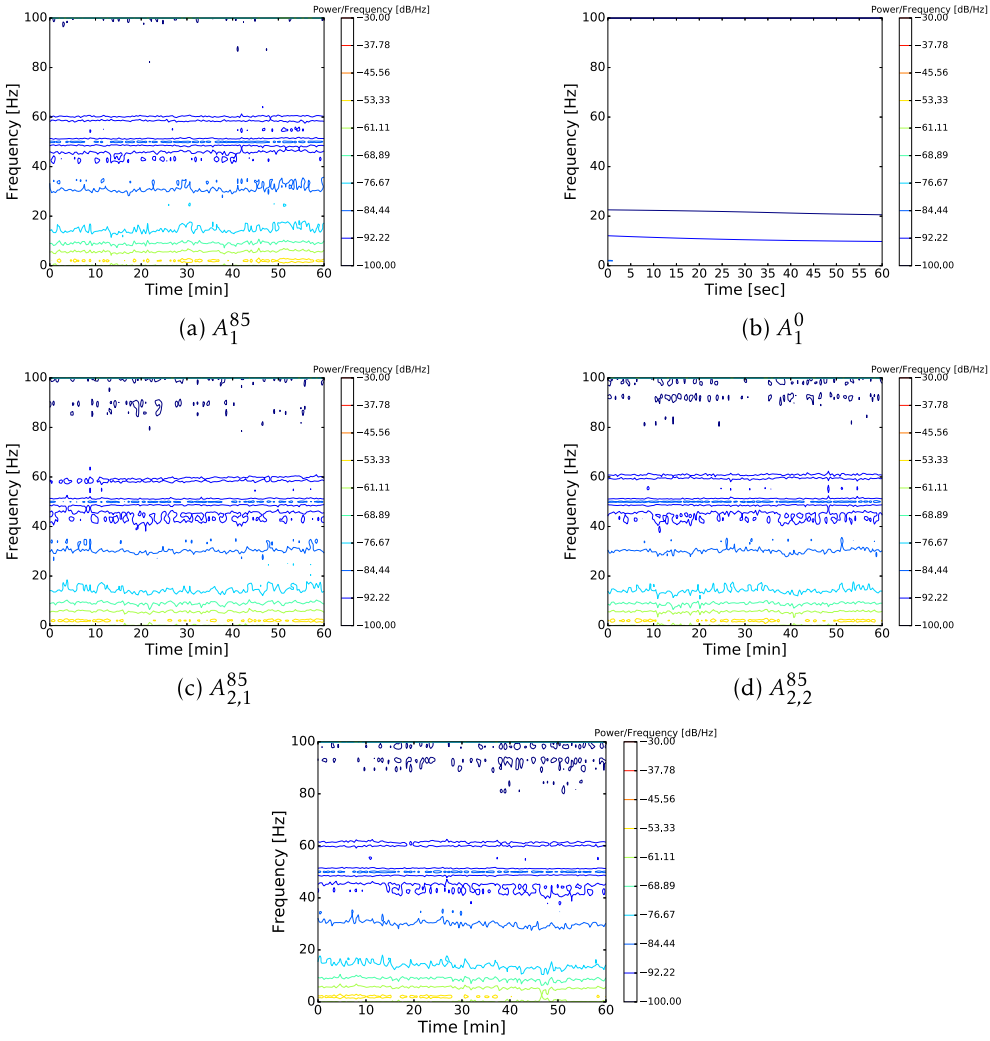

(a) A_1^{85}

(b) A_1^{0}

(c) $A_{2,1}^{85}$

(d) $A_{2,2}^{85}$

(e) $A_{2,3}^{85}$

Figure 5.2 – TFAR for 85A load (A_1^{85}, A_2^{85}) and for OCV mode (A_1^{0})

Wavelet

Wavelet results are presented in Fig. 5.3. We note the existence of some events (explosion of noise intensity) in all time domains. These events seems to be more pronounces for OCV mode, nevertheless it is necessary to take into account that the scale for OCV and load modes is different.

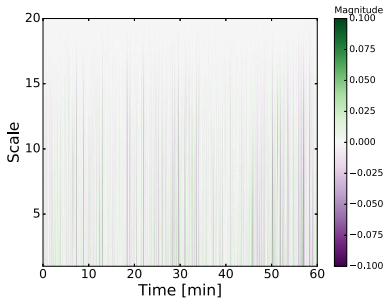

(a) A_1^{85}

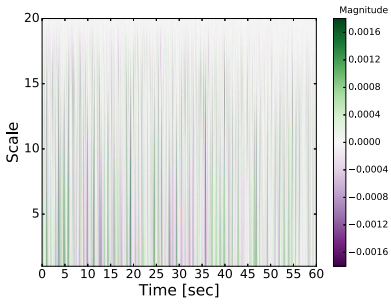

(b) A_1^{0}

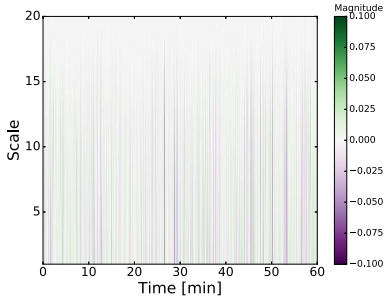

(c) $A_{2,1}^{85}$

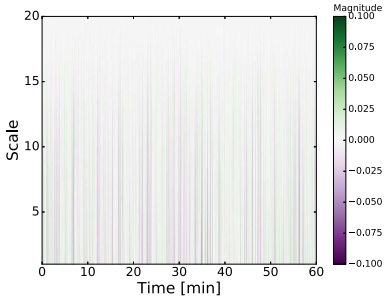

(d) $A_{2,2}^{85}$

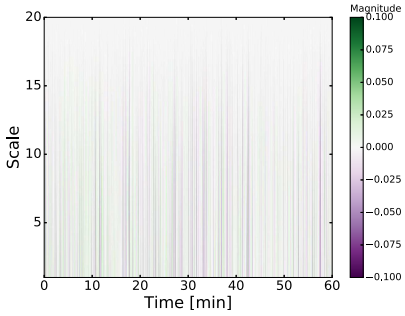

(e) $A_{2,3}^{85}$

Figure 5.3 – Wavelet for 85A load (A_1^{85}, A_2^{85}) and for OCV mode (A_1^{0})

5.1.2 Second campaign of measurements

Short-time Fourier Transform (STFT)

Short-time Fourier Transform (STFT) descriptors are presented below for OCV, 85A and 170A, respectively, in Fig.5.4, Fig.5.5 and Fig.5.6. As well as for the first campaign, we can see stable signature of dominant frequencies. Also, the noise intensity for OCV mode is much lower that for load modes. The noise intensity for 170A load is more important than the one for 85A load. The new phenomena in can be observed for 170A load, this is repetitive increasing of noise intensity (orange vertical lines in Fig. 5.4) each 7-8 minutes.

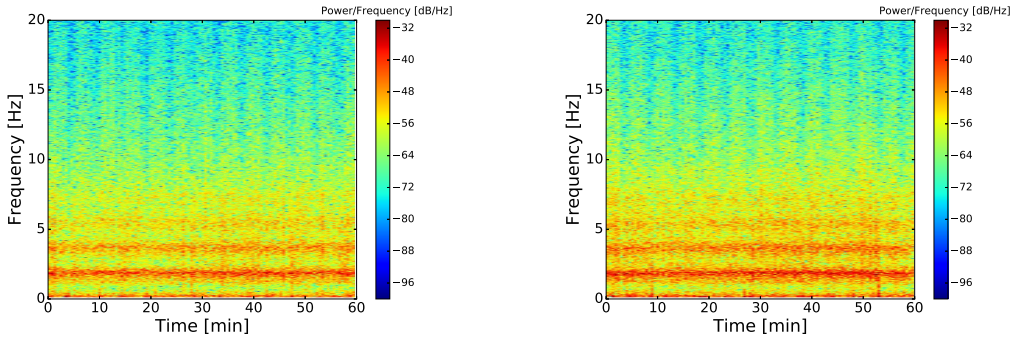

(a) $B_{1,1}^{170}$ (b) $B_{1,2}^{170}$

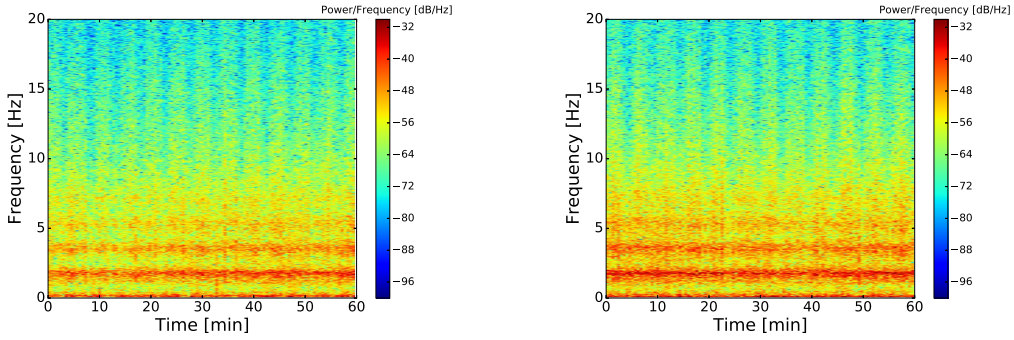

(c) B_{2}^{170} (d) B_{3}^{170}

Figure 5.4 – STFT for 170A load ($B_{1,1}^{170}$, $B_{1,2}^{170}$, B_{2}^{170} and B_{3}^{170})

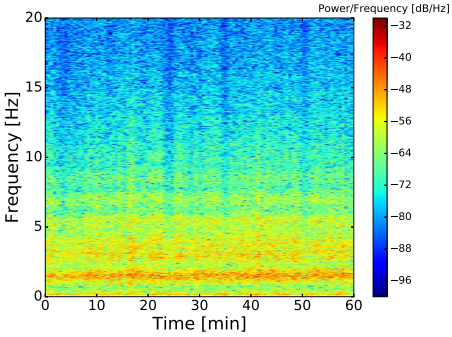

(a) B_1^{85}

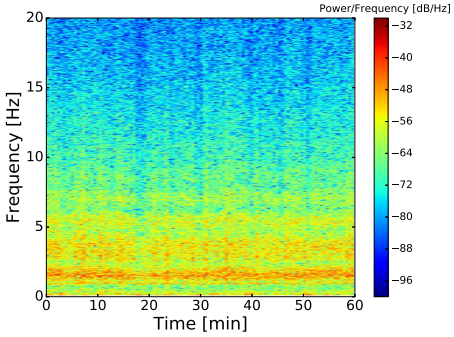

(b) B_2^{85}

Figure 5.5 – STFT for 85A load (B_1^{85} and B_2^{85})

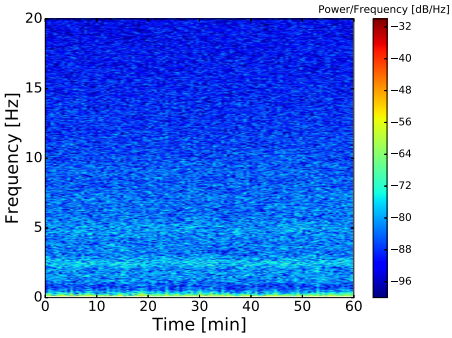

(a) B_1^0

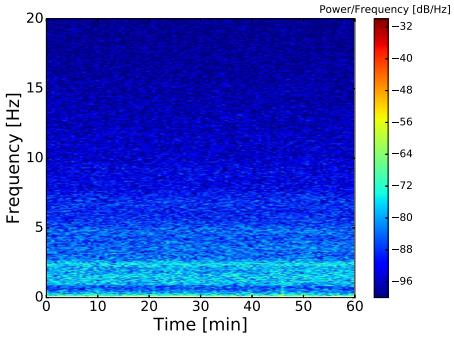

(b) B_2^0

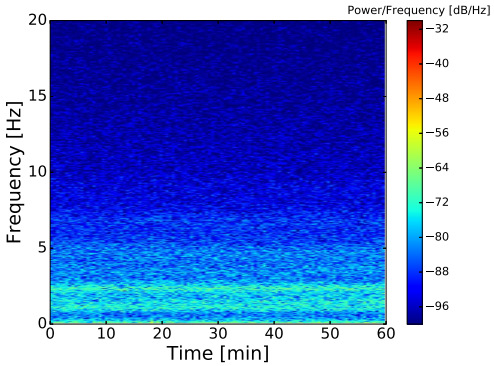

(c) B_3^0

Figure 5.6 – STFT for OCV mode (B_1^0, B_2^0 and B_3^0)

Time-Frequency Autoregressive (TFAR)

Descriptors in time-frequency domain generated by TFAR are presented below for OCV, 85A and 170A, see Fig.5.7, Fig.5.8 and Fig.5.9. As for the first campaign, the dominant frequencies become more pronounced in comparison with STFT. The repetitive increasing of noise intensity for 170A load transform now to the periodic fluctuations of the lines corresponding to dominant frequencies, for example for $f = 30Hz$. The OCV mode is clearly different from the load modes.

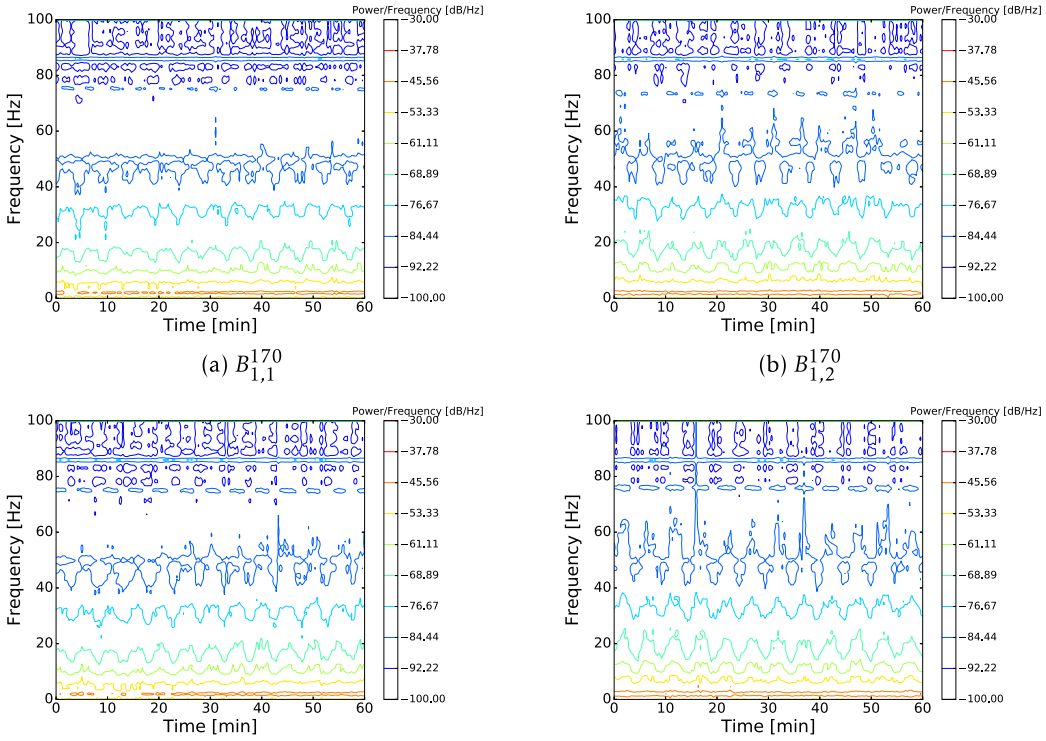

(a) $B_{1,1}^{170}$ (b) $B_{1,2}^{170}$

(c) B_2^{170} (d) B_3^{170}

Figure 5.7 – TFAR for 170A load ($B_{1,1}^{170}$, $B_{1,2}^{170}$, B_2^{170} and B_3^{170})

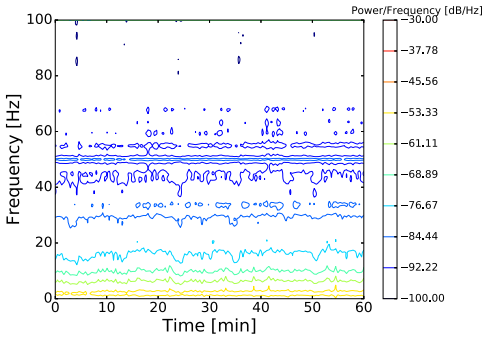

(a) B_1^{85}

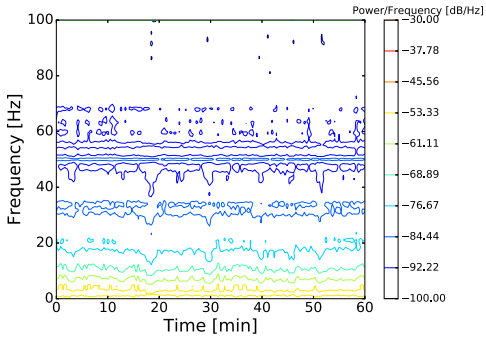

(b) B_2^{85}

Figure 5.8 – TFAR for 85A load (B_1^{85} and B_2^{85})

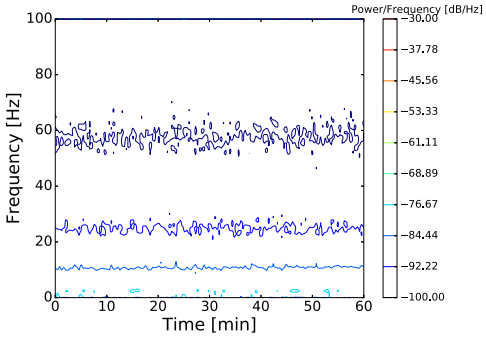

(a) B_1^0

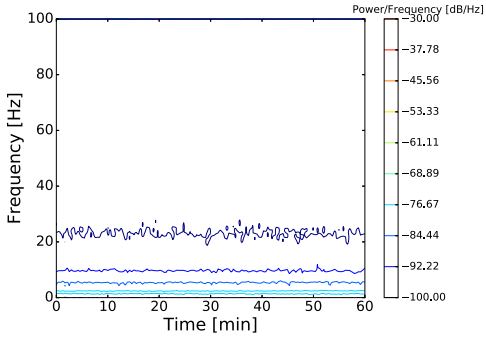

(b) B_2^0

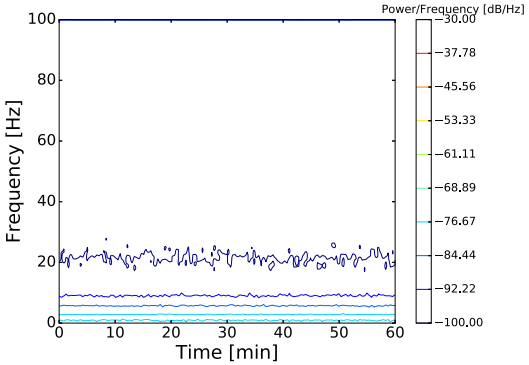

(c) B_3^0

Figure 5.9 – TFAR for OCV mode (B_1^0, B_2^0 and B_3^0)

Wavelet

Descriptors in time-frequency domain obtained by wavelet analyze are presented below for OCV, 85A and 170A, respectively, see Fig.5.10, Fig.5.11 and Fig.5.12. Some repetitive events with rather high frequency are visible for the load modes. These events are not visible for OCV mode.

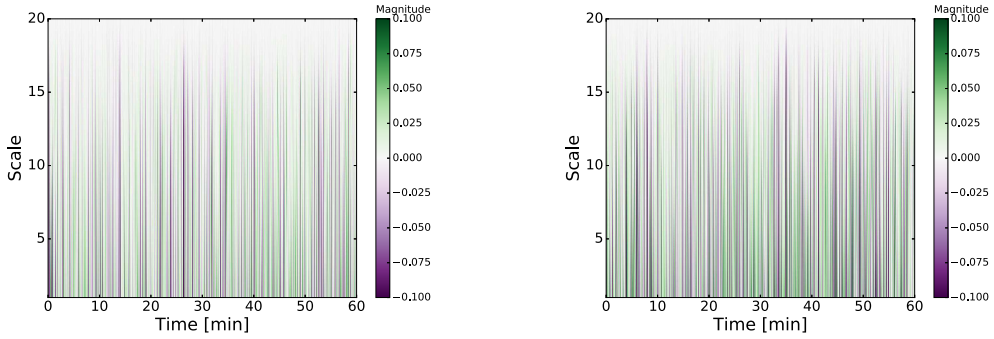

(a) $B_{1,1}^{170}$

(b) $B_{1,2}^{170}$

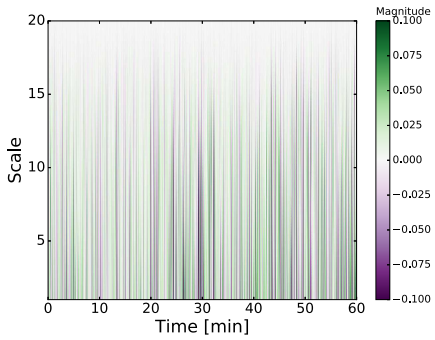

(c) B_{2}^{170}

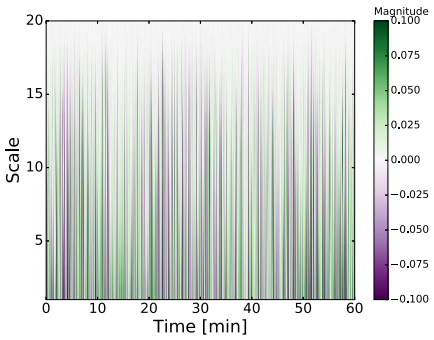

(d) B_{3}^{170}

Figure 5.10 – Wavelet for 170A load ($B_{1,1}^{170}$, $B_{1,2}^{170}$, B_{2}^{170} and B_{3}^{170})

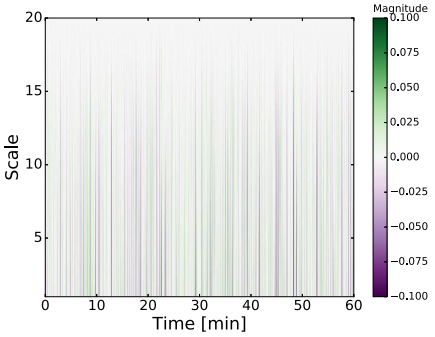

(a) B_1^{85}

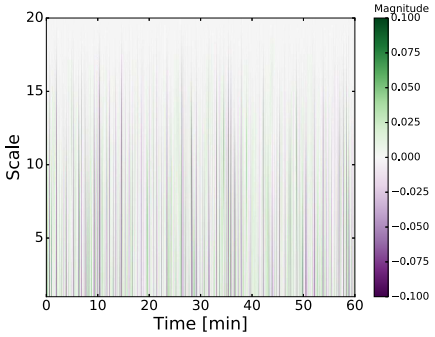

(b) B_2^{85}

Figure 5.11 – Wavelet for 85A load (B_1^{85} and B_2^{85})

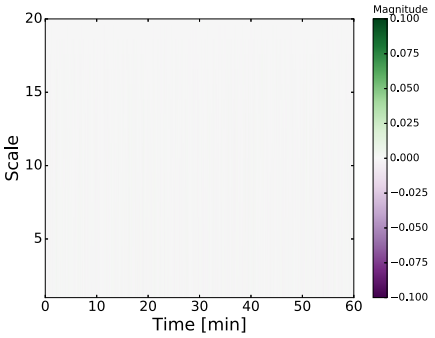

(a) B_1^0

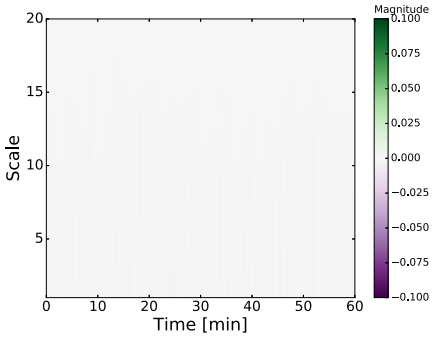

(b) B_2^0

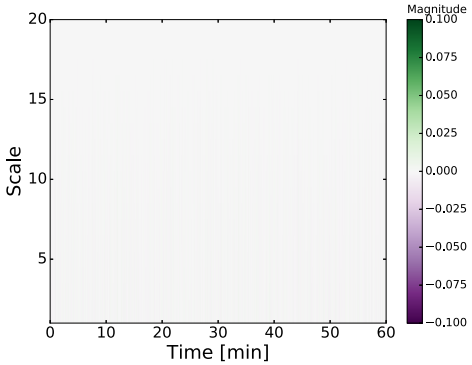

(c) B_3^0

Figure 5.12 – Wavelet for OCV mode (B_1^0, B_2^0 and B_3^0)

5.1.3 Third campaign of measurements

Short-time Fourier Transform (STFT)

Short-time Fourier Transform (STFT) descriptors are presented in Fig.5.13, Fig.5.14, Fig.5.15 and Fig.5.16 and the modes under load and stable dominant frequencies for all the modes.

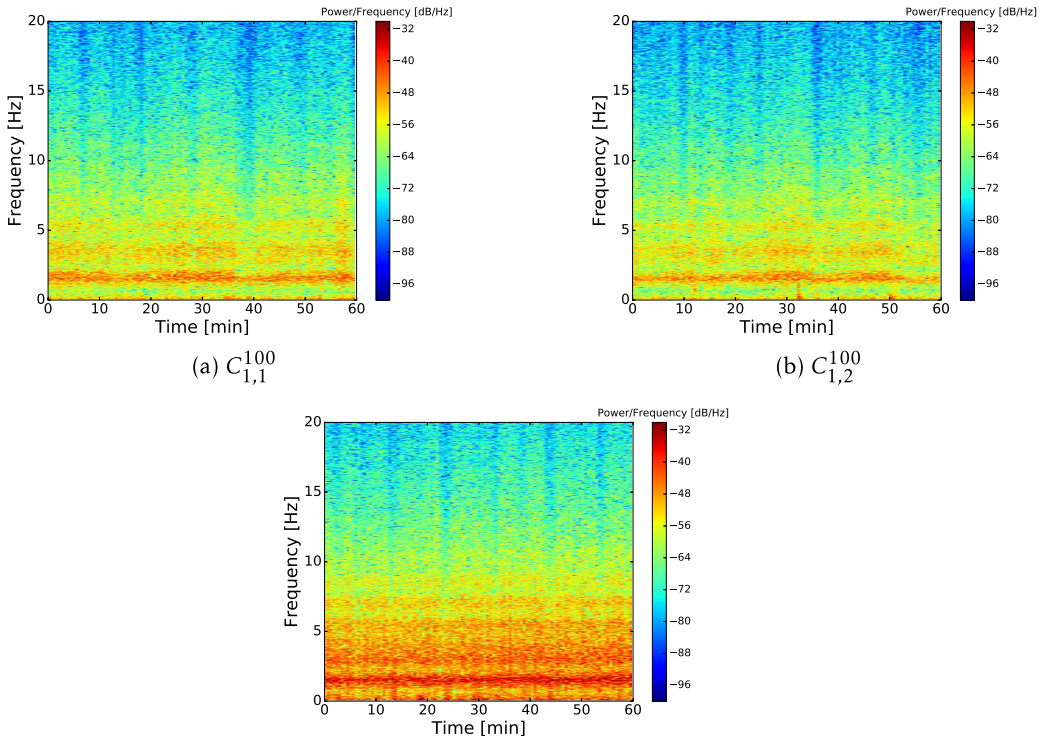

(a) $C_{1,1}^{100}$

(b) $C_{1,2}^{100}$

(c) $C_{1,3}^{100}$

Figure 5.13 – Implementation of STFT for 100A load (C_1^{100})

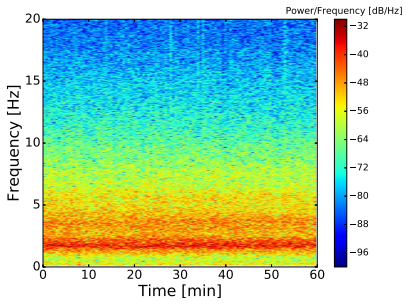

(a) $C_{1,1}^{50}$

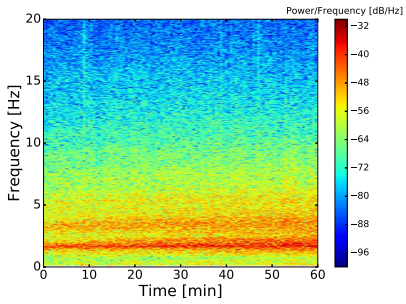

(b) $C_{1,2}^{50}$

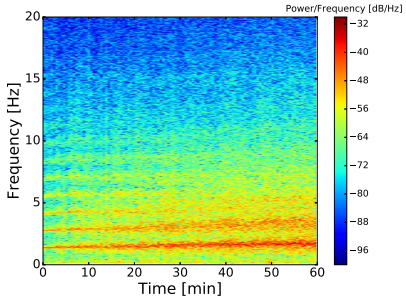

(c) $C_{1,3}^{50}$

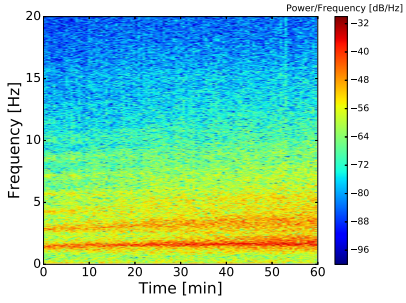

(d) $C_{1,4}^{50}$

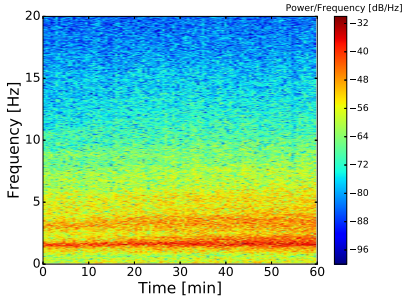

(e) $C_{1,5}^{50}$

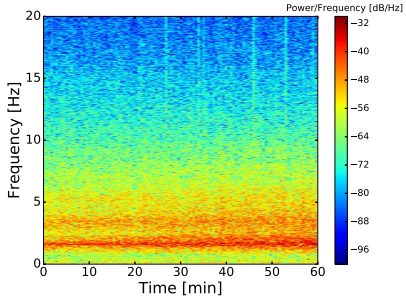

(f) $C_{1,6}^{50}$

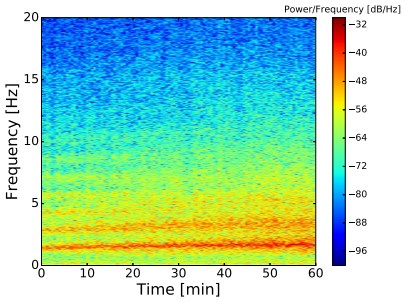

(g) $C_{1,7}^{50}$

Figure 5.14 – Implementation of STFT for 50A load (C_1^{50})

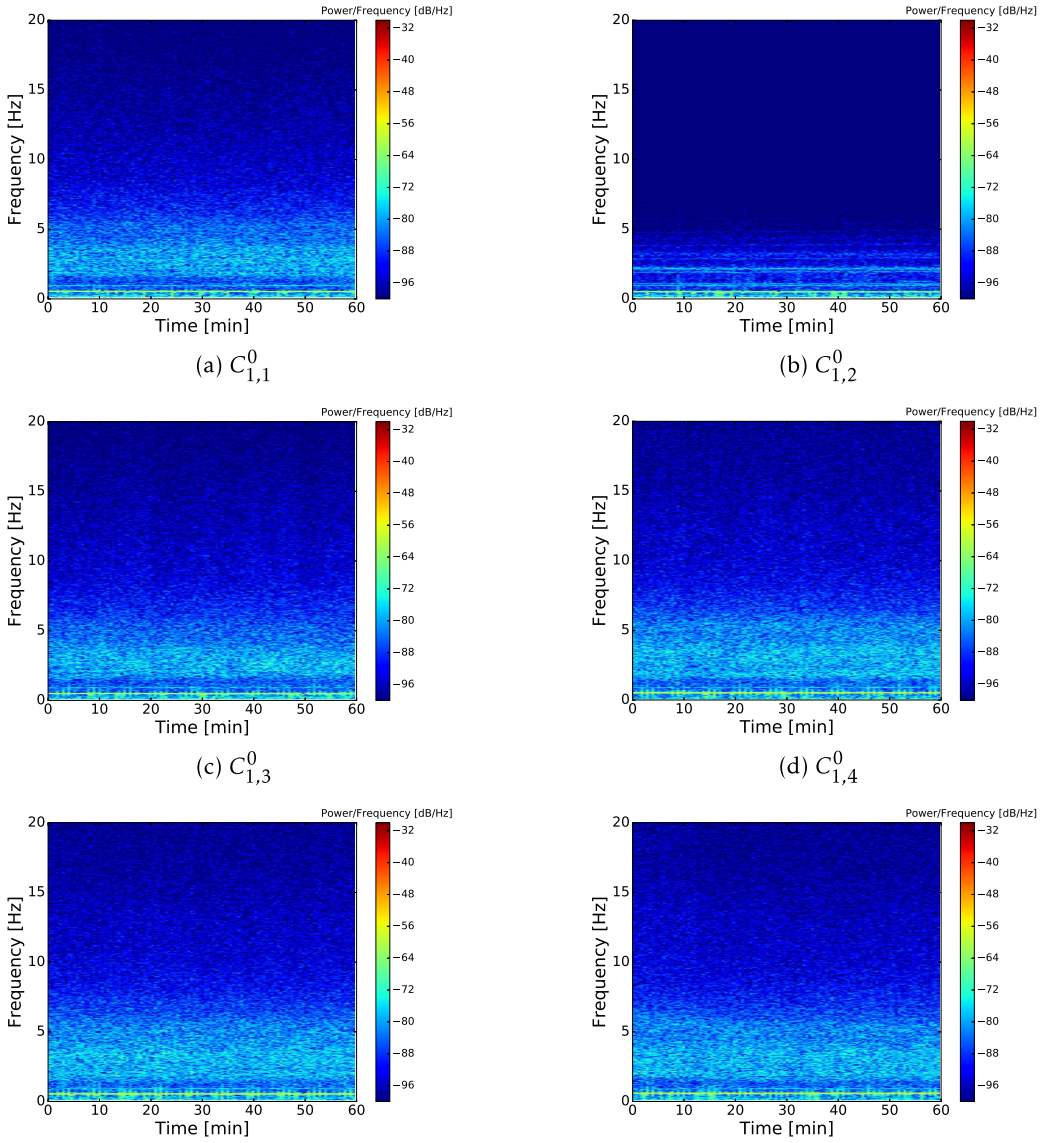

(a) $C^0_{1,1}$ (b) $C^0_{1,2}$

(c) $C^0_{1,3}$ (d) $C^0_{1,4}$

(e) $C^0_{1,5}$ (f) $C^0_{1,6}$

Figure 5.15 – Implementation of STFT for OCV mode(C^0_1)

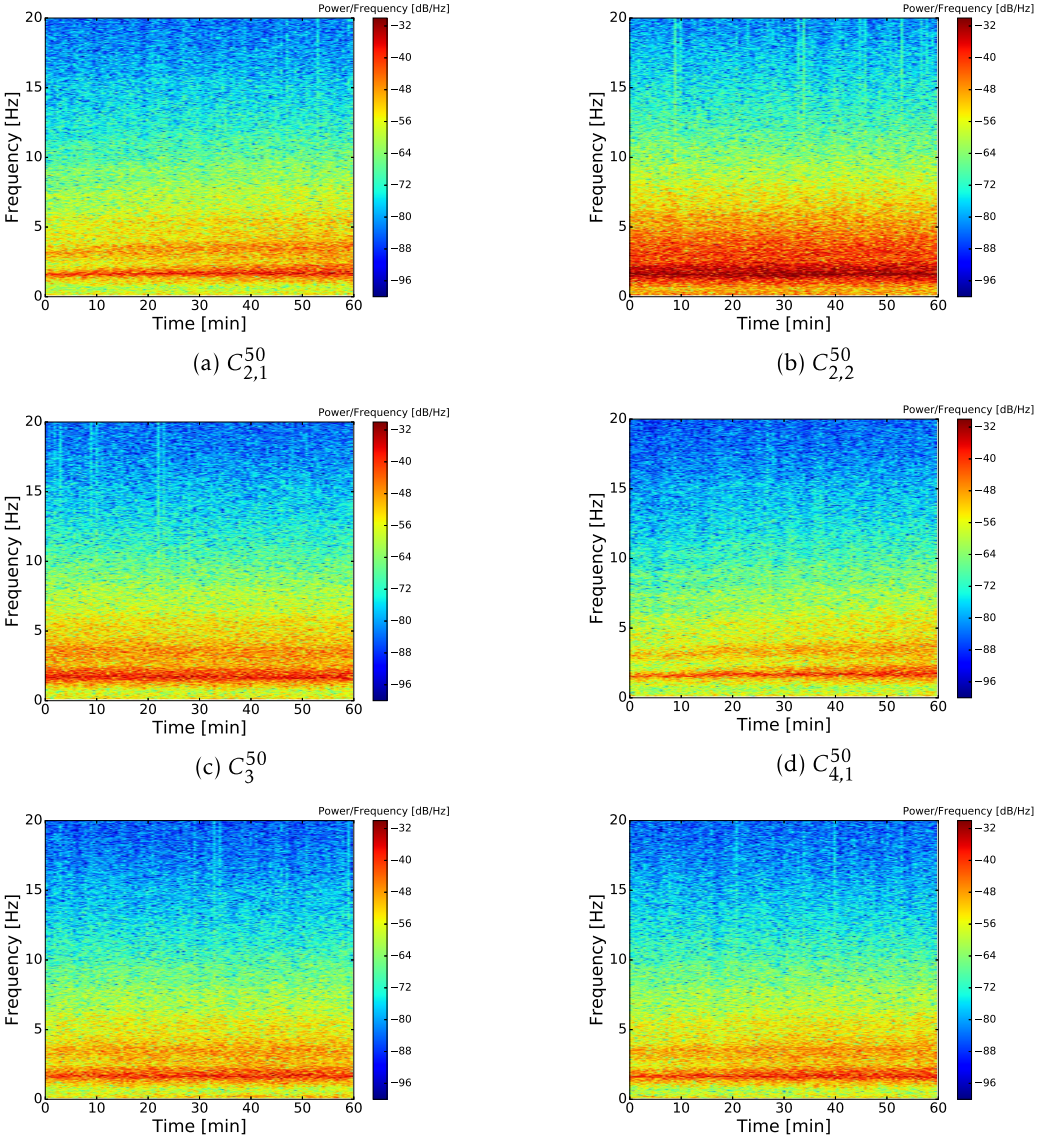

(a) $C_{2,1}^{50}$ (b) $C_{2,2}^{50}$

(c) C_{3}^{50} (d) $C_{4,1}^{50}$

(e) $C_{4,2}^{50}$ (f) $C_{4,3}^{50}$

Figure 5.16 – Implementation of STFT for 50A load (C_{2}^{50}, C_{3}^{50} and C_{4}^{50})

Time-Frequency Autoregressive (TFAR)

Time-Frequency Autoregressive (TFAR) descriptors are presented in Fig.5.18, Fig.5.19, Fig.5.20 and Fig.5.17. The dominant frequencies are very pronounced, the difference between OCV and load modes is clear. Some repetitive events for high frequency range ($f > 20Hz$) exist for load modes.

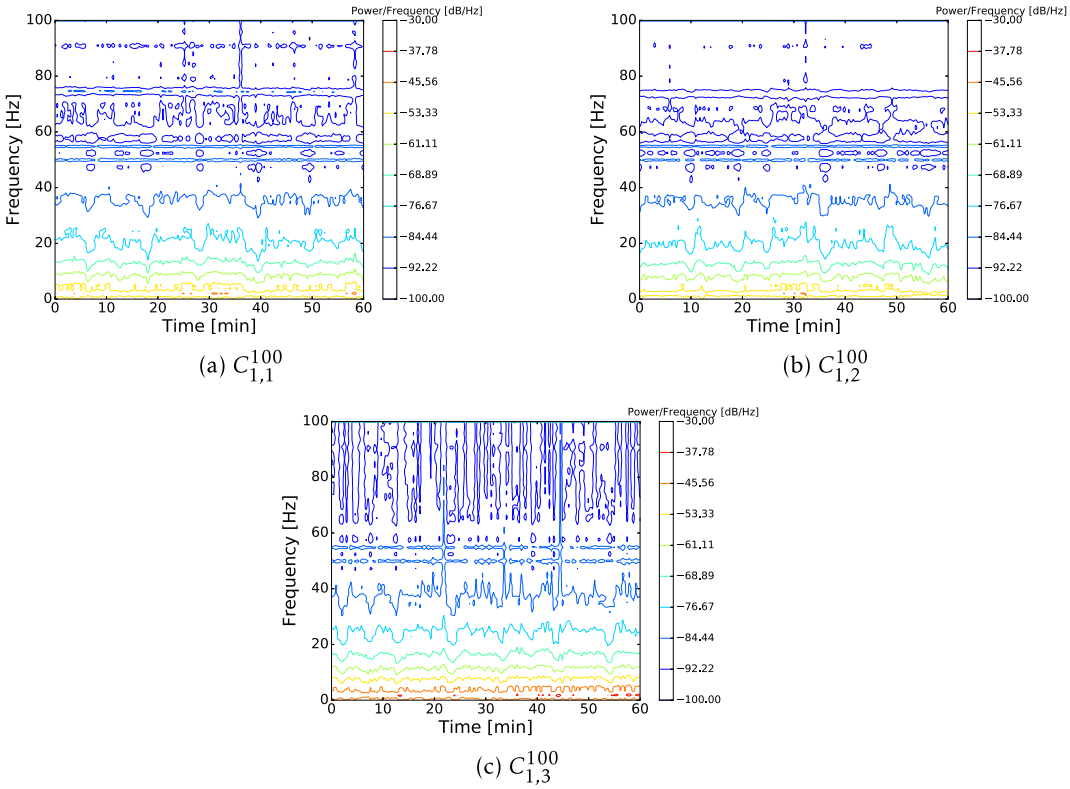

(a) $C_{1,1}^{100}$

(b) $C_{1,2}^{100}$

(c) $C_{1,3}^{100}$

Figure 5.17 – Implementation of TFAR for 100A load (C_1^{100})

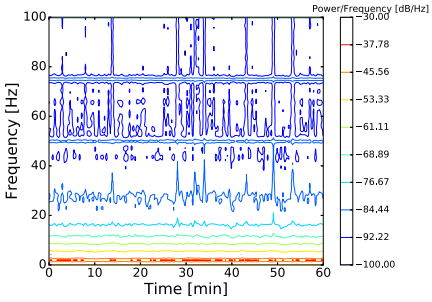

(a) $C_{1,1}^{50}$

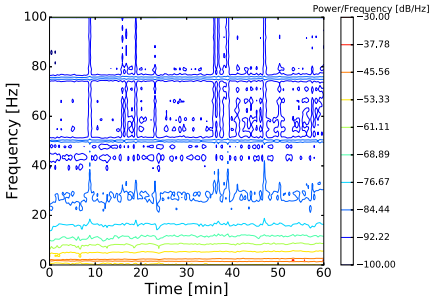

(b) $C_{1,2}^{50}$

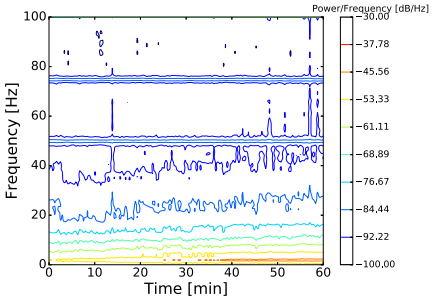

(c) $C_{1,3}^{50}$

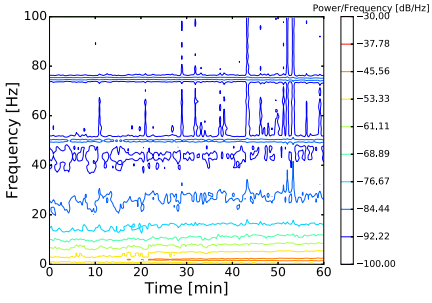

(d) $C_{1,4}^{50}$

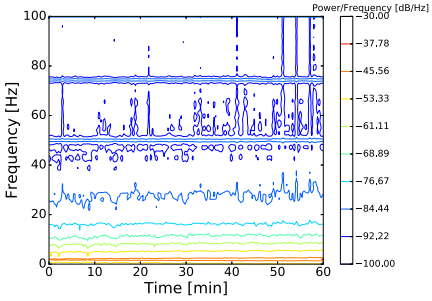

(e) $C_{1,5}^{50}$

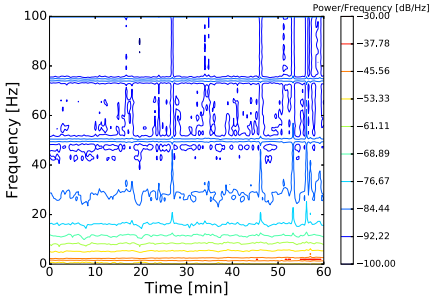

(f) $C_{1,6}^{50}$

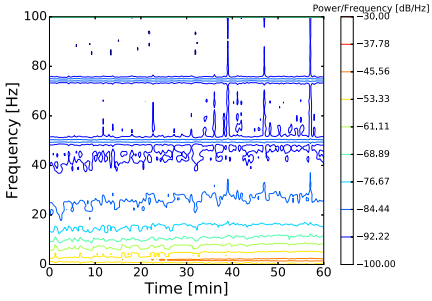

(g) $C_{1,7}^{50}$

Figure 5.18 – Implementation of TFAR for 50A load (C_1^{50})

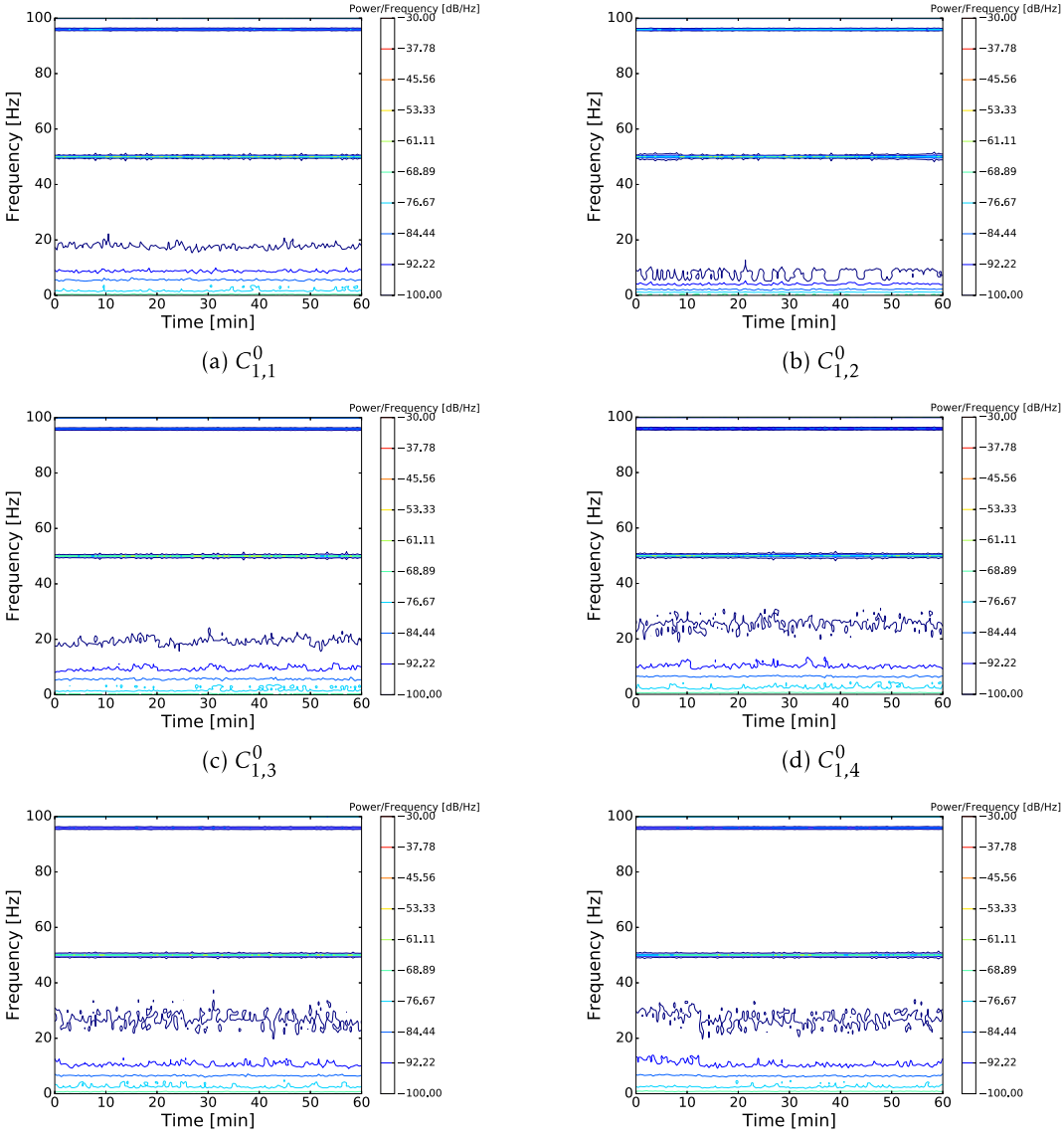

(a) $C^0_{1,1}$ (b) $C^0_{1,2}$

(c) $C^0_{1,3}$ (d) $C^0_{1,4}$

(e) $C^0_{1,5}$ (f) $C^0_{1,6}$

Figure 5.19 – Implementation of TFAR for OCV mode(C^0_1)

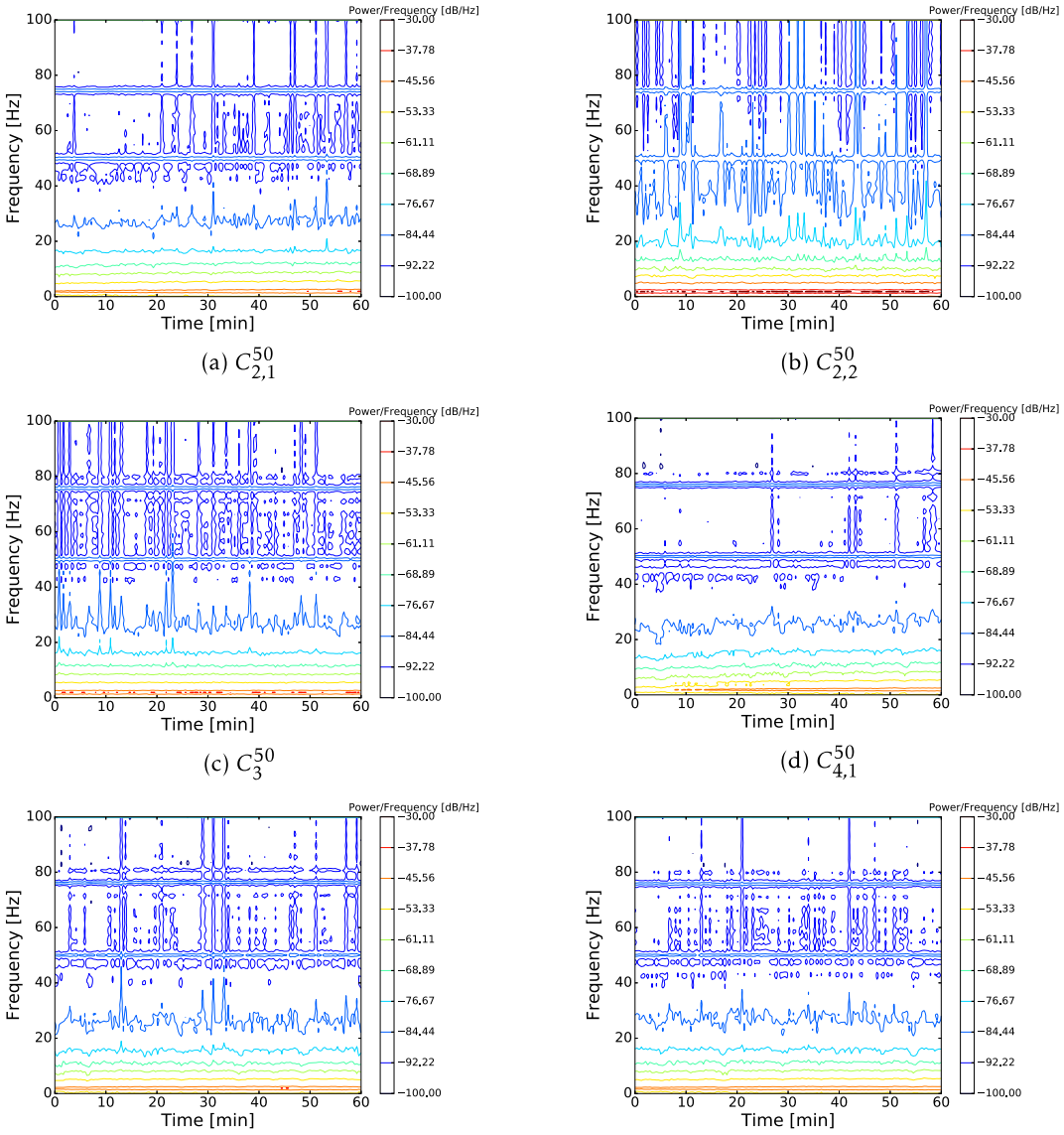

(a) $C_{2,1}^{50}$ (b) $C_{2,2}^{50}$

(c) C_{3}^{50} (d) $C_{4,1}^{50}$

(e) $C_{4,2}^{50}$ (f) $C_{4,3}^{50}$

Figure 5.20 – Implementation of TFAR for 50A load (C_{2}^{50}, C_{3}^{50} and C_{4}^{50})

Wavelet

Wavelet descriptors are presented in Fig.5.22, Fig.5.23, Fig.5.24 and Fig.5.21. High frequency repetitive events exist for load modes but are not visible for OCV mode.

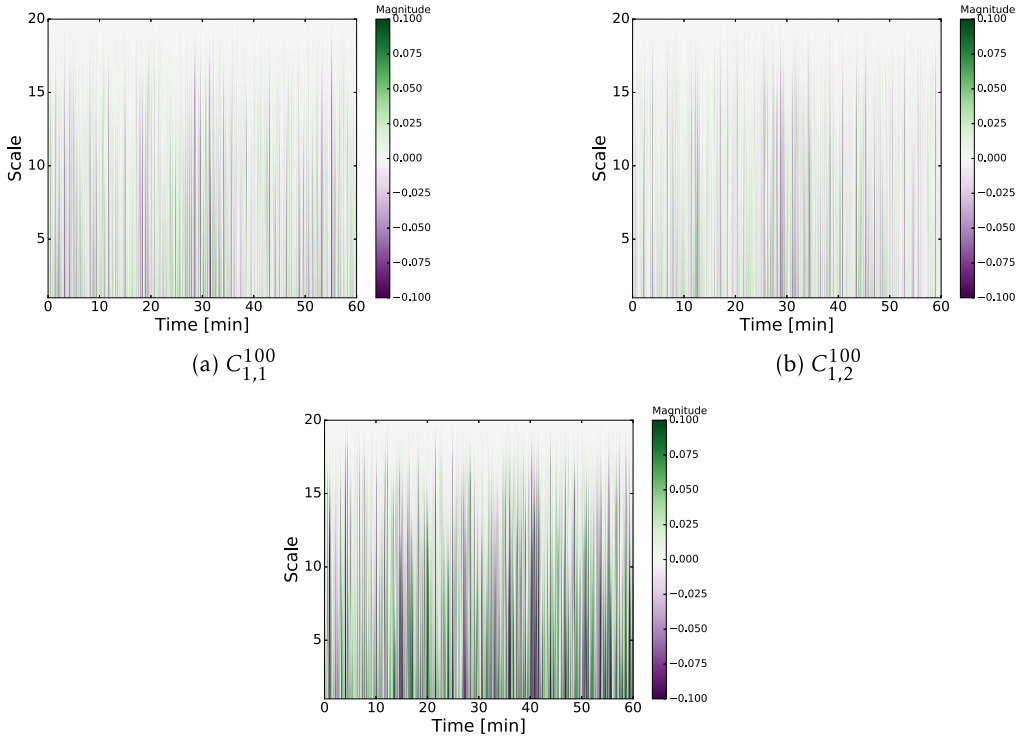

(a) $C_{1,1}^{100}$

(b) $C_{1,2}^{100}$

(c) $C_{1,3}^{100}$

Figure 5.21 – Implementation of Wavelet for 100A load (C_1^{100})

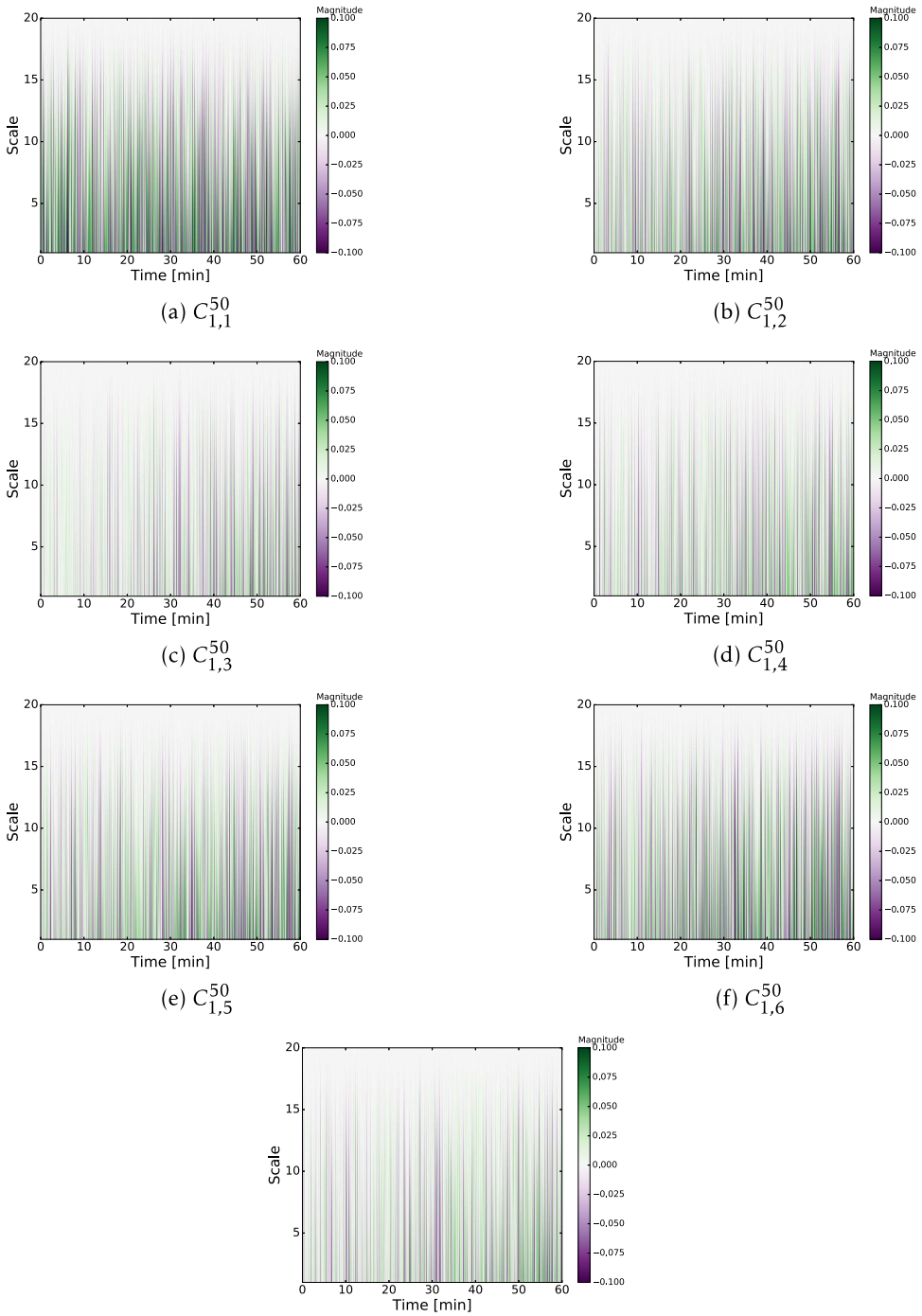

(a) $C_{1,1}^{50}$

(b) $C_{1,2}^{50}$

(c) $C_{1,3}^{50}$

(d) $C_{1,4}^{50}$

(e) $C_{1,5}^{50}$

(f) $C_{1,6}^{50}$

(g) $C_{1,7}^{50}$

Figure 5.22 – Implementation of Wavelet for 50A load (C_1^{50})

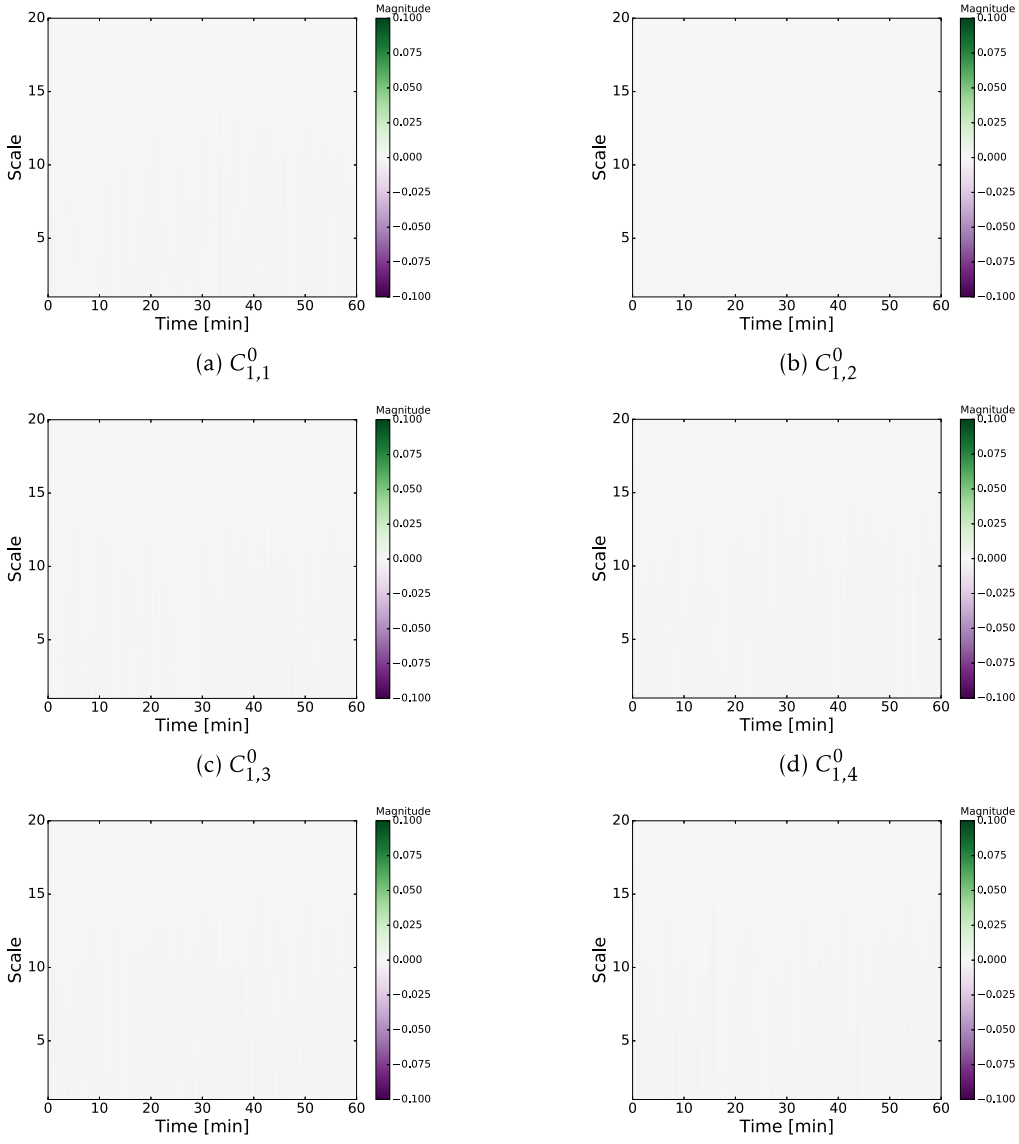

(a) $C^0_{1,1}$ (b) $C^0_{1,2}$

(c) $C^0_{1,3}$ (d) $C^0_{1,4}$

(e) $C^0_{1,5}$ (f) $C^0_{1,6}$

Figure 5.23 – Implementation of Wavelet for OCV mode(C^0_1)

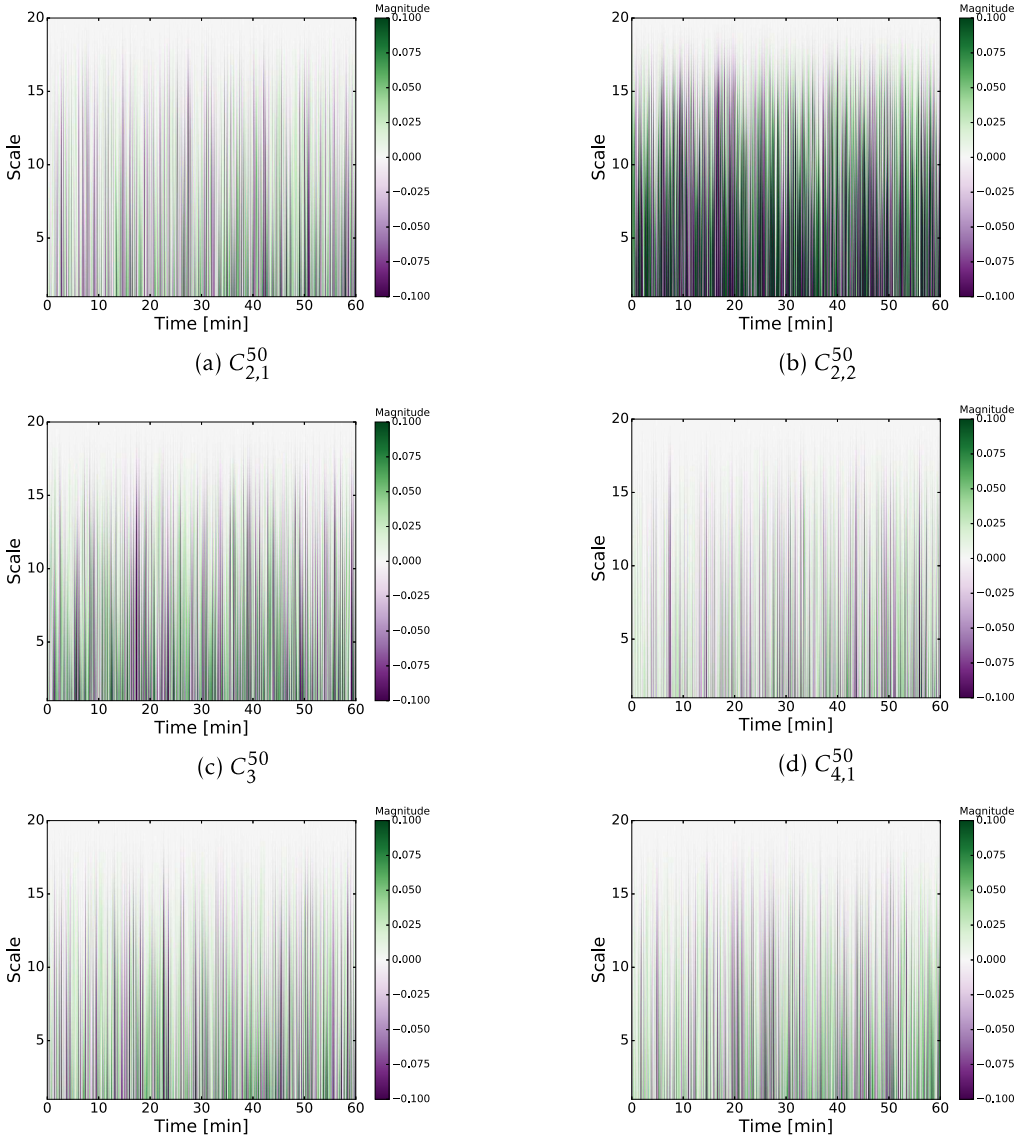

(a) $C_{2,1}^{50}$ (b) $C_{2,2}^{50}$

(c) C_{3}^{50} (d) $C_{4,1}^{50}$

(e) $C_{4,2}^{50}$ (f) $C_{4,3}^{50}$

Figure 5.24 – Implementation of Wavelet for 50A load (C_{2}^{50}, C_{3}^{50} and C_{4}^{50})

5.1.4 Fourth campaign of measurements

Statistical descriptors for continuous operation and OCV mode

Short-time Fourier Transform (STFT) descriptors for OCV, 85A and 110A load modes are presented in Fig.5.25. We can see results an important difference between noise signatures and the existence of stable dominant frequencies.

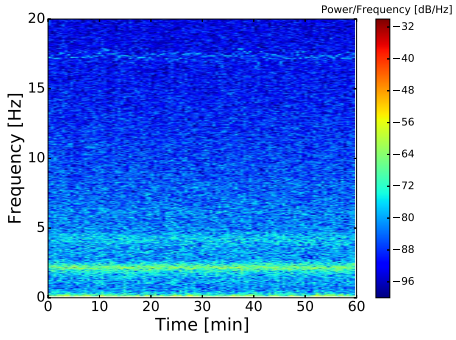

(a) D_1^0

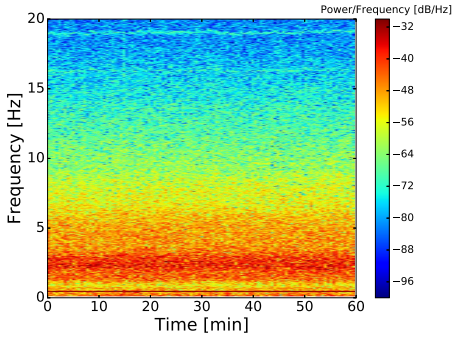

(b) D_1^{85}

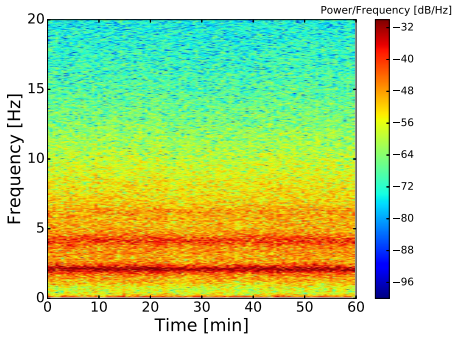

(c) D_1^{110}

Figure 5.25 – Implementation of STFT for 170A load(D_1^{110}), 85A load (D_1^{85}) and OCV mode (D_1^0)

Time-Frequency Autoregressive (TFAR) descriptors for different modes are presented in Fig.5.26. Interpretation is similar to the other campaigns.

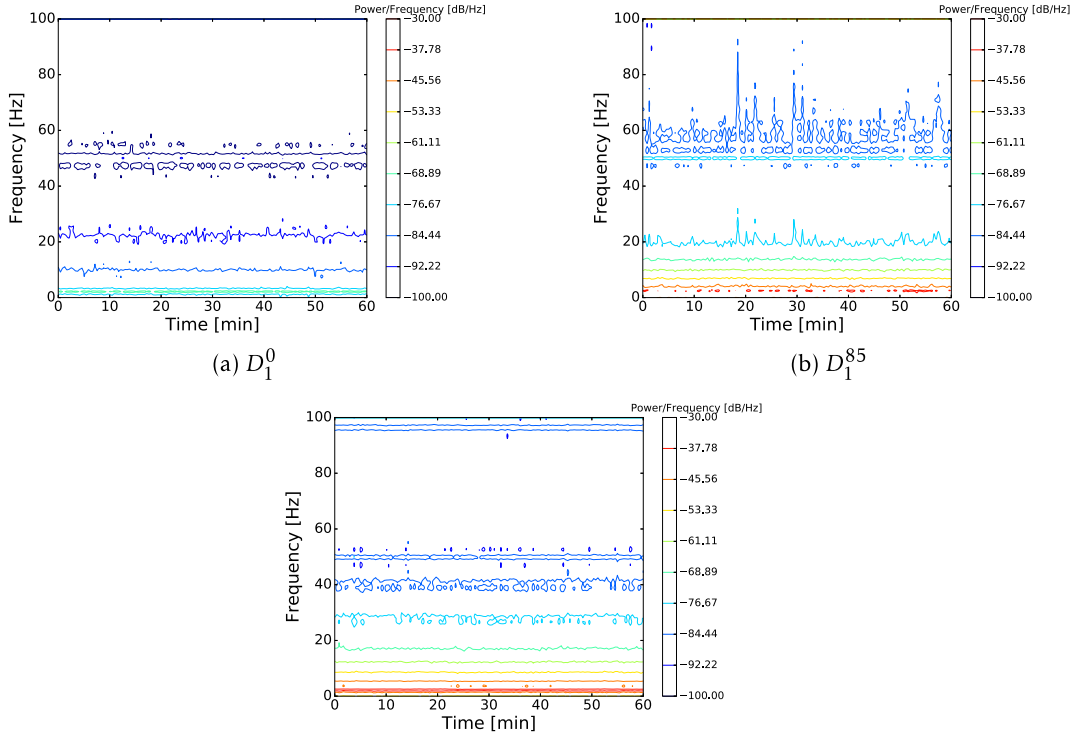

(a) D_1^0

(b) D_1^{85}

(c) D_1^{110}

Figure 5.26 – Implementation of TFAR for 170A load(D_1^{110}), 85A load (D_1^{85}) and OCV mode (D_1^0)

Wavelet descriptors for different loads are presented in Fig.5.27. High-frequency events are visible for load modes. These events have not been detected for OCV mode.

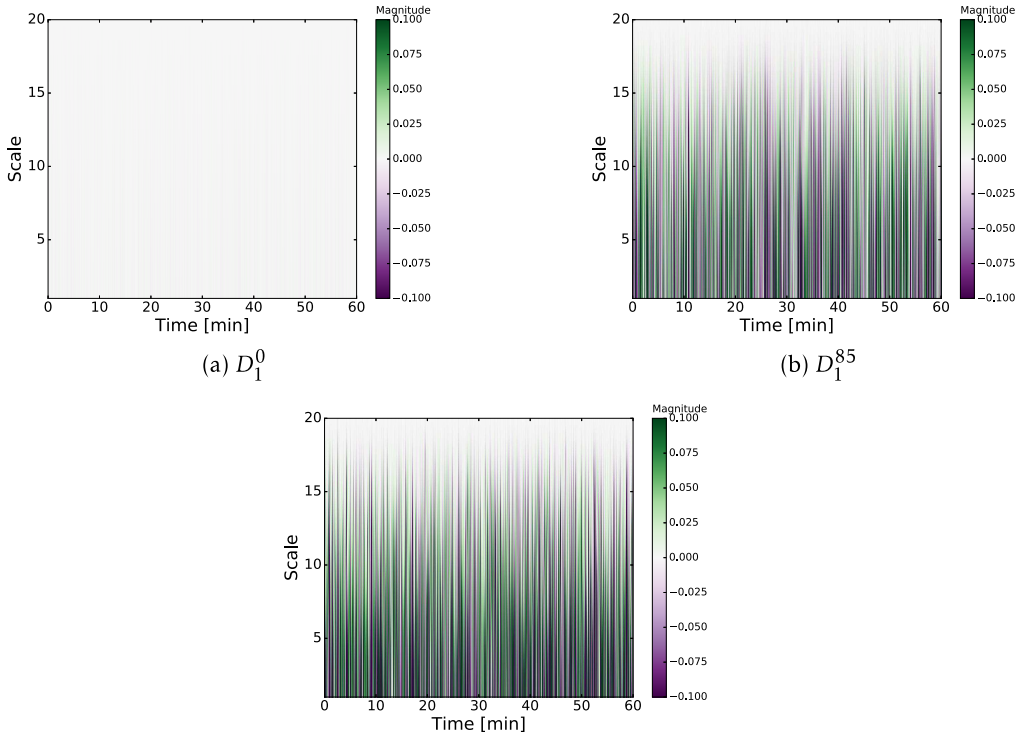

(a) D_1^0

(b) D_1^{85}

(c) D_1^{110}

Figure 5.27 – Implementation of Wavelet for 170A load(D_1^{110}), 85A load (D_1^{85}) and OCV mode (D_1^0)

Statistical descriptors for automotive operation mode

This operation mode concerns zones $D_1^{100(5)}$, $D_1^{50(5)}$, $D^{30(5)_1}$, $D_1^{20(5)}$ and $D_1^{10(5)}$. During this operation mode the load of stack has been changed repetitively between maximum I_{max} (I_{max} = 100A, 50A, 30A, 20A and 10A) and I_{min}=5A values, the duration of each cycle is equal to 60s and total time duration of each zone is equal to 1 hour. All part of cycling had been merged (we cut the parts corresponding to 1 minute). Visualization of merging signals can be seen in Fig. 4.89, Fig. 4.90 and Fig. 4.91 (Chapter 4).

Short-time Fourier Transform (STFT) descriptors for OCV, 85A and 100A load modes are presented in Fig. 5.28 and Fig. 5.29. We can see results an important difference between noise signatures and the existence of stable dominant frequencies. The following conclusions can be done:

- dominant frequency around 2 Hz is presented for all zones; for zone $D_1^{100(5)}$ we can see another dominant frequency around 5Hz (probably subharmonic)
- for all zones ($D_1^{30(5)}$) we can clearly observed some repetitive phenomena (vertical yellow lines and/or yellow spots) with characteristic time duration about 3 min.

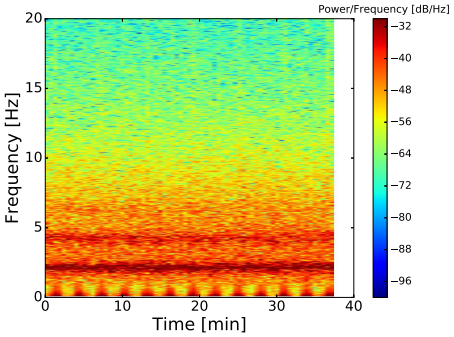

(a) $D_1^{100(5)}$

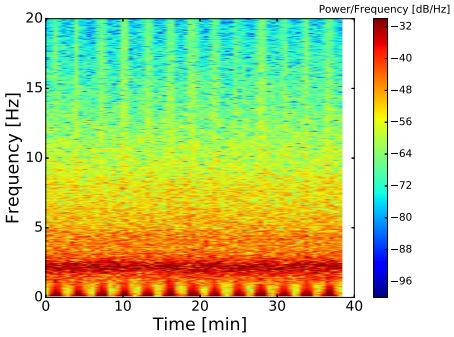

(b) $D_1^{50(5)}$

Figure 5.28 – Implementation of STFT for Automotive profile (100A ($D_1^{100(5)}$) and 50A ($D_1^{50(5)}$)

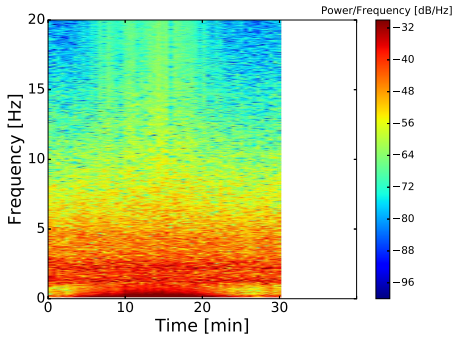

(a) $(D_1^{30(5)}$

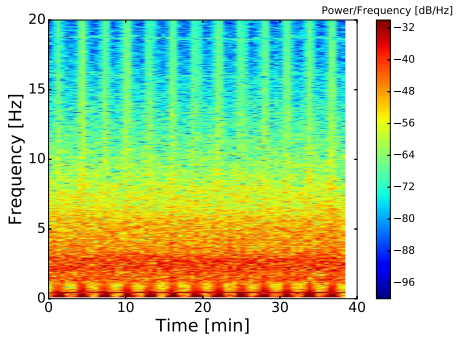

(b) $D_1^{20(5)}$

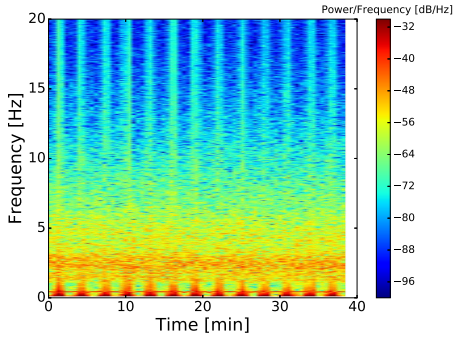

(c) $D_1^{10(5)}$

Figure 5.29 – Implementation of STFT for Automotive profile 30A ($(D_1^{30(5)}$), 20A ($D_1^{20(5)}$) and 10A ($D_1^{10(5)}$))

Time-Frequency Autoregressive (TFAR) descriptors are presented in Fig.5.30. We note the existence of dominant frequencies both in high ($f > 10Hz$) and low frequency ranges. Some repetitive events are also visible.

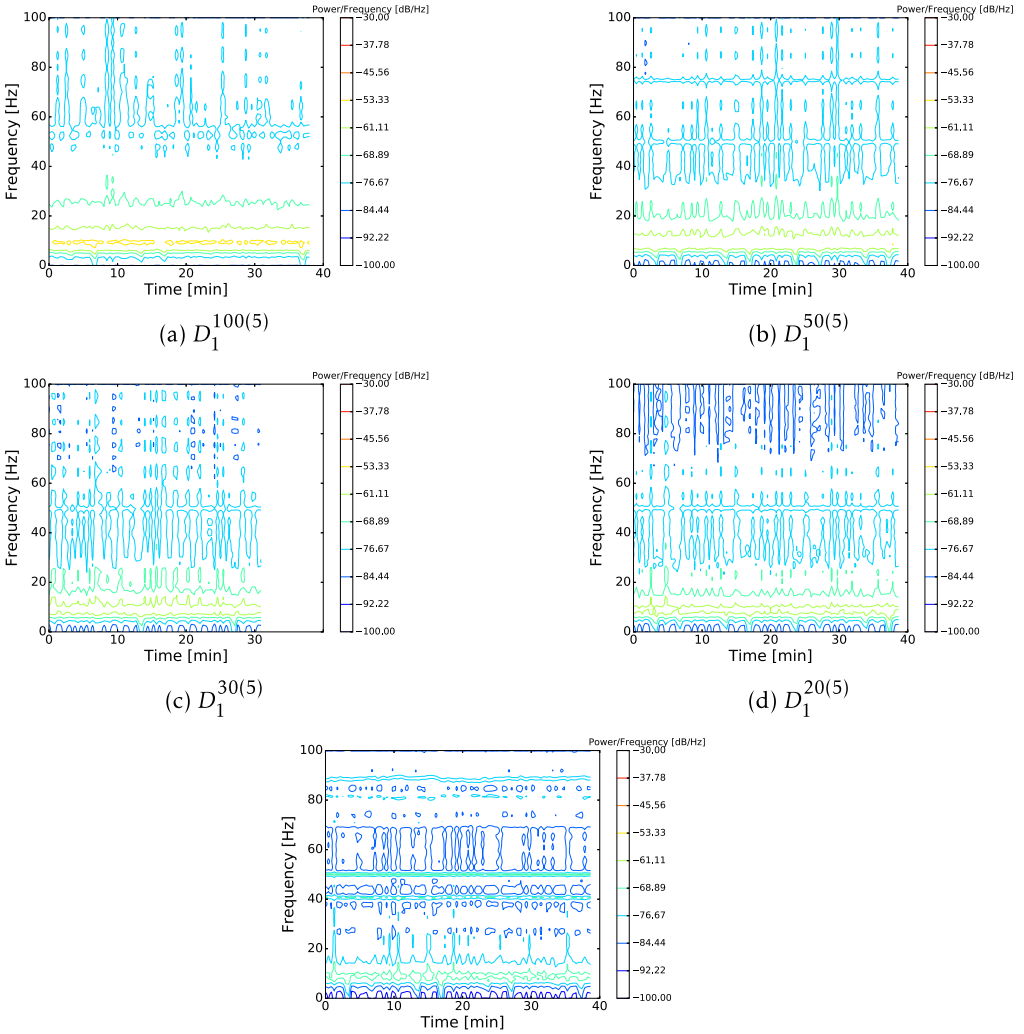

(a) $D_1^{100(5)}$ (b) $D_1^{50(5)}$

(c) $D_1^{30(5)}$ (d) $D_1^{20(5)}$

(e) $D_1^{10(5)}$

Figure 5.30 – Implementation of TFAR for Automotive profile (100A ($D_1^{100(5)}$), 50A ($D_1^{50(5)}$), 30A (($D_1^{30(5)}$), 20A ($D_1^{20(5)}$) and 10A ($D_1^{10(5)}$))

Wavelet descriptors are presented in Fig.5.31. For all zones we note existence of high repetitive events.

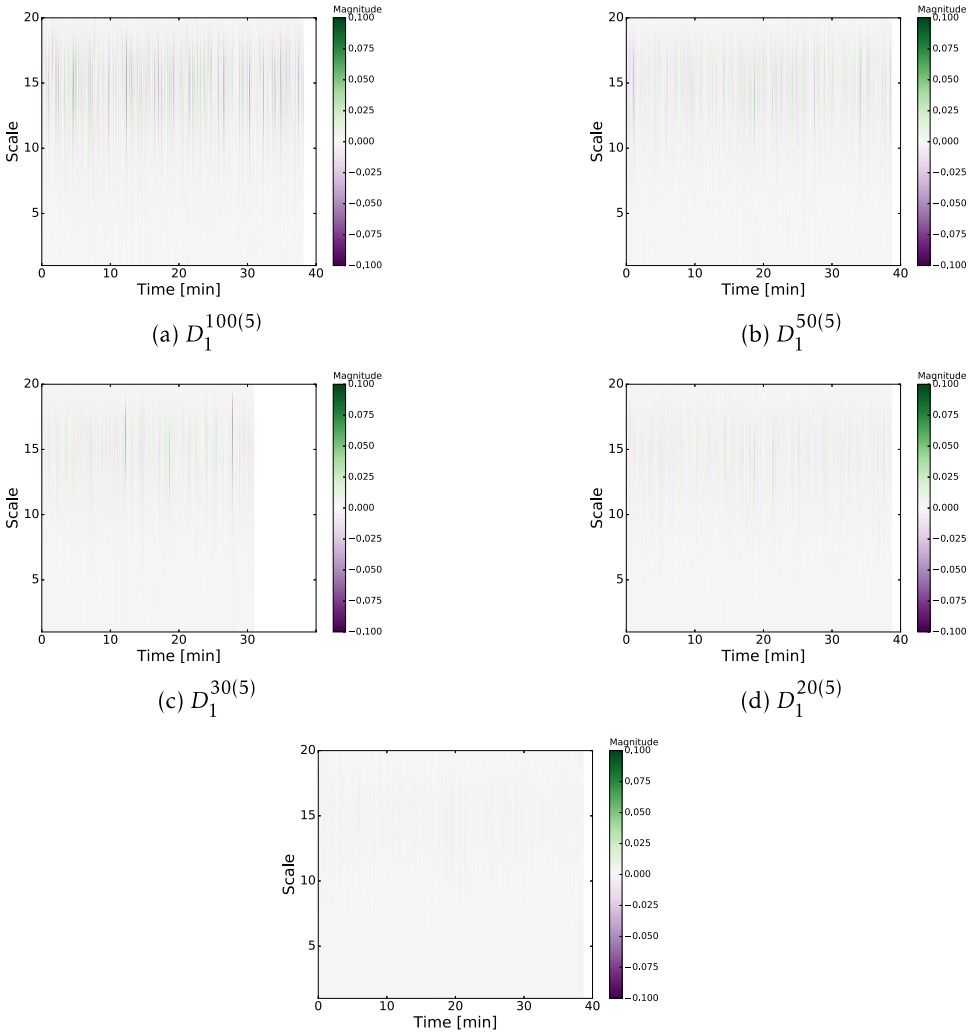

(a) $D_1^{100(5)}$

(b) $D_1^{50(5)}$

(c) $D_1^{30(5)}$

(d) $D_1^{20(5)}$

(e) $D_1^{10(5)}$

Figure 5.31 – Implementation of Wavelet for Automotive profile (100A ($D_1^{100(5)}$), 50A ($D_1^{50(5)}$), 30A (($D_1^{30(5)}$), 20A ($D_1^{20(5)}$) and 10A ($D_1^{10(5)}$))

Chapter 6

Application of noise diagnostic for characterization of PEM stack in different operational conditions.

Contents

Figures

The previous chapters 4, 5 have been devoted to the generation of different statistical descriptors in time, frequency and time-frequency domains. It was demonstrated that electrochemical noise diagnostic provides rich description of fuel cell stack. The noise signature obtained using different methods seems to be stable (repetitive) when operational conditions are constant and no perturbations occur during signal recording.

In this chapter we will try to understand what information can be extracted from the noise measurements with respect to influence of operational conditions on stack running. We note the specificity of our experiments which have serious limits regarding to the reproducibility of the tests. Indeed, during experimental campaigns stack running has been perturbed by planified (change of operational conditions, impedance and polarization curve measurements, aging) and non-planified (interrupt of hydrogen, etc.) events. All these events influence on noise signature because it is very sensitive. Thus, a lot of parameters influence simultaneously the stack operation and it is not easy to extract the governing factor. Moreover, in all the campaigns new stacks have been used and non-perfection of the stack manufacturing should be take into account as one of the parameters which also influence on noise signature. Thus, classification of noise signatures with the respect of different parameters meets principal difficulties and existence of artefacts should be accepted. It means, that we are looking for extraction of main tendencies which should be rectified in future studies.

Below we will try to understand the influence of noise signature on:

- current load
- relaxation processes after stack interruption
- type of stack polarization (cogeneration or automotive profiles)
- manufacturing (different stacks)
- aging

This information allows to use the noise diagnostic for practical applications, in particular development of prognostic tools, characterization of current technical state, estimation of manufacturing performance and understanding the physical processes in PEM stack. Sure, the present study is only the first step in this direction. As we have mentioned above, the noise signature is rich, sensitive and can be obtained by different methods. This is important because different governing factors can be extracted simultaneously from the same noise signature. From the other hand, the classification of noise signature with respect to governing factors is difficult, taking into account that it can be obtained in time, frequency and time-frequency domains. Each presentation of noise signature has advantages and disadvantages. Sometimes it is necessary to use interpretation of noise signature in different domains in order to clarify the influence of governing factors. Thus, we will start this chapter with some qualitative classification of obtained noise signatures in previous chapters using cross interpretation in frequency and time domains.

6.1 Cross interpretation of noise signature in time and frequency domains

Table 6.1 and Fig. 6.1 present noise signature of stack running at 85A load (second campaign) in time and frequency domains, respectively. This realization is taken only for illustration of cross interpretation.

Fig. 6.2 gives typical schematic representation of recorded PSD curves which reflects the main phenomena observed on Fig. 6.1, namely:

- low frequency flicker-noise component ($f < f_1$)
- high frequency flicker-noise component ($f > f_2$)

	original	32 seconds	8 seconds	2 seconds	0.3 seconds
μ, V	5.606	5.606	5.606	5.606	5.606
σ, mV	33.5	5.2	5.0	4.6	1.0
eps, 10^{-6}	5993	932	893	821	194
V_{max}, mV	5.661×10^3	12.6	15.1	36.2	19.2
V_{min}, mV	5.376×10^3	-61.1	-59.9	-54.6	-17.8
V_{p-p}, mV	284.4	73.8	75.0	90.9	37.1
M2, 10^{-6}	1128	27.3	25.0	21.1	1.1
M3, 10^{-9}	-127818	-380	-353	-245	-0.3
M4, 10^{-9}	20179	11	9.9	6.5	0
Sk	-3.37	-2.66	-2.81	-2.51	-0.25
KU	12.8	11.92	12.77	11.55	15.0

Table 6.1 – Statistical descriptors for 85A load (B_1^{85}) after detrending procedure with different time windows

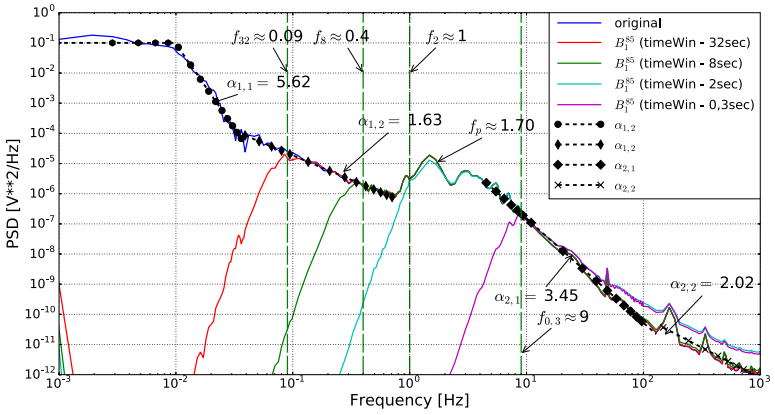

Figure 6.1 – PSD Welch with different time windows for 85 load (B_1^{85})

- intermediate frequency range ($f_1 < f < f_2$) where some dominant frequency $f_{pick} = f_p$ is presented with some subharmonics.

Low frequency flicker-noise can be characterized using one (α_1) or two ($\alpha_{1,1}$, $\alpha_{1,2}$) slopes. Low frequency "white-noise" plateau can be presented or not, depending on operational conditions. High frequency flicker-noise also can be characterized using one (α_2) or two ($\alpha_{2,1}$, $\alpha_{2,2}$) slopes. For example, for B_1^{85} realization, we can clearly identify low frequency "white-noise" plateau. Both, high and low frequency flicker-noise components for B_1^{85} realization are characterized by two slopes (low frequency - $\alpha_{1,1} = 5.62, \alpha_{1,2} = 1.63$, high frequency - $\alpha_{2,1} = 3.45, \alpha_{2,2} = 2.02$), see Fig. 6.1.

Our analyze presented in Chapter 4 for PSD curves shows that the main part of realizations can be interpreted using schema of Fig. 6.2. Sometimes some other pick frequencies with subharmonics are recorded as well. The detection of pick frequencies is more clear using noise signature in time-frequency domains, see the next paragraph 6.2.

The noise signature in time domain (Table 6.1) completes PSD description of the signal. Detrending procedure with different time windows plays a role of high pass band filter, the

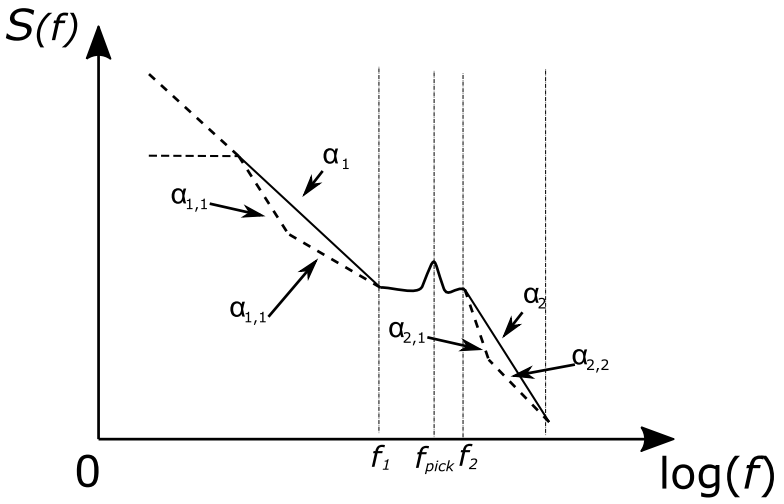

Figure 6.2 – Typical shape of PSD

corresponding cut frequencies are presented on Fig. 6.1, namely: $f_{32} \approx 0.09Hz$, $f_8 \approx 0.4Hz$, $f_2 \approx 1Hz$ and $f_{0.3} \approx 9Hz$.

We note a good quality of numerical filtering procedure. Only in very high frequency domain some difference between original and filtered signal can be observed.

Noise signature in time domain is given by standard deviation (σ) which is obtained using second moment of fluctuations M2 (noise energy) and by high order moments (M3,M4,...) or by their non-dimensional representation, namely skewness (Sk) and kurtosis (KU). The first line (μ) in Table 6.1 is a recorded stack voltage and $\varepsilon = \sigma/\mu$ is intensity of voltage fluctuations.

Naturally, the noise signature in time domain depends on the use of numerical filter (different time windows), thus we obtain different values of σ, ε, Sk, KU for different frequency domains. Roughly speaking, a following correspondence between numerical filters and recorded signals exists:

- dominant part of noise energy is located in low-frequency domain ($f < f_{32} \approx 0.09Hz$); this domain corresponds to low-frequency flicker-noise component, energy (σ) and time descriptors (Sk, KU) in this zone can be obtained using first column (original) in Table 6.1.
- high frequency flicker-noise component is described by the last (0.3 second) column, which corresponds to the frequency range $f > f_{0.3} \approx 9Hz$;
- frequency range ($f_{32} < f < f_{0.3}$) and corresponding columns (32s, 8s, 2s) reflects mainly the intermediate zone of Fig. 6.2.

For example, for realization B_1^{85} the low frequency zone $f < 0.09Hz$ accumulates $e_1 = \frac{1128-27.3}{1128} \cdot 100\% = 97.5\%$ of noise energy. This zone is characterized by large values of $Sk \approx -3.37$ and $KU \approx 12.8$. Using description of flicker-noise in terms of slopes, we should attribute to this zone the value $\alpha_{1,1} = 5.62$

The second part of low frequency flicker noise component with the slope $\alpha_{1,2} \approx 1.63$ is situated mainly in the range $f_{32} < f < f_8$, thus the second column characterizes this part of flicker-noise with $Sk \approx -2.66$ and $KU \approx 11.92$.

The intermediate zone is situated mainly in frequency range $f_8 < f < f_{0.3}$ and corresponding values of Sk and KU should be used. Pick frequency is equal to $f_p = 1.7Hz$. At last, high-frequency flicker noise component is situated mainly in the zone $f > f_{0.3} \approx 9Hz$. For this zone the last column in Table 6.1 should be taken for noise description with the values $Sk \approx -0.25$ and

$KU \approx 15.0$. We note the important decreasing of Sk for high-frequency flicker-noise component. In order to finalize the presentation of cross-interpretation, let us consider another realization B_2^0, which corresponds to OCV mode (running without load) during second campaign. The noise signature is given by Table 6.2 and Fig. 6.3

	original	32 seconds	8 seconds	2 seconds	0.3 seconds
μ, V	7.733	7.733	7.733	7.733	7.733
σ, mV	6.7	0.3	0.2	0.2	0.1
eps, 10^{-6}	874	48	37	33	11
V_{max}, mV	7.747×10^3	2.1	1.3	1.3	0.5
V_{min}, mV	7.719×10^3	-1.5	-1.3	-1.2	-0.5
V_{p-p}, mV	27.7	3.7	2.7	2.6	1.0
M2, 10^{-6}	45.6	136	0	0	0
M3, 10^{-9}	5.7	0	0	0	0
M4, 10^{-9}	4.0	0	0	0	0
Sk	0.01	0.25	0.59	0.61	0.19
KU	-1.08	0.39	0.74	0.76	1.50

Table 6.2 – Statistical descriptors for OCV (B_2^0) after detrending procedure with different time windows

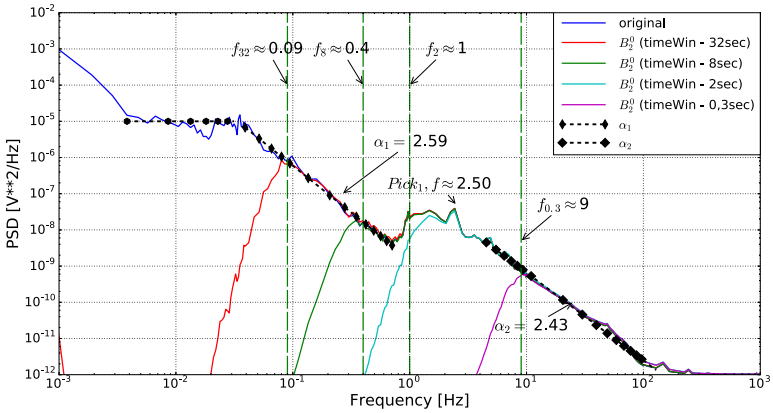

Figure 6.3 – PSD Welch with different time windows for OCV mode (B_2^0)

We note, that schema of Fig. 6.2 describes well this realization. The low-frequency flicker noise component is situated in the range $f_{32} < f < f_{0.3}$ and is characterized by one slope $\alpha_1 \approx 2.59$. Corresponding values of $Sk \approx 0.25$ and $KU \approx 0.39$. The high-frequency flicker-noise is situated in the zone $f > f_{0.3} \approx 9Hz$. This flicker-noise is characterized by one the slope $\alpha_2 \approx 2.43$ with $Sk = 0.19$ and $KU = 1.5$. The pick frequency in intermediate zone is equal to $f_p = 2.5Hz$. We note the clear difference between Sk and KU for two realizations. Indeed, for OCV mode in all the zones Sk and KU are small $|Sk| < 0.6$ and $|KU| < 1.5$.

6.2 Interpretation of noise signature in time-frequency domain

Fig. 6.4, Fig. 6.5, Fig. 6.6 and Fig. 6.7 present noise signature of B_1^{85} and B_2^0 realizations obtained in time-frequency domain using STFT and TFAR methods. This noise signature gives additional information with respect to detection of dominant frequencies and their subharmonics. Indeed, subharmonics in high frequency range become very visible on TFAR pictures. Moreover for OCV mode STFT reveals seconds dominant frequency $f \approx 1.6$ which is not visible on traditional PSD picture.

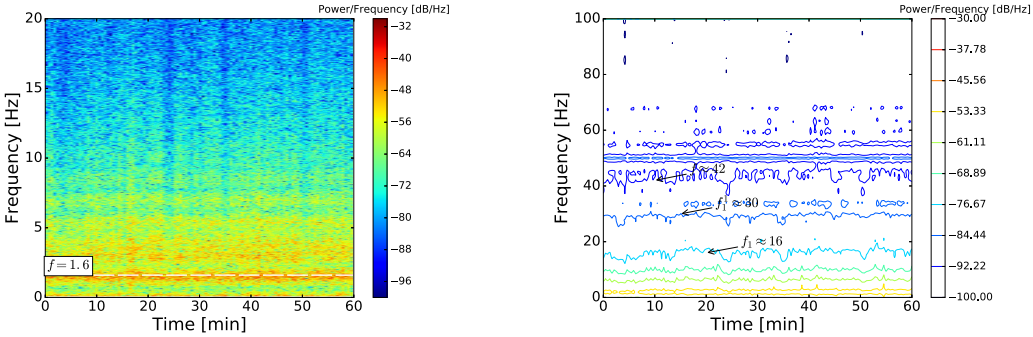

(a) STFT (b) TFAR

Figure 6.4 – STFT and TFAR for 85A load (B_1^{85})

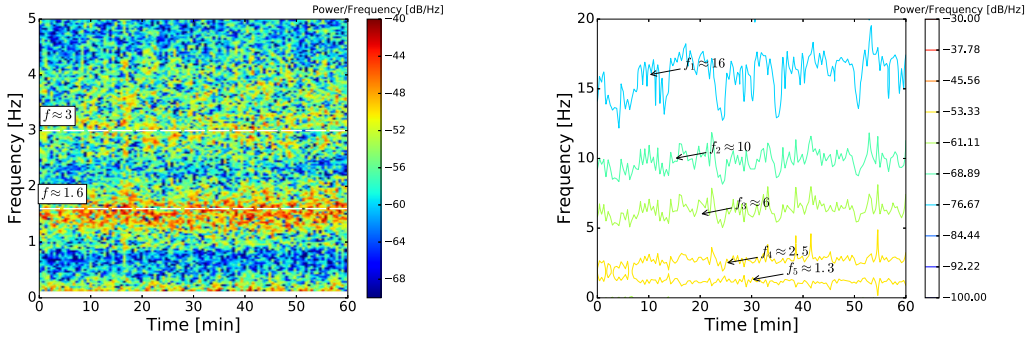

(a) STFT (b) TFAR

Figure 6.5 – STFT and TFAR for 85A load in low frequency range (B_1^{85})

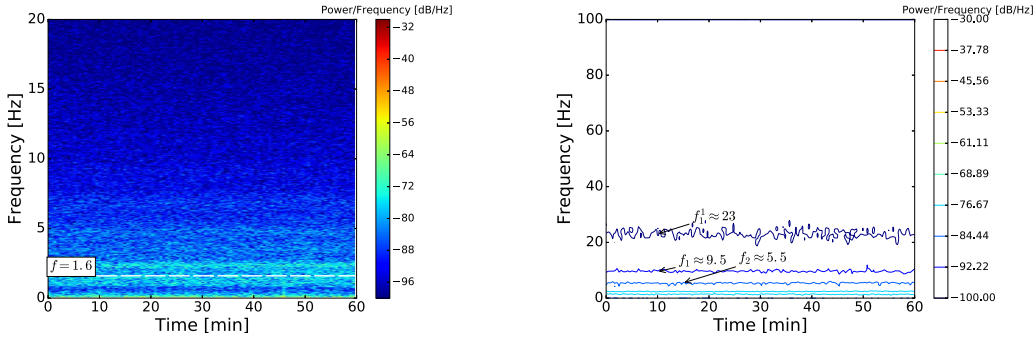

(a) STFT (b) TFAR

Figure 6.6 – STFT and TFAR for OCV mode (B_2^0)

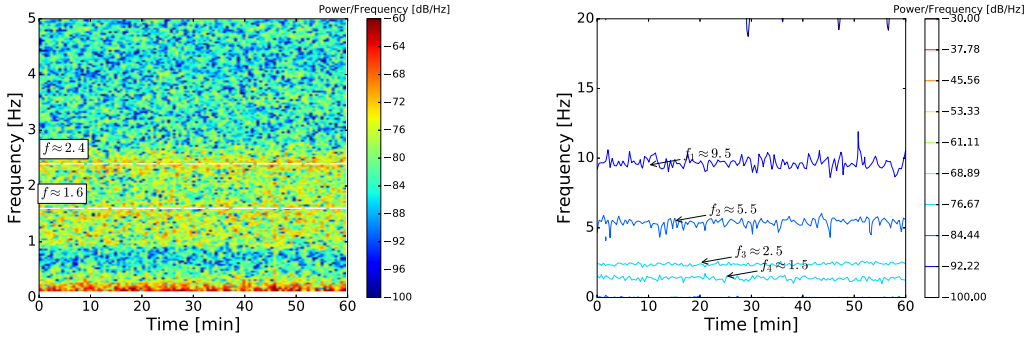

(a) STFT (b) TFAR

Figure 6.7 – STFT and TFAR for OCV mode in low frequency range (B_2^0)

6.3 Influence of low-frequency perturbations on noise signature

In this paragraph we discuss the repeatability of noise signature obtained in the same operational conditions. In the frame of the present study it was not possible to provide special repeatability experiments with respect to study of noise signature. Moreover, it is difficult to control perfectly all operational conditions, because a lot of parameters can influence on stack running. In order to answer on this question, we will compare the noise signatures recorded during the same campaign (it means using the same stack) and under the same constant load. In the next paragraph 6.4 the influence of current load on noise signature is discussed. The comparison of noise signatures for different stacks will be presented in paragraph 6.6.

Only three first campaign can provide the necessary information for repeatability studies. Indeed, in the 4th campaign mainly automotive profile has been studied and we have only two realizations with different constant load (85A and 110A). Fig. 6.8 presents four noise signatures in terms PSD recorded during the first campaign under 85A load. We note that after realization A_1^{85} the stack has been stopped for many hours due to the problem with hydrogen supply. One can see, that the stack interruption manifest a signature itself by some transient process that has a visible influence on noise signature in low frequency range. Nevertheless, in low frequency, perturbations do not change the noise frequency in intermediate and high frequency ranges ($f > 0.5Hz$).

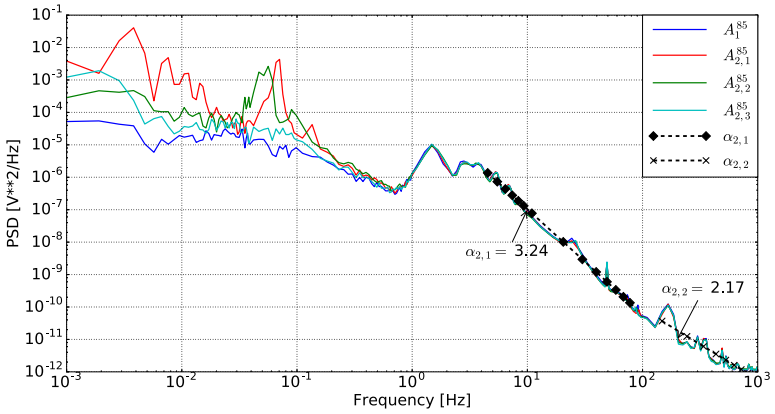

Figure 6.8 – PSD for 85A in 1st campaign

Fig. 6.9 presents four realizations under 170A load and two realization under 85 A load recorded during the second campaign. We note a very good repeatability of noise signature for a given load, in particular in intermediate and high frequency ranges. We note that running under 170A load has been affected by strong voltage fluctuations due to the problem with pressure regulation. These fluctuations influence significantly the low frequency noise signature, but do not influence on noise signature in intermediate and high frequency ranges.

Fig. 6.10 present three realizations under 100 A load and all realizations under 50A load recorded during third campaign. We note very good repeatability of noise signature in intermediate and high frequency ranges ($f > 0.5Hz$) despite of existence of some perturbations in low frequency domain.

Thus, our analyze show that for a given stack noise signature in intermediate and high frequency ranges ($f > 0.5Hz$) depends mainly on current load. Noise signature in low frequency

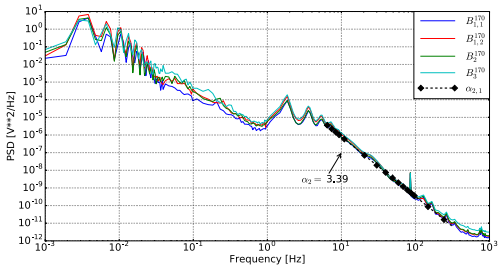

(a) 170A

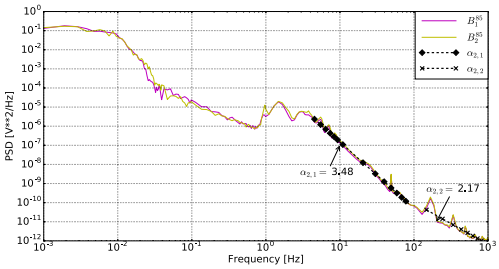

(b) 85A

Figure 6.9 – PSD for 170A and for 85A in 2nd campaign

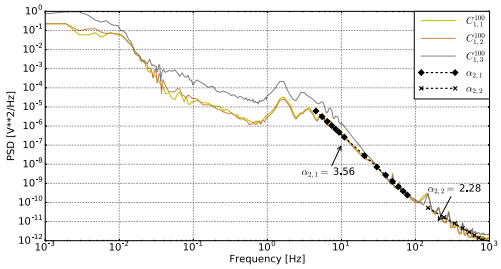

(a) 100A

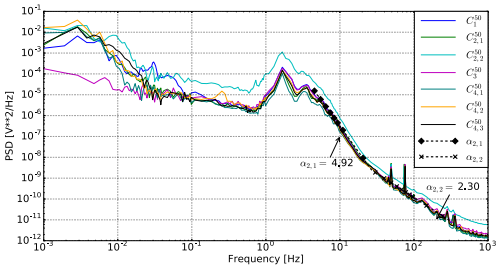

(b) 50A

Figure 6.10 – PSD for 100A and for 50A in 3rd campaign

range ($f < 0.5Hz$) is more sensitive, in particular to transient processes due to stack stoppage and pressure regulation.

6.4 Influence of current load on noise signature

In the previous chapter we have demonstrated that for the same constant current load the noise signature in terms of PSD is well reproducible, especially for intermediate and high frequency ranges. Thus, current load seems to be the main parameter determining noise signature for cogeneration profile. The dependence of noise signature on constant current load is discussed in this section. Noise signature for automotive profile (repetitive changing of load) will be discussed in the next paragraph 6.5. Fig. 6.11 illustrates the position of the points where noise signature has been recorded on the polarization curve.

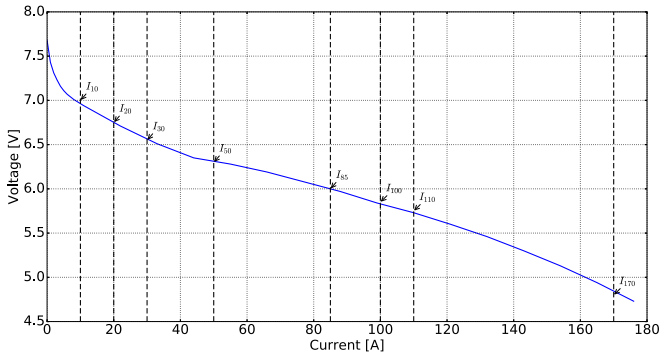

Figure 6.11 – Polarization curve

Fig. 6.12 demonstrates the dependence of the main dominant frequency fp, situated in the intermediate frequency range, on the current load. We note that this dominant frequency for all the loads is equal to $f_p = 1.75Hz$ with 8% accuracy. Noise signature under OCV mode is more sensitive than the one obtained under constant load. In particular, for OCV mode the dominant frequency lies in the range $2.2 < f_p < 2.5$. Calculated mean value for dominant frequency under OCV mode is equal to $f_p = 2.35$ with 15% accuracy.

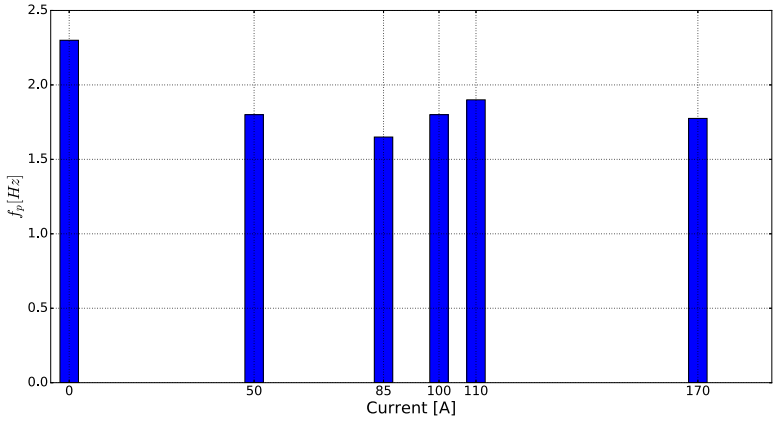

Figure 6.12 – Dependence of dominant frequency f_p on current load

Table 6.3 presents the slopes of high-frequency flicker noise for different current loads, the data are extracted from the figures presented in the previous paragraph 6.3.

	50A	85A	100A	170A
α_2	x	x	x	3.39
$\alpha_{2,1}$	4.92	3.48	3.56	x
$\alpha_{2,2}$	2.3	2.17	2.28	x

Table 6.3 – Dependence of slopes of high-frequency flicker noise component on stack load

Additional information concerning the influence of current load can be obtained using noise signature in time domain. This signature is characterized by the energy (or intensity) of noise and its moments (SK, KU) calculated for different time windows. The procedure has been explained in section 6.1 and Fig. 6.13, Fig. 6.14 and Fig. 6.15 illustrate the results of calculations. The intensity of fluctuations (*eps*) characterizes the energy of noise signal within the respective frequency range. In principal, this parameter can be obtained also by integration of corresponding PSD curves. The high order moments (SK and KU) cannot been obtained from PSD curves and give an additional information for noise signature.

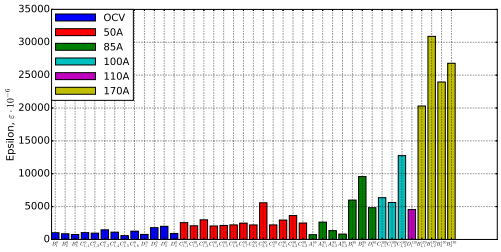

(a) low frequency range- "original"

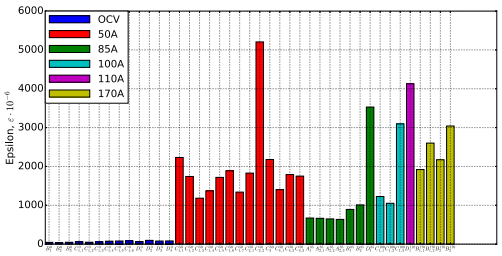

(b) intermediate frequency range - "time windows of 32, 8 and 2 seconds"

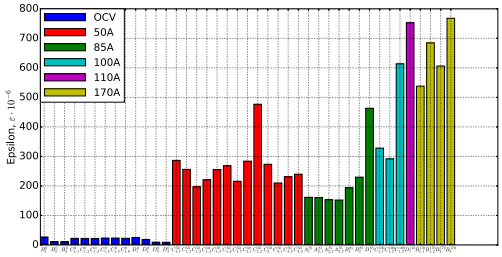

(c) high frequency range - "time windows of 0.3 seconds

Figure 6.13 – Dependence of noise intensity, epsilon on stack load

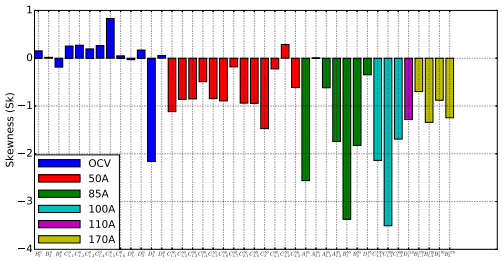

(a) low frequency range- "original"

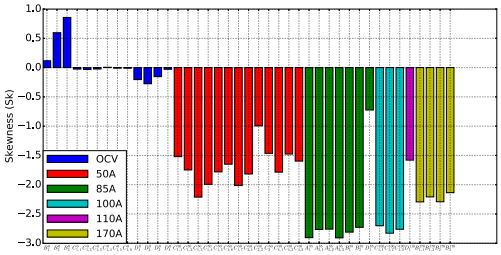

(b) intermediate frequency range - "time windows of 32, 8 and 2 seconds"

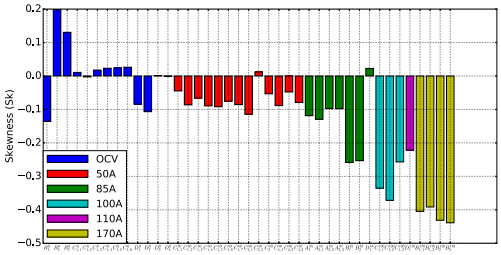

(c) high frequency range - "time windows of 0.3 seconds

Figure 6.14 – Dependence of skewness on stack load

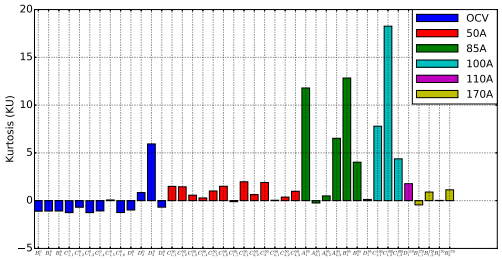

(a) low frequency range- "original"

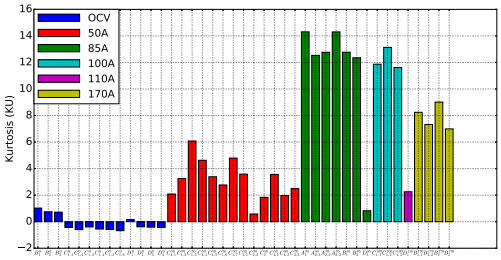

(b) intermediate frequency range - "time windows of 32, 8 and 2 seconds"

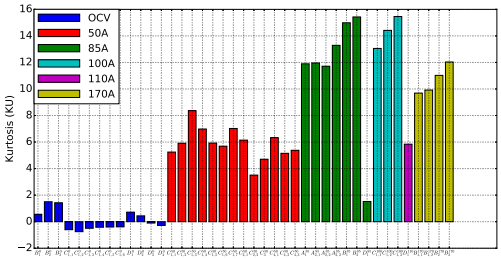

(c) high frequency range - "time windows of 0.3 seconds

Figure 6.15 – Dependence of kurtosis on stack load

We note the existence of some dispersion of calculated in time domain descriptors for the same load. It means that these descriptors can be more sensitive than the ones calculated in frequency domain. For further interpretation we use the mean value of calculated in time domain descriptors and present the results using Fig. 6.16, Fig. 6.18 and Fig. 6.18. Taking into account that standard deviation of the noise $\sigma = \mu \cdot \varepsilon$, we can plot the dependence σ for different frequency ranges, see Fig. 6.16.

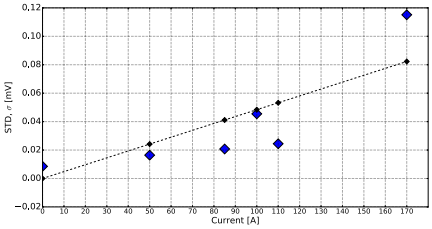

(a) low frequency - "original"

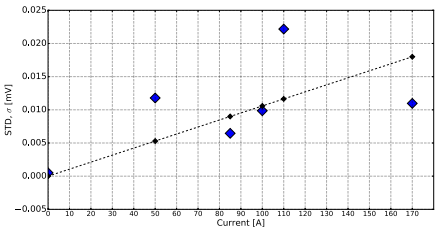

(b) Intermediate frequency - "time windows of 32, 8 and 2 seconds"

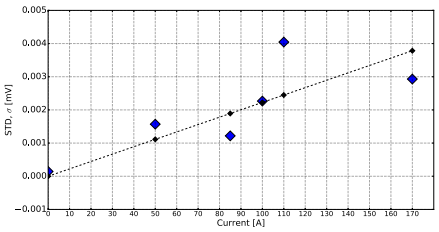

(c) high frequency - "time windows of 0.3 seconds

Figure 6.16 – Dependence of STD(σ) on stack load

It is interesting to check well-known empirical equation of Hooge[66, 71] which supposes that noise energy (σ^2) is proportional to the square of the mean current I. If this equation is valid, the dependence $\varepsilon(\mu)$ can be approximated by the straight line which is also plotted on Fig. 6.16.

We note that for all frequency domains our data relatively well meet with Hooge equation. The only one point has been treated as artefact, namely noise intensity at low-frequency range at 170A load. Indeed, for this load high-frequency fluctuations exist ($f < 0.05Hz$) due to the problem with pressure regulation. These fluctuations increase significantly the calculated noise energy but cannot been related with internal system noise.

Analyse of Sk data shows that for low and intermediate frequency ranges Sk is negative and relatively high $|SK| > 1$. For high-frequency range Sk decreases sharply $|Sk| < 0.4$.

Kurtosis (Fig. 6.18) for all frequency domains is important, it is difficult to extract some tendencies with respect to stack load.

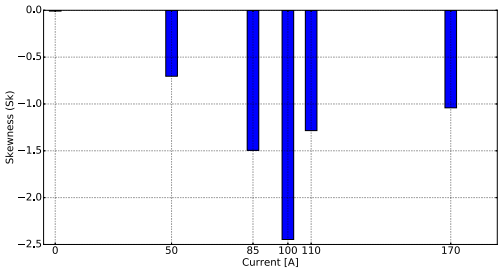

(a) low frequency - "original"

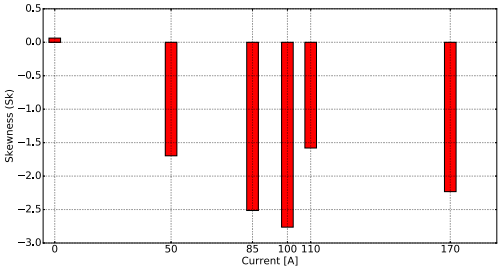

(b) Intermediate frequency - "time windows of 32, 8 and 2 seconds"

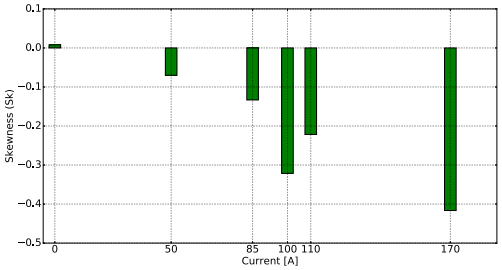

(c) high frequency - "time windows of 0.3 seconds

Figure 6.17 – Dependence of Sk on stack load

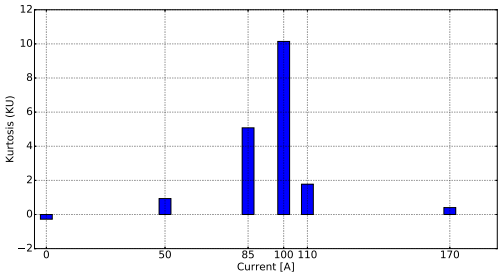

(a) low frequency - "original"

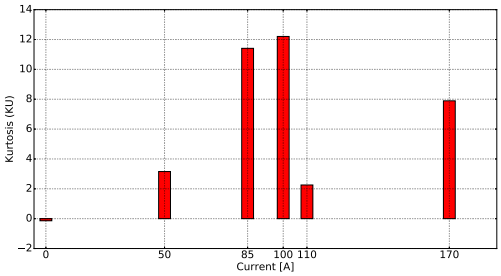

(b) Intermediate frequency - "time windows of 32, 8 and 2 seconds"

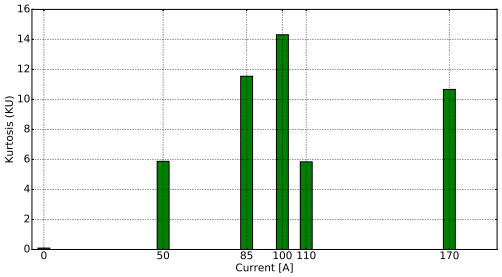

(c) high frequency - "time windows of 0.3 seconds

Figure 6.18 – Dependence of KU on stack load

6.5 Noise signature under automotive mode

The forth campaign of experiments concerns automotive profile, when current load changes repetitively between its maximum value I_{max} (100A, 50A, 30A, 20A, 10A) and minimum value $I_{min} = 5A$. The noise signature in frequency domain obtained for all I_{max} values is similar to the one obtained for co-generation profile, see Fig. 6.19, Fig. 6.20, Fig. 6.21, Fig. 6.22 and Fig. 6.23.

We note the existence of important perturbations in low frequency range ($f < 0.1Hz$) due to periodic mode of stack running with $f_{SW} = 0.025Hz$. Low frequency flicker-noise component is characterized by one slope and high-frequency flicker-noise component has two slopes. The values of these slopes, see Table 6.4, are rather stable with respect to I_{max} changing. We note also that dominant frequency in intermediate frequency range is more important ($f_p \approx 1.9$) in comparison to the one recorded for co-generation profile ($f_p \approx 1.75$).

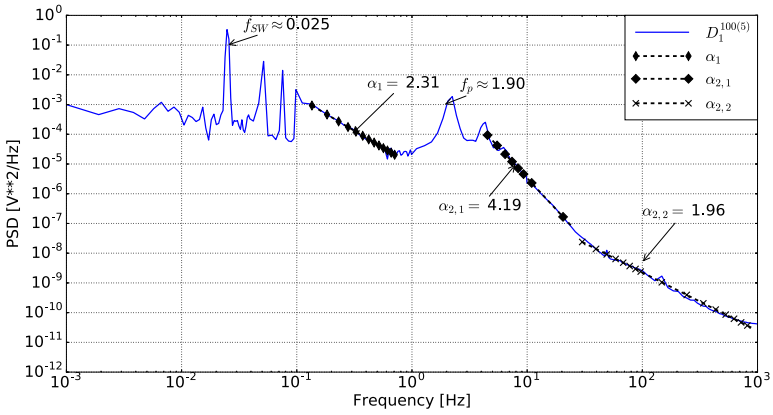

Figure 6.19 – PSD Welch for 100A/5A automotive mode ($D_1^{100(5)}$)

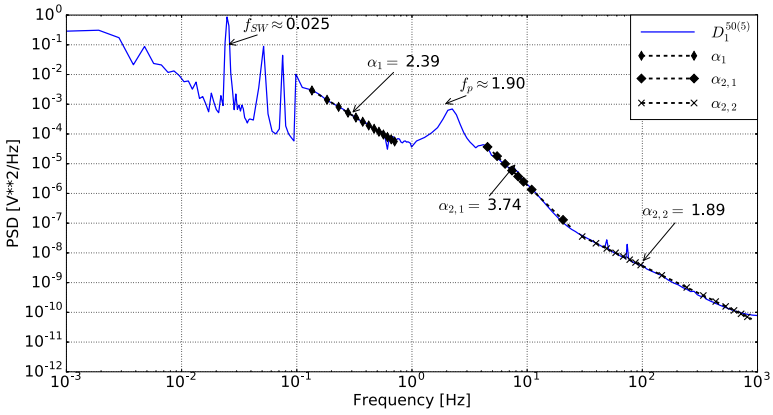

Figure 6.20 – PSD Welch for 50A/5A automotive mode ($D_1^{50(5)}$)

Fig. 6.24 and Fig. 6.25 present the comparison between noise signatures of automotive ("D") and co-generation profiles ("C") in frequency domain. We note that the signatures are similar in intermediate and high-frequency ranges. The noise intensity in these zones is more important for automotive profile.

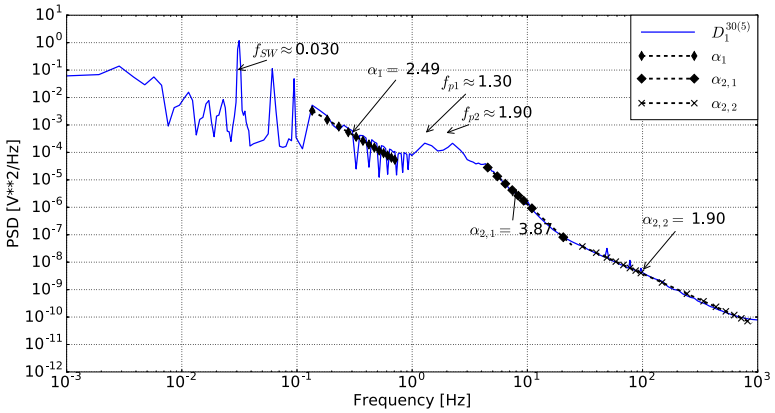

Figure 6.21 – PSD Welch for 30A/5A automotive mode ($D_1^{30(5)}$)

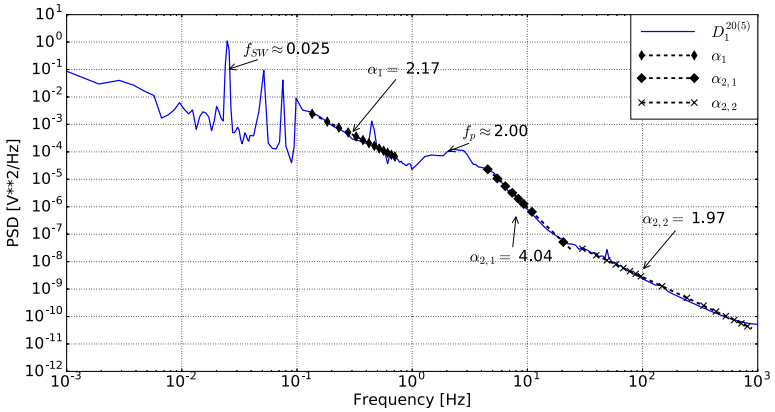

Figure 6.22 – PSD Welch for 20A/5A automotive mode ($D_1^{20(5)}$)

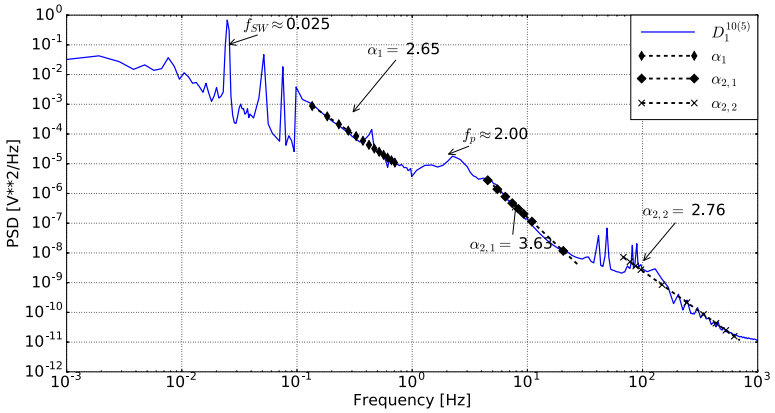

Figure 6.23 – PSD Welch for 10A/5A automotive mode ($D_1^{10(5)}$)

	10A	20A	30A	50A	100A
α_1	2.65	2.17	2.49	2.39	2.31
$\alpha_{2,1}$	3.63	4.04	3.87	3.74	4.19
$\alpha_{2,2}$	2.76	1.97	1.9	1.89	1.96

Table 6.4 – Dependence of slopes of flicker-noise components in current load I_{max}

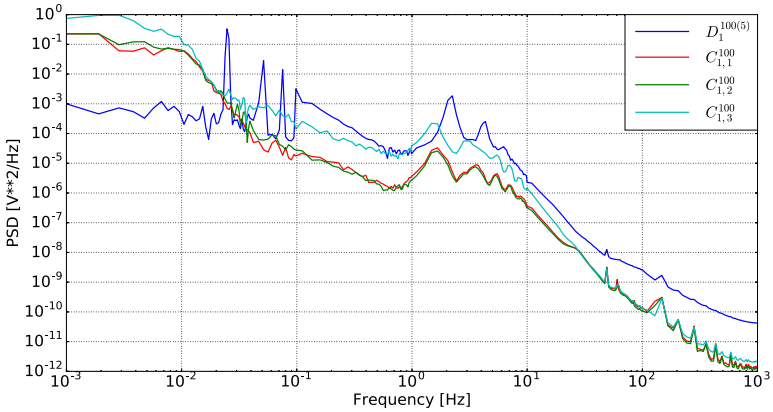

Figure 6.24 – Comparison of PSD Welch between automotive mode (100A/5A - $D_1^{100(5)}$) and continues operation (100A - C_1^{100})

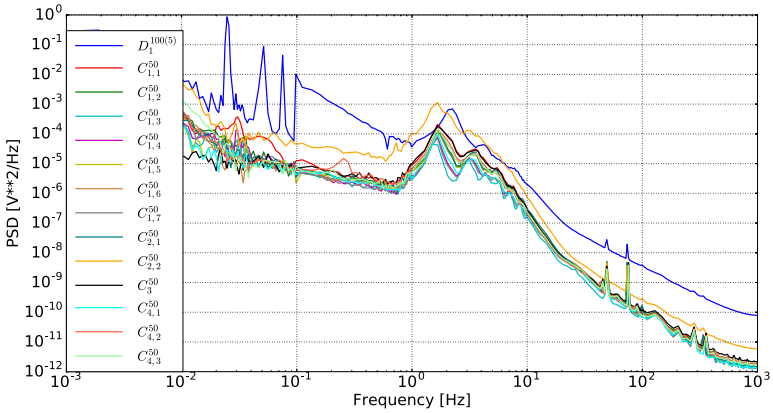

Figure 6.25 – Comparison of PSD Welch between automotive mode (50A/5A - $D_1^{50(5)}$) and continues operation (50A - C_1^{50},C_2^{50},C_3^{50},C_4^{50})

Fig.6.26, Fig.6.27 and Fig.6.28 complete the noise signature by using statistical descriptors in time domain. For comparison we add on these figures, the results previously obtained for co-generation profile for 50A and 100A loads.

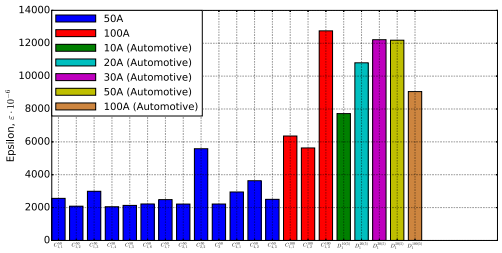

(a) low frequency range - "original"

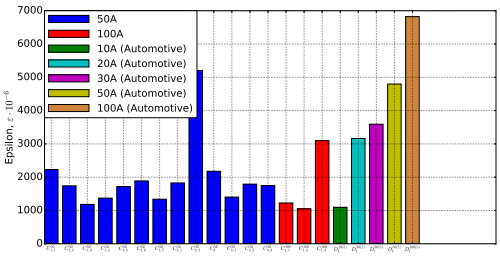

(b) intermediate frequency range - "time windows of 32, 8 and 2 seconds"

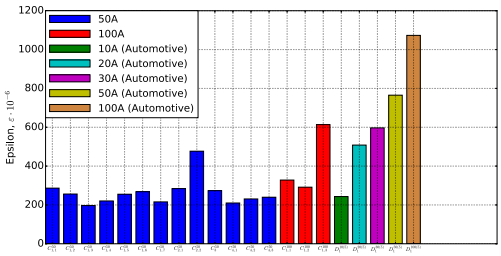

(c) high frequency range - "time windows of 0.3 seconds

Figure 6.26 – Dependence of epsilon on stack load

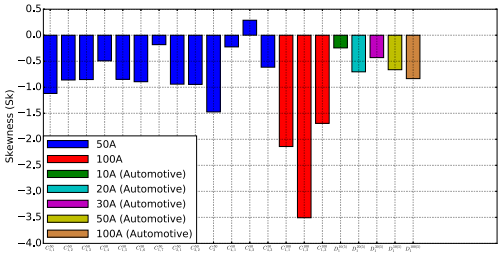

(a) low frequency range - "original"

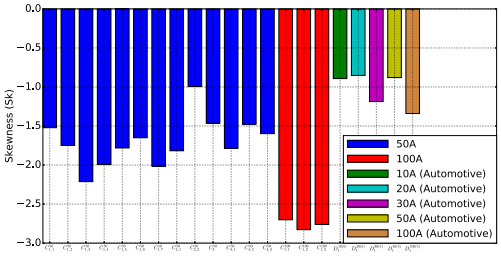

(b) intermediate frequency range - "time windows of 32, 8 and 2 seconds"

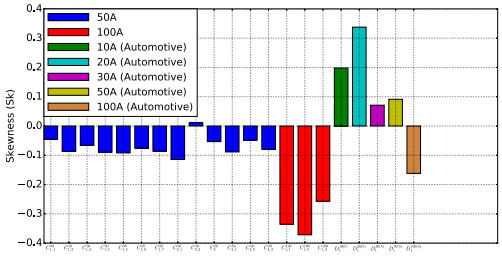

(c) high frequency range - "time windows of 0.3 seconds

Figure 6.27 – Dependence of skewness on stack load

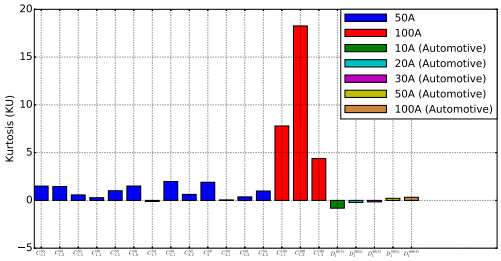

(a) low frequency range - "original"

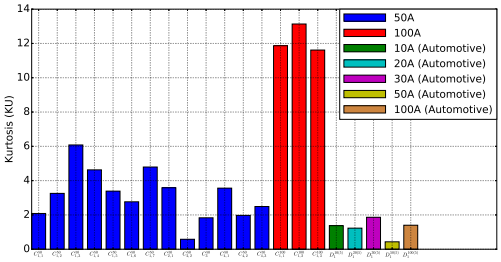

(b) intermediate frequency range - "time windows of 32, 8 and 2 seconds"

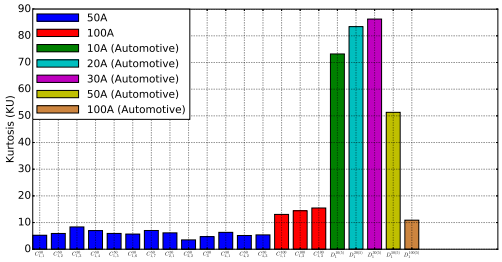

(c) high frequency range - "time windows of 0.3 seconds

Figure 6.28 – Dependence of kurtosis on stack load

Fig. 6.29, Fig. 6.30 and Fig. 6.31 present for automotive profile the dependence of STD, Sk and KU on stack load I_{max} for different frequency domains. For comparison we add on these figures the points corresponding to co-generation profile for 50A and 100A loads.

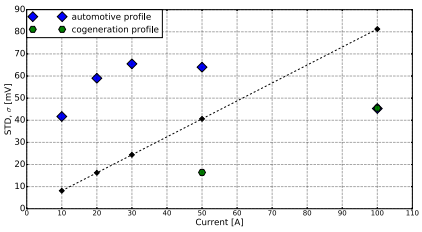

(a) low frequency - "original"

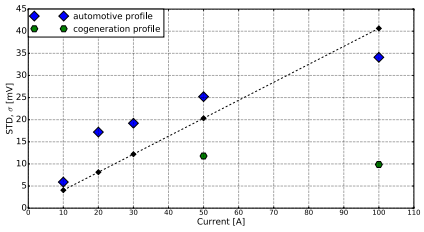

(b) Intermediate frequency - "time windows of 32, 8 and 2 seconds"

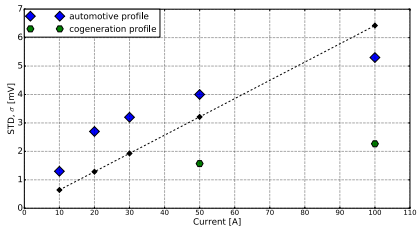

(c) high frequency - "time windows of 0.3 seconds

Figure 6.29 – Dependence of STD(σ) on stack load

We note that for low frequency range there is some divergence of obtained experimental results from Hooge equation. One of the possible interpretation deals with existence of important low frequency perturbation under automotive mode due to f_{SW} frequency, see Fig. 6.19, Fig. 6.20, Fig. 6.21, Fig. 6.22 and Fig. 6.23. The relative contribution of these perturbations is more important for small loads, whuch seem to be affected by this phenomenon.

Fig. 6.30 and Fig. 6.31 show the dependence of Sk and KU from stack load. We note very important increasing of KU value for high-frequency range for all the loads.

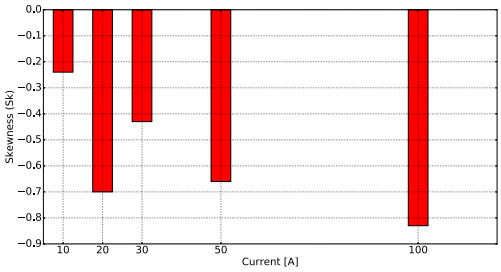

(a) low frequency - "original"

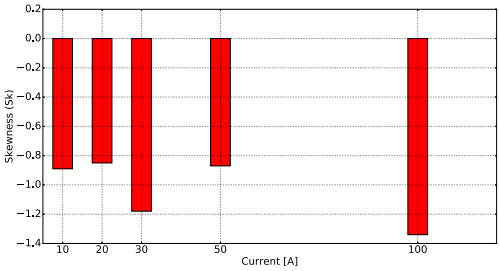

(b) Intermediate frequency - "time windows of 32, 8 and 2 seconds"

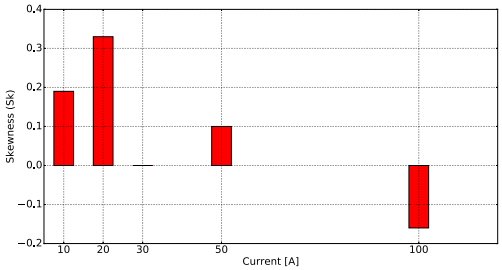

(c) high frequency - "time windows of 0.3 seconds

Figure 6.30 – Dependence of Sk on stack load

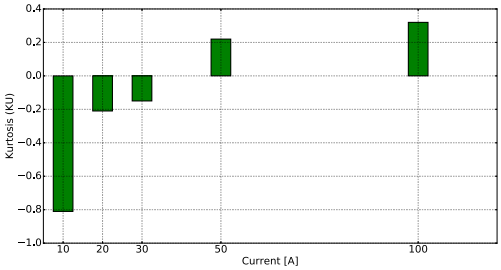

(a) low frequency - "original"

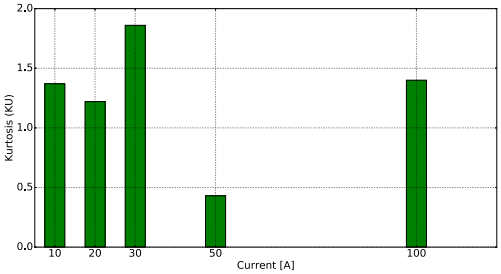

(b) Intermediate frequency - "time windows of 32, 8 and 2 seconds"

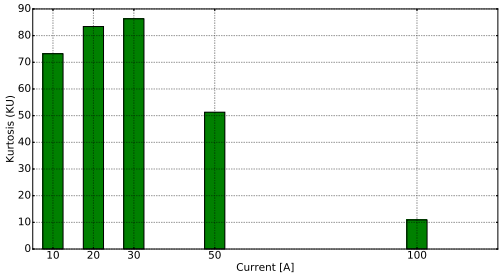

(c) high frequency - "time windows of 0.3 seconds

Figure 6.31 – Dependence of KU on stack load

6.6 On the possibility of using noise descriptors for aging studies and detection non-perfection of stack fabrication

Two interesting applications of noise diagnostic are related with aging studies and detection of possible defects during stack fabrication. In this paragraph we will discuss possible ways and difficulties related with these applications.

Concerning aging studies the natural way is selection of some noise descriptors in time, frequency or time-frequency domains and monitoring the time evolution of these descriptors. Usually the noise intensity is supposed to be responsible for characterization of system aging. Another idea deals with monitoring of noise structure which is characterized by high-order moments (Sk, KU). Also, is is possible to use monitoring of dominant frequencies. Generation of noise descriptors in time-frequency domain (STFT and especially TFAR) is a promising way.

The main difficulty deals with selectivity of using descriptor (or a set of descriptors). Indeed, it was shown above that a lot of parameters influence simultaneously on noise signature. Moreover, it is necessary to take into account computational costs which are determined by data recording frequency and duration of time interval using for generation of noise descriptors. At last, the influence of the trend related with system aging on generation of noise descriptors should be taken into consideration.

In our opinion, direct recording of fluctuation signals and numerical filtering is more promising than the use of analog filters. Indeed, aging experiments are very long, expensive and put the problem concerning reproducibility of results. It is difficult to choose apriori the parameters of analogous filter regarding the goals of aging experiment. From the other hand, direct recording of the signal with data storage allows to provide different filter and detrending procedures with the same physical signal. In this manuscript we do not discuss the results related with aging studies. Nevertheless, recorded data base and developed procedures for generation of noise descriptors can be used for this goal in future studies.

Concerning detection of possible defects during stack fabrication the following points can be noted. The natural way is the comparison of the noise signature of studied stack with the noise signature of a reference stack. For this aim, noise signature recorded under OCV or under well controlled operational conditions can be used. Sure, recording noise signature under OCV mode is more simple. Unfortunately, the obtained in the frame of the present study OCV noise signatures for different stacks (different campaign of measurements) are not enough reproducible. Indeed, no special affection have been taken for noise measurements under OCV mode. Providing OCV measurements in well controlled condition makes possible to obtain reproductible noise signatures[104].

In order to demonstrate the feasibility of noise diagnostic for comparison of different stacks we use here experiments provided under the same constant load in different campaigns, see Fig. 6.32.

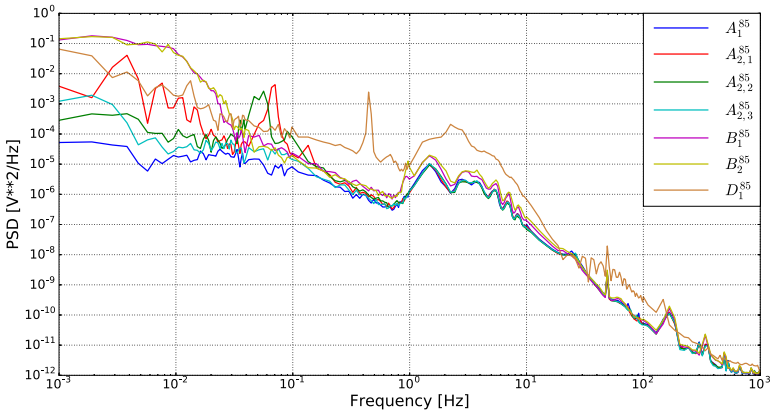

Figure 6.32 – Noise signature of three different stack at 85A load

Fig. 6.32 presents comparison of noise signatures for three different stacks in the same conditions (85A load). As we have discussed previously, low-frequency flicker-noise component ($f < 0.5Hz$) are sensitive to operational conditions. From the other hand, at the frequency range $f > 0.5Hz$ operational conditions do not influence noise signature. In this frequency range, the noise signature seems to be related mainly with internal physico-chemical processes within the stack. For two stacks (first and second campaigns) the noise signatures at high-frequency range coincide perfectly, the reproducibility is confirmed by 6 realizations. It is a good indicator, that these two stacks have no visible difference related with their fabrication. Contrary, the third stack (D_1^{85} realization) shows clear difference of noise signature at high frequency range. Moreover, intensity of noise for this stack in high frequency range is more important. In our opinion, this is an indicator of some defects related with stack fabrication.

General conclusions and perspectives

In the present study electrochemical noise diagnostic (END) has been used for characterization of 600 W PEM stacks. The advantage of noise diagnostic is related with a possibility to provide fine characterization of studied system in large frequency range without perturbation of its running. It is a relatively new experimental method which can complete or replace, when necessary, traditional instrumentation like electrochemical impedance spectroscopy.

Some papers concerning application of END for characterization of single PEM fuel cells can be found in the literature, nevertheless information concerning noise diagnostic of fuel cell stacks is missing. Another originality of the present study concerns utilization of END for stack monitoring during long time. These long-time measurements became possible thanks ANR French project « PROPICE » which has been oriented on the development of methods and instrumentation for fuel cell prognostic.

The first objective of this work was the development of suitable instrumentation allowing permanent registration with high sample frequency small voltage fluctuations (electrochemical noise) and simultaneous data storage. This instrumentation has been developed and successfully used during forth experimental campaigns provided in the site of FC LAB laboratory (Belfort) in the frame of «PROPICE» project. The developed instrumentation is based on National Instruments DAQ; for data storage a laptop is used and Labview © and Python © are used as software. Our measuring system allows simultaneous registration and data storage of 4 signals with sample frequency up to 50 KHz. In the frame of provided experiments we have used one channel and 2 KHz data recording for 1000 h permanent stack running.

Important point deals with instrumentation for noise measurements concerns filtering procedure. Usually analog filters are used for this purpose. We prefer to record signal directly without any analog filtering. It is a principal choice allowing to create a huge data base during a long physical experiment and after to use different methods of data treatment for obtaining the necessary information. In other words, we replace analog filter by numerical ones. In this way it is possible to control perturbations related with filtering procedure to take into account the special feature of recorded signals. The second objective was the development of methodology allowing the generation of different statistical descriptors for recorded stochastic signals. We put an attention for the signal detrending and signal filtering. The noise signature of the stack has been obtained in a large frequency range $0.001Hz < f < 1KHz$. Statistical descriptors have been obtained in time (moments), frequency (PSD) and time-frequency domains (STFT, TFAR, wavelets). Cross-interpretation of noise signature in different domains makes possible to improve understanding of different phenomena related with stack operation.

Developed instrumentation and procedures for the generation of statistical descriptors have been used to study the stack behaviour during forth experimental campaigns of long duration up to 1000 h. Three experimental campaigns concern stack running under the constant load (cogeneration profile) and the last one deals with automotive profile (load cycling between two levels).

We have shown that for all experimental campaigns it is possible to obtain stable and reproducible noise signature. This noise signature includes low-frequency ($f < 0.1Hz$) and high-frequency ($f > 10Hz$) flicker-noise components and intermediate frequency range ($0.1 < f < 10Hz$) where a stable dominant frequency f_p is clearly presented. The slopes of flicker-noise components, the values of dominant frequency, the moments (intensity, skewness, kurtosis) for different frequency ranges as well as space-time noise pictures (STFT, TFAR, wavelets) have been calculated for all operational conditions. We have demonstrated that low-frequency flicker-noise component is rather sensitive to operational conditions (transient processes after stack stoppage, low-frequency perturbations due to the problems with pressure regulation or load cycling). From the other hand, dominant frequency f_p and high-frequency flicker-noise component are not influenced by low frequency perturbations and reflect inner processes in fuel cell stack. The noise intensity under automotive profile in high frequency range is more important in comparison to cogeneration profile. We note also some difference in dominant frequency values : $f_p = 1.75Hz$ for cogeneration profile and $f_p = 1.9Hz$ for automotive profile.

It was shown that high-frequency flicker noise component under cogeneration profile is stable with respect to low frequency perturbations and is determined by stack load. The dependence of noise descriptors on stack load has been obtained. It was shown, that Hooge empirical relation describes rather well the noise intensity of the stack. In other words, we have shown that noise energy is proportional to the square of current load.

The noise signature under OCV mode is very different from the one recorded for cogeneration and automotive profiles. Qualitative character of OCV noise is the same : low-frequency ($f < 0.1Hz$) and high-frequency ($f > 10Hz$) flicker-noise components and intermediate frequency range with a dominant frequency f_p. Nevertheless, the noise intensity under OCV mode is much smaller and the character of the noise is very different from the one recorded for the running stack. This conclusion is supported by calculations of the moments (intensity, skewness, kurtosis) for different frequency ranges.

Thus, for the first time stable and well reproducible noise signature of PEM stack have been obtained and interpreted for cogeneration and automotive mode of running and for OCV conditions. Obtained noise signatures can be used to study the stack aging, detection of possible defects and to understand the physical processes in this electrochemical system. We have obtained preliminary results which demonstrate feasibility of noise diagnostics for detection of possible defects related with stack fabrication. Indeed, comparison of noise signatures of three different stacks running under the same constant load shown that two stacks demonstrate the same very stable and reproducible noise signature in high-frequency range. The signature of the third stack in the same operational conditions is different and noisier. It seems to be an indicator of possible defects related with stack fabrication.

The short term perspectives of the present study deal with :

- possibility to use the created data base for more detailed analysis ; in particular for study of stack aging under automotive profile and stack behavior during non-conventional modes of operation,
- developed instrumentation and methodology can be directly applied for recording of noise signatures of different electrochemical systems (fuel cells, electrolyzers, super-capacitances, batteries),
- noise signature can be detected simultaneously by four channels, thus it is possible to provide noise monitoring of different cells within the stack or/and different sensors (voltage/temperature ; voltage/temperature/pressure ; ...).

The long term perspectives deals with :

- application of noise diagnostic for aging studies,
- application of noise diagnostic for detection of possible defects during stack manufacturing,

- application of noise diagnostic for understanding of physico-chemical processes in electrochemical sources of energy.

Appendix A

Communications Personnelles

A.1 Articles

S. Martemianov, N. Adiutantov, Yu. K. Evdokimov, L. Madier, F. Maillard and A. Thomas, "New methodology of electrochemical noise analysis and applications for commercial Li-ion batteries". *Journal of Solid State Electrochemistry* 19 (**9**) :2803 - 2810, 2015.

E. Denisov, Yu. K. Evdokimov, R.R. Nigmatullin, S. Martemianov, A. Thomas, and N. Adiutantov, "Spectral method for PEMFC operation mode monitoring based on current (voltage) fluctuation analysis". *Scientia Iranica* 24 (**3**) :1437 - 1447, 2017.

R.R. Nigmatullin, S. Martemianov, Yu. K. Evdokimov, E. Denisov, A. Thomas, and N. Adiutantov, "New approach for PEMFC diagnostics based on quantitative description of quasi-periodic oscillations". *International Journal of Hydrogen Energy* 41 :12582 - 12590, 2016.

E. Denisov, Yu. K. Evdokimov, S. Martemianov, A. Thomas, and N. Adiutantov, "Electrochemical Noise as a Diagnostic Tool for PEMFC". *Fuel Cells* 17 (**2**) :225 - 237, 2017.

A.2 Conférences

E.S. Denisov, N.A. Adiutantov and A.Sh. Salakhova «Test bench with remote access for Proton Exchange Membrane Fuel Cell investigation». Nigmatullin's reading - 2013, Kazan, Russia, 2013, (Proceedings pp. 185-187, in Russian)

E.S. Denisov, N.A. Adiutantov and A.Sh. Salakhova «Automated system for estimation of parameters of electrochemical power sources equivalent circuit base on their transient responses». Engineering and scientific applications based on technology NI NIDAYS-2014 (NIDAYS-2014), Moscow, Russia, 2014, (Proceedings pp. 282-284, in Russian)

N. Adiutantov et *al.*, «Diagnostic des PEMFC par la mesure de bruit électrochimique». Conférence du GDR HySPàC "Hydrogène, Systèmes et Piles à Combustibles", Poitiers 2014, (Proceedings p. 51; oral presentation)

F. Maillard and N. Adiutantov et *al.*, «Diagnostic des systèmes électrochimiques par la mesure de bruit interne». Conférence du GDR HySPàC "Hydrogène, Systèmes et Piles à Combustibles", Poitiers 2014, (Proceedings p. 91; poster presentation by F. Maillard)

N. Adiutantov et *al.*, «Electrochemical noise as diagnostic tool for Proton Exchange Membrane (PEMFC)».International conference on Fundamentals and Development Fuel Cell (FDFC-2015), Toulouse, France 2015, (Proceedings electronic version)

N. Adiutantov et *al.*, «Spectral method for PEMFC operation mode monitoring based on current (voltage) fluctuation analysis». Conférence du GDR HySPàC "Hydrogène, Systèmes et Piles à Combustibles", Corse, France 2015, (Proceedings p. 56)

E. Denisov, N. Adiutantov et *al.*, «Diagnostics and prognostics of the hydrogen fuel cell». VIII international scientific and technical conference "Problems and prospects of development of aviation, surface transport and power engineering" (ANTE-2015), Kazan, Russia, October 19-21 2015 (Proceedings pp. 599-602).

N. Adiutantov et *al.*, «Fuel cell aging prediction based on Proni spectrum». VIII international scientific and technical conference "Problems and prospects of development of aviation, surface transport and power engineering" (ANTE-2015), Kazan, Russia, October 19-21 2015 (Proceedings pp. 603-606).

E. Denisov, N. Adiutantov et *al.*, «Spectral method for PEMFC operation mode monitoring based on current (voltage) fluctuation analysis». 3rd European Conference on Renewable Energy Systems (ECRES-2015), Antalya, Turkey, October 7-10 2015 (Proceedings electronic version).

E. Denisov, N. Adiutantov et *al.*, «New approach for PEMFC diagnostics based on quantitative description of quasi-periodic oscillations». 3rd European Conference on Renewable Energy Systems (ECRES-2015), Antalya, Turkey, October 7-10 2015 (Proceedings electronic version).

F. Maillard and N. Adiutantov et *al.*, «Measurements and Signal Processing of Li-ion Electrochemical Noise», 10th International Frumkin Symposium on Electrochemistry, Moscow, Russia, October 20-23 2015 (Proceedings p. 65).

F. Maillard, S. Martemianov and N. Adiutantov et *al.*, «Electrochemical Noise as Diagnostic Tool for Li-ion Batteries», 10th International Frumkin Symposium on Electrochemistry, Moscow, Russia, October 20-23 2015 (Proceedings p. 65).

S. Martemianov, F. Maillard, N. Adiutantov et *al.*, «Electrochemical Noise of commercial Li-ion batteries : methodology and possible applications». 10th International Frumkin Symposium on Electrochemistry, Moscow, Russia, October 20-23 2015, (Proceedings p. 22)

E. Denisov, N. Adiutantov et *al.*, «Quasi-distributed resistive sensor for steady-state field measurements». XII International Siberian Conference on Control and Communications (SIBCON-2016), Moscow, May 12-14 2016 (Proceedings pp. 1-5).

Appendix B

Prony

Figures

Results of applying Prony spectrum for generation statistical descriptors will bre presented in this section. The treatment procedure has been described in our article[101]. Signals with duration of 100 hours from 2nd campaign has been choosen for analyzing (B_1^{170} and B_2^{170}). The whole measured signal has been split into 10 successive equal parts to estimate its evolution in time. In each part the quasi-periodic processes has been identified. To describe quasi-periodic process 100 iterations for each part has been processed. This quantity is selected to obtain statistically-valid evaluations. The exemplary iterations and their medium value for the first part of the experimental data are presented in Fig. B.1. We can see that the quasi-periodic process has complex structure with not constant period and amplitudes.

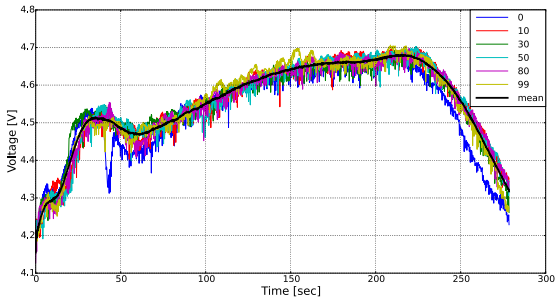

Figure B.1 – Exemplary iterations of quasi-periodic process and corresponding mean curve

As the result of the fitting procedure for the given set of iterations the number of modes K

and the decomposition coefficients Ac_k and As_k have been found. The corresponding results are demonstrated in Fig. B.2a. As we can see in order to provide a very accurate fit (RelErr (%) = 0.01%) only K = 20 modes are necessary. The value of the constant A(k=0) = -0.069. Results of the fitting is presented in Fig. B.2b.

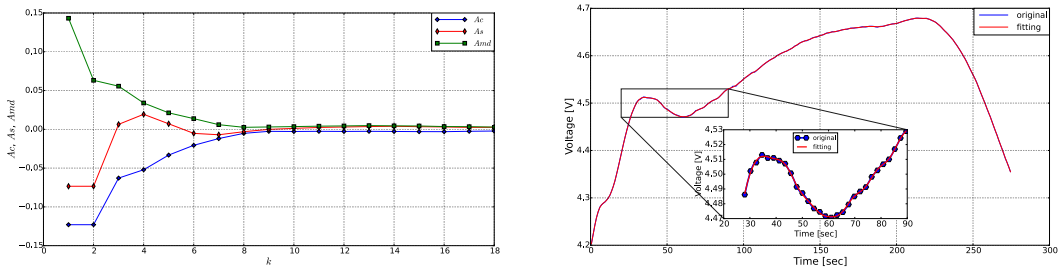

(a) [Dependence of the Prony decomposition coeffi-(b) Results of quasi-periodic processes fitting. As one cients Ac_k and As_k with respect to numbers of modes can see from this figure the relative value of the fitting m. The parameter k lies in the interval $1 < k < K/2$. error is very small and does not exceed the value 0.1%.

Figure B.2 – PSD of the first 10 hours with approximations (left side) and evolution of the parameters of a flicker noise component over time (right side)

At the same procedure, treatment procedure has been applied for $D^{100(5)_1}$. This signal contain a lot of signals under 100A with duration of 50 seconds, so we can select all of them during 1 hours. Signal of QP is presented in Fig. B.3.

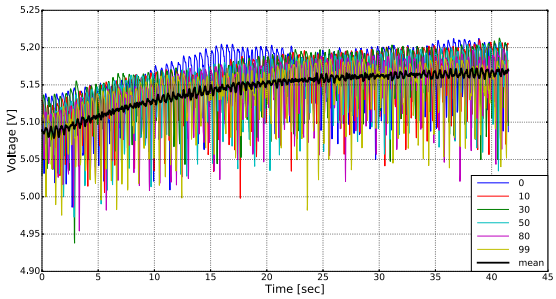

Figure B.3 – Exemplary iterations of quasi-periodic process and corresponding mean curve

Results of the fitting and corresponding spectrum are presented in Fig. B.4

As the result of the fitting procedure for the given set of iterations the number of modes K and the decomposition coefficients Ac_k and As_k have been found. The corresponding results are demonstrated in Fig. B.4b. As we can see in order to provide a very accurate fit (RelErr (%) = 0.01%) only K = 20 modes are necessary. The value of the constant A(k=0) = -0.069. Results of the fitting is presented in Fig. B.4a.

Usage decomposition coefficients Ac_k and As_k as descriptors allows us to make diagnosis or prognosis. More detailed information is presented in article [101].

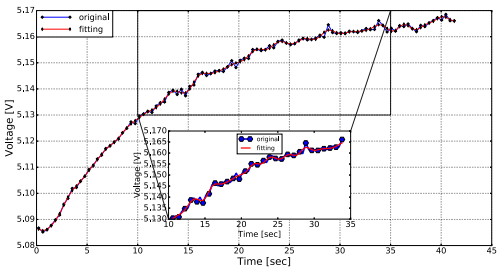

(a) Fitting of quasi-periodic processes

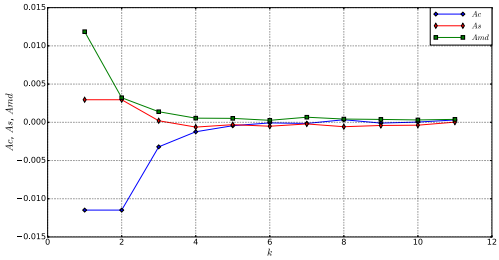

(b) Dependence of the Prony decomposition coefficients Ac_k and As_k with respect to numbers of modes m

Figure B.4 – Signal with approximations (left side) and Prony's spectrum (right side)

INTERNATIONAL JOURNAL OF HYDROGEN ENERGY 41 (2016) 12582–12590

Available online at www.sciencedirect.com

ScienceDirect

journal homepage: www.elsevier.com/locate/he

New approach for PEMFC diagnostics based on quantitative description of quasi-periodic oscillations

R.R. Nigmatullin [a], S. Martemianov [b], Yu.K. Evdokimov [a], E. Denisov [a,*], A. Thomas [b], N. Adiutantov [a,b]

[a] Kazan National Research Technical University named after A.N.Tupolev – KAI, 10, K.Marx Str., 420111, Kazan, Russian Federation

[b] Institut Pprime, UPR 3346 CNRS, Université de Poitiers, ENSMA, Batiment B25: 2, rue Pierre Brousse, TSA 41105, 86073 POITIERS Cedex 9, France

ARTICLE INFO

Article history:
Received 29 November 2015
Received in revised form
21 March 2016
Accepted 2 June 2016
Available online 27 June 2016

Keywords:
Fuel cell
Technical diagnostics
Quasi-periodic process
Prony's spectrum

ABSTRACT

One of the main disadvantages of the modern fuel cells (FC) is their relatively short non-failure operating time, and prediction of its technical condition is one of the most promising ways to solve this problem. Therefore, the development of effective methods applied to fuel cell diagnostics becomes extremely important. In this paper new approach for FC diagnostics based on the Prony's spectral analysis of the quasi-periodic (QP) processes is proposed. The results of FC voltage (current) signals analysis are presented. It is shown that the proposed approach is able to evaluate the FC technical state. The proposed method allows to increase the accuracy of the fluctuating processes description and can be considered as a reliable diagnostic tool for PEMFC.

© 2016 Hydrogen Energy Publications LLC. Published by Elsevier Ltd. All rights reserved.

Introduction

Fuel Cell (FC) technology obtains high potential to become one of main bases for power sources because of many reasons such as environmentally friendly behavior, high efficiency, and silent operation due to absence of moving parts. One of the most perspective systems in this area is the Proton Exchange Membrane Fuel Cells (PEMFC). This type of fuel cell operates at a relatively low temperature range 50–80 °C, has a high power density and a fast output power response on changing energy needs. PEMFCs have very high efficiency up to 0.83 [1] which can be additionally increased by using cogenerated waste heat to produce energy [2]. They are eminently suitable for stationary (power stations) and mobile (cars, aircrafts, telecommunications) applications. In spite of these advantages, they have significant drawbacks [3,4], such as high cost, catalyst degradation, complex water

Abbreviations: ADC, Analog-to-Digital Converter; EFP, Electric Fluctuation Phenomenon; FC, Fuel Cell; GPS, Generalized Prony's Spectrum; MEA, Membrane-Electrode Assembly; PEMFC, Proton Exchange Membrane Fuel Cell; QP, Quasi-Periodic; QPP, Quasi-Periodic Process; SRA, Sequence of the Ranged Amplitudes.

* *Corresponding author.*
E-mail address: genia-denisov@yandex.ru (E. Denisov).

http://dx.doi.org/10.1016/j.ijhydene.2016.06.011
0360-3199/© 2016 Hydrogen Energy Publications LLC. Published by Elsevier Ltd. All rights reserved.

management, insufficient reliability and durability. Consequently, many studies have been done in construction optimization [5], catalyst modification [6], understanding of water and thermal management [1,7]. Nevertheless all the previous drawbacks are not still eliminated, which impede the wide utilization of PEMFC.

The problems of FC reliability and durability can be solved by introducing dedicated diagnostics systems, which are able to estimate technical state and predict failures at the initial stages. Moreover, with an accurate control, a prognostic of the system can be done and allows neutralizing the effects of failures to keep high operational characteristics. Extended and detailed reviews of diagnostics, prognostics and health management methods used for PEMFC can be found in Refs. [3,4]. There are several common ways to develop the diagnostics techniques namely electrochemical impedance spectroscopy, current interruption method, and polarization curve analysis. The main disadvantage of these methods is the presence of FC operation mode interruption/perturbation during measuring procedures. However, there is also another diagnostics method using the diagnostic capabilities of FC electrical fluctuations [10–12] which can be done during FC operating and do not require any external influences. The main advantages of such approach are non-intrusiveness, rapidity (allows real time measurements) and high informativity [10].

It has been mentioned that fluctuation phenomena is common for fuel cells; this fact is confirmed by a large quantity of corresponding works [10–20]. Analysis of the results presented in the works reveals a lot of factors affecting on FC electrical fluctuation parameters: generated current [10,12,13,15–17], current distribution over membrane surface [15], membrane-electrode assembly (MEA) water balance [10,12,14,15], gas flow rate [12,16], stoichiometry [14,15] and pressure [10,19]. Moreover, fluctuations in electrochemical systems introduced by turbulent fluctuations of electrolyte (turbulent noise) have been studied intensively from the theoretical and the experimental points of view in Refs. [8,9].

It allows to conclude that fluctuation phenomena inside fuel cell is a general effect having strong dependence on PEMFC operation parameters and obviously on physical and chemical processes within the system. Therefore, the electric fluctuation phenomenon (EFP) can be potentially considered as a reliable and significant tool for PEMFC diagnostics.

The EFP within PEMFC can be classified on two significant classes: noise-like fluctuations and quasi-periodic (QP) oscillations. Both of these classes have a strong diagnostic features, in particular noise-like fluctuations [10–12] and QP oscillations [13–20]. It should be mentioned that the relative values of the QP oscillations with respect to the mean value of the generated voltage usually exceed 0.1%, while the noise-like fluctuations are less than 0.1%. By the other words, QP fluctuations measurement requires more simple equipment that reduces price and increase availability of the corresponding diagnostic systems. It should be noted that QP oscillations are not always observed within the total electrical signal of PEMFC, however, the oscillations exhibit a typical behavior for PEMFC operated under high currents [13,16] and usually correspond to high power output. Oscillation mode of PEMFC running under high currents is the typical regime; analyzing of QP oscillations can give very interesting possibilities for degradation process diagnostics.

This approach does not imply any perturbation of the operation mode and does not need any expensive measurement equipment. From the other hand a complex nature of the QP-oscillations requiring specific data treatment.

Lots of methods have been used for noise analysis in particular Fourier, wavelet, polynomial, and other types of signal-noise processing methods [21,22]. Nevertheless the question of QP processing interpretation is still open. Indeed, the Fourier analysis give a number of pseudo-harmonic components, while for wavelet approach there is no justification for selection of a proper wavelet.

In this article a new method based on the Prony transformation is proposed for analyzing of QP processes in PEMFC. The proposed method allows increasing accuracy of fluctuating processes description and can be considered as a reliable diagnostic tool for PEMFC.

Basic advantages of this new approach proposed by Nigmatullin R.R. [24,25] are presented below.

- (i) This approach can be tested on the existence of the QP phenomenon. The set of current measurements should be strongly-correlated with respect to mean measurement. Results of strongly-correlating verification are presented in Fig. 4, where we can see insufficient variance.
- (ii) After this test the applicability of Eq. (4) is justified.
- (iii) The fitting function as the solution of the functional equation (Eq. (6)) can be applied.
- (iv) The non-linear parameters as the exponential factor λ, the true value of the period T and limiting number of mode K are found easily by minimization of the value of the relative error (see Eq. (11)).

Other specific details of this approach are explained below.

Quantitative description of quasi-periodic oscillations

Formulation of the problem

Analysis of the available information sources shows that in the most cases PEMFC life tests are carried out in the galvanostatic mode. Degradation processes in this case lead to decreasing of cell voltage. These processes are usually observed in the presence of voltage oscillations [13–20] especially in cases, when PEMFC is run out with high current. Typical PEMFC oscillating signal is presented in Fig. 1 where the quasi-periodic components of signal are clearly observed. The exemplary signal is voltage variation of 8-cell PEMFC stack running in the galvanostatic mode of 170 A. In many works the voltage oscillations are analyzed and they demonstrate some correlation between parameters of these oscillations and physical and chemical processes that take place within FC. It is obvious that analysis of these phenomena can give a basis, that help to generate effective error status indicators for PEMFC, allowing to monitor its technical state.

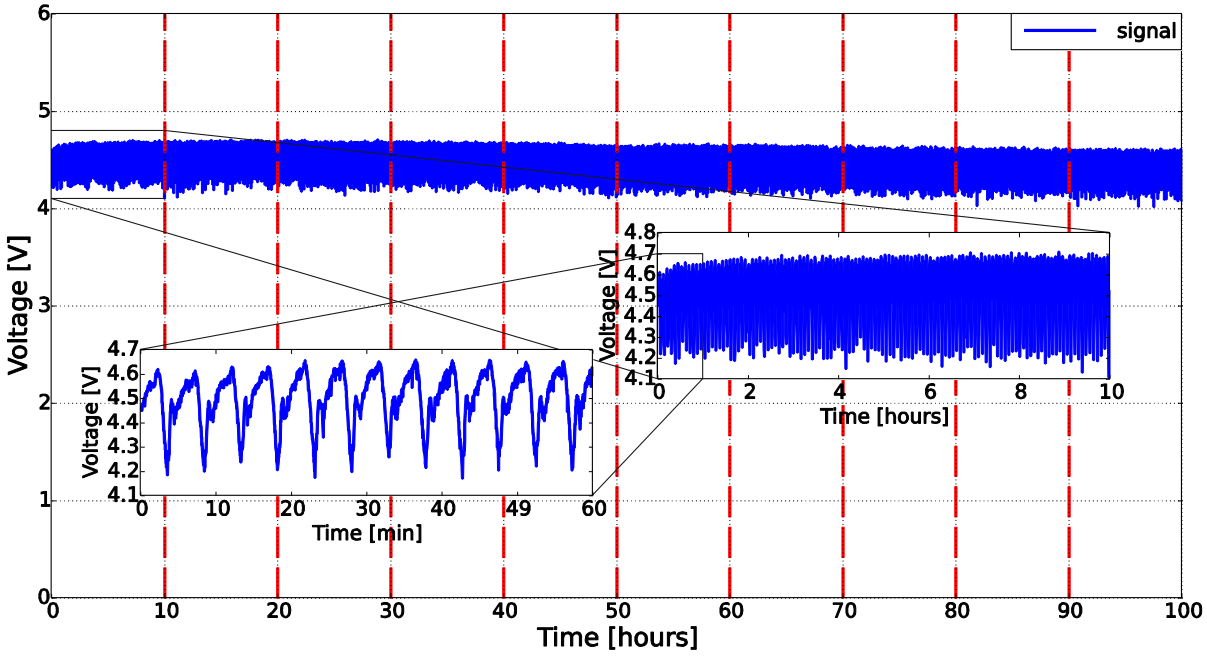

Fig. 1 – Typical voltage signal measured for 8-cell PEMFC stack operated in galvanostatic mode (170 A). Signal comprises clear strong quasi-periodic components.

In this paper we apply new approach based on the recognition of a wide class of quasi-periodic processes (QPP). Nigmatullin et al. [23,24] proved that a set of successive measurements has a memory and mathematically this tested hypothesis can be expressed as

$$F(x+LT)=\sum_{l=0}^{L-1} a_l F(x+lT)+b \tag{1}$$

Here x is experimentally controlled (input) variable that can coincide with time, frequency, wavelength and etc. T is a parameter that determines a period of the experiment with respect to the variable x, the set of the constants $\{a_l, b\}$ $(l = 0, 1, \ldots, L-1\}$ determines the length of the memory. It implies that part of the measurements is independent from each other, while others become dependent. The unknown constants $\{a_l, b\}$ can be found with the help of the linear least square method (LLSM). In the papers mentioned above we show the solutions of the functional equation (Eq. (1)) and described the algorithm that allows to reduce a wide set of measurements to the case of the short memory ($L = 2$). The existence of the QPP was confirmed on available set of data [23–25] and we expect that this phenomenon has a general character. We should stress here the following important fact. If all a_l coincides with the unit value and $b = 0$ then Eq. (1) is reduced to the situation of an "ideal" experiment (Eq. (2)) when all measurements become identical to each other. The solution in this case is trivial and can be presented in the form of the segment of the Fourier-series. For the shortest case $L = 1$ ($a \neq 1$, $b \neq 0$) the solution is expressed in the form of the segment of the series corresponding to the Prony decomposition containing minimal number of the fitting parameters. So, Eqs. (1) and (2) have different physical interpretation and this important fact should be taken into account in interpretation of the measured data. This new finding allows to suggest an intermediate model, when the strongly-correlated measurements corresponding to the tested hypothesis (Eq. (1)) can receive the unified fitting function expressed in the form of the finite segment of the Prony decomposition.

Elaboration of this approach is embarrassed by insufficient experimental database and difficulties of model describing of the oscillations, particularly when they have a quasi-periodic nature. To overcome these barriers, in frame of this work, an experimental investigation of PEMFC life tests has been carried out and new approach for oscillation description on the basis of QP processes analysis by the Prony's spectrum is proposed.

Treatment procedure

Basing on the general approach explained above and on the fact that Nigmatullin et al. [24] showed that the Generalized Prony's Spectrum (GPS) can be applied for description of quasi-periodic processes, it is proposed to use GPS [23] for describing fluctuating (oscillating) signals of PEMFC. The conventional Fourier's analysis cannot be directly applied for such kind of signals because it applicable only in the cases of "ideal" experiment, when the influence of the apparatus function is negligible. That is why the application of the Fourier transform in our case is questionable.

It is known that pure-periodic process with period T satisfies the following functional equation:

$$\mathrm{Pr}(t\pm T)=\mathrm{Pr}(t). \tag{2}$$

The general solution of this functional equation for a discrete set of data can be expressed in the form of the Fourier's series [24]. However, Nigmatullin R.R. et al. [23] showed

based on a large amount of available data that real measurements are described more accurately by the generalized functional equation (Eq. (3)):

$$F(t\pm T) = a(t)F(t) + b(t). \tag{3}$$

It means that the temporal evolution of some process taking place on the interval $t > T$ is based on events that took place in the nearest past ($t < T$). Eq. (3) for the strongly-correlated QP processes can be simplified and presented as

$$F(t\pm T) = aF(t) + b, \tag{4}$$

where a and b are real constants.

The solution of functional equation (Eq. (4)) can be found as follows [23,24]:

$$\begin{aligned} &a\neq 1 : F(t) = \exp(\lambda t)\Pr(t) + c_0, \lambda = \ln(a)/T, c_0 = b/(1-a);\\ &a\neq 1 : F(t) = \Pr(t) + bt/T. \end{aligned} \tag{5}$$

It can be shown that solution (Eq. (5)) corresponds to the Prony's series that includes exponential factors making the total process not pure periodical. As it directly follows from (Eq. (5)) the real QP measurements could be fitted by the following function

$$\begin{aligned} y(x) \cong F(t) = B + A_0\exp(\lambda x/T_x) + \\ + \sum_{k=1}^{K}[Ac_k\exp(\lambda x/T_x)\cos(2\pi kx/T_x) \\ + As_k\exp(\lambda x/T_x)\sin(2\pi kx/T_x)]. \end{aligned} \tag{6}$$

It includes the unknown set of amplitudes Ac_k and As_k ($k = 1, 2, \ldots, K$) and nonlinear parameters as: number of modes K, exponential factor λ and the period T_x.

Eq. (4) can be interpreted as repetition of a set of successive measurements corresponding to a supposition of stable (conserved) properties of the object under study. However this condition cannot be performed for a real system due to presence of a number of uncontrollable factors. In reality, it should be expected that the parameters depend on the number of a measurement m. In this case it is convenient to evaluate this dependence with respect to its mean measurement <y>.

$$y_m(x) = a_m < y(x) > + b_m, \tag{7}$$

Where

$$\begin{aligned} &< y(x) > = \frac{1}{M}\sum_{m=1}^{M} y_m(x),\ a_m = slope(< y >,\ y_m),\\ &b_m = intercept(< y >,\ y_m), \end{aligned} \tag{8}$$

Here M is total number of measurements. Nigmatullin R.R. et al. [23] showed that in the case of strong correlations of measurements in terms of Eq. (7) the solution (Eq. (5)) remains valid in the frame of a simple approximation.

$$a(t)\to < a > \equiv a,\ b(t)\to < b > \equiv b. \tag{9}$$

The real period T_x is not known (see Eq. (6)) but can be found from the fitting procedure as optimal value of the fitting parameter T_x. According to recommendation of [23] the desired value should be located approximately in the interval [$0.5T_{max}$, 2 T_{max}], where the value of T_{max} is estimate of the period T_x.

Therefore, the truncated Prony's series (Eq. (6)) can be used as a fitting function for description of a measuring signal. Traditionally, the main problem of expansion in Prony's series is extremely high computational cost especially for evaluation of the damping factor λ. This problem has been solved by R.R. Nigmatullin [23,24], where new approach for evaluation of the exponential factor λ directly from raw experimental data has been proposed. For this purpose all measurements clustered into three groups: up, mean, and down measurements according to criteria proposed [23]. Three mean functions calculated for each of the groups allows to estimate the desired range $\lambda \in [\lambda_{up}, \lambda_{dn}]$. The nonlinear parameters number of modes K, exponential factor λ, and period T_x and other parameters are estimated as result of the fitting. This approach significantly reduces calculation costs and increases accuracy of real signal description. The proposed algorithm includes in itself the following steps:

- (S1) Data acquisition;
- (S2) Test for strong correlations:

This test is based on analysis of all available measurements with the help of the plot $y_i \approx a_i <y> + b$. If, in the frame of the given fluctuations, they correspond to a set of straight lines, then this set can be considered as the strongly-correlated. From this simple analysis the desired equations (Eqs. (3)–(5)) describing this phenomenon can be derived.

- (S3) Clusterization of all measurements into 3 groups: down (dn), mean (mn), up;

This procedure is described in detail in paper [23] by R.R. Nigmatullin et al., however it needs probably in some additional explanation. More general expression corresponding to the presence of the memory phenomenon between successive measurements is expressed as [23,24].

$$F(t + LT) = \sum_{s=0}^{L-1} A_s F(t + sT) + B. \tag{10}$$

Here the constant L determines the limiting value between the strongly-correlated measurements. The set of constants A_s ($s = 0, 1, \ldots, L$) and B determines the measure of correlations between measurements. In many cases, this value L is not known. Therefore, in order to reduce this equation to the simplest case (Eq. (4)) the clusterization procedure is suggested. The relative slopes a_m from Eq. (7) after elimination of the unit value (corresponding to the mean measurement) are transformed to the sequence of the ranged amplitudes (SRA), where the measurements with maximal positive slope is placed on the left-hand side, while the measurement with minimal value of the negative slope will occupy the right-hand position. Being integrated this ordered distribution of the slopes form a bell-like curve shown in Fig. 5(i). Any real distribution of the relative slopes after integration will be located inside this bell-like curve. Based on the results of the model calculations for clusterization of all measurements on three independent groups the simple empirical procedure suggested: we simply line which is parallel to OX axis. The cross points with bell-like curve determine the desired number of measurements entering to each cluster – down (dn), mean (mn) and up; This procedure is shown in Fig. 5(i).

- (S4) Mean function calculation for each of three groups;

After realization of the procedure described in S3, it is easy to evaluate mean functions belonging to each cluster group because the number of measurements entering to each group is known.

- (S5) Correlations estimation and evaluation of λ range: λ_{up}, λ_{dn};

The plot of the functions *ydn(x)* and *yup(x)* with respect to *ymn(x)* allows to calculate the desired slopes a_{up}, that coinciding with the desired values λ_{up}, λ_{dn}.

- (S6) Fitting procedure allowing estimate all nonlinear fitting parameters of Prony decomposition based on the minimization of the value of the given relative error.

$$\mathrm{RelErr}(\%) = [stdev(\mathrm{y}(t) - F(t, K, T, \lambda))/mean|\mathrm{y}(t)|] \cdot 100\%. \quad (11)$$

The fitting of three nonlinear parameters (*K*, *T*, λ) are reduced to the minimization of the relative error surface because the desired limits for two param'eters are known.

This approach based on the verified QP phenomenon has the following remarkable properties:

- (i) It can be considered as noninvasive approach; it implies that identification and justification of the QP process in some complex system contains only error controllable transformations. Thanks to this property, this approach has definite advantages in comparison with invasive methods that contain uncontrollable errors. For example, (a) before the classic Fourier transform (that contains the well-known Hibbs oscillation problem), (b) before the wavelet transformations and other well-known methods, which contain uncontrollable errors and correlations. Many other well-known methods are unjustified and contain imposed suppositions.
- (ii) In the frame of the justified Prony's decomposition, all random sequences can be read quantitatively and, if necessary, can be compared with each other in terms of the reduced set of the fitting parameters.
- (iii) The suggested approach is free from unjustified suggestions related to the statistical nature of a noise and allows, based on the original criterion, to select the desired trend and relative fluctuations, which can be read independently from each other.

Results and discussion

Experimental installation

In frame of the present work, 8 cells hydrogen PEMFC (EPICEA v2) with cell surface of 220 cm^2 has been studied in Fuel Cell Laboratory (Belfort, France). All measurements were performed under galvanostatic mode for several different currents within the range 0–170 A for 2500 h continuously. The experimental installation has the following parameters: nominal power – 600 Watts, electrical current – 0–170 A; relative humidity of reactants – 50%; temperature of FC – 75–80 °C, absolute pressure within cell – 1, 5 bar, gas stoichiometry of Anode/Cathode – 1,5/2.

Voltage fluctuation measurement has been performed by the dedicated experimental equipment based on 24-bit Analog-to-Digital Converter (ADC) NI-9239 of National Instruments Inc. The digitized signal of ADC is transferred by means of NI Compact DAQ chassis NI USB-9162 to computer operated under LabVIEW based software control. ADC was operated under sampling frequency of 10 kHz. To minimize influence of measurement equipment ADC was configured with input impedance about 1 MOhm and connected to the output terminal of FC stack as shown in Fig. 2. Intrinsic noise of measurement equipment is about 70 μV.

Signal processing

The treatment procedure described in the part 2.2 has been applied to study QP processes of PEMFC under test for two series of measurements. Each series characterized by the constant operation conditions has 100 h duration and took place at the initial stage of whole 2500 h measurement procedures. For better understanding, we consider in detail treatment procedure for QP processes by the example of one of 100 h series of PEMFC operation with the load current of 170 A. The whole measured signal has been split into ten successive equal parts to estimate its evolution in time. In each part the quasi-periodic processes has been identified. One hundred iterations for each part have been processed to describe quasi-periodic process. This quantity is selected to obtain statistically significant evaluations. The exemplary iterations (with numbers 0, 10, 30, 50, 80, 99) and corresponding mean curve for the first part of the experimental data are presented in Fig. 3. We can see that the quasi-periodic process has complex structure and cannot be described by a constant period and the fixed set of amplitudes.

As it has been mentioned above to perform the proposed approach we should check the presence of strong correlations between measurements in terms of Eq. (7). One can remind here that the test for the strong correlations between two functions f_1 and $f_2 = a \cdot f_1 + b$ plotted with respect to each other is expressed in the form of the straight line segment. The result of the corresponding test is presented in Fig. 4 where the ranged amplitudes of the exemplary iterations of Fig. 3 are plotted with respect to the ranged amplitudes of the mean curves. The analysis of the figure shows that all dependencies

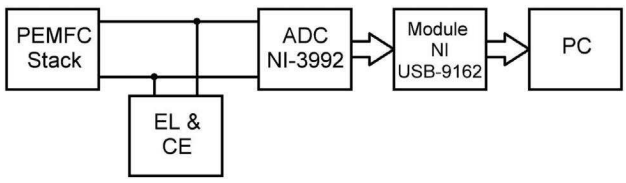

Fig. 2 – Diagram of connection of electrical signal measurement equipment to the PEMFC Stack: EL & CE – Electrical Load and Control Electronics, ADC – Analog-to-Digital Converter, PC – Personal Computer, Module NI USB-9162 – NI Compact DAQ chassis.

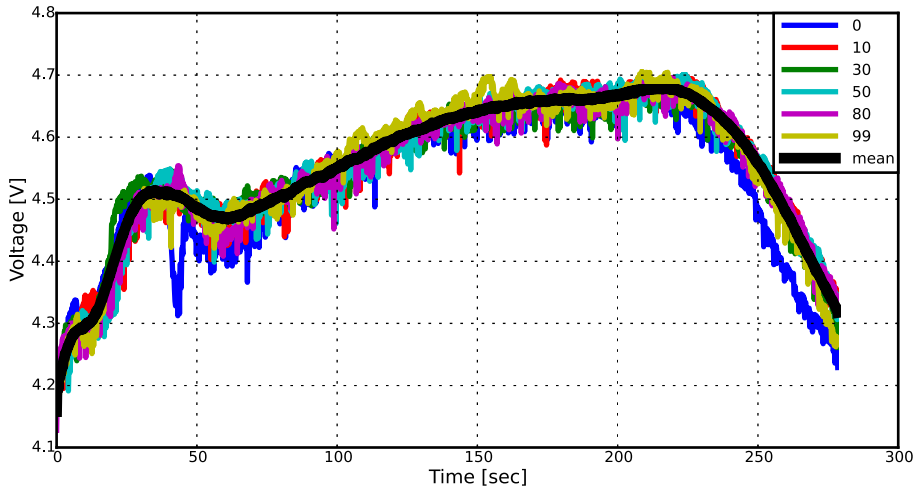

Fig. 3 – Exemplary iterations of quasi-periodic process and corresponding mean curve.

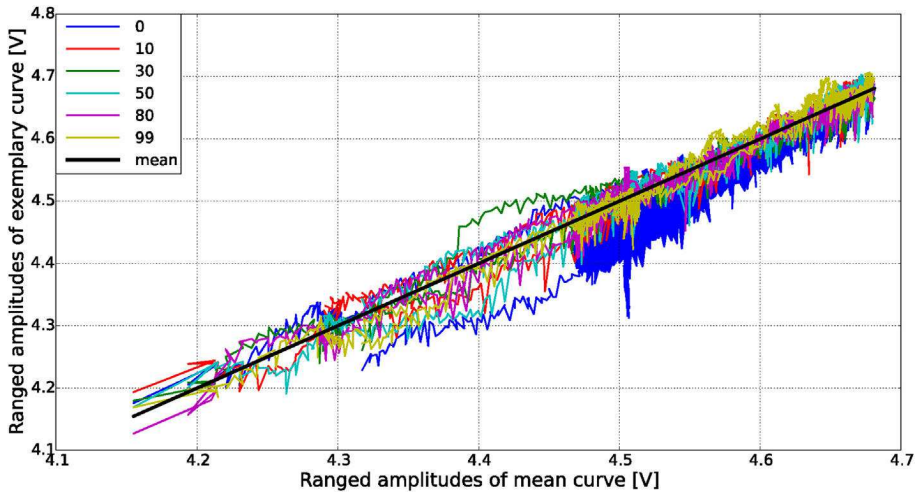

Fig. 4 – Test for strong correlations in terms of Eq. (7).

are close to linear and we have reason to prove the conclusion that the considered series have strong correlations. As we also can see in Fig. 4 the measurements are grouped into three sets in relation to the mean curve: up, mean (mn), and down (dn). The procedure of clusterization is shown more detailed in Fig. 5(i). This procedure is based on the series of the ranged amplitudes technique [25]. Fig. 5(i) presents result of integration of the signal series ranges (see Fig. 3) and its analog sorted in descending order. For the both signals the DC component has been eliminated before integration. In order to find the limits between up – mn clusters and dn – mn clusters, respectively, we draw a line which is parallel to the OX axis in the point corresponding to the maximum value of the integrated curve describing the signal series ranges. The

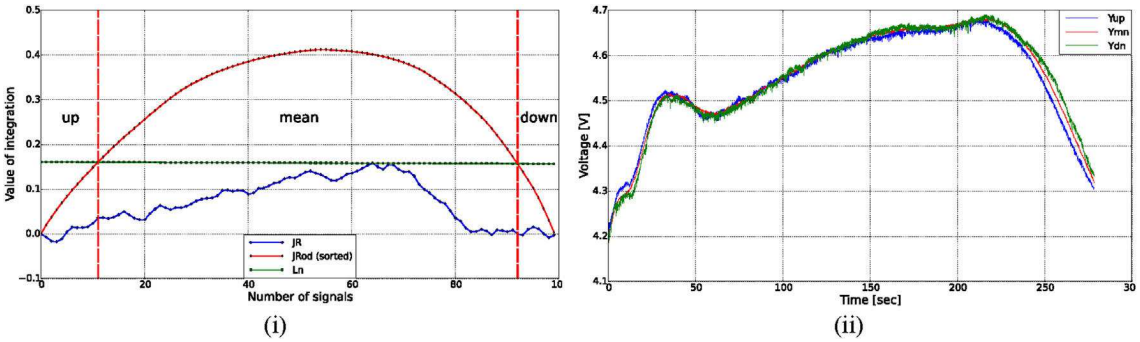

Fig. 5 – Procedure of clusterization (i) and mean functions for each of the groups (ii).

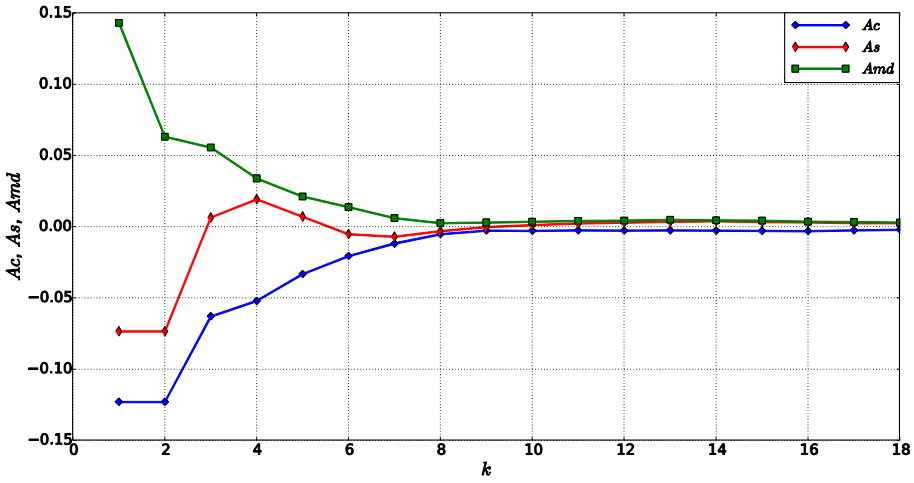

Fig. 6 – Dependence of the Prony decomposition coefficients Ac_k and As_k with respect to numbers of modes m. The parameter k lies in the interval $1 < k < K/2$.

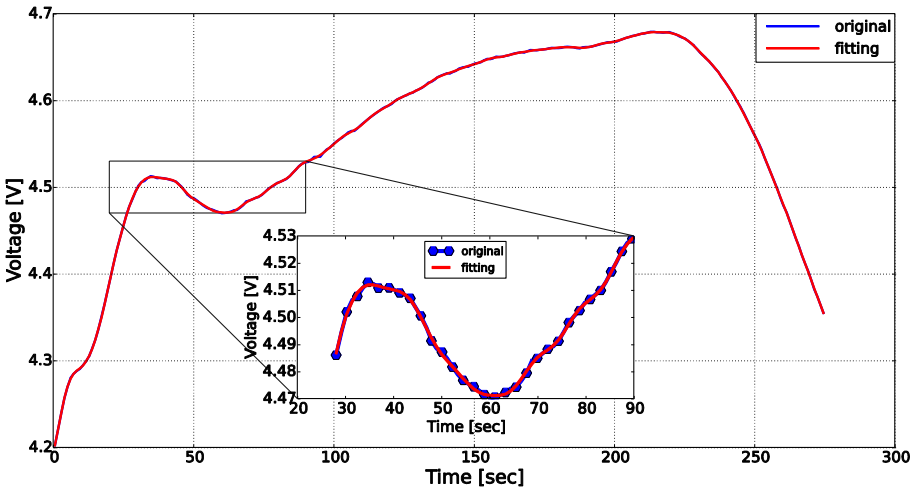

Fig. 7 – Results of quasi-periodic processes fitting. As one can see from this figure the relative value of the fitting error is very small and does not exceed the value 0.1%.

points of intercept separate the desired clusters ("up", "mean" and "down") from each other. Mean functions of the initial signals for each of these groups presented in Fig. 5(ii) are close to each other. This fact proves presence of strong correlation in the considered series and allows to find the range of the exponential factor λ.

All parameters of the Prony decomposition (Eq. (6)) were calculated as result of the fitting procedure for the analyzed set of iterations. Namely, the number of modes K and the decomposition coefficients Ac_k and As_k have been found from Eq. (11). The distributions of the decomposition coefficients Ac_k, As_k together with its modulus are depicted in Fig. 6. The

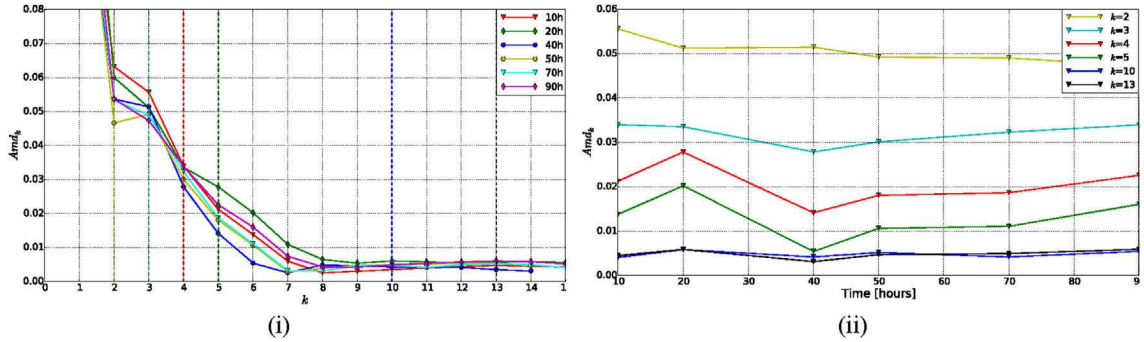

Fig. 8 – Evolution of the modulus decomposition coefficient for all modes (i), and for selected modes (ii).

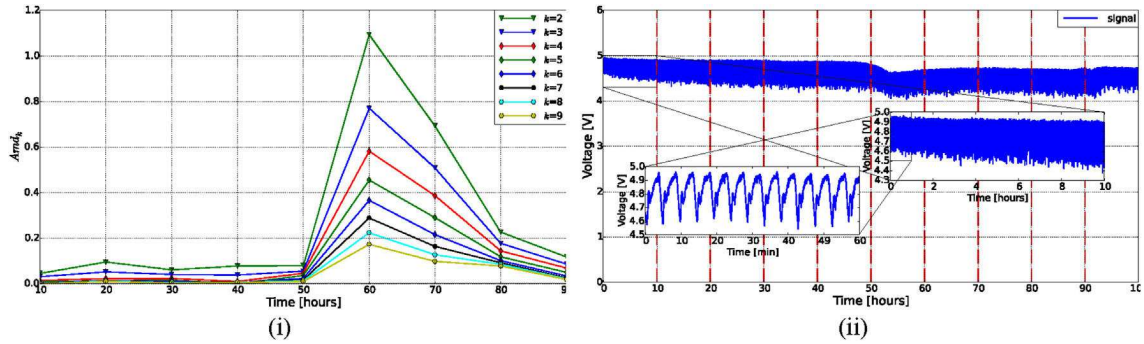

Fig. 9 – Evolution of the decomposition coefficients Amd_k for selected modes in case of fuel cell technical state changing (i), voltage signal corresponding to this time period(ii).

corresponding results are demonstrated in Fig. 6. As we can see in order to provide a very accurate fit (the value of the relative error – RelErr(%) = 0.1) only $K = 36$ modes are necessary. The value of the constant $A(k = 0) = -0.037$. The results of fitting are presented in Fig. 7.

Fig. 8(i) demonstrates the distribution of the modulus coefficients $Amd_k = \sqrt{(Ac_k^2 + (As_k^2))}$ with respect to the mode k, while Fig. 8(ii) shows the time evolution of the same coefficients. In this case fuel cell demonstrates very stable behavior. This fact is in a good agreement with energy characteristics of PEMFC operation not showing any degradation during this test.

Time evolution of the decomposition coefficients Amd_k for another 100-h period is shown in Fig. 9(i). We can see that after 60 h of operation coefficients Amd_k increase in many times and after it gradually decreases. This sharp increasing of coefficients corresponds to the moment of 4 percent loss in power produced by PEMFC (see Fig. 9(ii)). The reduced Prony's spectrum becomes very sensitive to any small changes that take place in a long sequence, while in the long sequence itself these degradations can be unnoticeable. This observation is explained clearly by Fig. 9(i). We cannot explain the physical and chemical reasons of this specific degradation phenomenon but with the help of the reduced Prony spectrum one can detect clearly the small changes "stretched" initially in time (see Fig. 9(ii) for comparison). It allows us to make a conclusion that coefficients Amd_k reflect current technical state of the PEMFC.

Conclusions

The present paper demonstrates that a quasi-periodic (QP) process treatment as a possible tool for PEMFC features diagnostics. One of the main difficulties of this approach deals with complex nature of the signal which requires a suitable data treatment procedure. Therefore, to solve this problem original method of data treatment based on generalized Prony's spectrum analysis has been proposed. This methodology allows to describe the quasi-periodic processes with a high accuracy using minimal number of modes and with reduced computational costs. It was shown that quasi-periodic oscillations (fluctuations of voltage in this case) depend on degradation processes inside PEMFC. These degradations can be efficiently described by using the decomposition coefficients of the generalized Prony spectrum.

In particular, it was shown that the informative parameter expressed as $Amd_k = \sqrt{(Ac_k^2 + (As_k^2))}$, is sensitive to technical monitoring state of PEMFC. The proposed Prony's decomposition method applied to the quasi-periodic voltage fluctuations of a PEMFC stack allows to enhance the accuracy of data treatment in terms of reliability and robustness. This method brings a new highlight on the results interpretation and will allow a possible prediction of the PEMFC failures.

Acknowledgments

This work has been supported by the ANR project PROPICE (ANR-12-PRGE-0001) funded by the French National Research Agency.

REFERENCES

[1] Barbir F. PEM fuel cells – theory and practice. Academic Press; 2012.
[2] Chen M, Andreasen SJ, Rosendahl L, Kær SK, Condra T. System modeling and validation of a thermoelectric fluidic power source: proton exchange membrane fuel cell and thermoelectric generator (PEMFC-TEG). J Electron Mater 2010;39(9):1593–600. http://dx.doi.org/10.1007/s11664-010-1270-9.
[3] Jouin M, Gouriveau R, Hissel D, Pera M-C, Zerhouni N. Prognostics and health management of PEMFC-state of the art and remaining challenges. Int J Hydrogen Energy 2013;38:15307–17. http://dx.doi.org/10.1016/j.ijhydene.2013.09.051.
[4] Petrone R, Zheng Z, Hissel D, Pera M, Pianese C, Sorrentino M, et al. A review on model-based diagnostics methodologies for PEMFCs. Int J Hydrogen Energy 2013;38:7077–91. http://dx.doi.org/10.1016/j.ijhydene.2013.03.106.
[5] Khazaee I, Ghazikhani M, Mohammadiun M. Experimental and thermodynamic investigation of a triangular channel geometry PEM fuel cell at different operating conditions. Sci Iran 2012;19(3):585–93. http://dx.doi.org/10.1016/j.scient.2011.11.039.
[6] Fang S-Y, Teoh LG, Huang R-H, Chao W-K, Lin T-J, Yang K-C, et al. Effect of adding zinc oxide particles to the anode catalyst layer on the performance of a proton exchange

membrane fuel cell. J Electron Mater 2014;43(9):3601–10. http://dx.doi.org/10.1007/s11664-014-3246-7.
[7] Thomas A, Maranzana G, Didierjean S, Dillet J, Lottin O. Measurements of electrode temperatures, heat and water fluxes in PEMFCs: conclusions about transfer mechanisms. J Electrochem Soc 2013;160:F1–14. http://dx.doi.org/10.1149/2.006303jes.
[8] Martemianov S, Legrand J, Skurygin EF. Turbulent mass transfer in the developing diffusion layer at large Schmidt numbers. Int J Heat Mass Transf 1999;42:2357–62. http://dx.doi.org/10.1016/S0017-9310(98)00321-4.
[9] Skurygin EF, Vorotyntsev MA, Martem'yanov SA. Space-time fluctuations of a passive impurity concentration within the diffusion boundary layer in the turbulent flow of a fluid. J Electroanal Chem 1989;259(1–2):285–93. http://dx.doi.org/10.1016/0022-0728(89)80052-X.
[10] Evdokimov YK, Denisov E, Martemianov S. Hydrogen fuel cell electrical noise and study of its diagnostics properties. Nonlinear World 2009;7(9):706–13.
[11] Martemianov S, Adiutantov N, Evdokimov YK, Madier L, Maillard F, Thomas A. New methodology of electrochemical noise analysis and applications for commercial Li-ion batteries. J Solid State Electrochem 2015;19(4):1–8. http://dx.doi.org/10.1007/s10008-015-2855-2.
[12] Evdokomov Y, Denisov E. Fluctuation-noise diagnostics of optical system power supply units based on fuel cell. Proc SPIE 2013;8787. http://dx.doi.org/10.1117/12.2020894. 87870E.
[13] Kadyk T, Kirscha S, Hanke-Rauschenbach R. Autonomous potential oscillations at the Pt anode of a polymer electrolyte membrane fuel cell under co poisoning. Electrochim Acta 2011;56(28):10593–602. http://dx.doi.org/10.1016/j.electacta.2011.05.005.
[14] Kulikovsky A, Scharmann H, Wippermann K. Dynamics of fuel cell performance degradation. Electrochem Commun 2004;6:75–82. http://dx.doi.org/10.1016/j.elecom.2003.10.018.
[15] Kulikovsky A, Scharmann H, Wippermann K. On the origin of voltage oscillations of a polymer electrolyte fuel cell in galvanostatic regime. Electrochem Commun 2004;6:729–36. http://dx.doi.org/10.1016/j.elecom.2004.05.015.
[16] Lopes PP, Ticianelli EA, Varela H. Potential oscillations in a proton exchange membrane fuel cell with a Pd–Pt/C anode. J Power Sources 2011;196(1):84–9. http://dx.doi.org/10.1016/j.jpowsour.2010.07.034.
[17] Zhang J, Datta R. Electrochemical preferential oxidation of co in reformate. J Electrochem Soc 2005;152(6):A1180–7. http://dx.doi.org/10.1149/1.1905983.
[18] Lu H, Rihko-Struckmann L, Sundmacher K. Spontaneous oscillations of cell voltage, power density, and anode exit co concentration in a PEM fuel cell. Phys Chem Chem Phys 2011;13:18179–85. http://dx.doi.org/10.1039/c1cp21984g.
[19] Niroumand AM, Merida W, Eikerling M, Saif M. Pressure-voltage oscillations as a diagnostic tool for PEFC cathodes. Electrochem Commun 2010;12(1):122–4. http://dx.doi.org/10.1016/j.elecom.2009.11.003.
[20] Zhang J, Datta R. Sustained potential oscillations in proton exchange membrane fuel cells with PtRu as anode catalyst. J Electrochem Soc 2002;149(11):A1423–31. http://dx.doi.org/10.1149/1.1511752.
[21] Xia D-H, Behnamian Y. Electrochemical noise: a review of experimental setup, instrumentation and DC removal. Russ J Electrochem 2015;51(7):593–601. http://dx.doi.org/10.1134/S1023193515070071.
[22] Wang R, Zhan Y, Zhou H. Application of transform in fault diagnostics of power electronics circuits. Sci Iran 2012;19(3):721–6. http://dx.doi.org/10.1016/j.scient.2011.06.013.
[23] Nigmatullin RR, Zhang W, Striccoli D. General theory of experiment containing reproducible data: the reduction to an ideal experiment. Commun Nonlinear Sci Numer Simul 2015;27(1):175–92. http://dx.doi.org/10.1016/j.cnsns.2015.02.024.
[24] Nigmatullin RR, Khamzin AA, Machado JT. Detection of quasi-periodic processes in complex systems: how do we quantitatively describe their properties? Phys Scr 2014;89(1):1–11. http://dx.doi.org/10.1088/0031-8949/89/01/015201.
[25] Nigmatullin R, Evdokimov Y, Denisov E, Zhang W. New methods of complex systems inspection: comparison of the ADC device in different operating modes. In: Computational problems in science and engineering, vol. 343 of lecture notes in electrical engineering. Springer International Publishing; 2015. p. 187–204. http://dx.doi.org/10.1007/978-3-319-15765-8_9.

Appendix C

Polarization curves and impedance measurements

Contents

Figures

C.1 Difference descriptors within campaign

Results of performing of electrochemical methods are presented in this section. Data has been obtained by colleagues of ANR "PROPICE" project.

C.1.1 1 campaign

Current density lower than 0.1 A/cm^2 and higher than 0.55 A/cm^2 are not allowed to perform electrochemical impedance spectroscopy (EIS) to obtain full resistance. Thereby, in according of the protocol of measurements EIS were adjusted as follows:

- sole spectrum of full resistance with current load of 85A ($I_{max}/2$) were obtained at T_0+1h,T_0+169 where T_0 is launch time of experiment;
- three spectrum of full resistance were obtained for current loads of 110A, 85A ($I_{max/2}$) and 20A at T_0+335 hours

Results of applying EIS in the range of 5kHz to 100mHz for equal current load with different times and for different current load (0.1 A/cm^2, 0.4 A/cm^2 and 0.5 A/cm^2) with the same time are presented as locus diagram in Fig.C.1. FC impedances for current load of 85A with different time of measurement are equal with small difference in low range frequencies ((Fig. C.1a). And as is obvious from Fig.C.1b diagram shows almost two time increase of impedance.

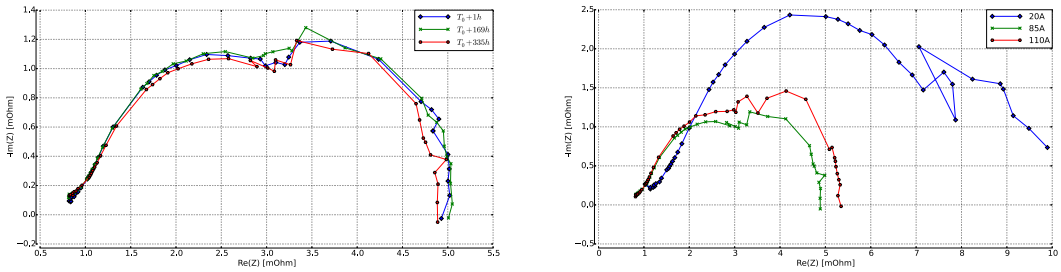

(a) FC impedance under current load of 85A with different measurement time

(b) FC impedance with different current load at the same measurement time

Figure C.1 – FC impedance

The polarization curves under decreasing current (Imax → 0) are registered with different operation time (T_0+1h,T_0+169,T_0+335h). Obtained polarization curves are presented in Fig.C.2.

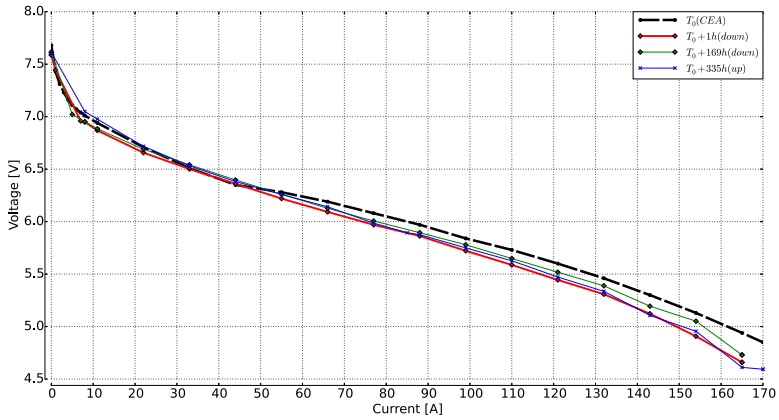

Figure C.2 – Polarization curves with different operation time and polarization curve obtained from CEA before delivering

As shown from polarization curves, there are insignificant increase of ohmic losses that are expressed to reducing the fuel cell voltage. From first measurement campaign. To achieve 1000 hours of operation, it is required to make modification in protocol of experiment notably the relative humidity.

C.1.2 2 campaign

Results of applying EIS over time are presented in Fig.C.3a for current load of 85A. Locus diagram is increased over time that characterize the degradation process. Also we can observed it in evolution of ohmic values from FC impedance that are collected in Table C.1, that are correspond to values at 5kHz and 100mHz, respectively. More clearly it is shown in Fig. C.4. The polarization curves under both mode decreasing (Imax → 0) and increasing (0 → Imax) current are registered with different operation time during all test time. Obtained polarization curves are presented in Fig.C.3b. As shown from polarization curves, there are also insignificant increase of ohmic losses like from first measurement campaign, but there are pronounced activation losses in the area of low current density in fuel cell operation that are probably evoked by degradation of MEA.

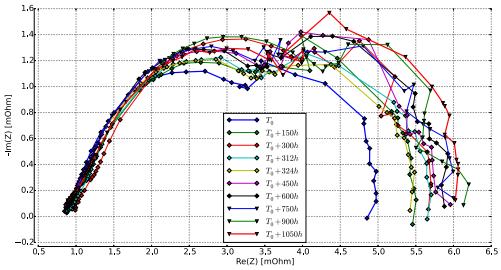

(a) Electrochemical Impedance Spectroscopy for 85A (4-5 cellules) load with different times

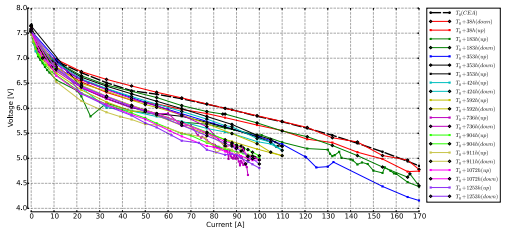

(b) Polarization curves

Figure C.3 – Pola and Spectra

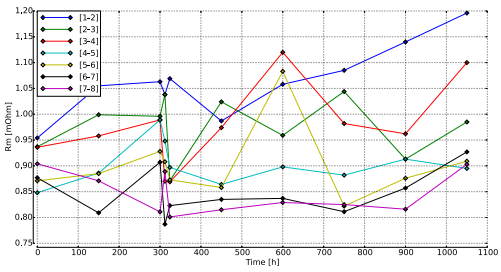

(a) Ohmic values at 5kHz

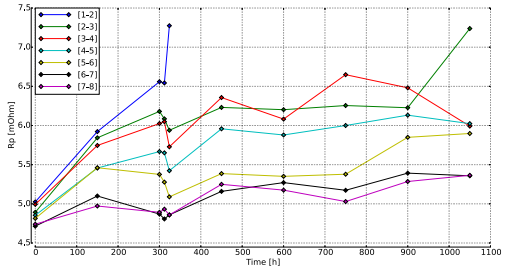

(b) Ohmic values at 100mHz

Figure C.4 – Evolution of Ohmic values

Table C.1 – Ohmic resistance

Group of cellules		[1-2]	[2-3]	[3-4]	[4-5]	[5-6]	[6-7]	[7-8]
Rm[mOhm]	T0	0.954	0.937	0.936	0.848	0.871	0.877	0.904
	T0+150h	1.055	0.999	0.958	0.886	0.885	0.809	0.871
	T0+300h	1.063	0.996	0.989	0.989	0.928	0.907	0.811
	T0+312h	1.038	1.038	0.8701	0.948	0.908	0.787	0.889
	T0+324h	1.069	0.871	0.869	0.897	0.873	0.823	0.801
	T0+450h	0.987	1.024	0.974	0.864	0.858	0.835	0.815
	T0+600h	1.058	0.959	1.12	0.898	1.083	0.837	0.829
	T0+750h	1.085	1.044	0.982	0.882	0.822	0.8112	0.825
	T0+900h	1.14	0.913	0.962	0.913	0.876	0.857	0.816
	T0+1050h	1.196	0.985	1.1	0.895	0.909	0.927	0.903
Rp[mOhm]	T0	5.025	4.892	4.993	4.854	4.814	4.715	4.740
	T0+150h	5.922	5.843	5.745	5.457	5.461	5.100	4.972
	T0+300h	6.559	6.18	6.025	5.667	5.376	4.869	4.892
	T0+312h	6.543	6.085	6.049	5.651	5.277	4.807	4.932
	T0+324h	7.274	5.939	5.728	5.423	5.089	4.859	4.858
	T0+450h	8.847	6.231	6.357	5.958	5.386	5.159	5.249
	T0+600h	9.579	6.202	6.082	5.879	5.351	5.271	5.175
	T0+750h	x	6.255	6.649	6	5.378	5.173	5.029
	T0+900h	x	6.227	6.481	6.132	5.849	5.392	5.285
	T0+1050h	x	7.238	5.992	6.024	5.898	5.358	5.364

J Solid State Electrochem
DOI 10.1007/s10008-015-2855-2

ORIGINAL PAPER

New methodology of electrochemical noise analysis and applications for commercial Li-ion batteries

S. Martemianov[1] · N. Adiutantov[1,2] · Yu. K. Evdokimov[2] · L. Madier[3] · F. Maillard[1] · A. Thomas[1]

Received: 1 April 2015 / Revised: 6 April 2015 / Accepted: 7 April 2015
© Springer-Verlag Berlin Heidelberg 2015

Abstract Electrochemical noise analysis (ENA) is performed on ICR 18650 commercial lithium-ion batteries. The interest of ENA relates with the possibility of in-situ diagnostics during charging or discharging of the battery. Thus, the extraction of small voltage fluctuations should take into account the time evolution of the mean signal. The non-stationary character of the phenomenon (charging and discharging battery) limits the use of traditional methods of signal filtering and attenuation, so a special methodology has been developed to calculate the noise standard deviation (STD). A good reproducibility of the results has been demonstrated, and V-shape form curves have been obtained with a minimum STD value at about 55 % of state of charge (SOC). It can be noted also that fast discharge provided with 3.3 Ω load is noisier than the slow one with 5 Ω load. Some promising results have been obtained regarding the possibility of battery state of health determination.

Keywords Lithium-ion battery · Electrochemical noise analysis · State of health · Aging

✉ S. Martemianov
serguei.martemianov@univ-poitiers.fr

[1] Institut Pprime, Université de Poitiers-CNRS-ENSMA, UPR 3346, 2 Rue Pierre Brousse, Bâtiment B25, TSA 41105, 86073 Poitiers Cedex 9, France

[2] Kazan National State Research University, 10 K. Marx street, Kazan, Russia

[3] DCNS/DGD/ASM/DI/ING/EN, St-Tropez, France

Introduction

In recent decades, much attention has been devoted to the development of electrochemical sources of energy, in particular, rechargeable lithium-ion (Li-ion) batteries [1–4]. These batteries are key components of the portable, computing, telecommunication equipment required today by the information-oriented society. Moreover, gaseous emissions from the burning of fossil fuels are polluting the air of large cities and creating global warming with dangerous consequences. These concerns initiate utilization of alternative sources of energy (solar radiation, wind, waves) that are variable in time and diffuse in space. All these sources require energy storage, and batteries provide a promising way in this direction.

Certainly, the progress in energy storage is much slower when compared with electronic industry where a doubling of memory capacity every 2 years follows well Moores' law prediction. Nevertheless, spectacular advances in electrochemical storage of energy via the emerging technologies of Ni-MeH, Li-ion batteries and fuel cells stimulate further R&D studies in physico-chemistry and engineering of electrochemical systems.

Economic impact of battery failures can be important when they are used in critical applications, and much attention has been devoted to the determination of state of health (SOH) of these systems. Existing diagnostic technologies such as conductance and impedance testing [5, 6] give only a partial answer on this question, and using alternative approaches seems to be very interesting. The present paper deals with electrochemical noise analysis (ENA) and its possible applications to studding rechargeable Li-ion batteries.

Noise measurements have been widely used not only in the 1960s in relation to communication systems [7] and

Published online: 23 April 2015

semiconductors [8] but also from time to time in electrochemical studies [9–12]. Electrochemical noise can be caused by different phenomena such as turbulent mass transfer [13–17], gas evolution [18–20], electrode corrosion [21–24] and passivation [25], or water transfer in fuel cells [26]. Usually ENA concerns small-size electrodes up to a few square centimetres. But for the practical applications related with commercial batteries, the active surface of the electrodes is much more important. The works of Professor M.A. Vorotyntsev and co-authors [13, 14], related to turbulent noise in electrochemical systems, have been demonstrated that relative intensity of the electrochemical noise is inverse to the electrode surface. For this reason, the ENA of commercial batteries is a delicate problem related with the extraction of very small voltage fluctuations, and very few measurements have been provided with real industrial systems [27, 28]. The interest of ENA relates with a possibility of in-situ diagnostics during charging or discharging of the battery. Thus, the extraction of small voltage fluctuations should take into account the time evolution of the mean signal. The non-stationary character of the phenomenon (charging and discharging battery) limits using of traditional methods of signal filtering and attenuation.

The main goal of the paper concerns the methodology of ENA with its application to monitoring of commercial Li-ion batteries. Special attention is given to the difficulties related with the extraction of very small voltage fluctuations during a battery's discharge. Some promising results related with the application of ENA for in-situ diagnostics of commercial batteries are presented as well.

Experimental setup

In the frame of the present work, electrical noise analysis (ENA) was applied to ICR 18650 commercial lithium-ion batteries; 18650-type is a cylindrical cell with a 3.7-V nominal voltage and 2.6-Ah rated capacity. To measure the low voltage fluctuations of lithium-ion batteries, experiments are performed in an appropriated experimental setup shown in Fig. 1. Battery voltage is measured by a 2182-Nanovoltmeter (Keithley) allowing, in the 10-mV range, to perform measurements with a nanovolt resolution. Nanovoltmeter is directly connected to a resistor divider that allows dividing by 500 the battery voltage and working in the 10-mV nanovoltmeter range (Fig. 2). Voltage is measured during battery discharges with two different loads, 3.3 and 5 Ω. To avoid, as much as possible, the electromagnetic interferences, the lithium battery, the divider and the load are placed into a metal box connected to the ground.

For discharge, the battery is maintained under a constant load until 5 % of state of charge (SOC) that takes approximately 2.5 h for 3.3 Ω and 4 h for 5 Ω. After each discharge, the battery is charged with a constant current of 0.5 A until the charging voltage of 4.2 V and kept at this constant voltage to the end of a current drop around 0.1 A. All measurements are performed with a frequency of 10 Hz using LabVIEW for data acquisition and Python for signal processing.

To validate and quantify the intrinsic noise of our experimental setup, voltage measurements have been performed without the battery. The battery has been replaced by a wire, and measurements of the voltage have been done for two circuits, one with nanovoltmeter plus wires and another with nanovoltmeter plus wires and divider.

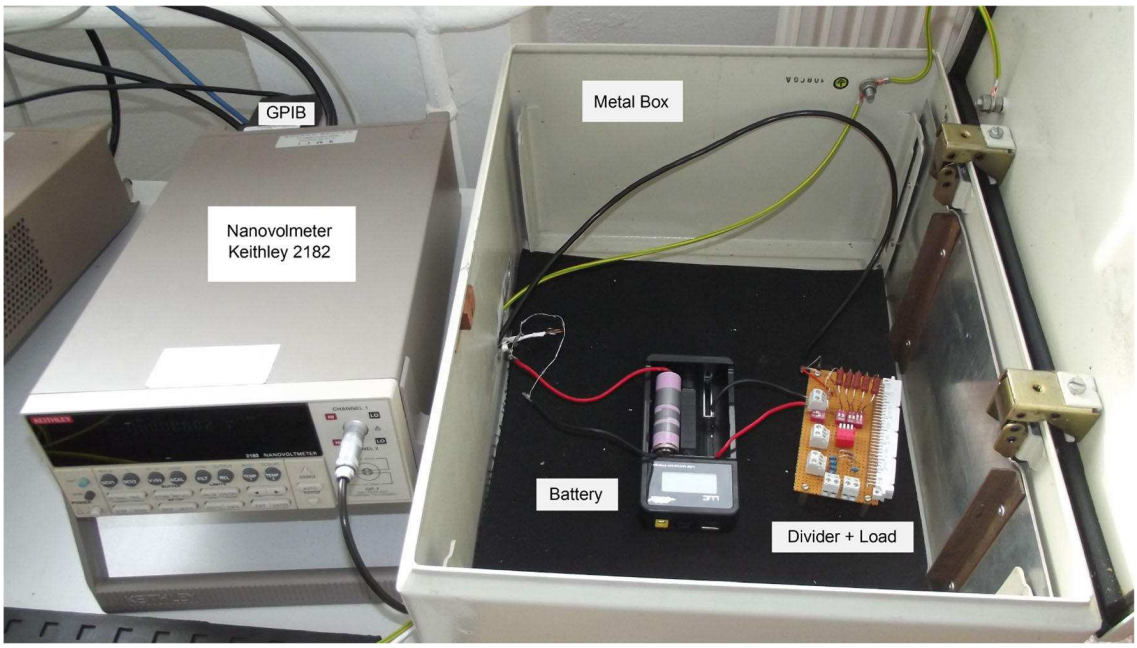

Fig. 1 Experimental setup for lithium-ion battery noise measurements

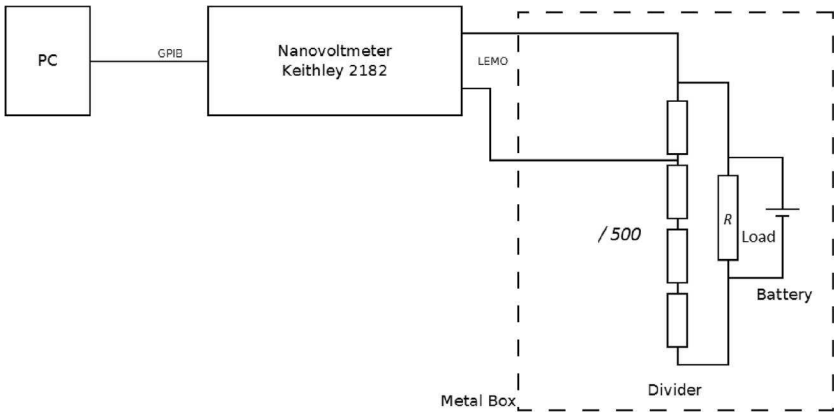

Fig. 2 Schema of experimental setup

Figure 3 shows intrinsic noise of the experimental setup during 400 s for the two abovementioned configurations. Measurements indicate that the apparatus noises are in the nanovolts order. The calculated standard deviation (STD) of the apparatus noise is equal to 2.74 nV for nanovoltmeter plus wire configurations (1) and 3.74 nV when divider is added (2). STD values are near the manufacturer values for the dc noise of the nanovoltmeter, which in the range of 10 mV, equals to 5 nV. So, the experimental setup was validated, and a STD of 5 nV has been accepted for the device noise.

Signal processing

Figure 4a shows a quasi-full discharge of the battery during 14,000 s (around 4 h). The discharge starts at the open-circuit voltage (OCV) of 3.98 V (charging voltage equals to 4.2 V) and run until 1.2 V. For signal processing, the total time domain have been divided into 20 pieces and the special procedure for the extraction of the noise fluctuations have been performed. Figure 4b shows the extracted voltage fluctuations for the tenth piece. The amplitude of the battery noise is in the microvolt order, 1000 times higher than the device noise (5 nV).

The procedure for the extraction of the noise fluctuations is the following: each of the 20 pieces contains approximately n=7000 experimental points (instantaneous voltage magnitudes); each of these 20 pieces is separated on time subintervals containing m points (m=50, 75 or 150). The signal in each sub-interval containing m experimental points is approximated by a n-order polynomial, and the signal fluctuations are calculated with respect to the mean value determined by this polynomial.

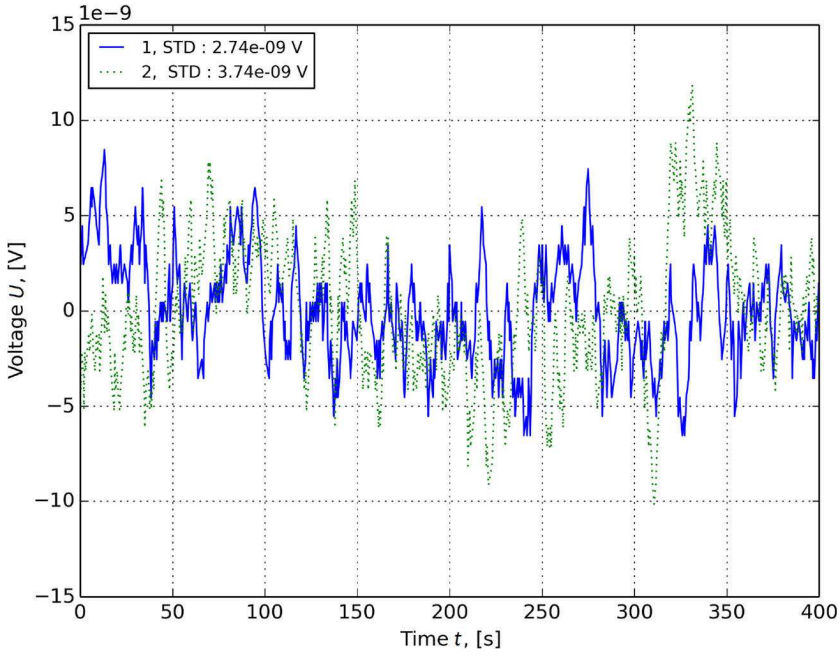

Fig. 3 Internal noise of experimental setup of **1** nanovoltmeter and wires and **2** nanovoltmeter, wires and divider

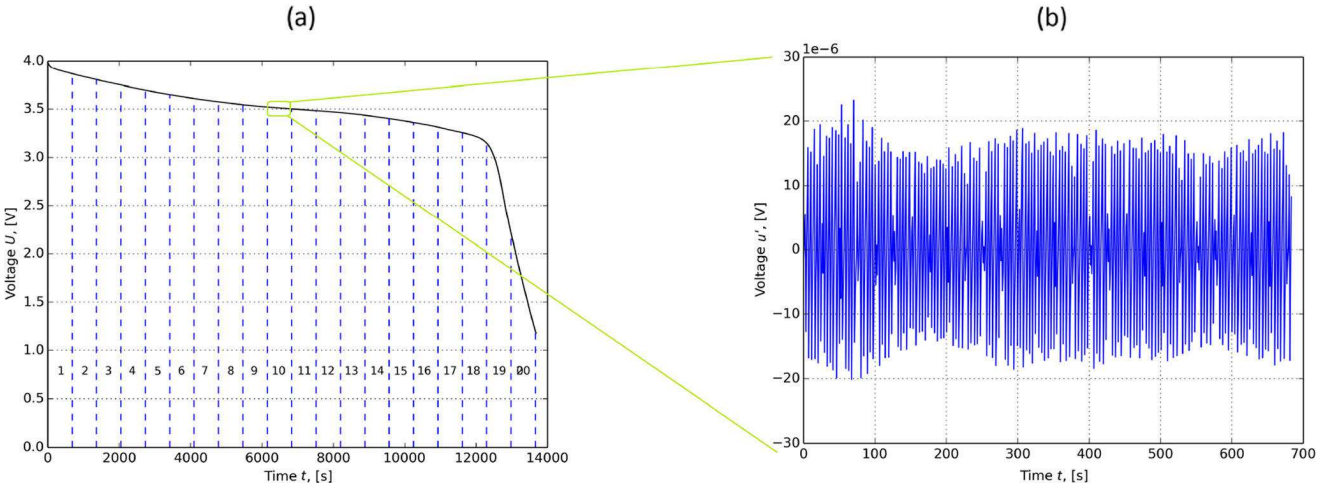

Fig. 4 **a** Discharge of Li-ion battery and **b** associated voltage fluctuations

Figure 5 illustrates the results of the signal processing when the steady-state and the linear approximation are used for determining the mean signal value. It is clear that the results (STD of voltage fluctuations) are very sensitive to data processing parameter, namely the value m, which characterises the time-span of the sub-interval where the signal fitting is provided. For this reason, the high-order polynomials have been used for the fitting of the mean signal value, as shown in Fig. 6. It can be seen that for high-order polynomials (n=5, 7, 9), the results are not sensitive to the data processing parameters (n and m). For the following, the data processing has been performed using n=7 and m=75 for extraction of the voltage fluctuations.

Experimental results and discussion

All obtained results are given in terms of state of charge (SOC) to permit the comparison for each discharge The noise (voltage fluctuations) of the lithium-ion battery is characterised by STD of the processing signal, and this STD is multiplied by 500 because the nanovoltmeter measures the voltage of the divider and not directly of the battery. The device noise of 5 nV is plotted for the comparison.

Influence of the discharge load

Voltage measurements have been performed for two different discharge loads of 3.3 Ω and 5 Ω for characterising the influence of a low (5 Ω) and fast discharge (3.3 Ω) on voltage drop and noise.

Figure 7 reflects the reproducibility of voltage drop during several discharges (mean) for each load. For three different batteries, five discharges are compared. After each discharge, the battery is charged until the charging voltage of 4.2 V. In overall, for each load, voltage drop is about 0.6 V until a SOC around 20 %. Figure 7 shows a good reproducibility for all discharges in each case; the voltage difference is 0.25 V (less

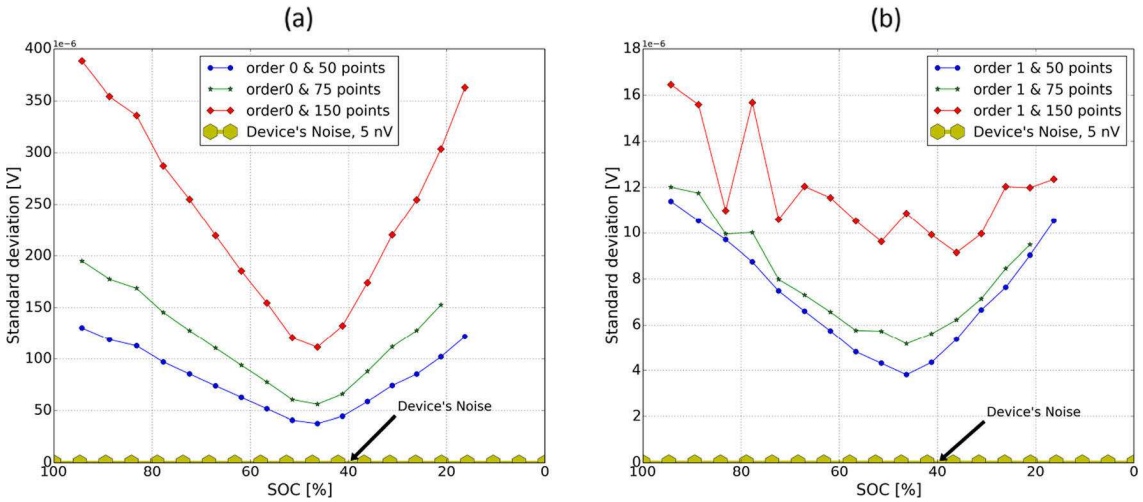

Fig. 5 Signal processing: STD of voltage fluctuations obtained using **a** steady-state and **b** linear approximations for determining the mean value

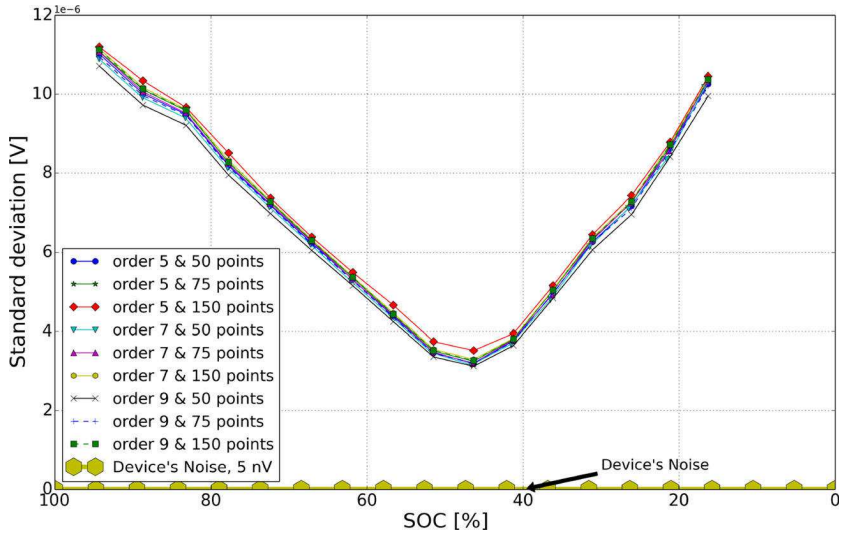

Fig. 6 Noise standard deviation of voltage fluctuations obtained using polynomial of order *n*: 5, 7 and 9 for determining the mean value

than 1 %) for all batteries and ten times lower (0.025 V) for the same battery after one discharge. A difference is noted for the started voltage between discharges with 5.5 Ω and 3.3 Ω load, but discharge curves are the same. Namely, started voltage is equal to 3.85 V for R=5.5 Ω (Fig. 7a) and to 3.75 V for R= 3.3 Ω (Fig. 7b).

Figure 8 shows a good reproducibility for the STD recording for each load. A maximal difference of 1 μV is measured for all batteries. The incertitude of 1 μV is reported on Fig. 9 where the comparison of the discharge for two loads is presented.

Figure 9 shows the comparison between noise measurements during discharges at different loads (5 Ω and 3.3 Ω) for the same battery. In both cases, a V-shape curve is founded with a minimum of 3.5 μV for 5.5 Ω load and 5 μV for 3.3 Ω load respectively at around 55 % of SOC. For each SOC, the STD for 3.3 Ω load is higher than the one for 5 Ω load. The difference around 6 μV at 95 % of SOC, 2 μV at 55 % of SOC and 4 μV at 18 % of SOC can be noted for STD with respect to a discharge at different loads. The test with 3.3 Ω load implies a faster discharge and a noisier drop voltage.

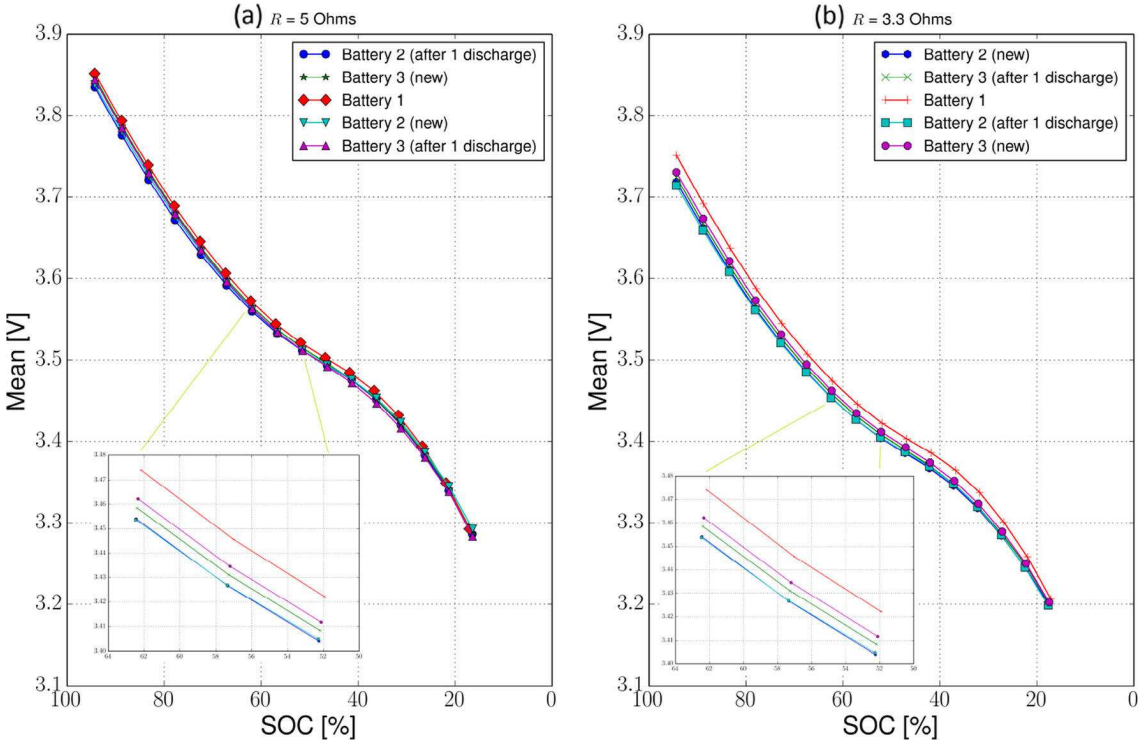

Fig. 7 Discharge of Li-ion battery with different load R **a** 3.3 Ω and **b** 5 Ω. Reproducibility of the mean measurements

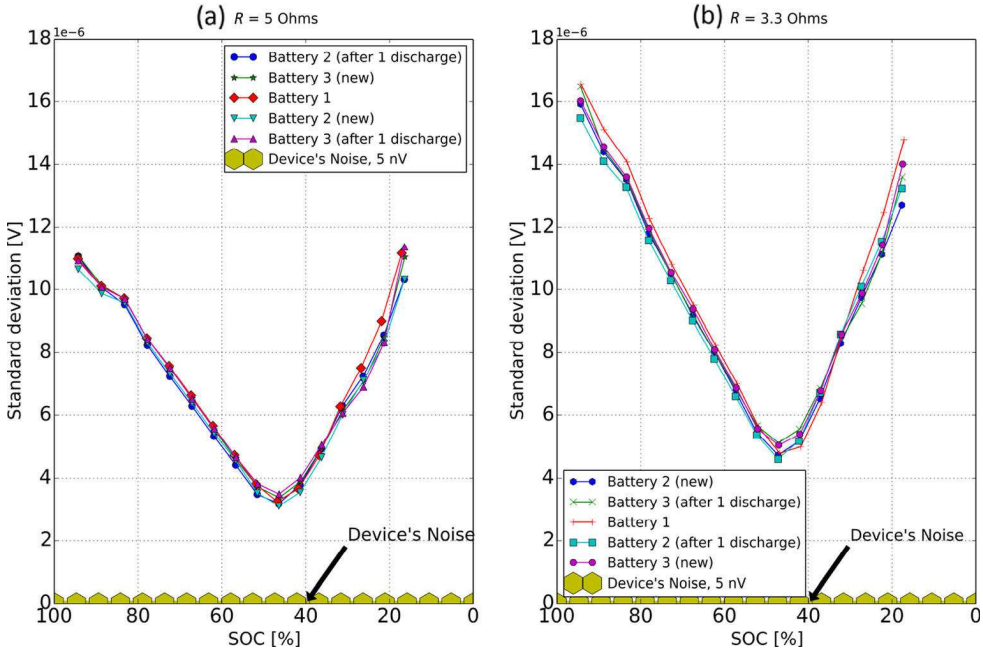

Fig. 8 Discharge of Li-ion battery with different load *R* **a** 3.3 Ω and **b** 5 Ω. Reproducibility of the noise measurements

Results show that voltage fluctuations and noise are more important near the OCV, decrease until a minimum at 55 % of SOC, that correspond to the inflexion point of the discharge (Fig. 7), and increases until 20 % of SOC. This V-shape curve can be related to the physical and electrochemical behaviour of the battery. Indeed, it can be supposed that for important SOC values (between 100 and 50 %), the battery discharge is governed mainly by the kinetics of electrochemical reactions (see the voltage drop curve in Fig. 7). Near the inflexion point which is situated around 50 % of SOC, the transport limitations begin to influence on the battery behaviour and become the governing factor for low SOC values. Thus, the decreasing part of the noise curve can be attributed to the noise of electrochemical reactions and the increasing part to the noise of transport phenomena.

It is interesting to note that both types of STD versus SOC behaviour have been noted in the literature. Thus, Baert and Vervaet [27] note the increasing of the noise voltage during discharge of Hoppecke batteries. Contrary, Martinet et al. [28] have presented the results concerning with Ni-MH batteries which indicate the decreasing of the noise power with SOC. The possible explanation relates with the influence of different phenomena (electrochemical and transport limitations) on the noise behaviour of different batteries.

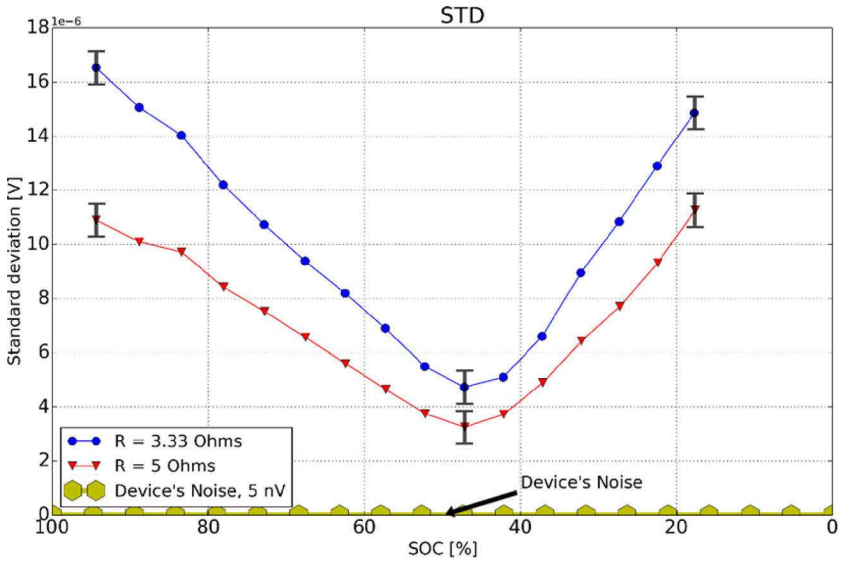

Fig. 9 Comparison of noise characteristics (STD) during discharge at different load *R* **a** 3.3 Ω and **b** 5 Ω for the same battery

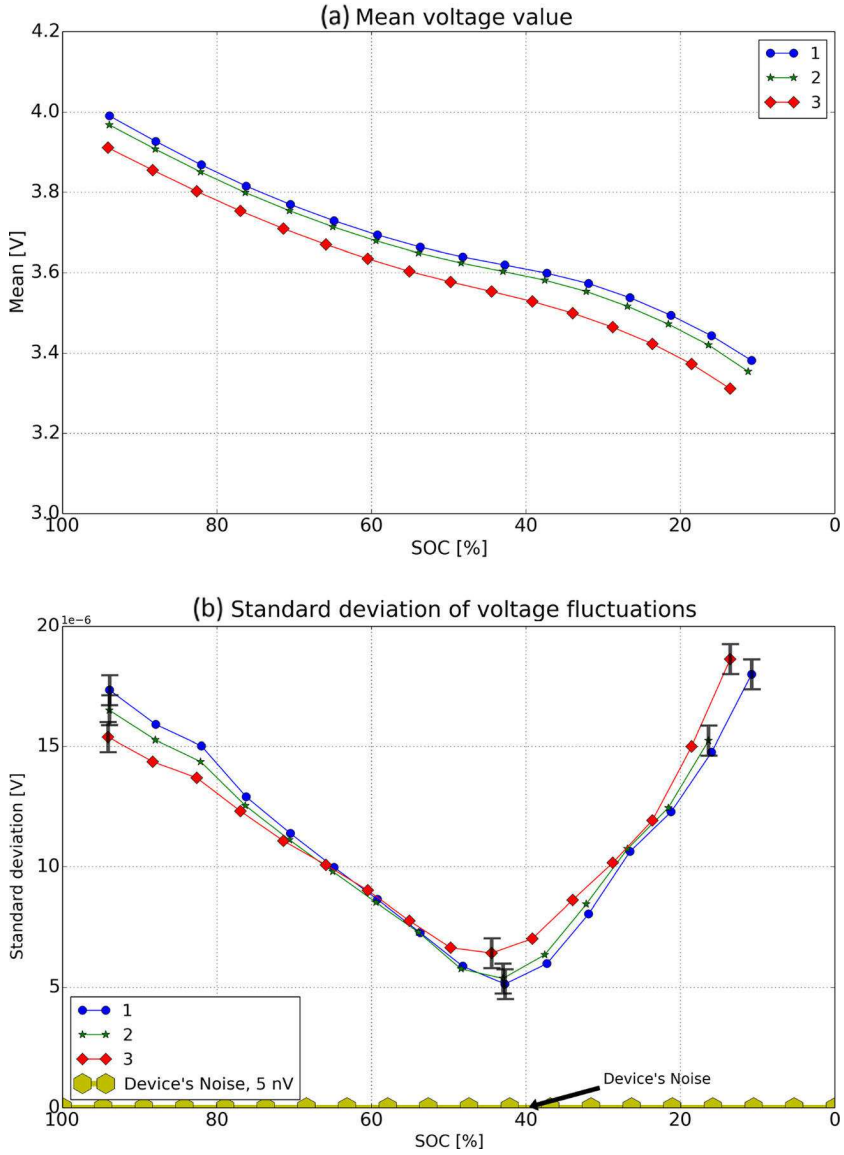

Fig. 10 Aging effect on **a** mean and **b** noise characteristics of the battery. **1** New battery, **2** after one short-circuit and **3** after ten short-circuits

Aging effect on the noise measurements

In this part, aging tests are performed via short-circuit cycling at ambient temperature. This aging test consists to short-circuit the battery during 2 h and to wait temperature equilibrium before start of another short-circuit. Figure 10 shows the drop of mean voltage (Fig. 10a) and noise characteristics (Fig. 10b) for a fresh battery, after one short-circuit and after a cycle of ten short-circuits. Figure 10a reflects that the voltage are decreased about 0.04 V after one short-circuit and about 0.1 V after ten short-circuits for all SOC. Voltage decrease is higher after ten short-circuit cycles, due to higher degradation processes in Li-ion battery. Figure 10b reflects the V-shape curve for the three state of health (SOH) with a variation of STD between 17 and 6 μV. For a SOC between 95 and 60 %, the STD of the fresh battery is higher than the battery after ten short-circuits. Around 55 % of SOC, a reverse occurs; STD (noise) of the aged battery, after ten short-circuit cycle, becomes higher than the fresh battery with a maximal difference at 45 % of SOC. At this SOC, STD after ten short-circuits is 6.5 μV against 5 μV for the fresh battery. The difference in the aging effect for low and high SOC can be related with the difference in preponderant effects (electrochemical or transport phenomena) which is governing the noise behaviour of the battery, but this issue needs more careful studies.

Conclusions

In this work, a methodology allowing to apply ENA for studying commercial batteries is presented. The commercial batteries have very important active surface of the electrodes and consequently very small voltage noise. The small voltage fluctuations have been extracted during

discharge of commercial Li-ion batteries using appropriated instrumentation (Nanovoltmeter) and a special data treatment procedure. This procedure is based on using high-order polynomials for fitting the mean signal value in small time windows. It is worth to note that the steady-state or the linear approximations for the fitting of the mean signal value do not allow correct extraction of the voltage noise during battery discharge because the noise characteristics depend dramatically in this case on data treatment parameters.

The noise standard deviation (STD) versus state of charge (SOC) has been measured for commercial Li-ion batteries, and good reproducibility of the results has been demonstrated. The obtained curves have a V-shape form with the minimum value at about 55 % of SOC. At our knowledge, this type of noise behaviour has never been published previously. Thus, the noise of the commercial Li-ion batteries is different on well-known noise sources. A possible explanation of a V-shape noise behaviour deals with superposition of different phenomena which governing the battery behaviour. For high SOC values, the electrochemical kinetics of the electrode's processes plays a dominant role while at small SOC values, the transport phenomena become more important.

It can be noted also that fast discharge provided with 3.3 Ω load is noisier than the slow one with 5 Ω load. Some promising results have been obtained with respect to possible monitoring of the battery's SOH by means of ENA. Indeed, at the minima of a V-shape curve, STD after ten short-circuits, is 6.5 μV against 5 μV for the fresh battery. This difference is much more important in comparison to the reached accuracy of ENA.

Acknowledgments This work pertains to the French Government Program "Investissements d'Avenir" (LABEX INTERACTIFS, reference ANR-11-LABX-0017-01). The authors are very thankful to Professor M.A. Vorotyntsev for his important contribution to scientific education and friendly support of scientific activities.

References

1. Tarascon JM, Armand M (2001) Nature 414:359–367
2. Scrosati B, Garche J (2010) J Power Sources 195:2419–2430
3. Goodenough JB, Kim Y (2010) Chem Mater 22:587–603
4. Barré A, Deguilhem B, Grolleau S, Gerard M, Suard F, Riu D (2013) J Power Sources 241:680–689
5. Huet F (1997) J Power Sources 70:59–69
6. Vorotyntsev M, Levi MD, Schechter A, Aurbach D (2001) J Phys Chem B 105:188–194
7. Bennett WR (1960) Electrical noise. McGraw Hill, London
8. Van Der Ziel A (1959) Fluctuation phenomena in semi-conductors. Butterworths Scientific Publication, London
9. Tyagai VA, Luk'yanchikova NB (1967) Soviet Electrochem 3:273–316
10. Tyagai VA (1971) Electrochim Acta 16:1647–1654
11. Grafov BM, Kanevskii LS, Astaf'ev MG (2005) J Appl Electrochem 35:1271–1276
12. Kanevskii LS, Grafov BM, Astaf'ev MG (2005) Russ J Electrochem 41:1091–1096
13. Vorotyntsev MA, Martem'yanov SA, Grafov BM (1984) J Electroanal Chem 1979:1–23
14. Skurygin EF, Vorotyntsev MA, Martem'yanov SA (1989) J Electroanal Chem 259:285–293
15. Martemyanov SA, Petrovsky NV, Grafov BM (1991) J Appl Electrochem 21:1099–1105
16. Martemianov S, Danaila L (2003) Fluctuation Noise Lett 3:L463–L471
17. Adolphe X, Danaila L, Martemianov S (2007) J Electroanal Chem 600:119–130
18. Gabrielli C, Huet F, Keddam M (1985) J Appl Electrochem 15: 503–508
19. Gabrielli C, Huet F, Keddam M, Macias A, Sahar A (1989) J Appl Electrochem 19:617–629
20. Hodgson DR (1996) Electrochim Acta 41:605–609
21. Searson PC, Dawson JL (1988) J Electrochem Soc 135:1908–1915
22. Mansfeld F, Xiao H (1993) J Electrochem Soc 140:2205–2209
23. Bertocci U, Gabrielli C, Huet F, Keddam M, Rousseau P (1997) J Electrochem Soc 144:31–37
24. Mansfeld F, Lee CC (1997) J Electrochem Soc 144:2062–2068
25. Gabrielli C, Huet F, Keddam M (1986) Electrochim Acta 31: 1025–1039
26. Evdokimov YK, Martemianov SA, Denisov ES (2009) Nonlinear World 7:706–713
27. Baert DHJ, Vervaet AAK (2003) J Power Sources 114:357–365
28. Martinet S, Durand R, Ozil P, Leblanc P, Blanchard P (1999) J Power Sources 83:93–99

Scientia Iranica D (2017) 24(3), 1437–1447

Sharif University of Technology
Scientia Iranica
Transactions D: Computer Science & Engineering and Electrical Engineering
www.scientiairanica.com

Spectral method for PEMFC operation mode monitoring based on electrical fluctuation analysis

E. Denisov[a,*], Yu.K. Evdokimov[a], R.R. Nigmatullin[a], S. Martemianov[b], A. Thomas[b] and N. Adiutantov[a,b]

a. *Kazan National Research Technical University named after A.N. Tupolev-KAI, 10 K. Marx St., 420111, Kazan, Russian Federation.*
b. *Institut Pprime, UPR 3346 CNRS, Université de Poitiers, ENSMA, Batiment B25:2, Rue Pierre Brousse - TSA 41105 - 86073 POITIERS Cedex 9, France.*

Received 2 December 2015; received in revised form 5 February 2016; accepted 10 May 2016

KEYWORDS
Fuel cell;
Technical diagnostics;
Flicker noise;
Water management.

Abstract. This work considers the possibility of applying electrochemical noise analysis to fuel cell diagnostics. Theoretical hypothesis and experimental result have shown that spectral characteristics of electrical fluctuations depend on water management processes inside the PEMFC. It has been established that the spectrum of electrical fluctuations in low frequency range has the nature of flicker noise. The frequency ranges of 0.1-1 Hz convenient for single cell as well as for stack diagnostics are revealed. The results show that the proposed approach can be considered as an effective tool to diagnose of fuel cells, namely allowing for prediction of drying and flooding.

© 2017 Sharif University of Technology. All rights reserved.

1. Introduction

There are many types of effective energy sources, but lately, scientists have been paying a great deal of attention to further researching the Polymer Exchange Membrane Fuel Cells (PEMFC) and Lithium-Ion (Li-Ion) batteries, which are the most promising energy sources for the near future. In the PEMFCs, hydrogen and oxygen are electrochemically combined to produce electrical energy without the essential interim step of heat production. It gives the PEMFC extremely high efficiency of up to 0.83 [1]. Reaction byproducts are water, and some waste heat is also used to produce additional power [2]. The PEMFC is considered an environmentally friendly source, since it does not produce greenhouse gas emissions.

Despite the mentioned advantages, the PEMFCs have insufficient operational characteristics, namely reliability and durability, which are strong barriers to their wide utilization. However, these problems can be solved by means of the PEMFC technical state diagnostics [3-6] adopted to detect and possibly predict failures at the initial stages and to try to neutralize the effects of failures to keep high operational characteristics. Development of corresponding methods and systems is an extremely difficult task since PEMFC operation is determined by several factors (pressure, reactant gases humidification, cell temperature, electrical operation mode, and others) and also considerably depends on the current technical state of membrane electrodes assembly and gas transport channels [1,7-9]. All these factors have a great deal of influence on energy conversion efficiency and operation stability. Therefore, in the current hydrogen energy industry on the basis of fuel cells, one of the problems is development of reliable diagnostic method of the fuel cell directly during its operation.

A lot has been written about dealing with diagnostic methods applied to fuel cells (see [3-5] and references therein), but the problem of developing

*. *Corresponding author. Tel.: +7 843 2389375; Fax: +7 843 2366032*
E-mail address: genia-denisov@yandex.ru (E. Denisov)

applicable and reliable diagnostic tools without any operation interruption has not been fully resolved. For development of the corresponding diagnostic systems, information properties of the PEMFC electrical noise and fluctuations are suggested for use within the scope of this work.

The latest research [7-10] shows that electric fluctuations reflecting physical processes occurring in electrochemical objects can be used for diagnostic purposes. Compared to other traditional electrochemical methods (polarization curve, electrochemical impedance spectroscopy, etc.), Electrical Noise Analysis (ENA) has many advantages such as rapidity, high informativity, and non-intrusiveness (the absence of external signal for the collection of experimental data). In this condition, the diagnostic method based on informational properties of electrical fluctuation is promising, since it allows for developing diagnostic systems which do not require perturbation of the FC operation mode [7,9]. At present, fluctuation phenomena during long-term operation mode occurring in the fuel cell are not fully explored. This work is dedicated to the development of diagnostic tools based on spectral characteristics of electrical fluctuations. It will enable the process of evaluating the degree of degradation of the equipment that allows for control of remaining useful life by changing the FC settings.

One of the main problems in the field of developing PEMFC systems is providing correct water management [11-19]. Analysis of the publications shows that great effort is directed at the understanding and quantitative description of water management processes [11,18,19] to identify influencing factors [13,15,17] for selection of materials [12], optimization of construction of the PEMFC [14], and control of the water management process [16]. The present work is focused on the problem of monitoring water management condition based on fuel cell electrical fluctuation analysis.

2. Spectral characteristics of electrical fluctuations of PEMFC

2.1. PEMFC electrical fluctuations

Electrical fluctuations are inherent properties of any electrochemical system and can be used for direct characterization of its condition. Diagnostic methods based on electrochemical noises are widely used for studying metal films and electrode corrosion, quality of passivation coatings, charging level estimation, and overcharging detection for electrochemical batteries, etc. An essential advantage of the noise (fluctuation) method is absence of any perturbation of electrochemical system by external probing signals. Observing electrical fluctuations during PEMFC operation could be divided into two large groups: (1) electrical noises (thermal, short, generation-recombination, and flicker noises), and (2) fluctuations caused by stochastic variation (instability) of electrical parameters of FC components. In this paper, we focus on the second group of fluctuations as they have a strong relationship with the PEMFC technical state and normally have large amplitudes making their measurement easier.

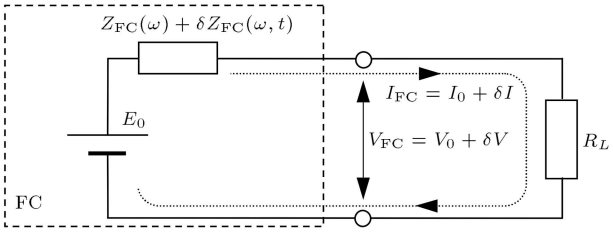

Figure 1. Origin of FC electrical current and voltage fluctuation.

During the FC operation process, stochastic variations (fluctuations) of the FC components of physicochemical parameters are observed. Due to the inconsistency of Membrane Electrode Assembly (MEA) for humidification modes, fluctuations of temperature and gas pressure maintenance of polymer membrane resistance, electrochemical reaction rates, diffusions coefficients, and double electrical layer thickness arise. These fluctuations cause stochastic variations of intrinsic FC electrical impedance $\delta Z_{FC}(\omega, t)$, and consequently provoke electrical current δI and voltage δV fluctuations (Figure 1).

Statistical parameters of such fluctuations should essentially depend on the current values of fuel cell physicochemical parameters and potentially have capacities which allow for realization of FC components' technical diagnostics. In other words, analysis of electrical current and voltage fluctuations can be considered as a basis for a reliable PEMFC diagnostic tool.

2.2. PEMFC electrical fluctuations caused by water condensation and evaporation processes

Within the scope of this work, the FC electrical fluctuations are understood as stochastic spontaneous variations of electrical current or voltage of FC. Such fluctuations take place even during operation under constant operational condition. The basic sources of the fluctuations are:

1. Instabilities in fuel and oxidized flows due to non-ideal construction of flow rate control systems;
2. Surges within flows of gases due to eddies caused by joints, abruptness, etc. within gas transport channels;
3. Variation in stoichiometry;
4. Variation of effective surface and activity of catalyst;

5. Water condensation and evaporation processes within gas transport channels and the MEA;
6. Condensed water drops blowing out and breaking by gas flows.

Each of these factors exerts influence on the FC electrical fluctuation spectrum. The effects of factors 1-3 could be significantly reduced by means of proper design of gas supply systems. The forth factor leads to long-term trends, reducing generating current. The influence of this factor could be significantly reduced by means of thorough cleaning of fuel and oxidizer.

Factor 6 is essential in case of large sizes of condensed drops and high gas flow rates [11]. During blowing off, a drop is "flattened" and the diameter of the drop increases in the contact area with the electrode surface:

$$d_d = K' c_D \mathrm{Re}^2, \tag{1}$$

where c_D is drag coefficient, K' is dimension factor (μm), Re is Reynolds number.

The additional possible source of electrical fluctuation observed during PEMFC operation is that of the condensation and evaporation processes in the region of Membrane Electrodes Assembly (MEA). These processes may provide drop formation on the membrane and electrodes which block reactants' delivery into the zone of electrochemical reaction. If we suppose that a water drop has a typical length scale (diameter, d), then the following area of a membrane surface is blocked:

$$S_b = \pi \times d^2/4. \tag{2}$$

The time variation of the blocked area leads to alteration of value of the produced current:

$$\delta I_{\mathrm{FC}}(t) = k \times S_b(t). \tag{3}$$

Here, k is proportionality factor.

As shown in [11] on the basis of empirical dependencies, growth of drop diameter during condensation within the MEA of the PEMFC could be described by the following equation:

$$D(t) = 0.62 \times t^{0.1}. \tag{4}$$

Here, t is time in seconds, and D is diameter of the drop in millimeters. The measurements have been carried out in 40 seconds under flow velocity 4,25 m/s. At the moment $t = 1$ s, the drop diameter was 0.62 mm [11]. Using dependences in Eqs. (3) and (4), it can be shown that such a growth of drop corresponds to the current variation:

$$\delta I_{\mathrm{FC}}(t) = 0.0961 \times k \times \pi \times t^{0.1}. \tag{5}$$

We can suppose that in general, current variations caused by condensation can be described by the following formula:

$$\delta I_{\mathrm{FC}}(t) = a \times t^{\alpha}, \tag{6}$$

where a is dimension proportionality factor, and α is a fractional factor.

Under the actual operating conditions, condensation and evaporation take place simultaneously within the MEA. The results of the reciprocal action of the two processes lead to drop diameter changes described by the equation:

$$D(t) = a_0 \times t^{\Delta\psi} = a_0 \times t^{(\alpha-\beta)}, \tag{7}$$

where $\Delta\psi = (\alpha - \beta)$; α and β are parameters corresponding to condensation and evaporation, respectively. Variation of drops diameters changes the blocked area of MEA's active layer:

$$S_b(t) = \pi \times a_0^2/4(t^{2\Delta\psi}). \tag{8}$$

It leads to changing of the current according to Eq. (3):

$$\delta I_{\mathrm{FC}}(t) \sim k\frac{\pi a_0^2}{4} t^{2\Delta\psi}. \tag{9}$$

Due to the presence within the MEA and gas transport channels, a great number of drops of different sizes (the greater part of which normally has small sizes) of condensation and evaporation cause complex fluctuation of effective membrane surface and corresponding electrical fluctuations. With standard tables of integral transform at hand [20], spectral representation of the current fluctuation can be expressed by the following equation:

$$\delta F_{I_{\mathrm{FC}}}(j\omega) = A_0 \frac{\Gamma(1+2\Delta\psi)}{(j\omega)^{1+2\Delta\psi}}, \tag{10}$$

where Γ is Gamma function, A_0 is proportionality coefficient, and $\Delta\psi = \alpha - \beta$.

Therefore, the Power Spectrum Density (PSD) of the electrical fluctuations corresponding to condensation-evaporation processes is expressed as:

$$S_I(\omega) \sim |\delta F_{I_{\mathrm{FC}}}(j\omega)|^2 = A_0^2 \frac{\Gamma^2(1+2\Delta\psi)}{(j\omega)^{2+4\Delta\psi}}. \tag{11}$$

Analysis of Eq. (11) shows that these fluctuations correspond to the flicker noise nature:

$$S(f) \sim \frac{1}{f^{\gamma}}, f \leq 1 \text{ Hz} \tag{12}$$

where $\gamma = 2 + 4\Delta\psi$.

These results show that electrical fluctuations contain information about the quality of water management inside the MEA, and therefore reflect the PEMFC technical state. Thus, electrical fluctuation can be considered as the basis for PEMFC diagnostic system whose diagnostic features will be analyzed in the experimental part of this work.

3. Experimental study of PEMFC electrical fluctuation

3.1. Experimental setup for PEM fuel cell fluctuation characteristics measurement

An automated measurement system for investigating fuel cell electrical fluctuation or the Fuel Cell Test Station (FCTS) has been developed for fluctuation measurement (Figure 2). This system consists of two parts: Fuel cell operability assurance subsystem and Electrical noise (fluctuation) measurement system. The BANC TEST installation produced by Fuel cell technologies Inc. was used for PEMFC operability assurance. This installation allows for choosing a type of oxidizer (oxygen or air) and control of seven fuel cell operation parameters: temperature of FC ($T_{\rm FC}$), humidity of fuel η_a, and oxidizer η_c gases, anode Q_a and cathode Q_c flow rates, anode P_a and cathode P_c backpressures.

The fuel cell operability assurance subsystem works in the following manner. Flow rate controllers (FRC1, FRC2) provide fuel cell anode and cathode with hydrogen and oxygen. Reactant gases can go directly to fuel cell inlets through the anode (AHS) and cathode (CHS) humidification systems in dependence on anode (AMS) and cathode (CMS) humidification mode of selector positions. Humidity of fuel, η_a, and oxidizer, η_c, is controlled by temperatures of anode T_{tHA} and cathode $T_{\rm HC}$ humidification systems, respectively. The backpressure controllers are placed after the fuel cell anode (ABPC) and cathode (CBPC) outlets. Cell temperature is set by the Temperature Controller (TC).

Temperature controllers of cell and both humidifiers are based on CN76122 T/C controllers with the accuracy of ± 0.25°C. Backpressure controllers have accuracy better than 2%. FCTS experimental setup operates under the control of computerized system of controls and measurements. Software has been created in the program environment LabVIEW 8.5 of National Instruments. The computerized system is connected to the anode (AFRC) and cathode (CFRC) flow rates controllers, allowing for maintaining flow rates with inaccuracy of less than 1% of the rated value.

The Impedance Measuring System (IMS) is based on the built-in BANC TEST installation impedance meter. The IMS allows for measuring FC impedance characteristics at the frequency range of 0.01 Hz - 40 Hz with relative error of real and imaginary part measurements lower than 0.25%. Electric Signal Measuring system (ESM) has been developed to measure FC electrical and fluctuation signals. A block diagram of this system is shown in Figure 2.

The fuel cell electric signal measuring system has two measuring channels. The developed two-channel measuring is based on data acquisition board NI PXI-5922 (National Instruments Inc.), and low-noise amplifier is made on the basis of the INA 103 microcircuit (Burr Brown Inc.), which has sensitivity better than 1.5 nV/Hz$^{0.5}$). NI PXI-5922 has a resolution of 24 bits at sampling rates of up to 50 kHz and the root-mean-square noise voltage $< 1\mu$V (Figure 3).

A two-channel noise measuring system provides measurement of complete FC voltage signal by the first channel:

$$V_{\rm FC} = V_0 + u(t). \tag{13}$$

Here, $V_0 = \overline{V_{\rm FC}}$ is DC component of FC voltage, $u(t)$ is fluctuation component of FC voltage, and only fluctuation component $u(t)$ of full signal in the frequency

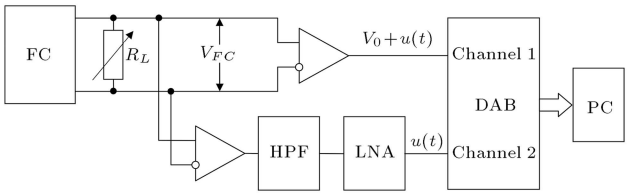

Figure 3. Block diagram of fuel cell electric signal measuring system.

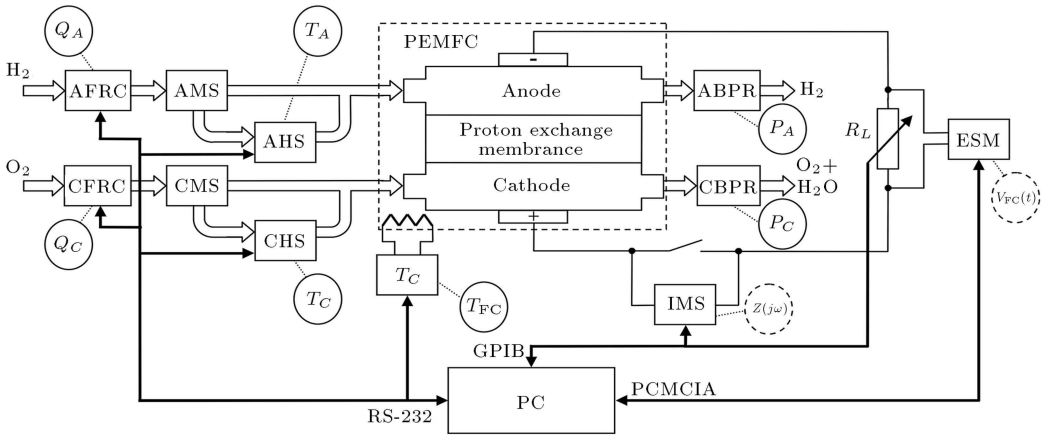

Figure 2. Block diagram of fuel cell testing system.

Table 1. Measurement information of system for single PEMFC analysis.

No.	Measured quantity	Notation	Unit	Type of quantity		Range	Accuracy
				Controlled	Measured		
1	FC temperature	T_{FC}	°C	+	+	0-100	±0.25°C
2	Temperature of anode humidification system	T_{HA}	°C	+	+	0-100	±0.25°C
3	Temperature of cathode humidification system	T_{HC}	°C	+	+	0-100	±0.25°C
4	Flow rate of anode gas	Q_A	ml/min	+	+	0-1000	1%
5	Flow rate of cathode gas	Q_C	ml/min	+	+	0-2000	1%
6	Anode backpressure	P_A	kPa	+	+	400	2%
7	Cathode backpressure	P_C	kPa	+	+	600	2%
8	Load resistance	R_L	Ohm	+	+	0.01-1000	0.1%
8	FC impedance	$Z(j\omega)$	Ohm	+	-	0-1000	0.25%
9	FC voltage	V_{FC}	V	+	-	0-5	0.6 μV

range 1 Hz-2k Hz by the second channel. A signal processing program has been also written in the program environment LabVIEW 8.5. Thus, the developed Fuel Cell Testing System allows for measuring 9 quantities describing fuel cell operation mode. Measurements of values, their notations, units of measurement, range, and accuracy are presented in Table 1.

3.2. Electrical fluctuation of a single PEMFC

The results presented in this section are obtained for a single PEMFC of the P'prime laboratory of the University of Poitiers (France). The Membrane Electrodes Assembly (MEA) of the considered fuel cell has been produced under the hot pressing method ($T = 120°\mathrm{C}$, $P = 7,8$ MPa, $t = 130$ s). Catalytic layers placed on the proton exchange membrane *Nafion* 117 contained 40% of mass fraction of Pt on carbon carrier unit *Vulcan* XC-72 with 0.5 mg/cm^2 platinum loading and 20% mass fraction of teflon PTFE. A hydrophobic carbon cloth has been used as the backing layer. Active surface area of square electrodes was equal to 5 cm^2. The MEA has been placed between two bipolar plates with gas transport channels having a single-channel serpentine configuration. The width and depth of the gas transport channels is 1 mm. The width of the copper current collector plate is also 1 mm.

An example of Power Spectral Density (PSD) $S''(f)$ of PEMFC fluctuation reduced to square average voltage $\overline{V_{\mathrm{FC}}}^2$ is measured for the operation mode corresponding to the following parameters:

$$T_{\mathrm{FC}} = 60°\mathrm{C}, \quad T_{\mathrm{HA}} = 50°\mathrm{C},$$

$$T_{\mathrm{HC}} = \text{dry (without humidification)},$$

$$Q_A = 600 \text{ ml/min}, \quad Q_c = 600 \text{ ml/min},$$

$$P_A = P_C = 300 \text{ kPa}, \tag{14}$$

which are presented in Figure 4.

The reduced PSD $S''(f)$ has been measured in the frequency range of 0.1-100 Hz. The lower frequency range limit has been chosen in order to enhance fluctuation from slow variations of generated electrical current (voltage) by frequency filtering. The upper frequency range limit (100 Hz) has been selected under the condition of a reliable measuring information, which obtains:

$$S(f) >> S_n(f), \tag{15}$$

where $S(f)$ is the PSD of PEM fuel cell microfluctuation, and $S_n(f)$ is PSD of measuring equipment intrinsic noises.

Graph $S''(f)$ (Figure 4) shows that fluctuations have a steadily decreasing character which can be described by fractional power dependence in accordance with theoretical speculations (see Section 2.2):

$$S'(f) \sim \frac{1}{f^{\gamma}}. \tag{16}$$

Fractional factor increasing in the range of 10-100 Hz can be increased by the shunting action of double-electrical layer capacity, C.

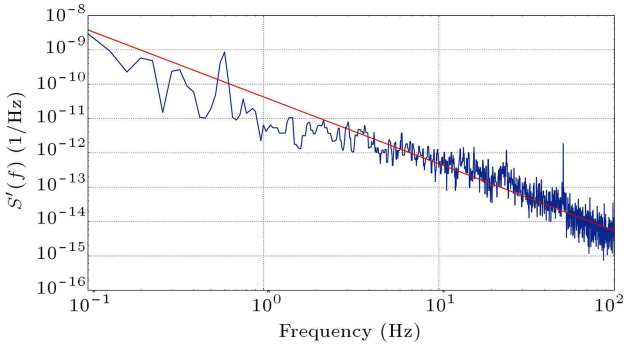

Figure 4. Typical power spectral density $S'(f)$ reduced to FC square of average voltage $\overline{V_{\mathrm{FC}}^2(t)}$ of PEMFC fluctuations measured in operation mode: $T_{\mathrm{FC}} = 60°\mathrm{C}$; $T_{\mathrm{HA}} = 50°\mathrm{C}$; $T_{\mathrm{HC}} =$ dry (without humidification); $Q_A = 600$ ml/min; $Q_C = 600$ ml/min; $P_A = P_C = 300$ kPa.

3.3. Single PEM fuel cell electrical fluctuation under different water management modes

Water balance substantially defines efficiency and stability of the PEM fuel cell operation. Water balance

control is generally carried out by variation of three parameters: FC temperature T_{FC}, anode T_{HA}, and T_{HC} cathode humidifiers temperature. For this reason, let us consider the influence of these parameters on FC electrical fluctuations arising during the FC operation.

FC temperature is one of the most important parameters defining the FC operation. Therefore, an analysis of influence on FC fluctuation is a task of the highest priority. The complexity of FC temperature characteristics investigation is caused by the fact that the fuel cell temperature directly defines water balance in the MEA.

Experimental results of the reduced PSD $S'(f)$ measured at different FC temperatures are presented in Figure 5. The analysis of these results allows us to conclude that electrical fluctuation at higher frequencies range ($f > 10$ Hz) demonstrates a slow decrease with the growth of a temperature, while low frequency fluctuations do not show a significant temperature dependence.

Dependence of the analysis of PEMFC fluctuation on anode humidifier temperature, T_{HA}, (Figure 6) does not reveal any significant dependency. It can be explained by the fact that anode reactions are not usually a limiting factor for PEMFC operation of efficiency and stability.

Reduced PSD $S'(f)$ of PEM fuel cell electrical fluctuation measured at different values of cathode humidifier temperature, T_{HC}, is presented in Figure 7. This figure shows that FC temperature has substantial influence on fluctuation spectral characteristics. Fluctuations at all frequencies remain almost constant with increasing temperature up to 40°C ($T_{HC} < 40$°C) and abruptly increase more than one order to higher temperatures (Figure 7).

Dependence of the hydrogen fuel cell impedance characteristic on anode humidifier temperature is presented in Figure 8. One can see that FC impedance absolute values $|Z_{FC}|$ at low frequency range ($f < 10$ Hz) have a character of dependence on temperature T_{HC} similar to the changing behavior of fluctuation characteristics kept at almost constant level in the temperature range of $T_{HC} < 40$°C and abrupt increase in the range of $T_{HC} > 40$°C. Strong temperature dependence of impedance and fluctuation characteristics can be explained by active water condensation on the MEA and gas transport channel surfaces when the

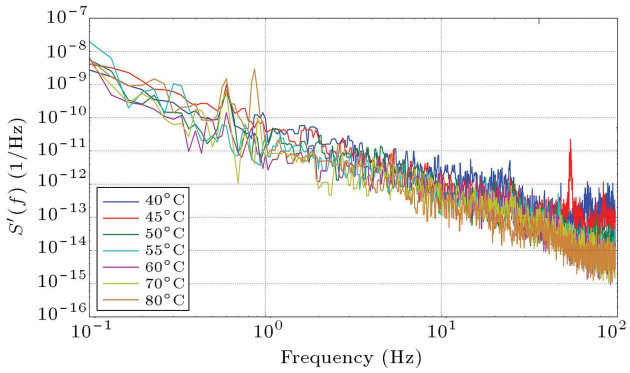

Figure 5. Reduced PSD $S'(f)$ of PEM fuel cell electrical fluctuation measured at different values of FC temperature T_{FC}.

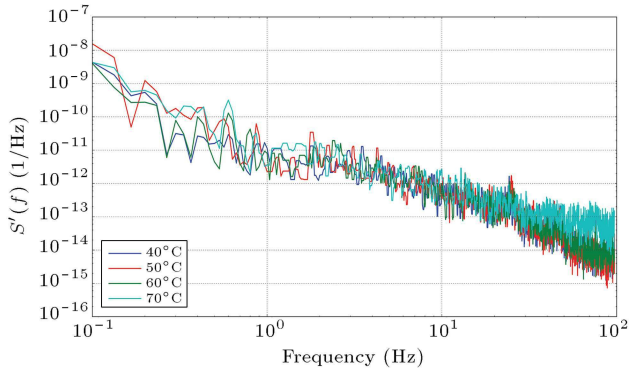

Figure 6. Reduced PSD $S'(f)$ of PEM fuel cell electrical fluctuation measured at different values of anode humidifier temperature T_{HA}.

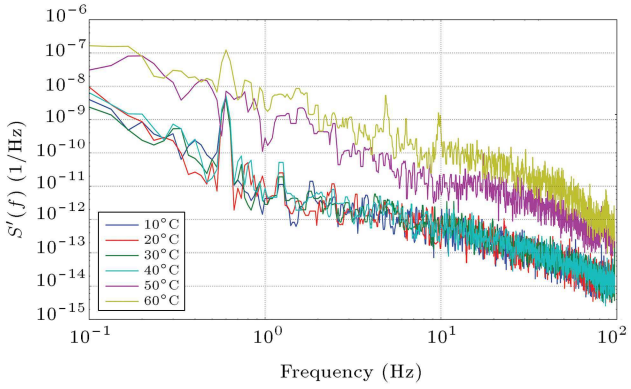

Figure 7. Reduced PSD $S'(f)$ of PEM fuel cell electrical fluctuation measured at different values of cathode humidifier temperature T_{HC}.

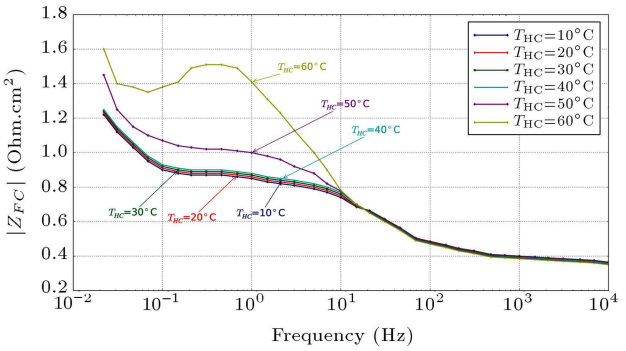

Figure 8. Dependence of FC impedance absolute values $|Z_{FC}|$ on frequency f at different cathode humidifier temperatures T_{HC}.

temperature of a PEM fuel cell T_{FC} becomes close to the dew point temperature of cathode gas. PEM fuel cell operation in this mode can lead to MEA active surface part blocking and non-uniformity of the current distribution along the membrane surface.

To check the above assumption that PEMFC fluctuation significantly depends on water management processes, the fluctuation characteristics have been studied in a flooding mode. The measurement of FC electrical fluctuation time dependence has been carried out (Figure 9) for a FC operating in the following operation mode: $T_{FC} = 60°C$; $T_{HA} = 70°C$; $T_{HC} = 70°C$; $Q_A = 600$ ml/min; $Q_C = 600$ ml/min; and $P_A = P_C = 300$ kPa. Such an operation mode due to high anode and cathode humidifier temperature leads to water excess in the MEA of the fuel cell. Figure 9 shows that the fuel cell fluctuations for this mode are characterized by a large quantity of short sharp impulses which affect the PSD increasing in a middle-frequency range (Figure 10). By a decrease of anode and cathode humidifiers' temperatures, the PSD of fluctuations has returned to its original form.

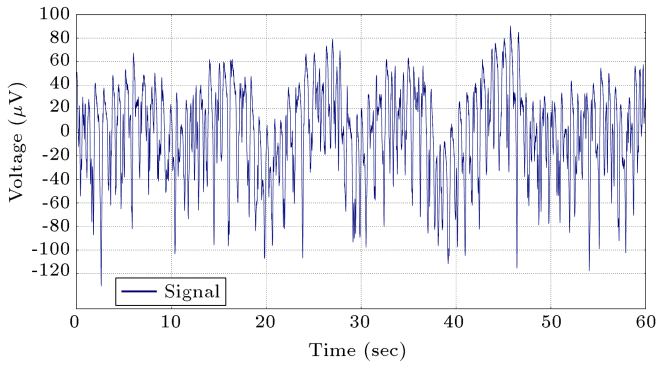

Figure 9. Electrical fluctuation time dependence for the PEM fuel cell operating at next operating mode: $T_{FC} = 60°C$; $T_{HA} = 70°C$; $T_{HC} = 70°C$; $Q_A = 600$ ml/min; $Q_C = 600$ ml/min; $P_A = P_C = 300$ kPa.

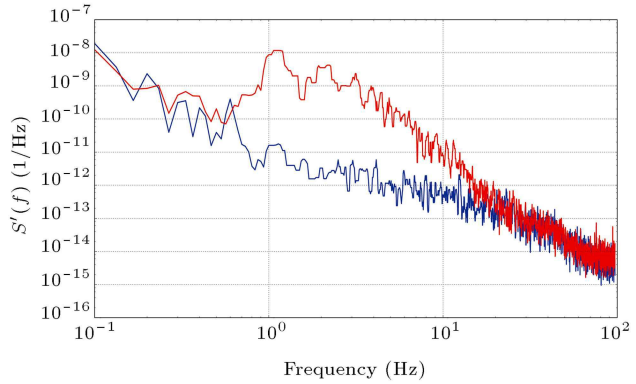

Figure 10. Electrical fluctuation PSD of the PEM fuel cell operating in operation mode: 1) $T_{FC} = 60°C$; $T_{HA} = 70°C$; $T_{HC} = 70°C$; $Q_A = 600$ ml/min; $Q_C = 600$ ml/min; $P_A = P_C = 300$ kPa; 2) $T_{FC} = 60°C$; $T_{HA} = 50°C$; $T_{HC} =$ dry; $Q_A = 600$ ml/min; $Q_C = 600$ ml/min; $P_A = P_C = 300$ kPa.

4. Results and discussion

Analysis of experimental results presented in Section 3.3 showed that electrical fluctuation depends on physical processes inside the PEMFC, especially on water condensation and evaporation processes in the MEA. It allows one to reasonably suppose that using the information properties of electrical fluctuations allows for developing an effective tool for PEMFC diagnostics. However, due to low maximum potential of single cell (less than 1.2 V), a PEMFC stack is usually used for practical application. Here, the question of applicability of the described approach was raised to estimate technical state of the stacks.

4.1. Experimental setup for PEMFC stack electrical fluctuation measurement

The Electrical Noise Analysis (ENA) was applied to study the 8-cell hydrogen PEMFC (EPICEA v2) with the cell surface of 220 cm^2 in Fuel Cell Laboratory (Belfort, France). The electrical parameters, such as voltage of stack and/or on each single stack cell, electrical current, impedance, etc., were measured in galvanostatic (0-170A) or potentiostatic (0-9V) modes. Electrical fluctuation measurement was performed by means of specific equipment based on NI-9239 of National Instrument Inc. The root mean square value of intrinsic noise of the equipment for fluctuation measurement is about 70 μV that is sufficient to measure FC voltage fluctuations.

To develop methods for diagnosis and prognosis of the PEMFCs, the state of health information on the current technical state of a PEMFC is required. The information was provided by the set of additional sensors. Test benches were equipped with sensors for temperature, pressure, humidity, and flow rate of reactants. All sensors are direct descriptors, i.e., using direct recording of physical parameters. A simplified diagram of sensor placement is shown in Figure 11. The main setup parameters are presented in Table 2.

Table 2. Technical characteristics of experiment for PEMFC stack electrical fluctuation analysis.

Characteristic	Value
Nominal power	600 Watts
Current	0-170 A
Relative humidity	50%
Temperature of FC	75-80°C
Absolute pressure	1.5 bar
Reagents stoichiometry of anode/cathode	1.5/2

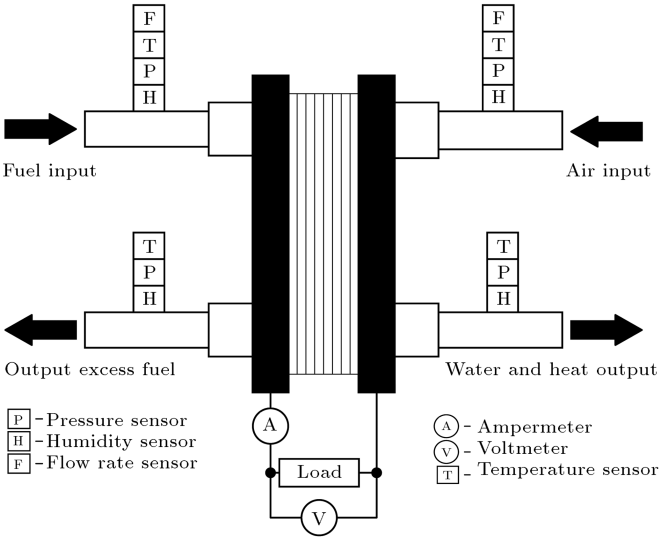

Figure 11. Acquisition of thermophysical parameters for generating direct descriptors.

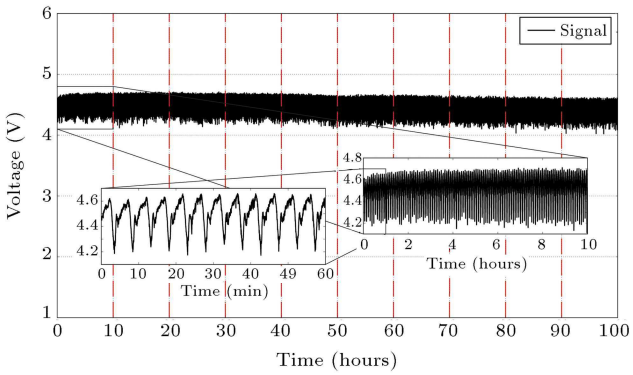

Figure 12. PEMFC voltage fluctuation in galvanostatic mode.

4.2. PEMFC stack electrical fluctuations

To realize an experimental study, a PEMFC was run galvanostatically for 100 hours with the current of 170A (772 mA/cm^2) with the other parameter listed in Table 2. Typical voltage fluctuations for 170A galvanostatic mode are presented in Figure 12. There are clearly-expressed quasi-periodic oscillations with the characteristic time of about 5 minutes. Within the structure of electrical fluctuations, there are also a lot of small stochastic signals distributed within wide ranges of frequencies and amplitudes.

Before applying ENA, the Direct Current (DC) and low frequency components have been removed using 5-order digital Butterworth high-pass filter with the cut-off frequency of 0.1 Hz. The frequency range has been chosen in accordance with the results obtained in Section 3.3 for a single PEMFC. To obtain spectral characteristics of electrical fluctuations, PSD has been calculated on the basis of Fast Fourier Transform (FFT).

PSDs of electrical fluctuations measured every 10 hours for a PEMFC run for 100 hours with the load current of 170A are presented in Figure 13. As one can see, PSD has a complex structure within the range of 100 mHz to 10 Hz. And, in particular, it is established that in a low frequency range, the fluctuation has the flicker-noise nature that coincides with the results obtained for a single PEMFC in Section 3.3. This experimental result also confirms the theoretical assumptions stated in Section 2.2. Distortion of fluctuations spectrum in higher frequency range can be explained by PEMFC control equipment operation. It is shown that since flicker-noise component of electrical fluctuation comprises diagnostic features reflecting technical state of a PEMFC, we will further focus on the corresponding frequency range lower than 1 Hz.

Figure 14 shows the evolution of fluctuation parameters estimated as values of PSD on specific frequencies. At the initial stage, all parameters that can be explained by operating process stabilization decrease. After 30 hours, all parameters have the increasing trend that can be caused by decreasing effective surface due to water accumulation within the MEA or by degradation of catalyst.

Due to the flicker-noise nature of PEMFC electrical fluctuations, it is interesting to analyze the possibil-

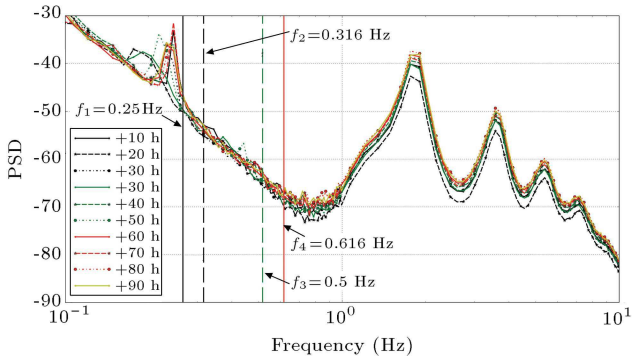

Figure 13. Power spectrum density of PEMFC stack voltage fluctuation.

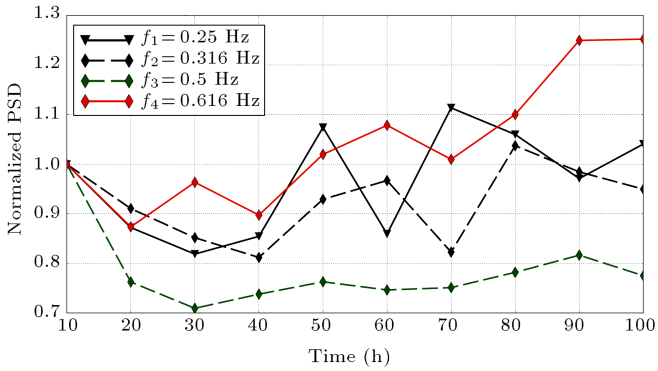

Figure 14. Evolution of the fluctuation parameters of PEMFC stack during 100 hours.

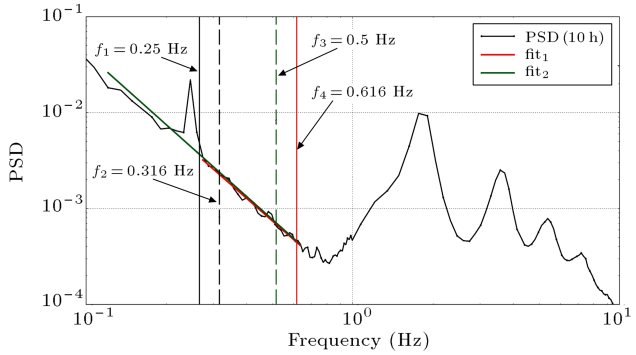

Figure 15. PSD of the first 10 hours with approximations.

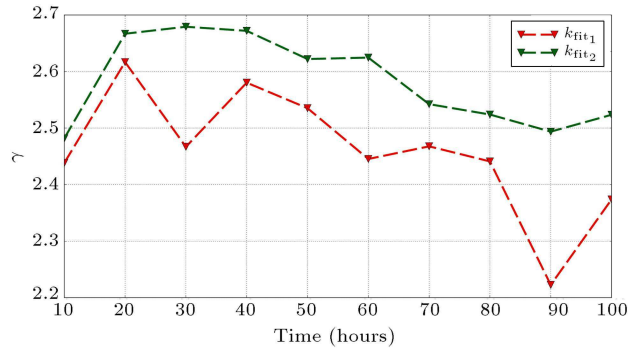

Figure 16. Evolution of the parameters of a flicker noise component over time.

ity of using the flicker-noise parameter γ (see Eq. (12)) to diagnose its technical state. This parameter is calculated as a result of fitting the PSD in double-logarithmic scale by the straight line. This fitting has been performed in two frequency ranges (see Figure 15) of 0.25 Hz to 0.65 Hz (range 1) and of 0.13 Hz to 0.65 Hz (range 2).

As seen in Figure 16, the parameter γ corresponding to the frequency range 2 (Figure 16, k_{fit2}) demonstrates a more stable trend and is more preferable to diagnostic procedures. This fact has strong physical interpretation: Wider frequency range has greater informative value. It should also be noted that the behaviors of parameter γ and PSD parameters at specific frequencies substantially coincide. At initial stages after setting new operation parameters (I = 170A), the parameter γ increases until stable operation condition is achieved. Value of γ after stabilization is equal to 2.67 that corresponds to $\Delta\psi = 0.167$. It means that condensation process slightly predominates over evaporation. After that, the parameter slowly decreases over time. So long as PEMFC stack works under high current density ($j = 0.77\text{A/cm}^2$), heating of membrane intensifies evaporation that leads to decreasing water content within MEA that is evidenced by the parameter γ decreasing. This conclusion is confirmed by the fact that the voltage of PEMFC stack also decreases. Here, we notice that both approaches can be used to organize diagnostics of the PEMFC. Parameter γ is more preferable since it is more stable, but it requires more computational resources for calculation.

5. Conclusions

The possibilities of spectral characteristics of electrical fluctuations of the PEMFC to perform diagnostic procedures for the PEMFC were observed. It has been theoretically shown that water management processes in the MEA involve electrical fluctuations with flicker-noise spectrum. This conclusion is confirmed by the experimental results which show a clear flicker-noise component in low frequency range (less than 10 Hz for a single PEMFC and less than 1 Hz for a PEMFC stack). It has been established that the PEMFC electrical fluctuation characteristic depends on water management processes in the cell. Therefore, analysis of the electric fluctuation provides an opportunity to predict drying or flooding of the membrane electrodes assembly which could lead to a dramatic decrease in the produced power.

On the basis of the experimental data, the frequency range (0.1-1 Hz) convenient as for single cell and as for stack diagnostic purposes was reduced. Analysis of experimental results allows for making the conclusion that the two types of diagnostic features estimated using PSD (flicker-noise parameter γ and PSD values at specific frequencies) sensitive to degradation processes inside the PEMFC can be found. It has been shown that parameter γ is more convenient for diagnostics application; however, parameters of other types are easier to measure.

The preliminary results indicate that noise measurement can be an effective tool for the fuel cell diagnosis, and the obtained results can be used to evaluate the degree of degradation of the object that would allow the control of remaining useful life by changing the FC settings. Thereby, fluctuation diagnosis can allow us to take a new step in the development of diagnostics and prognostics of electrochemical power sources.

Acknowledgements

This work has been supported by the ANR project PROPICE (ANR-12-PRGE-0001) funded by the French National Research Agency.

References

1. Barbir, F., *PEM Fuel Cells - Theory and Practice*, Academic Press (2012).
2. Chen, M., Andreasen, S.J., Rosendahl, L., Kær, S.K. and Condra, T. "System modeling and validation of

a thermoelectric fluidic power source: Proton exchange membrane fuel cell and thermoelectric generator (PEMFC-TEG)", *Journal of Electronic Materials,* **39**(9), pp. 1593-1600 (2010). DOI:10.1007/s11664-010-1270-9

3. Jouin, M., Gouriveau, R., Hissel, D., Pera, M.-C. and Zerhouni, N. "Prognostics and health management of PEMFC - state of the art and remaining challenges", *International Journal of Hydrogen Energy*, **38**, pp. 15307-15317 (2013). DOI:10.1016/j.ijhydene.2013.09.051

4. Petrone, R., Zheng, Z., Hissel, D., Pera, M., Pianese, C., Sorrentino, M., Becherif, M. and Yousfi-Steiner, N. "A review on model-based diagnostics methodologies for PEMFCs", *International Journal of Hydrogen Energy*, **38**, pp. 7077-7091 (2013). DOI:10.1016/j.ijhydene.2013.03.106.

5. Zheng, Z., Petrone, R., Péra, M.-C., Hissel, D., Becherif, M., Pianese, C., Steiner, N.Y. and Sorrentino, M. "A review on non-model based diagnostics methodologies for PEM fuel cell stacks and systems", *International Journal of Hydrogen Energy*, **38**(21), pp. 8914-8926 (2013). DOI:10.1016/j.ijhydene.2013.04.007

6. Wang, R., Zhan, Y. and Zhou, H. "Application of transform in fault diagnostics of power electronics circuits", *Scientia Iranica*, **19**(3), pp. 721-726 (2012). DOI:10.1016/j.scient.2011.06.013

7. Evdokimov, Yu.K., Denisov, E. and Martemianov, S. "Hydrogen fuel cell electrical noise and study of its diagnostics properties", *Nonlinear World*, **7**(9), pp. 706-713 (2009).

8. Martemianov, S., Adiutantov, N., Evdokimov, Y.K., Madier, L., Maillard, F. and Thomas, A. "New methodology of electrochemical noise analysis and applications for commercial li-ion batteries", *Journal of Solid State Electrochemistry*, **19**(4), pp. 1-8 (2015). DOI:10.1007/s10008-015-2855-2

9. Evdokimov, Yu. and Denisov, E. "Fluctuation-noise diagnostics of optical system power supply units based on fuel cell", *Proc. SPIE 8787*, pp. 87870E-87870E-11 (2013). DOI:10.1117/12.2020894

10. Claycomb, J.R., Brazdeikis, A., Miller, J.H., et al. "Nondestructive testing of PEM fuel cells", *IEEE Transactions on Applied Superconductivity*, **13**(2), pp. 211-214 (2003). DOI:10.1109/TASC.2003.813687

11. Zhang, F.Y., Yang, X.G. and Wang, C.Y. "Liquid water removal from a polymer electrolyte fuel cell", *Journal of The Electrochemical Society*, **153**(2), pp. A225-A232 (2006). DOI:10.1149/1.2138675

12. Fang, S.-Y., Teoh, L.G., Huang, R.-H., Chao, W.-K., Lin, T.-J., Yang, K.-C., Hsueh, K.-L. and Shieu, F.-S. "Effect of adding zinc oxide particles to the anode catalyst layer on the performance of a proton exchange membrane fuel cell", *Journal of Electronic Materials,* **43**(9), pp. 3601-3610 (2014). DOI:10.1007/s11664-014-3246-7

13. Katzel, J., Markotter, H., Arlt, T., Klages, M., Haussmann, J., Messerschmidt, M., Kardjilov, N., Scholta, J., Banhart, J. and Manke, I. "Effect of ageing of gas diffusion layers on the water distribution in flow field channels of polymer electrolyte membrane fuel cells", *Journal of Power Source*, **301**, pp. 386-391 (2016). DOI:10.1016/j.jpowsour.2015.10.004

14. Khazaee, I., Ghazikhani, M. and Mohammadiun, M. "Experimental and thermodynamic investigation of a triangular channel geometry PEM fuel cell at different operating conditions", *Scientia Iranica*, **19**(3), pp. 585-593 (2012). DOI:10.1016/j.scient.2011.11.039

15. Liu, X., Guo, H. and Ma, C. "Water flooding and two-phase flow in cathode channels of proton exchange membrane fuel cells", *Journal of Power Sources*, **156**, pp. 267-280 (2006). DOI:10.1016/j.jpowsour.2005.06.027

16. Song, M., Pei, P., Zha, H. and Xu, H. "Water management of proton exchange membrane fuel cell based on control of hydrogen pressure drop", *Journal of Power Sources*, **267**, pp. 655-663 (2014). DOI:10.1016/j.jpowsour.2014.05.094

17. Thomas, A., Maranzana, G., Didierjean, S., Dillet, J. and Lottin, O. "Thermal and water transfer in PEMFCs: Investigating the role of the microporous layer", *International Journal of Hydrogen Energy*, **39**, pp. 2649-2658 (2014). DOI:10.1016/j.ijhydene.2013.11.105

18. Zaffou, R., Yi, J.S., Kunz, H.R. and Fenton, J.M. "Temperature-driven water transport through membrane electrode assembly of proton exchange membrane fuel cells", *Electrochemical and Solid-State Letters*, **9**(9), pp. 418-422 (2006). DOI:10.1149/1.2218306

19. Zhan, Z., Wang, C., Fu, W. and Pan, M. "Visualization of water transport in a transparent PEMFC", *International Journal of Hydrogen Energy*, **37**, pp. 1094-1105 (2012). DOI: 10.1016/j.ijhydene.2011.02.081

20. Erdelyi, A., *Tables of Integral Transforms*, **1**, McGraw-Hill Inc. (1954).

Biographies

Evgenii Denisov is an Associate Professor of Department of Radio-Electronic and Information & Measuring Technology of Kazan National Research Technical University named after A.N. Tupolev-KAI (KNRTU-KAI). He received his PhD degrees in 2011 from University of Poitiers, France, and in 2012 from KNRTU-KAI. His research interests focus on technical diagnostics of electrochemical systems, hydrogen energetics, and digital signal processing.

Yury K. Evdokimov is a Full Professor, Head of Department of Radio-Electronic and Information &

Measuring Technology (RIIT) in Kazan National Research Technical University named after A.N. Tupolev-KAI (KNRTU-KAI). His main research interest is inverse operator problem and its applications in measuring technique, acoustics, and electrochemistry; fractal geometry and fractional operators for analysis and synthesis complex system; automation of measurement, control, and diagnosis; sensors.

Raoul Rashid Nigmatullin was born in Kazan, Tatarstan Republic, Russian Federation in 1947 year. He finished Kazan State University with honors in 1970 year. He defended his PhD thesis successfully in 1974 year, then his Doctorate thesis in 1992 year. As of 1997, he has become a Full Professor of the Theoretical Physics Department in Kazan State University. Before 2015, he has worked in Kazan Federal University. Since 2015, he has been working in Kazan National Research Technical University (KNRTU-KAI) in Radioelectronic and Informative-Measurements Technics Department. His scope of scientific interests is rather high and includes the fractal geometry, fractional calculus, dielectric spectroscopy, and development of new statistical methods for treatment of different random sequences. He is the author of more than 200 publications, and as the leading Russian scientist, he has more than 2000 citations.

Serguei Martemianov is a Full Professor of Chemical & Energy Engineering in University of Poitiers, France. He received his PhD degree in 1976 from Moscow State University, Russia. Afterwards, he has worked in Frumkin Institute of Electrochemistry (Moscow), INP de Grenoble (France) and in University of Poitiers since 1996. He is the author of monograph "Turbulent Diffusion Layer in Electrochemical Systems" and more than 100 articles in international journals. His research interests include turbulent mass transfer, transfer processes in electrochemical systems, electrochemical energetics (fuel cells, batteries), modeling of near interface transfer processes, and development of new instrumentation methods.

Anthony Thomas is an Associate Professor of Mechanical & Energy Engineering in University of Poitiers, France. He received his PhD degree in 2012 from University of Lorraine, France. His research interests include charge transfer, heat transfer, and mass transport into electrochemical systems, as PEM Fuel Cell & Electrolyser and Battery and associated metrology development.

Nikolai Adiutantov received his Diploma of Specialist in Information Security from Kazan Federal University, Kazan in 2012. He is currently pursuing his joint PhD degree in University of Poitiers, France and at Kazan National Research Technical University named after A.N. Tupolev-KAI (KNRTU-KAI). His primary research interest is focused on technical diagnosis of fuel cells, Li-ion batteries, etc.

Quasi-distributed resistive sensor for steady-state field measurements

E. Denisov, N. Adiutantov, Yu.K. Evdokimov,
A. Salakhova, G. Timergalina, T. Nikishin
Radio-Electronic and Information & Measuring Technology Department, Kazan National Research Technical University named after A.N. Tupolev - KAI
Kazan, Russian Federation
genia-denisov@yandex.ru

S. Martemianov, A. Thomas
Institut Pprime, UPR 3346 CNRS,
Université de Poitiers,
Poitiers, France
serguei.martemianov@univ-poitiers.fr

Abstract — **The quasi-distributed sensor allowing measuring of steady-state temperature fields has been proposed. The sensor comprises of thin sensing resistive elements arranged in grid structure. The sensor can be used in the system wherein only external boundary is available for measurement equipment connection such as PEMFC membrane electrode assembly. The proposed sensor can be adapted to measure other physical fields such as mechanical tension, deformations, etc.**

Keywords—distributed sensor; resistive sensor; themperature fields; measurement.

I. INTRODUCTION

Most of processes in technical systems can be considered as spatial-temporal fields (STF) of different physical nature. Such fields allow to describe state of the corresponding system with distributed parameters (SDP). Control of technical systems is based on measuring and monitoring conditions of the SDP. Here we can provide examples of mechanical stresses of building structures, temperature distribution within combustion chambers, etc. Therefore modern methods of accurate measurement of information about spatial-temporal fields are required. Consequently, development of new effective methods and devices of obtaining information about the state of SDP is an important task.

All of existing STF measurement techniques can be classified into three categories depending on the nature of contact which exists between the measuring device and object: (1) invasive (direct contact between measurement device and observed object, e.g., a thermocouple in a gas stream); (2) semi-invasive (remote observation of object properties, e.g., surface coatings whose color changes with temperature); (3) noninvasive (remotely sensed observations, e.g., infrared thermography). Nowadays, there are a lot of procedures of temperature measurements: (1) usage phase mapping based on use of the temperature dependence of the water proton chemical shift [1]; (2) usage high-intensity focused ultrasound therapy [2,3]; (3) IR methods, (4) usage continuously distributed sensors [4] (4) classical methods based on thermocouples, thermo resistors (5) and others. Conventional techniques and sensors allow to measure local, point-by-point characteristics of physical fields. Therefore it is required to use discrete distributed sensors (DDS) composed of many sensors leading to a considerable complication of the measuring equipment that affects on significant material costs.

STF measurement for diagnosis allows increasing operational characteristics, namely durability and reliability, for various technical systems, for example for Solid Oxide Fuel Cell (SOFC) operating at high operational temperatures (600 °C - 1000 °C). The main important component of SOFC design is the presence of uniform temperature distribution and minimization of thermal stresses between its components due to temperature difference [5]. Therefore, knowledge of temperature distribution allows obtaining the current density distribution within the SOFC stack [6].

The other example is Proton Exchange Membrane Fuel Cell (PEMFC) which is one of the most effective and perspective energy sources. However PEMFC performance significantly depends on operating conditions of its components first of all on temperature and water balance within membrane-electrodes assembly (MEA). Temperature distribution over membrane is very important characteristic since it defines conductivity of membrane and can be used as indicator of current distribution. The non-uniform distribution of current may induce local overheating and breakage of membrane. Thus the measurement of temperature distribution is very important parameter for further understanding physical processes inside PEMFC and improvement of its design.

One of the common ways of temperature measurement is usage of thermocouples due to their low cost, simplicity, robustness, size, and temperature range. In spite of the fact that their sensitivity as well as their response time are sufficient for many applications, they are less accurate than resistance temperature devices [7]. As mentioned above, for STF measurements it's required to use set of discrete sensors installed on the object, which may effect on procedure of measurement due to their quantities. However, in framework of this paper, circuit and its measurement procedure are proposed to eliminate of using complex equipment.

The reported study was funded by RFBR according to the research project No. 16-38-00464 мол_а

978-1-4673-8383-7/16/$31.00 ©2016 IEEE

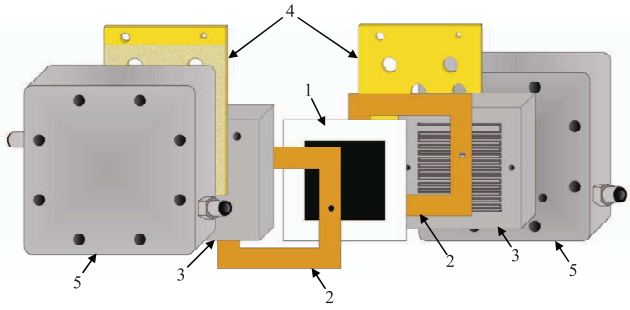

Fig. 1 PEM fuel cell construction: 1. – membrane electrodes assembly; 2. – gaskets; 3. – bipolar plates with gas transport channels; 4. – current collector plates; 5 – anode and cathode end plates.

II. Distributed Sensor

A. Distributed Sensor Structure

PEMFC is a complex technical system having a large number of components (Fig. 1): membrane electrode assembly, bipolar plates, current collectors, casing, etc.

MEA is the most important part of a PEMFC. It consists of polymer proton exchange membrane, porous electrodes and catalyst layer. For correct operation the membrane should be humidified and heated. Additional heat is generated by electrical current passing through membrane. Nonhomogeneous heating of membrane may lead to reducing PEMFC efficiency and even to mechanical breakage of membrane. Nonhomogeneous heating can be caused by a number of reasons such as nonuniform distribution of catalyst, nonuniform current distribution, etc. Therefore development of a reliable tool for temperature distribution over membrane of PEMFC is required. The tool should have high accuracy and negligible effect on PEMFC operation processes. The problem consists in that the electrodes have a large surface and are in close contact with membrane thus use of convenient sensors are almost impossible due to presence of large numbers of connecting wires.

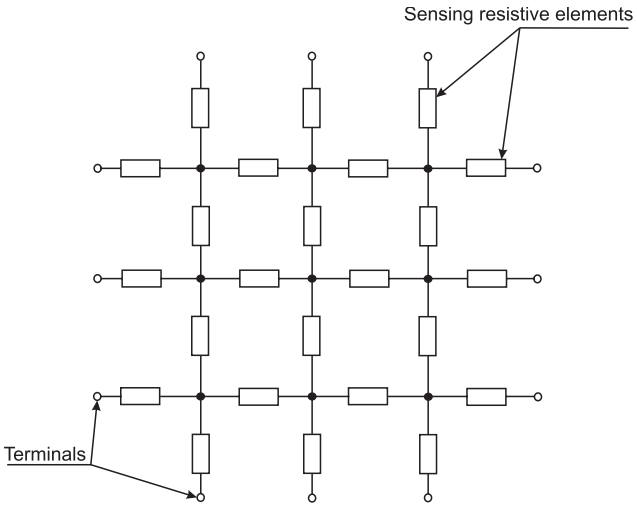

Fig. 2 Quasi-distributed resistive sensor.

To solve this problem a quasi-distributed resistive sensor is proposed. Distributed sensor consists of a number of spatial diversity sensible elements (Fig. 2). All sensing elements are the resistive elements of the same type (they should have sensitive to the same physical parameters and have the similar characteristics). The sensing elements are connected in grid structure as shown in Fig. 2. As we can only external terminals are available for the measurement equipment.

B. Princeples of Measurement

The measurement procedure of sensor is based on the following idea: calculate values of resistance basing on measured potentials of external terminals for different current distributions. To describe the procedure more accurate let us designate resistances and terminals as shown in Fig. 3. For clarity, only the case of square sensor topology, when the number of rows of the sensing elements is equal to the number of their columns, is considered. However all the conclusions will be also applicable for any rightangled topology.

If a current source I is connected between any two terminals as exemplarily shown in Fig. 4(a) it is possible to obtain a system of equations in accordance with convenient nodal analysis:

$$\mathbf{G} \cdot \vec{V} = \vec{j} \qquad (1)$$

here $\mathbf{G}$ is a conductance matrix, $\vec{V}$ is a nodal voltages vector, $\vec{j}$ is a current vectors. The conductance vector $\mathbf{G}$ is defined by the unknown resistors $R_{i,j}$. The number of resistors is $2N(N+1)$, where N is a number of intrinsic nodes in a row or a column of sensing elements. For the exemplary topology (Fig. 3) $N = 3$. Since we can directly measure potential of intrinsic nodes adjoining the external terminal, vector $\vec{V}$ comprises only N^2-4·(N-1) unknown potentials. It is obvious that the number of unknown variables $2N(N+1)+N^2$-4·(N-1) is less the number N^2 of equations in the system (1). However if we change current distribution by connection the current source to other terminals it becomes possible to obtain new systems comprising N^2 new equations and only N^2-4·(N-1)

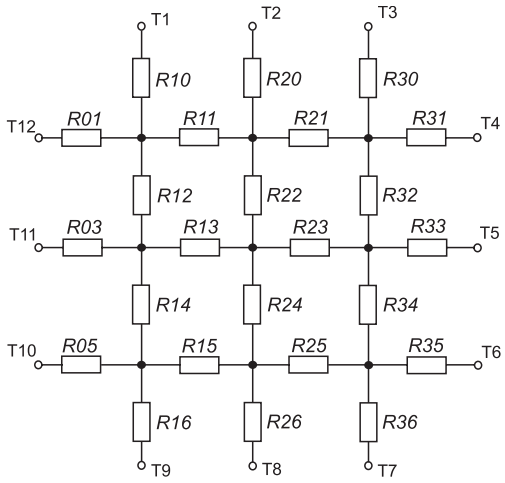

Fig. 3 Designations of quasi-distributed resistive sensor

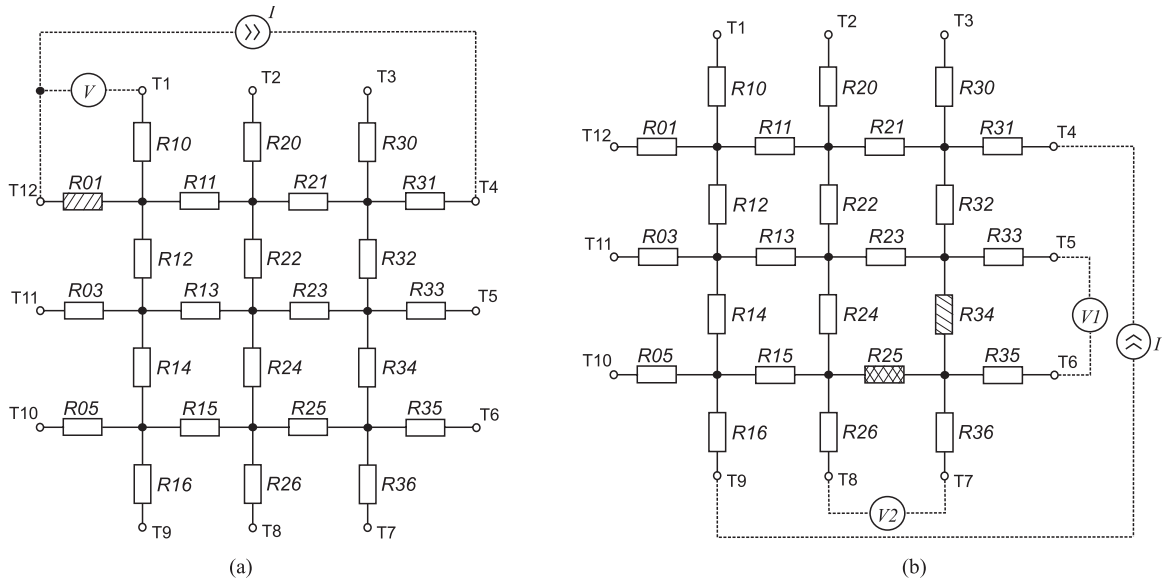

Fig. 4. Power sources and measurement equipment connection to the quasi-distributed resistive sensor

new unknown variables. It follows from the assumption that values of resistances still constant during the measurement procedure. After k iterations the system will comprise $2N(N+1) + k(N^2-2N+2)$ unknown variables and kN^2 equations. Consequently the following condition

$$2N(N+1) + k(N^2 - 2N + 2) < kN^2 \quad (2)$$

shall be true to have a possibility to solve equation and to calculate required values of resistances. Let us simplify the condition (2)

$$k > N(N+1)/(N-1). \quad (3)$$

Since the maximal value for k is a number of a 2-combination of a set $4N$ it can be shown that the considered extended system of equation can be solved for any N. In other words we proposed approach allows to obtain enough information to determine all resistances of the distributed sensor.

However the solution of the equation is difficult due to a great number of unknown variables and complex character of the equations. Therefore it was elaborated an iterative procedure allowing determining all resistances of the sensor.

1) External corner resistances

If the current source I is connected between terminals T_{12} and T_4 (Fig. 4(a)), the resistance R_{01} can be found as

$$R_{01} = (V_{T1} - V_{T12})/I, \quad (4)$$

where V_{T1}, V_{T12} are potential of the terminals T_1 and T_{12}. Here and below we suppose that the measurement equipment has high impedance and its input current can be neglected. The resistances R_{05}, R_{16}, R_{36}, R_{35}, R_{31}, R_{30}, R_{10} are determined by the same way.

2) Internal corner resistances

If we connect the current source between terminals T_4 and T_9 (Fig. 4(b)), the same current passes through resistances R_{25} and R_{34}. Thus it is possible to estimate ratio

$$R_{34}/R_{25} = (V_{T5} - V_{T6})/(V_{T7} - V_{T8}), \quad (5)$$

Let us connect the current source between T_4 and T_9 then the resistors R_{25} and R_{34} can be found as

$$R_{34} = (V_{T7} - V_{T5} + R_{34}/R_{25}\cdot(V_{T7} - V_{T8}))/I, \quad (6)$$

$$R_{25} = R_{34}/(R_{34}/R_{25}), \quad (7)$$

The resistances R_{11}, R_{12}, R_{21}, R_{32}, R_{14}, R_{15} are determined by the same way.

3) Middle external resistances

The resistor R_{26} can be determined as

$$R_{26} = (V_{T9} - V_{T7} + (V_{T5} - V_{T6})R_{25}/R_{34})/I, \quad (8)$$

when the source I is connected to terminals T_4 and T_8. Similarly the resistances R_{03}, R_{20}, R_{33} can be found.

4) Internal resistances

Let us calculate resistances R_{23} and R_{24}. Currents through resistances R_{23} and R_{24}

$$i_{24} = (V_{T7} - V_{T8})/R_{25} + (V_{T8} - V_{T10})R_{15}, \quad (9)$$

$$i_{23} = (V_{T7} - V_{T5})/R_{34} + (V_{T5} - V_{T4})R_{32}, \quad (10)$$

when the source I is connected between T_9 and T_3, and

$$i'_{24} = (V'_{T7} - V'_{T8})/R_{25} + (V'_{T8} - V'_{T10})R_{15}, \quad (9)$$

$$i'_{23} = (V'_{T7} - V'_{T5})/R_{34} + (V'_{T5} - V'_{T4})R_{32}, \quad (10)$$

when the source I is connected between T_{12} and T_6.

Taking into account what resistances R_{23} and R_{24} have the common point the values of resistances can be found according to the following equations:

$$R_{24} = (i'_{24}(V_{T5}\text{-}V_{T8}) + i_{24}(V'_{T5}\text{-}V'_{T8}))/(\, i_{24}i'_{23}\text{-}i_{23}i'_{24}), \quad (9)$$

$$R_{23} = (i'_{23}(V_{T5}\text{-}V_{T8}) + i_{23}(V'_{T5}\text{-}V'_{T8}))/(\, i_{24}i'_{23}\text{-}i_{23}i'_{24}), \quad (10)$$

The procedure of determination of the resistances R_{13}, R_{22} is analogous.

The described approach can be generalized for the bigger sensor comprising a greater number of sensitive elements. In this case the intrinsic layer of sensitive elements can be determined on the basis of the adjoined elements estimated during the previous step.

III. Model and Experimental Verification

The measurement procedure considered in the previous section is relatively complex. To check the applicability of the approach for real measurements, model and experimental verifications have been realized.

Quasi-distributed resistive sensor modeling was performed in Multisim of National Instruments Inc. in accordance with the design provided in Fig. 2. The following values of resistors have been chosen $R_{13} = R_{34} = 1.1$kOhm, $R_{22} = R_{25} = 2$kOhm and the others of 1kOhm. All measurements were carried out according to the measurement procedure described above. Simulation results showed that all nominal values of resistors can be found. In real-life environments, measurement equipment includes intrinsic noise. Therefore, to estimate noise influence on measurement procedure, simulation for several different intrinsic noise values were performed.

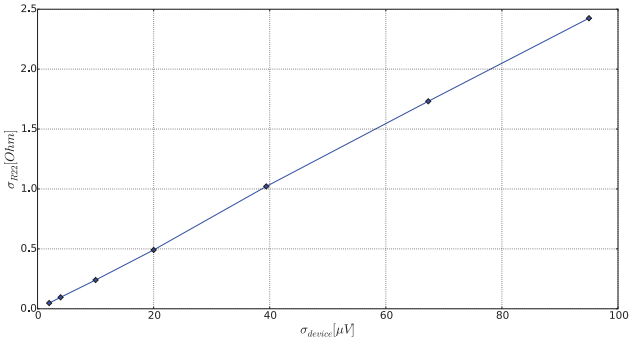

Fig. 5. Dependence of standard deviation of the measured resistor R22 on the intrinsic noises of measurement equipments.

TABLE I. Experimental Results

Resistor number	Value of resistor [Ohm]	
	Nominal (0.1% tolerance)	*Measured*
R01	1k	998.804
R03	1k	999.262
R05	1k	998.883
R10	1k	999.419
R12	1k	999.901
R14	1k	999.609
R16	1k	999.236
R11	1k	999.336
R13	1.1k	1101
R15	1k	998.782
R20	1k	999.063
R22	2k	2003
R24	1k	999.321
R26	1k	999.296
R21	1k	999.212
R23	1k	1000
R25	1.1k	1100
R30	1k	998.912
R32	1k	999.140
R34	2k	2002
R36	1k	999.090
R31	1k	999.030
R33	1k	999.090
R35	1k	999.284

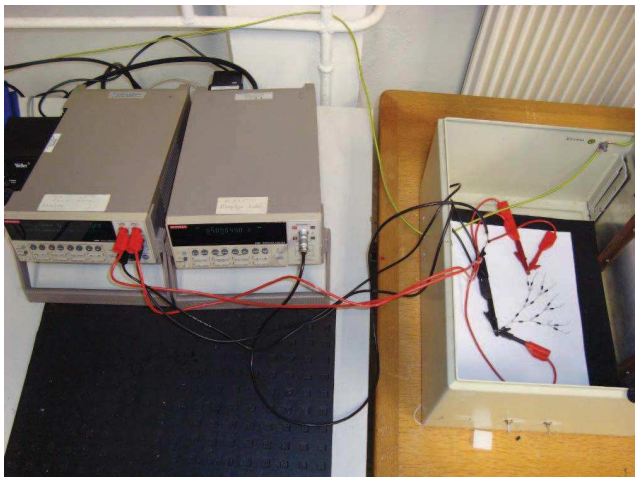

Fig. 6. Measurement equipment used to sensor data acquisition.

The results of simulation for the resistor R_{22} are provided in Fig. 5. This resistor has been chosen since it is one of the most difficult to determine in accordance with the proposed approach. As it can be seen from Fig. 5, there is linear dependence of the estimated resistance standard deviation on the standard deviation of the measurement equipment intrinsic noise. It can be found that the intrinsic noise of measurement equipment should not exceed the value of 20μV to obtain appropriate level of accuracy.

The provided approach has been also verified experimentally. Voltage measurements were performed by dedicated experimental equipment based on 2400-SourceMeter and 2182-Nanovoltmeter of Keithley allowing to perform measurements with a microvolt resolution within the range of 10V (Fig. 6). For the experimental verification the sensor has been presented as resistive circuits of Fig. 2 comprising resistors of 0,1% tolerance. The values of resistors and results of calculation are presented in Table 1. Analysis of the table allows to conclude that the accuracy of resistance measurement are better than 0,1%. This fact confirms that the proposed approach can be used to measure resistances of internal resistances with the accuracy enough to built temperature distributed sensor.

IV. Results and discussion

It has been shown a possibility of measurement resistances of grid structure using only external terminals. The accuracy of the measurements is enough to develop a distributed sensor allowing to measure the distributed physical parameters (temperature, pressure, mechanical stress and others).

The proposed distributed sensor consists of a large number of spatial diversity sensible elements. The sensor comprises of thin sensing resistive elements arranged in grid structure. All of sensing elements have the same type (they sensitive to one physical parameter and have similar characteristics) and based on resistive nature. The sensor can be fabricated from metal wires which are welded/soldered to each other and covered by passivating coating such as oxide layer or other.

Measurement procedure includes the following steps:

a) Connection of a current supply between two external terminals to produce some distribution of current;

b) Measurement of the external terminal voltages;

c) Calculation of resistances of sensing elements in accordance with approach disclosed in the Part II.

Thus the sensor has the following advantages:

(1) It allows to measure the distribution of physical field inside observed object, distributed physical parameters that are inaccessible for other measurement methods (sensor can be placed inside the object during its production, for example, in the membrane-electrode assembly of PEMFC, building constructions, etc.);

(2) Sensor is passive;

(3) It has a small sizes;

(4) It is simple for design and fabrication.

V. Conclusion

In this work, sensor design and corresponding measurement methodology allowing to determine physical field inside an object under test are proposed. Measurements of distributed physical fields are important to better understanding physical processes within different objects and to diagnose their technical state and can be provided by the proposed sensor. The sensor can be placed inside the object during its production. For example, it can be used effectively to measure temperature distribution within membrane-electrode assembly of proton exchange membrane fuel cells, building constructions, etc. The proposed sensor design was validated successfully using model and experimental data. It was approved that high accuracy can be provided by the sensor.

References

[1] Y. Ishihara, A. Calderon, H. Watanabe, K. Okamoto, Y. Suzuki, K. Kuroda and Y. Suzuki,. “A precise and fast temperature mapping using water proton chemical shift”, Magnetic Resonance in Medicine, vol. 34(6) , pp. 814-823, 1995.

[2] M. Pernot, M. Tanter, J. Bercoff, K.R. Waters, and M. Fink, “Temperature estimation using ultrasonic spatial compound imaging”, Ultrasonics, Ferroelectrics, and Frequency Control, IEEE Transactions, vol. 51(5), pp. 606-615, 2004.

[3] C. Simon, P. VanBaren, and E. S. Ebbini, “Two-dimensional temperature estimation using diagnostic ultrasound”, Ultrasonics, Ferroelectrics, and Frequency Control, IEEE Transactions, vol. 45(4), pp. 1088-1099, 1998.

[4] Y.K. Evdokimov and S. Martemianov, “Continuously distributed sensors for steady-state temperature profile measurements: main principles and numerical algorithm”, International journal of heat and mass transfer, vol. 47(2), pp. 329-340 (2004).

[5] W.B. Guan H.J. Zhai, L. Jin, C. Xu and W.G. Wang, “Temperature measurement and distribution inside planar SOFC stacks”, Fuel cells, vol. 12(1),pp. 24-31.

[6] S. Celik, B. Timurkutluk and M.D. Mat, “Measurement of the temperature distribution in a large solid oxide fuel cell short stack”, International Journal of Hydrogen Energy, vol. 38(25),pp. 10534-10541 (2013).

[7] P.R.N. Childs, J.R. Greenwood and C.A. Long, “Review of temperature measurement”, Review of scientific instruments, vol. 71(8), pp. 2959-2978, (2000).

DOI: 10.1002/fuce.201600077

Electrochemical Noise as a Diagnostic Tool for PEMFC▲

E. S. Denisov[1]*, Y. K. Evdokimov[1], S. Martemianov[2], A. Thomas[2], N. Adiutantov[1,2]

[1] Kazan National Research Technical University named after A.N. Tupolev – KAI, 10, K. Marx st., 420111 Kazan, Russian Federation
[2] Institut Pprime, UPR 3346 CNRS, Université de Poitiers, ENSMA, Batiment B25: 2, rue Pierre Brousse – TSA 41105 – 86073 Poitiers Cedex 9, France

Received April 08, 2016; accepted September 21, 2016; published online ■■■

Abstract

A promising direction for improving proton exchange membrane fuel cells (PEMFCs) is the increase of their reliability and operating time without failure. Therefore, the problem of a reliable diagnostic tool is important. It has been theoretically deduced that a non uniform current distribution causes the increase of power spectral density of the flicker-noise component of electrical fluctuations, which was experimentally confirmed for the case of excess humidification. Theoretical investigations allow to conclude that other reasons of current non uniformity, for example incorrect stoichiometry, can lead to similar results as well. Experimental findings show that the behavior and parameters of electrical fluctuations depend on the fuel cell operation mode and technical state of its components. This paper shows that electrical fluctuations reflect physical processes inside the fuel cell. Thus, the electrical fluctuations can be considered as a reliable diagnostics tool for PEMFC.

Keywords: Current Distribution, Current Distribution Measurement, Electrical Fluctuations, Fuel Cell Monitoring, PEMFC, Water Management

1 Introduction

The search for the most efficient power plants and engines is required to solve the problem of depleting fossil fuels and to build a new necessary infrastructure for energy delivery from a power source to an end consumer. A promising direction for developing power sources is hydrogen energy, especially proton exchange membrane fuel cell (PEMFC) which has low emissions and high efficiency (in theory 83%, in practice 40–50%, with hydrogen as fuel around 50%) [1–3]. PEMFC operates at the temperature range 50–90 °C, provides high current density (more than 1 A cm^{-2}) and a fast output power response when energy needs are changing [3].

In spite of the fact that these systems have many advantages, they have unsolved challenges of increasing reliability and durability up to a level that pushes their wide commercial utilization [3]. PEMFC power source is a complex system which contains PEMFC stack and many auxiliaries, e.g., air pumps and fans, mass flow controllers, reactant storages, gas humidifiers and purifiers, a temperature controlling system etc. that are responsible for maintaining the stack in operating conditions, which provides the demanded power output over the required lifetime.

The requirement of a long-term operation is hard to define due to the complexity of the system, physical and chemical processes, as well as the degradation of PEMFC components. An analysis of degradation phenomena was made by Jouin et al. [4]. According to [4], the proton exchange membrane and electrodes with catalyst layers are key elements of non-nominal operation, which most likely lead to failures, system degradation or even its death.

One of the main purposes of a polymer membrane is to transport protons from one electrode to another and to prevent electrons transfer and crossover of reactant gases [5]. The ionic conductivity of such membranes strongly depends on the temperature and water content, which should be maintained in the optimal ranges [6]. Poor water management may lead to degradation phenomena within PEMFC due to the following reasons: membrane electrodes assembly (MEA) dehydration or flooding, corrosion of electrodes, catalyst layers,

▲ *Paper presented at the 6th International Conference on Fundamentals and Development of Fuel Cells (FDFC2015), February 3 – 5, 2015 held in Toulouse, France.*

[*] *Corresponding author, genia-denisov@yandex.ru*

 © 2016 WILEY-VCH Verlag GmbH & Co. KGaA, Weinheim

and other components [7]. The mentioned reasons can cause the decrease in the electrochemical active surface area (ECSA) of electrodes, forming a non uniform current distribution, mechanical stresses, etc. [4, 6–10]. The non uniform current distribution may lead to local overheating that causes the degradation of a membrane, which can take place in case of an unfavorable transient operation or poor water management [4]. Appropriate management of stoichiometry is also a major factor determining the lifetime of PEMFC [3].

Thus, PEMFC operation is determined by a large set of parameters (pressure, humidity of supplied gases, cell temperature, electrical operational mode, etc.). It substantially depends on the actual technical state of the membrane electrode assembly and gas transport channels considerably influencing energy conversation efficiency and the stability of operation. Thereby, the important issue for improving PEMFC power sources is understanding degradation mechanisms and early detection of effects caused by the mechanisms.

There are a lot of methods to diagnose PEMFC technical state [4, 11], but some of them can be singled out. For example, the transparent fuel cell allows to visualize water accumulation processes inside the fuel cell [12]. Neutron radiography is an imaging technique allowing to see water distribution across the membrane electrolyte assembly (MEA) through graphite of bipolar plates, which are commonly used for fuel cells, without any perturbation of FC operation [13]. Shimpalee et al. [14] studied distributions of current, temperature by three-dimensional electrochemical model for commercial PEMFC systems. Gagliardo et al. [15] investigated PEMFC operation with neutron radiography and a segmented circuit board to localize the current distribution. However, commercial implementation of diagnosis system may increase installation costs. Therefore, an effective tool is required to diagnose the technical state of PEMFC and in particular to detect an inhomogeneous current distribution which can speed up degradation processes inside PEMFC.

One of the promising ways to solve the problem is the use of diagnostic capabilities of PEMFC current or voltage fluctuations. Electrical fluctuations are inherent properties of any electrochemical system and could be used to direct characterization of its state. Diagnostic methods based on electrochemical noises are widely used for studying metal films and corrosion of electrodes [16–19], quality of passivation coatings [20, 21], estimation of state-of-charge and detection of overcharge for electrochemical batteries [22, 23], etc. An essential advantage of noise (fluctuation) method is absence of any perturbation of the electrochemical system by external probing signals. Fluctuations in electrochemical systems introduced by turbulent fluctuations of electrolyte (turbulent noise) have been intensively studied from the theoretical and experimental points of view in [24–28]. The approaches which allow estimating the technical state of electrochemical power sources are presented in [23, 29–35].

The main goal of the presented research is to develop a new approach which allows for detecting a non uniform current distribution based on PEMFC electrical fluctuation measurement. The importance of this work is confirmed by the fact that the non uniform current distribution is an indicator of incorrect and inhomogeneous operation of PEMFC.

2 Electrical Fluctuations and their Diagnostic Capabilities

2.1 PEMFC Electrical Fluctuations

Electrical fluctuations observed during PEM fuel cell operation can be divided into two large groups: (i) electrical noises (thermal, short, generation-recombination, and flicker) and (ii) fluctuations caused by the random variation of electrical parameters of FC components.

Stochastic variations of FC components physicochemical parameters are observed during the FC operation process. The fluctuation of polymer membrane resistance, electrochemical reaction rates, diffusion coefficients and thickness of a double electrical layer are caused by the inconstancy of membrane electrode assembly (MEA) humidification modes, temperature and gas pressure control [36]. These fluctuations create stochastic variations of intrinsic FC electrical impedance $\delta Z_{FC}(\omega, t)$ and, as a consequence, an electrical current δI and voltage δV fluctuations (Figure 1).

Statistical parameters of fluctuations depend on the present fuel cell's physical and chemical state and potentially have capacities, which allow implementation of FC components technical diagnostics [23, 29, 33, 34, 37]. In other words, the analysis of FC electrical current and voltage fluctuations will allow to obtain information about the actual values of membrane resistance, electrochemical reaction rate, and states of gas-diffusion and catalytic layers.

2.2 Hydrogen Fuel Cell Electrical Fluctuation Capabilities

FC electrical noise diagnostic capacities can serve as an example of electrical current nonuniformity caused by insufficient oxygen supply, which leads to a considerable decrease in FC reliability and unstable operation.

It has been shown in articles [29, 36] that FC electrical fluctuations have a large flicker-noise component. It means that the power spectral density of this component could be described by Hooge's Eq. (1) [38, 39]:

$$S_I(f) = \frac{\alpha_H \cdot I_0^2}{N \cdot f^{\gamma}} \tag{1}$$

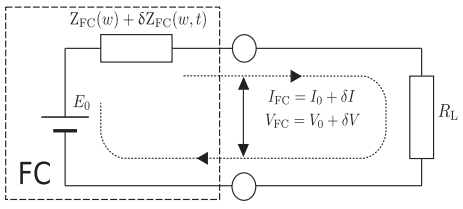

Fig. 1 Origin of FC electrical current and voltage fluctuation.

 © 2016 WILEY-VCH Verlag GmbH & Co. KGaA, Weinheim

where I_0 is an electrical current flow through the studied specimen, α_H is the Hooge parameter, N is a total number of charge carriers in specimen, f is the frequency in Hz, γ is a fractional exponent.

The current density through membrane, in a generic case, could be expressed as the function of two variables $j(x, y)$, where x, y are Cartesian coordinates (Figure 2). The vector of current density $j(x, y)$ is perpendicular to the surface of the membrane (xy-plane). The surface is remapped to a rectangular shape, which is presented by a rectangle with L_x and L_y lateral lengths on elementary $\Delta S = \Delta x \cdot \Delta y$ plots (Figure 2). In this case, constant electrical current flowing through elementary ΔS plot cross-section with $(i\Delta x, j\Delta y)$ coordinates is equal to

$$I_{i,j} = j(i\Delta x, j\Delta y)\Delta S \tag{2}$$

that results in flicker-noise appearance according to Eq. (1):

$$S_I(f, i\Delta x, j\Delta y) = \frac{\alpha_H j^2(i\Delta x, j\Delta y)(\Delta S)^2}{C \cdot \Delta S \cdot h \cdot f^\gamma} \tag{3}$$

where C is charge carriers concentration in membrane, h is membrane thickness.

In accordance with experimental data [38, 40] it is possible to assume the correlation between current flicker-noises in various points of membrane as weak. Therefore, the power spectral density (PSD) of a total flicker-noise signal could be estimated as an algebraic sum of particular spectral densities:

$$S_I(f) = \sum_{j=0}^{N_y} \sum_{i=0}^{N_x} s_I(f, i\Delta x, j\Delta y) \tag{4}$$

or

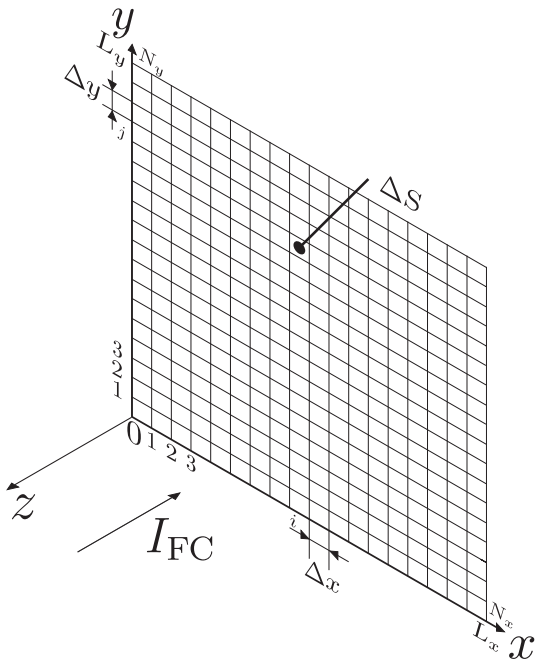

Fig. 2 Membrane surface decomposition on elementary plots ΔS.

$$S_I(f) = \sum_{j=0}^{N_y} \sum_{i=0}^{N_x} \frac{\alpha_H \cdot j^2(i\Delta x, j\Delta y) \cdot \Delta S}{C \cdot h \cdot f^\gamma} \tag{5}$$

If $\Delta S \to 0$, an integral is obtained over the membrane surface

$$S_I(f) = \int_{S_0} \frac{\alpha_H j^2(x, y)}{C \cdot h \cdot f^\gamma} dS \tag{6}$$

where $S_0 = L_x \cdot L_y$ is the total active surface of a FC polymer membrane. Thus, PSD of flicker-noise signal is proportional to surface integral Eq. (6) calculated on active membrane surface.

If $\alpha \cdot S_0$ part of membrane surface S_0 is blocked, the current flow through this part is also blocked or strongly reduced. The reason for such blockage could be membrane overheating, blockage of catalyst surface by condensate or membrane defects, or an inhomogeneous distribution of active catalyst. It can be assumed that current distribution along unblocked membrane $(1–\alpha)S_0$ surface is homogeneous. When the FC is operated under galvanostatic mode, wherein the current is considered as constant

$$I_{FC} = I_0 = \text{const.} \tag{7}$$

the current distribution through unblocked membranes surface can be estimated by the next equation

$$j(x, y) = \frac{I_0}{S_e} = \frac{1}{1 - \alpha} \frac{I_0}{S_0} \tag{8}$$

where S_e is the electrochemical active surface area (ECSA), S_0 is a whole membrane surface, $\alpha = S_e / S_0$ is the parameter of membrane surface usage efficiency.

The power spectral density of current noise can be found on the basis of Eq. (6) in the following way:

$$S_I(f) = K(\alpha) \frac{\alpha_H I_0^2}{N \cdot f^\gamma} \tag{9}$$

where $K(\alpha) = \dfrac{1}{1 - \alpha}$.

Under the partial blockage of FC, the polymer membrane power spectral density grows in $K(\alpha)$ times (Figure 3).

In another example, it is supposed that FC gas transport channels have single-channel serpentine configuration. Figure 4 shows the geometry with w_c channel width and L total length. Due to oxygen consumption in electrochemical reactions proceeding in PEMFC, the electrical current density decreases with the growth of distance from the gas transport channel inlet. The current distribution along the gas transport channel can be described by the following equation [33, 41]:

$$j(z) = \bar{j} \cdot K_\lambda \left(1 - \frac{1}{\lambda}\right)^{\frac{z}{L}} \tag{10}$$

 © 2016 WILEY-VCH Verlag GmbH & Co. KGaA, Weinheim

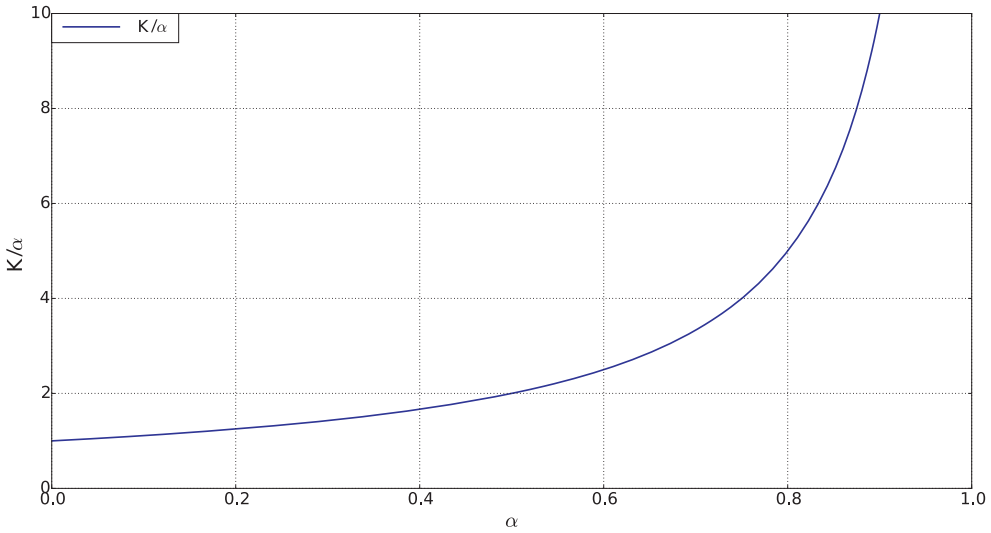

Fig. 3 Dependence of $K(\alpha)$ coefficient on α parameter of membrane surface usage efficiency.

where

$$K_\lambda = -\lambda \ln\left(1 - \frac{1}{\lambda}\right) \tag{11}$$

λ is the stoichiometric ratio, $\bar{j}$ is a mean current density through FC polymer membrane surface, z is a distance from the gas inlet along the channel. It can be shown that

$$w_c \int_0^L j(z)dz = w_c \cdot L \cdot \bar{j} = I_0 \tag{12}$$

where I_0 is the total current through FC polymer membrane surface. If it is assumed that the gas transport channels cover the whole active membrane S_0 uniformly, the surface integral Eq. (6) could be replaced by the curve integral

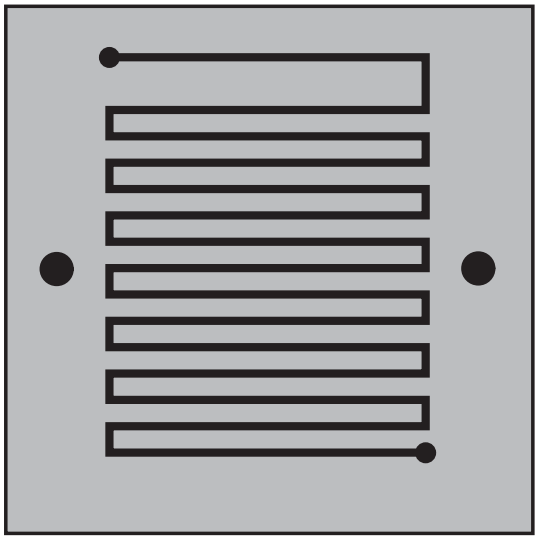

Fig. 4 Gas transport channel geometry.

$$S_I(f) = \int_L \frac{\alpha_H w_c j^2(x,y)}{C \cdot h \cdot f^\gamma} dl \tag{13}$$

which can be reduced to the next form

$$S_I(f) = \int_0^L \frac{\alpha_H w_c j^2(z)}{C \cdot h \cdot f^\gamma} dz \tag{14}$$

Combining Eq. (14) and Eq. (10), it is possible to obtain:

$$S_I(f) = \left(2 - \frac{1}{\lambda}\right) \frac{\alpha_H w_c^2 K_\lambda L}{2C \cdot h \cdot f^\gamma} \tag{15}$$

Taking into account Eq. (12) and the fact that charge carriers number is equal to $N = C{\cdot}h{\cdot}w_c{\cdot}L$, Eq. (15) can be reduced to

$$S_I(f) = V_\lambda \frac{\alpha_H \cdot I_0^2}{N \cdot f^\gamma} \tag{16}$$

where

$$V_\lambda = \left(2 - \frac{1}{\lambda}\right) \frac{K_\lambda}{2} \tag{17}$$

Comparing Eq. (1) and Eq. (15) shows that flicker-noise level is increased V_λ times under the non uniform current distribution on the membrane surface produced by progressive exhaustion of oxygen concentration along the gas transport channel. The function of V_λ related to the stoichiometry λ, which is presented in Figure 5, shows that PSD of flicker-noise increases with decrease of λ relation. For example, when λ changes from 1.1 to 1.05, the flicker-noise PSD increases in 1.3 times.

Therefore, any non uniform current distribution produced by other reasons (for example local membrane overheating,

 © 2016 WILEY-VCH Verlag GmbH & Co. KGaA, Weinheim

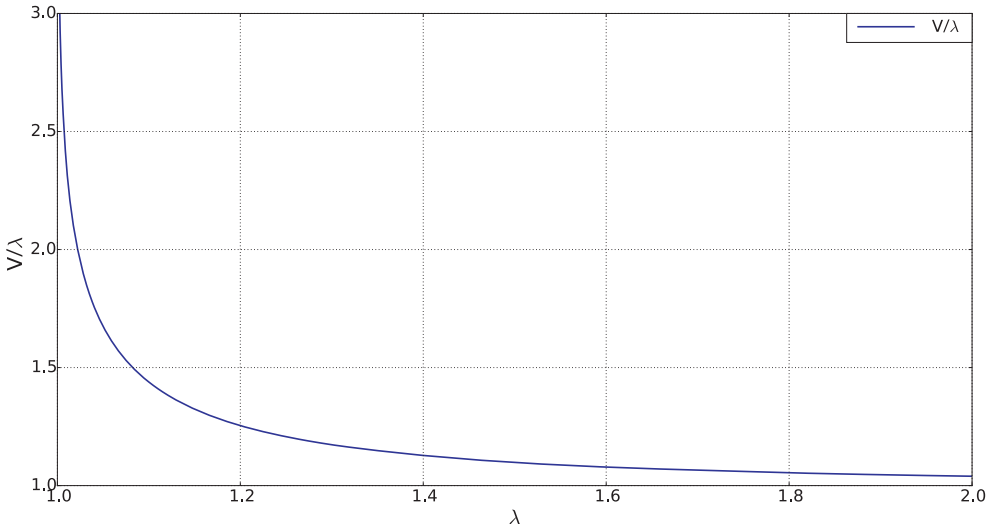

Fig. 5 Dependents of $V(\lambda)$ from stoichiometric coefficient λ.

catalyst layer blockage, membrane defects, etc.) will have an effect on the spectral characteristic of electrical noises.

It can be shown that in frame of the second model example, flicker-noise power spectrum is also inversely proportional to effective surface $S_e = \alpha \cdot S_0$ of MEA during insufficient oxygen supply of cathode. In this case, the membrane surface usage efficiency parameter could also be estimated as

$$\alpha = \frac{S_{I_0}(f)}{S_I(f)} \tag{18}$$

where $S_{I_0}(f)$ is the electrical fluctuation PSD in nominal operation mode, when the whole MEA surface is used effectively and $\alpha \to 1$. This case corresponds to a full usage of the surface, when a perfect distribution of the gases on the inhomogeneous distributed active surface of a fuel cell takes place.

The analysis of electrical noises characteristics for PEMFC can detect non uniform current distribution along the proton exchange membrane. This is an important result for technical diagnostics of the FC, because such operating modes considerably decrease fuel cell remaining useful life [33].

As mentioned above, the parameters and characteristics of PEMFC electrical current and voltage fluctuation essentially depend on its state. Physical and electrochemical parameters of the PEMFC, e.g., polymer membrane resistance, effective double electrical layer capacity, generated current and others, which determine FC durability and reliability are varied during operation. These parameters effect the FC electrical fluctuation behavior [29, 34, 42]. This circumstance gives possibilities to develop FC diagnostic system based on electrical noise and fluctuation measurements. The important advantage of such system is the possibility to carry out diagnostics directly during FC operation without variation or interruption of operation mode. Literature review has shown that electrochemical noise analysis is the most perspective FC diagnostic method which does not require operating mode perturbation [29, 30, 33, 34, 37]. For that reason, the development of FC fluctuation-noise diagnostic method is an important task.

3 Experimental Installation

In the previous section, it was theoretically shown that the PEMFC electrical fluctuations are depended on active cell surface and current distribution over the membrane surface when the flicker noise oscillations are presented. In this section, a test of a single PEMFC is presented. The membrane electrodes assembly (MEA) of the considered fuel cell has been produced under the hot pressure method (T = 120 °C, P = 7.8 MPa, t = 130 s) in the P'prime laboratory of University of Poitiers (France). The catalytic layer was placed on the proton exchange membrane Nafion 117, contained 40% of mass fraction of Pt on carbon carrier unit Vulcan XC-72 with 0.5 mg cm^{-2} platinum loading and 20% mass fraction of Teflon PTFE. A hydrophobic carbon cloth has been used as the backing layer. The surface area of square electrodes was equal to 5 cm^2. The MEA has been placed between two bipolar plates with gas transport channels having single-channel serpentine configuration. The width and depth of gas transport channels was 1 mm and the width of the copper current collector plate was 1 mm.

An automated measurement system for electrical fluctuation investigation of fuel cells or the fuel cell test station (FCTS) has been developed and used for the PEM fuel cell fluctuation-noise characteristics measurement. The block diagram of this system is presented in Figure 6. This developed system consists of two parts: operability assurance subsystem and electrical noise measurement system. The *BANC TEST* installation produced by Fuel Cell Technologies, Inc. was used for PEMFC operability assurance. This installation allows to choose the type of oxidizer (oxygen or air) and to control seven fuel cell operation parameters: the temperature of FC

 © 2016 WILEY-VCH Verlag GmbH & Co. KGaA, Weinheim

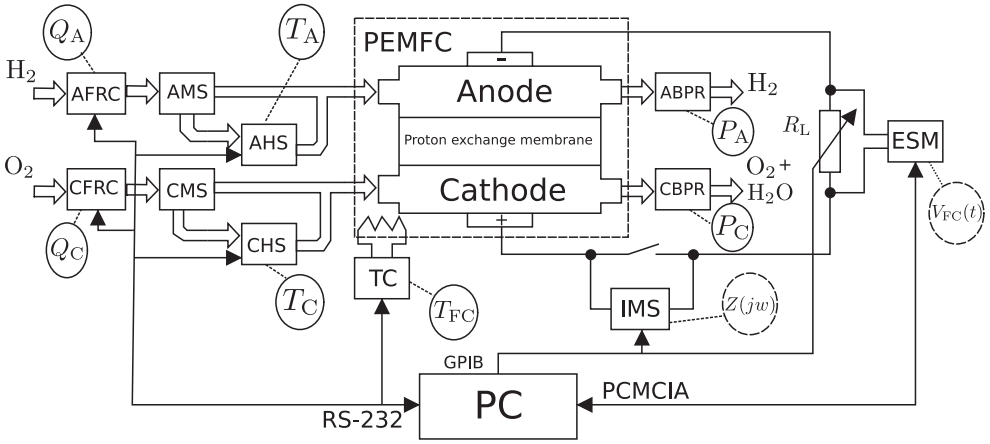

Fig. 6 Block diagram of fuel cell testing system: AFRC/CFRC are anode/cathode flow rate controllers; AMS/CMS are anode/cathode humidification mode selectors; AHS/CHS are anode/cathode humidification systems; ABPR/CBPR are anode/cathode backpressure regulators; TC is temperature controller; ESM is electric signal measuring system; IMS is impedance measuring system; PC is personal computer.

T_{FC}, the humidity of fuel and oxidizer gases, the anode Q_a and the cathode Q_c flow rates, the anode P_a and the cathode P_c backpressures.

The operability assurance subsystem works in the following way. The flow rate controllers (AFRC, CFRC) provide anode/cathode of fuel cell with hydrogen/oxygen. The reactant gases can go directly to fuel cell inlets through the anode (AHS) and cathode (CHS) humidification systems, which is controlled by the anode (AMS) and cathode (CMS) humidification mode selectors. The humidity of fuel and oxidizer is controlled by the temperatures of the anode T_{HA} and the cathode T_{HC} humidification systems. The backpressure regulators are placed after the fuel cell anode (ABPR) and cathode (CBPR) outlets. The cell temperature is set by the temperature controller (TC).

The temperature controllers of the cell and both humidifiers are based on CN76122 T/C controllers which have an accuracy of ± 0.25 °C. FCTS experimental setup is controlled by a computerized system via a LabVIEW program. The computerized system is connected with the anode (AFRC) and the cathode (CFRC) flow rates controllers, which allow maintaining flow rates with inaccuracy of less than 1% from the rated value.

The impedance measuring system (IMS) is based on the built-in BANC TEST installation impedance meter. The IMS allows measuring FC impedance characteristics at a frequency range from 0.01 Hz up to 40 Hz with relative error of real and imaginary parts less than 0.25%.

The electric signal measuring system (ESM) has been developed to measure the electrical fluctuation signals of the FC. The block diagram of this system is presented in Figure 6.

The fuel cell measuring system has two channels. The developed two-channel measurement is based on the data acquisition board NI PXI-5922 (*National Instruments, Inc.*), and low-noise amplifier made on the INA 103 microcircuit (*Burr Brown, Inc.*), which has a sensitivity better than 1.5 nV $Hz^{-0.5}$. The NI PXI-5922 has a resolution of 24 bits at sampling rates up to 50 kHz and the root-mean-square noise voltage < 1 μV (Figure 7).

The two-channel noise measurement system provides the complete FC voltage signal by the first channel

$$V_{FC} = V_0 + u(t) \tag{19}$$

where $V_0 = \overline{V_{FC}}$ is the DC component of FC voltage and $u(t)$ is the fluctuating component of FC voltage. The second channel measures only the fluctuating component $u(t)$ of full signal in the frequency range of 1 Hz – 2 kHz.

The developed fuel cell testing system is able to measure nine quantities, which describe the fuel cell operation mode. A summary of the measured values, their notation, units, and ranged accuracy can be found in Table 1.

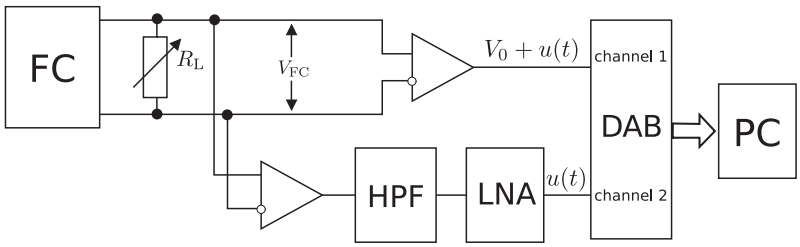

Fig. 7 Block diagram of fuel cell electric signal measuring system: FC is fuel cell; R_L is the electrical load; HPF is high pass filter; LNA is low noise amplifier; DAB is data acquisition board; PC is personal computer.

 © 2016 WILEY-VCH Verlag GmbH & Co. KGaA, Weinheim

Table 1 Measurement information of fuel cell testing system.

No.	Measured Quantity	Notation	Unit	Type of quantity		Range	Error
				Controlled	Measured		
1	FC temperature	T_{FC}	°C	+	+	0–100	±0.25 °C
2	Temperature of anode humidification system	T_{HA}	°C	+	+	0–100	±0.25 °C
3	Temperature of cathode humidification system	T_{HC}	°C	+	+	0–100	±0.25 °C
4	Flow rate of anode gas	Q_A	mL min^{-1}	+	+	0–1,000	1%
5	Flow rate of cathode gas	Q_C	mL min^{-1}	+	+	0–2,000	1%
6	Anode backpressure	P_A	kPa	+	+	400	2%
7	Cathode backpressure	P_C	kPa	+	+	600	2%
8	Load resistance	R_L	Ohm	+	+	0.01–1,000	0.1%
8	FC impedance	$Z(j\omega)$	Ohm	–	+	0–1,000	0.25%
9	FC voltage	V_{FC}	V	–	+	0–5	0.6 µV

4 Results and Discussion

4.1 General Description of PEMFC Electrical Fluctuations

Figure 8 shows a typical power spectral density $S'(f)$ of the fluctuation reduced to the mean square voltage of the PEMFC. The operation mode of PEMFC, in this case, has been characterized by the following set of parameters:

$$T_{FC} = 60\,°C;\ T_{HA} = 50\,°C;\ \text{without humidification;}$$
$$Q_A = 10\ \text{mL s}^{-1};\ Q_C = 10\ \text{mL s}^{-1};\ P_A = P_C = 300\ \text{kPa}. \quad (20)$$

Further, $S'(f)$ is reduced to square of mean voltage $\overline{V_{FC}}^2$ power spectral density of electrical fluctuations in contrast to $S(f)$, which corresponds to the absolute value of fluctuation PSD.

The reduced PSD $S'(f)$ is more preferable for FC technical state diagnostics because it allows to exclude effects related to the selection of electrical operation point.

The reduced PSD $S'(f)$ has been measured in a frequency range between 0.1 and 100 Hz (cp. Figure 8). The lower frequency range limit has been chosen with the purpose to enhance FC micro-fluctuation from slow macro and middle level fluctuations by frequency filtering. The upper frequency range limit (100 Hz) has been selected from the condition of a reliable measuring information, obtaining

$$S(f) >> S_n(f) \quad (21)$$

where $S(f)$ is the PSD of PEMFC fluctuation (cp. Figure 8), $S_n(f)$ is PSD of measuring equipment intrinsic noises (cp. Figure 7).

Figure 8 shows that fluctuations have a steadily decreasing character which can be described by fractional power dependence

$$S'(f) \sim \frac{1}{f^{\gamma}} \quad (22)$$

where $\gamma = 1.6$ is the fractional factor.

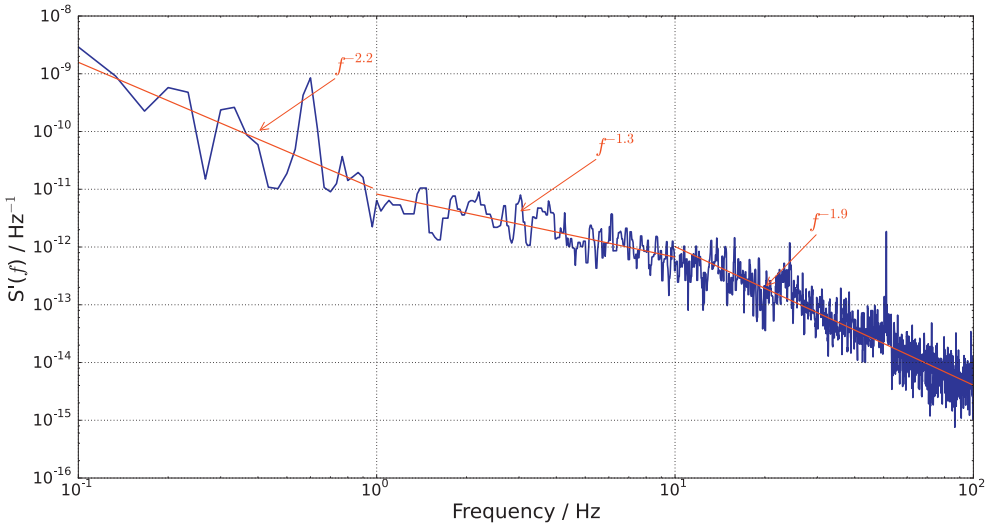

Fig. 8 Typical power spectral density $S'(f)$ reduced to square of mean voltage of PEMFC fluctuation measured in nominal operation mode.

 © 2016 WILEY-VCH Verlag GmbH & Co. KGaA, Weinheim

Therefore, the conclusion that PEM fuel cell fluctuations have a flicker-noise character can be made.

However, considering Figure 8, it is possible to conclude that the slope of $S'(f)$ in logarithmic scale has three frequency fields with different values of fractional factor $\gamma - \gamma', \gamma'', \gamma'''$:

$$S'(f) \sim \begin{cases} \frac{1}{f^{\gamma'}}, & f \leq 1Hz; \\ \frac{1}{f^{\gamma''}}, & 1Hz < f \leq 10Hz; \\ \frac{1}{f^{\gamma'''}}, & 10Hz \leq f \leq 100Hz, \end{cases} \quad (23)$$

where $\gamma' = 2.2; \gamma'' = 1.3; \gamma''' = 1.9$ are the fractional factors.

Such behavior of PSD $S'(f)$ can be related to the presence of several fluctuation sources within PEMFC.

Since it is possible to divide the reduced PSD $S'(f)$ into three fields Eq. (23), the next dimensionless energy parameters σ, σ', σ'', σ''' (see Table 2) and fractional factors γ', γ'', γ''' Eq. (23) can be used for quantitative description of the PEM fuel cell fluctuations.

The measurements of the reduced PSD $S'(f)$ have been carried out for the same PEM fuel cell 10 times for ten different days and have shown good reproducibility [27].

4.2 PEM Fuel Cell Electrical Fluctuations at Different Operation Modes

As shown above, the fuel cell electrical operating point position is specified by a load resistance R_L variation that changes the electrical voltage V_{FC}, and the current I_{FC}. The electrical current I_{FC} is considered as indicator of electrochemical process intensity, which should enlarge the increase of the reduced PSD $S'(f)$. In order to verify this assumption, the root-mean-square (RMS) parameter σ'' (for medium frequency range, 1 Hz < f < 10 Hz) depending on the FC average electrical current I_{FC} has been formed (cp. Figure 9). It shows that RMS values of the FC electrical fluctuation parameter σ'' grow with increasing current I_{FC}. In this case, "the growth rate" increases several times in the field of high currents (I_{FC} > 1.5 A, see Figure 9), when the limiting effect of mass transfer processes intensifies and problems of excess cathode water production appear.

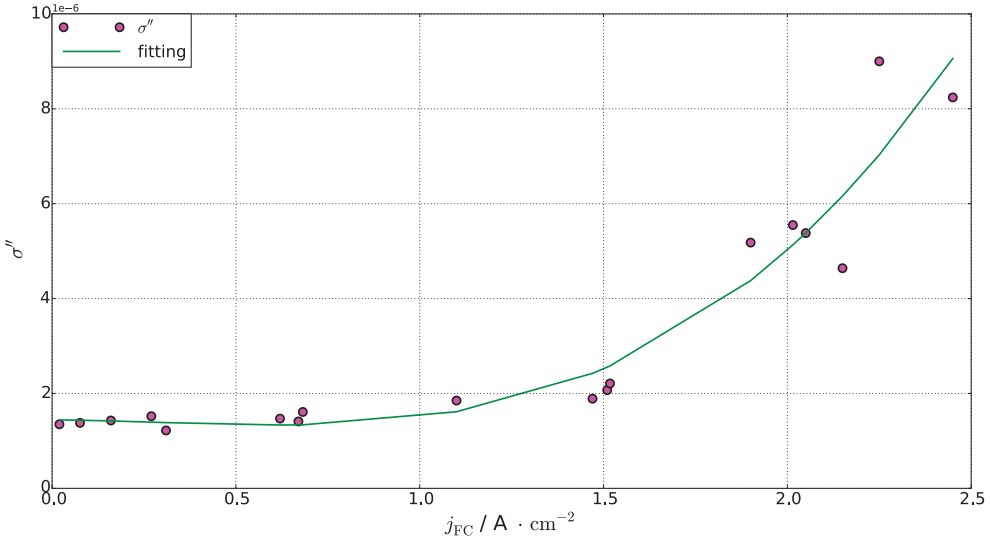

Fig. 9 Medium frequency range RMS parameter σ'' of PEM fuel cell electrical fluctuation dependences on FC average electrical current density j_{FC}.

Table 2 Energy parameters of PEM fuel cell fluctuation.

No.	Parameter	Notation	Definition	Frequency range / Hz
1	Reduced root-mean-square value of FC micro-fluctuation	σ	$\sigma = \left(\int_{0.1}^{100} S'(f) df \right)^{0.5}$	0.1–100
2	Reduced root-mean-square value of FC micro-fluctuation in low frequency range	σ'	$\sigma' = \left(\int_{0.1}^{1} S'(f) df \right)^{0.5}$	0.1–1
3	Reduced root-mean-square value of FC micro-fluctuation in medium frequency range	σ''	$\sigma'' = \left(\int_{1}^{10} S'(f) df \right)^{0.5}$	1–10
4	Reduced root-mean-square value of FC micro-fluctuation in high frequency range	σ'''	$\sigma''' = \left(\int_{10}^{100} S'(f) df \right)^{0.5}$	10–100

 © 2016 WILEY-VCH Verlag GmbH & Co. KGaA, Weinheim

It should be noted that the parameter σ'' shows a stronger dependence on the current. In other words, a medium frequency component (1 Hz < f < 10 Hz) of fluctuation spectrum is the most sensitive to the position of electrical operating point.

The reduced PSD $S'(f)$ of PEM fuel cell electrical fluctuations, measured at different values of cathode humidifier temperature T_{HC}, is presented in Figure 10. This figure shows that the FC temperature has a substantial influence on fluctuations of spectral characteristics. It can be noticed that the FC fluctuations grow in all frequency ranges, when temperature increases. Figure 11 illustrates the growth of a higher frequency range fluctuations σ''', which remains almost constant up to 40 °C and increases more than 10 times at 60 °C.

The temperature dependencies on fluctuation characteristics can be caused by water condensation on MEA and gas transport channels surfaces, when temperature of PEM fuel cell T_{FC} becomes close to dew-point temperature of cathode gas. The PEM fuel cell operation in this mode can lead to MEA active surface part blocking and non uniformity of current distribution along membrane surface. This observation fits well with the results obtained from the theoretical investigation of the Section 2.2. The high degree of MEA humidification should lead to a significant appearance of liquid water and therefore to a partial blockage of membrane surface. For that reason, it makes the current distribution non uniform and the electrical fluctuations increase.

It has been shown above that the power spectral density of electrical fluctuation has strong influence on the technical state of membrane electrodes assembly and fuel cell operating modes. In consequence, the electrical fluctuations potentially have diagnostic features, allowing to develop a technical diagnostic system for PEMFC systems.

One of the most complex technical problems, which should be handled during PEM fuel cell operation, is the management

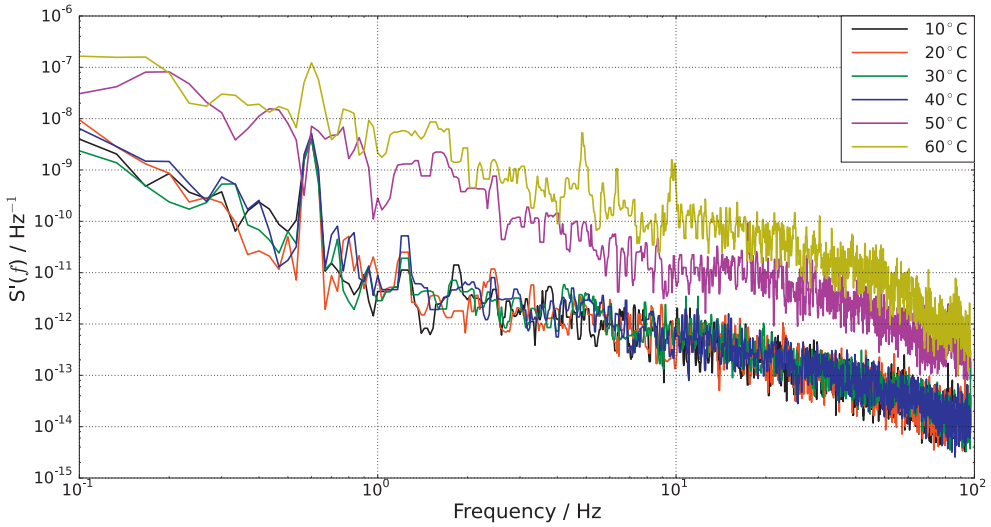

Fig. 10 Reduced PSD $S'(f)$ of PEM fuel cell electrical fluctuation measured at different values of cathode humidifier temperature T_{HC}.

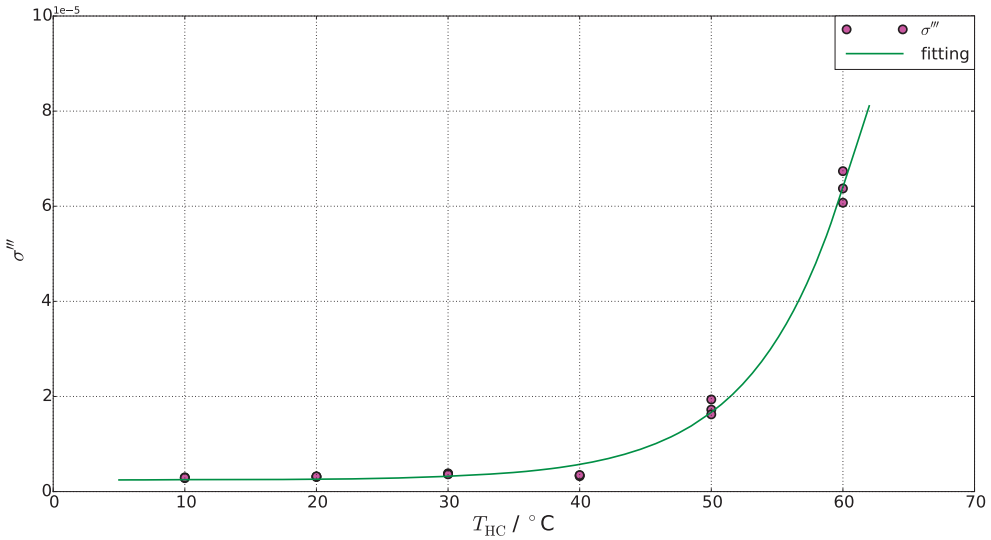

Fig. 11 High frequency range RMS parameter σ''' of PEM fuel cell electrical fluctuation dependencies on cathode humidifier temperature T_{HC}.

 © 2016 WILEY-VCH Verlag GmbH & Co. KGaA, Weinheim

of water balance. In this case, two types of failures are possible: water flooding and drying. Both failures lead to considerable decreasing of FC efficiency and energy production. Therefore, diagnostics and early detection of trends towards these failures are an important problem for increasing the PEMFC reliability and operation time without failure. It has been shown by Evdokimov et al. [29] that the characteristics of PEM fuel cell electrical fluctuations have the highest dependency on parameters, determining humidification mode of FC membrane electrodes assembly. Thus, it can be assumed that FC electrical fluctuations have features, allowing to diagnose excess or insufficient humidification of FC MEA.

The parameters σ′, σ′′, and σ′′′ can be considered as diagnostic criteria, which are specified as a root-mean-square value of PEM fuel cell electrical fluctuation in the three different frequency ranges. The specific frequency ranges might depend on the FC design and have to be estimated experimentally.

The nominal operation mode, as shown in Figure 12, is specified by high stability of operating voltage V_{FC} and parameters σ'_V, σ''_V, and σ'''_V. Here

$$\sigma'_V = \sigma' \cdot V_{FC},\ \sigma''_V = \sigma'' \cdot V_{FC},\ \sigma'''_V = \sigma''' \cdot V_{FC} \qquad (24)$$

where σ′, σ′′, and σ′′′ are reduced RMS values of PEM FC electrical fluctuations measured in three frequencies ranges: 0.1–1 Hz, 1–10 Hz and 10–100 Hz, respectively (see Table 2), V_{FC} is the FC operating voltage. The graphs presented in Figure 12 show that relative variations of parameters σ'_V, σ''_V, and σ'''_V from its mean values do not exceed 20%.

When the PEM fuel cell is operated under low or high humidification of membrane electrodes assembly, in nominal mode (Figure 13, section T_{HA} = 50 °C), the operating voltage V_{FC} and the electrical fluctuations parameters σ'_V, σ''_V, and σ'''_V remain on the same level (relative derivation of its values are not higher than 10%). The FC operation mode changes after the anode humidifier temperature decreases to the value T_{HA} = 30 °C, corresponding to low humidification of MEA. The operating voltage V_{FC} begins to oscillate periodically, going down to magnitude ~0.02 V. The FC operation mode becomes unstable due to insufficient humidification of MEA. The oscillations of voltage V_{FC} can be explained in the following way. If a constant ohmic resistance is used as the electrical load R_L and is connected to the FC, the electrical current $I_{FC} = V_{FC} / R_L$ flows though MEA. The current I_{FC} induces additional heating of MEA and consequently reduces water content in it. This effect leads to an increasing resistance inside the proton exchange membrane and decreasing of the current I_{FC} and voltage V_{FC}.

The following shutdown of anode humidifier (Figure 13, without humidification) leads to the additional decreasing of water quantity, entering the MEA (very low humidification). The water quantity becomes insufficient for restoring the FC voltage even in case of long-term operation at minimal value of I_{FC}.

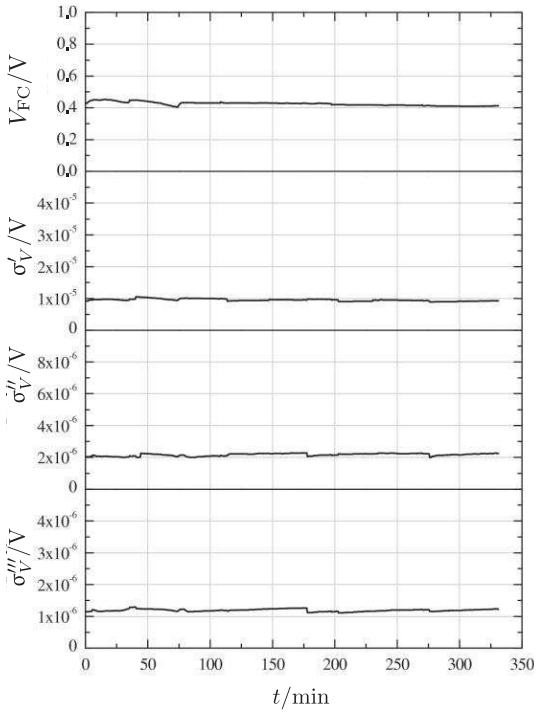

Fig. 12 Time dependencies of operating voltage V_{FC} on unreduced PEMFC electrical fluctuations parameters σ'_V, σ''_V, and σ'''_V under the nominal (optimal) operation mode.

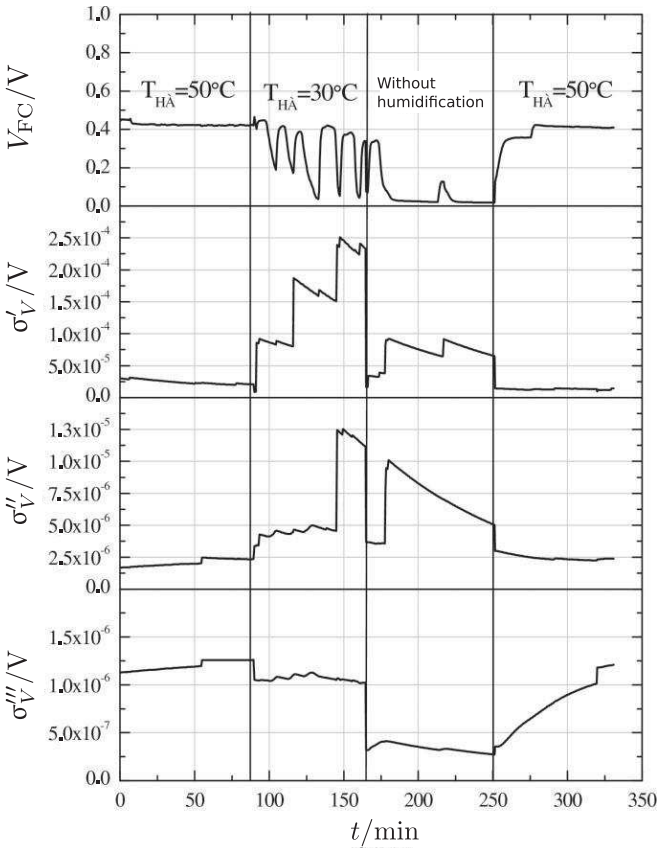

Fig. 13 Variation of the operating voltage V_{FC} on the unreduced PEMFC electrical fluctuations parameters σ'_V, σ''_V, and σ'''_V during insufficient humidification of membrane electrodes assembly.

 © 2016 WILEY-VCH Verlag GmbH & Co. KGaA, Weinheim

Returning to the operating parameters, which are corresponding to nominal operation mode Eq. (20), restores the voltage V_{FC} and changes the electrical fluctuation parameters back to the initial level.

The operation modes, resulting in insufficient MEA humidification and drying of polymer membrane (Figure 13, sections T_{HA} = 30 °C and without humidification), cause more than double increase of electrical fluctuations RMS values in lower frequencies σ'_V and medium frequencies σ''_V ranges. Contrarily, the higher frequency range fluctuations parameter σ'''_V decreases to 20% for the operation mode with T_{HA} = 30 °C and becomes 3 times lower without additional humidification of the anode gas.

The PEM fuel cell operation during increased MEA humidification is presented in Figure 14. This figure shows that the operating voltage V_{FC} and electrical fluctuations parameters σ'_V, σ''_V, and σ'''_V do not change significantly during FC operating in nominal mode. A slow decrease of operating potential V_{FC} (~ 1.4 μV s^{-1}) appears when the operation mode is changed by additional humidification of cathode gases at T_{HC} = 50 °C. In this case, the time intervals over several minutes are characterized by a considerable increase of σ''_V and σ'''_V appears. A short-time (< 1 min) increase (of 2–5 times) for σ'_V is observed in the low-frequency range.

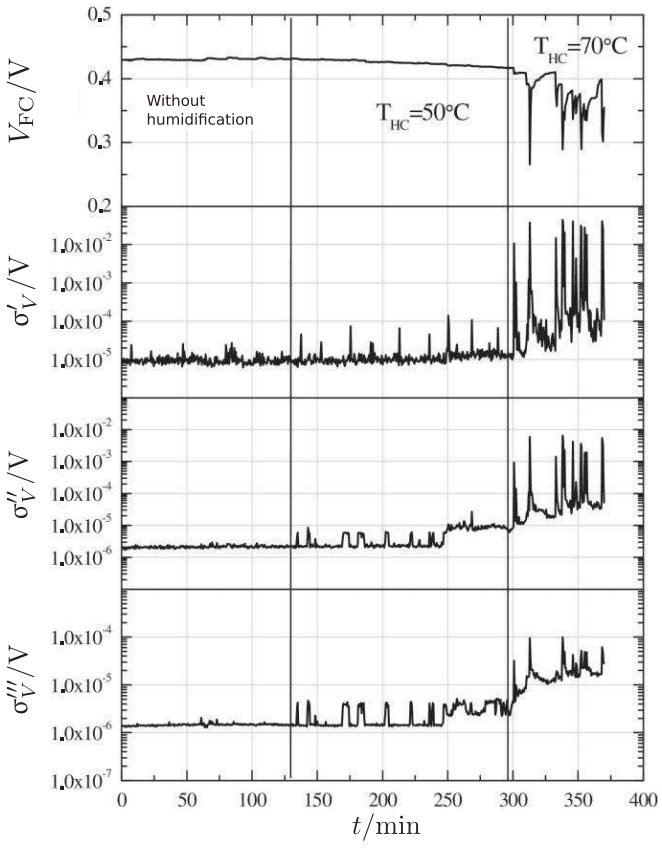

Fig. 14 Variation of the operating voltage V_{FC} on the unreduced PEMFC electrical fluctuations parameters σ'_V, σ''_V, and σ'''_V during excess humidification of membrane electrodes assembly.

If the PEMFC operating mode changes again, after increasing cathode humidifier temperature up to T_{HC} = 70 °C, the voltage V_{FC} becomes unstable. In addition, fluctuations in σ'_V and σ''_V become 100 times higher, while σ'''_V grows by 10 times. The last mode is characterized by high humidification of the MEA, which creates water condensation in the gas transport channels.

Thereby, both variants of FC operation mode failures, connected with the non-nominal water balance, lead to variation of fluctuations parameters. It is possible to recognize modes of excess and insufficient humidification of MEA by the different behaviors of σ'_V, σ''_V, and σ'''_V. In case of insufficient humidification, the electrical fluctuation in low and medium frequency ranges increases, while high-frequency fluctuations decrease and *vice versa*. During excess humidification, at the beginning stage, the electrical fluctuations increase in medium and high-frequency ranges, but for higher humidification, fluctuations increase in all frequency ranges.

5 Conclusion

The analysis of the obtained results allows to conclude that fluctuation phenomena inside fuel cell are a general effect. The electrical fluctuation analysis can be used to obtain the information about a PEM fuel cell's physical state. The possibility of non uniform current distribution detection on the basis of PEMFC electrical fluctuation measurements was shown.

It has been theoretically deduced and experimentally confirmed for the case of excess humidification, that nonuniform current distribution increases the PSD of the flicker-noise component. Theoretically, other reasons of current non uniformity, for example incorrect stoichiometry, can also lead to similar results.

The experimental measurement of fuel cell electrical fluctuations has been carried out for different operation modes. The experimental result shows that the electrical fluctuations depend on the FC operation mode and the physical state of its components. The dependences of PEMFC fluctuations PSD on its operation parameters have been measured to investigate a correlation between FC electrical fluctuations and its physical state.

During the investigation of the experimental data, three parameter were found to characterize the electrical fluctuations of a PEMFC: σ′ at low frequency range (f < 1 Hz), σ′′ at middle frequency range (1 Hz < f < 10 Hz), and σ′′′ at high frequency range (10 Hz < f). The results of the study show that the parameters σ′, σ′′, σ′′′ could be used as diagnostic features for estimating the FC state. In case of insufficient humidification of MEA, the increase of fluctuations in low and medium frequency ranges occurs, while high-frequency fluctuations decrease. During the excess humidification of MEA, at the beginning stage, medium and high-frequency fluctuations increased. During higher humidification, the fluctuations in all frequency ranges increased.

© 2016 WILEY-VCH Verlag GmbH & Co. KGaA, Weinheim

In the end, electrical fluctuations can be considered as a reliable tool for PEMFC diagnostics and might be used as additional information for a prognosis of remaining useful life.

Acknowledgements

The reported study has been supported by the ANR project PROPICE (ANR-12-PRGE-0001) funded by the French National Research Agency and was partially funded by RFBR according to the research project No. 16-38-00464 mol_a.

List of Symbols

Latin letters

C	concentration of charge carriers
C_{dl}	double electrical layer capacity / F
f	frequency / Hz
h	membrane thickness / mm
I	current / A
j	current density / A cm^{-2}
K	dimensionless coefficient
L	length / cm
N	number of elements
P	pressure / Pa
Q	flow rate / mL s^{-1}
R	resistance / Ω
S_I	power spectrum density
S_e	electrochemical active surface area / cm^2
S_0	whole membrane surface / cm^2
t	time / s
T	temperature / °C
u	voltage fluctuation component / V
V	voltage / V
V_λ	dimensionless coefficient
w_c	channel width / mm
x	Cartesian coordinate / cm
y	Cartesian coordinate / cm
Z	electrical impedance / Ω
z	coordinates measured along the channel length / cm

Greek Letter

α	parameter of membrane surface usage efficiency
α_H	Hooge parameter
γ	fractional factor
λ	stoichiometric ratio
σ	reduced root-mean-square value
σ_v	root-mean-square value / V

Sub/Superscripts

a	anode
c	cathode
FC	fuel cell
HA	anode humidification system
HC	cathode humidification system

References

[1] F. Barbir, *Int. J. Energy Res.* **2008**, *32*, 369.
[2] T. A. H. Ratlamwala, A. H. El-Sinawi, M. A. Gadalla, A. Aidan, *Int. J. Energy Res.* **2012**, *36*, 1121.
[3] F. Barbir, *PEM Fuel Cells – Theory and Practice*, Academic Press, **2012**.
[4] M. Jouin, R. Gouriveau, D. Hissel, M.-C. Pera, N. Zerhouni, *Reliability Engineering & System Safety* **2016**, *148*, 78.
[5] C. S. Gittleman, F. D. Coms, Y.-H. Lai, in Polymer Electrolyte Fuel Cell Degradation (Eds. M. Mench, E. C. Kumbur, T. N. Veziroglu), *Academic Press*, **2012**, 15.
[6] A. Collier, H. Wang, X. Yuan, J. Zhang, D. Wilkinson, *Int. J. Hydrogen Energy* **2006**, *31*, 1838.
[7] W. Schmittinger, A. Vahidi, *J. Power Sources* **2008**, *180*, 1.
[8] R. Borup, J. Meyers, B. Pivovar, Y. S. Kim, R. Mukundan, N. Garland, D. Myers, M. Wilson, F. Garzon, D. Wood, P. Zelenay, K. More, K. Stroh, T. Zawodzinski, J. Boncella, J. E. McGrath, M. Inaba, K. Miyatake, M. Hori, K. Ota, Z. Ogumi, S. Miyata, A. Nishikata, Z. Siroma, Y. Uchimoto, K. Yasuda, K.-I. Kimijima, N. Iwashita, *Chem. Rev.* **2007**, *107*, 3904.
[9] J. Wu, X. Z. Yuan, J. J. Martin, H. Wang, J. Zhang, J. Shen, S. Wu, W. Merida, *J. Power Sources* **2008**, *184*, 104.
[10] M. Jouin, R. Gouriveau, D. Hissel, M.-C. Pera, N. Zerhouni, *Int. J. Hydrogen Energy* **2014**, *39*, 481.
[11] M. Jouin, R. Gouriveau, D. Hissel, M.-C. Pera, N. Zerhouni, *Int. J. Hydrogen Energy* **2013**, *38*, 15307.
[12] F. Y. Zhang, X. G. Yang, C. Y. Wang, *J. Electrochem. Soc.* **2006**, *153*, 225.
[13] P. Boillat, D. Kramer, B. Seyfang, G. Frei, E. Lehmann, G. G. Scherer, A. Wokaun, Y. Ichikawa, Y. Tasaki, K. Shinohara, *Electrochem. Commun.* **2008**, *10*, 546.
[14] S. Shimpalee, S. Greenway, D. Spuckler, J. W. V. Zee, *J. Power Sources* **2004**, *135*, 79.
[15] J. J. Gagliardo, J. P. Owejan, T. A. Trabold, T. W. Tighe, *Nucl. Instrum. Methods Phys. Res., Sect. A* **2009**, *605*, 115.
[16] U. Bertocci, C. Gabrielli, F. Huet, M. Keddam, P. Rousseau, *J. Electrochem. Soc.* **1997**, *144*, 37.
[17] P. C. Searson, J. L. Dawson, *J. Electrochem. Soc.* **1988**, *195*, 1908.
[18] M. G. Astafiev, L. S. Kanevskii, B. M. Grafov, *Russ. J. Electrochem.* **2006**, *42*, 523.
[19] B. M. Grafov, L. S. Kanevskii, M. G. Astafiev, *J. Appl. Electrochem.* **2005**, *35*, 1271.
[20] A.-M. Lafront, F. Safizadeh, E. Ghali, G. Houlachi, *Electrochim. Acta* **2010**, *55*, 2505.
[21] T. Okada, *J. Electrochem. Soc.* **1993**, *140*, 1261.

 © 2016 WILEY-VCH Verlag GmbH & Co. KGaA, Weinheim

[22] S. Martinet, R. Durand, P. Ozil, P. Leblanc, P. Blanchard, *J. Power Sources* **1999**, *83*, 93.
[23] S. Martemianov, N. Adiutantov, Yu.K. Evdokimov, L. Madier, F. Maillard, A. Thomas, *J. Solid State Electrochem.* **2015**, *19*, 1.
[24] M. Vorotyntsev, S. Martem'yanov, B. Grafov, *Zh Eksp Teor Fiz (JETF)* **1980**, *79*, 1797.
[25] M. Vorotyntsev, S. Martem'yanov, B. Grafov, *J. Electroanal. Chem. Interfacial Electrochem.* **1984**, *179*, 1.
[26] S. Martemyanov, E. Skurygin, J. Legrand, *Int. J. Heat Mass Transfer* **1999**, *42*, 2357.
[27] E. Skurygin, M. Vorotyntsev, S. Martem'yanov, *J. Electroanal. Chem. Interfacial Electrochem.* **1989**, *259*, 285.
[28] X. Adolphe, L. Danaila, S. Martemianov, *J. Electroanal. Chem.* **2007**, *600*, 119.
[29] Yu. K. Evdokimov, E. Denisov, S. Martemianov, *Nonlinear World* **2009**, *7*, 706 (in Russian).
[30] Yu. Evdikomov, E. Denisov, *Proc SPIE* **2013**, *8787*, 87870E.
[31] R. K. Arun, W. Bekelea, A. Ghatak, *Electrochim. Acta* **2013**, *87*, 489.
[32] T. Kadyk, S. Kirscha, R. Hanke-Rauschenbach, *Electrochim. Acta* **2011**, *56*, 10593.
[33] A. Kulikovsky, H. Scharmann, K. Wippermann, *Electrochem. Commun.* **2004**, *6*, 75.
[34] A. Kulikovsky, H. Scharmann, K. Wippermann, *Electrochem. Commun.* **2004**, *6*, 729.
[35] P. P. Lopes, E. A. Ticianelli, H. Varela, *J. Power Sources* **2011**, *196*, 84.
[36] E. Denisov, *Nonlinear World* **2008**, *6*, 483.
[37] B. Legros, P.-X. Thivel, Y. Bultel, R. P. Nogueira, *Electrochem. Commun.* **2011**, *13*, 1514.
[38] S. Kogan, *Electronic Noise and Fluctuations in Solids*, Cambridge University Press, **1996**.
[39] C. Claeys, E. Simoen, *J. Electrochem. Soc.* **1998**, *145*, 2058.
[40] S. M. Kogan, *Soviet Physics Uspekhi* **1985**, *28*, 170.
[41] A. Kornyshev, A. Kulikovsky, *Electrochim. Acta* **2001**, *46*, 4389.
[42] E. Denisov, *Electronics and information technology* **2009**, *1* (in Russian).

 © 2016 WILEY-VCH Verlag GmbH & Co. KGaA, Weinheim

Bibliography

[1] *Annual Energy Outlook 2015* (2015). URL: http://www.eia.gov/forecasts/AEO/pdf/0383(2015).pdf.

[2] *World Energy Resources: 2013 Survey* (2013). URL: http://www.worldenergy.org/wp-content/uploads/2013/09/Complete_WER_2013_Survey.pdf.

[3] *Climate Change 2014: Mitigation of Climate Change* (2014). URL: http://www.ipcc.ch/report/ar5/wg3/.

[4] *World Energy Outlook - Executive Summary* (2014). English. URL: http://www.iea.org/publications/freepublications/publication/world-energy-outlook-2014---executive-summary---english.html.

[5] *Trends in global CO2 emissions* (2014).

[6] *EROI of Global Energy Resources: Preliminary Status and Trends* (2012).

[7] P. Corbo, F. Migliardini, and O. Veneri. *Hydrogen Fuel Cells for Road Vehicles*. Ed. by P. Corbo. Springer, 2011.

[8] J. J. Romm. *The Hype about Hydrogen: Fact and Fiction in the Race to Save the Climate*. Island Press, 2004. URL: http://www.islandpress.org/book/the-hype-about-hydrogen.

[9] F. Barbir. *PEM Fuel Cells - Theory and Practice*. Academic Press, 2012.

[10] M. Cifrain and K. Kordesch. "Hydrogen/oxygen (air) fuel cells with alkaline electrolytes". *Handbook of Fuel Cells – Fundamentals, Technology and Applications*. Vol. 1. 4. John Wiley & Sons Ltd., 2010. Chap. 14, 267–280. DOI: 10.1002/9780470974001.f104013.

[11] S. Lu et al. "Alkaline polymer electrolyte fuel cells completely free from noble metal catalysts". *Proceedings of the National Academy of Sciences*. Vol. 105. 52. 2008. 20611–20614. DOI: 10.1073/pnas.0810041106.

[12] M. Schulze, E. Gülzow, and G. Steinhilber. "Activation of nickel-anodes for alkaline fuel cells". *Applied Surface Science* **179**: 251–256, 2001. DOI: 10.1016/S0169-4332(01)00291-4.

[13] V. V. Kharton. *Solid State Electrochemistry II: Electrodes, Interfaces and Ceramic Membranes*. Ed. by V. V. Kharton. John Wiley & Sons, 2011. DOI: 10.1002/9783527635566.

[14] S. Revankar and P. Majumdar. *Fuel Cells: Principles, Design, and Analysis*. CRC Press, 2014.

[15] F. Barbir, H. Gorgun, and X. Wang. "Relationship between pressure drop and cell resistance as a diagnostic tool for PEM fuel cells". *Journal of Power Sources* **141**: 96–101, 2005. DOI: 10.1016/j.jpowsour.2004.08.055.

[16] A. S. Lohoff et al. "Extending the lifetime of direct methanol fuel cell systems to more than 20,000 h by applying ion exchange resins". *International Journal of Hydrogen Energy* **41**: 15325–15334, 2016. DOI: 10.1016/j.ijhydene.2016.06.207. URL: http://www.sciencedirect.com/science/journal/03603199.

[17] E. T. Services. *Fuel Cell Handbook (Seventh Edition)*. EG&G, 2004. URL: https://www.netl.doe.gov/File%20Library/research/coal/energy%20systems/fuel%20cells/FCHandbook7.pdf.

[18] B. Legros et al. "First results on PEMFC diagnosis by electrochemical noise". *Electrochemistry Communications* **13**: 1514–1516, 2011. DOI: 10.1016/j.elecom.2011.10.007.

[19] O. Himanen. "Characterization of Transport Phenomena in Small Polymer Electrolyte Membrane Fuel Cells". PhD thesis. Helsinki University of Technology, 2008.

[20] M. Schulze et al. "Degradation of sealings for PEFC test cells during fuel cell operation". *Journal of Power Source* **127**: 222–229, 2004. DOI: 10.1016/j.jpowsour.2003.09.017.

[21] J. Wu et al. "A review of PEM fuel cell durability: Degradation mechanisms and mitigation strategies". *Journal of Power Sources* **184**: 104–119, 2008. DOI: 10.1016/j.jpowsour.2008.06.006.

[22] D.-H. Ye and Z.-G. Zhan. "A review on the sealing structures of membrane electrode assembly of proton exchange membrane fuel cells". *Journal of Power Source* **231**: 285–292, 2013. DOI: 10.1016/j.jpowsour.2013.01.009.

[23] D. Bograchev et al. "Stress and plastic deformation of MEA in running fuel cell". *International Journal of Hydrogen Energy* **33**: 5703–5717, 2008. DOI: 10.1016/j.ijhydene.2008.06.066.

[24] C.-H. Chien et al. "Compression of Seals in PEM Fuel Cells". *Conference Proceedings of the Society for Experimental Mechanics Series*. Vol. 5. 183–192. 2011. DOI: 10.1007/978-1-4419-9798-2_22.

[25] J. Tan et al. "Degradation of elastomeric gasket materials in PEM fuel cells". *Materials Science and Engineerin* **445–446**: 669–675, 2007. DOI: 10.1016/j.msea.2006.09.098.

[26] S. Cleghorn et al. "A polymer electrolyte fuel cell life test: 3 years of continuous operation". *Journal of Power Source* **158**: 446–454, 2006. DOI: 10.1016/j.jpowsour.2005.09.062.

[27] G. Chen et al. "Electrochemical durability of gas diffusion layer under simulated proton exchange membrane fuel cell conditions". *International Journal of Hydrogen Energy* **34**: 8185–8192, 2009. DOI: 10.1016/j.ijhydene.2009.07.085.

[28] W.-M. Yan et al. "Optimal microporous layer for proton exchange membrane fuel cell". *Journal of Power Sources* **195**: 5731–5734, 2010. DOI: 10.1016/j.jpowsour.2010.03.041.

[29] J. M. Morgan and R. Datta. "Understanding the gas diffusion layer in proton exchange membrane fuel cells. I. How its structural characteristics affect diffusion and performance". *Journal of Power Source* **251**: 269–278, 2014. DOI: 10.1016/j.jpowsour.2013.09.090.

[30] J. P. Owejan et al. "Water Transport Mechanisms in PEMFC Gas Diffusion Layers". *Journal of the Electrochemical Society* **157**: B1456–B1464, 2010. DOI: 10.1149/1.3468615.

[31] D. Malevich et al. "Investigation of Charge-Transfer and Mass-Transport Resistances in PEMFCs with Microporous Layer Using Electrochemical Impedance Spectroscopy". *Journal of the Electrochemical Society* **156**: B216–B224, 2009. DOI: 10.1149/1.3033408.

[32] T. Kim, S. Lee, and H. Park. "A study of water transport as a function of the micro-porous layer arrangement in PEMFCs". *International Journal of Hydrogen Energy* **33**: 8631–8643, 2010. DOI: 10.1016/j.ijhydene.2010.05.123.

[33] W.-K. Lee et al. "The effects of compression and gas diffusion layers on the performance of a PEM fuel cell". *Journal of Power Sources* **84**: 45–51, 1999. DOI: 10.1016/S0378-7753(99)00298-0.

[34] J. Pauchet et al. "Performance loss of proton exchange membrane fuel cell due to hydrophobicity loss in gas diffusion layer: Analysis by multiscale approach combining pore network and performance modelling". *International Journal of Hydrogen Energy* **37**: 1628–1641, 2012. DOI: 10.1016/j.ijhydene.2011.09.127.

[35] M. Schulze et al. "Combined electrochemical and surface analysis investigation of degradation processes in polymer electrolyte membrane fuel cells". *Electrochimica Acta* **52**: 2328–2336, 2007. DOI: 10.1016/j.electacta.2006.05.063.

[36] Z. Fishman and A. Bazylak. "Heterogeneous Through-Plane Porosity Distributions for Treated PEMFC GDLs I. PTFE Effect". *Journal of the Electrochemical Society* **158**: B841–B845, 2011. DOI: 10.1149/1.3594578.

[37] Y. Lasbet et al. "A chaotic heat-exchanger for PEMFC cooling applications". *Journal of Power Sources* **156**: 114–118, 2006. DOI: 10.1016/j.jpowsour.2005.08.030.

[38] A. Kumar and R. G. Reddy. "Effect of channel dimensions and shape in the flow-field distributor on the performance of polymer electrolyte membrane fuel cells". *Journal of Power Sources* **113**: 11–18, 2003. DOI: 10.1016/S0378-7753(02)00475-5.

[39] S.-J. Lee et al. "Corrosion-resistant component for PEM fuel cells". *Journal of Power Sources* **131**: 162–168, 2004. DOI: 10.1016/j.jpowsour.2004.01.008.

[40] W. Schmittinger and A. Vahidi. "A review of the main parameters influencing long-term performance and durability of PEM fuel cells". *Journal of Power Sources* **180**: 1–14, 2008. DOI: 10.1016/j.jpowsour.2008.01.070.

[41] G. Hinds. *Performance and durability of PEM fuel cells: a review*. Ed. by G. Hinds. National Physical Laboratory Teddington, UK, 2004. URL: http://www.npl.co.uk/upload/pdf/NPL_Report_DEPC-MPE_002.pdf.

[42] M. Jouin et al. "Degradations analysis and aging modeling for health assessment and prognostics of PEMFC". *Reliability Engineering & System Safety* **148**: 78–95, 2016. DOI: 10.1016/j.ress.2015.12.003.

[43] G. Sasikumar, J. Ihm, and H. Ryu. "Dependence of optimum Nafion content in catalyst layer on platinum loading". *Journal of Power Sources* **132**: 11–17, 2004. DOI: 10.1016/j.jpowsour.2003.12.060.

[44] E. Antolini et al. "Influence of Nafion loading in the catalyst layer of gas-diffusion electrodes for PEFC". *Journal of Power Sources* **77**: 136–142, 1999. DOI: 10.1016/S0378-7753(98)00186-4.

[45] S. S. Kocha. "Polymer Electrolyte Fuel Cell Degradation". S. S. Kocha, ed. Chap. Electrochemical Degradation: Electrocatalyst and Support Durability, 89–214. Academic Press, 2012. DOI: 10.1016/B978-0-12-386936-4.10003-X.

[46] S. Dhanushkodi et al. "Carbon corrosion fingerprint development and de-convolution of performance loss according to degradation mechanism in PEM fuel cells". *Journal of Power Sources* **240**: 114–121, 2013. DOI: 10.1016/j.jpowsour.2013.03.033.

[47] R. Borup et al. "Scientific Aspects of Polymer Electrolyte Fuel Cell Durability and Degradation". *Chemical Reviews* **107**: 3904–3951, 2007. DOI: 10.1021/cr0501821.

[48] W. Bi and T. Fuller. "Modeling of PEM fuel cell Pt/C catalyst degradation". *Journal of Power Sources* **178**: 188–196, 2008. DOI: 10.1016/j.jpowsour.2007.12.007.

[49] C. Gittleman, F. Coms, and Y.-H. Lai. "Polymer Electrolyte Fuel Cell Degradation". Chap. Membrane Durability: Physical and Chemical Degradation, 15–88. Academic Press, 2012. DOI: 10.1016/B978-0-12-386936-4.10002-8.

[50] A. Collier et al. "Degradation of polymer electrolyte membranes". *International Journal of Hydrogen Energy* **31**: 1838–1854, 2006. DOI: 10.1016/j.ijhydene.2006.05.006.

[51] J. Mainka. "Local impedance in H2/air Proton Exchange Membrane Fuel Cells (PEMFC). Theoretical and experimental investigations". PhD thesis. Université Henri Poincaré, 2011.

[52] C. Yang et al. "A comparison of physical properties and fuel cell performance of Nafion and zirconium phosphate/Nafion composite membranes". *Journal of Membrane Science* **237**: 145–161, 2004. DOI: 10.1016/j.memsci.2004.03.009.

[53] J. Wu et al. "Diagnostic tools in PEM fuel cell research: Part II Physical/chemical methods". *International Journal of Hydrogen Energy* **33**: 1747–1757, 2008. URL: http://www.sciencedirect.com/science/article/pii/S0360319908000712.

[54] S. Kwaka et al. "New fabrication method of the composite membrane for polymer electrolyte membrane fuel cell". *Journal of New Materials for Electrochemical Systems* **4**: 25–29, 2001. URL: http://www.groupes.polymtl.ca/jnmes/modules/journal/index.php/content0623.html.

[55] Z. Zheng et al. "A review on non-model based diagnosis methodologies for PEM fuel cell stacks and systems". *International Journal of Hydrogen Energy* **38**: 8914–8926, 2013. DOI: 10.1016/j.ijhydene.2013.04.007.

[56] R. Petrone et al. "A review on model-based diagnosis methodologies for PEMFCs". *International Journal of Hydrogen Energy* **38**: 7077–7091, 2013. DOI: 10.1016/j.ijhydene.2013.03.106.

[57] M. Jouin et al. "Prognostics of PEM fuel cell in a particle filtering framework". *International Journal of Hydrogen Energy* **39**: 481–494, 2014. DOI: 10.1016/j.ijhydene.2013.10.054.

[58] M. Jouin et al. "Prognostics and Health Management of PEMFC - State of the art and remaining challenges". *International Journal of Hydrogen Energy* **38**: 15307–15317, 2013. DOI: 10.1016/j.ijhydene.2013.09.051.

[59] Z. Li et al. "Data-driven diagnosis of PEM fuel cell: A comparative study". *Control Engineering Practice* **28**: 1–12, 2014. URL: http://www.sciencedirect.com/science/article/pii/S0967066114001002.

[60] J. Wu et al. "Diagnostic tools in PEM fuel cell research: Part I Electrochemical techniques". *International Journal of Hydrogen Energy* **33**: 1735–1746, 2008. URL: http://www.sciencedirect.com/science/article/pii/S0360319908000700.

[61] X. Yuan et al. "AC impedance technique in PEM fuel cell diagnosis - A review". *International Journal of Hydrogen Energy* **32**: 4365–4380, 2007. URL: http://www.sciencedirect.com/science/article/pii/S036031990700328X.

[62] M. Rubio, A. Urquia, and S. Dormido. "Diagnosis of PEM fuel cells through current interruption". *Journal of Power Sources* **171**: 670–677, 2007. URL: http://www.sciencedirect.com/science/article/pii/S0378775307013596.

[63] A. Thomas et al. "Thermal Effect on Water Transport in Proton Exchange Membrane Fuel Cell". *Fuel Cells (Weinheim, Germany)* **12**: 212–224, 2012. URL: http://onlinelibrary.wiley.com/doi/10.1002/fuce.201100100/full.

[64] A. Thomas et al. "Measurements of Electrode Temperatures, Heat and Water Fluxes in PEMFCs: Conclusions about Transfer Mechanisms". *Journal of the Electrochemical Society* **160**: 191–204, 2013. DOI: 10.1149/2.006303jes.

[65] A. Thomas et al. "Thermal and water transfer in PEMFCs: Investigating the role of the microporous layer". *International Journal of Hydrogen Energy* **39**: 2649–2658, 2014. DOI: 10.1016/j.ijhydene.2013.11.105.

[66] F. Hooge, T. Kleinpenning, and L. K. J. Vandamme. "Experimental studies on 1/f noise". *Reports on Progress in Physics* **44**: 479–532, 1981. DOI: 10.1088/0034-4885/44/5/001.

[67] F. N. Hooge. "1/f noise sources". *IEEE Transactions on Electron Devices* **41**: 1926–1935, 1994. DOI: 10.1109/16.333808.

[68] E. Denisov. "Les bruits et les fluctuations électriques d'une pile à combustible de type PEM et leurs propriétés diagnostiques". PhD thesis. Université de Poitiers, 2011.

[69] J. B. Johnson. "Thermal Agitation of Electricity in Conductors". *Physical Review* **32**: 97–109, 1928. DOI: 10.1103/PhysRev.32.97.

[70] H. Nyquist. "Thermal Agitation of Electric Charge in Conductors". *Physical review* **32**: 110–113, 1928. DOI: 10.1103/PhysRev.32.110.

[71] C. Claeys and E. Simoen. "Noise as a Diagnostic Tool for Semiconductor Material and Device Characterization". *Journal of the Electrochemical Society* **145**: 2058–2067, 1998. DOI: 10.1149/1.1838597.

[72] L. Du, Y. Zhuang, and Y. Wu. "1/f Noise separated from white noise with wavelet denoising". *Microelectronics Reliability* **42**: 183–188, 2002. DOI: 10.1016/S0026-2714(01)00249-9.

[73] D.-H. Xia and Y. Behnamian. "Electrochemical Noise: A Review of Experimental Setup, Instrumentation and DC Removal". *Russian Journal of Electrochemistry* **51**: 593–601, 2015. DOI: 10.1134/S1023193515070071.

[74] M. Vorotyntsev, S. Martem'yanov, and B. Grafov. "Temporal correlation of current pulsations at one or several electrodes: A technique to study hydrodynamic fluctuation characteristics of a turbulent flow". *Journal of Electroanalytical Chemistry and Interfacial Electrochemistry* **179**: 1–23, 1984. DOI: 10.1016/S0022-0728(84)80270-3.

[75] E. Skurygin, M. Vorotyntsev, and S. Martem'yanov. "Space-time fluctuations of a passive impurity concentration within the diffusion boundary layer in the turbulent flow of a fluid". *Journal of Electroanalytical Chemistry and Interfacial Electrochemistry* **259**: 285–293, 1989. DOI: 10.1016/0022-0728(89)80052-X.

[76] S. A. Martemyanov, N. V. Petrovskiy, and B. M. Grafov. "Turbulent pulsations of the microelectrode limiting diffusion current". *Journal of Applied Electrochemistry* **21**: 1099–1102, 1991. DOI: 10.1007/BF01041455.

[77] S. Martemianov and L. Danaila. "On the study of electrochemical turbulent noise in a stirred vessel". *Fluctuation and Noise Letters* **3**: L463–L471, 2003. DOI: 10.1142/S0219477503001555.

[78] X. Adolphe, L. Danaila, and S. Martemianov. "On the small-scale statistics of turbulent mixing in electrochemical systems". *Journal of Electroanalytical Chemistry* **600**: 119–130, 2007. DOI: 10.1016/j.jelechem.2006.04.023.

[79] R. A. Cottis. "Interpretation of electrochemical noise data". *Corrosion* **57**: 265–285, 2001. DOI: 10.5006/1.3290350.

[80] U. Bertocci et al. "Noise Resistance Applied to Corrosion Measurements: I. Theoretical Analysis". *Journal of The Electrochemical Society* **144**: 31–37, 1997. URL: http://jes.ecsdl.org/content/144/1/31.

[81] P. C. Searson and J. L. Dawson. "Analysis of Electrochemical Noise Generated by Corroding Electrodes under Open-Circuit Conditions". *Journal of the Electrochemical Society* **135**: 1908–1915, 1988. DOI: 10.1149/1.2096177.

[82] S. Martinet et al. "Application of electrochemical noise analysis to the study of batteries: state-of-charge determination and overcharge detection". *Journal of Power Sources* **83**: 93–99, 1999. URL: http://www.sciencedirect.com/science/article/pii/S0378775399002724.

[83] S. Martemianov et al. "New methodology of electrochemical noise analysis and applications for commercial Li-ion batteries". *Journal of Solid State Electrochemistry* **19**: 1–8, 2015. DOI: 10.1007/s10008-015-2855-2.

[84] Y. K. Evdokimov, E. Denisov, and S. Martemianov. "Hydrogen Fuel Cell Electrical Noise and Study of its Diagnostics Properties". *Nonlinear world* **7**: 706–713, 2009.

[85] Y. Evdokimov and E. Denisov. "Fluctuation-noise diagnostics of optical system power supply units based on fuel cell". *Proc. SPIE* **8787**: 87870E1–87870E-11, 2013. DOI: 10.1117/12.2020894.

[86] Y. Tan et al. "Study on Glucose Biofuel Cells Using an Electrochemical Noise Device". *Electroanalysis* **20**: 1599–1606, 2008. DOI: 10.1002/elan.200804220.

[87] A. N. Kolmogorov. "The local structure of turbulence in incompressible viscous fluid for very large Reynolds numbers". *Dokl. Akad. Nauk SSSR*. Vol. 30. 4. JSTOR. 1941. 301–305. URL: http://www.jstor.org/stable/51980.

[88] A. N. Kolmogorov. "Dissipation of energy in the locally isotropic turbulence". *Proceedings: Mathematical and Physical Sciences* **434**: 15–17, 1991. URL: http://www.jstor.org/stable/51981.

[89] U. Bertocci et al. "Drift Removal Procedures in the Analysis of Electrochemical Noise". *CORROSION SCIENCE* **58**: 337–347, 2002. DOI: http://dx.doi.org/10.5006/1.3287684.

[90] F. Principato and G. Ferrante. "Skewness and kurtosis of 1/f noise in semiconductor devices". *Microelectronics Reliability* **40**: 1969–1973, 2000. URL: http://www.sciencedirect.com/science/article/pii/S0026271400000676.

[91] S. Marple. *Digital spectral analysis with applications*. Ed. by S. Marple. Englewood Cliffs, 1987.

[92] A. I. Solonina et al. *Digital signal processing and Matlab*. BHV-Peterburg, 2013.

[93] J. B. Allen, M. Hill, and L. R. Rabiner. "A unified approach to short-time Fourier analysis and synthesis". *Proceedings of the IEEE* **65**: 1558–1564, 1977. DOI: 10.1109/PROC.1977.10770.

[94] R. A. Altes. "Detection, estimation, and classification with spectrograms". *The Journal of the Acoustical Society of America* **67**: 1232–1246, 1980. DOI: 10.1121/1.384165.

[95] A. H. Costa and S. Hengstler. "Adaptive time–frequency analysis based on autoregressive modeling". *Signal Processing* **91**: 740–749, 2011. DOI: 10.1016/j.sigpro.2010.07.020.

[96] R. R. Nigmatullin, W. Zhang, and D. Striccoli. "General theory of experiment containing reproducible data: The reduction to an ideal experiment". *Communications in Nonlinear Science and Numerical Simulation* **27**: 175–192, 2015. DOI: 10.1016/j.cnsns.2015.02.024.

[97] R. R. Nigmatullin, A. A. Khamzin, and J. T. Machado. "Detection of quasi-periodic processes in complex systems: how do we quantitatively describe their properties?" *Physica Scripta* **89**: 1–11, 2014. DOI: 10.1088/0031-8949/89/01/015201.

[98] A. Kulikovsky, H. Scharmann, and K. Wippermann. "On the origin of voltage oscillations of a polymer electrolyte fuel cell in galvanostatic regime". *Electrochemistry Communications* **6**: 729–736, 2004. DOI: 10.1016/j.elecom.2004.05.015.

[99] A. Kulikovsky, H. Scharmann, and K. Wippermann. "Dynamics of fuel cell performance degradation". *Electrochemistry Communications* **6**: 75–82, 2004. DOI: 10.1016/j.elecom.2003.10.018.

[100] J. Zhang and R. Datta. "Sustained Potential Oscillations in Proton Exchange Membrane Fuel Cells with PtRu as Anode Catalyst". *Journal of the Electrochemical Society* **149**: A1423–A1431, 2002. DOI: 10.1149/1.1511752.

[101] R. Nigmatullin et al. "New approach for PEMFC diagnostics based on quantitative description of quasi-periodic oscillations". *International Journal of Hydrogen Energy* **41**: 12582–12590, 2016. DOI: 10.1016/j.ijhydene.2016.06.011.

[102] K. Nishida et al. "Measurement of liquid water content in cathode gas diffusion electrode of polymer electrolyte fuel cell". *Journal of Power Sources* **195**: 3365–3373, 2010. URL: http://www.sciencedirect.com/science/article/pii/S0378775309023350.

[103] A. Thomas et al. "Heat fluxes and electrodes temperature in a proton exchange membrane fuel cell". *Mechanics & Industry* **1**: 1–6, 2012. DOI: https://doi.org/10.1051/meca/2012021.

[104] R. Maizia et al. "Proton exchange membrane fuel cell diagnosis by spectral characterization of the electrochemical noise". *Journal of Power Sources* **342**: 553–561, 2017. DOI: https://doi.org/10.1016/j.jpowsour.2016.12.053. URL: http://www.sciencedirect.com/science/article/pii/S0378775316317487.

Development of instrumentation and methodology for noise diagnostic of PEMFC stacks

Abstract

Fuel cell technology development requires adequate diagnostic tools, in particular for monitoring the state of health of industrial systems (stacks) under operating conditions. Traditional diagnostic tools require to stop or disrupt the system operating. This thesis aims at the development of an innovative and non-intrusive approach for the diagnostic of PEM (Proton Exchange Membrane) fuel cell stacks. The methodology is based on the measurement of small electrical fluctuations (electrochemical noise). To measure this noise, a high frequency signal acquisition system was used without prior analog filter. These measurements were obtained within the ANR project « Propice » using four measurement campaigns with the collaboration of FCLAB and CEA LITEN. Electrochemical noise Measurements, over several weeks, made it possible to build a rich database. To process these data, different statistical approaches in time, frequency and tempo-frequency domains have been used for the generation of reliable and robust descriptors. It has been shown that the measurement of noise makes it possible to obtain a rich signature of the PEM stacks in a wide frequency range. This signature reflects the various physico-chemical phenomena and it is very sensitive to the operating parameters of the system. The evolution of this signature in short time analysis can be used for an in-situ diagnostic of the state of health of commercial stacks under real operating conditions and for the development of prognostic strategies.

Keywords: electrochemical noise, instrumentation, methodology, statistical descriptors, diagnostic, prognostic, fuel cell, pemfc stack

---

Développement d'une instrumentation et méthodologie par l'étude des bruits électrochimiques pour le diagnostic des stacks de pile à combustible de type PEMFC

Résumé

Le développement de la technologie « piles à combustible » nécessite l'utilisation d'outils de diagnostic adéquats notamment pour le monitoring de l'état de santé des systèmes industriels (stacks) dans les conditions réelles de fonctionnement. L'utilisation des moyens traditionnels de diagnostic nécessite l'arrêt ou la perturbation du fonctionnement du système. Le travail de cette thèse vise le développement d'une approche innovante non intrusive pour le diagnostic des stacks PEM (Proton Exchange Membrane), basée sur la mesure des petites fluctuations électriques (bruits électrochimiques). Pour mesurer les bruits, un système d'acquisition des faibles signaux à haute fréquence a été utilisé sans filtrage analogique préalable. Ces mesures ont été dans le cadre du projet ANR « Propice » pour quatre campagnes de mesures avec la collaboration du FCLAB et du CEA LITEN. Les mesures des bruits électrochimiques, sur plusieurs semaines, ont permis de construire une base de données extrêmement riche. Pour traiter ces données, différents approches statistiques dans le domaine temporel, fréquentiel et tempo-fréquentiel ont été utilisés pour la génération de descripteurs fiables et robustes. Il a été démontré que la mesure des bruits permet d'obtenir une riche signature des stacks PEM dans un vaste domaine fréquentiel. Cette signature reflète les différents phénomènes physico-chimiques et est très sensible aux paramètres de fonctionnement du système. L'évolution de cette signature au court de temps peut être utilisée pour le diagnostic in-situ de d'état de santé des stacks commerciaux dans les conditions réelles de fonctionnement et pour le développement des moyens de pronostic.

Mots clés : bruit électrochimique, instrumentation, méthodologie, descripteurs statistiques, diagnostic, pronostic, pile à combustible, stack pemfc

---

Institut Pprime
SP2MI - Téléport 2 – 11 boulevard Marie et Pierre Curie – BP 30179 F86962 Futuroscope Chasseneuil Cedex – France

Résumé de la thèse en Français

Introduction

Dans un contexte où la demande énergétique, basée essentiellement sur l'énergie fossile, est irrémédiablement en croissance et qu'une crise environnementale risque de bouleverser nos habitudes, un nouveau mix énergétique doit être imaginé. En effet, la gestion globale de l'énergie est aujourd'hui intégrée dans une stratégie de développement qui inclut, au-delà de l'aspect écologique, des aspects sociaux et économiques. C'est pourquoi au cours des dix dernières années, de nombreuses alternatives ont été développées pour surmonter cette une éventuelle pénurie d'énergie, notamment par l'utilisation d'énergies renouvelables telles que l'énergie éolienne, hydraulique, ou solaire.

Cependant, l'utilisation unique des énergies renouvelables ne permet pas aujourd'hui de répondre à la demande énergétique mondiale en raison de leur faible efficacité et variabilité. Donc, de nouvelles formes de production d'énergie sont développées, en particulier les piles à combustible associées au vecteur hydrogène. En effet, la technologie des piles à combustible a un potentiel élevé pour devenir l'une des principales bases pour les sources d'énergie en raison d'un comportement respectueux de l'environnement, d'une haute efficacité, et d'un fonctionnement silencieux en raison de l'absence de pièces mobiles. L'un des systèmes les plus mis en avant dans ce domaine sont les piles à membrane à échange de protons (PEMFC). Les PEMFC sont une technologie prometteuse pour convertir l'énergie chimique en l'énergie électrique et en chaleur pour les applications mobiles (transport, électronique portable) et les applications stationnaires (générateur auxiliaire, énergie de conversion / stockage). Malgré les indéniable progrès réalisés au cours des dernières décennies, certains obstacles technologiques doivent être surmontés pour permettre un développement économique viable. Parmi les différents aspects actuellement étudiés, nous pouvons mentionner l'obligation de la réduction des coûts de fabrication, augmenter la fiabilité et la durée de vie des systèmes de piles à combustible ainsi que de développer la mise en œuvre de diagnostic et d'outils fiables de pronostique.

Ce travail de thèse s'inscrit donc dans cette problématique et concerne plus particulièrement le développement de l'instrumentation et de la méthodologie du bruit électrochimique pour le diagnostic des piles PEMFC. Le développement de la technologie des piles à combustible nécessite des outils de diagnostic adéquats, en particulier pour le suivi de l'état de santé de systèmes industriels (piles) dans des conditions de fonctionnement.

Cette thèse vise le développement d'une approche innovante et non intrusive pour le diagnostic des PEM (Proton Exchange Membrane) piles à combustible. La méthodologie est basée sur la mesure de petites fluctuations (bruit électrochimique). Pour mesurer ce bruit, une acquisition de signal à haute fréquence a été utilisé sans filtre analogique préalable. L'aspect fondamental est de comprendre à travers l'utilisation de l'analyse du bruit, les phénomènes physiques internes se déroulant dans la pile, similaire à l'impédance électrochimique, mais avec l'avantage que le bruit électrochimique est non intrusif (pas de perturbation du système avec un signal d'excitation).

Ces mesures ont été obtenues dans le cadre du projet ANR «PROPICE» en utilisant quatre campagnes de mesures avec la collaboration de FCLAB, EIFER et CEA LITEN. Trois d'entre elles sont basées sur le profil de micro-cogénération et la quatrième est basée sur le profil automobile. Les mesures de bruit électrochimique, sur plusieurs semaines (1000h) pour chaque campagne, en rendu possible la construction d'une base de données riche. Sûrement, les difficultés de stockage (big data) et l'analyse à long terme a été rencontré et surmonté dans ce travail.

Pour traiter ces données, différentes approches statistiques en temps, fréquence et tempo-fréquence les domaines ont été utilisés pour la génération de descripteurs fiables et robustes. Cela a été montré que la mesure du bruit permet d'obtenir une signature riche des piles PEM dans une large gamme de fréquence. Cette signature reflète les différents phénomènes physico-chimiques et il est très sensible aux paramètres de fonctionnement du système. L'évolution de cette signature peut être utilisée pour un diagnostic in situ de l'état de santé des piles commerciales dans des conditions réelles de fonctionnement et pour le développement de stratégies pronostiques.

Ce manuscrit est divisé en six chapitres. Le chapitre 1 présente l'état de l'art du carburant technologies cellulaires. Le chapitre 2 met en évidence le principe, les limites et le diagnostic du PEMFC. Ce chapitre se concentre sur les méthodes qui permettent le diagnostic de la technologie PEMFC. Le chapitre 3 est dédié à l'analyse de bruit électrochimique et son application sur le diagnostic des piles à combustibles. Ce chapitre est basé sur la présentation de différentes méthodologies de signaux et en particulier sur les méthodes de « detrending » et les méthodes mathématiques pour la génération les descripteurs statistiques est expliquée. Dans le chapitre 4, les descripteurs statistiques générés au cours des expériences fournis dans le cadre du projet ANR "PROPICE" sont présentés dans les domaines temporels et fréquentiels. Ces descripteurs et leurs évolutions sont présentés pour les quatre campagnes et fournis différentes

signatures pour chaque analyse, dans le domaine temporel et fréquentiel et pour chaque campagne. Le chapitre 5 met l'accent sur l'utilisation de méthodes temps-fréquence pour générer des descripteurs statistiques dans les deux domaines en même temps. Cette application de l'analyse temps-fréquence donne quelques signatures sous forme de « tableau » des piles à combustible pour les quatre campagnes du projet. Au chapitre 6, le croisement de toutes les méthodes et tous les résultats sont faits. L'objectif de ce chapitre tes de donner quelques conclusions sur les descripteurs statistiques et les signatures en temps, fréquence et domaine temps-fréquence. La comparaison des signatures générées par des descripteurs statistiques entre les points de fonctionnement des quatre campagnes met en évidence la puissance de l'analyse du bruit électrochimique pour fournir des résultats très intéressant et des signes remarquables des phénomènes physiques au sein d'une pile PEMFC, éléments essentiels pour son bon diagnostic et son pronostic futur. Enfin, une conclusion générale résume le travail effectué au cours de cette thèse et suggère des perspectives pour les travaux futurs.

Chapitre 1 : Piles à combustible – état de l'art

Les énergies fossiles et notamment le charbon est la première source d'énergie utilisée par l'homme. Cette utilisation a commencé au début du 18ème siècle et a permis la première révolution industrielle. Aujourd'hui encore le charbon reste une énergie primaire primordiale pour notre civilisation. Un nouveau paradigme et mix énergétique doit être inventé avec une collaboration entre les sources d'énergies, renouvelables et/ou fossiles et les vecteurs énergétiques permettant leur acheminement (Figure 1.1).

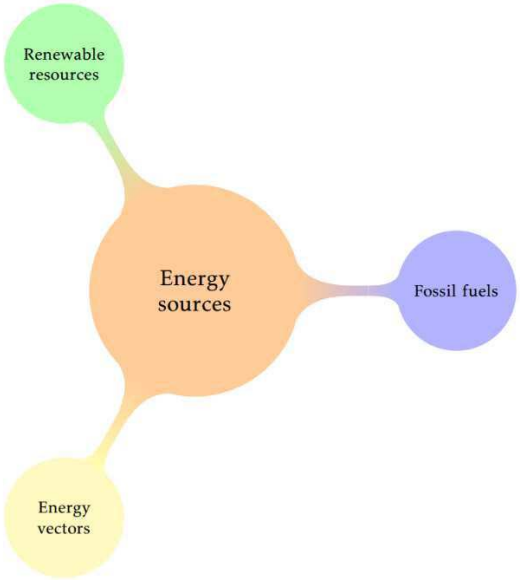

Figure 1.1 – Différentes types d'énergie

Une utilisation raisonné et sobre de l'énergie avec l'incorporation de plus en plus grande des renouvables est un solution au défi énergétique de demain. Vis-à-vis du caractère intermittent et variable des énergies renouvelables, l'hydrogène apparait comme un vecteur intéressant pour le stockage de l'énergie.Toutefois son aspect vertueux devra être corrélé à une production verte et faiblement émmettrice de CO2. Les différents moyens de production de l'hydrogène sont présentés figure 1.2 et l'on constate que sa production est majoritairement faite à partie d'énergie fossile.

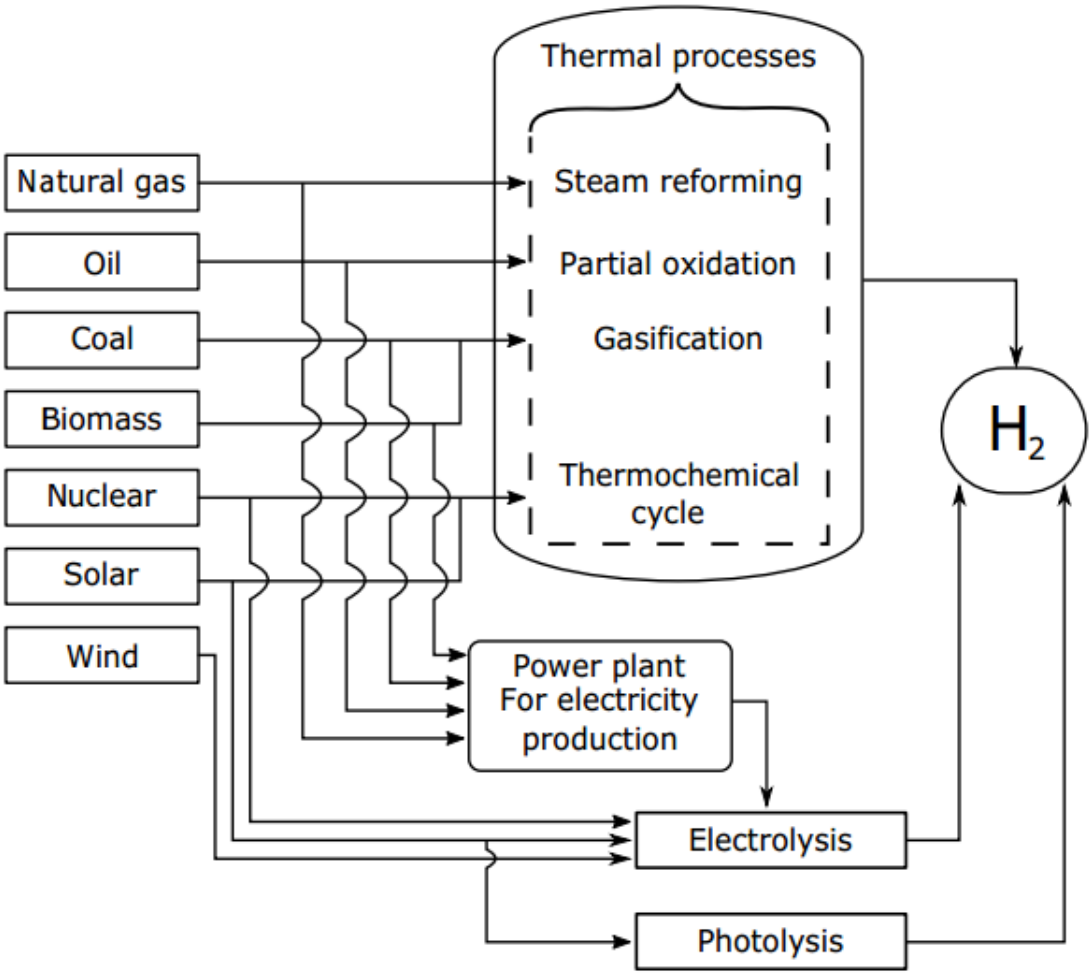

Figure 1.2 – Schéma des principaux moyens de production de l'hydrogène

A partir d'une production d'hydrogène plus « vert », les piles à combustibles permettent elle de convertir énergie chimique en énergie électrique et chaleur. Les différents types de piles à combustibles utilisées, leurs technologies, leurs puissances ainsi que leurs avantages et désavantages sont rappelés tableau 1.1.

Type of FC	AFC	PEMFC	DMFC	PAFC	MCFC	SOFC
Name	Alkaline Fuel Cell	Polymer Exchange Membrane Fuel Cell	Direct Methanol Fuel Cell	Phosphoric Acid Fuel Cell	Molten Carbonate Fuel Cell	Solid Oxide Fuel Cell
Electrolyte	KOH Solution (Aqueous solution of potassium hydroxide in a matrix)	Polymer Membrane proton conductive (Perfluorosulfonic acid)	Polymer Membrane proton conductive	Phosphoric acid (Phosphoric acid soaked in a matrix)	Li_2CO_3 and K_2CO_3 melted in a matrix of $LiAlO_2$ (solution of litium, and/or potassium carbonates, soaked in a matrix)	ZrO_2 and Y_2O_3 (Yttria stabilized zirconia)
Catalyst	Nikel, Platine-palladium	platine	platine, platine/Ruthénium	platine	Nikel-Chrome	Lanthanum strontium manganite
Ions in the electrolyte	OH^-	H^+	H^+	H^+	CO_3^{2-}	O^{2-}
Operating temperature	80 °C-90 °C	50 °C-90 °C, typically 80 °C	60 °C-130 °C	150 °C-210 °C	600 °C-700 °C	700 °C-1000 °C
Fuel	H_2	H_2 (pure or reformed)	Methanol	H_2 (pure or reformed)	H_2 (pure or reformed)	H_2 (pure or reformed)
Oxidants	O2 (pure)	Air	Air	Air	Air	Air
Applications	space, transport, military	portable, transport, stationary	portable	transport, stationary (distributed generation)	stationary (distributed generation)	transport (APU), stationary (auxillary power, distributed generation)
Power range	10W-100 kW	1W-300 kW	1W-300 kW	1 kW-300 kW, 100 kW module	300 kW-3 MW, 300 kW module	1 kW-2 MW
Electrical efficiency	60-70 %	50-65 %	FC: 20-30%	40-50 %	55-65 %	55-65 %
Advantages	very high performance at the cathode low cost components	high energy density, quick start/stop, low temp	low operating range, easy storage and transportation,	Mature technology, good reliability, low cost electrolyte	high efficiency, large choice of catalyst, fuel flexibility, suitable for CHP	high efficiency, large choice of catalyst, fuel flexibility, suitable for CHP
Disadvantages	usage pure gas, sensitivity to impurities, electrolyte management	expensive components, water management	expensive catalyst, methanol crossover	expensive catalyst, evaporation of the acid, long start-up time, low power density	long start-up time, corrosion, low power density	long start-up time, high temperature, components relatively expensive

Tableau 1.1 – Principales caractéristiques des différents types de piles à combustible

La technologie des piles à combustibles et notamment des PEMFC fait face au triptyque, faible cout, grande durabilité et haute performance. Il est difficile d'obtenir ces trois points en même temps et une hiérarchisation du développement des composants de la pile à combustible doit être fait (figure 1.3).

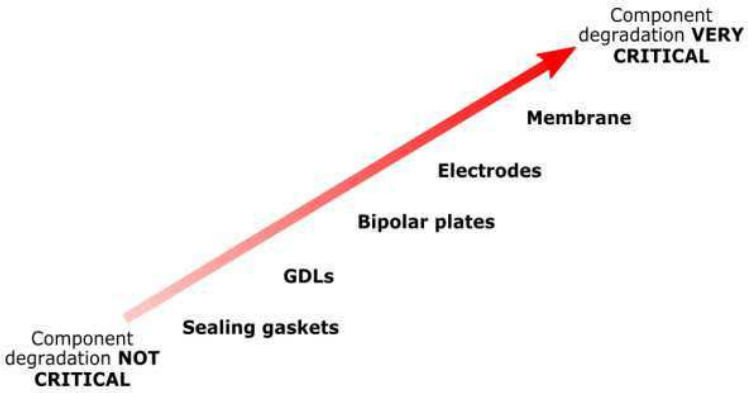

Figure 1.3 – Hiérarchie des composants critiques d'une pile à combustible

Les aspects critiques à l'heure actuelle se situent au niveau des membranes, utilisant des composés chers et venant de la chimie du fluor principalement, et des électrodes utilisant du platine (métal rare) et du carbone assujetti à une corrosion forte à fort potentiels. Les plaques bipolaires et notamment leur design participe au cout élevé de ce type de technologie.

Chapitre 2 : Les piles PEMFC – Principe, limitations et diagnostic

Dans ce chapitre nous nous sommes intéressés à présenter le principe de fonctionnement, les limitations et les différents techniques de diagnostic pouvant être utilisées pour les piles PEMFC. Les différents composants d'une pile PEMFC sont présentés figure 2.1.

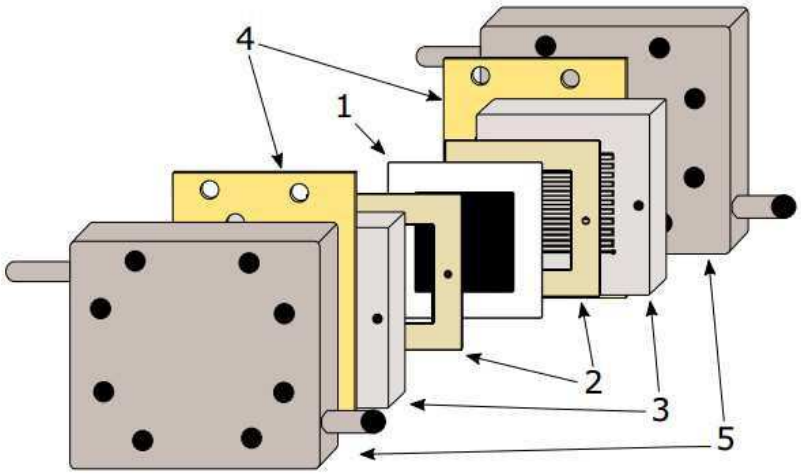

Figure 2.1 – Assemblage d'une PEMFC. 1- assemblage membrane-électrode, 2- joints, 3- plaques d'alimentation, 4- plaques collectrices de courant, 5- plaques de serrage

La nature et la fonction de chaque composant est détaillé dans le document principal. Un accent est fait sur leur mode de dégradations et quelles méthodes pourrait être employer pour en assurer leur diagnostic. La figure 2.2 présente tous les capteurs qui peuvent être installé sur un banc de pile à combustible et les différents paramètres physiques qui peuvent être mesurés pendant les campagnes de mesure. Tous ces paramètres tels que le débit, la pression, la température, l'humidité relative des gaz, le courant et la tension du stack et des cellules qui le compose permettent d'obtenir une base de données riches de signaux et ainsi le développement de méthodologies fines et complètes afin d'obtenir les performances et un diagnostic riche du système.

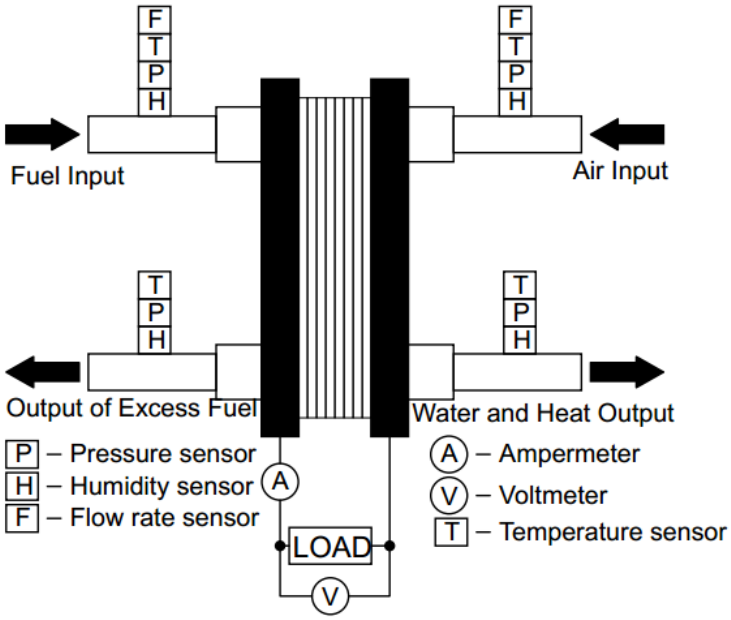

Figure 2.2 – Différents capteurs mis en place sur le banc d'essai pour la génération des descripteurs statistiques

Les différentes signaux d'acquisitions obtenus dans ce travail sont présentés figure 2.3.

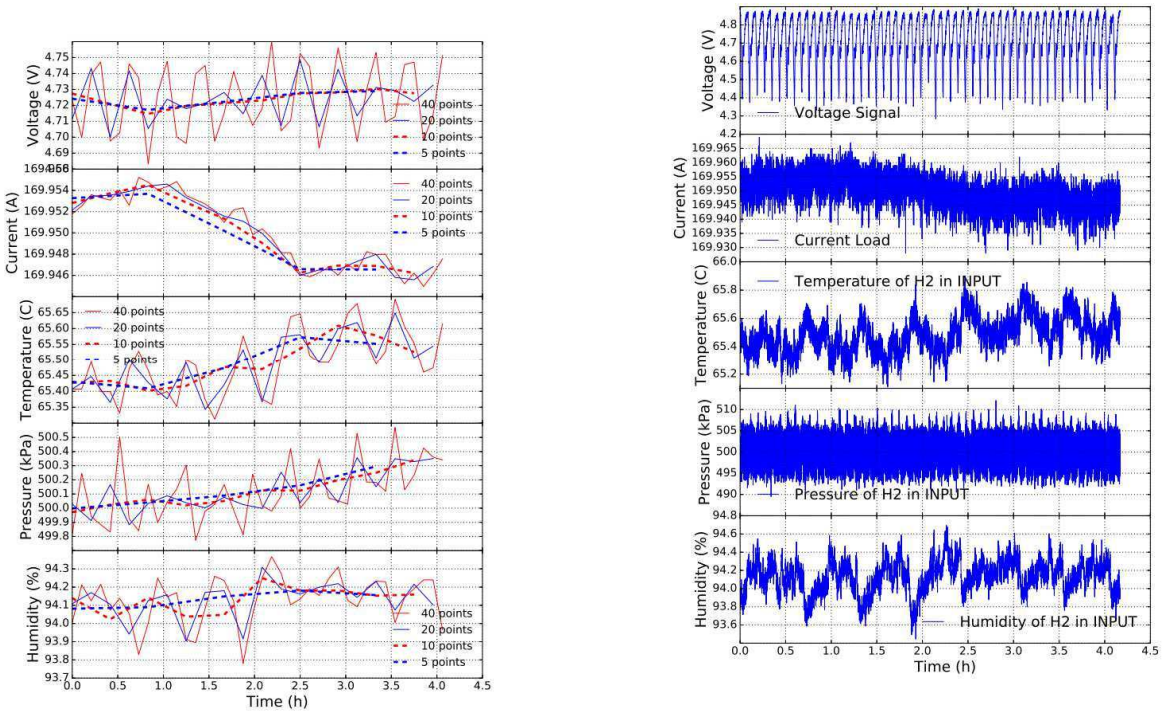

Figure 2.3 – Signaux d'acquisition des différents capteurs

Chapitre 3 : Le bruit électrochimique appliqué au diagnostic des piles à combustible

Le chapitre 3 est consacré à la présentation des différents bruits pouvant exister et une attention particulière s'est porté sur le bruit électrochimique et sa caractérisation possible comme outil de diagnostic pour les stacks PEMFC. Une méthodologie de traitement du signal y est présentée et particulière sur la présentation des différentes méthodes de « deterending » d'un signal c'est-à-dire la suppression de sa composante continue. La méthodologie employée ici c'est faible à l'aide d'une analyse à court terme en découpant le signal par morceaux et en appliquant un polynôme de degré 5 pour différente tailles de fenêtres.

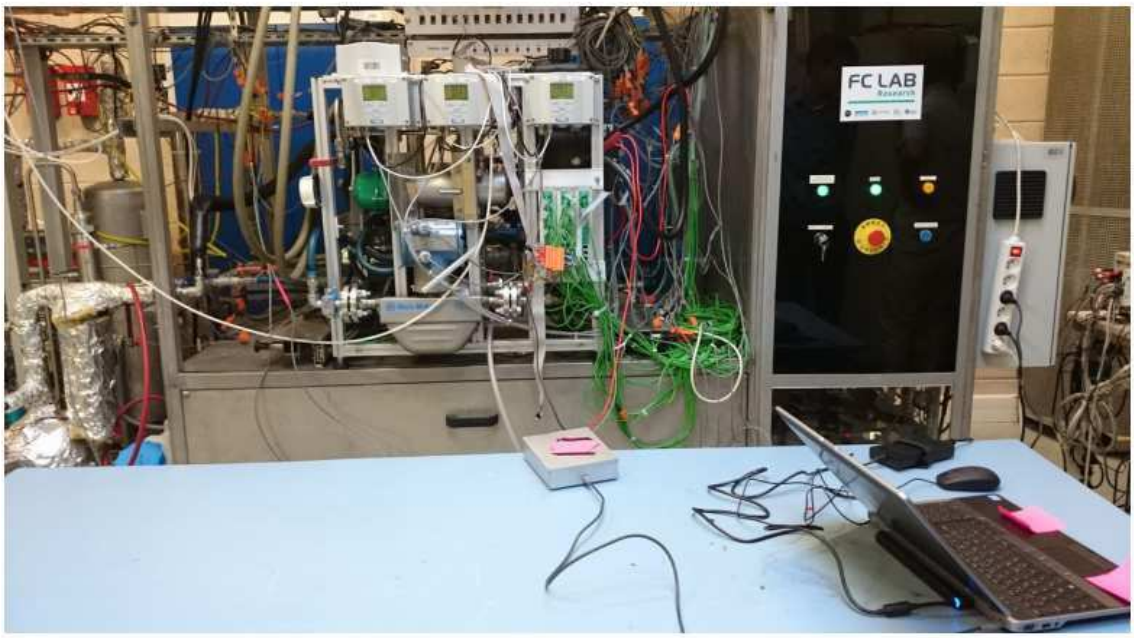

Figure 3.1 – Banc d'essai

La figure 3.1 montre le dispositf expérimental utilisé pour ce travail avec le stack PEMFC développé par le CEA, la carte d'acquisition National Instrument® permettant une acquisition des signaux à hautes fréquences (50kHz) sur une grande résolution (24 bits) et le PC permettant de sauvegardé et créé la base de données sur plusieurs milliers d'heures d'enregistrements (plus de 5000h - big data). La figure 3.2 précise que notre mesure se fait sans filtrage analogique au préalable (AC), c'est-à-dire de manière direct (DC). Cela permet de ne pas perdre d'information dû à l'utilisation d'un filtre analogique non adapté et si besoin d'appliquer par la suite un filtrage numérique sans pertes d'informations cruciales.

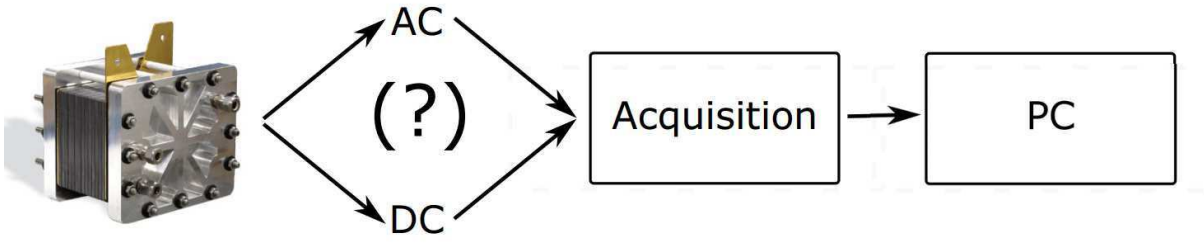

Figure 3.2 – Diagramme permettant l'acquisition direct du signal

La figure 3.3 présente notre technique polynomiale à court-terme de « detrending », c'est-à-dire la suppression de la composante continue de notre signal de tension. On peut voir cette procédure comme l'application d'un filtre numérique.

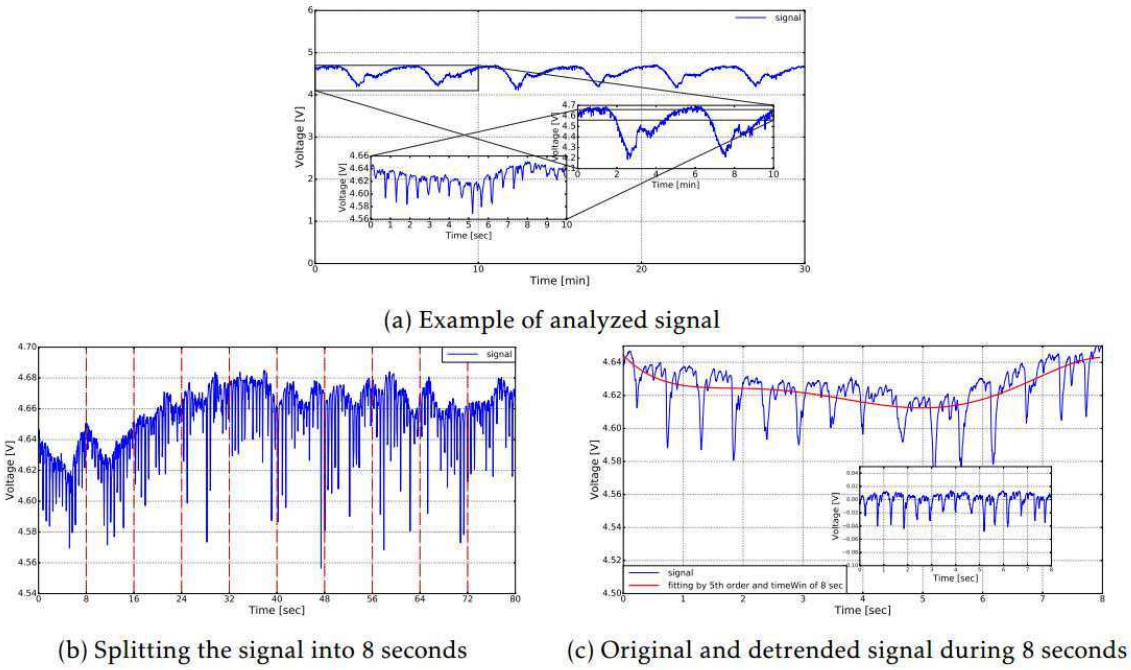

Figure 3.3 – Procédure de suppression de la composante continue

La figure 3.4 nous renseigne sur l'impact de la taille des fenêtres et de l'ordre du polynôme utilisés utilisés sur le detrending du signal. Car l'analyse à court terme oblige de choisir la taille (le nombre de point) à prendre dans chaque fenêtre.

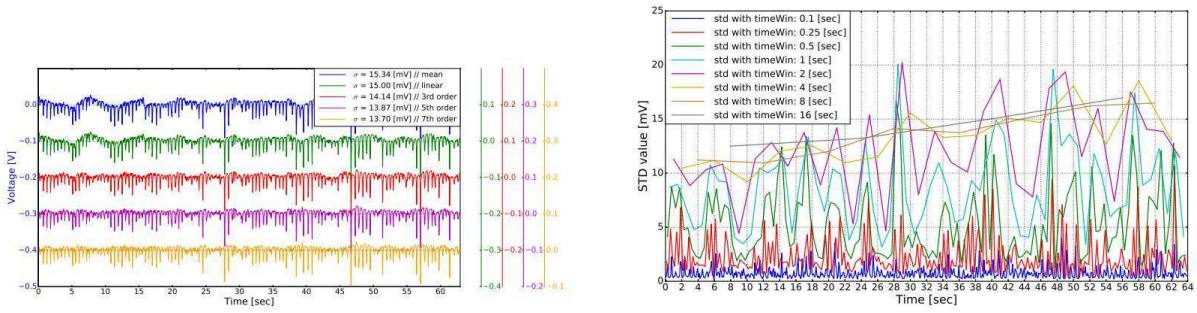

Figure 3.4 – Influence de la taille de la fenêtre et de l'ordre du polynôme utiliser pour la suppression de la composante continue du signal

La figure 3.5 montre l'impact des différentes méthodes de « detrending » d'un signal et valide l'utilisation d'un polynôme de degré 5 sur des fenêtres à court terme (découpage du signal sur des petites fenêtres 32, 8, 2 et 0.3 secondes).

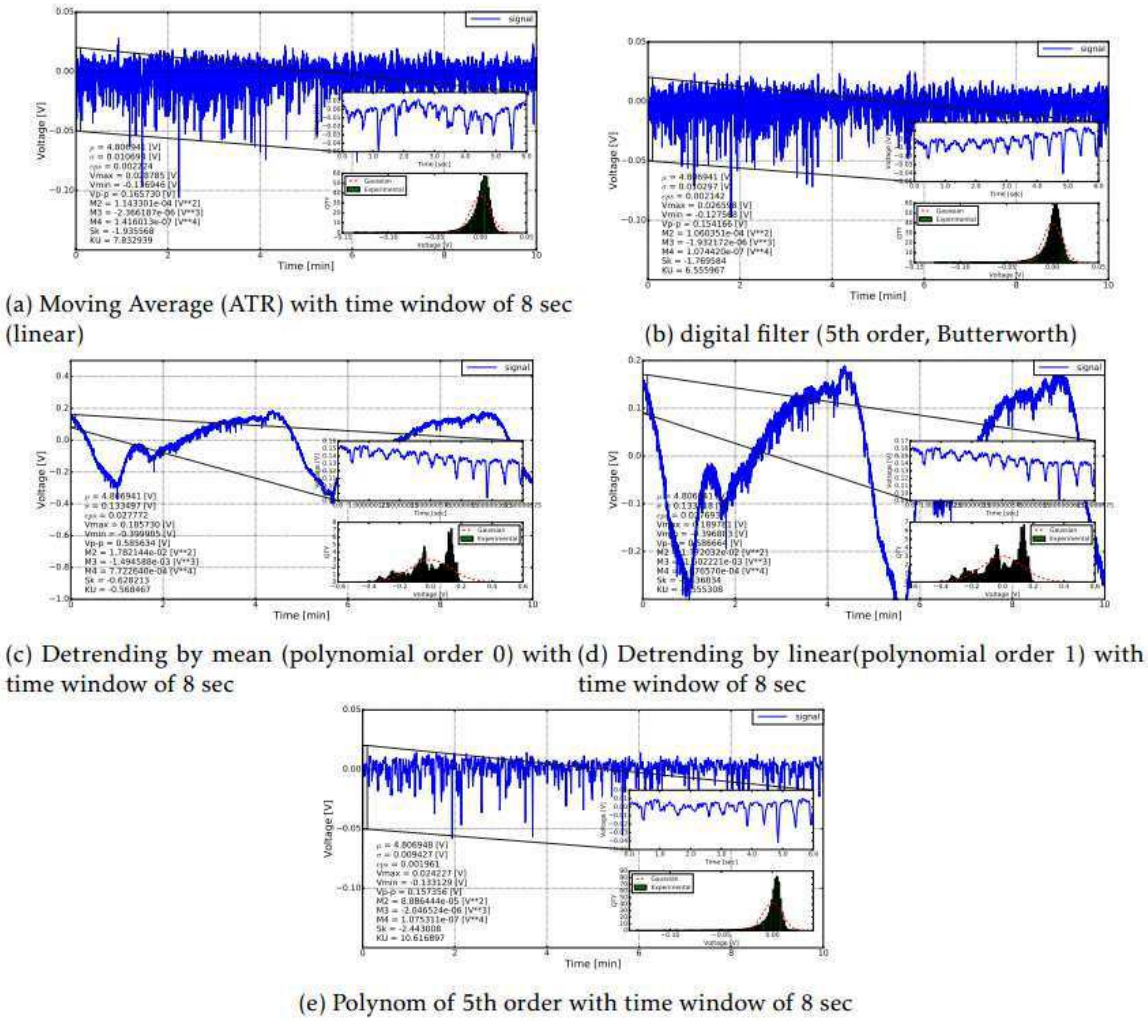

(a) Moving Average (ATR) with time window of 8 sec (linear)

(b) digital filter (5th order, Butterworth)

(c) Detrending by mean (polynomial order 0) with time window of 8 sec

(d) Detrending by linear(polynomial order 1) with time window of 8 sec

(e) Polynom of 5th order with time window of 8 sec

Figure 3.5 – Evolution du bruit après l'utilisation de différentes techniques de suppression de la composante continue du signal

Chapitre 4 : Descripteurs statistiques du bruit obtenus dans le domaine temporel et fréquentiel

Le chapitre 4 est consacré à la présentation des résultats obtenus sous forme de descripteurs statistiques dans le domaine temporel et fréquentiel. Le début du chapitre est consacré à la présentation en détail des campagnes de mesures faites dans le cadre du projet national ANR « Propice » en partenariat avec le FCLAB, EIFIER et le CEA Liten. L'objectif du projet était de se mettre dans des conditions de vieillissements des stacks de piles à combustible PEMFC pour deux profils : le profil stationnaire pour simuler des applications de micro-cogénération (Figure 4.1) et le profil transitoire pour simuler des applications automobiles (Figure 4.2).

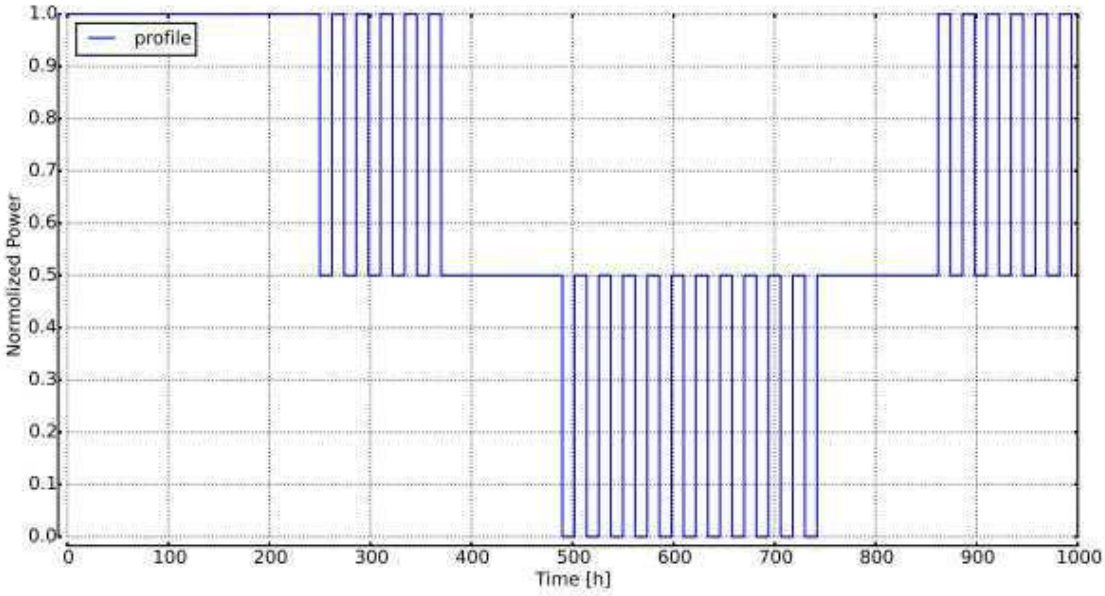

Figure 4.1 – Profil utilisé pour la campagne de micro-cogénération

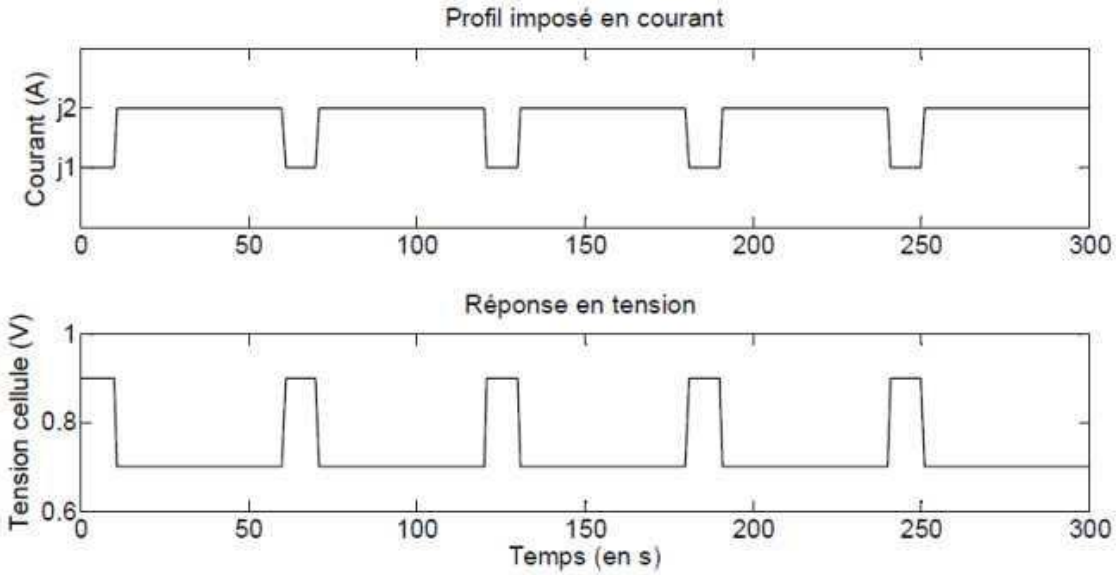

Figure 4.2 – Profil utilisé pour la campagne automobile

Quatre campagnes de mesures ont ainsi été effectués tout au long du projet qui a duré 3 ans. Trois campagnes sur la micro-cogénération et une la quatrième sur l'application automobile. Les figures 4.3, 4.4, 4.5 et 4.6 montrent les mesures de tension obtenus pour les quatre campagnes et la partie rouge met en lumière les mesures effectuées à hautes fréquences essentielles pour l'analyse du bruit électrochimique.

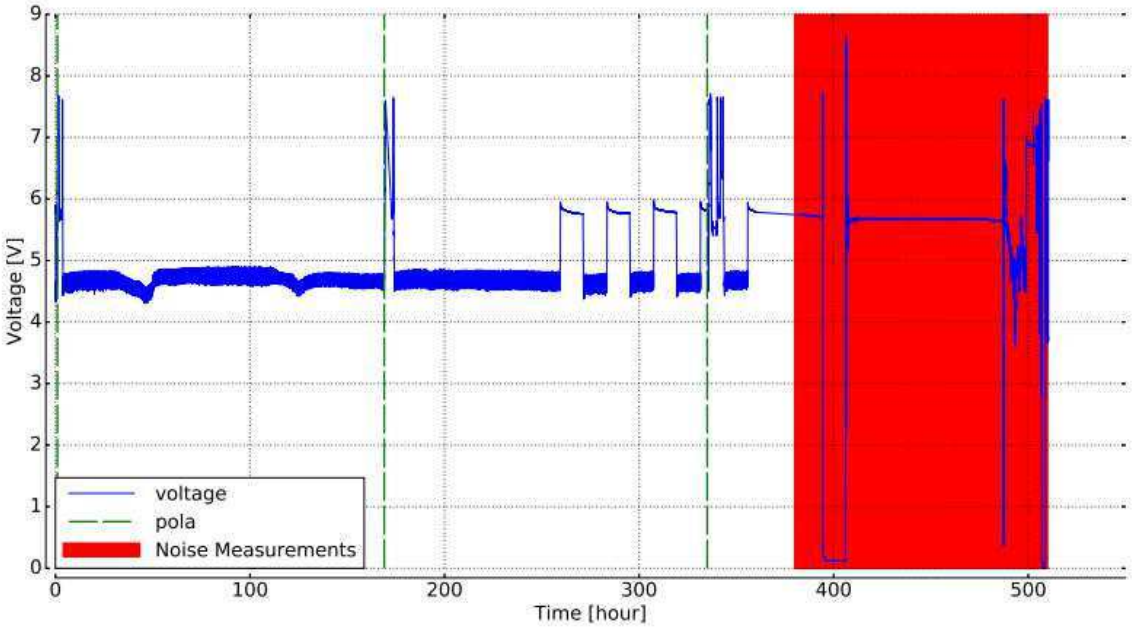

Figure 4.3 – Variation de tension pour la 1ère campagne de mesure – micro-cogénération

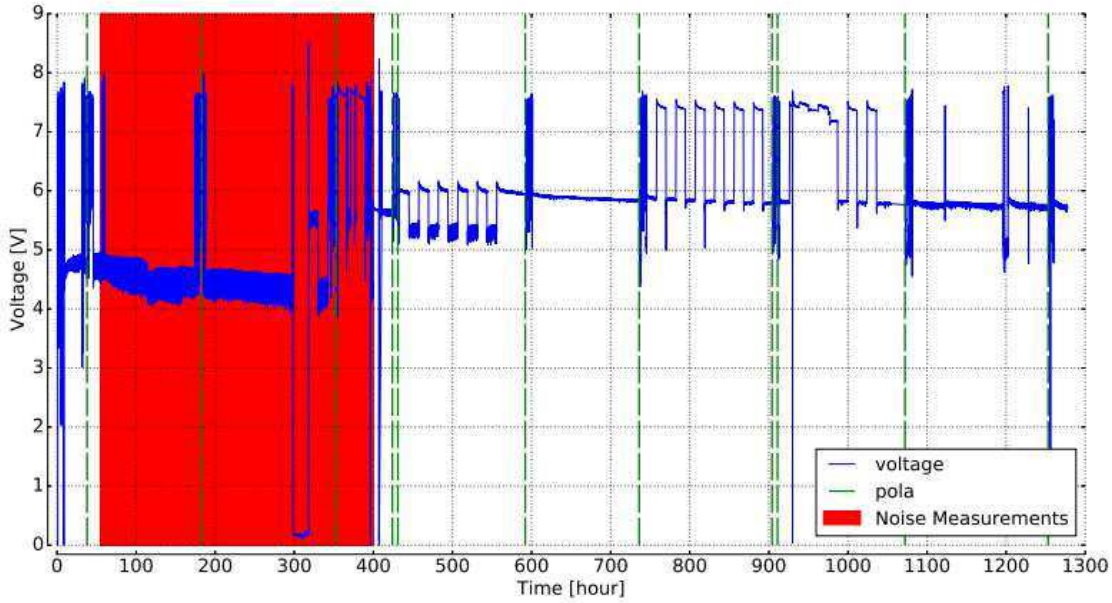

Figure 4.4 – Variation de tension pour la 2ème campagne de mesure – micro-cogénération

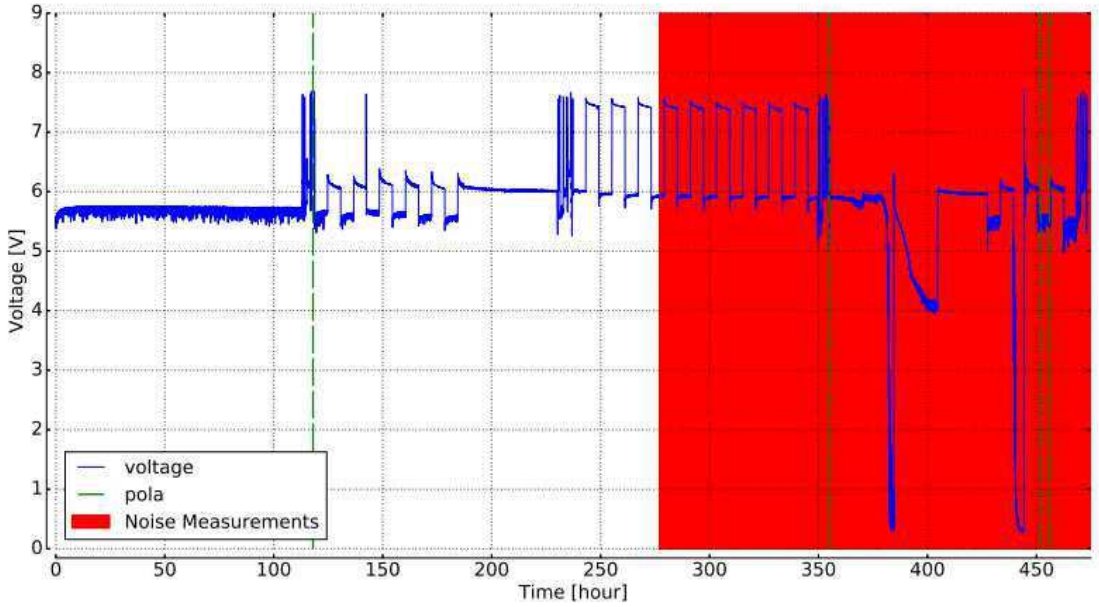

Figure 4.5 – Variation de tension pour la 3ème campagne de mesure – micro-cogénération

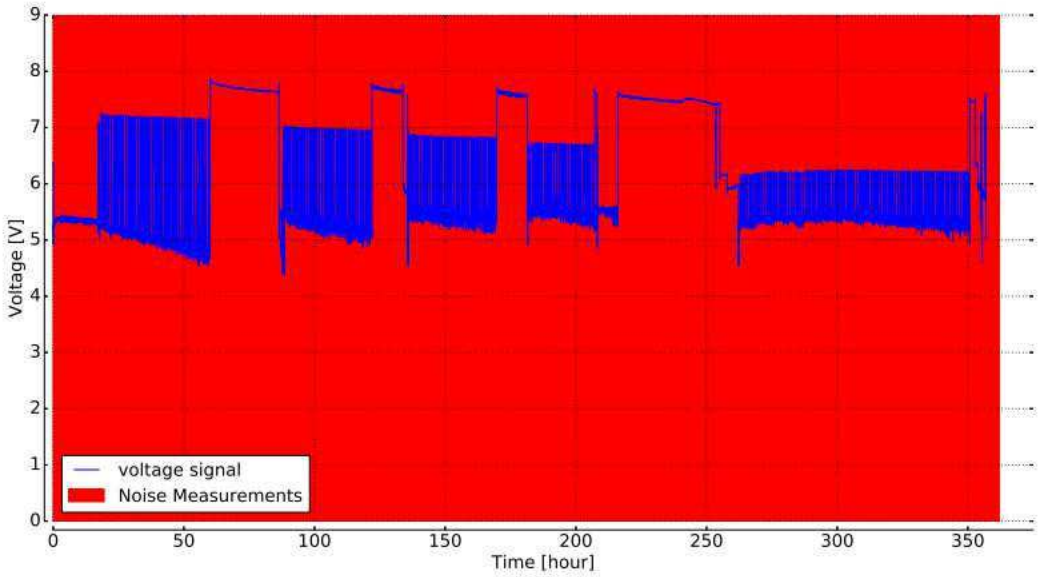

Figure 4.6 – Variation de tension pour la 4ème campagne de mesure - automobile

La suite du chapitre est consacrée aux résultats obtenus pour chaque campagne et à différentes zones de mesures dans le domaine temporel à travers l'utilisation de descripteurs statistiques (moyenne, écart-type, moments d'ordre supérieurs, Skewness, Kurtosis) et les signatures dans le domaine fréquentiel des bruits par l'utilisation de spectre calculé à l'aide d'une transformé de Welch (transformée de Fourier paramétrique). Tous ces résultats sont résumés par la figure 4.7 jusqu'à la figure 4.18. L'évolution de ces descripteurs et leurs significations sont discutées en détail dans le document principal.

1ère campagne

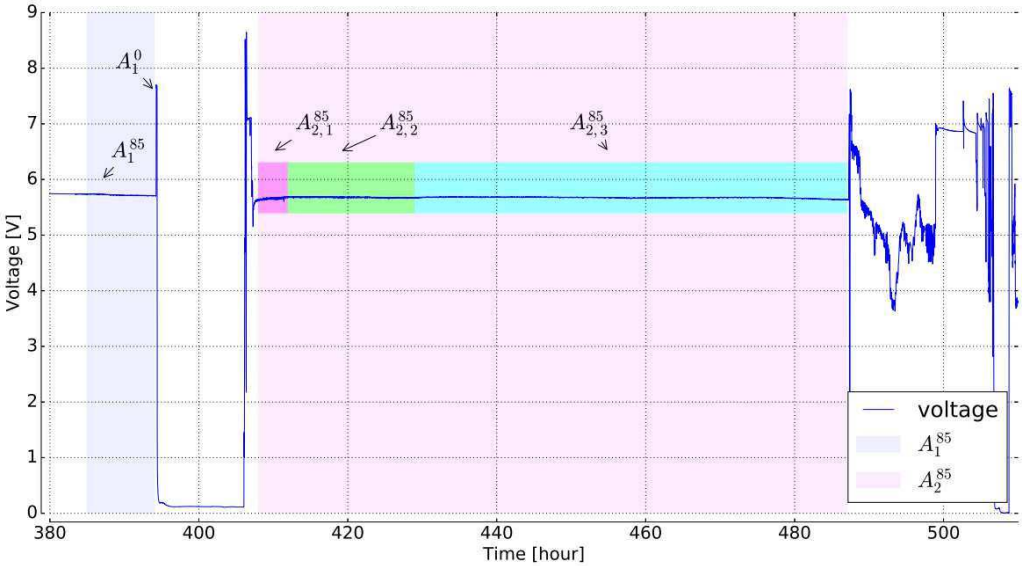

Figure 4.7 – Sélection des zones pour la 1ère campagne

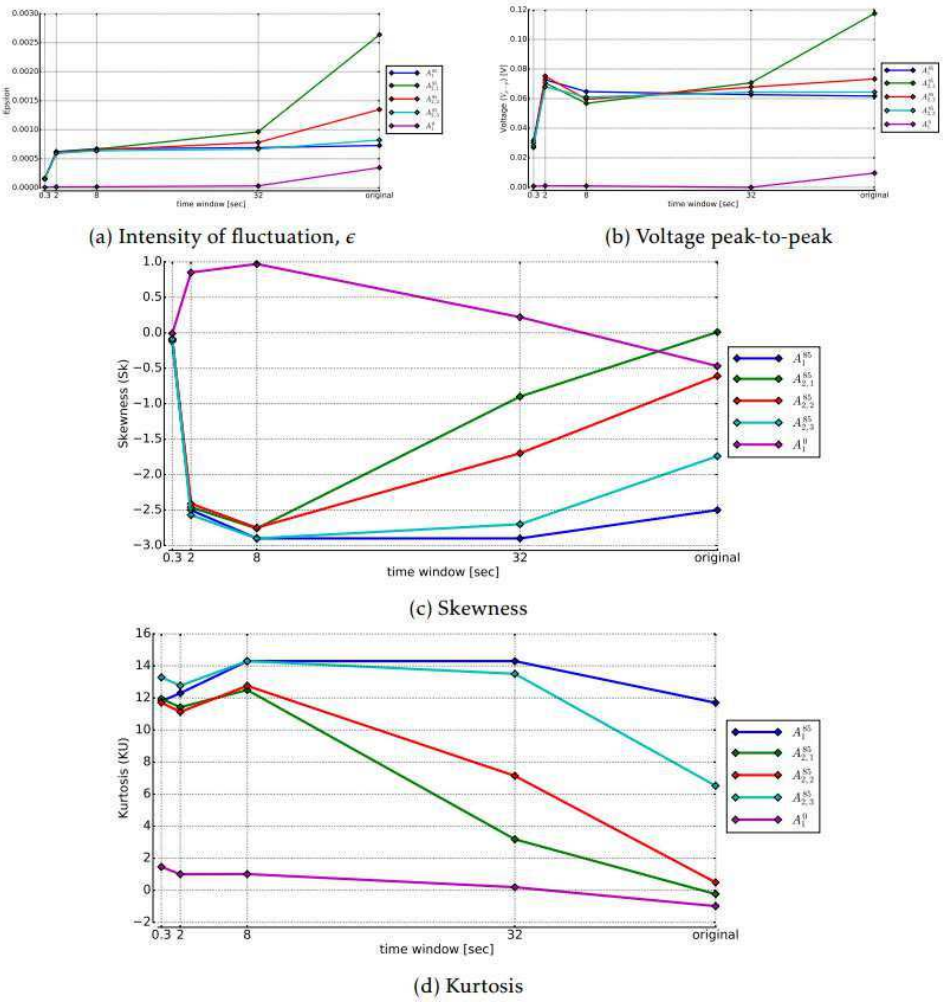

Figure 4.8 – Dépendance des descripteurs statistiques avec la fenêtre de temps – 1ère campagne

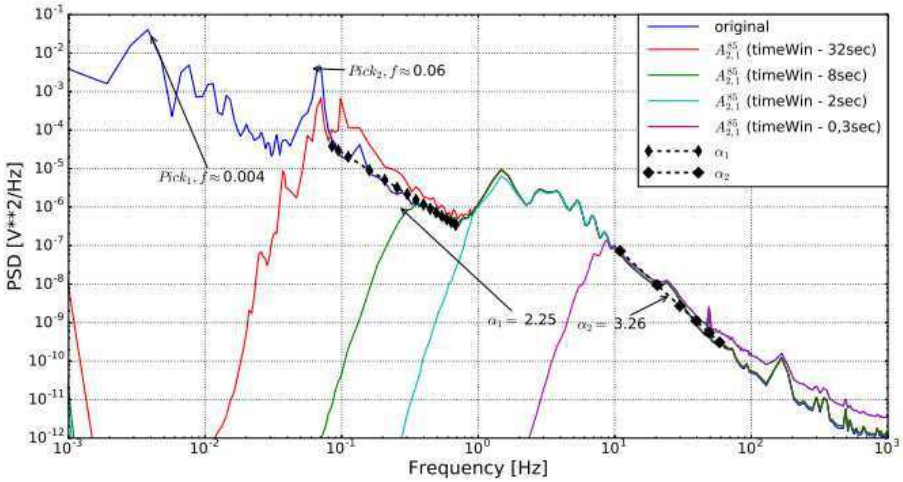

Figure 4.9 – Spectres obtenus avec différentes fenêtres de temps – 1ère campagne

2mee campagne

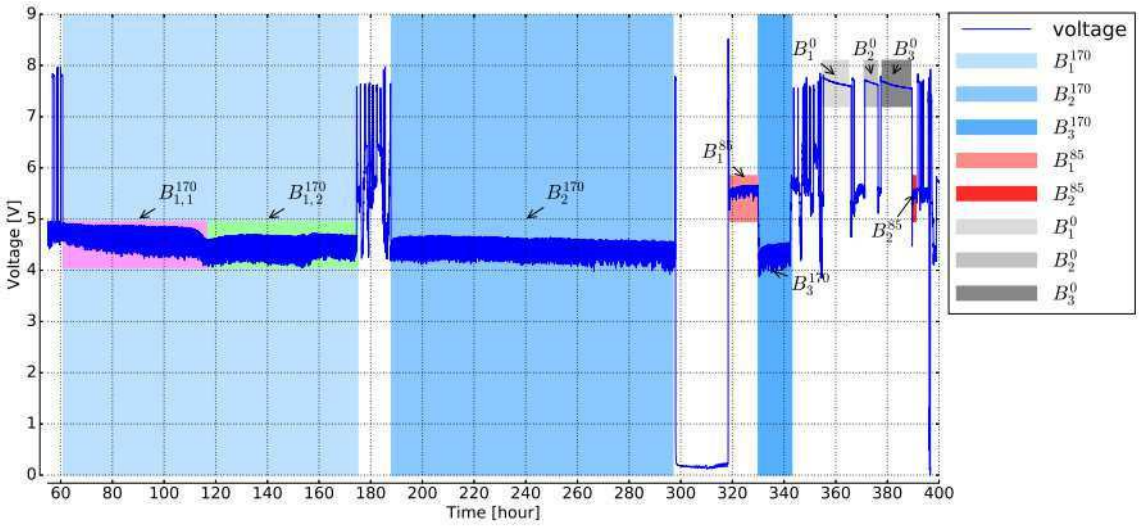

Figure 4.10 – Sélection des zones pour la 2ème campagne

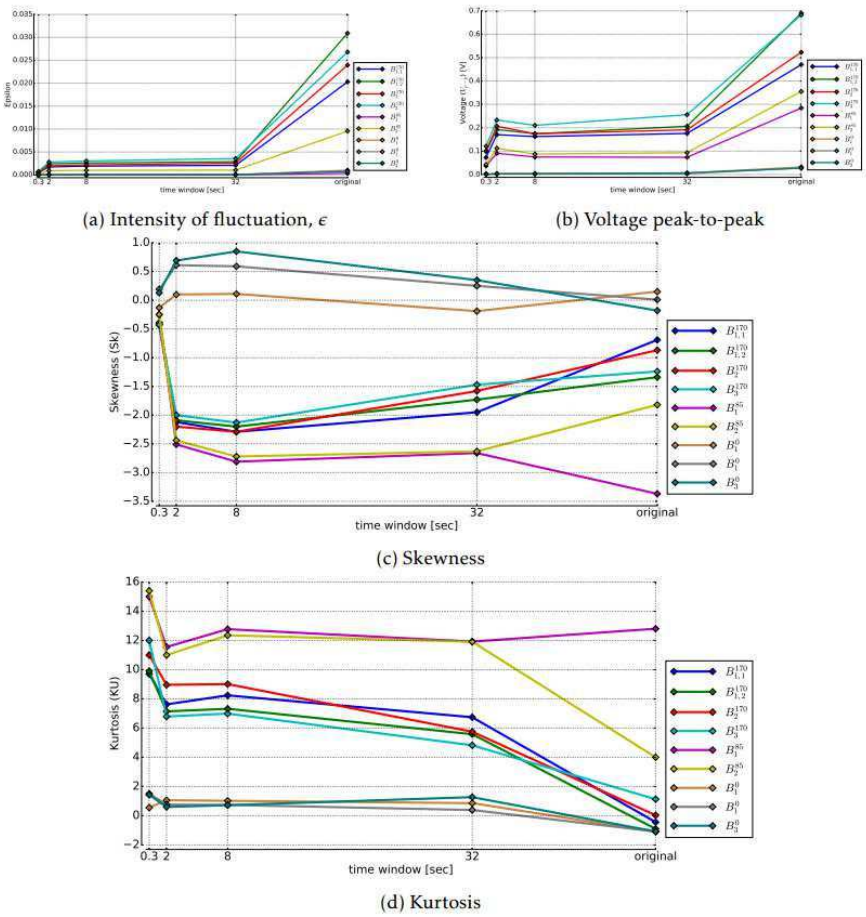

Figure 4.11 – Dépendance des descripteurs statistiques avec la fenêtre de temps – 2ème campagne

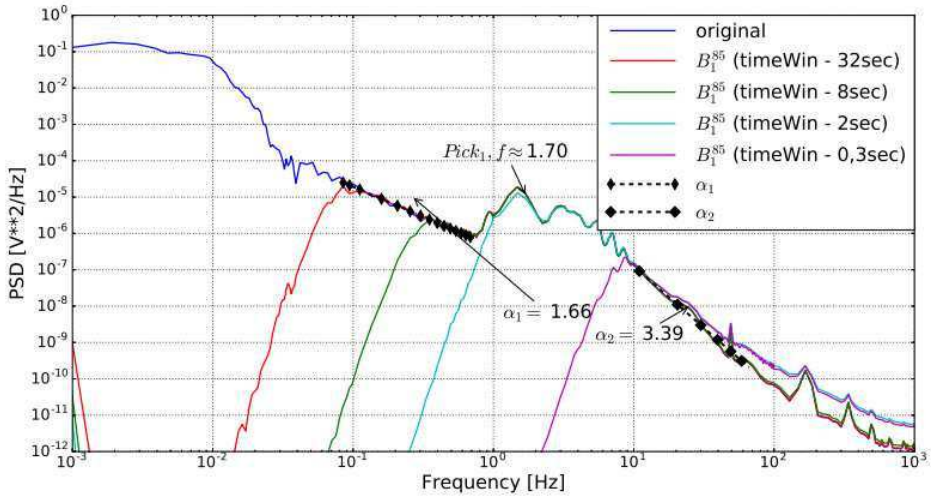

Figure 4.12 – Spectres obtenus avec différentes fenêtres de temps – 2ème campagne

3mee campagne

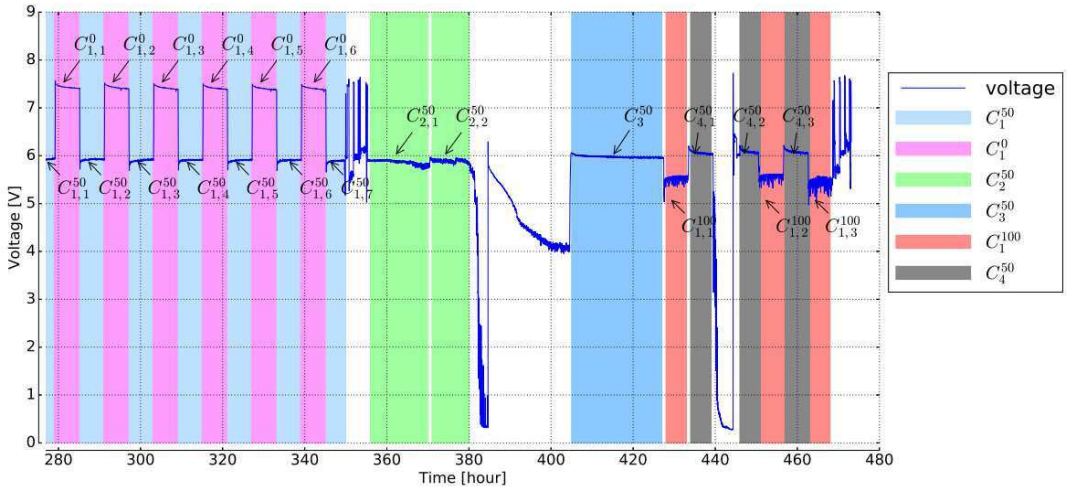

Figure 4.13 – Sélection des zones pour la 3ème campagne

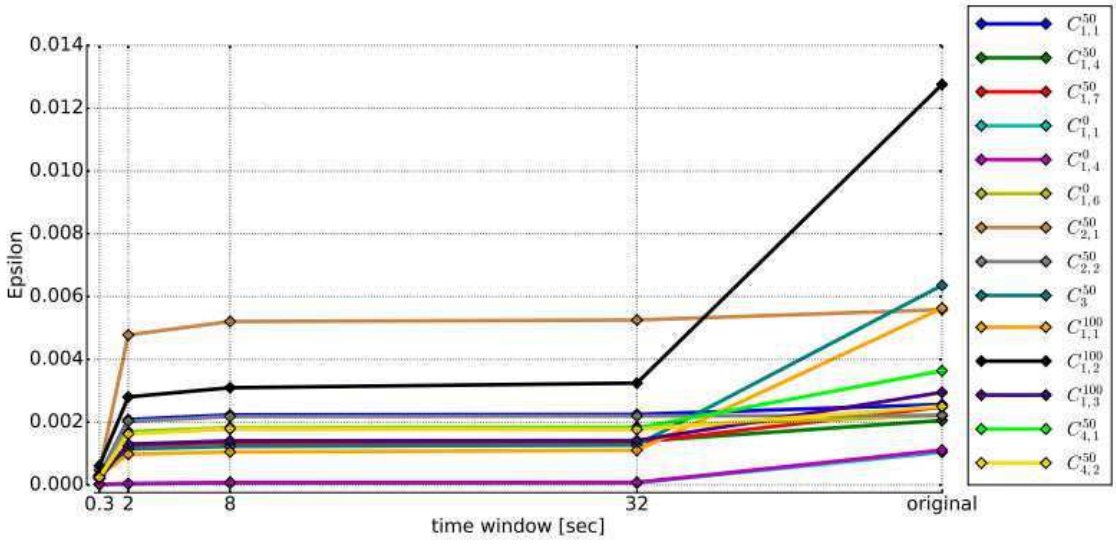

Figure 4.14 – Dépendance des descripteurs statistiques avec la fenêtre de temps – 3ème campagne

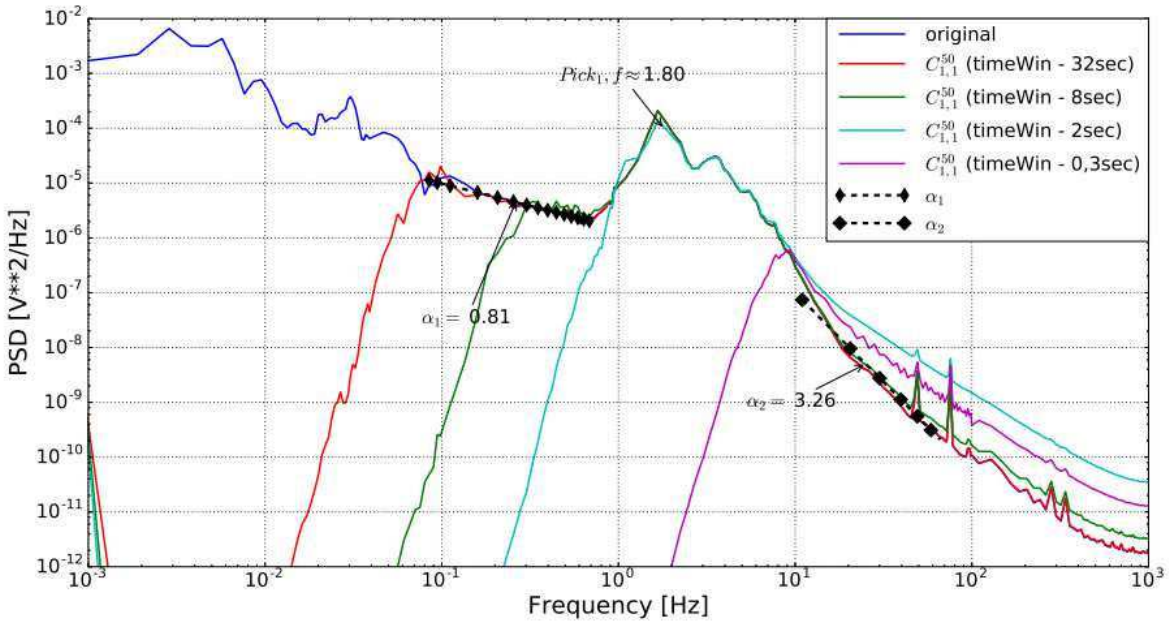

Figure 4.15 – Spectres obtenus avec différentes fenêtres de temps – 3ème campagne

4mee campagne

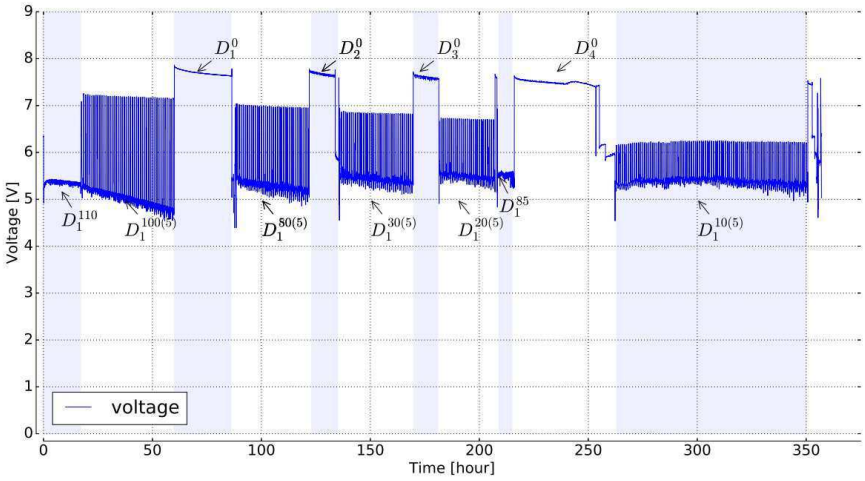

Figure 4.16 – Sélection des zones pour la 4ème campagne

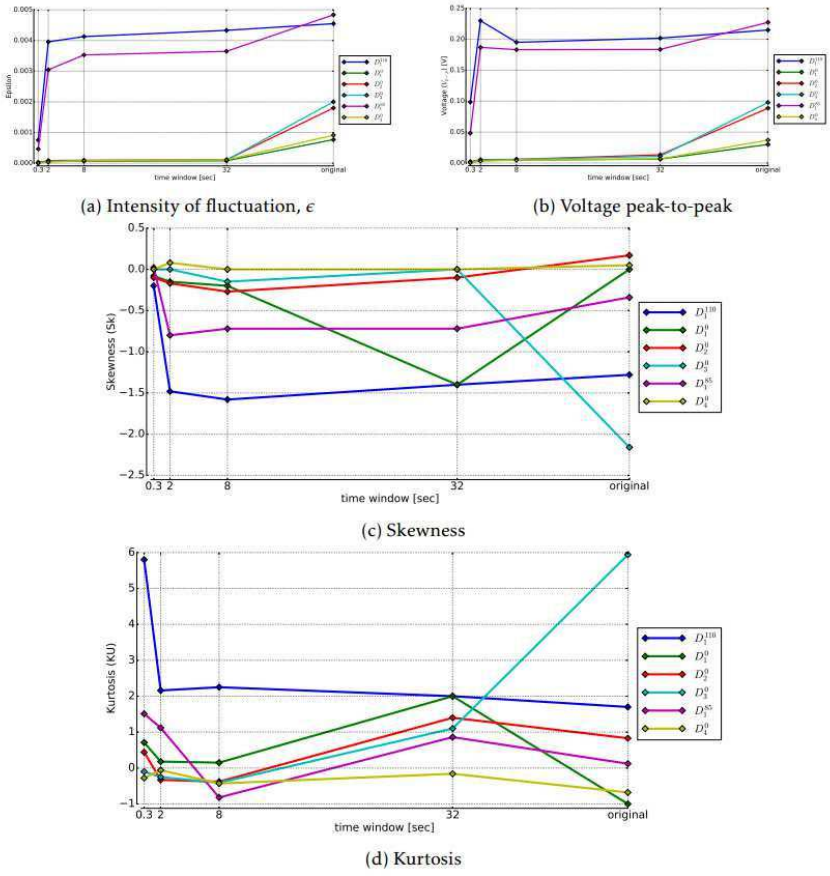

Figure 4.17 – Dépendance des descripteurs statistiques avec la fenêtre de temps – 4ème campagne

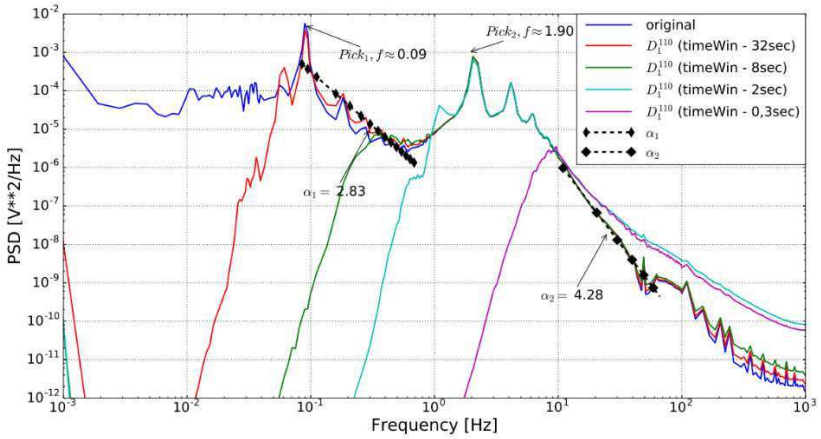

Figure 4.18 – Spectres obtenus avec différentes fenêtres de temps – 4ème campagne

Chapitre 5 : Descripteurs statistiques du bruit obtenus dans le domaine tempo-fréquentiel

Le chapitre 5 se consacre cette fois-ci à la présentation des résultats pour les 4 campagnes de mesures avec l'utilisation d'outils permettant de générer des descripteurs dans le domaine tempo-fréquentiels. Trois méthodes sont utilisées : La transformée de Fourier à court-terme, la transformée tempo-fréquentiel autorégressive et les ondelettes. Les résultats de l'application de ces 3 méthodes sont montrés figure 5.1, 5.2 et 5.3 pour la campagne automobile ici, 4ème campagne. L'évolution des scalogrammes obtenus permet de tirer plusieurs descripteurs et signatures dans mauvais ou bon fonctionnement du stack de pile à combustibles.

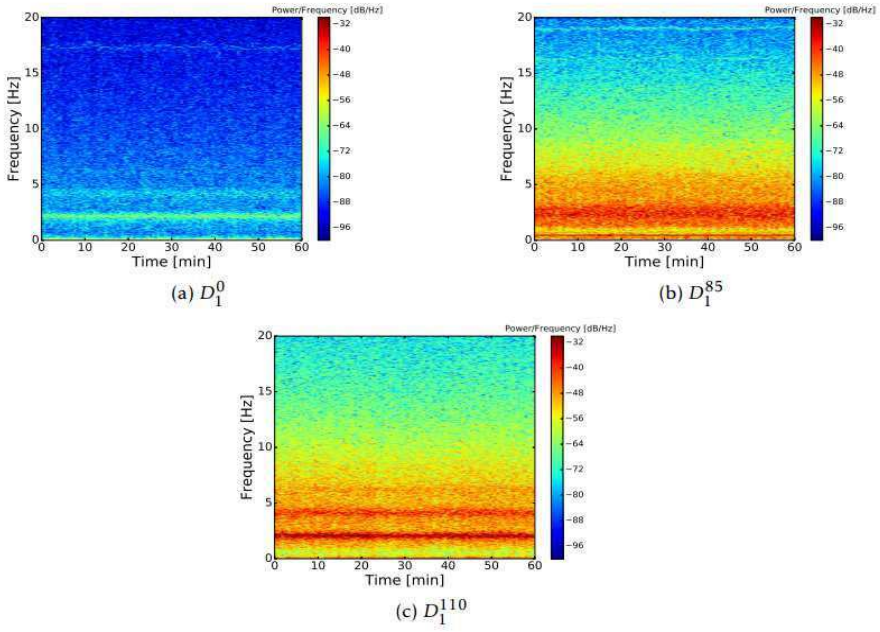

Figure 5.1 – Transformée de Fourier au temps-court – 4ème campagne

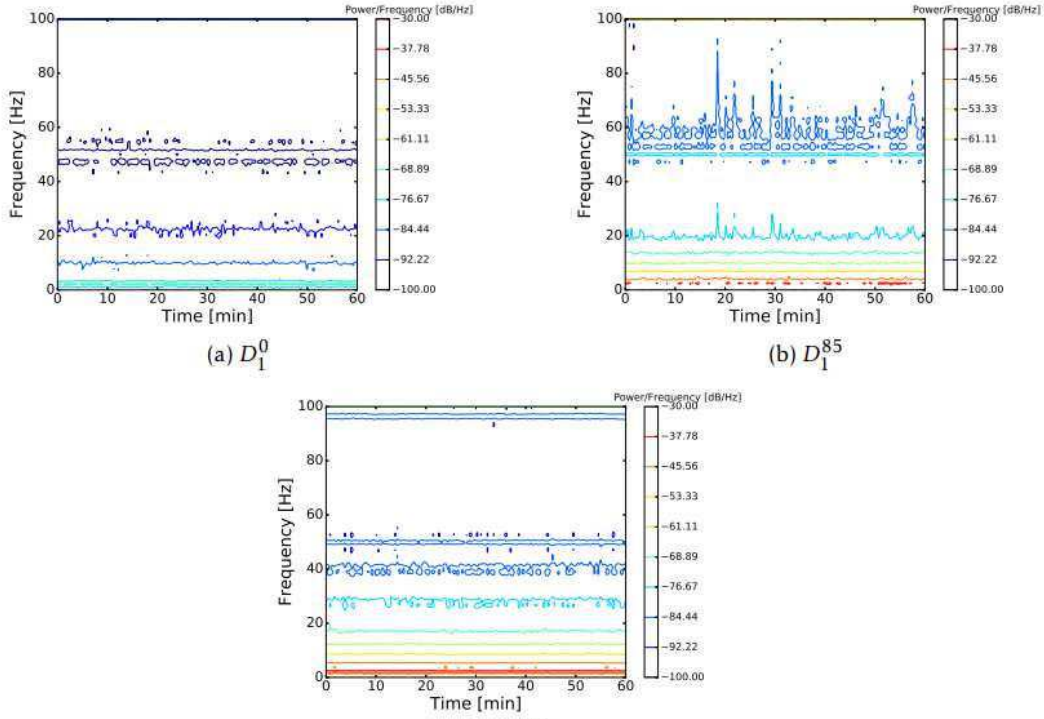

Figure 5.2 – Transformée en temps-fréquence autorégressive – 4ème campagne

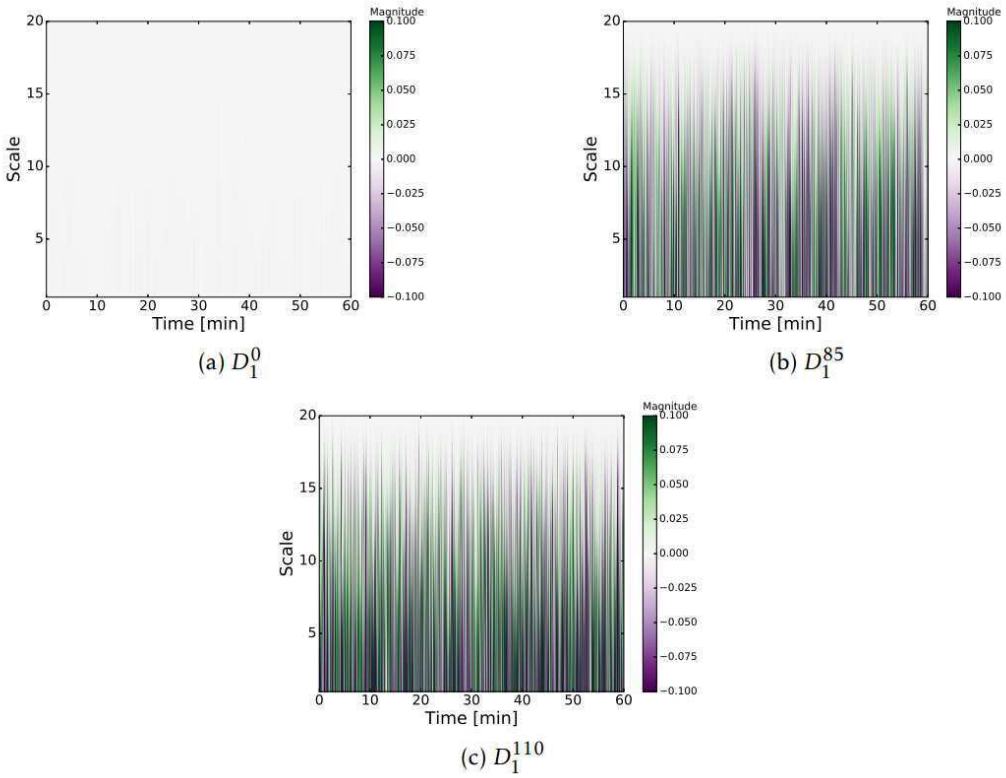

Figure 5.3 – Transformée en ondelettes – 4ème campagne

Chapitre 6 : Application du diagnostic par les bruits pour la caractérisation des stacks pile à combustibles pour les différentes conditions expérimentales.

Le chapitre 6 test le chapitre résumé qui permet la comparaison croisée de toutes les campagnes et de tous les descripteurs générés dans les domaines temporel, fréquentiel et tempo-fréquentiel. Ce regard croisé permet l'interprétation pertinente et novatrice des différentes signatures obtenus à l'aide de l'analyse des bruits électrochimiques comme outils de diagnostic pour les stack de pile à combustible de type PEMFC. Il permet de mettre en lumière tout le travail de description et présentation des résultats fait précédemment dans le document.

	original	32 seconds	8 seconds	2 seconds	0.3 seconds
μ, V	5.606	5.606	5.606	5.606	5.606
σ, mV	33.5	5.2	5.0	4.6	1.0
$eps, 10^{-6}$	5993	932	893	821	194
V_{max}, mV	5.661×10^3	12.6	15.1	36.2	19.2
V_{min}, mV	5.376×10^3	-61.1	-59.9	-54.6	-17.8
V_{p-p}, mV	284.4	73.8	75.0	90.9	37.1
M2, 10^{-6}	1128	27.3	25.0	21.1	1.1
M3, 10^{-9}	-127818	-380	-353	-245	-0.3
M4, 10^{-9}	20179	11	9.9	6.5	0
Sk	-3.37	-2.66	-2.81	-2.51	-0.25
KU	12.8	11.92	12.77	11.55	15.0

Table 6.1 – Descripteurs statistiques à 85 A avec différentes fenêtres de temps – 2ème campagne

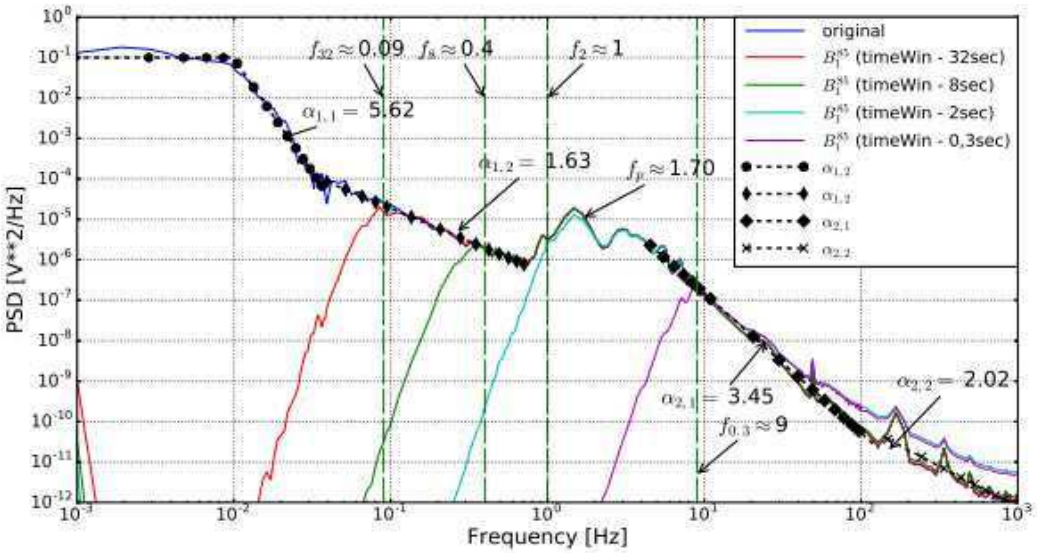

Figure 6.1 – Spectres obtenus avec différentes fenêtres de temps à 85 A – 2ème campagne

La comparaison du tableau 6.1 et de la figure 6.1 permet de montrer qu'il y a trois zones de fréquences qui présente un comportement radicalement différent en fonction de la taille des fenêtres utilisés (pas de fenêtre, signal original – « low frequency », fenêtres de 30, 8 et 2secondes – « intermediate frequency » et fenêtre de 0.3s – « high frequency »). De manière analogue à la spectroscopie d'impédance, l'utilisation de filtre numérique (variation de la taille des fenêtres) permet de dégager différentes signatures dans les différents domaines fréquentiels. Ainsi il est possible de faire un lien en les résutalts obtenus dans le domaine temporel (tableau 6.1) et les résultats obtenu dans le domaine fréquentiel (figure 6.1),ici pour le point de mesure à 85A au sein de la 2ème campagne.

La figure 6.2 résumé la signature spectrale très propre obtenu pour toutes les campagnes. L'analyse de la variation des pentes (α) et de f_{pick}, permet une quantification des signatures obtenues par l'analyse du bruit (fluctuations de tension).

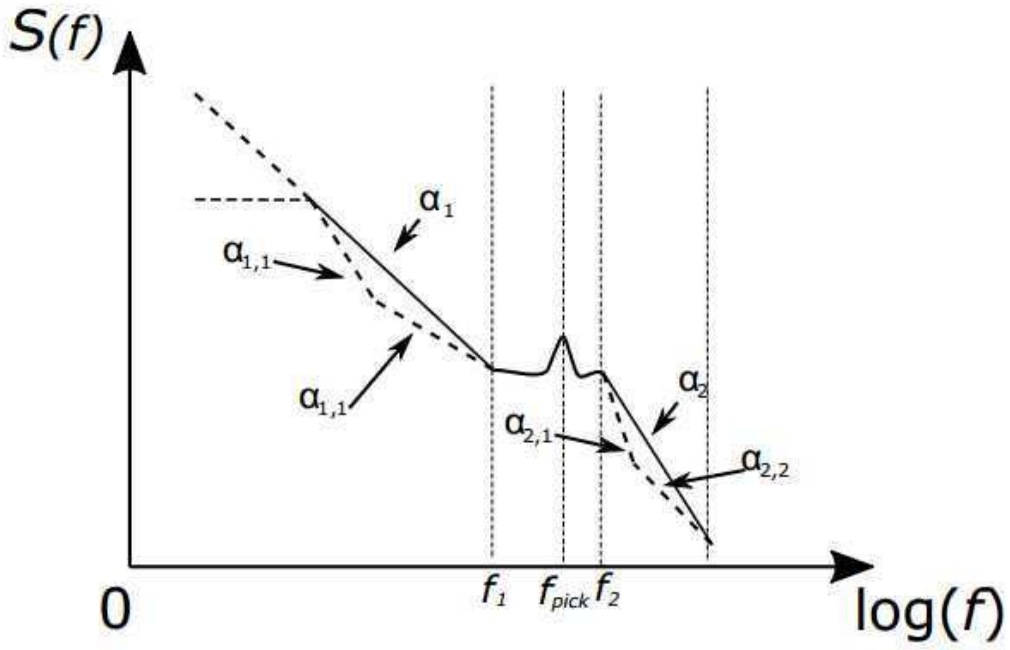

Figure 6.2 – Tendance typique des spectres obtenus

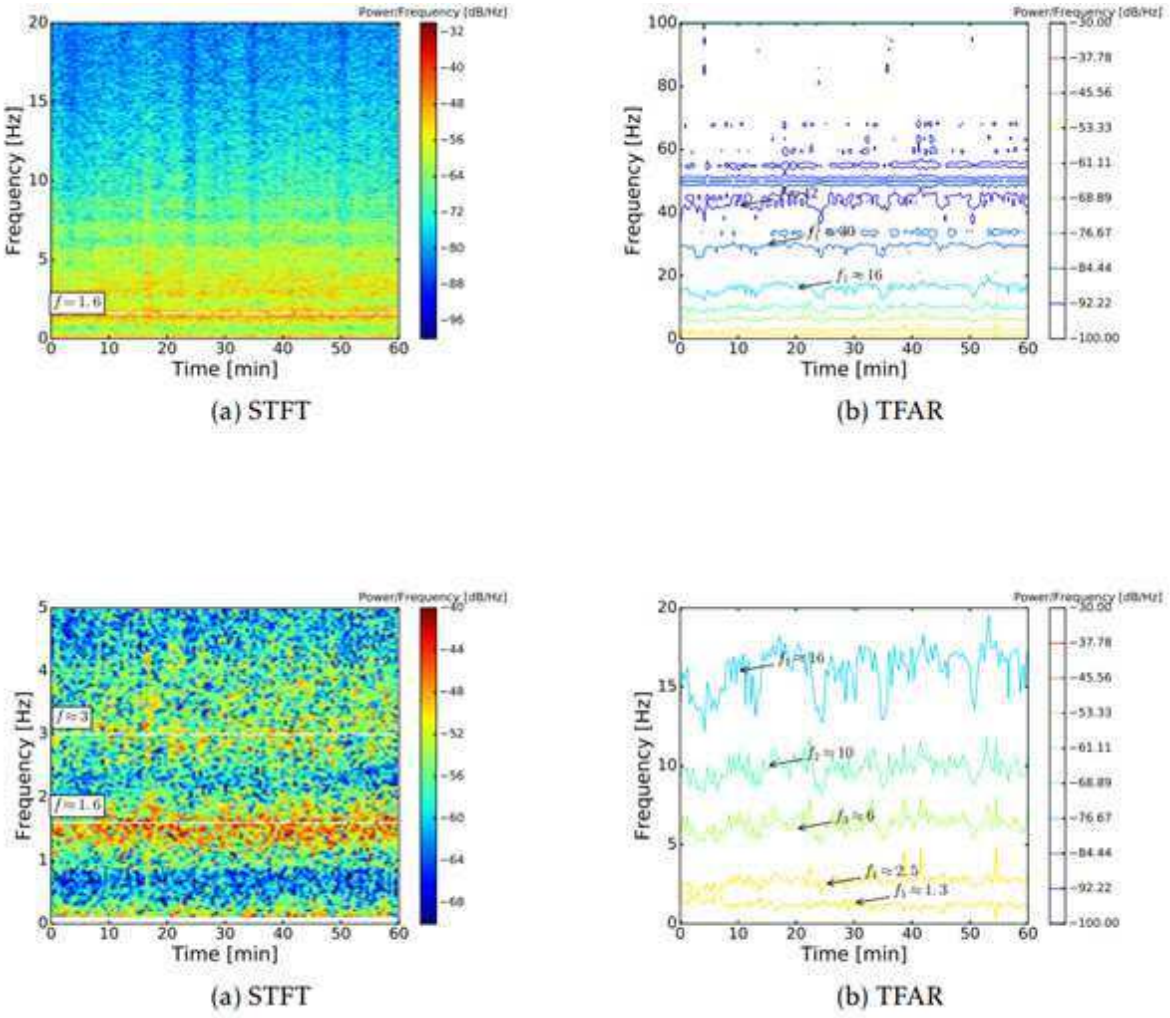

Figure 6.3 – Analyses temps –fréquences à 85 A - 2ème campagne

La figure 6.3 montrent la comparaison au point de fonctionnement à 85a pour la 2ème campagne pour les descripteurs du domaine tempo-fréquentiel. On observe des tensions caractéristiques notamment 1.6 Hz et ces sous harmoniques que l'on peut comparer à f_{pick} du spectre fréquentiel.

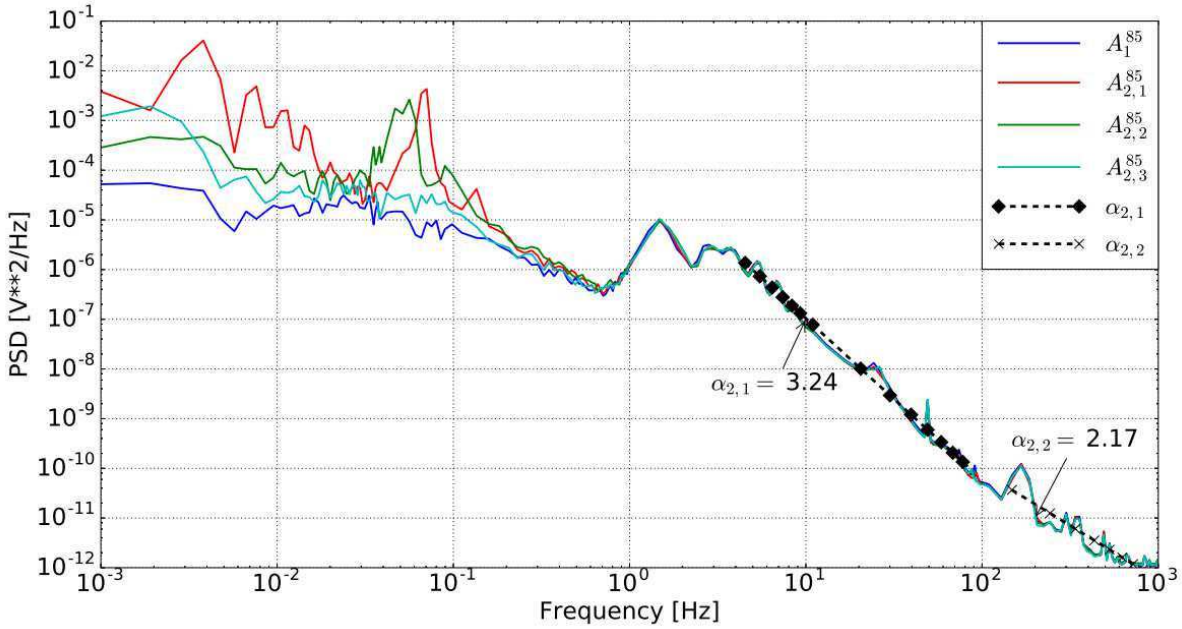

Figure 6.4 – Spectre de comparaison des zones – 1ère campagne

La figure 6.4 permet de mettre en lumière les différentes observées au sein d'une même campagne, ici 1ère campagne en les différentes zones au niveau de la basse fréquence (f<0.1 Hz) du spectre fréquentiel. On observe que notre signature spectrale est très robuste et que les variations en basse fréquences peuvent être corrélées au vieillissement du stack après plusieurs centaines d'heures.

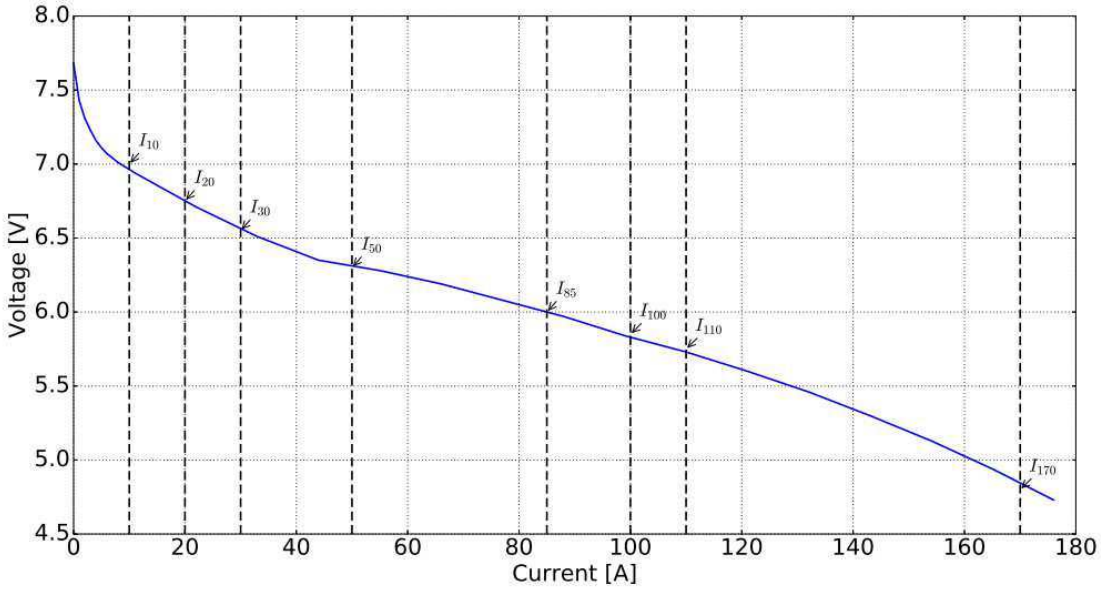

Figure 6.5 – Courbe de polarisation

La figure 6.5 présente la courbe de polarisation (performance électrique) obtenue pour les stacks PEMFC utilisés dans le projet « PROPICE » et dans cette thèse. La figure 6.6 montre l'évolution du f_{pick}, signature robuste de nos spectres, en fonction du courant. Cette fréquence peut tous à fait servir d'indicateur pour le diagnostic et son évolution en fonction du temps pour le pronostic des stack de pile à combustible.

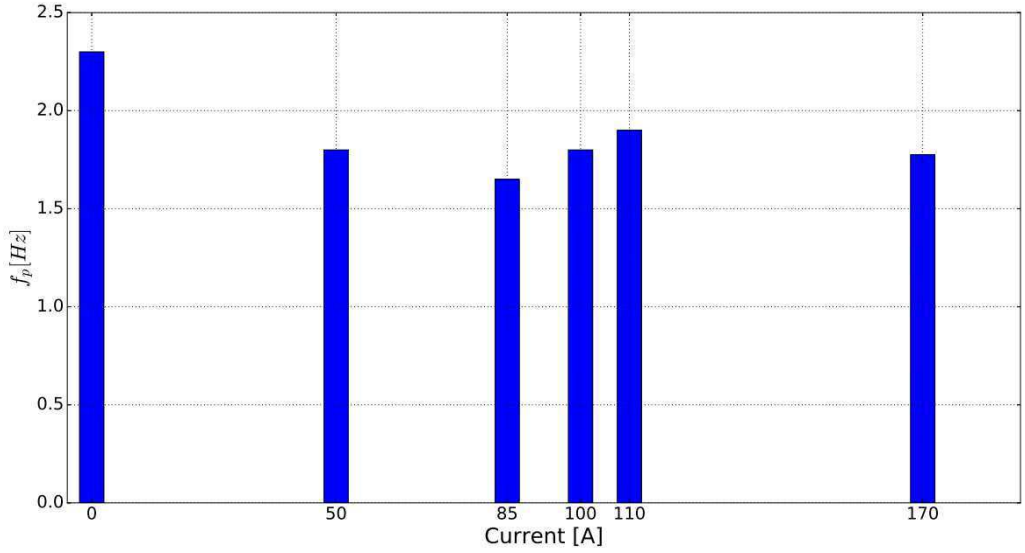

Figure 6.6 – Dépendance de la fréquence de pic avec le courant

La figure 6.7 présente un exemple de la variation l'intensité du bruit (écart-type) pour tous les campagnes de mesures. On peut observer que ce descripteur évolue fortement avec le courant et la taille des fenetres. Une plus petite taille de fenetre, c'est-à-dire à des fréquences plus grande permet d'obtenir une plus grande sensibilité à un courant donné (comparaison d'une même couleur).

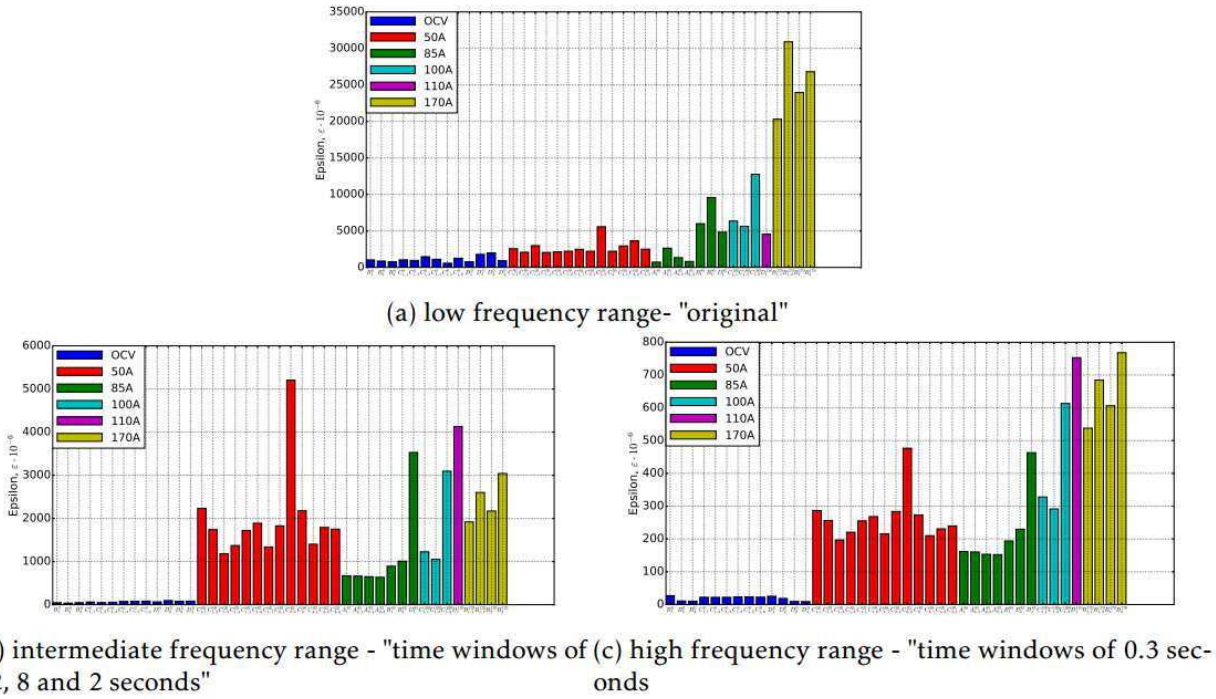

(a) low frequency range- "original"

(b) intermediate frequency range - "time windows of 32, 8 and 2 seconds"

(c) high frequency range - "time windows of 0.3 seconds

Figure 6.7 – Dépendance de l'intensité du bruit électrochimique pour toutes les campagnes de mesures

La figure 6.8 permet de mettre en lumière le caractère très différent du profil automobile (D) au profil de micro-cogénération (C). En effet, on observe que la signature spectrale de la campagne automobile présente de forte fluctuations entre 10^{-3} et 1 Hz.

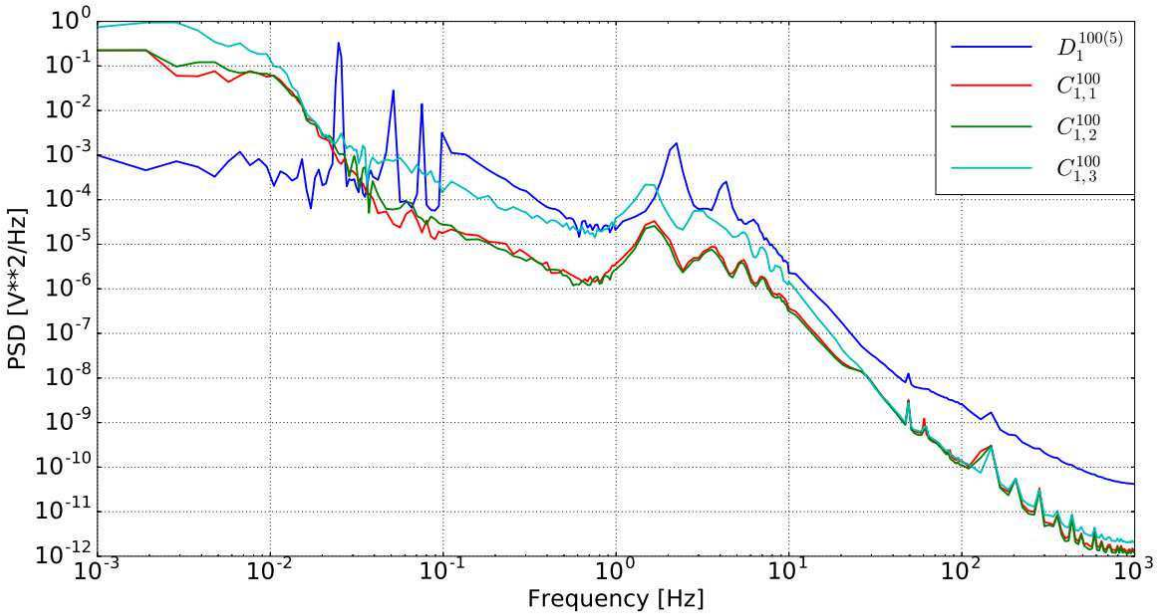

Figure 6.8 – Comparaison des spectres entre la 3ème et 4ème campagne

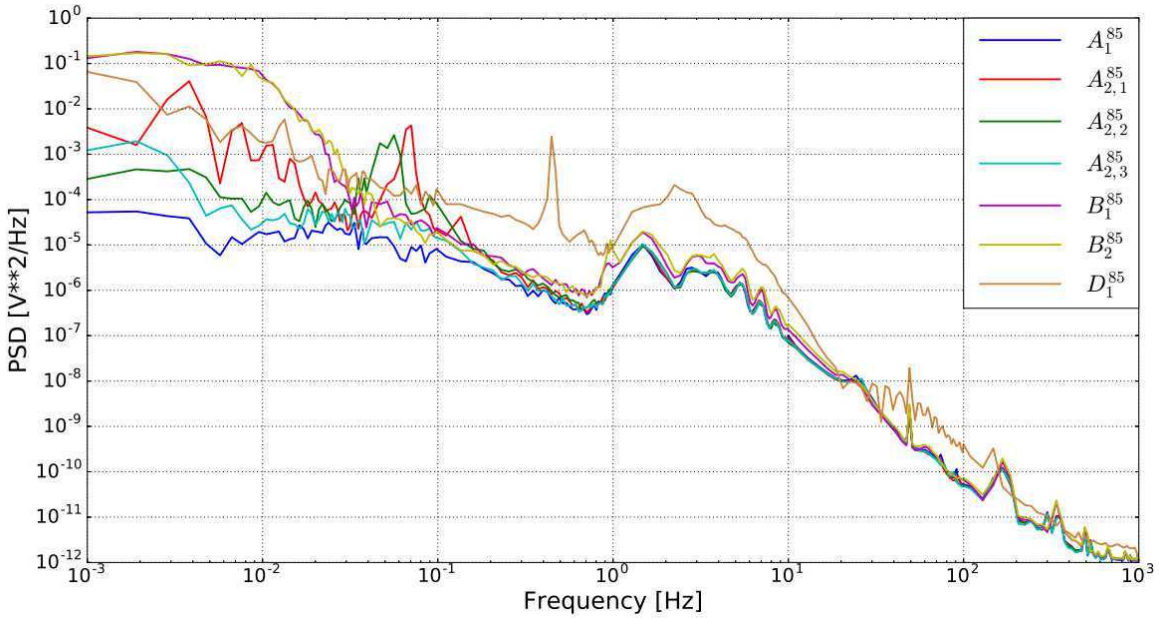

Figure 6.9 – Signature du bruit dans le domaine fréquentiel pour 3 différentes stacks

Fig. 6.9 présente la comparaison des signatures de bruit pour trois stacks (A, B et D) différents dans la même condition (courant de 85A). Comme nous l'avons discuté précédemment, la basse fréquence (f <0.5Hz) est sensible aux conditions de fonctionnement. D'autre part, pour les gammes de fréquence f > 0.5 Hz les conditions de fonctionnement n'influencent pas la signature sonore. Dans cette gamme de fréquences, la signature du bruit semble être liée principalement aux processus physico-chimiques internes la pile. Pour deux piles (première - A et deuxième campagne - B) les signatures de bruit à haute fréquence les signatures coïncident parfaitement, la reproductibilité est confirmée par les 6 réalisations. C'est un bon indicateur, que ces deux stacks n'ont aucune différence visible liée à leur fabrication. Au contraire, le stack automobile (réalisation D1 85) montre une différence nette de signature de bruit à haute fréquence. De plus, l'intensité du bruit pour cette pile dans la plage des hautes fréquences est plus importante. Dans notre opinion, ceci est un indicateur de certains défauts liés à la fabrication des piles.

Conclusions générales et perspectives

Dans la présente étude, le diagnostic du bruit électrochimique (END) a été utilisé pour la caractérisation de stack PEM de 600 W. L'avantage du diagnostic par les bruits est lié à la possibilité de fournir une caractérisation fine du système étudié dans une large gamme de fréquences sans perturbation de son fonctionnement. C'est une méthode expérimentale relativement nouvelle qui peut compléter ou remplacer, quand nécessaire, l'instrumentation traditionnelle comme la spectroscopie d'impédance électrochimique. Quelques articles concernant l'application de END pour la caractérisation des piles à combustible PEM simples peuvent être trouvé dans la littérature, néanmoins des informations concernant le bruit de diagnostic des stack de piles à combustible est manquant. Une autre originalité de la présente étude concerne l'utilisation de END pour la surveillance du stack pendant des campagnes longues (plisseurs milliers d'heures). Ces mesures de longue sont devenues possibles grâce au projet ANR français «PROPICE» axé sur le développement de méthodes et de instrumentation pour le pronostic des piles à combustible.

Le premier objectif de ce travail était le développement d'une instrumentation adaptée permettant l'enregistrement permanent avec de fluctuations de tension à fréquence d'échantillonnage élevée (bruit électrochimique) et le stockage simultané des données. Cette instrumentation a été développée et utilisée lors des 4 dernières campagnes expérimentales réalisées sur le site du laboratoire FC LAB (Belfort) dans le cadre du projet «PROPICE». L'instrumentation développée est basée sur une carte d'acquisition National Instruments DAQ et pour le stockage de données, un simple ordinateur portable est utilisé et Labview © et Python © sont utilisés comme logiciel de pilotage et traitement. Notre système de mesure permet l'enregistrement simultané et le stockage de données de 4 signaux avec fréquence d'échantillonnage jusqu'à 50 kHz. Dans le cadre des expériences fournies, nous avons utilisé un enregistrement de données sur un canal et un fréquence d'échantillonnage de 2 kHz pour un fonctionnement en pile permanent de 1000.

Un point important au niveau de l'instrumentation pour les mesures de bruit concerne la procédure de filtrage. Habituellement, les filtres analogiques sont utilisés à cette fin. Nous préférons enregistrer le signal directement sans aucun filtrage analogique. C'est un choix primordial permettant de créer une énorme base de données au cours d'une longue expérience physique et après d'utiliser différentes méthodes de traitement du signal pour obtenir l'information nécessaire. En d'autres termes, nous remplaçons le filtre analogique par des filtres

numériques. De cette façon il est possible de contrôler les perturbations liées à la procédure de filtrage pour prendre en compte toutes les caractéristiques particulières des signaux enregistrés.

Le deuxième objectif était le développement de la méthodologie permettant la génération de différents descripteurs statistiques pour des signaux stochastiques enregistrés. Nous avons attaché une attention particulière à la suppresion de la composante continue (« detrending ») du signal et à son filtrage. La signature du bruit de la pile a été obtenu dans une large gamme de fréquences 0.001Hz <f <1KHz. Les descripteurs statistiques ont été obtenus en temps (moments), en fréquence (PSD) et dans le domaine temps-fréquence (STFT, TFAR, ondelettes). L'interprétation croisée de la signature de bruit dans différents domaines permet d'améliorer la compréhension des différents phénomènes liés au fonctionnement de la pile.

L'instrumentation développée et les procédures pour la génération de descripteurs statistiques ont été utilisé pour étudier le comportement de la pile au cours des campagnes expérimentales de longue durée jusqu'à 1000 h. Trois campagnes expérimentales concernent le fonctionnement de la pile sous un courant constant (profil de cogénération) et le dernier concerne le profil de l'automobile (cycle de courant entre deux niveaux). Nous avons montré que pour toutes les campagnes expérimentales, il est possible d'obtenir des signatures de bruit reproductible. Cette signature, sous forme de pente – flicker noise, de bruit inclut la basse fréquence (f <0.1 Hz) et à haute fréquence (f> 10 Hz) et plage de fréquence intermédiaire (0.1 < f <10 Hz) où une fréquence dominante stable fpick est clairement présentée.

La variation des pentes, des valeurs de fréquence dominante, des moments (intensité, asymétrie, kurtosis) pour différentes gammes de fréquences ainsi que des images de bruit spatio-temporel (STFT, TFAR, ondelettes) ont été calculés pour toutes les conditions opérationnelles. Nous avons démontré que le bruit de à basse fréquence est plutôt sensible aux conditions opérationnelles (processus transitoires après l'arrêt de la pile, perturbations à basse fréquence dues aux problèmes de régulation de pression ou de cyclage de charge). D'autre part, la fréquence dominante fpick et le composant flicker-noise à haute fréquence sont ne sont pas influencés par les perturbations à basse fréquence et reflètent les processus internes de la pile à combustible. L'intensité du bruit sous le profil de l'automobile dans la gamme de haute fréquence est plus importante en comparaison au profil de cogénération le montre. Nous notons également une différence dans les valeurs de fréquence dominante : fpick = 1.75 Hz pour le profil de cogénération et fpick = 1.9 Hz pour le profil automobile.

Il a été montré que le composant du flicker-noise à haute fréquence sous le profil de cogénération est stable et est déterminée par le courant de la pile. La dépendance de ces descripteurs de bruit sur le courant du stack a été obtenue. Nous avons montré que l'énergie du bruit est proportionnelle au carré du courant.

La signature de bruit en mode OCV est très différente de celle enregistrée pour la cogénération et les profils automobiles. Le caractère qualitatif du bruit OCV est le même : basse fréquence (f <0.1Hz) et haute fréquence (f> 10Hz) flicker-noise et la gamme de fréquence intermédiaire présente une fréquence dominante fpick. Néanmoins, l'intensité du bruit en mode OCV est beaucoup plus petite et le caractère du bruit est très différent de celui enregistré pour le courant. Cette conclusion est soutenue par les calculs des moments (intensité, asymétrie, kurtosis) pour différentes gammes de fréquences.

Ainsi, pour la première fois, une signature du bruit stable et bien reproductible d'un stack de pile PEMFC a été obtenu et interprété pour la cogénération et le mode automobile sous différents courants et pour l'OCV. Les signatures de bruit obtenues peuvent être utilisées pour étudier le vieillissement de la pile, la détection de possibles défauts et comprendre les processus physiques dans ce système électrochimique. Nous avons obtenu des résultats préliminaires qui démontrent la faisabilité des diagnostics de bruit pour la détection de défauts possibles liés à la fabrication de la pile. En effet, la comparaison des signatures de bruit de trois différents stacks fonctionnant sous le même courant constant a montré que deux piles démontrent la même signature de bruit très stable et reproductible dans la gamme de hautes fréquences. La signature du troisième stack dans les mêmes conditions opérationnelles est différente et plus bruyante. Il semble être un indicateur d'un défaut possibles liés à la fabrication du stack.

Les perspectives à court terme de la présente étude portent sur :

• la possibilité d'utiliser la base de données créée pour une analyse plus détaillée ; en particulier pour l'étude de vieillissement du stack sous profil automobile et le comportement du stack dans des modes non conventionnels d'opération,

• l'instrumentation développée et la méthodologie peuvent être directement appliquées pour l'enregistrement de signatures par le bruit de différents systèmes électrochimiques (piles à combustible, électrolyseurs, supercapacités, batteries),

• la signature du bruit peut être détectée simultanément par quatre canaux, il est donc possible d'assurer la surveillance du bruit de différentes cellules dans un empilement et / ou de différents capteurs (tension / température, pression, ...).

Les perspectives à long terme concernent :

• l'application du diagnostic en ligne du bruit pour les études de vieillissement,

• l'application d'un diagnostic de bruit pour la détection de défauts éventuels lors de la fabrication de la pile,

• application du diagnostic de bruit pour la compréhension des processus physico-chimiques dans les sources d'énergie électrochimiques.